europhysics
conference
abstracts

15th European Conference on

Controlled Fusion and Plasma Heating

Dubrovnik, May 16—20, 1988

Editors: S. Pešić, J. Jacquinot

Contributed Papers
Part III

Published by: European Physical Society

Editor: Dr. J. Heijn, Petten

ging Editor: G. Thomas, Geneva

VOLUME 12B Part III

XV
FUSION
DUBROVNIK
1988

15th European Conference on

Controlled Fusion and Plasma Heating

Dubrovnik, May 16—20, 1988

Editors: S. Pešić, J. Jacquinot

Contributed Papers
Part III

E F G H I J

EUROPHYSICS CONFERENCE ABSTRACTS is published by the
European Physical Society, © 1988

Preface

The 15th European Conference on Controlled Fusion and Plasma Heating was organized by the Boris Kidrič Institute of Nuclear Sciences, Belgrade, Yugoslavia, on behalf of the Plasma Physics Division of the European Physical Society (EPS). It was held in Cavtat, near Dubrovnik, from 16 to 22 May 1988.

The 15th Conference concentrates on experimental and theoretical aspects of Plasma Confinement and Plasma Heating. The programme, format and schedule of the meeting was determined by the International Programme Committee, which was appointed by the Plasma Physics Division Board of the EPS. The Programme Committee selected 19 invited and 24 oral contributed papers.

This volume contains all accepted contributed papers received in due time by the Organizers. It is published in the Europhysics Conference Abstracts Series and it follows the rules for publication of the EPS. The 4–page extended abstracts were reproduced photographically using the camera ready manuscripts submitted by the authors who are therefore responsible for the quality of the presentation. Post-deadline papers are not included in this volume.

All invited papers will be published in a special issue of the journal "Plasma Physics and Controlled Fusion". This journal may also publish rapidly an extended version of contributed papers, following an accelerated refereeing procedure.

The Organizers would like to acknowledge the support of the Serbian Science Research Council and the technical assistance of the Publishing Department of the Boris Kidrič Institute of Nuclear Sciences. The Conference has been organized under the general sponsorship of the Union of Yugoslav Societies of Mathematicians, Physicists and Astronomers, member of EPS.

April 1988 The Editors

International Programme Committee

J. Jacquinot (Chairman), JET, Abingdon, United Kingdom
S. Pešić (Vice–Chairman), IBK, Belgrade, Yugoslavia
K. Appert, CRPP, Lausanne, Switzerland
H. Bodin, Culham Lab., Abingdon, United Kingdom
G. Briffod, CENG, Grenoble, France
F. Engelmann, NET, Garching, F. R. Germany
L. Kovrizhnykh, GPI, Moscow, USSR
K. Lackner, IPP, Garching, F. R. Germany
E. Sindoni, University of Milan, Milan, Italy
M. M. Škorić, IBK, Belgrade, Yugoslavia

Organizing Committee

M. M. Škorić (Chairman), IBK, Belgrade
S. Pešić, IBK, Belgrade
Đ. Jović, IBK, Belgrade
Đ. Miljanić, IBK, Belgrade
Lj. Hadžievski, IBK, Belgrade
S. Pavićević, Yugotours, Belgrade

Contents

Paper Identification

Each paper is identified with a 6 character code printed on the top right corner of the first page. The code *u v wx yz* has the following structure:

- *u* – type of contribution; *u* = I, O, P for invited paper, oral and poster contributed paper
- *v* – the day of event; *v* = 0, 1, 2,...,9 for Monday morning, Monday afternoon, Tuesday morning,..., to Friday afternoon
- *wx* – the topic and subtopic of the contribution
- *yz* – the poster board number: *yz* = 01, 02,...,99

Note that the authors of oral contributed papers are given the possibility to post their contributions. Therefore, the data in the code refer to the corresponding poster presentation.

Example

P 8 E2 47

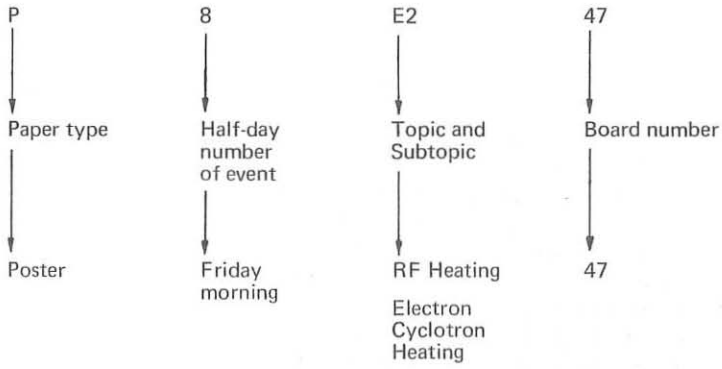

Title List of Contributed Papers

A. TOKAMAKS

E1. Experiments

A2. H Mode

A3. Theory

B. STELLARATORS

C2. Other Alternative Magnetic Confinement Schemes

D. PLASMA EDGE PHYSICS

E. RF HEATING

E1. Ion Cyclotron Heating

E2. Electron Cyclotron Heating

E3. Lower Hybrid Heating

E4. Alfven Wave and Other RF Heating Methods

F. CURRENT DRIVE AND PROFILE CONTROL

F1. Lower Hybrid Current Drive

F2. Other Profile Control Methods

G. NEUTRAL BEAM INJECTION HEATING

H. DIAGNOSTICS

J. INERTIAL CONFINEMENT PHYSICS

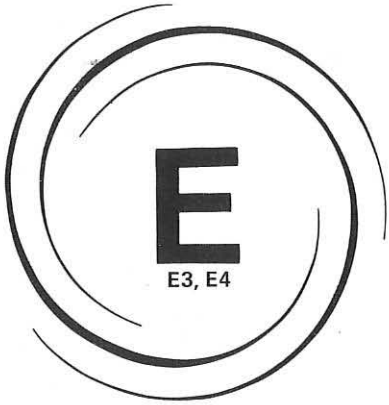

RF Heating

LH POWER ABSORPTION AND ENERGY CONFINEMENT DURING COMBINED LOWER HYBRID AND NBI HEATING ON JT-60

F.X. Söldner[1], K. Ushigusa, T. Imai, Y. Ikeda, K. Sakamoto, Y. Takase[2] and JT-60 Team

Japan Atomic Energy Research Institute
Naka-machi, Naka-gun, Ibaraki-ken, Japan

ABSTRACT

Combined heating with Lower Hybrid waves and neutral beams was studied on JT-60 with total powers up to 30 MW. The same incremental energy confinement time is found in combined operation as for both heating methods individually. LH heating is most efficient in the density range $\bar{n}_e = 2\text{-}3\times10^{13}\,cm^{-3}$. Degradation of the LH heating rate at higher density may be attributed to poor penetration of waves with low $N_{\parallel}$ into the central region according to the accessibility condition. The LH-generated suprathermal electron population diminishes with simultaneous NBI. Fast ion tails with energies up to twice the beam injection energy are formed by absorption of LH waves on the beam ions.

HEATING REGIME

The divertor tokamak JT-60 (R_o = 3.1 m, a = 0.9 m, $I_p \leq 3.2$ MA, $B_t \leq 4.8$ T) is equipped with high power additional heating systems /1/. NBI (E_o = 75 keV, P ≤ 20 MW) had been combined with LH current drive at low density previously /2/. Improved current drive efficiency and an improvement in the energy confinement were obtained in this operation. The latter is related to a modification of the current profile by LHCD /3/. In this paper the extension of combined application of LH and NBI to higher densities will be discussed. The current drive effects are reduced in this regime due to the $1/\bar{n}_e$-dependence of η_{LHCD} and heating dominates. In all these experiments LH waves are launched from three different grill antennae with wave spectra at low $N_{\parallel}$ ($\bar{N}_{\parallel}$= 1.7/1.8, f_o = 2 GHz). Most discharges are performed in divertor configuration where the plasma density can be better controlled.

The heating efficiency is given by the incremental energy confinement time $\tau_E^{inc} = \Delta W_p/\Delta P$, where ΔW_p is the change in plasma stored energy upon change in the total input power ΔP. In Fig. 1, τ_E^{inc} versus injected LH-power is shown for LH-heating of both Ohmic and NBI-heated target plasmas in the density range $\bar{n}_e = 2\text{-}3\times10^{13}\,cm^{-3}$. In the case of LH heating into OH plasmas, τ_E^{inc} was determined in two ways: from flat-top pulses and from slow LH-power ramps (the power range is denoted by the solid lines in Fig. 2). With ramps, the incremental energy confinement time can be determined within only one discharge from: $\tau_E^{inc} = \dfrac{\Delta W_p/\Delta t}{\Delta P/\Delta t}$. Flat-top and ramp values agree well. The energy content W_p is taken from diamagnetic measurements. They are in good agreement with kinetic data. No systematic difference in

1 on leave from Max-Planck-Institut für Plasmaphysik, Garching, FRG
2 on leave from Plasma Fusion Center, MIT, USA

τ_E^{inc} is seen for Ohmic and beam heated target plasmas. The slightly higher values for τ_E^{inc} at low power are probably due to the change of confinement scaling from OH- to L-Mode scaling in this range. The same heating efficiency is obtained for LH+NBI as for NBI alone at high power, with $\tau_E^{inc} \approx 50$ ms. Therefore the heating is additive. The energy confinement times are the same for NBI and NBI+LH and no synergetic effects on confinement are seen in the range of medium densities ($\bar{n}_e \leq 4\times10^{13}cm^{-3}$).

The LH-heating efficiency depends strongly on density. This is shown in Fig. 2 where LH is switched on during NBI, still within the rise time of $\bar{n}_e$ and W_p^* from NBI. The density increases from ~$2\times10^{13}cm^{-3}$ to ~$5\times10^{13}cm^{-3}$ during the LH-pulse. After start of the rf, the stored energy rises with a steeper slope. At a density of $\bar{n}_e \approx 4.5\times10^{13}cm^{-3}$, the heating from LH saturates and at $\bar{n}_e \approx 4.5\times10^{13}cm^{-3}$, W_p^* is nearly back at the level of NBI alone. The density dependence of LH heating in combination with NBI is summarized in Fig. 3. The incremental confinement time due to additional LH heating, $\tau_{E,LH}^{inc} = (\Delta W/\Delta P)_{LH}$ is plotted versus $\bar{n}_e$ for a large range of plasma conditions. The strong decrease with increasing density can be explained with degrading LH power penetration into the central plasma region due to the accessibility limitation. The experimental points for $\tau_{E,LH}^{inc}(\bar{n}_e)$ are well fitted with a curve giving the fraction of accessible power inside half radius /4/. The same result was obtained also from power balance calculations for LH heating on ASDEX /5/.

HEATING MECHANISM

Suprathermal electrons are generated by LH waves at low density as seen from the strong increase of hard X-ray radiation and suprathermal ECE. Landau damping on these fast electrons determines the absorption of LH waves in the plasma. With simultaneous NBI the intensity of hard X-ray radiation and also of the suprathermal ECE is reduced for densities above $\bar{n}_e \approx 1.5\times10^{13}cm^{-3}$. For the hard X-ray radiation this is shown in Fig. 4. There the results of two experimental periods and different working gases are summarized. Though the absolute levels of the signals vary due to different wall materials employed, the characteristic density dependence remains the same.

In the same range of densities high energy ion tails extending far above the beam injection energy are formed if LH is combined with NBI. This acceleration of beam ions by LH-waves is shown in Fig. 5 in the charge exchange spectrum of a neutral particle analyzer viewing the plasma periphery on a perpendicular line of sight. In the combination of LH+NBI therefore the generation of suprathermal electrons is reduced on the expense of power absorption by fast ions. Single pass ray tracing calculations show that for the experimental conditions, $N_\perp$ can become sufficiently high so that resonant absorption of LH wave power on beam ions can occur.

A possibility to prevent such interaction of the LH waves with the ions might be top or bottom launching where the waves could propagate to the central region with smaller $N_\perp$ values due to reduced toroidal effects. On the other hand, the formation of a suprathermal ion distribution with combined LH+NBI operation might offer an attractive way to increase considerably the fusion yield.

ACKNOWLEDGEMENTS

The authors wish to thank the members of JAERI who have contributed to the JT-60 project. They also wish to express their gratitude to Drs. S. Mori, K. Tomabechi and M. Yoshikawa for their continuous encouragement and support. One of the authors (F.X. S.) would like to express his gratitude to Dr. M. Yoshikawa for his support in arranging a stay on JT-60 and he would like to thank all members of the JT-60 team for their help and hospitality.

REFERENCES

/1/ Yoshikawa M. et al., Proc. 11th Conf. on Plasma Phys. and Contr. Nucl. Fusion Research, IAEA-CN-47/A-I-1, Kyoto (1986).
/2/ Imai, T. et al., ibid, IAEA-CN-47/K-I-2, Kyoto (1986).
/3/ Yoshino, R. et al., Plasma Physics and Controlled Fusion 29, 1377 (1987)
/4/ Ushigusa, K. et al., to be published.
/5/ Söldner, F. et al., 12th Europ. Conf. on Contr. Fusion and Plasma Physics, Budapest 1985, Vol. II, p.244.

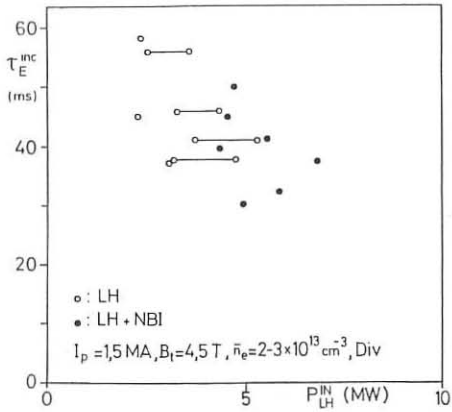

Fig. 1: Incremental energy confinement time τ_E^{inc} versus P_{LH} for Ohmic (o) and beam heated (o) target plasmas $P_{NBI} \leq 20$ MW. Solid lines between open circles denote the range of power ramps where $\tau_E^{inc} = W_p/P_{LH}$.

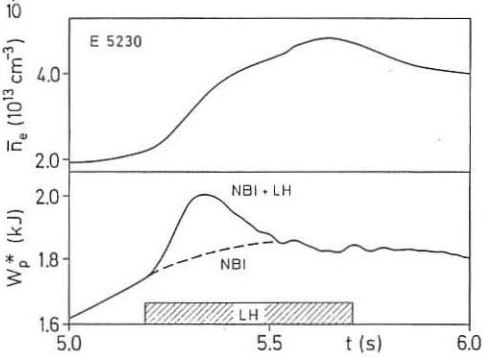

Fig. 2: Temporal evolution of $\bar{n}_e$ and W_p^* with LH (P=6MW) + NBI (P=18MW). NBI: 4.5 - 6.6 s, I_p = 4.5 T.

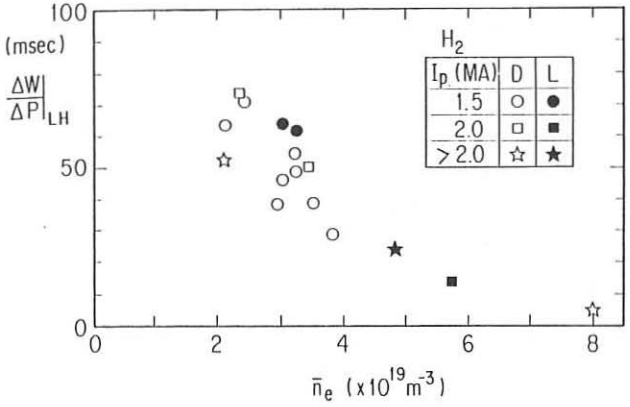

Fig. 3: Incremental energy confinement time $\tau_{E,LH}^{inc} = (\Delta W/\Delta P)_{LH}$ versus $\bar{n}_e$ for LH-heating into NBI-heated target plasmas.

Fig. 4: Hard X-ray intensity (E > 260 keV) versus $\bar{n}_e$ for LH injection into Ohmic and NBI heated target plasmas.

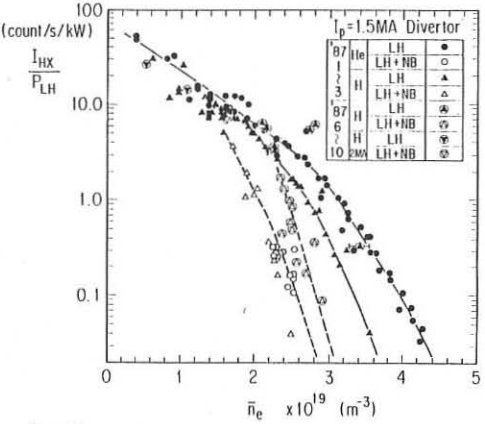

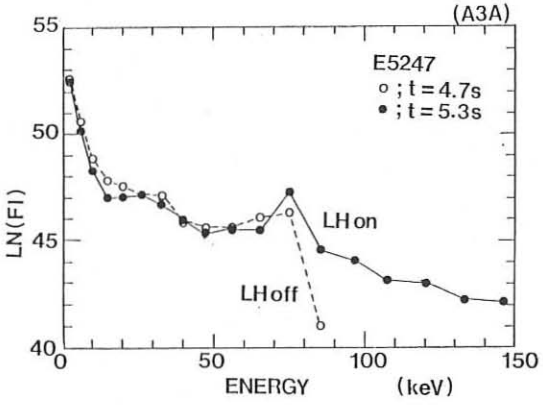

Fig. 5: Charge exchange spectra during NBI+LH and NBI alone from a charge exchange analyzer on a perpendicular line of sight through the plasma periphery.

LOWER HYBRID EXPERIMENTS AT 8 GHz IN FT

F. Alladio, E. Barbato, G. Bardotti, R. Bartiromo, G. Bracco, F. Bombarda, G. Buceti, P. Buratti, E. Caiaffa, A. Cardinali, R. Cesario, F. Crisanti, R. De Angelis, F. De Marco, M. De Pretis, D. Frigione, L. Gabellieri, R. Giannella, M. Grolli, S. Mancuso, M. Marinucci, G. Mazzitelli, F. Orsitto, L. Panaccione, V. Pericoli-Ridolfini, L. Pieroni, S. Podda, G.B. Righetti, F. Romanelli, D. Santi, F. Santini, S.E. Segre G. Tonini, A.A. Tuccillo, O. Tudisco, G. Vlad, V. Zanza*

Associazione EURATOM-ENEA sulla Fusione, Centro Ricerche Energia Frascati,
C.P. 65 - 00044 - Frascati, Rome, Italy

INTRODUCTION

Lower Hybrid heating in FT Tokamak was extensively applied and studied in the last few years at frequency of 2.45 GHz and RF power ≤ 450 kW [1,2]. Good heating results and sawtooth activity control were obtained [3] without a significant impurity enhancement up to a density of 5×10^{13} cm^{-3}. In order to work at much higher densities a new Lower Hybrid system with a frequency of 8 GHz has been installed on FT. The possibility of this heating method is tested and studied in view of the FTU machine where 8 MW of RF power at 8 GHz will be injected.

Four Varian VKX-7879A tubes, with f = 8 GHz, 125 kW each, have been installed directly in the torus hall to minimize losses in the transmission lines. These consist of a few meters of standard guide WR137. Each klystron feeds a column of a 4×4 grill through a compact 1:4 power divider. As with previous 2.45 GHz grills, each waveguide has its own ceramic window brazed at ~ 15 cm from the mouth, the inner dimensions being 5×35 mm. The whole structure can move radially 3 cm to optimize the coupling. The 4-waveguide excitations were mainly phased as 00ππ and 0π0π. The relative spectra are shown in Fig. 1. Preliminary results were reported in Ref. [4,5].

Due to the loss in the transmission and to the system dimensions and performance, the results reported hereafter were obtained up to a maximum RF power coupled to the plasma of 220 kW.

TRANSMISSION AND COUPLING

Due to the narrow size of the waveguides it is impossible to insert any system of guide conditioning. Thus, the only remaining way to condition the grill is to send the RF into the plasma. The system was able to transmit a power density of about 10

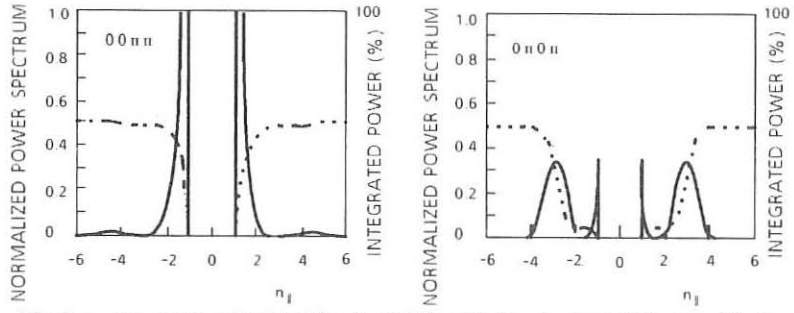

Fig. 1 - $n_\parallel$-spectrum calculated for the 8 GHz grill for phasing at 00ππ and 0π0π

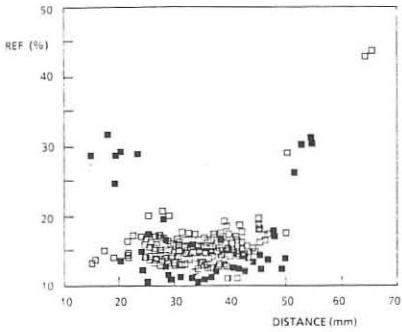

Fig. 2: Net reflection coefficient vs the distance between plasma and grill mouth, full dots for phasing 00ππ

kW/cm^2 without any particular care. At higher power levels some spikes on the reflected power signals appear, triggering the switch off of the system which automatically resets after ~ 5 ms. Generally a few RF long pulses (~ 500 ms) at a slightly lower power are sufficient to avoid the tripping of the system at the next power step, and so on. This behaviour indicates the need for grill conditioning, at least at higher power density.

We have checked the coupling properties of the 8 GHz LH radiofrequency over a wide range of plasma parameters for the two phasings 00ππ and 0π0π. As shown in Fig. 2 reflection values about of 15% are obtained for all the plasma conditions for appropriate values of the antenna to plasma edge distance.

In the best coupling conditions, Langmuir probes measurements indicate a boundary density at the grill mouth, ranging from 0.2-1×10^{13} cm^{-3} quite in agreement with the theoretical expectation [6] $n_b/n_{cutoff} \geq n^2_{\parallel}$, where n_b is the density in front of the grill mouth. The maximum power density injected into the plasma has been 10 kW/cm^2, while the average power density at the grill mouth has been 8.6 kW/cm^2. This is due to a problem on the first column of the grill. As a consequence the power distribution was not perfectly balanced on all the four columns and was limited for safe and routine operations to a level of 220 kW coupled to the plasma.

EXPERIMENTAL RESULTS

The RF power was launched in FT with the two spectra of Fig. 1 corresponding to a slower wave speed (by phasing 0π0π) and to a faster one (00ππ). The plasma parameters were B_T = 6-8 T, Ip = 300-500 kA, $\bar{n}$ = 0.4-3.5×10^{14} cm^{-3}.

The total fraction of the coupled RF power over the ohmic power did not exceed 0.40. Clear effects due to RF were observed on electrical conductance, σ, and on the ECE signals up to $\bar{n}$ = 3.5×10^{14} cm^{-3}. No fast neutral tails were detected. The enhancements during the RF pulse of the conductance σ and ECE signals were increasing with RF power as reported in Fig. 3 for $\bar{n}_e$ = 1.2×10^{14} cm^{-3}.

In Fig. 4 we report the increase of ECE normalized to the fraction of the RF to the OH power and in Fig. 5 the conductance enhancement, Δσ, (also normalized) vs the plasma density. The ECE singal continuously decreases as the density increases while the normalized Δσ, after an initial decrease, becames roughly constant with density.

Two processes can be effective in explaining these results. As density increases, collisionality reduces the tail of the electron distribution function. Another effect related to the reduction of suprathermal tails at high densities, is due to the dc electric field. This cannot freely accelerate electrons with $V_{\parallel} \leq V_{cr} \equiv$ the Dreicer critical velocity. The marginal condition for resonating electrons $V_{cr} = V_{\parallel} = c/n_{\parallel min}$, where $n_{\parallel min}$ is found by the accessibility in the spectrum of Fig. 1, yields a value for density $\bar{n}_e \simeq 8\times10^{13}$ cm^{-3}. This seems to correspond to the different behavior of Δσ in Fig. 5.

Therefore, we can assume with a wide margin of confidence that suprathermal contributions to Δσ and Δl_ω are negligible above n = 1×10^{14} cm^{-3}. The effects at high density can be explained by an increase of the average temperature of about 20 eV.

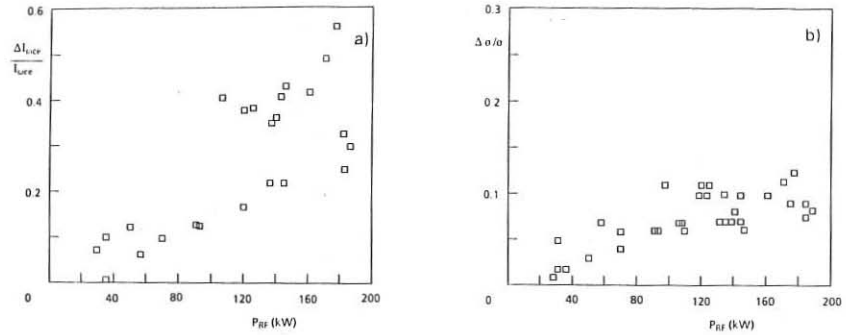

Fig. 3: Relative variations of ECE signals a) and of the electrical conductance σ b) with RF power for $\bar{n}_e \simeq 1.2 \times 10^{14}$ cm^{-3}, B_T = 6 and 8 T

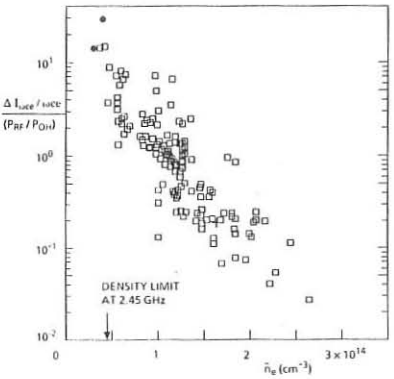

Fig. 4: Relative variation for the ECE signal normalized with coupled P_{RF}/P_{OH} vs $\bar{n}_e$ for discharges with P_{RF} >100 kW and B_T = 6 and 8 T (full dots refer to 2.45 GHz results)

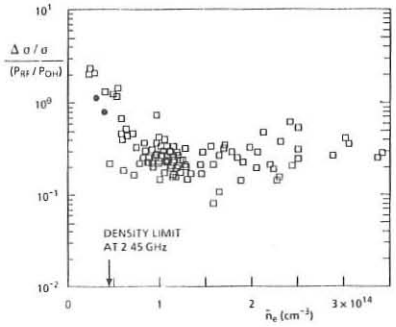

Fig. 5: Relative variation of the conductiance σ normalized with coupled P_{RF}/P_{OH} vs $\bar{n}_e$ for discharges with P_{RF} >100 kW and BT = 6 and 8 T(full dots refer to 2.45 GHz results)

This is of the same order, but somewhat lower, than what is expected with simple power balance. It may be connected to a wide radial deposition of RF power since at high densities only the slower excitation (0Π0Π) was used.

Finally, the frequency spectrum of the signal collected by an external RF probe shows for some discharges a wide broadening of the pump, as seen in Fig. 6. In a few other cases secondary peaks appear also [5]. These effects are evident only in discharges at relatively high density but with low current (I_p < 400 kA) and low temperature. In these discharges where secondary peaks or pump broadening alone are present, the observed values of Δσ (and of ECE enhancement at lower densities) are much below the typical values shown in Figs 4,5. For high current discharges (I_p > 500 kA, B_T = 8 T) where temperature due to ohmic power is higher, it is possible to avoid secondary peaks and to reduce pump broadening (up to the present working limit of 3.5×10^{14} cm^{-3}) by adjusting the plasma horizontal position [7].

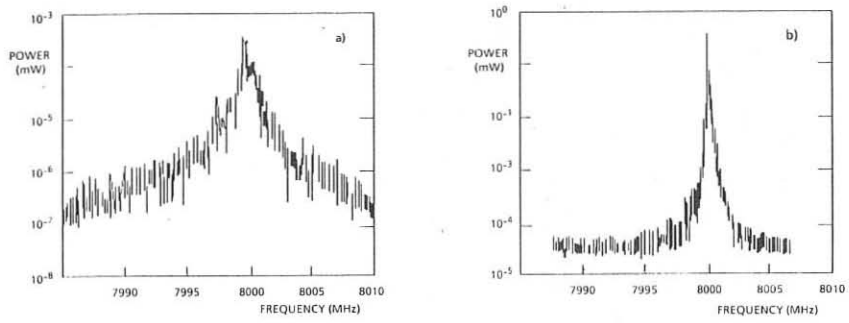

Fig. 6: Frequency spectra measured by RF probe a) with and b) without large broadening

CONCLUSIONS

Experiments with a new Lower Hybrid system at 8 GHz have been carried out in FT up to a coupled power of 220 kW. The analysis of the results indicates the following main points:

- In FT at 8 GHz, a very high power density up to 10 kW/cm^2 was injected routinely. This figure perhaps is not a limit since it might be increased by better and longer conditioning.
- The density limit for wave-electron interaction (electron mode responsible for heating and current drive in many experiments) is known to increase with frequency [8,9]. FT results at 8 GHz indicate this density limit is higher than 3.5×10^{14} cm^{-3}.
- As observed in FT at 2.45 GHz, secondary peaks and pump broadening may be avoided by increasing the plasma current [1]. Also at 8 GHz, similar behavior is observed even at the maximum density of 3.5×10^{14} cm^{-3}. By comparison with the 2.45 GHz experiments with the same target plasma, the density threshold for parametric decay instability appears to increase with frequency.

FOOTNOTE AND REFERENCES

* Permanent address: Dipartimento di Fisica, Univeristà Roma I, Roma, Italy

[1] F. Alladio et al., *Proc. 4th Int. Symp. on Heating in Toroidal Plasmas*, Roma, 21-28/3/84. Vol. I, p. 546 (1984)

[2] F. Alladio et. al., *Proc. 12th Europ. Conf. on Controlled Fusion and Plasma Phys.*, Budapest, 2-6/9/85, Vol. Ia, p. 179 (1986)

[3] F. Alladio et al., *Proc. 12th Europ. Conf. on Controlled Fusion and Plasma Phys.*, Schliersee, 14-18/4/86, Vol. 10c, part. III, p. 327 (1987)

[4] F. Alladio et al., *Proc. of 7th Topical Conf. on Applications of RF power to Plasmas*, Kissimmee, 4-6/5/87

[5] F. Alladio et al., *Proc. of 7th Topical Conf. on Applications of RF power to Plasmas*, Kissimmee, 4-6/5/87

[6] F. Santini, *Course and Workshop on Applications of RF Waves to Tokamak Plasmas*, Varenna, 5-14/9/85, Vol. I, p. 251

[7] R. Cesario, R. McWilliams, V. Pericoli-Ridolfini, *Interaction of the Lower Hybrid Pump Wave with FT Edge Plasma* (this conference).

[8] F. Alladio et al., Nucl. Fusion, **24**, 725 (1984)

[9] T.G.Wegrowe, G. Tonon, *Proc. 5th Topic Conf. on RF Heating*, Madison, Winsconsin, 1983

LOWER HYBRID PARAMETRIC INSTABILITIES IN THE FT PLASMA

*A. Cardinali, R. Cesario, F. Paoletti**

Associazione EURATOM-ENEA sulla Fusione, Centro Ricerche Energia Frascati
C.P. 65, 0044 Frascati, Rome, Italy

1 INTRODUCTION

In the heating and current drive experiments in tokamaks with rf power near the lower-hybrid frequency a typical activity of the probe rf signals is observed when the plasma density reaches values high enough [1].

We are interested to search for the role of the parametric instabilities in producing the observed spectra. Occurring mainly in the colder and outer regions of the plasma, this phenomenon can modify the characteristics of the launched waves and prevent the propagation towards the plasma centre.

In this paper we present the results of the study of the parametric instabilities obtained by solving numerically the complete parametric dispersion relation, taking under consideration a wide range of frequencies where different channels of instabilities could be involved.

2 PARAMETRIC DISPERSION RELATION AND DECAY INSTABILITIES

We consider the propagation, in a plasma magnetized by a static magnetic field B_T, of a lower-hybrid pump wave (ω_0, $\mathbf{k}_0$) with finite extent which decays into a low frequency mode (ω_1, $\mathbf{k}_1$) and two high frequency sidebands ($\omega_1 \pm \omega_0$, $\mathbf{k}_1 \pm \mathbf{k}_0$). The plasma is assumed locally homogeneous, i.e. $k_\perp \gg |\nabla n/n|, |\nabla T/T|$, where $k_\perp$ is the perpendicular (to B_T) wavevector of the involved waves and n and T are the plasma density and temperature.

Following Tripathi et al. [2] the parametric dispersion relation is:

$$\varepsilon(\omega_1, k_1) = \frac{\mu^+}{\varepsilon(\omega_1 + \omega_0, k_1 + k_0)} + \frac{\mu^-}{\varepsilon(\omega_1 - \omega_0, k_1 - k_0)} \qquad (1)$$

where $\varepsilon(\omega, \mathbf{k}) \equiv 1 + \chi_i(\omega, \mathbf{k}) + \chi_e(\omega, \mathbf{k})$ is the dielectric function and χ_i, χ_e are the linear susceptibilities, $\mu^\pm$ are the upper and lower sideband coupling coefficients.

Whe have solved numerically the equation (1) with respect to the complex frequency $\omega_1 \equiv \omega_{1R} + i\gamma$. For a given numerical calculation we have assumed one of the plasma and rf parameters $n, T, B_T, P_{RF}, k_{0\parallel}, k_{\parallel}^\pm, k_\perp^\pm, k_{1\parallel}, k_{1\perp}$, as independent variable, keeping fixed the others.

We have considered the FT plasma where the density and temperature profiles are defined in Ref. [3].

The electric field amplitude is calculated in term of the injected rf power using the WKBJ method [4].

In this section we consider the absolute instability which is characterized by a growth rate $\gamma > 0$, keeping under consideration two ranges of frequencies $\omega_{1R} \ll \omega_{ci}$ and $\omega_{1R} \geq \omega_{ci}$.

2a) Range $\omega_{1R} \ll \omega_{ci}$ In the range of very low frequencies, for a tokamak plasma with $T_e \simeq T_i$, we expect that the ion sound waves are heavily damped on the particles, being $\omega_{1R} \approx k_{1\parallel} v_{thi} \ll k_{1\parallel} v_{the}$. The solution of Eq. (1) which gives parametric instabilities driven by ion sound quasimodes for the case of FT plasma and a pump wave with frequency $\omega_0/2\pi$ = 2.45 GHz, are described in Ref. [5].

2b) Range of $\omega_{1R} \geq l\omega_{ci}$; l = 1,2,3, ... In this range we have found that the parametric instabilities are mainly driven by ion cyclotron quasimodes being $|\varepsilon(\omega_1, \underline{k}_1)| \gg 1$.

Figure 1a shows the behaviour of the growth rate vs the real part of the frequency. The plasma parameters are related to the plasma border in the case of high density regime: n = 1×10^{14} cm^{-3}, T $\simeq$ 150 eV r/a $\simeq$ 0.9. The rf characteristics of the pump wave are: $n_{0\parallel}$ = 2, P_{RF} = 4 kW and δ^- = 90°. Figure 1b shows the growth rate vs the real part of the frequency for the same parameters as Fig. 1a, but with $n_{0\parallel}$ = 7. We note the change of the shape of the peacks which becomes non monotonic.

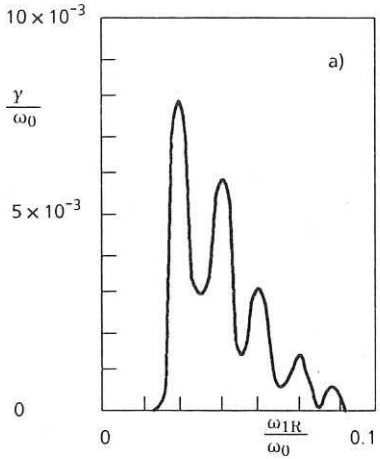

Fig. 1: a) A numerical solution of Eq. (1) when $k_{1\perp}$ is varied in a broad range of values where parametric instabilities driven by ion cyclotron quasimodes are recovered. Here γ/ω_0 is plotted vs ω_{1R}/ω_0 in a deuterium plasma, B_T = 60 kG, n = 5×10^{13} cm^{-3}, T = 20 eV, $k_{0\parallel} c/\omega_0$ = 2, $k_{1\parallel} c/\omega_0$ = 7, δ^- ∢ $k_\perp^-$, $k_{0\perp}$ = 90°, P_{RF} = 4 kW

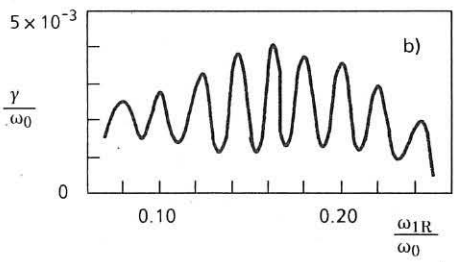

Fig. 1b) This numerical solution is referred to the case of a pump with $k_{0\parallel} c/\omega_0$ = 8 and $k_{1\parallel} c/\omega_0$ = 13, n = 8×10^{13} cm^{-3}, T = 150 eV and the other parameters as Fig. 1a

3 CONVECTIVE THRESHOLDS

The threshold for the onset of a parametric instability involving a pump of finite extent is set by the propagation of the decay waves out the region of the pump wave [7]. For an homogeneous plasma the spatial growth factor is:

$$\Lambda = \frac{B}{|v_{g1\xi}|} L_{0\xi} \qquad (2)$$

where:

$$B = \frac{\mu^2}{k} \left(\frac{\partial \varepsilon_R}{\partial \omega} \Big|_{\omega-\omega_0} \right)^{-1} \mathrm{Im} \left| \frac{\chi_e (1+\chi_i)}{\varepsilon(\omega_1, k_1)} \right|$$

$$v_{g1\xi} = - \frac{\partial \varepsilon_1 / \partial k_1}{\partial \varepsilon_1 / \partial \omega_0} \Big|_{\xi} = (\omega_0 - \omega_{1R}) \left| 1 - \frac{\omega_{LH}^2}{(\omega_0 - \omega_{1R})^2} \right| \left(\frac{\cos\theta}{k_{1x}} - \frac{\mathrm{sen}\,\theta}{k_{1z}} \right)$$

$$\theta = \mathrm{arc\,tg} \left| \frac{k_{0z}}{k_{0x}} \right|$$

$$L_{0\xi} = L_{0z} \frac{k_{0z}}{k_{0x}}$$

being L_{0z} the width of the antenna along the toroidal direction.

For parametric instabilities to be of some significance must be: $A \geq 1$.

3a) Case with: $\omega_{1R} \ll \omega_{ci}$. The maximum amplification factor can be found by a variation of the angle between the perpendicular wavevectors of the pump wave and the lower sideband [8].

Figure 2 shows the behaviour of the convective thresholds vs the value of $k_{1\parallel} c/\omega_0$ for an angle value of $\delta^- = 20°$, ($\delta^- \equiv \sphericalangle\, k_\perp^-, k_{0\perp}$) we observe that for $k_{1\parallel} c/\omega_0 \geq 10$ the threshold is ≤ 1 kW. The frequency of the pump wave is $\omega_0/2\pi = 2.45$ GHz.

3b) Case with: $\omega_{1R} \geq l\omega_{ci}$; $l = 1,2, \ldots$. We have assumed $\delta^- = 90°$ for maximizing the homogeneous growth rates. The behaviour of the power threshold for the case $l = 1$ is reported in Ref. [6]. In calculating the convective threshold for the instabilities driven by ion cyclotron quasimodes with high harmonic number we have assumed the parameters related to the solutions, as in Fig. 1b. The estimated power threshold is $P_{th} \simeq 20$ kW which is in a good agreement with the experimental observation on FT [6].

CONCLUSIONS

The result of the analysis is that parametric instabilities involving ion sound quasimodes can occur at the border of FT plasma. The estimated convective thresholds are in the range of the RF power used in the experiment. Moreover this instabilities can be related to the observed spectral broadening of the launched wave.

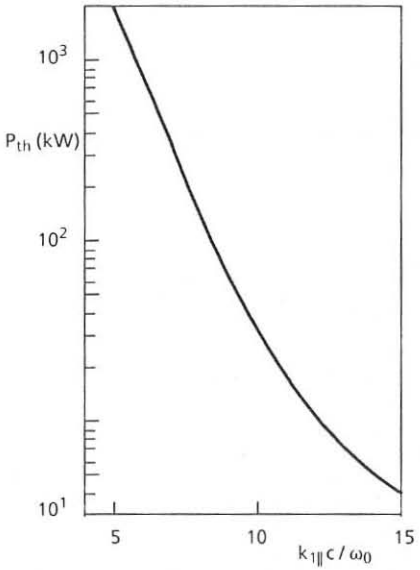

Fig. 2: Convective power threshold vs $k_{1\parallel} c/\omega_0$ for $\delta^- \measuredangle k_\perp^-$, $k_{0\perp} = 20°$, The plasma parameters are: $n = 5 \times 10^{13}$ cm^{-3}, $T_e = T_i = 20$ eV. The parameters of the pump wave are: $\omega_0/2\pi = 2.45$ GHz, $k_{0\parallel} c/\omega_0 = 2$

As regards to the instabilities driven by ion cyclotron quasimodes with high harmonic number l we have found a power threshold of $\simeq$ 10 kW for $l \simeq 10$, assuming for the pump wave $n_{0\parallel} = 7$. This result can be related to the observation of the rf spectra.

As regards to the rf spectra observed in FT in the LH experiment at the frequency of 2.45 GHz, which shows many secondary peacks, our analysis shows that this phenomenon can be related to parametric instabilities driven by ion cyclotron quasimodes with high harmonic number, if a $n_{\parallel 0}$ - broadening of the pump wave is supposed to occur at the plasma border.

FOOTNOTE AND REFERENCES

* ENEA Student

[1] F. De Marco, *Course and Workshop on Application of RF to Tokamak Plasma, Int. School of Plasma Phys.* Varenna, September 1984, Vol. 1, p. 313

[2] V.K. Tripathi, C.S. Liu and C. Grebogi, Phys. Fluids, **22**, 301 (1979)

[3] V. Pericoli-Ridolfini, Plasma Phys. and Controlled Fusion, **27**, 493 (1985)

[4] P.M. Bellan and M. Porkolab, Phys. Fluids, **23**, 96 (1974)

[5] A. Cardinali, R. Cesario, *Proc. 14th Europ. Conf. on Controlled Fusion and Plasma Phys.*, Madrid,22-26/6/87, vol. 11, III, p. 907 (1987)

[6] R. Cesario, V. Pericoli-Ridolfini, Nucl. Fusion, **27**, 435 (1987)

[7] C.S. Liu, and P.K. Kaw, in Advance in Plasma Phys., Ed. by A. Simon and W.B. Thompson (Wiley, N.Y.) **6**, 87 (1976)

[8] E. Villalon, A. Bers, Nucl. Fusion, **20**, 243 (1980)

INTERACTION OF THE LOWER HYBRID PUMP WAVE WITH FT EDGE PLASMA

R. Cesario, R. Mc Williams, V. Pericoli Ridolfini*

Associazione EURATOM-ENEA sulla Fusione, Centro Ricerche Energia Frascati, C.P. 65 - 00044 - Frascati, Rome, Italy

INTRODUCTION

The phenomena involved in the interaction of the lower hybrid waves with the edge plasma in FT, were studied during the heating experiment with the new 8 GHz equipment [1], to compare and contrast with the work done with the old 2.45 GHz power supply system [2,3]. Additionally we propose an interpretation of the results on the basis of models described elsewhere in more detail [4,5].

The main FT plasma parameters for this work were: line averaged density $\bar{n}$ = $0.3 \div 3.6 \times 10^{14}$ cm^{-3}; current I_p = 280÷600 kA; toroidal field B_T = 6 and 8 T; coupled RF power P_{RF} = 100÷200 kW. The scrape off plasma was characterized by means of Langmuir probes which gave the local density and temperature. The RF waves are characterized through the spectral analysis of the radiation collected by a small loop antenna external to the vacuum vessel.

Previous results with the 2.45 GHz system showed that the most interesting effects occur either at low plasma density, $\bar{n} \leq 4 \times 10^{13}$ cm^{-3}, where the RF waves drive strong modifications in the edge plasma [6], or at high density $\bar{n} \geq 1.2 \times 10^{14}$ cm^{-3}, where the spectral width of the pump wave broadens and numerous secondary peaks appear in the spectrum [2,3]. These clearly originate in the edge plasma and scale with the main plasma parameters, as do the edge plasma parameters.

The following remarks are divided according to the density regime studied.

LOW DENSITY EFFECTS

For the 8 GHz experiment no spectacular effects on the scrape-off plasma were found like those described in [6] for 2.45 GHz, namely no density reduction of a factor ~ 10 and no temperature increase of ~ 30 eV inside the RF grill radius. Onle a few shots at very low density $\bar{n} \approx 3 \times 10^{13}$ cm^{-3}, showed a density decrease of about 20% ÷ 30% together with a small D_α brightness drop, but no clear temperature increase was seen within the experimental error bars. However, a systematic study of the conditions required to observe these effects has not been conducted yet.

Both the 2.45 GHz and 8 GHz results can be accounted for in term of ponderomotive effects and edge plasma heating due to lower hybrid electric field in front of the RF grill [4]. The wave field raises the average electron kinetic energy by an amount proportional to f^{-2}, where f is the wave frequency, causing a density reduction of a Boltzmann factor ~ e^{-a/f^2}, where a depends only on wave amplitude and plasma temperature. Once formed, this perturbation spreads along the magnetic field at roughly the sound speed [4], affecting a large part of the palsma surface. Model predictions, shown in Fig. 1, agree satisfactorily with experiment.

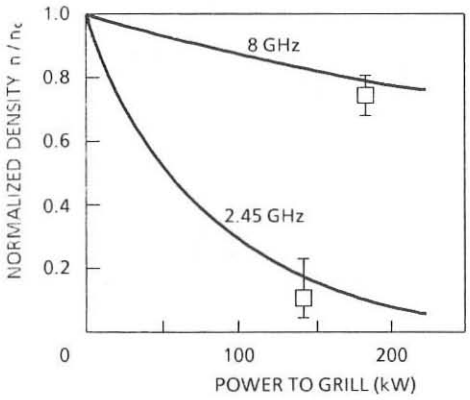

Fig. 1: Density reduction in the FT edge plasma as a function of the injected power.
Full line: theory, □: experiment

The importance of understanding and controlling the mechanism governing such modifications lies in the effect that they have on recycling and possibly on the global confinement properties [7].

HIGH DENSITY EFFECTS

As mentioned above, when the plasma density is increased modification in the RF waves become visible. The experimental data, presented in Fig. 2, lead us to consider three different regimes.

The first is characterized by narrow pump spectral broadening, ~ 0.6 MHZ at -10 db for $\bar{n} \sim 2\times10^{14}$ cm^{-3}, and large pump signal level (Fig. 2a) with noticeable change in bulk plasma conductance. Figure 2b shows the relative change of the conductance normalized to the ratio (RF power)/(ohmic power).

The second regime is characterized by a pump spectral width about three times broader, much lower pump level (see Fig. 2c) and very little effects, if any, on the main plasma.

Finally in the third regime the pump spectral width becomes very large (~ 6 MHz) and the first satellite wave emerges from the noise [8]. Its frequency shift corresponds to the ion cyclotron frequency evaluated at the outer plasma edge and it appears only with large pump spectral broadening, just as for the 2.45 GHz case. The onset of the first satellite can be predicted satisfactorily by extending the model calculation in [3] to the 8 GHz case and taking into account the actual edge densities, which for these shots turn out to be more than two times higher than those predicted by the FT scaling laws [9] and used in [3]. Also for this regime no effect of the RF on the main plasma is observed.

So, it appears that the alteration of the wave properties (i.e. its spectral broadening) is strictly correlated to the absence of effects on the main plasma, perhaps more clearly than for the 2.45 GHz experiment. In fact, in the 2.45 GHz case the upper density threshold to heating, can be accounted for as due to a *switching* of the RF interaction from electrons to ions, both predicted [10] and observed [11], which efficiently depletes the pump power. For the 8 GHz experiment no such mechanism is either expected or found (no fast neutral tails were produced), but no conductance increase, or other bulk effect, is observed when the pump spectral width exceeds ~ 1.3 MHz at -10 db.

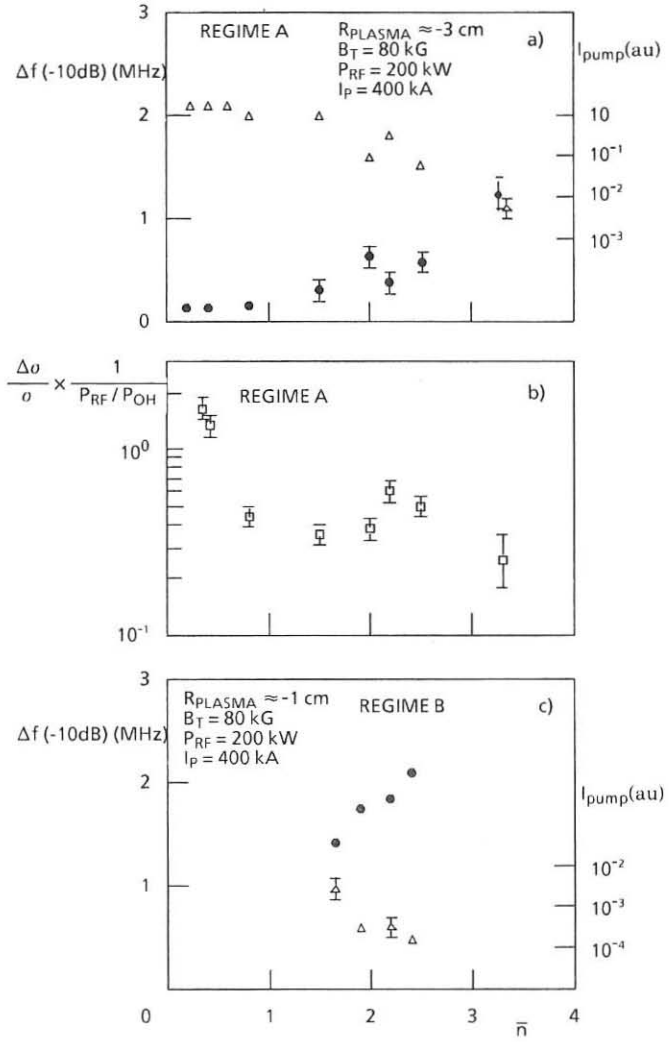

Fig. 2: a,b) regime A; c) regime B. • full pump spectral width at -10 db (MHz); Δ logarithm of the pump power level; □ relative conductance variation of the plasma upon application of the 8 GHz power normalized to the ratio P_{RF}/P_{OH}, only for regime A. For regime B this quantity is zero within the experimental errors

The access to a particular regime can be controlled by adjusting some macroscopic plasma parameters. Current and density are already known to affect the wave propagation properties [3]. The present data establish the importance of the horizontal

position, too. Indeed the second regime shots differ from the first ones only for an outward plasma shift, that is towards the RF grill, of 1.5÷2.0 cm. The third regime shots, on the other hand, show a bit smaller outward shift ($\leq$ 1 cm) together with lower current and central temperature (about factor $\leq$ 2) compared to the first ones.

It was shown experimentally and was confirmed by model calculations [3] that the importance of the plasma current and density follows from the modifications they induce in the edge plasma, at least as far as the onset of the first satellite is concerned. It has been found also [5] that the pump spectral broadening might originate in the edge plasma through parametric instabilities involving ion sound quasi modes. The threshold powers are calculated to have a very deep minimum (< 1 kW) near the limiter radius, indicating a strong sensitivity to the local values of temperature and density. In this framework, a horizontal plasma shift can influence the pump spectral width by varying the density and temperature just in that region where the threshold power drops. Indeed a shift of the last closed magnetic surface relative to the limiter alters the edge magnetic topology and, as a consequence, changes the local balance between the input and output power and particles, which, in turn determines the values of n_e and T_e. This qualitative argument is supported by Langmuir probe data. All the shots with outward shifts show higher edge densities compared to the others, but similar temperatures. Hence, the pump wave will encounter high density regions when the temperature is still low. This drops the threshold power for the parametric instabilities, favoring these processes.

CONCLUSIONS

We have studied the interaction of the RF lower hybrid waves with the edge plasma. Comparisons between the 2.45 and 8 GHz experiment have been made and some mechanisms for the phenomena observed have been proposed. Another macroscopic plasma parameter, i.e. the horizontal position, has been recognized to be of importance in determining the edge parameters and hence the RF effects on the whole plasma.

FOOTNOTE AND REFERENCES

* Permanent address: Physics Dept., Univ. of California, Irvine, CA 92717 (USA)

[1] FT Group, *Lower Hybrid Experiments at 8 GHz in FT* (this conference)
[2] R. Cesario, V. Pericoli-Ridolfini, *Proc. 12th Europ. Conf. on Controlled Fusion and Plasma Phys.*, Budapest, 2-6/9/85, vol. 9F, II, p. 220 (1986)
[3] R. Cesario, V. Pericoli-Ridolfini, Nucl. Fusion, **27**, 435 (1987)
[4] R. Mc Williams and N.S. Wolf, Phys. Rev. **A25**, 1247 (1982)
J.R. Wilson and K.L. Wong, Phys. Fluids, **25**, 675 (1982)
R.W. Motley, Phys. Fluids, **23**, 2050 (1980)
[5] A. Cardinali, R. Cesario, *Proc. 14th Europ. Conf. on Controlled Fusion and Plasma Phys.*, Madrid,22-26/6/87, vol. 11, III, p. 907 (1987)
[6] V. Pericoli-Ridolfini, Plasma Phys. and Controlled Fusion, **27**, 715 (1985)
[7] R. De Angelis, G. Tonini, *Proc. 12th Europ. Conf. on Controlled Fusion and Plasma Phys.*, Budapest, 2-6/9/85, vol. 9F, II, p. 690 (1986)
[8] F. Alladio et al., *Proc. of 7th Topical Conf. on Applications of RF Power to Plasmas*, Kissimmee, 4-6/5/87, p. 131
[9] V. Pericoli-Ridolfini, Plasma Phys. and Controlled Fusion, **27**, 493 (1985)
[10] T.G. Wegrowe, F. Engelmann, Comm. on Plamsa Phys. and Controlled Fusion, **8**, 211 (1984)
[11] F. Alladio et al., Nucl. Fusion, **24**, 725 (1984)

LOWER HYBRID ION HEATING IN FT-2 TOKAMAK

V.N.Budnikov, V.V.Djachenko, L.A.Esipov, M.A.Irzak, E.R.Its, S.I.Lashkul, A.D.Lebedev, S.Y.Petrov, A.Yu.Stepanov, O.N.Shcherbinin, V.O.Aleksandrov*, I.E.Sakharov*

A.F.Ioffe Physical-Technical Institute, Leningrad, USSR
*M.I.Kalinin Polytechnic Institute, Leningrad, USSR

We present here the investigation of lower hybrid (LH) ion heating efficiency as a function of RF power level. The experiments have been carried out on the FT-2 tokamak /1/, R = 55 cm, a = 8 cm, with the following plasma parameters: B_T = 2.3 T, I_p = 33 kA, $\bar{n}_e = 3.6 \times 10^{13}$ cm^{-3}, $T_e(0)$ = 450 eV. A two waveguide grill installed on the lower field side of the tokamak has been used to inject 25÷200 kW of LHRF power with the duration up to 8 ms at a frequency of f_o = 925 MHz. Ion temperature profiles have been measured by the 5-channel charge-exchange analyzer.

In Fig.1 we display the time-history of the main plasma parameters for the Ohmic discharge and for the LH heating discharge with 160 kW of RF power. All changes shown in Fig. 1, increased with the increasing RF power.

The time sequence of the electron density profiles $n_e(r)$, measured by the 2-mm interferometer, is shown in Fig.2.

The electron temperature profile $T_e(r)$, measured by the second harmonic of the ECE, is presented in Fig.3; no changes in $T_e(r)$ were observed during RF pulse. The neutral hydrogen density profile $n_H(r)$ has been calculated from the charge exchange neutrals flux. For the Ohmic discharge $n_H(a) \approx 3.10^{10}$ cm^{-3} and this value did not increase during RF pulse. The value of Z_{eff} for both types of the discharge was ≤ 2.

When LH power has been injected into plasma, the bulk ion heating and the fast ions tail generation with $T_t > 600$÷1000 eV have been observed. The time evolution of the $T_i(0)$ is plotted in Fig.4. It can be seen, that ΔT_i has a week de-

pendence on RF power level. At P_{RF} = 25 kW the highest heating rate η = 10^{14} eV/kW.cm^3 has been obtained; at higher power levels η decreased roughly inversely proportional to the RF power. Ion energy confinement time, deduced from the derivative dT_i/dt, Fig.4, was 2.8 ms at P_{RF} = 30 kW, and 1.2 ms at P_{RF} = 160 kW. The relaxation of T_i after the end of RF pulse occured with the characteristic time $\tau_{Ei} \approx 3$ ms; it should be noted that in the Ohmic discharge $\tau_{Ei} \approx 3$ ms. At the same time the particle confinement time during LH pulse was improved. It followes from the fact that the neutral hydrogen density n_H and the impurity density $n_I \sim \mathcal{J}_I/n_e$ kept constant, whereas n_e increased, Fig.2, with the characteristic time of 4.5 ms, which is 2 times larger than the decrease time for n_e after the end of RF pulse, 2.2 ms. The same effect has been observed both in the ion heating experiments and in the current drive experiments in a low density plasma on JFT-2 /2/ and Versator /3/.

The evaluation of the energy input into the ions can be done using the balance equation:

$$4\pi^2 R r \, \varkappa_{i\,ef} \nabla T_i = W_{RF} + W_{ei} - W_{cx} - 1.5 \frac{d}{dt} \int_V n_i T_i \, dV \qquad (1)$$

where W_{RF} is the absorpted RF power, W_{ei} is the power input from electrons to ions, W_{cx} is the charge exchange losses. All the values are calculated for the cylinder with a radius r and a length $2\pi R$. For the evaluation of $\varkappa_{i\,ef}$ in RF discharge we used the value of $\varkappa_i$ obtained in the OH discharge, but the latter was modified taking the plasma parameters disturbed during RF. In the flat-top stage of ΔT_i the calculated value was W_{RF} = 13 kW for P_{RF} = 30 kW and W_{RF} = 30 kW for P_{RF} = 160 kW. It should be marked that the estimation by the relation:

$$W_{RF} + W_{ei} - W_{cx} = \bar{n}_i \bar{T}_i V / \tau_{Ei} \qquad (2)$$

where V = 7.10^5 cm^3 is the plasma volume and τ_{Ei} is deduced from the derivative $dT_i(0)/dt$, results in W_{RF} = 17 kW for

P_{RF} = 30 kW and W_{RF} = 62 kW for P_{RF} = 160 kW. These values are higher than those, obtained by (1), when for RF discharge we used the $\varkappa_{i\ell f}$ from OH discharge. However the experimental values of $\tau_{E\ell}$ during RF heating are smaller. This discrepancy could be explained by the enhancement of the ion heat conductivity during LHRF injection.

The estimation of the energy losses with the fast ions can be done by the charge exchange and bolometric measurements. The energy flux of the charge exchange neutrals with the energy E > 1000 eV was W_{cx} = 3 kW for P_{RF} = 30 kW and W_{cx} = 6 kW for P_{RF} = 160 kW. The fast rise of the bolometric signal on the first millisecond of the RF pulse and its fast decay after the turn off of the RF could be also associated with the fast particles, /4/. This estimation shows, that the fast particle losses are W_t = 6 kW for P_{RF} = 30 kW and W_t = 12 kW for P_{RF} = 160 kW. The excess of W_t over W_{cx} can be explained by the fact that the total energy flux on the wall includes not only the neutrals, but the charged particles too. And it should be taken into account that the power losses with the fast ions is τ_{cx}/τ_d times higher, than W_{cx} (τ_{cx} is the charge exchange time and τ_d is the confinement time for banana or localy trapped ions). The ratio of τ_{cx}/τ_d can amount up to ten. Therefore the low value of RF power deposition into the bulk ions could be explained by the energy losses through the fast ions.

REFERENCES

1. Budnikov V.N. et al., Fiz.Plasmy (Sov.J.Plasma Phys.), 1984, 10, p.485-492.
2. Uechara K., Nagashiwa T. In: Heating in Toroidal Plasmas, Grenoble, 1982, 2, p.485-503.
3. Porkolab M. et al., ibid, p.469-483.
4. Clement M. et al. In: Heating in Toroidal Plasmas, Roma, 1984, 1, p.634-640.

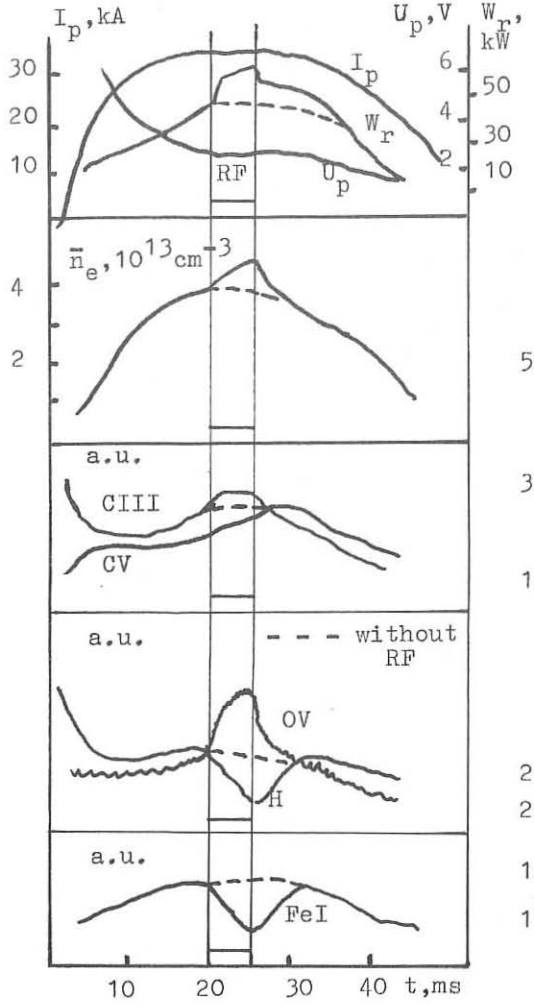

Fig.I

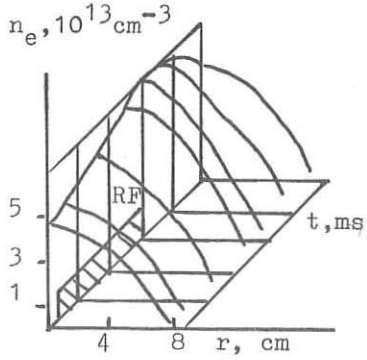

Fig.2

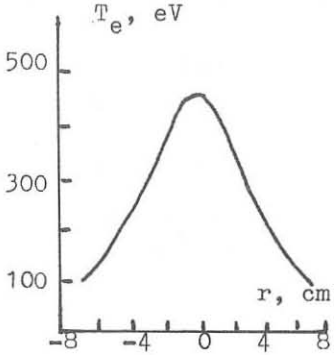

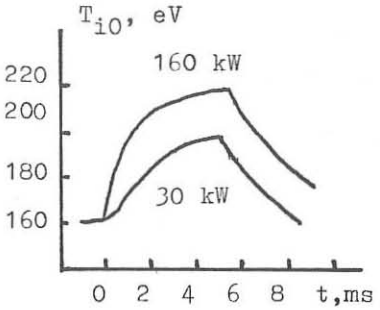

Fig. 4

LOWER HYBRID WAVES ABSORPTION STUDIES IN FT-2 TOKAMAK

V.N.Budnikov, V.V.Djachenko, L.A.Esipov, M.A.Irzak, E.R.Its, A.D.Lebedev, K.M.Novik, A.Yu.Stepanov, O.N.Shcherbinin, V.O.Aleksandrov*, I.E.Sakharov*

A.F.Ioffe Physical-Technical Institute, Leningrad, USSR
* M.I.Kalinin Polytechnic Institute, Leningrad, USSR

Lower hybrid (LH) ion heating experiments on tokamaks vary in results. On Petula and JFT-2 bulk ion heating has been reported, while on ASDEX, PLT, FT only fast ions tail generation has been observed (see Ref. in /1/). In our experiments on FT-2 tokamak we saw the peculiarities of both types of experiments. In this paper we present some experimental data, which can be usefull for understanding the mechanism of LH wave propagation and absorption in tokamak plasmas.

In the FT-2 (R = 55 cm, a = 8 cm /2/) experiments described below, the main plasma parameters were in the following ranges: B_T = 1.3÷2.7 T, I_p = 20÷35 kA, T_{eo} = 300÷500 eV, $\bar{n}_e = (1 \div 4.5).10^{13}$ cm^{-3}. For LH ion heating an externally based 2 waveguide grill has been used to inject the microwave power $P \leq 200$ kW at f_o = 925 MHz with a good coupling ($R \leq 10\%$). The ion temperature in OH and LH regimes has been deduced from the charge exchange analysis. Perpendicular ion energy spectra with and without LHRF pulse are shown in Fig. 1. In this picture both bulk ion heating and fast ions tail generation can be seen. In a dense plasma with $\bar{n}_e = 4.5 \times 10^{13}$ cm^{-3} and B_T = 2.7 T ion temperature increased from 180 up to 260 eV, when 80 kW of RF power was injected. Heating rate in this case was $\eta = 4.10^{13}$ eV/cm^{3}kW. The same result has been obtained for similar plasma parameters in Petula B experiment /3/ and has been explained by the theoretical model based on the strong slowing of the heating wave in radial direction near the linear transformation point (LTP) and the

stochastic mechanism of ions acceleration in the field of the strongly slowed wave. Nevertheless in some of our experiments we saw effects that were not in agreement with this model.

In Fig.2 we display a plot of the central ion temperature without RF and with 80 kW RF power; and the value of the flux of fast neutrals with the energy E = 1875 eV versus $\bar{n}_e$ for B_T = 2.7 T. The jump of the flux with E = 1875 T near $\bar{n}_e = 2.10^{13}$ cm^{-3} can be seen. Such a jump is usually explained by the appearance of LTP in the plasma volume /4/. In our conditions for $Z_{eff} = 2$ and $\bar{n}_e = 2.4 \times 10^{13}$ cm^{-3} LTP appears in the center of plasma column and the jump of F could be associated with the appearance of LTP in the center. However it is not so: there is no jump of T_{io} near $\bar{n}_e = 2.4 \times 10^{13}$ cm^{-3}, hence the jump of F is not connected with the fast ions generation in the plasma center.

Besides, it was established, that the bulk ion heating and the fast ions tail generation took place for the very small densities and magnetic fields, when there was no LTP. For instance, at B_T = 1.3 T, $\bar{n}_e = 1.8 \times 10^{13}$ cm^{-3}, P_{RF} = 30 kW we obtained bulk ion heating from 85 up to 160 eV, with the haeting rate $\eta = 4.10^{13}$ eV/cm^{3}kW, Fig.1. In these conditions the maximum possible slowing factor of the electron plasma waves excited by the grill is $N_\perp$ = 90 for $N_\parallel$ = 3. In the experiments the generation of ions with minimum energy E_B = 500 eV ($v_{iB} = 3.5 \times 10^7$ cm/c) was observed. Taking into account the accelerating condition $v_i \geq v_{ph}$ we can suppose that the waves with $N_\perp = c/v_{ph} = c/v_{iph} = 850$ exist in the plasma. There is no linear mechanism for such a strong slowing of LH waves in plasma with the above mentioned parameters. The flux of neutrals with E = 1500 eV versus $\bar{n}_e$ is shown on Fig.3, the fluxes for the different magnetic fields are of the same value, although they depend on $\bar{n}_e$. So the jump of $F(\bar{n}_e)$ does not follow the LH resonance curve $\mathcal{E}(n_e, B) = 0$, Fig.4, even qualitatively and takes place on a line n_e = const.

Thus, the fast ions generation depends only on the plasma density. This allows us to make a conclusion, that the wave process, responsible for the fast ions generation in its turn depends only on n_e. But exactly in the edge plasma the perpendicular wave vector of the electron plasma wave depends only on n_e: $k_\perp = k_\parallel \sqrt{n_e/n_c}$, where n_c is the critical density for LH wave, $k_\parallel$ is determined by grill. Estimations show, that this condition is safisfied when $n_e \leq (1\text{-}2).10^{13}$ cm^{-3}. So we can suppose that some nonlinear processes, in particular parametric instabilities, stimulating the fast ions generation, take place in the vicinity of $n_e = (1\text{-}2).10^{13}$ cm^{-3}, where $\omega_o \approx 1.5\, \omega_{LH}$

Parametric instability studies have been done by the high frequency probe, located near the grill. The generation of the satellites, shifted for f_{ci}, $2f_{ci}$, $3f_{ci}$ (f_{ci} is the ion cyclotron frequency on $r \approx 6.5$ cm) to the red side from f_{LH}, has been observed. The power thresholds of the satellites decrease with plasma density. This decreasing dependence correlates with the increase of neutral fluxes, Fig.3. Parametric spectra have been obtained also by the enhanced scattering of 4 mm microwaves method, /5/. The extraordinary waves have been launched from the inner side of the torus at the cross-section shifted from the grill position to 90°. The spectrum of the scattered signal from the region r = + 6 cm is shown on Fig.5. It is broader than the spectrum, obtained by the high frequency probe.

REFERENCES

1. Golant V.E., Fedorov V.I., RF Plasma Heating in Toroidal Plasmas (in Russian), Moscow, Energoatomizdat, 1984, p. 116-141.
2. Budnikov V.N. et al., Fiz.Plasmy (Sov.J.Plasma Phys), 10, 1984, p.485-492.
3. Van Voutte D. et al., In: Heating in Toroidal Plasmas, Rome, 1, 1984, p.554-570.
4. Gladkovsky I.P. et al., Fiz.Plasmy (Sov.J.Plasma Phys.), 5 1978, p.512-518.
5. Aleksandrov V.O. et al., Voprosy atomnoy nauki i tekhniki, ser.Termojaderny sintez (Nuclear Fusion) 1, 1986, p.30.

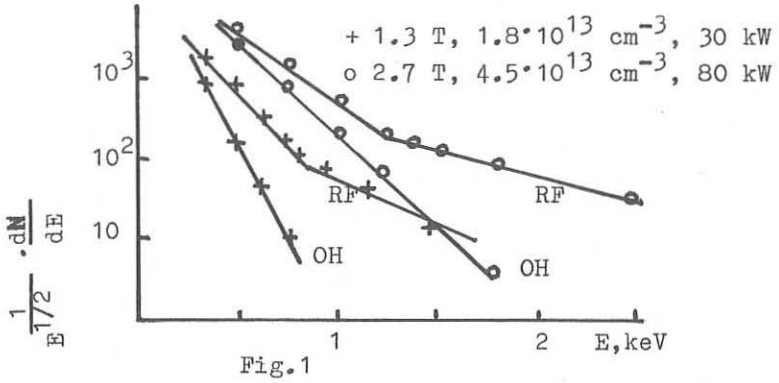

Fig.1

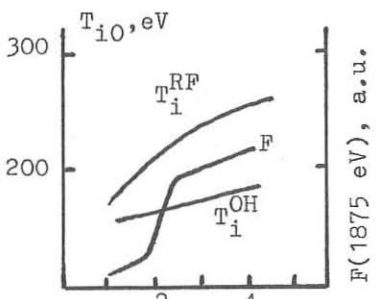

Fig.2 $\bar{n}_e, 10^{13}cm^{-3}$

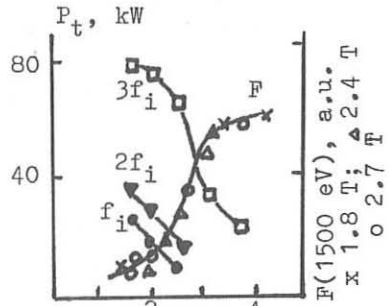

Fig.3 $\bar{n}_e, 10^{13}cm^{-3}$

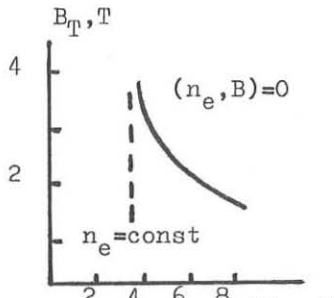

Fig.4

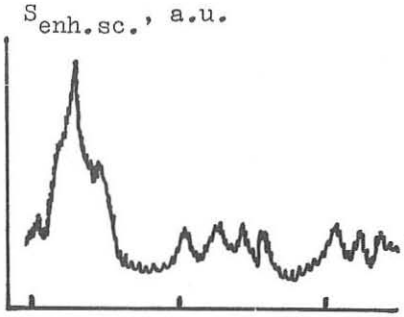

Fig.5

ION HEATING IN THE TOKAMAK FT-1 AT FREQUENCIES $\omega_0 < \omega_{LH}$

Yu.F.Baranov, V.V.Dyachenko, M.M.Larionov, L.S.Levin, G.A. Serebreny.
A.F.Ioffe Physical-Technical Institute, Academy of Science of the USSR, Leningrad.

In experiments on Lower Hybrid Resonance Heating (LHRH) most of the HF power goes to produce high energy ions (nonthermal "tails"). Their behaviour is determined by a drift in the tokamak magnetic field. Effective LHRH can be expected only when the losses of these ions are small. In earlier experiments in the FT-1 Tokamak /1,2/ it was shown that the behaviour of the energic ions depends on the position of antennae relative to the direction of the toroidal ion drift. The optimal position is at the bottom (or at the top) of a discharge chamber, when the ion drift is directed from the antenna into the plasma volume.

This paper is concerned with the determination of the LHRH efficiency and some aspects of the ion energy distibution. The results were obtained mainly by the charge exchange (CX) analysis.

The tokamak FT-1 parameters were: R = 62 cm, a = 15 cm; $B \leq 1.2$T; I = 45 kA; q(a) = 4.5; $\bar{n}_e = (1\text{-}1.5)10^{13}$ cm^{-3}; $Z_{eff} = 3.5$; the filling gas was hydrogen. A magnetron generator (ω_0 = 360 MHz) was used to launch into the plasma a power of 30-50 kW in 10 ms pulses. The frequency ω_0 was lower than LHR frequency at the discharge axis and the LHR surface was localized near the periphery at r = (0.7-0.8)a. Two rod antennae were introduced into the chamber through coaxial insulator. They partially embraced the plasma column from the top and from the bottom sides (Fig.1). A corrugated slow--wave structure was mounted inside the chamber. Antennae together with the structure excited in a plasma E-polarized slow wave with N 2.

During a HF pulse the density increase was 15-20%, the increase of radiation losses and SXR - 40-50%, so Z_{eff} did not change significantly. During the LHRH the ion distribution becomes nonmaxwellian, so a thorough analysis of CX data was nesessary to find the true value of Ti increase in a bulk plasma.

The typical CX spectra for ohmic heating (OH) (3) and the LHRH by the upper (2) and the lower (1) antennae are shown in Fig.2. The toroidal drift was directed upward. The intensity of high energy part of spectrum 1 is higher than of spectrum 2. Moreover, the slope in the energy range 300--1200 eV changed, which may be due to the total temperature increase from 140 to 220 eV. Spectrum 4 was obtained 1 ms after the termination of the LHRH pulse by the lower antenna. The nonmaxwellian part of the spectrum decayed during that time. The slope of the remaining part of the spectrum shows T 180eV. Also remarkable is the excess of the par-

ticles having E>1600 eV. So the operation of the lower antenna provides Δ Ti $\simeq$ 80 eV at the power of 20 kW introduced into a plasma. The upper antenna is less effective, Δ Ti is about 15-20 eV.

In the initial OH regime at Ti = 140 eV; $T_e(0)$ = 500 eV; $\bar{n}_e = 1{,}3 \cdot 10^{13}\,cm^{-3}$ the power transfered to the ions is $P_{ei} \simeq 17$ kW; the ion energy confinement time is $\tau_{ei} \simeq 3$ ms. The oscilloscope traces of CX fluxes (Fig.3) clearly show the different time behaviour of "tail" (E = 2400 eV) and thermal (E = 980 eV) ions. The former disappears practically instantly after the LHRH pulse termination; the latter decay with τ = 2 ms. The significant difference in time constants between the high and low energy ions allows one to determine the thermal part of an energy spectrum, 300--1200 eV, in which the ion temperature is measured.

According to the theory, in the LH wave field the ions acquire the transverse component of their energy. Supposing that the nonthermal "tails" were absent in "longitudinal" ion distributions, we carried out an experiment where the CX atoms leaving the plasma at small angles to the magnetic field were analysed, using the reflection of neutrals from a moveable aluminium mirror located in the limiter "shadow". The CX spectra obtained in perpendicular (1) and longitudinal (2) directions in the OH and the LHRH regimes are shown in Fig.4. Unexpectedly, the perpendicular and longitudinal spectra were found to be similar. The former reflects the energy distribution of locally and toroidally trapped ions, the latter the energy distribution of the passing ones. Both spectra consist of two components during the LHRH and possess "tails" with the short lifetime.

Taking into account Z_{eff} the ion isotropisation time $\tau_{ii} \simeq 0{,}25$ ms for E = 1000 eV and 1 ms for E = 2400 eV. The observed ion lifetime for E = 2400 eV is much less than 1 ms. Nevertheless, the longitudinal spectra are similar to the transverse ones and the ion velosity distribution is apparently isotropic.

CX spectra of deuterium added in small amount (7%) to the hydrogen were found to be similar to the hydrogen spectra in having thermal and "tail" parts under the LHRH (Fig.4). Thus the attempt to find conditions under which the observed spectra are thermal and undisrurbed during the LHRH have failed. But the analysis of the time evolution of CX fluxer after the termination of the LHRH pulse made it possible to find the thermal part of the disturbed energy distribution.

The experiment on ion heating and Ti evolution was modelled numerically. The transport coefficients for the OH regime in FT-1 were used in the model. The calculated Ti(0) evolution is shown in Fig.5 in the case of P = 40 kW. The heating is localized at the discharge axis (1) and at

the radii of 7.5(2) and 11 cm (3). The CX data are also shown. Apparently, Ti rise would have been higher in the case of the of the most affective central heating.

The dependence of Δ Ti during the LHRH at P = 40 kW on the plasma mean density $\bar{n}_e$ is shown in Fig.6. To find the temperature, the energy range of 300-1200 eV was used as previously. Δ Ti increases with the density. This seems to be due to the collision frequency rise and fast ion termolisation improvement. The heating efficiency at $\bar{n}_e = 1.5 \cdot 10^{13}$ cm^{-3} is $\eta = 4 \times 10^{13}$ eV$\cdot$cm^{-3} kW^{-1}. Fig.6 shows the data on the optimally located lower antenna. Under the same conditions the upper antenna and previously used antenna mounted at the outer side of the chamber were much less effective, $\eta < 1 \cdot 10^{13}$ eV$\cdot$cm^{-3} kW^{-1}.

Thus, the experimental evidence shows that the appropriate localization of the antenna for the LHRH into account the direction of the toroidal drift can increase the heating efficiency, especially in a dense plasma at relatively low generator frequency, when the LHR zone is near the periphery. The effect of kinetic convection /3/ appears to make a contribution. Accelerated near the periphery by the LH wave ions drift towards the plasma center, where they lose their energy in collisions and become trapped. Possibly, the traditional location of the LHRH antennae (grills) on the outside torus wall in experiments with dense plasma is not effective, because the accelerated ions become toroidally or locally trapped near the periphery. They are later easely lost due to the CX or drift.

REFERENCES

/1/. V.V.Dyachenko et al. Proc. XIth Europ. Conf. on Contr. Fusion and Plasma Physics, Aachen, 1983, v. 1, p. 461.

/2/. D.G.Bulyginsky et al. Proc. Xth ICPPCNFR, London, 1984, v. 1, p. 491.

/3/. E. L. Berezovsky et al. Nuclear Fusion, 1983, v. 22, N 12, p. 1575.

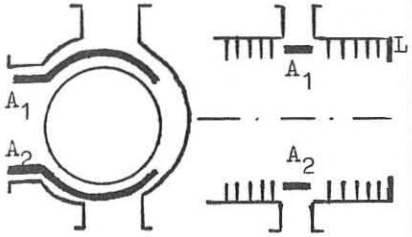

Fig.1

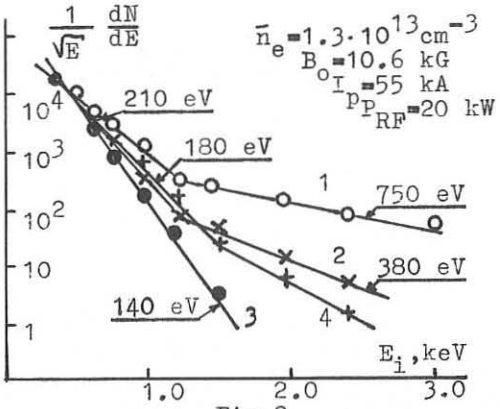

Fig.2

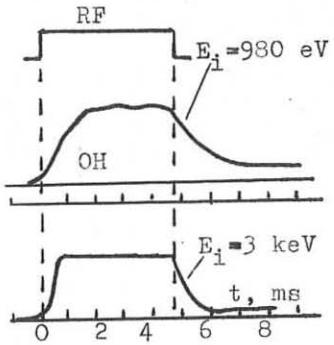

Fig.3

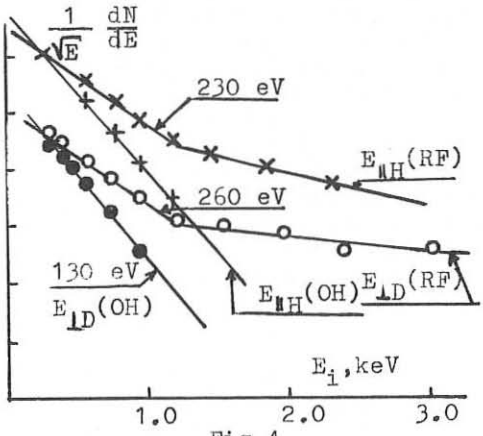

Fig.4

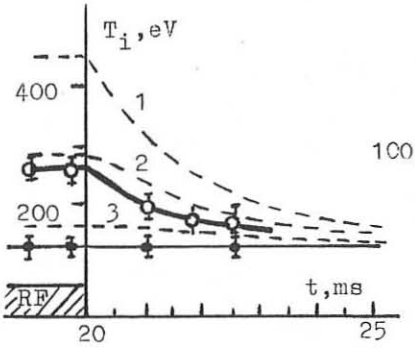

Fig.5

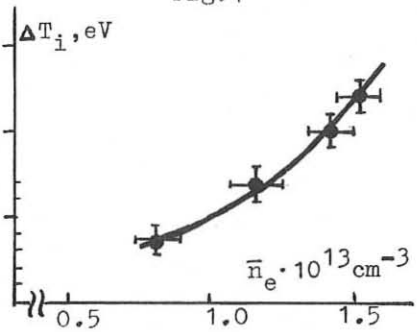

Fig.6

HIGH EFFICIENCY KLYSTRONS FOR LOWER HYBRID HEATING APPLICATIONS

E.W. McCune
Varian Associates, Inc.
611 Hansen Way
Palo Alto, CA 94303 USA

INTRODUCTION

Plasma heating, using the lower hybrid resonance method, requires very high power at frequencies in the range of 0.5 to 15 GHz. Desired power source characteristics include, along with high-power capability, good reliability with high efficiency. The klystron amplifier is traditionally preferred for generating of high power levels at these frequencies. Klystrons have demonstrated good reliability while providing high power at good efficiency[1].

Efficiency is an important consideration for high-power amplifiers. Much effort has been devoted to establishing the design parameters which determine the interaction efficiency of klystrons.[2] This work utilized computer-aided design to optimize the beam and circuit interaction to provide maximum output power. Klystrons designed in this manner have demonstrated efficiencies of up to 75% although values of 50% to 60% are routinely achieved in practical devices.

Another method is available for enhancing operating efficiency of microwave tubes. By incorporating a decellerating electric field in the collector region, one can recover energy from the spent electron beam with consequent overall efficiency improvement. This design approach, referred to as "depressed collector operation," has been routinely used for traveling-wave tube designs but until recently has not been applied to klystrons for a variety of technical reasons. These technical problems have been overcome, and the technology is now available to allow klystron designs with exceptional efficiency performance.[3]

DEPRESSED COLLECTOR DEVELOPMENT PROGRAM

Power consumption of the amplifier klystron is a particular concern for UHF television stations. A program to develop a depressed collector UHF-TV klystron was initiated in June 1984 with broad support from the television community and from NASA. A computer-aided design was subsequently constructed and evaluated.[4,5]

The Varian VKP-7555S five-cavity klystron was selected as the test vehicle for the multistage depressed collector (MSDC) performance evaluation. This klystron provides 60 kW output power at the television frequencies of 700 to 850 MHz. Figure 1 is a photograph of the tube showing the collector at the upper end enclosed in a metal shield to minimize rf interference. The collector is composed of five elements, each operated at a different potential to provide the decellerating electric field for the electron beam. The operating conditions for the electron beam are 24.5 kV and 5 amperes. The collector elements operate with evenly divided potentials with just over 6 kV between each electrode. Typical power supply schematics are shown in Figure 2.

Measurements of current distribution to the collector elements were performed as a function of rf drive power. The results are shown in Figure 3. For no rf drive essentially all the beam current goes to electrode four, which is at a depressed potential of 0.75 times beam voltage. As drive increases, I_4 drops rapidly as I_3 increases, followed by I_2 then I_1. It is interesting to note that up to 10% of the current goes to element five which is at cathode potential and, consequently, does not involve power supply power.

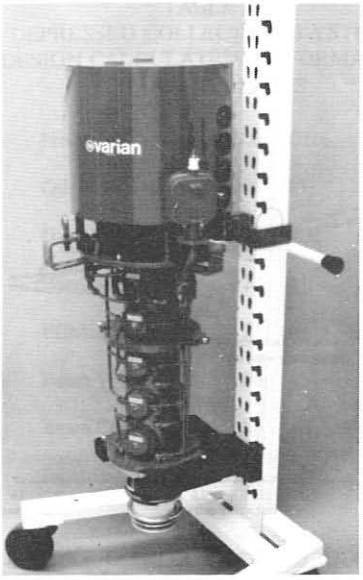

FIGURE 1

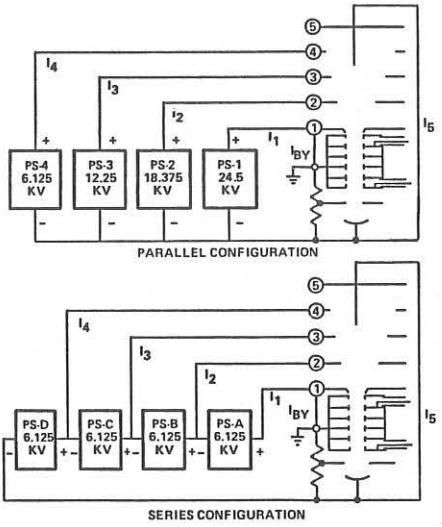

FIGURE 2. SCHEMATICS

With the measured performance characteristics, the collector efficiency was determined. This is the ratio of power recovered to spent beam power, plotted in Figure 4 along with the predicted value obtained by computer analysis. The measured performance compares closely with the previously calculated values supporting the accuracy of our computer modeling technique. The power distribution as a function of rf output level is shown in Figure 5. The power recovery (and efficiency enhancement) is greatest for operation below saturation. Even at saturation, however, the efficiency of this klystron is increased from 52% to 72% by employing the depressed collector design.

APPLICATION TO PLASMA HEATING

Using our computer-aided design technology, we evaluated potential depressed collector klystron designs appropriate for plasma heating application. In particular, we evaluated a design to provide 1 MW of power at 2 GHz. A four-stage collector design similar to that demonstrated on the UHF-TV klystron was used. The operating characteristics of this klystron design are listed in Table I. The basic interaction efficiency is 55%, which is increased to 77% by the power recovery achieved by the depressed collector.

The current distribution to the collector elements was determined, followed by the calculation of power supply requirements. The current and power requirements for power supplies of the parallel configuration, as shown in Figure 2, were evaluated and are listed in Table II.

The design analysis included evaluation of both electrical and mechanical characteristics to assure an adequate design from all viewpoints. In particular, the heat dissipation capability was evaluated to assure adequate thermal capability.

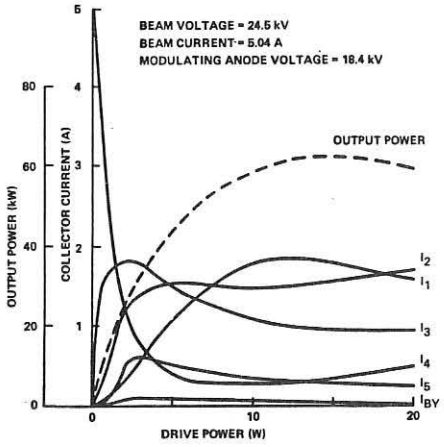

FIGURE 3. CURRENT DISTRIBUTION

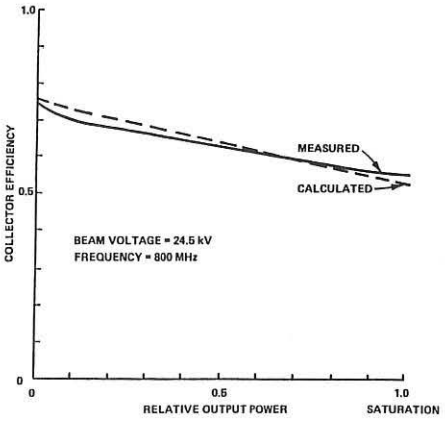

FIGURE 4. KLYSTRON COLLECTOR

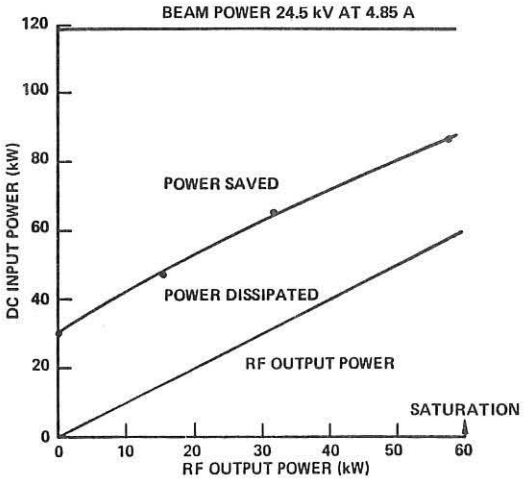

FIGURE 5. CALCULATED POWER DISTRIBUTION

TABLE I
DEPRESSED COLLECTOR KLYSTRON
DESIGN CALCULATED PERFORMANCE
CHARACTERISTICS

Frequency	2.0	GHz
Output Power	1000	kW
Gain	47	dB
Bandwidth	22	MHz
Efficiency	77	%
Beam Voltage	80	kV
Beam Current	22.6	A
Input Power	1300	kW

TABLE II
POWER SUPPLY REQUIREMENTS
PARALLEL CONFIGURATION

Power Supply Number	Voltage		Saturation Output	No Drive
1	80 kV	Current	8.31	.04 A
		Power	664.8	3.2 kW
2	60 kV	Current	7.18	0.18 A
		Power	430.8	10.8 kW
3	40 kV	Current	4.27	0.76 A
		Power	170.8	30.4 kW
4	20 kV	Current	1.66	21.64 A
		Power	33.2	432.8 kW
TOTAL		Current	21.42	22.62 A
		Power	1299.6	477.2 kW

CONCLUSION

Depressed collector technology holds promise for significant improvement of klystron efficiency. Computer modeling suggests designs with a predicted efficiency improvement of 1.35; tube performance data is slightly better at 1.38 (52% increased to 72%). To date, three UHF-TV klystrons of this design have been constructed and evaluated. All have provided similar performance. Using our computer modeling codes, we have evaluated other designs and have determined that depressed collector technology can be applied to high-power klystrons of the type used for plasma heating and similar improvements in efficiency can be expected.

REFERENCES

(1) McCune, E.W.: "Klystrons for Present and Future Lower Hybrid Resonance Applications", presented at the 4th International Symposium on Heating in Toroidal Plasmas, Rome, March 1984.

(2) Lien, E.L.: "High Efficiency Klystron Amplifiers", in Conv. Rec. MOGA 70 (8th International Conference, Amsterdam, Sept. 1970).

(3) Kosmahl, H.G.: "Modern Multistage Depressed Collectors — A Review", proceedings of the IEEE, November 1982.

(4) McCune, E.W.: "A UHF-TV Klystron Using Multistage Depressed Collector Technology", *IEEE IEDM Tech. Digest,* December 1986.

(5) McCune, E.W.: "Klystron Performance Using a Multistage Depressed Collector", *IEEE IEDM Tech. Digest*, December 1987.

THE SATURATION OF PURELY GROWING INSTABILITY DUE TO PARAMETRIC EXCITATION OF CONVECTIVE CELLS IN PLASMA

P.K.Shukla
Faculty of Physics and Astronomy, Ruhr University Bochum, F.R.Germany

V.N.Pavlenko, V.G.Panchenko
Institute for Nuclear Research of the Ukrainian Academy of Sciences, Kiev, USSR

The convective cell mode is a zero-frequency, purely damped, electrostatic mode involving only particle motion and perturbations in the direction perpendicular to the external magnetic field. These convective cell modes play a very important role in the anomalous transport processes and particles diffusion of magnetized plasmas [1,2].
It is known that in the magnetized plasma subjected the RF-pump wave a lower-hybrid waves can parametrically excite purely growing instabilities by coupling with purely damped convective cells [3]. In the report the nonlinear mechanism of purely growing convective cells instability stabilization due to the scattering of charged particles by suprathermal plasma fluctuations is presented. This process is described by the effective collision frequency ν_{eff} that determines the efficiency of the RF power dissipation in the plasma.
Consider the electron-ion plasma immersed in the magnetic field $\vec{B}_0 = B_0 \vec{z}$ and subjected the influence of an RF pump wave field $\vec{E}(t) = E_0 \vec{y} \cos\omega_0 t$ with frequency ω_0 near the lower-hybrid frequency $\omega_{LH} = \omega_{pi}\left(1 + \omega_{pe}^2/\Omega_e^2\right)$ ($\omega_{p\alpha}$ and Ω_α) are the Langmuir and gyrofrequency of the plasma patricles of kind α).
As it follows from [4], we can represent the electric field fluctuation spectral density in the form

$$\langle \delta\vec{E}\,\delta\vec{E}\rangle_{\omega,\vec{k}} = \frac{1}{\varepsilon_E(\omega,\vec{k})}\left\{\langle \delta\vec{E}^2\rangle^{o}_{\omega,\vec{k}} + \frac{\nu^2}{4}(\chi_e^{o})^2 \times\right.$$

$$\left.\times\left[\frac{\langle \delta E^2\rangle^{o}_{\omega+\omega_o,\vec{k}}}{|\varepsilon_1(\omega+\omega_o,\vec{k})|^2} + \frac{\langle \delta\vec{E}^2\rangle^{o}_{\omega-\omega_o,\vec{k}}}{|\varepsilon_{-1}(\omega-\omega_o,\vec{k})|^2}\right]\right., \qquad (1)$$

where $\nu = k_\perp E_o c/\omega_o B_o$, $\langle \delta E^2\rangle^{o}_{\omega,\vec{k}}$ and $\langle \delta\vec{E}^2\rangle^{o}_{\omega\pm\omega_o,\vec{k}}$ are the common correlation spectral functions of the non-interacting particles in the magnetized plasma in the absence of the pump field. The nonlinear dielectric permittivity $\varepsilon_E(\omega,\vec{k})$ is defined by the expression

$$\varepsilon_E(\omega,\vec{k}) = \varepsilon_o(\omega,\vec{k}) + \frac{\nu^2}{4}\chi_e^{o}\chi_i^{o}\left[\frac{1}{\varepsilon_1(\omega+\omega_o,\vec{k})} + \frac{1}{\varepsilon_{-1}(\omega-\omega_o,\vec{k})}\right], \qquad (2)$$

where $\varepsilon_{\pm1}(\omega\pm\omega_o,\vec{k})$ are the dielectric permittivities related to the upper and lower side-band respectively, $\varepsilon_o(\omega,\vec{k}) = 1+\chi_e^{o}+\chi_i^{o} = 0$ is the dispersion equation for the convective cells (χ_e^{o} and χ_i^{o} are the electron and ion plasma susceptibilities at the frequency $|\omega| \ll \omega_o$). We are interested in electrostatic short-wavelength ($k\rho_i \gg 1$, ρ_i is the ion Larmor radius) two-dimensional ($k_z = 0$) perturbations. Since the ion gyroradius is longer than the Debye length, collective effects due to the short-wavelength modes should be taken into account. The expression for χ_e^{o} and χ_i^{o} in this case are given by $\chi_e^{o} = 1/k^2 r_{De}^2$, $\chi_i^{o} = 1/k^2 r_{Di}^2\left(1 + i\,\frac{3(\pi+1)}{8\pi^{1/2}}\,\frac{\nu_i k\rho_i}{\omega}\right)$ and from the dispersion equation $\varepsilon_o(\omega,\vec{k}) = 0$ we have

$$\omega = -i\nu_i\,\frac{k\rho_i}{1+k^2 r_{Di}^2} \qquad (3)$$

The parametric coupling of the lower-hybrid pump wave with purely damped convective cell mode (3) is described by the equation

$$\varepsilon_E(\omega, \vec{k}) = 0. \tag{4}$$

From the dispersion equation (4) one can obtain the growth rate and the threshold of purely growing instability. In particular, the threshold strength of the electric field related to the excitation of such parametric instability is

$$E_{th}^2 = 8 \frac{\omega_0^2 B_0^2}{c^2} r_{De}^2 \frac{\Gamma}{\omega_{LH}}, \tag{5}$$

where Γ is the linear damping rate of the lower-hybrid wave for the case $k_z = 0$, $\Gamma = \left(\frac{\omega_{pi}^2 \nu_i}{\omega_0^3} + \frac{k_x^2 \omega_{pe}^2}{k^2 \Omega_e^2} \frac{\nu_e}{\omega_0}\right)\left(2\frac{\omega_{pi}^2}{\omega_0^3}\right)^{-1}$ [5]. It is easy to show that the intensity of the fluctuations increases infinitely in the instability threshold region $I_{\vec{k}} \sim \left(1 - E_0^2/E_{th}^2\right)^{-1}$ at $E_0 \to E_{th}$. We show that allowance for the additional wave damping due to charged particle scattering by suprathermal fluctuations leads to the stabilization of purely growing instability. We introduce the effective collision frequency as the property descriptive of charged particle scattering by turbulent fluctuations of an electrostatic field in the plasma. In the assumption that the main contribution to the collision integral is given by the term associated with the particle turbulent diffusion in velocity space we have the following equation for ν_{eff}.

$$\nu_{eff} = \frac{2 m_e \omega_0^2}{e^2 E_0^2 n} \int \frac{d\omega}{2\pi} \int \frac{d\vec{k}}{(2\pi)^3} \frac{\omega}{4\pi} \langle \widetilde{\delta\vec{E}\,\delta\vec{E}} \rangle_{\omega,\vec{k}} \sum_{\alpha} \operatorname{Im} \chi_\alpha^0, \tag{6}$$

where $\langle \widetilde{\delta\vec{E}\,\delta\vec{E}} \rangle_{\omega,\vec{k}}$ is the spectral density of the turbulent fluctuations in the plasma in the region above threshold

($E_0 > E_{th}$). The value of the correlator $\langle \delta\vec{E}\,\delta\vec{E} \rangle_{\omega,k}$ can be obtained from eq. (1), in which the eigen frequencies of the plasma are taken to be $\omega_j + i\nu_{eff}$ (ω_j are the eigen frequencies of the plasma in the absence of an pump field). The direct calculation shows that the fluctuations associated with the parametric excitation of the convective cells give the main contribution to the turbulent fluctuation spectral density. Assuming the condition $\nu_{eff.} > \Gamma,\ \nu_i k \rho_i$ to be fulfilled we obtain from the eq. (6)

$$\nu_{eff.} = \Gamma \frac{E_0^2}{E_{th}^2} \tag{7}$$

The expression (7) is held in the region

$$\frac{\nu_i k \rho_i}{\Gamma} < \frac{E_0^2}{E_{th}^2} < \frac{1}{\delta} \frac{\omega_{pe}^2}{\Omega_e^2} \frac{\omega_{LH}}{\Gamma} \tag{8}$$

We mention that for typical parameters of the hot plasma in which the lower-hybrid waves are used for the RF plasma heating the effective collision frequency which is defined by (7) exceeds both the linear damping of the lower-hybrid wave and the dissipation of the convective cell due to the ion gyroviscosity.

References

1. Okuda H., Dawson J.M. (1973) Phys. Fluids 16, 408.
2. Shukla P.K., Yu M.Y., Rahman H.U., Spatschek K.H. (1984) Phys. Reports 105, 207.
3. Yu M.Y., Shukla P.K. (1976) Phys. Letters 58A, 175.
4. Pavlenko V.N., Panchenko V.G., Revenchuk S.M. (1986) Sov. Phys. JETP 64, 50.
5. Shukla P.K., Yu M.Y., Spatschek K.H. (1977) Nuovo Cimento 41, 46.

LOW-HYBRID WAVE PROPAGATION AFFECTED BY A RANDOM MEDIUM LARYER

PAN Chuan-Hong QIU Xiao-Ming
Southwestern Institute of Physics, Leshan, Sichuan, China

ABSTRACT Making use of the stochastic model, we have studied the low-hybrid wave scattering by the density fluctuations in the edge-regions of Tokamak plasmas. The dispersion relation under considerstion includes not only the $\underset{\sim}{E}\times\underset{\sim}{B}$ convective derivation term but also the electromagnetic correction term. The results show us that the transmission coefficient decreases, whereas the reflection coefficient increases when the electromagnetic efect is takken into account.

1. BASIC EQUATIONS

The density fluctuations near the edge-plasma-region have been observed experimentally in number of present day Tokamaks. These fluctuations are generally thought to be due to a host of micro- and macro-instibilities as well as various stages of turbulence[1]. The effect of density-fluctuation on LH (low-hybrid) wave propagation has been discussed in some papers. An important theoritical model advanced by Morales and Lee[2] is called "nonlinear filamentation of low-hybrid cones" In addition to this, a stochastic madel has been developed by Papanicoloau[3], Morrison and Grossmann[4] et al. We use this model in our present work to discuss the LH wave scattering by the density fluctuation. Our model is similar to that of Grossmann[4] except including an electromagnetic correction term in this paper.

We consider a slab geometry. In our model problem, we let the plasma be contained in the region $-\infty<x<l$, density fluctuation layer (scattering layer) be located in $0<x<l$, vacuum region be assumed for $l<x<\infty$, LH wave impinge the plasma at $x=l$. Besides, we also assume that the plasma density is independent of z coordinete, magnetic field is uniform and tangent to z direction, density fluctuation is a stationary state, i.e.

$$B=B_0\hat{z},\quad n(x)=n_0[1+\xi(x)],\quad \langle\xi\rangle=\langle d\xi/dx\rangle=0 \qquad (1)$$

where $\xi(x)\equiv\delta n/n_0$ is the fluctuation quantity, which is considered to be a real function with zero mean.

In the electrostatic limit, $\underset{\sim}{E}=-\nabla\Phi$. The potential of the LH wave, Φ, obeys Poisson's law $\nabla\cdot(\underset{\approx}{\varepsilon}\cdot\nabla\Phi)=0$. If we introduce an electromagnetic correction term, the dispersion relation becomes

$$\nabla \cdot (\underset{\approx}{\varepsilon} \cdot \nabla \Phi) + D\Phi = 0 \qquad (2)$$

where $\underset{\approx}{\varepsilon}$ is the dielectric tensor and the second teom on the left hand side denotes the electromagnetic correction. Under the cold plasma approximation, $\varepsilon = \varepsilon_{\perp} (\hat{x}\hat{x}+\hat{y}\hat{y}) + \varepsilon_{\parallel}\hat{z}\hat{z} + i\varepsilon_{w} (\hat{x}\hat{y}-\hat{y}\hat{x})$. Besides, $D = (w^2/c^2)\,[-\varepsilon_{\parallel}\varepsilon_{\perp}+\varepsilon^2_{w}]$, In the hybrid frequency range $(\Omega_e >> \omega >> \Omega_i)$. $\varepsilon_{\parallel} = 1+\omega^2_{pe}/\Omega^2_e - \omega^2_{pi}/\omega^2 \approx 1$. $\varepsilon_{w} = \omega^2_{pe}/(\omega\Omega_e)$, $\varepsilon_{\perp} = 1-\omega^2_{pe}/\omega^2 - \omega^2_{pi}/\omega^2 \approx -\omega^2_{pe}/\omega^2$. Where $\Omega_e = eB/(m_e c)$, $\omega^2_{pe} = <\omega^2_{pe}>(1+\xi)$ are the electron gyro-frequency and the electron plasma frequency reapectively, $<\omega^2_{pe}> = 4\pi n_e e^2/m_e$, $\xi = 0$ outside the scattering layer.

Substituting these relations into Eq. (2) and noting that $\omega/\Omega_e << 1$, we obtain

$$\nabla^2_{\perp}\Phi - i\underset{\sim}{A} \cdot \nabla\Phi + (1+\xi)\,[\,-(<\omega^2_{pe}>/\omega^2)\,\nabla^2_{\parallel} + <D>]\,\Phi = 0 \qquad (3)$$

with $\underset{\sim}{A} \equiv M\hat{z} \times \nabla\xi$, $M \equiv <\omega^2_{pe}>/(\omega\Omega_e)$, $<D> \equiv (\omega^2/c^2)\,(\omega^2_{pe}/\omega^2)\,[1+M\omega/\Omega_e]$. Carrying out the Fourier transform in both y and z directions, $\Phi = u(x)\exp[i(k_y y + k_z z) - i\omega t]$, leting the inciden wave have unity amplitude and noting that the normalized refrective index in the vacuum is μ, we gain analytically the solutions of $u(x)$ in both vacuum region and quite plasma. In the scattering layer, function $u(x)$ satifies

$$d^2u/dx^2 + k^2_0\,\{1+\varepsilon\,\xi(x) + \varepsilon\, C(d\xi/dx) + G[\,1+\varepsilon\,\lambda\,\xi(x)\,]\,\}\,u = 0 \qquad (4)$$

Where $\tilde{k}^2_0 \equiv k^2_0 - k^2_z$, $k^2_0 \equiv <\omega^2_{pe}>k^2_z/\omega^2$, $g \equiv <D>/\tilde{k}^2_0$, $C \equiv -Mk_z/k^2_0$, $\lambda \equiv \tilde{k}^2_0/k^2$, $\varepsilon \equiv \varepsilon/\lambda$; ε represents the extent of fluctuation and is considered to be a small quantity, i.e. $\xi \to \varepsilon\,\xi(x)$, $\xi(x) \to O(1)$;

From the continuity of u and du/dx at x=l and the analytical form of the potential invacuum region, we obtain a random differential equation

$$\begin{aligned} dR/dl = i\tilde{k}_0(1+g)^{1/2}/2\mu\,[\,(1-\mu^2) + \tilde{\varepsilon}(1+\lambda g)/(1+g)\,\xi(l) \\ + \tilde{\varepsilon}\,C/(1+g)\,\xi_x(l)\,] \cdot \{R\exp[\,i\mu\tilde{k}_0(1+g)^{1/2}l \\ + \exp[\,-i\mu\tilde{k}_0(1+g)^{1/2}l\,]\,\}^2 \end{aligned} \qquad (5)$$

where R denotes the reflection coefficient $\xi_x \equiv d\xi/dx$. By leting $\mu = 1$, $g = 0$ and $C = 0$, we reproduce Papanicoloau's result' from Eq. (5). Of cause, we can use Hashminskii's thoery to solve Eq.(5) as same as doing in Ref.3. We here use a simple way instead of Papanicoloau's method, to get the reflaction coefficient (or transmission coefficient).

2. CONCLUSION AND DISCUSSION

Let $r > 0$ be the correlation length of fluctuation quantity ξ, and let us define $t \equiv x/r$, $L \equiv l/r$, $\bar{K}^2 \equiv r^2\tilde{k}^2_0(1+g)$. We find from Eq. (4) that the function $u = u(t)$ satisfies

$$d^2u/dt^2+\bar{k}^2(1+\tilde{\varepsilon}\,\bar{\xi})\,u=0. \qquad (6)$$

If the dimensionless variable t is thought to be a timelike argument, the original boundary value problem can be discussed as an initial value problem. In Eq.(11)

$$\bar{\xi}(t)\equiv[(1+\lambda g)/(1+g)]\,\xi(t) + \{C/[r(1+g)]\}(d\xi/dt), \qquad (7)$$

is a more general process. If $\xi(t)$ is assumed to be a Brownian process, we can prove that $\bar{\xi}(t)$ satisfies all of the hypotheses given in Ref.3, $\bar{\xi}(t)$ is still a Brownian process. Therefore, the precious theory developed by Morrison et al. can be used to discuss Eq.(6). Comparing Eq.(11) with the basic equation given in Ref.1, we obtain the mean or expected value of the fronsmitted power, which takes the form

$$1/\mu<|T|^2>=[4\sqrt{2}e^{-\bar{s}/4}/(\sqrt{\pi}\bar{s})]\int_0^\infty dv\,\{ve^{-v2}/[\theta+\cosh(2\sqrt{\bar{s}}v)]^{1/2}\} \tanh^{-1}\{\sqrt{2}\sinh(\sqrt{\bar{s}}v)/[\theta+\cosh(\sqrt{\bar{s}}v)]^{1/2}\}+0(\tilde{\varepsilon}^2). \qquad (8)$$

To get this result, Morrison et al. have assumed that no power-absorption takes place in scattering layer, i.e. $|T|^2=1-R|^2$. This result can be illustrated as follows. We can see from Eig.1 that the trens-mitted wave power power decreases monotonically with S increasing. In Eq.(13),

$$\bar{S}\equiv\tilde{\varepsilon}^2L(\bar{k}^2/2)\,\bar{I}(2\bar{k}),\quad \theta\equiv(\mu^2+1)/(2\mu) \qquad (9)$$

$\bar{I}(2\bar{k})$ is (one-half) the power spectral density of the generalized process $\bar{\xi}$. Let the two-point correlation function of the original process ξ, $\rho(\Delta x)\equiv<\xi(x+\Delta x)\cdot\xi(x)>$, be given by[1]

$$\rho(\Delta x)=\exp[-\xi_0^{-2}(\Delta x)^2] \qquad (10)$$

with $\xi_0\equiv 1/r$. We can derive a relation

$$\bar{I}(2\bar{k})=\{(1+\lambda g)^2/(1+g)^2+4C^2\bar{k}^2[r^2(1+g)^2]\}\,I(2\bar{k}) \qquad (11)$$

where $I(2\bar{k})$ is (one-half) the power spectral density of process ξ.

Under the large angle scattering condition $k_0^2<<\xi_0^{-2}$, we can prove that

$$\bar{S}=F(C.g)\,S \qquad (12)$$

with

$$F(C,g)=[1+g+4c^2k_0^2(1-k_\nu^2/k_0^2)]\,(1-k_\nu^2/k_0^2)\cdot\exp[4(k_0/\xi_0)^2(k_\nu/k_0)^2(1+g)]/\exp(4k_0^2/\xi_0^2)$$
$$S=(\varepsilon^2Lr^2k_0^2/2)\,I(2k_0). \qquad (13)$$

Where S is a dimensionless parameter defrned by Morrison et al. If we drop both the $\tilde{E}\times\tilde{B}$

convective derivative term and the electromagnetic correction term (i.e. leting C=0 and g=0), $\bar{S}=S$

Equation (14) shows that in the strong scattering limit, $k_0^2 \ll \xi_0^{-2}$, the parameter $\bar{S}$ gets larger when $C \neq 0$ and /or $g \neq 0$. Otherwise, we have known from Fig. 1 that the larger the parameter $\bar{S}$ is, the smaller the transmitted power will be. In other words, more power will be scattered when the LH wave propagates through the density fluctuation region if the electromagnetic effect is taken into account, We also note that $g \approx 1/N_\parallel$, where $N_\parallel$ is the parallel refrective index. In the typical Alcator C current-drive experiment the initial value of $N_\parallel$ is approximatoly 2-3, $g \sim 0.1$-0.25, $\bar{S}$ increeses by a factor of 10% or more due to the electromagnetic correction. As a result, the transmitted wave power decreases. However, in the Alcator C heating experiment $N_\parallel$ may be 3-5, in this case the increment of parameter $\bar{S}$ is less important, the electromagnetic effect on LH wave propagation is not considerable.

The conclussion is that after introducing an electromagnetic correction term the transmitted wave power lowers, or more power will be scattered by the density fluctuation layer.

REFERENCES

1. W. Grossmann et al., Phys. Fluids, 28, 1783(1985).
2. G. J. Morales and Y. C. Lee, Phys, Rev, Lett, 35, 930(1975).
3. G. C. Papanicoloatl, SIAM J. Appl. Math., 21, 13(1971).
4. J. A. Morrison et al., Commun. Pure. Appl. Math., 24, 473(1971)

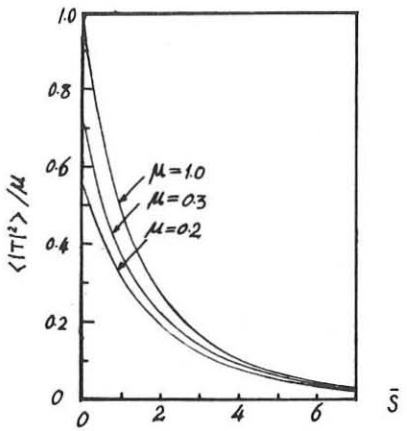

EFFECTS OF THE ALFVEN WAVE HEATING ON THE TCA PLASMA STUDIED BY THE DYNAMICAL RESPONSE

B. Joye, J.B. Lister and J.-M. Moret

Centre de Recherche en Physique des Plasmas
Association Euratom - Confédération Suisse
EPFL - LAUSANNE (Switzerland)

Studies of the dynamical response of the plasma to modulated Alfvén Wave Heating (AWH) power and to modulated gas puffing in ohmic conditions have been performed on TCA. In both cases, the radial profile of the phase of the electron temperature response exhibits a low value inside the q=1 radius, indicating the presence of a central thermal energy source. Absolute comparison of the gain and the phase in the two cases leads to the conclusion that the electron temperature perturbation during AWH is dominated by the influence of the density variation, with a peaked kinetic energy modulation profile. This at least partly explains the previously reported high performances of the AWH results.

Introduction Dynamical plasma response has been extensively used on TCA as a powerful and systematic approach to interpret AWH experiments [1]. The present study concentrates on the analysis of the soft X-ray flux as an electron temperature measurement . Experiments were carried out both during r.f. heating and in purely ohmic conditions.
TCA plasmas (a=0.18 m, R=0.61 m, B_φ=1.52 T) are heated by Alfvén Waves at 2.0 - 2.5 MHz launched by 8 phase-coherent antennae. Dynamical response measurements are performed either by sinusoidally modulating the r.f. power or the gas valve between 50 and 500 Hz or by superimposing a δ function. In the first case, a given signal y(t') is fitted in a time window of 5 to 50 ms to the form : $y(t') = Re(Y(t)) \cdot \cos(\omega t) + Im(Y(t)) \cdot \sin(\omega t) + \langle y \rangle(t) + d\langle y \rangle/dt\,(t) \cdot (t-t')$. This method has the same properties as a classical Fourier transform but allows a good time resolution even with a non-integer number of cycles and transient conditions with significant drift. In the second case, a transmittance, expressed as a rational function of $z=e^{sT}$ (s is the Laplace variable and T the sampling period), is identified by means of the Stieglitz method [2]. The advantage of the latter technique is that the frequency response can be determined in one shot and without using a specific waveform excitation. Comparison of the two analyses gives excellent agreement.

Dynamical response of the electron temperature to AWH Profiles of the normalised gain and of the phase of the soft X-ray response to a modulated r.f. power exhibit two distinct regions : the inner volume of the discharge displays the lowest gains and phases; outside a well defined radius both the gain and the delay increase. A plasma current scan between 55 kA and 125 kA clearly demonstrated that this separation surface is linked to the sawtooth inversion radius : results for 125 kA and 85 kA are plotted in Fig. 1 (a) and (b). At the highest frequencies used ($\geq$ 200 Hz), the phase profile inside q=1 becomes slightly convex. Therefore the outermost part of the inner volume possesses the lowest phase,

accompanied by a small peak on the amplitude, indicating the presence here of a thermal energy source. The large jump in phase outside this radius is associated with the good thermal insulation of the q=1 region, a property also observed on TFR during pellet injection [3]. Surprisingly, the phase profile is not affected by the positions of the resonance layers near which the wave energy is theoretically predicted to be absorbed.

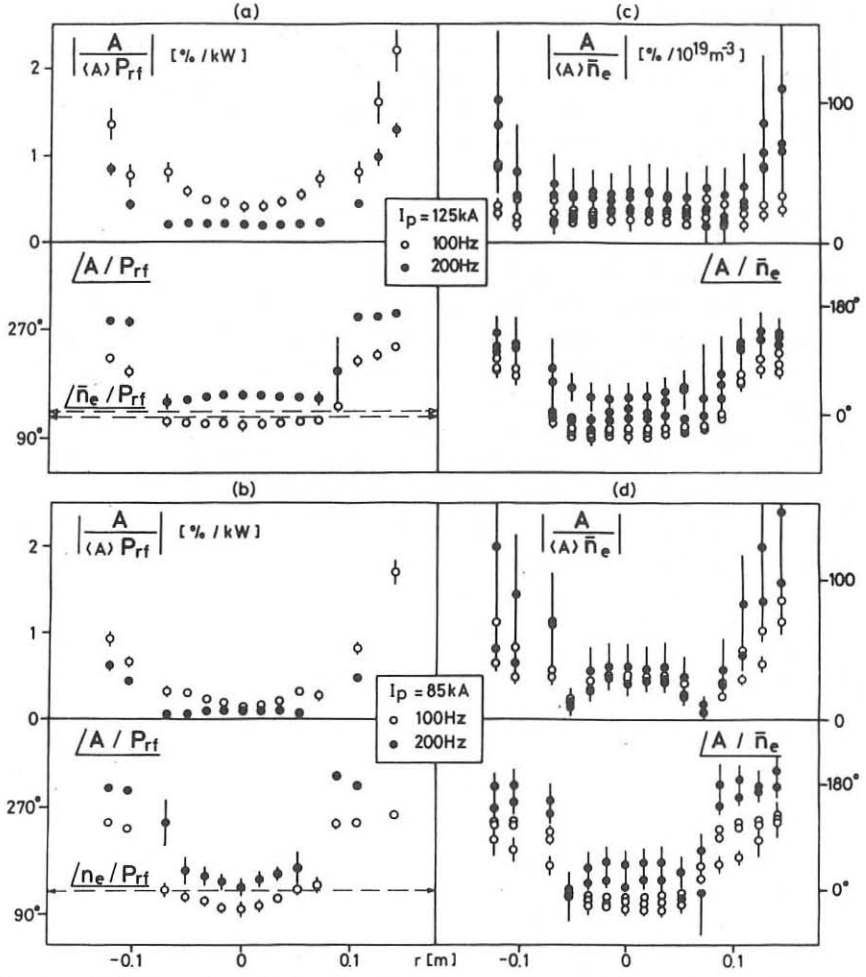

Fig. 1 *Relative gain and phase profile of the response of the soft X-ray, (a) and (b) during r.f. power modulation, (c) and (d) with gas valve modulation, (a) and (c) at 125kA, (b) and (d) at 85kA.*

At modulation frequencies much higher than the inverse local confinement time, the local energy is related to the local power deposition by an integration, giving a phase of 90°. The observed lowest phase however always tends towards 180° at high frequency. The diagnostic spatial resolution (18 mm) was checked to be adequate by carrying out the measurement during a current ramp, in order to make any possible 90° point cross through the visible chords. The only possible explanation in such a case is that the wave energy is not directly thermalised but there is an indirect mechanism driven by the r.f. power subsequently producing a thermal perturbation, such that a 90° delay can be generated. None of the damping mechanisms involved in Alfvén wave absorption has a sufficiently long characteristic time constant to produce this delay.

Dynamical response of the electron temperature to modulated gas puffing

AWH is accompanied by a large density increase. In order to quantify the influence of the density variation , the response of the soft X-ray signals to modulation of the gas valve was measured in purely ohmic discharges (Fig. 1(c, d)). The gain and phase profiles display the same characteristics as before : a low phase inner region and a shrinking of this volume when I_p is decreased. The phase on the axis however is close to zero or even negative, showing that n_e is not the driving mechanism but is only useful for comparison. The parallel can be extended further : if we choose as phase origin the phase between $\mathbf{n}_e$ and $\mathbf{P}_{rf}$, the phase profiles cannot be distinguished from each other even in absolute values ; both r.f. power and gas valve modulation produce identical relative amplitudes proportional to $|\mathbf{n}_e|$ (Fig. 2). The sawtooth period was previously found to be modulated out of phase by the r.f. power [1], a feature that can also be reproduced by sinusoidal gas puffing.

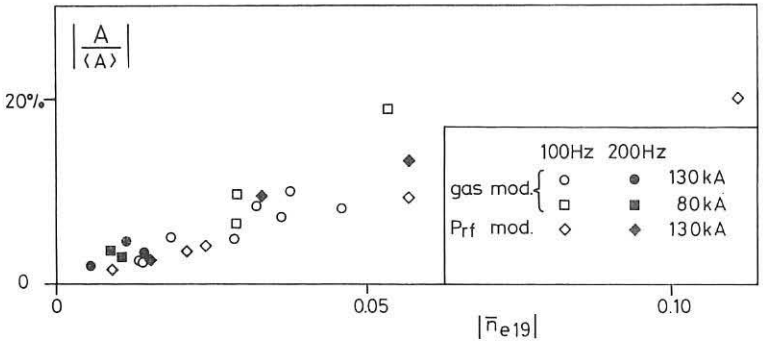

Fig. 2 Relative modulation amplitude during both r.f. power and gas valve modulation as a function of the density modulation amplitude.

Discussion The present discussion addresses the consequences of the previous results to the interpretation of AWH experiments and some considerations about the possible mechanism underlying the observations. A rough estimation of the perturbed electron thermal energy profile gives a peak to mean ration near 5 and in the r.f. case a volume integrated value matching $|P_{rf}|$. This goes a long way to explain previously reported AWH results yielding an astonishingly high heating efficiency and central power deposition estimated by radial power balance [4] or by sawtooth slope analysis [5]. In the case of direct electron heating, the expected modulation amplitude would be comparable to, or smaller than, the observed effect of the density. The superposition of the two contributions would lead, if placed in quadrature, to a maximum phase difference of 45°, experimentally difficult to identify. The dominant role of the density also explains the lack of sensitivity of the phase profile to the resonance layer position. In the two previous cases, a temperature perturbation arising from edge cooling can be discounted, as the source clearly originates inside or near q=1. Modifications of the confinement properties are also excluded : any power dependence of the thermal conductivity would give rise to a phase varying with the r.f. power amplitude, which was not the case in the experiments. The evident link with the current profile via the q=1 radius and the peakedness of the electron kinetic energy modulation amplitude may be symptomatic of a form of temperature profile consistency in both ohmic and heated conditions. A possible modulation of the local ohmic power or a possible exchange between internal poloidal magnetic and plasma kinetic energy cannot be excluded : as experimental evidence, the relative modulation amplitude of the Shafranov parameter $\beta + l_i/2$ is always smaller than the central soft X-ray chord modulation.

Conclusion Dynamical analysis of the plasma response to r.f. power and gas valve modulation have clearly shown that two perturbations can produce similar temperature responses. This response is characterised by a central thermal source certainly linked to the current profile and whose origin remains unknown. This presents an example of the difficulty in interpreting a non-stationary heating experiment while the ohmic behaviour of the target plasma is so badly understood.

Acknowledgement We would like to thank all the members of the TCA team. This work is partially supported by the Fonds National Suisse de la Recherche Scientifique.

References

[1] Joye B. et al., 1988, Dynamical plasma response to additional heating, accepted for publication in Plasma Phys. and Cont. Fus..
[2] de Larminat Ph., Thomas Y., Automatique des systèmes linéaires, Flammarion, Paris.
[3] TFR Group, 1987, 14th EPS Conf. Contr. Fus. Plasma Phys. (Madrid) **1**, 29.
[4] A. de Chambrier et al., 1985, X IAEA Conf. on Plasma Phys. and Contr. Nucl. Fus. Research (London) **I**, 551.
[5] Besson G. et al., 1986, Plasma Phys and Contr. Fus. **28**, 1291.

SHAFRANOV PARAMETER LIMITS FOR OHMIC AND R.F. HEATED PLASMAS IN TCA

B. Joye, J.B. Lister and F. Ryter*

Centre de Recherches en Physique des Plasmas
Association Euratom - Confédération Suisse
E.P.F.L, Lausanne, Switzerland

*present address: IPP, Garching, F.R.G.

An ohmic study is presented to define the experimental dependence of the value of $(\beta + l_i/2)$ derived from the Shafranov equation. The Alfvén Wave Heating pulse causes an increase in both $(\beta + l_i/2)$ and density, and with R.F., the value of $(\beta + l_i/2)$ is significantly greater than the ohmic scaling. However, the maximum R.F. values never exceed the maximum achieved ohmic values. As this limit is approached, the m=2 activity increases, as in the ohmic case, and we show that this increase correlates well with the increase in $(\beta + l_i/2)$.

Results : This paper studies the increase in $(\beta + l_i/2)$ measured during Alfvén Wave Heating (f~2.5 MHz) on the TCA tokamak (R, a = 0.61, 0.18 m, $B_\phi \leq 1.51$ T, $I_p < 135$ kA, D_2), and compares the results with ohmically heated discharges. When the R.F. pulse is applied, there is a significant and rapid increase in the value of the Shafranov $(\beta + l_i/2)$ calculated from the vertical field and plasma current. The origins of this increase, whether mainly β, mainly $l_i/2$ or both, are discussed in a companion paper [1]. Figure 1 illustrates the changes in $(\beta + l_i/2)$ when different R.F. power levels are applied, for a range of plasma currents and three excitation conditions (driving predominantly n=4, n=1 and n=2 waves). The increase in $(\beta + l_i/2)$ is largest for low plasma currents and most effective for the n=4 modes. Since, under our standard conditions, the n=4 resonance surfaces are in the outer part of the plasma, this result is at first sight surprising. This whole issue is further complicated by the substantial increase in density which occurs during the R.F. pulse.

In order to proceed further, we have studied the values of $(\beta + l_i/2)$ obtained in quasi-stationary ohmic discharges for three values of toroidal field (0.78, 1.16, 1.51 T) and plasma currents from 40-135 kA. The wide range of values obtained, Fig. 2a, can be reduced to an extremely good description of the density dependence by using the quantity $\Lambda^* \cdot (I_p/130\ \text{kA})$ where $\Lambda^* = (\beta + l_i/2 - 0.7)$. The value 0.7 was selected to give the least deviation in the data. This quantity does not itself appear to have any absolute merit. However, we can redraw Fig. 2b scaled by $1/B_\phi$ in which $\Lambda^* \cdot (I_p/130\ \text{kA}) \cdot (1.51\ \text{T}/B_\phi)$ is a well defined

function of $\overline{n_e}/B_\phi$, the Murakami parameter. That is to say the value of $\Lambda^*(\overline{n_e})$ divided by the value of β_p at the Troyon limit is determined by the fraction of the operational density range in ohmic conditions. The selected value 0.7 chosen to generate Λ^* corresponds to the minimum value of $(\beta + l_i/2)$ at high current (q_a=3), being roughly $l_i/2$ for q_a=3. At lower currents $(\beta + l_i/2 - 0.7)$ does not correspond to β, since the $l_i/2$ contribution is then larger (Fig. 1a).

When we look at non-stationary ohmic discharges, $(\beta + l_i/2)$ can be higher than predicted by the stationary scaling, for example during a rapid density ramp-up. An example is shown as a dashed line trajectory in Fig. 2b.

At the higher levels of R.F. power, the discharge evolution follows a much higher trajectory in the same plane and the maximum $(\beta + l_i/2)$ values achieved were shown in Fig. 1. Figure 2 shows the same results versus the plasma density and a certain alignment is already visible. With some hindsight we replot the data on the $\Lambda^* \cdot (I_p/130\ kA)$: $\overline{n_e}$ plane, Fig. 4, with a typical trajectory shown as a dashed line. The R.F. accessed region is way above the quasi-stationary ohmic scaling, and exceeds the trajectory for hard gas-puffing. The different plasma currents and excitation modes are now indistinguishable. The most noticeable feature is that the maximum $\Lambda^* \cdot (I_p/130\ kA)$ does not exceed the maximum ohmic value, that is, the ohmic value near the density limit ($\overline{n_e} \sim 8 \times 10^{19} m^{-3}$). At the lowest densities the effect of the R.F. is most marked, that is, when the ohmic discharge is "weakest".

The data shown in Fig. 4 are those obtained in pulses which did not disrupt. On trying to exceed this experimentally observed limit, a disruption will ensue, characterised by a progressive increase in the $B_{\theta a}(m=2)$ amplitude. This form of disruption is similar to the density limit disruption, but at a lower density, one at which there would be no significant m=2 activity in a quasi-stationary ohmic discharge. However, when we consider $\Lambda^* \cdot (I_p/130\ kA)$ as the determining parameter the phenomenology of the two types of disruption is similar, Fig. 5. The details of the excited spectrum are, however, important as already noted [2], and can systematically alter the dependence of Fig. 5, but not by very much. The observation that the disruptions are most likely to occur near a mode threshold corresponds to the observation that the highest point in the $\Lambda^* \cdot (I_p/130\ kA)$: $\overline{n_e}$ plane is also frequently close to a mode threshold.

The power levels in Fig. 1 (a,b,c) are much lower than the available R.F. power. It has always been considered that the n=2 excitation is preferable in that much more R.F. power can be delivered than for n=1, n=4. On reanalysing the highest power data, the trajectories of those shots do, nonetheless, lie within the distribution of Fig. 4. We had found a way of increasing the power acceptance in conditions in which the increase in $(\beta + l_i/2)$ had virtually saturated. In general, the longer R.F. pulses with lower ramp-rates produced less marked increases in $(\beta + l_i/2)$, and tolerated a greater level of R.F. power.

Discussion : These results show that all the quasi-stationary ohmic data can all be described by a simple law relating $(\beta + l_i/2)$ to the Troyon limit and the Murakami factor for a given density. In this parameterisation, the maximum achieved $(\beta + l_i/2)$ is simply studied for varying plasma conditions, and we find that, although we exceed the ohmic conditions for low density plasmas, we do not exceed the maximum value for $\overline{n_e}=8\times10^{19}m^{-3}$.

Acknowledgements : This work was partly funded by the Fonds National Suisse de la Recherche Scientifique.

References

[1] Th. Dudok de Wit at al., paper presented at this conference.
[2] K. Appert et al., 1987 Int. Conf. on Plasma Physics, Kiev, USSR, 1987. (LRP 321/87)

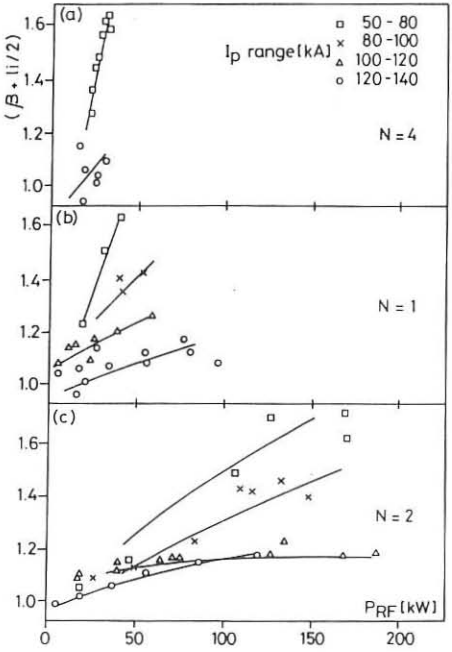

Fig. 1 $(\beta + l_i/2)$ achieved as a function of both delivered R.F. power and plasma current for a) n=4 b) n=1 c) n=2 [B_ϕ=1.51 T, f=2.5 MHz, D_2].

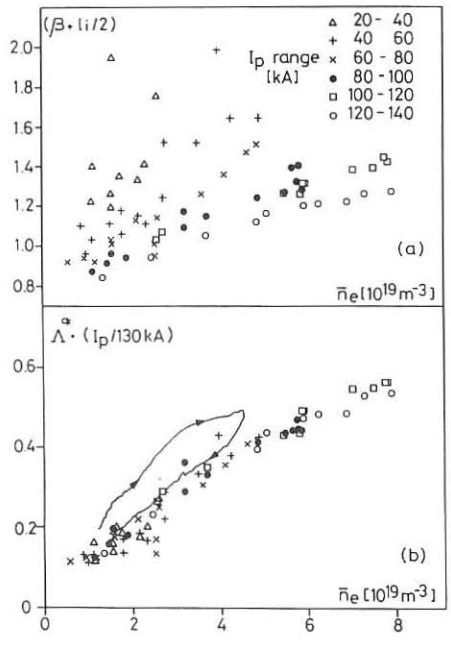

Fig. 2 a) $(\beta + l_i/2)$ as a function of n_e for ohmic discharges with different plasma currents b) $\Lambda^* \cdot (I_p/130$ kA) for the same data [B_ϕ=0.78, 1.16, 1.51 T, D_2].

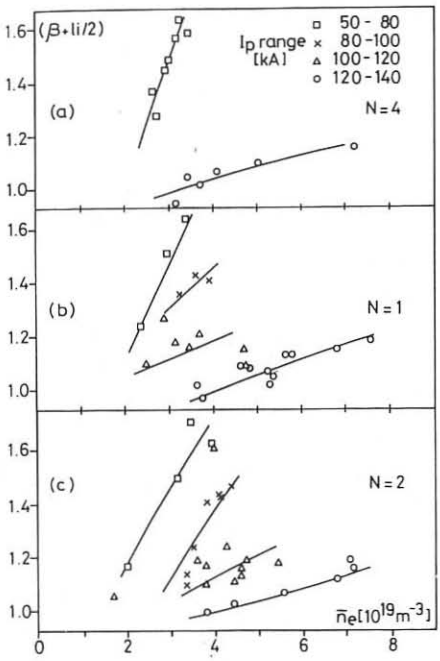

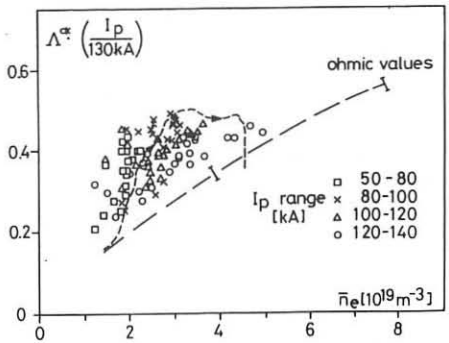

Fig. 4 R.F. discharges in the $\Lambda^* \cdot I_p : \bar{n}_e$ plane, for different plasma currents [B_ϕ=1.51 T, f=2.5 MHz, D_2].

Fig. 3 The data of Fig. 1 replotted as a function of the maximum density reached. ←

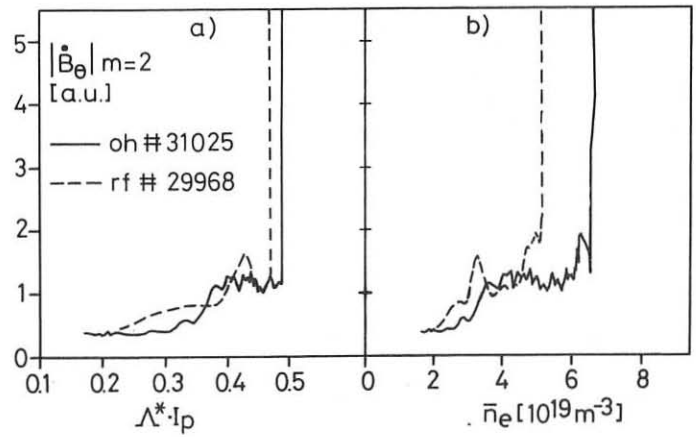

Fig. 5 Evolution of the m=2 amplitude as a function of a) $\Lambda^* \cdot I_p$ and b) $\bar{n}_e$ for ohmic and R.F. discharges.

ION TEMPERATURE EVOLUTION DURING ALFVEN WAVE HEATING IN TCA

A.de Chambrier, B.P.Duval, J.B.Lister, F.J.Mompeán* and J.-M.Moret

Centre de Recherches en Physique des Plasmas
Association Euratom - Confédération Suisse
E.P.F.L. Lausanne, Switzerland
* seconded from C.I.E.M.A.T., Madrid, Spain

ABSTRACT: The application of Alfvén Wave Heating, (AWH), is accompanied by an electron density (n_e) rise and an increase in the ion temperature, (T_i), measured with a Neutral Particle Analyser (NPA). A study was performed and a formula developed to model the T_i in non stationary ohmic discharges, to determine if the T_i increase is simply due to n_e. When compared with AWH discharges, the observed T_i is consistently higher than predicted by the ohmic model, indicating an additional source due to the RF. T_i also reflected the evolution of the AW spectra and reaches a maximum at the onset of a new continuum ie: when the resonant surfaces are in the outer half of the minor radius. T_i was investigated with modulated RF power, and a modulated gas puff, measuring the phase and amplitudes of the T_i rise relative to the perturbation. We conclude that the RF appears to have a direct effect on the T_i.

Introduction: The results described were obtained on the TCA tokamak (R, a = 0.61, 0.18m, I_p up to 170kA, B_ϕ up to 1.51T, Deuterium Plasma). T_i was measured with a five channel NPA obtained from the A.F.IOFFE Institute [1]. The installation, calibration, and operation of this spectrometer on TCA is described in detail by [2]. Additional RF heating was provided at a frequency of 2.0 - 2.5MHz with pulses up to 80msec long and delivered RF power up to 200kW. The details of the Alfvén Wave launching scheme are described in detail by [3] and a resumé of its application to TCA has been given by [4]. To recall the relevant features of this heating scheme, (N,M) are the toroidal and poloidal mode numbers of the exciting antennae structure and (n,m) are the mode numbers of the wave driven in the plasma. The RF energy is predicted to be damped by the electrons which have approximately the same thermal velocity as the Alfvén wave speed.

The RF pulse produces a rapid increase in $(\beta+l_i/2)$, the soft X-ray flux, n_e (see Fig 1b), and the flux in the NPA channels. For certain plasma conditions, the T_i measured by the NPA increases significantly [2].

Ohmic Study: The understanding of T_i is complicated by the increasing n_e, so the plasma may not be considered quasi-stationary. As n_e increases, the power transfer rate from the increased electron-ion collisionality leads to a T_i increase. An early effort to estimate this indirect heating term [5] suggested that the increase in T_i was greater than expected simply from ne. The timescale of the n_e increase makes a quasi-stationary analysis inadequate, obliging us to consider terms depending on dn_e/dt and dT_i/dt. The increase in T_i is observed to saturate at both high I_p and n_e. This saturation may be explained by the reduction in the collisional transfer from the electrons, and here only discharges for which I_p was constant are

considered. The ion power balance can be simply written, valid for an ill-defined central region, as:

$$dW_i/dt = 3/2\ e\ (dT_i/dt\ n_e + T_i\ dn_e/dt) = P_{ei} - 3/2\ e\ T_i\ n_e/\tau_{ei}$$

where W_i is the power of the ions, and, for the moment, all losses have been lumped together using an energy confinement time τ_{ei}. An empirical form $\tau_{ei}(n_e) = C\ n_e^a$ was chosen to reproduce the quasi-stationary form of $T_i(n_e)$. Fig. 1a) shows the results of this fit together with the experimental n_e trace exhibiting excellent agreement with the experimental trace. By introducing impurity gas puffs, we concluded that an unsupportably high impurity contamination would be required to significantly alter this analysis.

T_i During RF Heating: Applying the RF pulse leads to an increase in all the NPA channel fluxes the estimated T_i. The measured neutral particle energy spectrum before, during and after an RF heating pulse remains Maxwellian. The T_i increase is largest when the pre-RF T_i was lowest, and rises linearly with RF power, and saturates with the large n_e increase. For a discharge with AWH, the T_i calculated the ohmic model, and the measured n_e, differs from the measured value, Fig.1b. T_i increases at the start of the RF pulse, instead of the decrease which would be predicted by $dW_i/dt = 0$, suggesting that the model is incomplete.

In order to "correct" the simulation we would need to change at least one of the terms in the ion power balance. We could:

1) Add a term labelled "Direct Ion Heating" for which there is no theoretical support.
2) Modify P_{ei} by an anormaly factor which switched on during the RF pulse.
3) Suddenly reduce the ion losses by increasing τ_{ei} during the RF pulse.
4) Assuming that the incoming plasma is convected at high temperature.

Since in our analysis T_i is the result of these terms, we can not distinguish between these possibilities. In conclusion, we see the presence of a term that has the effect of directly heating the ions which is not accounted for by our ohmic model.

Effect of the Excited Spectrum: In the previous section, we treated one specific RF excitation condition with toroidal mode number n=2. As n_e increases with RF, the excited spectrum changes [4]. From the assumption of an RF induced ion power balance term, we might expect some spectral RF dependence. Three main excitation structures were driven with M=1 [3], and Hydrogen and Deuterium working gas was used, thus changing the spectral condition. The increase in T_i can change at the threshold of a Discrete Alfvén Wave, (DAW), signalled by an increase in the antennae loading curves. The form of the n_e increase can also change at this point and the maximum T_i is no longer obtained at the maximum value of n_e.

Figure 2 plots the maximum values of T_i and n_e during the RF pulse, not necessarily obtained simultaneously, for discharges with the same initial n_e and a range of RF powers. As the maximum n_e increases roughly linearly, T_i tends to increase. The RF power at which n_e rose sufficiently to cross the next Alfvén Wave threshold is marked by a vertical arrow. In this example, above this critical power, the maximum achieved T_i actually decreases. This

shows that the increase in T_i can be a strong function of the position in the AW spectrum, and is most "efficient" before a new threshold which corresponds to the RF resonance layers being far out in the plasma edge. Once the threshold is crossed, the new resonance surface, which is most important, is near the plasma centre. This new surface appears to have less effect on T_i.

RF Modulation Discharges: The RF power was sinusoidally modulated at 100Hz and the phase and amplitude response of n_e and T_i investigated. The analysis considers the T_i response as the sum of the change in the electron-ion collisional term, the n_e modulation and a postulated "direct" heating term. The magnitude of the direct term deduced from this analysis was larger than the supplied RF power indicating that the model is quantitatively deficient. Interestingly, the phase of the T_i response relative to the RF power was observed to slide between two quasi-stationary values across the passage of a DAW, Fig. 3, which correlates with the discontinuity observed with continuous RF heating. In a similar comparison to that above, the response to a modulated gas puff was investigated. The modulation frequency was limited to 30Hz by the relatively slow response of n_e to the gas valve, but no phase slide, similar to that with RF, was found. The linear analysis of the gas puff modulation experiments could also be interpreted as an increase in the ion energy confinement, but smaller than that observed with the RF.

Conclusions: This paper investigates the reaction of the ion temperature to Alfvén Wave Heating. The analysis has been handicapped by the n_e rise associated with the RF, which requires that many time dependent terms be included in the ion power balance. The n_e rise was modelled by a time dependent ion loss term for an ohmic discharge with a gas puff induced n_e rise. The RF heating induced n_e rise did not agree with this model, which lead us to consider a direct effect of the RF on T_i. An attempt made to calculate this term using RF modulation experiments, although tending to confirm the need for such a term, gives a value with an unreasonably high magnitude. Since the n_e rise with Alfvén Heating is not yet understood, it could still be argued that this postulated term could be solely due to a difference in the dynamics of the RF and gas puff. This could not explain the discontinuities in the T_i behaviour coincident with strong spectral RF features like the DAW. We thus conclude that T_i is in some way directly influenced by the RF, although we can not identify the term responsible.

In preliminary results, the RF induced n_e rise is observed to saturate with time. Using this, and the recent prolongation of the plasma pulse on TCA, and the ability of our RF generator to give longer pulses we hope to be able to continue these experiments with more stationary plasma conditions.

Acknowledgment: We would like to thank all the members of the TCA team for the machine operation and diagnostic information. This work is partially supported by the Fonds National Suisse de la Recherche Scientifique.

References:

[1] AFROSIMOV V.V. et al. Sov. Phys. Tech. Phys. 20 1 (1975)
[2] de CHAMBRIER A. Doctoral thesis 712 EFPL/CRPP LRP 345/88 (1988)
[3] COLLINS G.A. et al. Plas. Phys. Fluid. 29 2260 (1986)
[4] BESSON G. et al. Plas. Phys. & Contr. Fus. 28 1291 (1986)
[5] BEHN R. et al. Plas. Phys. & Contr. Fus. 26 173 (1984)

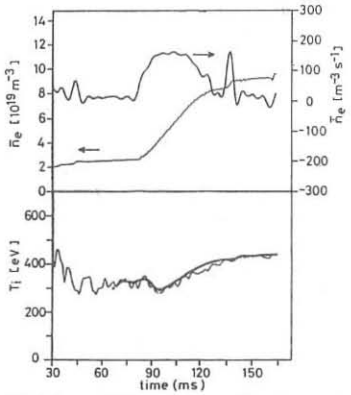

Fig 1a) ne and Ti for a discharge with a strong gas puff. The ohmic model fitted Ti is shown Bold

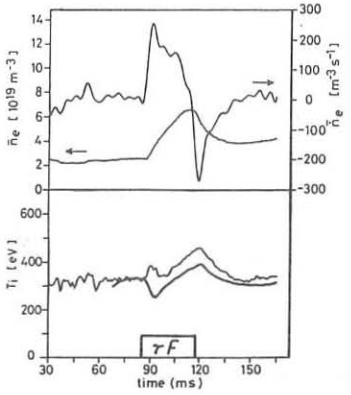

Fig 1b) As above, but for a Discharge with RF heating. The Ohmic model fit (Bold) is no longer in good agreement.

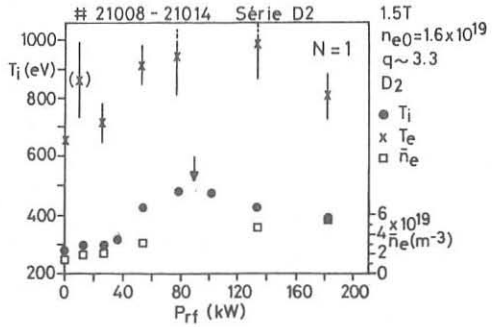

Fig 2) The maximum values of Ti and ne for a series of discharges with N=1 and the same initial density with a scan of RF power. The power at which the RF spectrum crosses a DAW is marked by a vertical arrow.

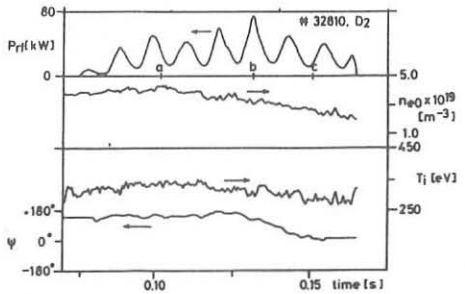

Fig 3) RF modulation experiment showing the deduced n_e and T_i. The phase of the T_i modulation relative to the RF is shown. As ne drops, there is DAW resonance, across which the phase is seen to change between two quasi-stationary values.

KINETIC AND CURRENT PROFILE EFFECTS OF ALFVEN WAVES IN THE TCA TOKAMAK

G.G. Borg, A.A. Howling, B. Joye, J.B. Lister, F. Ryter* and H. Weisen

Centre de Recherches en Physique des Plasmas
Association Euratom - Confédération Suisse
E.P.F.L., Lausanne, Switzerland

*present address: IPP, Garching, F.R.G.

Recent Alfvén wave experiments in the TCA tokamak show new evidence of the importance of kinetic effects and the influence of plasma conditions on the Alfvén wave. The R.F. magnetic field measured at the plasma edge reflects unambiguously the resonance of the kinetic wave eigenmodes in the plasma centre. The measured values of the resonance Q-factor of the principal eigenmodes are lower than predicted by the code by a factor of 3 to 20, although all expected damping mechanisms are included in the code. Alternative damping mechanisms are discussed and the best candidates proposed after quantitative evaluation. The R.F. itself modifies the plasma in such a way that the coupling strength can change very strongly. The experimental observations and the results of the code show that the current profile is certainly the best candidate which can affect the coupling in this way, implying that the R.F. pulse is able to influence the plasma current profile.

Observations of kinetic effects at the edge : In the kinetic description of AWH, the surface compressional wave mode converts to the KAW in the vicinity of the Alfvén Wave resonance layer (ARL). As the ARL moves outwards, standing waves of increasing order are formed due to reflection at the plasma centre. These standing waves, which occur for all (n,m) modes, appear as a sequence of resonances on the loading and edge plasma wavefield at a higher density than the principle DAW.

A comparison between experiment and the cylindrical kinetic code ISMENE [1] for the n=2 edge plasma wavefield is shown in Fig. 1, where the experimental, cold and kinetic theory fields have been plotted in the complex plane. From the figure it may be concluded that the resonances are a kinetic effect. The resonances disappear when the KAW is damped before reaching the plasma centre and so indicate approximately when energy deposition ceases to be central.

Width of the DAW resonance peaks : An important discrepancy between theory and experiment is the value of the quality factor, Q, for the DAW resonances. Figure 2a shows the experimental (2,1) Q as a function of

plasma current and R.F. power and Fig. 2b shows the theoretical Q for two representative current profiles as a function of plasma current. According to Fig. 2a, the DAW affects the plasma in such a way that its Q increases with R.F. power.

A comparison of the figures shows that the experimental Q is about 10 times lower than the theoretical Q, even though the kinetic code includes those damping mechanisms, electron Landau damping, transit time magnetic pumping and electron-ion collisions, known to be important for the damping of shear Alfvén waves. The theoretical Q is not a strong function of the electron temperature, or its profile.

Three mechanisms have been proposed which could lead to a lower Q than predicted and which are not contained in the model of a hot quiescent plasma.

Enhanced collision frequency due to MHD turbulence has been observed to lead to lower than predicted Q's for magnetoacoustic waves [2]. Calculations using the kinetic code with 1000 times the electron-ion collisionality revealed a negligible change in Q since the kinetic damping mechanisms dominate for TCA conditions. Turbulence enhanced electron-ion collisions do not therefore explain the low observed Q.

In toroidal geometry a DAW may couple to KAWs of several different surfaces already present in the plasma. This coupling, not contained in the cylindrical theory, could provide an additional energy loss channel for the DAW. Analysis of such coupling would require a 2D kinetic code. However, we have made numerical simulations based on coupled circuits, using the experimental observation that the KAW n_e at the (2,0) resonant layer increases by a factor of 5 during the passage of the (2,1) DAW. These reveal that the power transfer is insufficient to explain the observed Q. Until toroidal coupling is properly modelled, however, the energy loss of the DAW cannot be determined unambiguously.

Since the DAW resonance is density and plasma current dependent, a noise modulation of the average values of these parameters, or their profiles, will modulate the resonance condition and lead to a smearing of the resonance curve. Changes of ~ 3 % in $\overline{n}_e$ and ~ 10 % in I_p, required to reduce Q enough, would be too large. Plasma current and density profile wobulations are, therefore, most likely responsible for the low observed Q.

Effect of R.F. power on the Alfvén Wave spectrum : At high power levels in AWH, discontinuities are observed to occur in the plasma parameters at the continuum thresholds [3]. At the thresholds, the rate of density rise decreases or even changes sign and a drop in the plasma internal inductance (l_i) has been proposed to accompany a transient drop in R_{pl} [3,4].

Further evidence for a drop in l_i is shown in Fig. 3a. The density begins to decrease after the (2,1) threshold, however, the DAW fails to

reappear due to a drastic loss of loading as the spectrum is reswept. This is surprising since the DAW is relatively insensitive to plasma parameters provided the profiles of density and current are held fixed. The DAW loading decreases very rapidly for flat density profiles as the profiles become flatter; however, the change in density profile required to completely eliminate the DAW is larger than measured. Numerical calculations show that the DAW loading and coupling (R_{ant}/Q) are also strong functions of the plasma current profile, increasing linearly with l_i as shown for the coupling in Fig. 3b for the (2,1) DAW over a wide range of current profiles. Fig. 3b indicates that a flattening of the current profile can cause the DAW coupling to become vanishingly small, however, the interpretation is complicated by the presence of β in the experimental $\Lambda = (\beta + l_i/2)$ measurement. The problem of current profile modification is also treated in [5].

Conclusion : Results have been presented which show clear evidence that certain effects of Alfvén waves cannot be explained by the simple quiescent cold plasma MHD theory. Kinetic effects must be included to fully describe the standing KAWs observable in the edge plasma wavefield. Current or density profile wobulation appears the best candidate to explain the low observed Q. Static current profile changes occurring at continuum thresholds seem the best candidate to explain a markedly reduced DAW loading in experiments where the spectrum is reswept by a descending density.

Acknowledgements : This work was partly funded by the Fonds National Suisse de la Recherche Scientifique.

References

[1] Appert et al., (1987), in Proc. 7th Int. Conf. on Plasma Physics, Kiev, Invited papers Vol. 2, 1230.
[2] C. Ritz et al., (1982), Hel. Phys. Acta 55, p. 354.
[3] G. Besson et al., (1986), Plas. Phys. and Contr. Fuscon. 28, p. 1291
[4] K. Appert et al., (1987), in Proc. 7th Int. Conf. on Plasma Physics, Kiev
[5] Th. Dudok de Wit et al., (1988), Alfvén Wave Heating and its effects on the Tokamak Current Profile, this conference.

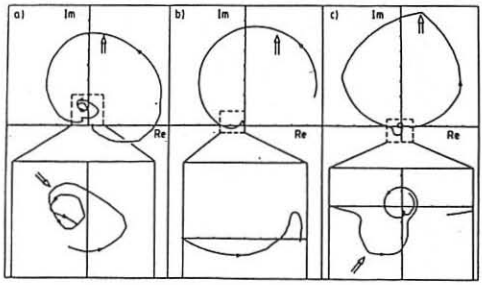

FIG. 1. The RF magnetic wavefield of the (2,1) DAW and KAW resonances plotted in the complex plane: a) experiment b) cold model c) kinetic model.

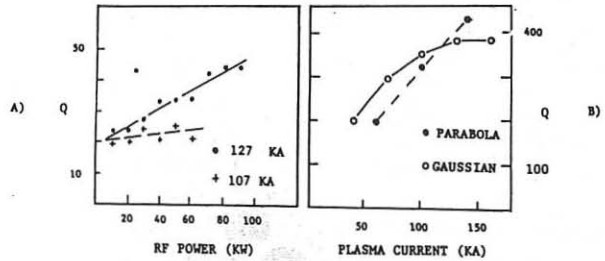

FIG. 2 A) measured Q of(2,1) DAW vs RF power.
B) Calculated Q of (2,1) DAW vs plasma current. using a parabolic and a Gaussian profile.

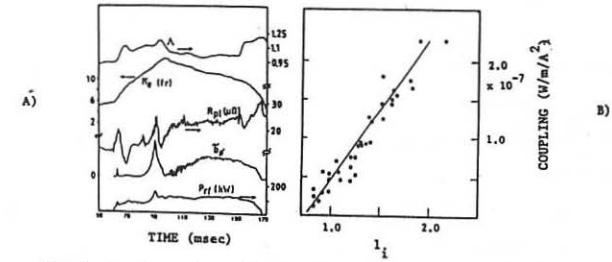

FIG. 3 A) Loss of coupling to DAW during density fall. Note change in lambda.
B) DAW coupling vs plasma internal inductance calculated from code using a wide range of plasma current profiles.

ALFVEN WAVE HEATING STUDIES IN THE TORTUS TOKAMAK

M.J. BALLICO, M.H. BRENNAN, R.C.CROSS, J.A. LEHANE and M.L. SAWLEY

Plasma Physics Dept. University of Sydney, Sydney 2006 Australia

Although Faraday shields are an integral part of ICRF heating antennas, it has not been clear whether a shield is necessary for Alfven wave heating since the excitation frequency and antenna voltage is low. Unshielded antennas are used in several Alfven wave heating experiments, for example in the TCA tokamak at Lausanne and in the PRETEXT tokamak at Austin. Although significant bulk heating is observed in these experiments, there is also evidence of a strong modification of the edge plasma. In TCA it is observed [1] that the antenna loading resistance decreases as the applied RF power increases and there is a large, uncontrolled increase in the line-averaged density during the RF pulse.

In this paper, we present the results of an experiment to compare shielded and unshielded antennas for Alfven wave heating in the TORTUS tokamak. It is shown that the addition of shields acts to suppress the density rise observed with unshielded antennas. The shields also act to minimise power deposited in the edge plasma by reducing the Langmuir currents drawn by the antennas and by reducing direct wave excitation in the edge plasma.

The TORTUS tokamak has a major radius of 44cm and minor radius 10cm. The experiments described below were conducted with a toroidal field $B_\phi \sim 0.7T$, and a plasma current $I_p \sim 20$ kA up to 20ms duration. Two antennas were used, situated above and below the plasma at the same toroidal location and phased to excite odd (mainly $m = \pm 1$) modes. All current carrying elements in the antennas were perpendicular to the toroidal magnetic field to minimise direct excitation of the shear Alfven wave in the edge plasma. Each antenna was equipped with a removable aluminium Faraday shield, as shown in Fig. 1. The shields contained vertical slots aligned in the toroidal direction and were coated

with titanium nitride to reduce sputtering. The antennas were driven with an RF pulse of duration 2ms, and up to 20kW input power, applied 9ms after the beginning of the discharge, at a fixed frequency 5.0MHz (corresponding to $\omega/\omega_{ci} = 0.55$). Several Alfven resonance surfaces for low toroidal modes $|n| \leq 4$, $m = \pm 1$ were present simultaneously in the plasma.

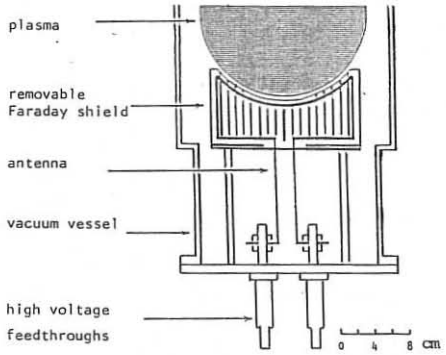

Fig.1. Schematic diagram of one antenna

Figure 2 shows the effect on n_e of applying RF power to the unshielded antennas. The density rise during the RF pulse is often sufficient to disrupt the plasma. The density rise is proportional to the RF power, but is totally suppressed when the shields are added.

The presence of the shields also results in a significant reduction in the antenna loading resistance, R_{ant}, defined as the increase in series resistance of each antenna (above the vacuum resistance) due to the plasma. Results are shown in Fig. 3. The value of R_{ant} for unshielded antennas decreases with increasing input power, as observed in TCA. A much weaker dependence of R_{ant} on input power is observed with shielded antennas. The antenna loading arises from a combination of the desired coupling to the bulk plasma and dissipation in the plasma edge. The results in Fig. 3. suggest that a significant fraction of the input power to unshielded antennas is deposited in the plasma edge.

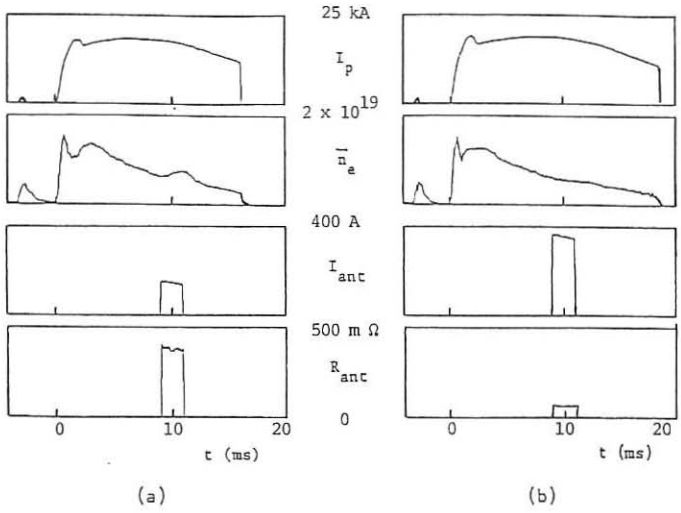

Fig. 2 Typical results for (a) unshielded and (b) shielded antennas at the same input power P ~ 8 kW.

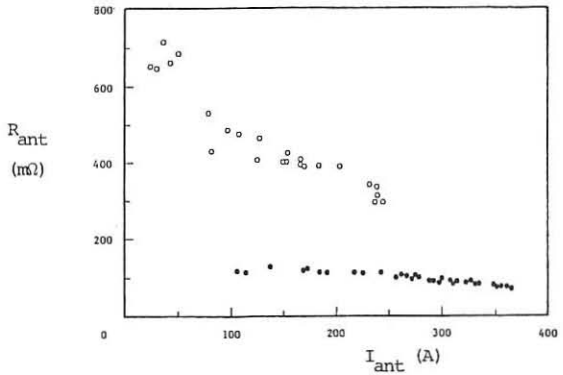

Fig. 3 Antenna loading resistance, R_{ant}, vs antenna current, I_{ant}, for shielded (•) and unshielded (o) antennas.

There are two mechanisms which we have identified in this experiment by which the input power can be deposited in the edge plasma. The

first is dissipation due to Langmuir currents drawn by the antennas. The Langmuir current was evident as a second harmonic component in the antenna current and was much larger when the antennas were unshielded. Both the shielded and unshielded antennas were allowed to float electrically with respect to the vacuum vessel and were observed to charge negatively to about 1 kV, as expected if the ion saturation current drawn during negative cycles balances the electron current drawn during positive cycles.

A second mechanism for edge dissipation was identified by measurement of the wave fields in the plasma edge. The wave fields were measured with a probe array, oriented to detect the b_θ magnetic field component. The array was inserted in a quartz tube surrounding the plasma poloidally at r = 11.2cm and location 180° toroidally from the antennas. The poloidal variation of b_θ can be interpreted in terms of direct excitation of shear waves, principally at the ends of the antennas [2]. Although the $b_\theta(\theta)$ structure was observed to be insensitive to the presence or absence of shields, the amplitude of the directly excited shear wave was significantly larger for unshielded antennas, as shown in Fig.4.

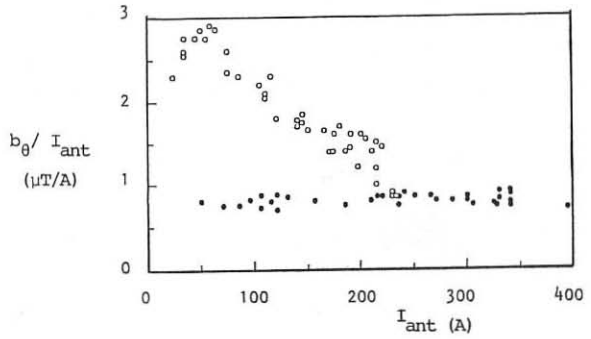

Fig.4. Poloidally averaged b_θ amplitude, normalised to the antenna current, I_{ant}, vs. I_{ant}, for shielded (•) and unshielded (o) antennas.

[1] Collins G.A. et al, (1986) Phys. Fluids **29**, 2260.
[2] Ballico M.J. et al, (1987) Proc. 14th Eur.Conf.CFPP,Madrid,**11D**,865.

TWODIMENSIONAL COMPUTATION ON ALFVEN HEATING OF A TOROIDAL PLASMA.

M.V.Dmitrieva, A.A.Ivanov, A.V.Sidorova, V.F.Tishkin, A.P. Favorsky

Keldysh Institute of Applied Mathematics USSR Academy of Sciences

A.G.Elfimov, F.M.Nekrasov, V.P.Sidorov

Vekua Institute of Physics and Technology, Sukhumi, USSR.

1.On studing Alfven plasma heating in tokamaks, it is of importance to concider natural twodimensional inhomogeneities of plasma parameters and magnetic field. Analytical and numerical analyses of MHD equations [1,2] in a linear approximation show that a local Alfven resonance in a torus is realized on magnetic surfaces only, in the neighbourhood of these surfaces refered as resonant ones, a HF power is absorbed. However, according to the unidimensional computations [3,4] , the absorbed power distribution depends upon the damping length of a kinetic Alfven wave which appears in the local resonance neighbourhood due to the conversion phenomenon. Thus, it becomes clear that kinetic effects should be considered in a twodimensional geometry. To this end, a twodimensional programme for solving numerically Alfven plasma heating problems in tokamak devices (ALKITOR 5) has been developed. Maxwell equations describing propagation, transformation and absorption of HF fields in a plasma and their generation by antennas are taken as initial ones. A driving system is fed by HF currents distributed along a toroidal helical antenna of radius $r = b$ the currents having a surface density of: $j_\theta = j_\theta^0 e^{i(M\theta + N\varphi - \omega t)}$ $j_\varphi = j_\varphi^0 e^{i(M\theta + N\varphi - \omega t)}$ is found from the condition: $div \vec{j} = 0$ The antenna is situated between the plasma($r = a$) and the conducting wall ($r = c$).

As it is known [3,4] ,plasma electromagnetic properties are defined by the dielectric permeability tensor. Here, we have used the local tensor approximation [3-5] for $T_e \gg T_i$, values of the components being defined by the magnetic surface radius. For the sake of simplicity, the surfaces have been assumed to be circular and coaxial. The unique numerical scheme created is based on a method of supporting operator which allowed to obtain conservative difference

schemes [5]

2. Computations are given for Alfven heating of a toroidal plasma of T-7 tokamak parameters [5]. Fig.1 shows the Fourrier-amplitudes $|E_m^r|^2$ for $m=1,0$ harmonics (antenna $M=1, N=2$) for MHD and kinetic computations. The HF field in a local resonance is multimode. The coupling between neighbouring local resonances can be greater in kinetic model due to the kinetic Alfven wave propagation. If to decrease the frequency in such a way that the local resonance $m=1$ should be absent, the so-called " under-threshold "excitation of $m=0$ local resonance would be expected. Fig.2 shows energy absorption on $m=0$, $\omega < \omega_{Hi}$. It follows from the theoretical and numerical analysis that the coupling between the harmonics of the local resonance eigenfunction is defined by $E_{M\pm1}/E_M \sim (Nq+M)\frac{r}{R}$ If this parameter value is of the order or greater than unity, the inter-mode coupling becomes stronger and several corresponding local resonances arise(see Fig.3),resulting in considerable angular and radial departures of the energy absorption profile(Fig.4) from that of the local MHD mode.

3. Conclusions:

a)In comparison with those of MHD the neighbouring local resonances can be coupled due to a kinetic wave,its damping length being greater than the distance between the resonances.

b)Using HF currents in an antenna with a preferentional mode $M=1$, the local resonance $m=0$ can be excited close to the plasma centre and the power absorbed in this resonance is maximum if the $m=1$ is absent.

c)Fourrier-analysis of HF fields has shown that at $(Nq+M)\,r/R \geq 1$ positions of toroidal local resonances do not coincide wiht those of their cylindrical analogues. A HF field structure is multimodal with approximatly equal amplitudes of several harmonics(up to 5 in number).

REFERENCES:

1. Kieras C.,Tataronis J.,J.Plasma Phys.1982,v.28,p.395.
2. Appert K.,Balet B.,Gruber R.,Troyon F.,Nucl. Fus.,1982, 22,p.903.
3. Boordo O.S.,Gorin V.V.,Dmitrenko A.G., Elfimov A.G., Fisika Plasmy 1983,9, p.697.
4. Dmitrieva M.V.,Grishanov N.I., Ivanov A.A.,et al. Preprint N 197,Keldysh Inst.Appl.Math.,Moscow, 1986.

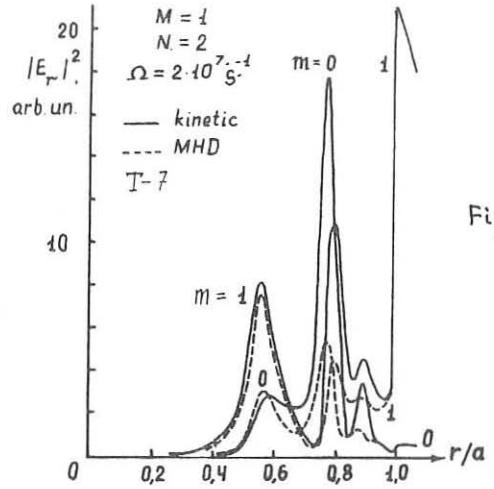
M = 1
N = 2
Ω = 2·10^7 s^-1
kinetic
MHD
T-7
|E_r|^2
arb.un.
20
10
0
m = 0
1
m = 1
0
1
0
0,2
0,4
0,6
0,8
1,0
r/a

Fig.1.

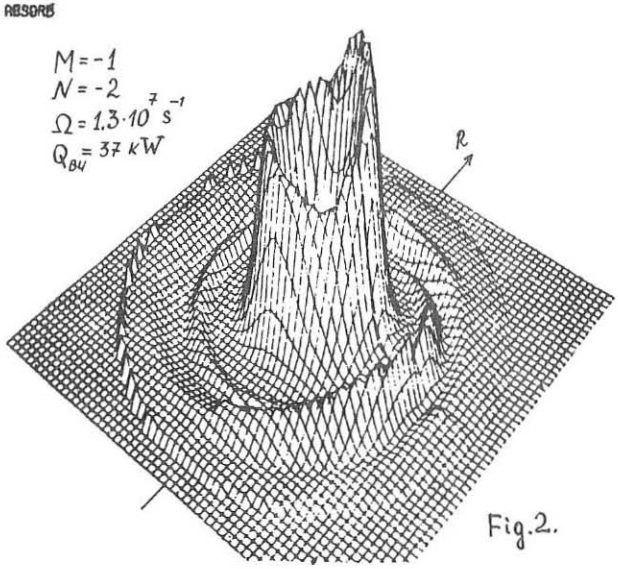
ABSORB
M = -1
N = -2
Ω = 1.3·10^7 s^-1
Q_BW = 37 kW
R

Fig.2.

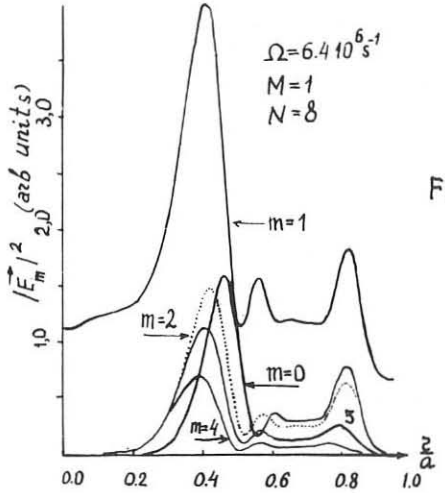

Fig.3.

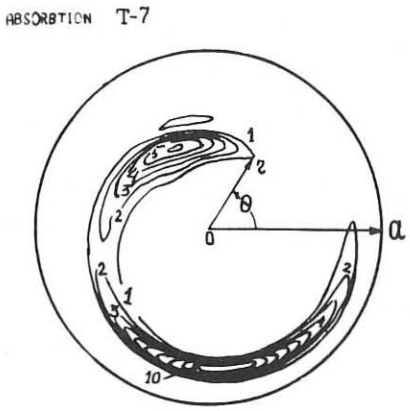

1 0.01840
2 0.03681
3 0.05521
4 0.07362
5 0.09202
6 0.11043
7 0.12883
8 0.14724
9 0.16564
10 0.18405

$\Omega = 6.4\ 10^6\ s^{-1}$
M=1
N=8
$\frac{a}{R} = 0.23$
$I_p = 0.15$ MA

Fig.4.

ALFVEN RESONANCE ABSORPTION IN A MAGNETOFLUID

D A Diver and E W Laing

Department of Physics and Astronomy,
University of Glasgow,
Glasgow G12 8QQ,
United Kingdom.

1. Introduction

In this paper, we tackle wave propagation in a warm MHD plasma, with non-uniform magnetic field. Earlier work in this area has concentrated on the Alfven resonance alone [1,2]. The novelty of this approach is the simultaneous treatment of both the Alfven and one of the magnetosonic singularities. The extra singularity has been noted in the past, [3,4] but we are unaware of any consistent treatment of both. We calculate reflection and absorption coefficients self-consistently by modelling the wave behaviour locally.

2. The magnetofluid model

Consider a one-fluid description of a perfectly conducting plasma with a scalar pressure. The relevant fluid equations are [5]

$$\frac{D\rho}{Dt}+\rho\nabla\cdot\mathbf{u}=0,\quad \frac{D\mathbf{u}}{Dt}=-\nabla p+(\nabla\times\mathbf{B})\times\frac{\mathbf{B}}{\mu_0},\quad \mathbf{E}+\mathbf{u}\times\mathbf{B}=0,\quad \frac{D}{Dt}(p\rho^{-\gamma})=0,\quad \frac{\partial\mathbf{B}}{\partial t}=\nabla\times(\mathbf{u}\times\mathbf{B}),\quad \nabla\cdot\mathbf{B}=0$$

where $D/Dt=\partial/\partial t+\mathbf{u}\cdot\nabla$ denotes the advective derivative, and the dependent variables have the usual meanings. These equations form a closed system, and so provide a complete mathematical description of all the physical processes of the model.

Restricting attention to small amplitude waves, it is sufficient to consider the linearised perturbation problem, in which the static equilibrium is

$$\mathbf{u}_0=0,\quad \mathbf{E}_0=0,\quad \nabla p_0=(\nabla\times\mathbf{B}_0)\times\mathbf{B}_0/\mu_0,\quad p_0\rho_0^{-\gamma}=constant. \tag{1}$$

The equations for the perturbed quantities may be combined self-consistently, yielding

$$\rho_0\ddot{\mathbf{u}}_1=\nabla[\gamma p_0\nabla\cdot\mathbf{u}_1+\mathbf{u}_1\cdot\nabla p_0]+[\nabla\times(\nabla\times(\mathbf{u}_1\times\mathbf{B}_0))]\times\mathbf{B}_0/\mu_0+(\nabla\times\mathbf{B}_0)\times[\nabla\times(\mathbf{u}_1\times\mathbf{B}_0)]/\mu_0. \tag{2}$$

In this paper, we will consider a plasma in which the equilibrium field $\mathbf{B}_0$ is plane stratified in the z direction :

$$\mathbf{B}_0=\hat{\mathbf{x}}B_{0x}(z)+\hat{\mathbf{y}}B_{0y}(z)=B_0(z)[\hat{\mathbf{x}}\cos\theta+\hat{\mathbf{y}}\sin\theta]. \tag{3}$$

The angle θ is a constant, and so this is the simplest non-uniform field satisfying $\nabla\cdot\mathbf{B}_0=0$.

This imposed variation now dictates the spatial structure of the pressure and density parameters. As a consequence, the spatial variations in the plasma are characterised by the functional dependence of the fundamental velocities, c_a and c_s.

Using the algebraic manipulation system REDUCE [6], we may eliminate u_x and u_y in favour of u_z in order to arrive at an equation for u_z :

$$\xi\psi u_z''+(\phi+\lambda\frac{q'}{q})u_z'+\psi q\,u_z=0 \tag{4}$$

where we have dropped the subscripts 0 and 1, and where the coefficients are defined as follows :

$$q = \omega^4 - k_x^2 V^2 \omega^2 + k_x^4 c_s^2 c_a^2 \cos^2\theta, \quad \xi = \omega^2 V^2 - k_x^2 c_s^2 c_a^2 \cos^2\theta, \quad \psi = \omega^2 - k_x^2 c_a^2 \cos^2\theta$$

$$\phi = \tilde{c_a^2}[(2-\gamma)\omega^4 + k_x^2\omega^2(c_a^2(\gamma-2) - 2c_s^2)\cos^2\theta + 2k_x^4 c_a^2 c_s^2 \cos^4\theta], \quad \tilde{c_a^2} = (\rho_0 c_a^2)'/(2\rho_0)$$

$$+ k_x^2 c_s^{2\prime}(\omega^2 - k_x^2 c_a^2 c_s^2 \cos^2\theta)(c_a^2 \sin^2\theta + c_s^2) + k_x^2 c_a^{2\prime}[\omega^2 V^2 \sin^2\theta - k_x^2 c_s^2 (c_a^2 \sin^2\theta + c_s^2)\cos^2\theta]$$

$$\lambda = k_x^2[k_x^2 c_a^2 c_s^2 \cos^2\theta(c_a^2 \sin^2\theta + c_s^2) - \omega^2(c_a^4 \sin^2\theta + c_s^4 + 2c_a^2 c_s^2 \sin^2\theta)]$$

When the equilibrium magnetic field is constant, then Fourier transforming in z yields $k_z^2 \xi\psi - \psi q = 0$, which is simply the expected dispersion relation [5].

Returning to the full problem, with non-uniform $\mathbf{B}_0$ and oblique wavevector ($k_x \neq 0$), we must tackle (4) in its full complexity. Note that there are four possible singularities in (4), namely the zeros of ψ, ξ and q . We will concentrate on the Alfven singularity $\psi = 0$ and one of the roots of q, which are close together for small θ.

3. A model comparison equation

In order to make progress in the analytical solution of this ODE, we will take the following form for ψ and q :

$$q = q_0 z\,, \quad \psi = \psi_0(z-\delta), \quad q_0 = (\partial q)/(\partial z)_{\delta/2}, \quad \psi_0 = (\partial\psi)/(\partial z)_{\delta/2}.$$

Note that λ may be written in the form $\lambda = -(a + b\psi)$, $a = 2k_x^2\omega^2 c_a^2 c_s^2 \sin^2\theta$, $b = k_x^2(c_s^4 + c_a^4)$, and so we incorporate this feature into our modelling, which will concentrate primarily on the effects of the singularities on the wave properties of the model, all other terms being taken as constants. Thus (4) becomes

$$\psi_0 \xi_0 (z-\delta)u'' + (\phi_0 - (a + b\,\psi_0(z-\delta))/z)u' + \psi_0 q_0 z\,(z-\delta)u = 0, \tag{5}$$

where we evaluate ψ_0, ϕ_0, a, b at $z = \delta/2$. Note that we have dropped the subscript z on the velocity.

It is most convenient to rescale the ODE so that the singularities are situated at the origin and the point $z = 1$. However, we must treat the special case of $\theta = 0$ separately, since in this case, $\delta = 0$ and there is only one singularity.

3.1. coincident roots : $\theta = 0$

Setting $\delta = 0$ in (5) yields the equation

$$z\,u'' + A_0 u' + C_0 u = 0. \tag{6}$$

This equation is of standard form, and has solution

$$u = z^{\frac{1}{2}(1-A_0)} K_{1/p}(\kappa z^{3/2}), \quad \kappa = 4(1-2s)/(3(A_0-1))\sqrt{C_0}, \quad p = 3/(1-2s), \quad 1-2s = \pm(1-A_0).$$

Note that there is total reflection in this case, independent of the details of A_0, C_0 and p.

3.2. separated singularities : $\theta \neq 0$

It is convenient in this situation to rescale the singularities in order that they occur at the origin and unity. Thus we make a change of independent variable, $\eta = z/\delta$, $\delta \neq 0$, to arrive at

$$\eta(\eta-1)u_{\eta\eta} + (A\,\eta + B)u_\eta + C\,\eta^2(\eta-1)u = 0, \tag{7}$$

$$A = (\phi_0 - b\,\psi_0)/(\xi_0\psi_0), \quad B = (b\,\psi_0\delta - a)/(\delta\xi_0\psi_0), \quad C = (\delta q_0)/(\xi_0)\sigma^2.$$

Note that the coefficients are now non-dimensional, and that the fundamental parameters of the problem can be taken as

$$\theta, \quad \beta = c_s^2/c_a^2, \quad \nu = (k_x^2 c_a^2)/\omega^2, \quad \sigma = k_x\delta, \quad G = (1/B_0)(\partial B_0)/(\partial z). \tag{8}$$

4. Local solutions

We construct an approximate solution at the origin by retaining in the coefficients of the ODE only those terms which are significant when $\eta \approx 0$. The resulting equation and solution is

$$\eta u_{\eta\eta} - B u_\eta + C\eta^2 u = 0, \quad u_0 = \eta^{\frac{1}{2}(1+B)} J_{\pm(1+B)/3}[2/3\sqrt{C}\,\eta^{3/2}]. \tag{9}$$

The solution at $\eta=1$ may be approximated in a similar way, by first making the change of variable $\zeta=\eta-1$. The equation here, with its solution is then

$$\zeta u_{\zeta\zeta} + (A+B)u_\zeta + C\zeta u = 0, \quad u_1 = \zeta^{\frac{1}{2}(1-A-B)} J_{\pm\frac{1}{2}(1-A-B)}[\sqrt{C}\,\zeta]. \tag{10}$$

For the overall picture in this analysis, we require the behaviour of u for large η. Taking the leading terms in each coefficient for large η, we have

$$\eta u_{\eta\eta} + A u_\eta + C\eta^2 u = 0, \quad u_\infty = \eta^{\frac{1}{2}(1-A)} J_{\pm(1-A)/3}[2/3\sqrt{C}\,\eta^{3/2}]. \tag{11}$$

At this stage we know both the local and global behaviour of the waves. However, before any physical interpretation of these forms can be made, we need to know A, B and C in terms of the fundamental plasma parameters (8). Note that these parameters are not all independent, since there are underlying assumptions about the propagation characteristics of the plasma.

In fact, we may use $\beta \approx \beta_{plasma}$ as an expansion parameter, and from Taylor expansion of q and ψ, we can identify eventually, omitting the details,

$$\nu \simeq 1+\tfrac{1}{2}\theta^2, \quad \delta \simeq \beta\theta^2/G. \tag{12}$$

Note that we have made the approximations $\mu \simeq 1-\theta^2$ and $q_s \simeq -1/\beta$. In addition, we have used $\partial\nu/\partial z = \nu(1+2\beta)G/\beta$, $\partial\beta/\partial z = -(\gamma+2\beta)G$. We may also calculate to leading order,

$$A \simeq -2\theta^2, \quad B \simeq \theta^2, \quad C \simeq -\theta^2\sigma^2/\beta, \tag{13}$$

where we have taken $q_s \simeq -1/\beta$.

Knowing all the coefficients as functions of the fundamental parameters, we can now procede with the interpretation of the local and asymptotic forms u_0, u_1, and u_∞.

5. Boundary conditions and the reflection coefficient

Assuming $G > 0$, then the asymptotic solution u_∞ demands oscillatory solutions for $\eta \ll 0$, and evanescent solutions for $\eta \gg 0$. This scenario is equivalent to propagation from the low field side.

Since this is a physical wave problem, we require bounded evanescent behaviour for $\eta \gg 0$. Thus the appropriate form of u_1 must be

$$u_1 = \zeta^m K_m(\kappa_1\zeta), \quad \zeta > 0, \quad m = \tfrac{1}{2}[1-A-B], \quad \kappa_1 = |C|^{\frac{1}{2}}. \tag{14}$$

Moreover, since u_0 must be oscillatory for $\eta < 0$, we can take

$$u_0 = \eta^{3m/2}\left[D_1 H_l^{(1)}(\kappa_0\eta^{3/2}) + D_2 H_l^{(2)}(\kappa_0\eta^{3/2})\right] \quad \eta < 0, \quad l = (1+B)/3, \quad \kappa_0 = 2|C|^{\frac{1}{2}}/3 \tag{15}$$

with D_1 and D_2 being constants to be determined.

Let the solutions u_0, u_1 be valid at the common point $\eta_c \in]0,1[$, so that an approximate overall solution may be constructed by matching function and gradient at η_c. Hence, for a consistent description, we must have

$$u_0(\eta_c) = u_1(\eta_c), \quad (\partial u_0/\partial\eta)_{\eta_c} = (\partial u_1/\partial\eta)_{\eta_c}. \tag{16}$$

However, we cannot apply (16) directly to (14) and (15) without first analytically continuing the forms u_0 and u_1 into the region $\eta \in]0,1[$.

Again, omitting the details, the matching of the analytically continued solutions yields two linear algebraic equations in D_1 and D_2. Inverting these yields an expression for the reflection coefficient :

$$|R|^2 = [\,4\eta_c^2(\eta_c-1)^2[9/4\eta_c K_l'^2 F_m\ \kappa_0^2 + K_l^2 F_m(')\ \kappa_1^2] + 3\sqrt{\eta_c}(K_l^2)' F_m'\eta_c^2(\eta_c-1)^2\ \kappa_0\kappa_1 \quad (18)$$
$$+ [3\sqrt{\eta_c}(K_l^2)' F_m\ \kappa_0 + 2K_l^2 F_m'\ \kappa_1]\tau\eta_c(1-\eta_c) + K_l^2 F_m\tau^2\,]$$

$$[\,4\eta_c^2(1-\eta_c)^2[9/4\eta_c F_l(') F_m\ \kappa_0^2 + F_l F_m(')\ \kappa_1^2] + 3\sqrt{\eta_c}[F_l' F_m'\ \kappa_1 + 4W_l W_m\cos(m\pi)]\eta_c^2(1-\eta_c)^2\ \kappa_0\kappa_1$$
$$+ [3\sqrt{\eta_c}F_l' F_m\ \kappa_0 + 2F_l F_m'\ \kappa_1]\tau\eta_c(1-\eta_c) + F_l F_m\tau^2\,]$$

where

$$F_l = \pi^2 I_l^2 + K_l^2 + 2\pi I_l K_l \sin(l\pi),\quad F_m = \pi^2 I_m^2 + K_m^2,\quad F_m(') = \pi^2 I_m'^2 + K_m'^2,$$

and similarly for $F_l(')$, where $'$ denotes differentiation with respect to the relevant Bessel function argument, and $\tau = 3l - (3l - 2m)\eta_c$, $W_j = \pi(I_j K_j' - I_j' K_j)$.

At first sight, (18) looks rather daunting, but close inspection reveals certain symmetries. Note for instance that the role played by K_l^2 in the numerator is taken by the function F_l in the denominator, and also that the expression is evenly weighted in κ_0 and κ_1. The different Bessel function arguments at zero and unity account for the extra term $\sqrt{\eta_c}$ associated with every factor of κ_0.

Although no value of η_c has been specified at this stage, clearly $\eta_c = \frac{1}{2}$ is the most appropriate choice, since it is the point with respect to which all local parameter values and gradients were defined.

A small argument expansion of the formula can be taken to reveal limiting behaviour. Taking

$$K_\nu(z) \simeq \tfrac{1}{2}\Gamma(\nu)(\tfrac{1}{2}z)^{-\nu},\qquad I_\nu(z) \simeq (\tfrac{1}{2}z)^\nu/\Gamma(1+\nu).$$

we may take the leading term expansion to be $F_l \simeq C_-\kappa_0^{-2l} + C_0$, $F_m \simeq D_-\kappa_1^{-2m}$. where $C_0, C_\pm$ and D_- are defined in terms of the appropriate Bessel expansions.

Consequently, we have

$$|R|^2 = (\varepsilon_0 C_-)/(\varepsilon_0 C_- + \varepsilon_1 C_0\kappa_0^{2l}),\quad |C_{abs}|^2 = (\varepsilon_1 C_0\kappa_0^{2l})/(\varepsilon_0 C_- + \varepsilon_1 C_0\kappa_0^{2l}), \quad (19)$$
$$\varepsilon_0 = [1/4(9/8l^2 + m^2) + 3/\sqrt{8}lm - (\tfrac{1}{2}(3\sqrt{2}l + 2m)\tau + \tau^2],\quad \varepsilon_1 = [1/4(m^2 - 9/8l^2) - m\tau + \tau^2].$$

Note that we may take $\kappa_1 = 3/2\kappa_0 = |C|^{1/2} \simeq 2\times10^{-17}\sqrt{n}\,a\,\omega\sqrt{\beta}\theta^3/B_0$ where a is the tokamak minor radius.

6. Discussion

Note that for $\theta = 0$, $|C_{abs}| = 0$, in keeping with the general result of (6). At first glance, it would appear that the results (19) imply very small absorption, but it should be kept in mind that (19) is merely the small argument expansion of (18), the full and general reflection formula. If instead $|C|^{1/2}$ were large, for example if the wave frequency was of order of GHz rather than MHz, then the I_l would dominate over K_l, leading to very much smaller reflections and therefore enhanced absorption.

7. Acknowledgments

We are grateful for useful comments on this work from Dr. C N Lashmore-Davies. One of us (DAD) would like to acknowledge funding from UKAEA Culham Laboratory.

8. References

[1] L Chen, A Hasegawa : Phys. Fluids, **17** , 1399, 1974.
[2] J A Tataronis, W Grossman : Nuclear Fusion, **16** , 667, 1976.
[3] H Grad : Proc. Nat. Acad. Sci. USA, **70** , 3277, 1973.
[4] K V Appert, R Gruber : Phys. Fluids, **17** ,1471, 1974.
[5] J P Goedbloed : Lecture Notes on Ideal Magnetohydrodynamics, Rijnhuizen Report 83-145.
[6] REDUCE 3.3 User's Manual, High Level Hardware Ltd, Windmill Road, Oxford, 1987.

ALFVÉN WAVE HEATING OF TOROIDAL PLASMAS WITH NON-CIRCULAR CROSS SECTIONS

Satish Puri

MPI für Plasmaphysik, EURATOM Association, Garching bei München

Toroidal plasmas of non-circular cross sections display an enhanced coupling to Alfvén waves. Antenna loading resistance increases with the plasma elongation resulting in typical antenna $Q \approx 8$ *corresponding to* $V_A < 10\sqrt{P}\,kV$ *and* $I_A < \sqrt{P}\,kA$, *where* P *is the antenna input power in MW. Simultaneously, the radial penetration of the radiofrequency energy into the plasma improves, enabling heating near the plasma core. Alfvén wave heating offers an attractive alternative to the ICRF heating schemes, possessing such important advantages as (i) lower antenna voltage, (ii) well defined absorption process insensitive to the precise plasma composition, and (iii) relative freedom from surface effects. Consequently, Alfvén waves are eminently suited for the heating of the Stellerator, the Doublet, and the non-circular Tokamak plasmas.*

1. INTRODUCTION

Coupling to Alfvén waves is primarily dictated [1,2] by the choice of the toroidal wave number n. The loading resistance increases rapidly with n, reaching a maximum for $n \approx 8$. The reason for this behaviour is traced [2] to the improvement in the conversion efficiency from the compressional to the torsional mode near the resonance layer for larger values of ω/ω_{ci}. The prospect of having to install up to sixteen antennas around the torus circumference is, in any case, unavoidable for coupling approximately $100\,MW$ of radiofrequency power to attain thermonuclear ignition.

The antenna loading is relatively insensitive to the remaining plasma and antenna parameters [1], with the important exception of the radial location of the Alfvén resonance layer. This is because the close juxtaposition of the oppositely phased adjacent antenna sections needed for obtaining $n = 8$ causes a rapid radial evanescence of the antenna field. As a result, the resonant absorption layer in cylindrical geometry has to be located at $r_A/r_p \geq .67$, where r_A is the radial location of the Alfvén resonance and r_p is the plasma radius. This limitation may constitute the most serious drawback of otherwise promising features of Alfvén wave heating.

In this paper it is pointed out that the non-circular cross section plasma configurations of practical thermonuclear interest promote significantly improved antenna loading while simultaneously obviating the radial energy penetration problem.

2. ALFVÉN WAVE PENETRATION INTO THE PLASMA CORE

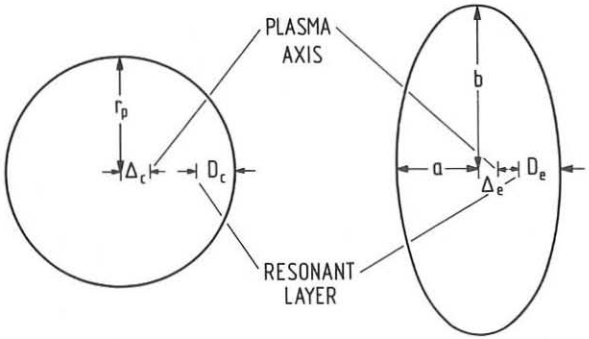

Fig.1 Improved Alfvén wave penetration in a plasma of non-circular cross section.

In Refs.[1, 2] it was shown that the Alfvén waves can penetrate a cylindrical plasma to a depth $D_c \sim r_p/3$ (Fig. 1) for $n = 8$. In the case of a plasma with an elliptical cross section of elongation $\varepsilon = b/a$ (a and b are the semiminor and semimajor axis, respectively), using $r_p = a\sqrt{\varepsilon}$, one obtains $D_e \sim a\sqrt{\varepsilon}/3$. The finite $\beta_{pol} \sim 1$ causes an outward shift of the plasma axis by an amount $\Delta_c \approx r_p/A$ and $\Delta_e \approx a/A$, where A is the torus aspect ratio. For the elliptical geometry, the distance of the resonance surface from the plasma center, measured along the minor axis is given approximately by $(a - D_e - \Delta_e) \approx .25a$, for an elongation $\varepsilon = 2$. This implies the possibility of depositing the wave energy near the plasma core, thereby removing a major hurdle in the practical application of Alfvén wave heating to thermonuclear plasmas. Although both ε and β_{pol} play comparable roles in improving the penetration depth, the full benefit of β_{pol} must await the appearance of hotter, denser plasmas.

Another effect capable of significant improvement in the penetration depth is the outward shift in the cutoff position due to an increase in ϵ_x' and a lower effective value of n_y in plasmas of non-circular cross sections. The amount of this shift may be estimated from Eq.(A8) of Ref.[2]

$$\gamma_1 = \epsilon_x - n_z^2 = \pm\frac{1}{2}\frac{\epsilon_x'}{k_0 n_y} - \frac{1}{2}\left(\frac{\tilde{\epsilon}_y}{n_y}\right)^2 , \qquad (1)$$

where the two terms on the right originate from the gradient and the enhanced Hall effect, respectively. Restoring the position of the cutoff by changing the frequency would result in further increase in the penetration depth. Alternatively, the shift in the cutoff might be utilized to enhance the antenna loading as described in Sec. 3.

3. ENHANCED ANTENNA LOADING

For cylindrical plasmas it is possible to obtain $Q \approx 17$ under optimum conditions [2]. In comparison with the ICRF case, the low frequency operation for the Alfvén wave heating allows coupling at considerably lower voltages. As mentioned in the preceding section, a further reduction in the antenna voltage is anticipated for plasmas of non-circular cross sections. The shift in the cutoff position causes an increase in the value of β (see Appendix A in Ref.[2]) by a factor $\sim \sqrt{\varepsilon}(2-\varepsilon^{-1}) \approx 2$ for $\varepsilon = 2$. This has an effect equivalent to increasing the toroidal wave number n by a factor of $\sqrt{2}$ without the attendant increase in the radial evanescence. The estimated antenna loading would increase by a factor > 2 with a resultant $Q \approx 8$, corresponding to $V_A < 10\sqrt{P}\,kV$ and $I_A < \sqrt{P}\,kA$, where P is the antenna input power in MW.

Further improvement in coupling is contributed by the decreased evanescence due to the smaller effective value of n_y in a non-circular cross section plasma. This effect will become important in the case of the future requirements of recessed antenna configurations. Compared to the ICRF case, Alfvén wave coupling is insensitive to the antenna separation from the plasma due to the inherently large evanescent region.

4. EDGE AND IMPURITY HEATING

Presence of a longitudinal electric field component in the absence of Faraday shielding would couple rf energy to the torsional surface wave [3], capable of surface heating of the plasma electrons and causing a density rise. An improper alignment of the Faraday screen gives rise to moderate coupling to the surface wave as well [2]. A properly designed Faraday screen completely closed on its sides, precluding the leakage of longitudinal electric fields, would eliminate this source of plasma surface heating.

Heavy ion impurity atoms could be accelerated to potentially damaging energies, unless care is exercised in limiting the electric field in front of the Faraday shield to $E_\perp \leq 7.1(T_{max}/A)^{1/2}\, B_0\, kV/m$, where $T_{max}(eV)$ is the maximum admissible impurity ion energy, A is the atomic number and $B_0(T)$ is the toroidal magnetic field [4].

The longitudinal electric fields, shielded by completely solid Faraday screen sides will continue to persist within the Faraday shield chamber with capability to accelerate charged ions within the enclosure to full antenna voltages. Although a segmented antenna construction will tend to limit the maximum energy gain, it would still be necessary that the front of the Faraday screen allows no access to charged particles. Such a condition might be obtained by using overlapping slanted vanes in the form of a Venetian blind [4].

Unlike ICRF heating, Alfvén waves do not couple to alpha particles, are not affected by the presence of impurities, and are insensitive to the precise plasma composition.

5. DISCUSSION

Alfvén wave heating has lacked credibility due to the poor radial penetration limited to $r/r_p \geq .67$ [1,2]. We have endeavoured to resolve this problem in this paper. Non-circular plasma configurations considerably enhance the penetration capabilities of the Alfvén waves while simultaneously improving antenna loading.

The Alfvén wave heating of plasma electrons is unlikely to be a limitation in the higher density plasmas, and the fact that the energy goes in the longitudinal velocity component may prove to be ultimately beneficial. It appears increasingly unlikely that even ICRF could be used for directly heating the majority ion species.

Alfvén wave coupling displays remarkable freedom from a host of surface effects, namely (i) at the low operation frequency, the existence of longitudinal electric field component is suppressed in a properly shielded antenna resulting in virtual absence of the torsional surface mode. The small amount of energy coupled to the surface mode is absorbed by the uncontained electrons at the plasma edge. (ii) The coupling is not affected by the alpha particles and is immune to the precise plasma composition.

Sputtering due to the acceleration of heavy ion impurities can be checked by limiting the antenna voltages in conformity with the ambient magnetic field. Once again, the importance of working at low Q and hence at large toroidal wave number n becomes evident. However, only an experiment would reveal the success of these measures, considering the complex transport and surface effects called into play.

On the experimental side, there is a regrettable lack of work in this field. The extant high power Alfvén wave heating experiments have been performed in an extremely unfavourable parameter range with $n \sim 2$ and without the benefit of a Faraday screen, predictably accompanied by plasma production and density rise.

6. CONCLUSION

In the light of the arguments presented here, particularly regarding the possibility of superior penetration in plasmas with non-circular cross-sections, we believe that there is compelling evidence in support of a concerted effort in the experimental direction. Alfvén wave heating may well turn out to be an important contender for the heating of thermonuclear plasmas.

REFERENCES

[1] PURI, S., Nuclear Fusion **27** (1987) 229.
[2] PURI, S., Nuclear Fusion **27** (1987) 1091.
[3] BALLICO, M. J., CROSS, R. C., BRENNAN, M. H., LEHANE, J. A., SAWLEY, M. L., Plasma. Phys. and Contr. Fusion (submitted).
[4] PURI, S., Present Conference (Paper E1).

ALFVEN WAVE COUPLING IN LARGE TOKAMAKS

G.G. Borg, A.J. Knight, J.B. Lister, K.Appert and J.Vaclavik

Centre de Recherches en Physique des Plasmas
Association Euratom - Confédération Suisse
E.P.F.L., Lausanne, Switzerland

Supplementary plasma heating by Alfvén waves (AWH) has been extensively studied both theoretically and experimentally for small, low temperature plasmas. However, only a few studies of AWH have been performed for fusion plasmas. In this paper the cylindrical kinetic code ISMENE [1] is used to address problems of AWH in a large tokamak. The results of calculations are presented which show that the antenna loading scales with frequency and vessel dimensions according to ideal MHD theory. A sample scaling of the experimental antenna loading measured in TCA to the loading predicted for a fusion plasma is presented. We discuss whether this loading leads to a realistic antenna design. The choice of a suitable antenna configuration, mode number and operating frequency is presented for NET parameters with a typical operating scenario.

Introduction : In a hot plasma, AWH is effected by antenna excitation of a fast magnetosonic wave which mode converts to the kinetic Alfvén wave (KAW) at surfaces in the plasma where the Alfvén wave dispersion relation is satisfied locally [2]

$$\omega^2(\varepsilon) = [n+m/q(\varepsilon)]^2 \; B_o^2/(\mu_o \rho(\varepsilon))/R^2 \qquad (1)$$

In equation (1) n and m are the toroidal and poloidal mode numbers, B_o the total field, R the major radius, ω the operating circular frequency (much less than the ion cyclotron frequency), ρ and q are the plasma mass density and safety factor as a function of $\varepsilon=r/a$, a being the minor radius.

In this study the machine parameters of the NET DN configuration [3] are modified to the cylindrical equivalent values; major radius (R)=5.18 m, minor radius (a)=2.17m, toroidal field (B_o)=5.0T, plasma current (I_p)=10.8MA, burn temperature (T)=14keV (on axis) and electron density (n_e)=$18\times10^{19}m^{-3}$ (on axis) with a 50:50 D/T fuel mixture.

Scaling of Antenna Loading in AWH : Scaling laws allow one to predict the antenna loading at a fixed point in the spectrum (n, m, ε and both antenna and vessel geometry fixed in equation (1)) under a change in ω, R, ρ or B_o.

Scaling laws are useful because:

a) Codes are restricted to simplified plasma, antenna and vessel geometries.
b) Such laws give increased confidence in the loading predictions if the validity of the plasma model has already been established experimentally [2].

According to ideal MHD, the antenna loading at a fixed point in the Alfvén spectrum increases linearly with the driving frequency and is independent of the plasma density and magnetic field.

The antenna loading, R_A, normalised to ω, is plotted versus the logarithm of the on axis density in Fig. 1a using ISMENE for the basic NET dimensions. We have chosen $\varepsilon=0.67$ and $(n,m)=(-1,-1)$, $(-2,-1)$, $(-4,-1)$ and $(-8,-1)$. Satisfactory agreement is obtained for $n=-1$, -2, and -4 for $n_e(0)>10^{18}m^{-3}$. At low densities a discrepancy results from finite frequency effects.

In ideal MHD, the antenna loading scales linearly with the major radius at a fixed point in the spectrum provided that the plasma, antenna and vessel geometries are held fixed. This law is checked by shrinking and expanding the basic NET configuration with ω, B_o constant, $n_e \sim 1/R^2$, $a \sim R$ and $I_p \sim R_p$ so that equation (1) remains invariant. This scaling law is checked in Fig. 1b for $|n|=1$, 2, 4, 8 and $|m|=1$ and demonstrates that an antenna loading obtained in, for example, ASDEX would lead to only a $\sim\pm10\%$ error in predicting the NET loading.

An example of how scaling laws can be used to predict the loading is shown in Fig. 1c. The TCA experimental loading for $n=2$ excitation [2], $f=2.5$ MHz, $R=0.61$ and $B_o=1.51$T is scaled to a NET equivalent loading with $f=0.5$MHz, $R=5.18$ and $B_o=5.0$T. The ISMENE load is adjusted to agree as well as possible with the TCA experiment and the NET equivalent, and scaled loadings are then calculated directly. The agreement is better than 10% in the (2,1) continuum for more than a factor of 8 increase in the vessel dimensions. For $n>2$ the agreement would be somewhat worse due to finite frequency effects.

Choice of Suitable Mode and Frequency : In NET there are 16 oblique and 8 radial access ports equispaced toroidally in each case with a 20cm blanket into which the antenna has to be recessed [4]. In addition, we restrict our discussion to unshielded [2], poloidal antennas although future experiments may reveal the utility of Faraday shields and tilted antennas [5].

In AWH it is desirable to have the largest possible number of antennas due to the phase coherence of the wave launching. Consistent with this, the number and the size of the available ports, we choose 8 low field side poloidal antennas with poloidal half angle 90° and toroidal half angle <5° (Fig. 2a).

Taking into account the Fourier spectrum of the antenna, ISMENE

calculated loads are presented in Fig. 2b for $|n|=1,2,4,8,16$ and $|m|=0,1,3$ using the optimum phasing for each mode, and $\varepsilon=0.67$. This calculation shows that n=4, 8, m=1 and n=16, m=0 at f=1.08, 1.98 and 3.77MHz respectively give the greatest total antenna loading. The maximum load occurs at n=2.5R/a ~6 in agreement with [6] and [7]. This loading at 500-1000mΩ gives an r.m.s. antenna current of 10kA for 50MW power input, and leads to a feasible technological requirement.

It should be noted that the actual loading will depend on the antenna geometry model, in particular the recess. Studies of this question have shown that an antenna flush with the torus wall can have a substantial loading, of the order of 15% of the no-wall case. The flush-wall configuration for a plasma-wall spacing of 0.1m and an equal recess depth, has the same antenna loading for n=8, as an antenna one third away from the same wall without a recess.

The radial location of the principle resonance layers excited during an n=8 and n=4 heating scenario is shown in Fig. 2c during the heating and fuelling phase to ignition in NET [8]. N=8 with all antenna currents in phase at f=2.16MHz begins the heating phase at $\rho=3.6\times10^{-7}kg/m^{-3}$ (D/T) with a change of frequency to 1.08MHz and n=4 at $\rho=4.8\times10^{-7}kg/m^{-3}$. The power deposition is approximately local (20% of the minor radius) and is equally divided between the m/n>0 and the m/n<0 layers.

Conclusion : Calculations have been presented which demonstrate that the scaling laws of ideal MHD can be used to predict antenna loadings in large tokamaks from those obtained in small tokamaks. An $|n|=4$, 8, $|m|=1$ scenario has been discussed.

Acknowledgements : This work was funded under the NET contract 251/86-10/FU CH/NET. We are endebted to Dr. J-G. Wegrowe for stimulating discussions.

References

[1] K. Appert et al. (1987), in Proc. 7th Int. Conf. on Plasma Physics, Kiev, Invited Papers, Vol. 2, 1230.
[2] G. Collins et al., Phys. of Fluids 29 (1986) 2260.
[3] F. Engelmann, 1986, Concept and Parameters of NET, NET Report EUR-fu/XII-80/86/64.
[4] E. Salpietro et al, NET Basic Machine, NET Report, 1988.
[5] F. Hofmann et al., Nucl. Fusion 24 (1984) 1679.
[6] K. Appert et al., (1980) Plas. Phys. and Contr. Fus. Res., Vol. II, IAEA-CN-38/D-1-1.
[7] A.G. Kirov et al., RF Systems for Alfvén Wave Heating of Large Tokamaks, IAEA Technical Workshop on RF Heating and Current Drive, Moscow, 1987.
[8] F. Engelmann et al., NET Physics Basis, NET Report, 1988.

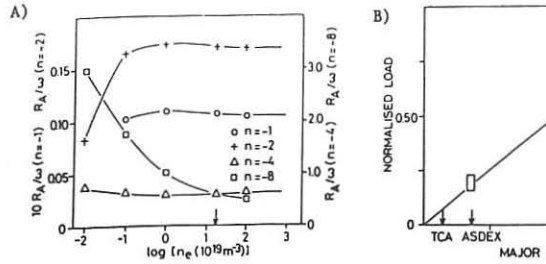

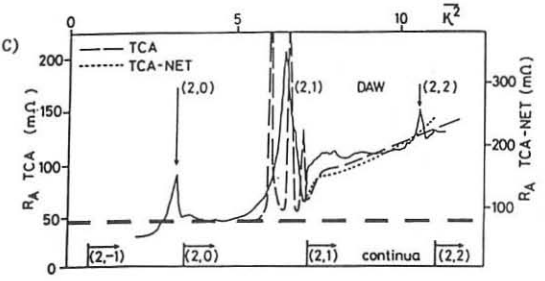

Fig. 1a Scaling of antenna load with frequency.

Fig. 1b Scaling vs major radius

Fig. 1c Scaling of TCA to NET equivalent plasma. Scaled load on right axis.

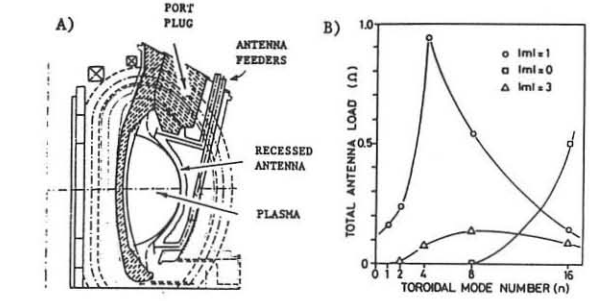

Fig. 2a Antenna configuration in NET.

Fig. 2b Load vs n for 8 sector antenna

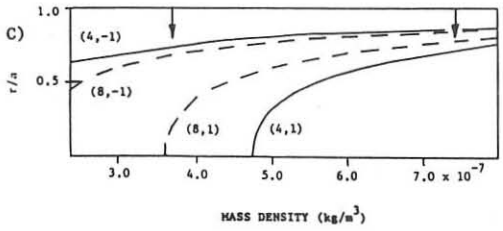

Fig. 2c ARL positions in an n = 4 and 8 heating scenario. Arrows indicate the heating phase.

PROPAGATION OF A MAGNETICALLY GUIDED ALFVEN BEAM IN THE EDGE PLASMA

R.C. CROSS

Plasma Physics Dept., University of Sydney, Sydney 2006 Australia

An RF heating antenna located at the plasma edge will, in general, launch both the fast and a slow wave. In the Alfven wave heating scheme, the slow wave is the torsional Alfven wave. In ICRF, the slow wave is either the ion cyclotron or the ion-ion hybrid wave. All three slow waves are observed [1] to be guided along steady magnetic field lines passing through or near the antenna and are therefore constrained to propagate in the edge plasma. In this paper, the effect of a strong density gradient on wave guidance in the edge plasma is examined. Since finite frequency effects do not play a significant role in wave guidance [1], we consider only ideal MHD effects. The advantage is that an exact solution is obtained, without the need for a WKB treatment.

Specifically, we consider propagation of a guided wave in plasma which is homogeneous in the z direction but inhomogeneous in a direction perpendicular to a steady uniform magnetic field, $\mathbf{B} = \hat{\mathbf{z}}\, B$. If the plasma resistivity and kinetic pressure are neglected, then low frequency waves in the plasma can be described by the ideal MHD equations $\mathbf{E} + \mathbf{v} \times \mathbf{B} = 0$ and $\rho \partial \mathbf{v}/\partial t = \mathbf{j} \times \mathbf{B}$, and Maxwell's equations $\nabla \times \mathbf{b} = \mu_o \mathbf{j}$ and $\nabla \times \mathbf{E} = -\partial \mathbf{b}/\partial t$ where $\mathbf{b}$ is the wave magnetic field. For small perturbations of the form $f(r,\theta)\exp i(k_z z - \omega t)$ it is easy to show that the z component of $\mathbf{b}$ satisfies the relation

$$\frac{1}{r}\frac{\partial}{\partial r}\left(\frac{r}{F}\frac{\partial b_z}{\partial r}\right) + \frac{1}{r^2}\frac{\partial}{\partial \theta}\left(\frac{1}{F}\frac{\partial b_z}{\partial \theta}\right) + b_z = 0 \qquad (1)$$

where $F = \omega^2/v_A^{\,2} - k_z^{\,2}$ and $v_A^{\,2} = B^2/\mu_o \rho$. The other components of $\mathbf{b}$ are

$$b_r = \frac{ik_z}{F}\frac{\partial b_z}{\partial r} \qquad \text{and} \qquad b_\theta = \frac{ik_z}{rF}\frac{\partial b_z}{\partial \theta} \qquad (2)$$

Solutions of (1) are normally found by Fourier analysis in the θ direction, with $\partial/\partial\theta = im$, where m is the azimuthal wave number. If

$m \neq 0$, equation (1) is singular at the Alfven resonance surface defined by $F = 0$. At the resonance surface, $r = r_o$, b_z is finite and continuous, $b_r \propto \ell n(r - r_o)$ and $b_\theta \propto 1/(r-r_o)$. At $r = r_o$, **b** is therefore polarised in the resonance surface.

Equation (1) also admits *non-singular* solutions, provided that $\partial b_z/\partial r$ and $\partial b_z/\partial \theta$ are both zero when $F = 0$. These solutions, which have not previously been noticed, described magnetically guided torsional Alfven waves which are decoupled from the compressional wave since there is no singular or resonance surface. The direction of **b** in a guided mode follows from (2), which indicates that $(\mathbf{b} \times \nabla b_z)_z = 0$. The wave magnetic field lines in the r,θ plane are therefore perpendicular to constant b_z contours. Since the $F = 0$ surface forms a constant b_z contour when $\partial b_z/\partial r = \partial b_z/\partial \theta = 0$, the wave magnetic field lines cross the $F = 0$ surface at right angles.

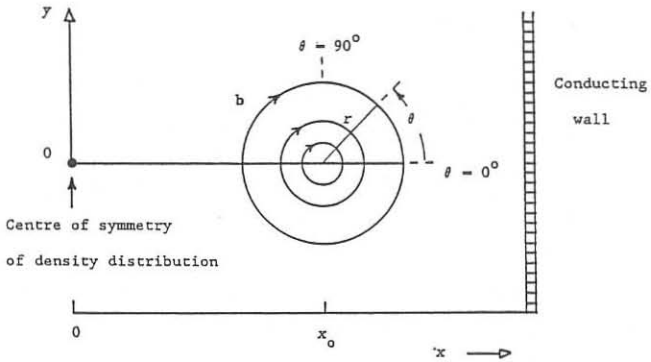

Fig. 1 Wave magnetic field lines, **b**, in the x–y plane for a guided torsional wave propagating in the z direction.

Consider, for example, the wave field distribution shown in Fig. 1 where $b_r = 0$ for all r,θ. Note that the $r = 0$ origin is located in a region where the density gradient is finite. This example is chosen since it represents, in the case of a homogeneous plasma, the wave field generated by a current element in the z direction. Current elements perpendicular to **B** do not couple to the torsional wave, at

least in ideal MHD. Since $b_r = 0$, the first term in (1) is zero. Equation (1) then has an exact analytical solution

$$b_z = b_o \sin\theta \tag{3}$$

provided that

$$F = -\frac{F_o r \cos\theta}{1 - F_o r^3 \cos\theta} \tag{4}$$

where b_o and F_o are arbitrary constants. From (2), the variation of b_θ is given by

$$b_\theta = -\frac{ik_z b_o}{F_o r^2}(1 - F_o r^3 \cos\theta) \tag{5}$$

Suppose that the $r = 0$ origin is near the edge of the plasma, with coordinates $x = x_o$, $y = 0$, as shown in Fig. 1. Since $F = 0$ at $\theta = \pm 90^o$ (ie at $x = x_o$), v_A must remain constant in the y direction at $x = x_o$. Hence

$$k_z = \omega/v_A(x_o) \tag{6}$$

and

$$\rho = \rho(x_o)\left[1 - \frac{v_A^2(x_o)F_o r\cos\theta}{\omega^2(1 - F_o r^3\cos\theta)}\right] \tag{7}$$

where $\rho(x_o)$ and $v_A(x_o)$ are respectively the density and Alfven speed at $x = x_o$. This profile reduces to a linear ramp profile $\rho = \rho_o(1 - x/a)$ if we set $F_o = \omega^2/(v_{Ao}{}^2 a)$, $v_{Ao}{}^2 = B^2/(\mu_o\rho_o)$, $x = x_o + r\cos\theta$ and assume that $F_o r^3 \ll 1$. The assumption $F_o r^3 \ll 1$ is satisfied for most conditions of interest and is always satisfied at sufficiently small r. Consider typical tokamak parameters $v_{Ao} \sim 5 \times 10^6$ m/s, $a \sim 0.3$ m and let $\omega \sim 10^7$ r/s. Then $F_o \sim 13$ m^{-3} and $F_o r^3 \ll 1$ when $r < 0.1$ m. For these parameters, $b_\theta \propto 1/r^2$ from (5) and $|b_z/b_\theta| \sim F_o r^2/k_z$. For example, at $r \sim 0.02$ m, $|b_z/b_\theta| \sim 0.005$. Homogeneous plasma results are recovered as $a \to \infty$, in which case $F_o \to 0$ and $b_z/b_\theta \to 0$.

Since b_θ varies as $1/r^2$, the wave is strongly localised near the $y = 0$, $x = x_o$ origin. The singularity at $r = 0$ can be avoided by including the effects of finite resistivity or finite electron mass. At large r, the field lines will not remain circular if they intersect a

conducting wall boundary. However, this effect is not significant, for two reasons. Firstly, the energy density in the wave field decreases as $1/r^4$ away from the $x = x_o$ origin, so the wave energy near the boundary is insignificant (assuming that x_o is not very close to the boundary). Secondly, the wave energy propagates almost exactly along the steady magnetic field lines and not towards the boundary. The direction and magnitude of the energy flux is given by the Poynting vector

$$\mathbf{S} = \frac{\mathbf{E} \times \mathbf{b}}{\mu_o} = \frac{\omega}{\mu_o k_z} \left[-\hat{\mathbf{x}}(b_x b_z) - \hat{\mathbf{y}}(b_y b_z) + \hat{\mathbf{z}}(b_x^2 + b_y^2) \right]$$

When $b_z = 0$, $\mathbf{S}$ is exactly parallel to the steady field. If the wave has a small b_z component, some energy will propagate across the steady field lines. However, as shown above, $b_z / |b_\perp|$ may be well below 0.01 for typical laboratory conditions and the energy flux across field lines is then negligible. Furthermore, the direction of energy flow across the steady field is parallel to $\mathbf{b}_\perp$, where $\mathbf{b}_\perp = \hat{\mathbf{x}}\, b_x + \hat{\mathbf{y}}\, b_y$. The wave magnetic field lines in Fig. 1 therefore indicate the direction of energy flow perpendicular to **B**. No energy escapes through surfaces bounded by these curves. It is clear from Fig. 1 and the fact that the energy flow is primarily in the z direction that the wave is guided by the steady magnetic field and the plasma boundary has no significant effect on the wave motion. It is also evident that the wave is not refracted by the density gradient.

For a ramp profile, we have shown that a guided wave is decoupled from the compressional wave, despite the fact that ω lies in the Alfven continuum. It contains a continuous spectrum of high k_x and k_y components but a unique k_z component. A guided wave is therefore not phase-mixed by the density gradient and does not locally satisfy the dispersion relation $\omega/k_z = v_A(x,y)$ at all points in the plasma cross-section. Solutions for a parabolic density profile will require a numerical solution of (1) with finite b_r, b_θ and b_z. It is anticipated that a guided wave in a parabolic profile will have similar properties to those found for the density ramp.

[1] Borg G. and Cross R.C., (1987) Plasma Phys. and Contr. Fus. **29**, 681.

PLASMA TOROIDICITY EFFECTS ON ALFVEN RESONANCES

A.G.Elfimov

I.N.Vekua Institute of Physics and Technology, Sukhumi, USSR

1. Theoretical investigations on linearized MHD equations /1/ have shown that singular solutions related with a local Alfven resonance in a torus may occur at magnetic surfaces only. However, computations /2,3/ and tokamak Alfven heating experiments /4/ revealed that under the local resonance conditions in a torus, a whole spectrum of HF field poloidal harmonics each of them giving rise to its own local resonances and absorbing the HF power.

In the present paper a theoretical analysis of eigenfunction is given and eigenvalues are found for local MHD and kinetic Alfven resonance frequencies of a toroidal plasma with concentric magnetic surfaces. The analysis has been done within the frame of Maxwell equations where plasma properties are defined by permability tensor within the local approximation /3,5/ for each of magnetic surfaces with the three directions specified (radial -r, parallel -3 and binormal -b). Further the tensor components $\varepsilon_{rr}=\varepsilon_1=\omega_{pe}^2/(\omega_{ci}^2-\Omega^2)=\varepsilon_{bb}$ and $\varepsilon_{33}=\varepsilon_3=-\omega_{pe}^2/\Omega^2$ are used. For a hot plasma ($c_A<v_{Te}$), an approximate value of $\varepsilon_3\simeq(\omega_{pe}^2/k_z v_{Te}^2)(1+\sqrt{\frac{\pi}{2}}\frac{\Omega}{k_z v_{Te}})$ is taken.

2. In order to analyze the behaviour of a short wavelength (kinetik) Alfven wave in a toroidal plasma at its generation by an antenna structure with the given frequency Ω and the longitudinal wave number n , one may use a radial approximation of the geometric optics: $\vec{E}=\vec{E}\,exp\,i\left[\int \varkappa dr' + n\zeta - \Omega t\right]$. Here the value of $|\varkappa|\gg 1/r$ is calculated for each of magnetic surfaces as an eigenvalue of the following equation:

$$\frac{\partial}{\partial\theta}\left(\frac{R}{r}\frac{\partial E_r}{\partial\theta}\right)+\frac{2in h_\zeta}{h_\theta}\frac{\partial E_r}{\partial\theta}+\frac{rR}{h_\theta^2}\left[\left(1-\frac{\varkappa^2c^2}{\varepsilon_3\Omega_0^2}\right)\varepsilon_1\frac{\Omega^2}{c^2}-k_\zeta^2\right]E_r=0 \quad (1)$$

where $k_\zeta=n h_\zeta/R$; $R=R_0+r\cos\theta$ and h_θ, h_ζ are poloidal and toroidal projections of the $\vec{B}/B$ magnetic field unit vector. This equation is valid far from the local resonance neigbourhood.

3. In order to study local resonances one should refer to the MHD limit /2/ when $\varepsilon_3\to\infty$ and $E_\zeta\to 0$. In such a case fields in the $r=r_A$ local resonance neigbourhood have following singularities: $\vec{E}_b=E_b\,h(r-r_A)exp\,i(n\zeta-\Omega t)$; $E_r=\frac{E_b}{r-r_A}exp\,i(n\zeta-\Omega t)$.

Fields of such pattern suggest that the equation for eigenfunction in a local resonance coincides with Eq.(1) for $\varkappa\equiv 0$.

Since one has $\varepsilon_1=\varepsilon_0+2\sum\tilde{\varepsilon}_M\cos M\theta$ for the general case, Eq.(1) is identified as Hill type equation with periodic coefficients. If periodic coefficients are included in the equations with small parameters r^2/R_0 and $\tilde{\varepsilon}_M/\varepsilon_0\ll 1$, then, using the method of "stretched" parameters /6/ Eqs.(1) (with $\varkappa=0$) may be given as:

$$\Omega^2=\Omega_0^2(1+\Delta_1+\Delta_2+\dots)\ ;\quad E_r=\sum_s E_s^{(m)}\exp i(m+s)\theta \qquad (2)$$

Substituting Exp.(2) for the local resonance equation when $2|nq+m|\neq S$, S – a natural number, one obtains:

$$[\varepsilon_0(\Omega_0R_0q/c)^2-(m+nq)^2]E_0^{(m)}=0;\ \Delta_1=0\ ;\ E_0^{(m)}\neq 0\ . \qquad (3a)$$

is a local Alfven resonance condition for the mode m within the cylindrical approximation:

$$[1\pm 2(m+nq)]E_{\pm1}^{(m)}=(rE_0^{(m)}/2R_0)\left[3\varepsilon_0(\Omega_0R_0q/c)^2+(nq)^2-m_0(m\pm1)\right] \qquad (3b)$$

is the first correction to the eigenfunction $E_0^{(m)}$.

From the second approximation, one can find Δ_2, a toroidal correction to the local frequency eigenvalue (3a) at the given magnetic surface:

$$[2\Delta_2+3(r/R_0)^2](\Omega_0R_0q/c)^2=(nq^2r/R_0)^2+$$

$$\left(\frac{r}{R_0}\right)^2\frac{[3\varepsilon_0(\Omega_0R_0q/c)^2+(nq)^2-m^2]^2+m^2+4m(m+nq)[3\varepsilon_0(\Omega_0R_0q/c)^2+(nq)^2-m^2]}{4(m+nq)^2-1} \qquad (3c)$$

Eqs.(3) become invalid if $4(m+nq)^2=S^2$ This violation follows from crossing of m and $m\pm S$ local resonances. Such a crossing for the case of $S=1$ was considered in Ref.(1) within the MHD approximation. In this case in the continuum for the m mode a gap is formed at the crossing position with $m\pm1$. Similar gaps are formed in the continuum for m and $m=m-M$ modes if the tensor component ε_1 is strongly modulated over the poloidal angle by the $M>1$ mode: $\varepsilon_1\simeq\varepsilon_0+2\tilde{\varepsilon}_M\cos M\theta$. Strong modulation is possible, e.g., due to the cyclotron resonance for small additions ($n_z\ll n_i$) of heavy impurities when $\Omega\simeq k_\parallel c_A(0)\simeq\omega_{cz}\ll\omega_{ci}$.

For the case of such modulation at the crossing position of the m and m_1 modes, the eigenvalue of the local resonance frequency Ω_0^2 gets an addition:

$$\Delta_1^{\pm}=\frac{c^2[M-2(m+nq)]M}{2\varepsilon_0(\Omega_0R_0q)^2}\pm\sqrt{\left(\frac{c^2[M-2(m+nq)]M}{2\varepsilon_0(\Omega_0R_0q)^2}\right)^2+\frac{\tilde{\varepsilon}_M^2}{\varepsilon_0^2}} \qquad (4)$$

This addition is twosigned which means that there is no local resonance (or gap in continuum) for the following frequency values: $\Omega_0^2(1+\Delta_1^-)<\Omega<(1+\Delta_1^+)$. In the neighbourhood of such a gap, the eigenfunction has an equal mixture of modes:

$$E^{(m)}\simeq E^{(m_1)};\quad E_r\simeq E_0^{(m)}\exp im\theta+E_0^{(m_1)}\exp im_1\theta\ .$$

Thus, the attempts to excite a local resonance at Ω_0 will lead to the generation of the $m=m-M$ harmonics. For the m_1 mode, there exists another local resonance (see Fig.1) which is close to the plasma surface ; this resonance is

responsible for the main energy absorption. In order to avoid this situation, it is necessary to generate the m mode local resonance at the surfaces having weak poloidal modulation of ε_1 for the $M>2(m+nq)$ mode.

4. For kinetic Alfven waves, eigenfunctions and eigenvalues can be found in a similar way (as described in Item 3). To define them ($\varepsilon_0(1-\varkappa^2c^2/\varepsilon_3\Omega_0^2)$ must be substituted for ε_1 in Expressions (3a - 3c) and (4). Hence, it follows that the eigenvalue $\varkappa$ at the magnetic surface given will be :

$$\varkappa^2=(\varepsilon_3\Omega_0^2/c^2)\{1+\Delta-[(nq+m)c/(\varepsilon_0 R_0\Omega_0)]^2\} \qquad (5)$$

In this case, if the frequency is chosen such that it gets into gap in the continuum for the m mode (i.e., when there is no local resonance), the correction value, Δ , is defined by Exp.(4) and local radial wavenumber eigenvalue for a slow (kinetic) wave will be: $\varkappa^2=\pm\varepsilon_3(\Omega\tilde{\varepsilon}_M/c\varepsilon_0)^2$.

Hence, we may conclude that within the Alfven continuum gap there exists a slow (kinetic) wave with a bimodal structure. These modes have the same order of amplitudes:

$$E_z=(E_0^{(m)}\exp im\theta+E_0^{(m_1)}\exp im_1\theta)\exp i\Big[\int_0^z\varkappa dz'+n\zeta-\Omega t\Big].$$

5. In order to complete the analysis of Alfven HF generation in a torus, one has to find fields in the neighbourhood of all the possible conversion surfaces ($z=z_{Am}$). Here we shall presume that for neighbouring $m\pm1$ modes we have no crossings of local resonances. Within the neighbourhood of a conversion surface we obtain an approximate from Maxwell equations:

$$\frac{\partial^2E_z}{\partial z^2}+\frac{\varepsilon_3}{\varepsilon_1}\Big\{\frac{h_\theta^2}{zR}\Big[\frac{\partial}{\partial\theta}\Big(\frac{R}{z}\frac{\partial E_z}{\partial\theta}\Big)+\frac{2inh_z}{h_\theta}\frac{\partial E_z}{\partial\theta}\Big]+\Big(\varepsilon_1\frac{\Omega^2}{c^2}-k_z^2\Big)E_z=\Psi \qquad (6)$$

Here $\Psi(z,\theta)$ is an arbitrary function defined by the fields of the neighbouring points ($z_{A\,m\pm1}$) and by that of an excited HF circuit.

We expand solutions for Eq.(6) in eigenfunctions $\{E_m^{(s)}\}$/2,3/ of Eq.(1) at $\varkappa=0$ for a set of local resonances characterized by the following values of s : $E_z=\sum_s P_s(z)E^{(s)}(z,\theta)$

On a given magnetic surface this system of functions proves to be orthogonal one with the weight of

$$\alpha=(R/R_0)\exp\Big[2inq\int^\theta d\theta'/(1+\tfrac{z}{R_0}\cos\theta')\Big].$$

Then with the $z/R_0\ll1$ smallness considered in the conversion surface neighbourhood $|z_{Am}-z|\ll z_{Am}$, the following equation will hold:

$$\frac{d^2P_m}{dz^2}+\frac{\varepsilon_3}{\varepsilon_1}\frac{\Omega^2}{c^2}\frac{d\varepsilon_1}{dz}(z-z_{Am})=\Phi_m \qquad (7)$$

If the HF fields are generated by a HF circuit with the mode M_0 dominating, the resonances at $m=M_0\pm1$ side harmonics may be driven only for the case when the Φ_m value differs from zero. For the case when the kinetic wave damping depth (L_z) is greater than the distance between the neighbourhood

local resonances located far enough from each other ($L_z > |z_{A M_0} - z_A| \gg z_A \sqrt[3]{\varepsilon_3/\varepsilon_1}$) a coupling between neighbouring local resonances may be expected due to kinetic Alfven waves from the main (M_0) and lateral modes ($M_0 \pm 1$).

REFERENCES

1. Kieras C., Tataronis J. J.Plasma Phys. 1982,v.28,p.395.
2. Appert K., Gruber R.,Balet B., Troyon F. Nucl.Fus. 1982, v.22, p.903.
3. Dmitrieva M.V., Grishanov N.I.,Ivanov A.A. et al.Preprint 197 issued by M.V.Keldysh Institute of Applied Mathematics, Moscow, 1986.
4. Appert K., Collins G.A.,Hofman F. et al. Phys. Rev. Letters 1985, v.54, p.1671.
5. Dolgopolov V.V.,Kryukov A.V.,Romanov S.S. Preprint issued by Kharkov Institute of Physics and Technology, TSNIIATOMINFORM, Moscow, 1985.
6. Naiffe A. in the book;"Introduction into Methods of Perturbations", Moscow, "Mir" publishers, 1984, p.262.

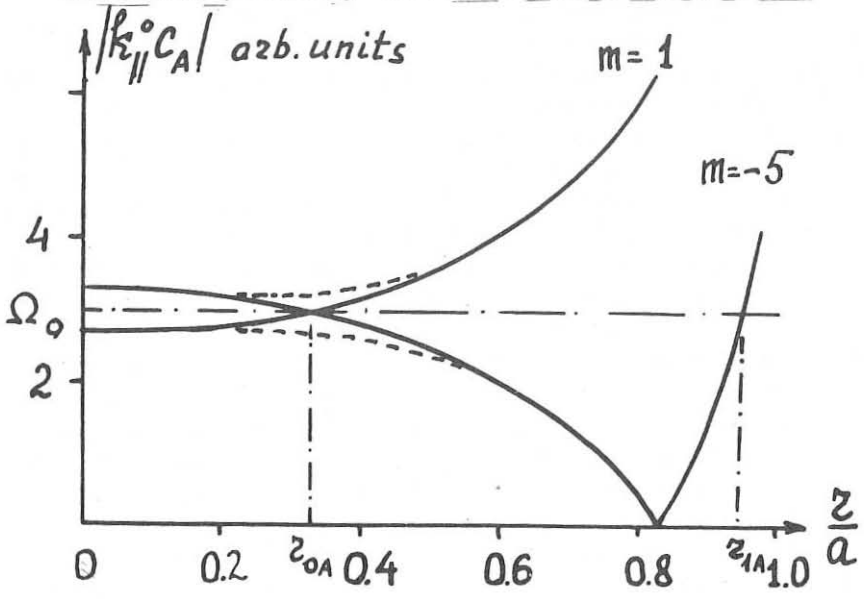

Fig.1. Schematic diagram showing the local resonance frequency versus the magnetic surface radid for poloidal m=1; -5 modes in a straight cylinder (solid line) and a thin torus (broken line) for $N = 2$, $q_0 = 0{,}9$.

ON THE LOCAL POWER ABSORPTION OF HF WAVES IN HOT INHOMOGENEOUS PLASMAS

M. Brambilla, T. Krücken

Max-Planck Institute für Plasmaphysik, Garching bei München, W. Germany

1. - The power dissipated per unit volume by a plane wave propagating in a uniform plasma is [1]:

$$P_{abs} = \frac{\omega}{8\pi} \vec{E}_0^* \cdot \underline{\underline{\epsilon}}^A \cdot \vec{E}_0 \tag{1}$$

where $\underline{\underline{\epsilon}}^A$ is the antihermitean part of the dielectric tensor. P_{abs} differs from $\langle \vec{J} \cdot \vec{E} \rangle$ by the divergence of a vector having the dimensions of a power flux. This kinetic correction to the Poynting flux,

$$\vec{T} = \frac{\omega}{16\pi} \vec{E}_0^* \cdot \frac{\partial \underline{\underline{\epsilon}}^H}{\partial \vec{k}} \cdot \vec{E}_0 \tag{2}$$

is due to space dispersion. In a hot plasma the mean collisional free path of charged particles typically exceeds the wavelength by a large factor: as a consequence the h.f. current $\vec{J}$ is a nonlocal functional of $\vec{E}$, a fact reflected in the dependence of the dielectric tensor $\underline{\underline{\epsilon}}$ on the wavevector $\vec{k}$.

Due to space dispersion, Maxwell equations in non-homogeneous plasmas are generally integro-differential. Only in plane-stratified or cylindrical geometry, assuming the perpendicular wavelength to be much greater than the average Larmor radius, it is possible to obtain purely differential approximations to the wave equations. Finite Larmor Radius wave equations have recently received much attention, as they provide the theoretical description of mode conversion and absorption in ICR heating of fusion oriented [2]-[5]. To obtain quantitative information about power deposition profiles, it is also necessary to know the appropriate generalisation of (1) to the non-homogeneous case.

Even the knowledge of an adequate approximation for the constitutive relation, however, is not sufficient to establish the form of the local power dissipated per unit volume. Indeed, the wave equations do not offer any clue to distinguish within $\langle \vec{J} \cdot \vec{E} \rangle$ the irreversible part P_{abs} from the reversible kinetic flux $\mathrm{div}\vec{T}$. The necessity of reverting to first principles to evaluate P_{abs} has been recognised by McVey et al. [6] (cfr. also [7]), who suggest to start from:

$$\int_{-\infty}^{t} P_{abs}^{\alpha} dt' = Z_\alpha e \int d\vec{v} \left\langle \int_{-\infty}^{t} dt' \left\{ \mathrm{Re}\left[\vec{E}(\vec{r}', t') \right] \cdot \vec{v}' \right\} \{ \mathrm{Re}[f_\alpha(\vec{v}', \vec{r}', t')] \} \right\rangle_t \tag{3}$$

Here f_α is the solution of the linearised Vlasov equation for species α; $\vec{r}'$, $\vec{v}'$ are the characteristics of this equation, i.e. represent the unperturbed trajectory of a particle

having velocity $\vec{v}$ at point $\vec{r}$ at time t. The r.h. side is easily recognised to be the total energy gained by all particles of species α up to time t, averaged over the fast time scale ω^{-1}. It is assumed that the field has been adiabatically switched on, $|\vec{E}|^2 \to 0$ for $t \to -\infty$. In the case of a time harmonic wave, this means $\gamma = \mathrm{Im}\omega > 0$, $\gamma \to 0+$, which leads to the correct prescription to handle the singularities due to resonant particles on the r.h. side of (3). It should also be clear that to apply (3) one must assume sufficient collisions to ensure that particle trapping by the wave negligible; this is at the same time the condition for the validity of the linearised Vlasov equation.

2. - The result obtained in [6] by applying Eq. (3) to a plane-stratified plasma in the small Larmor approximation can be generalised to all situations in which $\vec{r}'$, $\vec{v}'$ can be evaluated in the drift approximation. Under this quite unrestrictive condition

$$\int_{-\infty}^{t} P^{\alpha}_{abs} dt' = \frac{Z_\alpha^2 e^2}{2m_\alpha} \int d\vec{v}\; e^{2\gamma t} \mathrm{Re}\left\{ \int_{-\infty}^{t} dt' e^{-i\omega^*(t-t')} \left(\vec{E}^*(\vec{r}') \cdot \vec{v}'\right) \cdot \right.$$
$$\left. \int_{-\infty}^{t'} dt'' e^{i\omega(t-t'')} \left[\left(\vec{E}(\vec{r}'') + \frac{\vec{v}''}{c} \times \vec{B}(\vec{r}'') \right) \cdot \frac{\partial F_\alpha}{\partial \vec{v}''} \right] \right\} \tag{4}$$

Using the group properties of the particle trajectories and the fact that the unperturbed distributions F_α depend only on constants of the motion, and assuming for simplicity local thermal equilibrium, this can be simplified to

$$P^{\alpha}_{abs} = \frac{\omega}{4\pi} \frac{\omega_{p\alpha}^2}{v_{th\alpha}^2} \int d\vec{v}\, F_{M\alpha}(v^2, \vec{r}_g) \lim_{\gamma \to 0} \frac{2\gamma}{\omega} \mathrm{Re}\left\{ \int_{-\infty}^{t} dt' e^{-i\omega^*(t-t')} \left(\vec{E}^*(\vec{r}') \cdot \vec{v}'\right) \right.$$
$$\left. \int_{-\infty}^{t'} dt'' e^{i\omega(t-t'')} \left[\vec{E}(\vec{r}'') \cdot \left(\vec{v}'' - \frac{v_{th\alpha}^2}{2\Omega_{c\alpha}} \vec{b} \times \vec{\nabla} \log F_{M\alpha} \right) \right] \right\} \tag{5}$$

where $\vec{b} = \vec{B}_o / B_o$, $F_{M\alpha}$ is the Maxwell distribution, and $\vec{r}_g = \vec{r} + \left(\vec{v} \times \vec{b}\right) / \Omega_{c\alpha}$ is the particle guiding center. The second term in the t'' integral is easily recognised as the one responsible for low frequency drift instabilities ($\omega << \Omega_c$); in the ICR frequency range it can be consistently neglected. An integration by parts then allows to recast P^{α}_{abs} in the form:

$$P^{\alpha}_{abs} = \frac{\omega}{8\pi} \frac{\omega_{p\alpha}^2}{\omega^2} \int d\vec{v}\, F_{M\alpha}(v^2, \vec{r}_g) \lim_{\gamma \to 0} \frac{2\gamma}{\omega} \left| -i\omega \int_0^\infty d\tau e^{i\omega\tau} \left(\vec{E}(\vec{r}') \cdot \frac{\vec{v}'}{v_{th\alpha}} \right) \right|^2 \tag{6}$$

Here the integrand is positive defined: in this approximation *energy flows always from the waves to the particles at each point of space.* This result seems to contraddict recent analysis of the generalised Plasma Dispersion Function in tokamak geometry [8], [9].

The difficulty is easily removed by realising that the locally negative contibutions to $\langle \vec{J} \cdot \vec{E} \rangle$ found by these Authors belong to $\mathrm{div}\vec{T}$ rather than to P^{α}_{abs}.

Although physically plausible, the above expression for P^{α}_{abs} is only acceptable if it is in agreement with the formal conservation theorem of Maxwell-Vlasov equations. To prove that this is the case it is necessary and sufficient to show that the difference between P^{α}_{abs} and $\langle \vec{J}_{\alpha} \cdot \vec{E} \rangle$ is the divergence of a vector. Indeed it can be shown that [10]

$$\langle \vec{J}_{\alpha} \cdot \vec{E} \rangle = P^{\alpha}_{abs} + \mathrm{div}\vec{T}^{\alpha} \tag{7}$$

with

$$\vec{T}^{\alpha} = \frac{1}{8\pi} \frac{\omega_{p\alpha}^2}{\omega^2} \int d\vec{v}\, \vec{v} F_{M\alpha}(v^2, \vec{r}_g) \left| -i\omega \int_0^{\infty} d\tau e^{i\omega\tau} \left\{ \vec{E}(\vec{r}') \cdot \frac{\vec{v}'}{v_{th\alpha}} \right\} \right|^2 \tag{8}$$

3. - It is instructive to apply Eq. (6) in the homogeneous limit. In this case the most general time-harmonic field can be written

$$\vec{E}(\vec{r}, t) = \int dk_{\parallel} \int d\psi\, \vec{E}(k_{\parallel}, \psi) e^{-i\left[k_{\parallel} z + k_{\perp}(x\cos\psi + y\sin\psi) - \omega t\right]} \tag{9}$$

where $k_{\perp} = k_{\perp}(\omega, k_{\parallel})$ has to satisfy the dispersion relation, but does not depend on $\psi = \mathrm{atan}(k_y/k_x)$; parallel and perpendicular refer to the direction of the static magnetic field. Eq. (6) then becomes:

$$\begin{aligned} P^{\alpha}_{abs} = \frac{\omega}{8\pi} \frac{\omega_{p\alpha}^2}{\omega^2} \int dk_{\parallel} \int dk'_{\parallel} \int d\psi \int d\psi' \, \mathrm{Re} \Bigg\{ & e^{i(\vec{k}-\vec{k}')\cdot\vec{r}} \\ & \int d\vec{v} F_{M\alpha}(v^2) \exp i \left[\frac{k_{\perp} v_{\perp}}{\Omega_{c\alpha}} \sin(\phi + \psi) - \frac{k'_{\perp} v_{\perp}}{\Omega_{c\alpha}} \sin(\phi + \psi') \right] \\ & \lim_{\gamma \to 0} \frac{2\gamma}{\omega} \left[\sum_n \frac{\omega}{\omega - i\gamma - n\Omega_{c\alpha} - k_{\parallel} v_{\parallel}} \left(\vec{V}^{\alpha}_n(\vec{k}) \cdot \vec{E}(k_{\parallel}, \psi) \right) \right] \cdot \\ & \left[\sum_{n'} \frac{\omega}{\omega + i\gamma - n'\Omega_{c\alpha} - k'_{\parallel} v_{\parallel}} \left(\vec{V}^{\alpha}_{n'}(\vec{k}') \cdot \vec{E}^*(k'_{\parallel}, \psi') \right) \right] \Bigg\} \end{aligned} \tag{10}$$

with

$$\vec{V}^{\alpha}_n \cdot \vec{E} = v_{\perp} \left[E_x \frac{n\Omega_{c\alpha}}{k_{\perp} v_{\perp}} J_n \left(\frac{k_{\perp} v_{\perp}}{\Omega_{c\alpha}} \right) + i E_y J'_n \left(\frac{k_{\perp} v_{\perp}}{\Omega_{c\alpha}} \right) \right] + v_{\parallel} E_z J_n \left(\frac{k_{\perp} v_{\perp}}{\Omega_{c\alpha}} \right) \tag{11}$$

Now it is not difficult to show that

$$\begin{aligned} \lim_{\gamma \to 0} \frac{2\gamma}{\omega} \left\{ \frac{\omega}{\omega - i\gamma - n\Omega_{c\alpha} - k_{\parallel} v_{\parallel}} \right\} \left\{ \frac{\omega}{\omega + i\gamma - n'\Omega_{c\alpha} - k'_{\parallel} v_{\parallel}} \right\} = \\ 2\pi\delta \left(\frac{\omega - n\Omega_{c\alpha} - k_{\parallel} v_{\parallel}}{\omega} \right) \delta\left(k_{\parallel} - k'_{\parallel} \right) \delta_{n,n'} \end{aligned} \tag{12}$$

so that finally

$$P^{\alpha}_{abs} = \frac{\omega}{8\pi}\frac{\omega^2_{p\alpha}}{\omega^2}\int dk_{\parallel}\int d\psi\int d\vec{v}\, F_{M\alpha}(v^2)\sum_n 2\pi\delta\left(\frac{\omega - n\Omega_{c\alpha} - k_{\parallel}v_{\parallel}}{\omega}\right)|\vec{V}^{\alpha}_n\cdot\vec{E}|^2 \quad (13)$$

According to this equation, P^{α}_{abs} has two remarkable properties (not independent from each other): *a) it is constant along the static magnetic field*; and *b) it is the sum of independent contributions from each partial wave.* Both properties follow from the fact that P^{α}_{abs} bears no memory of phase relations between partial waves. They can easily be shown to hold also for the FLR wave equations in a plane-stratified plasma.

By contrast, $\langle\vec{J}\cdot\vec{E}\rangle$ is generally a function of z, showing the interference between partial waves normally to be expected for quadratic forms in the field amplitude, and is not positive definite. The averaging along $\vec{B}_o$ leading to (13) is clearly due to the free streaming of charged particles, and this equation can only be valid if the collisional mean free path is large compared with the parallel wavelength of all partial waves, as assumed above. On the other hand, the wave must have a stationary amplitude for times longer than the collision time: for shorter transients the distinction between P^{α}_{abs} and div$\vec{T}$ loses sharpness, as indicated by the existence of echo effects in weakly collisional plasmas.

Finally the case of a plane wave in a homogeneous plasma is recovered by narrowing the spectral width of the wavepacket (9) so that

$$|\vec{E}(k_{\parallel},\psi)|^2 \to |\vec{E}_0|^2\delta\left(k_{\parallel}-k_{\parallel 0}\right)\delta\left(\psi-\psi_0\right) \quad (14)$$

It is straightforword to check that in this limit (13) reduces to (1), as it should.

REFERENCES.

[1] T.H. Stix, The theory of Plasma Waves, McGraw Hill, N.Y. (1961).

[2] D.G. Swanson, Phys. Fluids **24** (1981) 2035.

[3] P.L. Colestock, R.J. Kashuba, Nucl. Fusion **23** (1983) 763.

[4] M. Brambilla, M. Ottaviani, Plasma Phys. Contr. Fusion **27** (1985) 919.

[5] T. Martin, J. Vaclavik, Helv. Phys. Acta **60** (1987) 471.

[6] B.D. McVey, R.S. Sund, J.E. Sharer, Phys. Rev. Lett. **55** (1985) 507.

[7] J. Vaclavik, K. Appert, Plasma Phys. Contr. Fusion **29** (1987) 257.

[8] S.-I. Itoh, K. Fukuyama, K. Itoh, K. Nishikawa, J. Phys. Soc. Japan **54** (1985) 1800.

[9] D.W. Faulconer, Plasma Phys. Contr. Fusion **29** (1987) 433.

[10] M. Brambilla, T. Krücken, to be published.

A GYROKINETIC DESCRIPTION OF CYCLOTRON RESONANCE ABSORPTION IN TOROIDAL PLASMAS

R. O. Dendy and C. N. Lashmore-Davies

Culham Laboratory, Abingdon, Oxon, OX14 3DB. England
(EURATOM/UKAEA Fusion Association)

The resonance between plasma particles and electromagnetic waves whose frequency coincides with the local cyclotron frequency is sensitive both to the thermal motion of the particles and to the geometry of the magnetic field. A systematic, self-consistent description of the effect of magnetic field inhomogeneity on high-frequency resonance is offered by gyrokinetic theory. This is a development of the Vlasov equation in terms of variables which reflect the underlying physics of charged particle motion in inhomogeneous magnetic fields, and takes full account of finite Larmor radius effects. Using standard techniques of gyrokinetic theory [1-9], we write perturbations to the distribution function in the form

$$\delta f = \frac{q}{m}\,\delta\phi\,\frac{\partial F_o}{\partial \varepsilon} + \sum_{\ell=-\infty}^{\infty} \langle \delta H \rangle_\ell \, e^{-i\ell\alpha} \qquad (1)$$

Here F_o is the equilibrium distribution function $\varepsilon = v^2/2$, $\delta\phi$ is the perturbed electrostatic potential, α is the gyroangle, and $\langle\rangle_\ell$ denotes the Fourier transform with respect to α. The evolution of $\langle \delta H \rangle_\ell$ is governed by the gyrokinetic equation [1-9], which for our purposes is

$$\langle L_g \rangle_\ell \langle \delta H \rangle_\ell = \frac{iq}{m}\left(\frac{\omega \partial F_o}{\partial \varepsilon} + \frac{\ell\Omega}{B}\frac{\partial F_o}{\partial \mu}\right) \qquad (2)$$

Here μ is the magnetic moment, and $\langle L_g \rangle_\ell$ is the lth harmonic component of the Vlasov operator. In our case

$$\langle L_g \rangle_\ell = v_\parallel \hat{e}_z \cdot \nabla_{\underline{X}} - i(\omega - \ell\Omega) + \underline{v}_d \cdot \nabla_{\underline{X}} \qquad (3)$$

where $\hat{e}_z$ is the direction of $\underline{B}$, Ω is the local cyclotron frequency, $\underline{v}_d$ is the standard drift velocity due to magnetic field inhomogeneity, and

$$\underline{X} = \underline{x} + \underline{v} \times \hat{e}_z/\Omega \qquad (4)$$

relates the guiding centre position $\underline{X}$ to the particle position $\underline{x}$. Maxwell's equations are expressed with argument $(\underline{x},t)$, so that it is ultimately necessary to transform back from $\underline{X}$ to $\underline{x}$. This is achieved by considering quantities that vary as exp $(i\underline{k}.\underline{x})$, which are denoted by subscript $\underline{k}$.

Let us consider a specific equilibrium magnetic field,

$$\underline{B} = B_o(1 + x/L_B)\hat{\underline{e}}_z, \tag{5}$$

define $\Omega_o = eB_o/mc$, and assume F_o to be Maxwellian. We consider electromagnetic perturbations, whose wavevector $\underline{k} = k_\perp (\underline{e}_x \cos\xi + \hat{\underline{e}}_y \sin\xi)$. Application of the gyrokinetic methods outlined above yields

$$\delta f_{\underline{k}} = -\frac{2n_o q}{mV_T^5 \pi^{3/2}} e^{-V^2}\left[\delta\phi_{\underline{k}} - \langle\delta\phi\rangle_{o\underline{k}} + \sum_{\ell\neq 0} \frac{\omega L_B}{\ell V_T} \frac{\langle\delta\phi\rangle_{\ell\underline{k}}}{V_y - \zeta_\ell} e^{i\ell\alpha}\right] \tag{6}$$

$$\langle\delta\phi\rangle_{\ell\underline{k}} = e^{i(k_x\rho V_y - k_y\rho V_x)}\left\{(\delta\phi_{\underline{k}} - V_z\frac{V_T}{c}\delta A_{\parallel\underline{k}})J_\ell(k_\perp\rho V_\perp) e^{i\ell\xi}\right.$$

$$\left. + \frac{V_\perp}{2}\frac{V_T}{c}\delta A_{\perp\underline{k}}\left[e^{-i\Theta}J_{\ell+1}(k_\perp\rho V_\perp)e^{i(\ell+1)\xi} + e^{i\Theta}J_{\ell-1}(k_\perp\rho V_\perp)e^{i(\ell-1)\xi}\right]\right\} \tag{7}$$

Here $\underline{V}$ is the dimensionless velocity, V_T the thermal velocity, $\rho = V_T/\Omega_o$ is the Larmor radius at $x = 0$, $\delta\underline{A}_{\underline{k}} = \delta A_{\parallel\underline{k}}\hat{\underline{e}}_z + \delta A_{\perp\underline{k}}(\hat{\underline{e}}_x\cos\Theta + \hat{\underline{e}}_y\sin\Theta)$, and

$$\zeta_\ell = L_B(\omega - \ell\Omega(x))/\ell V_T \tag{8}$$

The drift velocity $\underline{v}_d$ plays a negligible role provided $k_y\rho \ll 1$. By multiplying $\delta f_{\underline{k}}$ by $\underline{V}$, and then integrating over all velocities, we have obtained an expression for the current density $\delta\underline{J}_{\underline{k}}$ associated with the perturbation, in terms of $\delta\phi_{\underline{k}}$ and $\delta\underline{A}_{\underline{k}}$. This generalised expression explicitly includes the inhomogeneity of the magnetic field, through the parameter L_B and the variable ζ_ℓ. It is clear from Eq.(6) that ζ_ℓ will appear in $\delta\underline{J}_{\underline{k}}$ as the argument of the plasma dispersion function Z. By substituting our expression for $\delta\underline{J}_{\underline{k}}$ into Maxwell's equations, which in the Coulomb gauge take the form

$$(k^2 - \omega^2/c^2)\delta\underline{A}_{\underline{k}} = 4\pi\delta\underline{J}_{\underline{k}}/c - \omega\,\underline{k}\,\delta\phi_{\underline{k}}/c, \tag{9}$$

we obtain dispersion relations for waves propagating through a plasma in the plane perpendicular to the inhomogeneous magnetic field of Eq.(5). Here, we consider two examples in the single mode, small Larmor radius approximation: the first Bernstein mode, and the Ordinary mode.

In both cases, wave damping occurs in a limited region of plasma about the resonant surface. The effects of inhomogeneity need therefore be included fully only in the resonant term in the summation over ℓ harmonics. Following the procedure outlined above, we first take the divergence of Eq.(9) and substitute for $\delta\underline{J}_{\underline{k}}$. We set $k_y = 0$, so that the perpendicular electrostatic wave propagates into the gradient of magnetic field strength. This yields the dispersion relation for the first Bernstein mode

$$1 = \frac{\omega_p^2}{\omega^2 - \Omega^2} + \frac{i}{8}\frac{\omega_p^2}{\Omega}\frac{L_B}{V_T}k_x\rho\left[1 + \zeta_2 Z(\zeta_2 - ik_x\rho/2)\right] \tag{10}$$

where ω_p is the species plasma frequency. For ions in a tokamak plasma, $\omega_{pi}^2/\Omega_i^2 >> 1$. Consider first the homogeneous plasma limit of Eq.(10), setting $\zeta_2 >> 1$. This gives waves with $\omega \lesssim 2\Omega_i$, such that

$$k_x^2 = -\frac{8}{3}\frac{\Omega_i(\omega-2\Omega_i)}{v_{Ti}^2} \tag{11}$$

We have recovered the familiar result that in a homogeneous plasma, ion Bernstein waves propagate for $\omega < 2\Omega_i$, are cut-off at $\omega = 2\Omega_i$, and are evanescent for $\omega > 2\Omega_i$. In the general inhomogeneous case described by Eq.(5) with L_B/ρ finite, Eq.(10) shows that ion Bernstein modes are damped:

$$k_x\rho(1+ik_x\rho\zeta_2) = i\frac{8}{3}\frac{V_T}{\Omega L_B}\frac{1}{[1+\zeta_2 Z(\zeta_2)]} \tag{12}$$

when $k_x\rho << |\zeta_2|$. This wave-particle resonance was first noted in [7] where, however, $\ell=1$ and the wave was taken to propagate perpendicular to the gradient in magnetic field strength. Eq.(12) indicates that the ion Bernstein wave no longer possesses a well-defined cut-off. Over a width of a few Larmor radii, depending on ρ/L_B ion Bernstein waves change smoothly from undamped propagation, via strong damping, to evanescence.

Next, we consider the Ordinary mode propagating close to the fundamental electron cyclotron frequency. Taking the scalar product of $\hat{\underline{e}}_z$ with Eq.(9), and again substituting for $\delta\underline{J}_k$ from the expression derived from Eqs.(6) - (8), we obtain

$$c^2k_\perp^2 = \omega^2 - \omega_p^2 + \omega_p^2\frac{\omega L_B}{V_T}\frac{k_\perp^2\rho^2}{4}Z(\zeta_1) \tag{13}$$

We take a perturbation expansion $k_\perp = k_{\perp o} + \delta k$, where $c^2k_{\perp o}^2 = \omega^2-\omega_p^2$ and $\omega = \Omega_o$. Then Eq.(13) yields

$$\text{Im}\ \delta k = \frac{\pi^{1/2}}{8}\frac{\omega_p^2}{\Omega_o^2}\frac{V_T^2}{c^2}\frac{\Omega_o L_B}{V_T}k_{\perp o}\exp(-\zeta_1^2) \tag{14}$$

By Eqs.(5) and (8), $\zeta_1 = -\Omega_o x/V_T$. Substituting this in Eq.(14), we obtain the optical depth

$$\tau = 2\int_{-\infty}^{\infty}\text{Im}\ \delta k(x)dx = \frac{\pi}{4}\frac{\omega_p^2}{\Omega_o^2}\frac{V_T^2}{c^2}k_{\perp o}L_B \tag{15}$$

This expression is identical to that obtained from standard treatments [10] that include the relativistic mass variation of the electron.

In conclusion, we note that the effect of magnetic field inhomogeneity on cyclotron motion and wave-particle resonance has been included self-consistently from the beginning of the gyrokinetic calculations presented here. This is a basic difference from standard approaches to the problem, where a locally homogeneous plasma description is used, and inhomogeneity enters only at the end of the calculation when the value of $\omega-\Omega(\underline{x})$ is specified. The gyrokinetic approach has enabled us to examine a new cyclotron resonant wave-particle damping process, related to that first identified in [7]. We have calculated the absorption resulting from this process for two classes of wave mode, both propagating perpendicular to the magnetic field and into the gradient of magnetic field strength. First, the ion Bernstein wave was considered, where the $\ell=2$ ion cyclotron resonance produces a continuous transition from undamped propagation, via strong damping, to evanescence, rather than the snarp cutoff of standard theory. Second, the Ordinary mode ($\ell=1$ electron cyclotron resonance) was examined nonrelativistically, and the damping profile for the new process was obtained. The optical depth was found to equal that obtained using standard methods in a relativistic treatment. A complete theory of Ordinary mode absorption will therefore require the inclusion of both relativistic mass variation and the intrinsic effects of magnetic field inhomogeneity on cyclotron resonance.

REFERENCES

[1] R.J.Hastie, J.B.Taylor, and F.A.Haas, Ann.Phys. 41, 302 (1967).
[2] J.B.Taylor and R.J.Hastie, Plasma Phys. 10, 479 (1968).
[3] P.H.Rutherford and E.A.Frieman, Phys. Fluids 11, 569 (1968).
[4] T.M.Antonsen and B.Lane, Phys. Fluids 23, 1205 (1980).
[5] P.J.Catto, W.M.Tang, and D.E.Baldwin, Plasma Phys. 23, 639 (1981).
[6] L.Chen and S.T.Tsai, Phys. Fluids 26, 141 (1983).
[7] X.S.Lee, J.R.Myra, and P.J.Catto, Phys. Fluids 26, 223 (1983).
[8] L.Chen and S.T.Tsai, Plasma Phys. 25, 349 (1983).
[9] R.G.Littlejohn, Phys. Fluids 27, 976 (1984).
[10] M.Bornatici, R.Cano, O.De Barbieri, and F.Engelmann, Nucl. Fusion 23, 1153 (1983).

DYNAMICAL SELF-FOCUSING OF THE HIGH POWER FEL RADIATION IN A MAGNETIZED PLASMA

A.Cardinali(+), M.Lontano, A.M.Sergeev(*)

Istituto di Fisica del Plasma, EUR/ENEA/CNR Ass., Milano, Italy;

(+)Associazione EURATOM/ENEA sulla Fusione, CRE Frascati (Roma), Italy;
(*)Institute of Applied Physics, Soviet Academy of Science, Gorky, USSR.

1. Introduction

The next FEL operations in ECRH scenarios /1/ will be characterized by an AC regime in which a sequence of short pulses of EM radiation will be injected in the tokamak plasma. Each RF pulse will have a very high peak power ($P \gtrsim 10$ GW) concentrated in a very short time length ($\tau_p \gtrsim 50$ nsec). These features will lead to the possibility of the uprising of non linear effects, during a single shot, without achieving the steady state.

This paper is devoted to the study of the self-effects /2/ of the FEL radiation, polarized in the OM and propagating in a direction almost perpendicular to the external magnetic field. The unstable character of the FEL-beam plasma system and the related process of "focus" formation are studied in a dynamical framework /3/. Typical time and space scales of self-focusing are computed, showing that this non linear process will strongly change the traditional view of the ECRH scenarios.

2. Formulation of the problem

We choose a model of homogeneous plasma, in the region $x \gg 0$, placed in a uniform and constant magnetic field $\underline{B} = B\underline{e}_z$. This simple picture is allowed since the self-focusing, has no resonant character and it does not depend on density and magnetic field gradients in the plasma.

We assume that the density has the form $n = n_o + \delta n$ and that the electric field of the OM under consideration can be represented in the form $\underline{E} = \underline{e}_z [\mathcal{E}(\underline{r},t)\exp(i\omega t - ik_x x) + c.c.]$; the slowly varying in time and space amplitude $\mathcal{E}(\underline{r},t)$ and the relative density perturbation $\delta n/n_o$ satisfy, respectively, the equations:

$$-2iK\frac{\partial \mathcal{E}}{\partial x} - 2i\frac{\omega}{c^2}\frac{\partial \mathcal{E}}{\partial t} + \frac{\partial^2 \mathcal{E}}{\partial y^2} + \alpha\frac{\partial^2 \mathcal{E}}{\partial z^2} - \frac{\omega_{pe}^2}{c^2}\frac{\delta n}{n_o}\mathcal{E} = 0 \qquad (1)$$

$$\frac{\partial^2}{\partial t^2}\frac{\delta n}{n_o} - V_s^2 \nabla_\perp^2 \frac{\delta n}{n_o} + \hat{\Gamma}\frac{\partial}{\partial t}\frac{\delta n}{n_o} = \frac{e^2}{4 M m \omega^2}\nabla_\perp^2 |\mathcal{E}|^2 . \qquad (2)$$

Here the following definitions have been adopted: $\alpha = 1 - \omega_{pe}^2/\omega^2$, $k = \alpha^{1/2}\omega/c$, ω_{pe} is the electron plasma frequency computed on n_o, $V_S = [(T_e + 3T_i)/M]^{1/2}$ is the longitudinal sound velocity, $\hat{\Gamma}$ is a spatial operator responsible for the collisionless damping of the low frequency motion. Furthermore $\nabla_\perp^2 = \partial^2/\partial z^2 + \delta\,\partial^2/\partial y^2$ is the Laplace operator in the y,z-plane and $\delta = 0$

or 1 depending on the magnitude of the non linear time scale τ_{NL}: if $\tau_{NL}\omega_{Bi} \gg 1$ magnetized ion-sound waves are excited and $\delta = 0$; if $\tau_{NL}\omega_{Bi} \ll 1$ the maximum response belongs to the usual ion-sound oscillations and $\delta = 1$.

The steady state analysis of the eqs.(1),(2), which is not suitable for the description of realistic pulsed FEL operations, can be interesting for sake of comparison with the results of the dynamical treatment. Neglecting the time derivatives we obtain a cubic non linear Scrödinger equation which describes the self-focusing of the incident radiation. For a Gaussian distribution at the plasma boundary, $\mathcal{E}(x=0,y,z) = A\exp(-y^2/L_y^2 - z^2/L_z^2)$, we can define a critical power $[P_{cr} = (c/4\beta)(L_z/L_y)(1 + \alpha L_y^2/L_z^2)$, where $\beta = \frac{\omega_{pe}^2}{\omega^2}\frac{e^2}{4mc^2(T_e + 3T_i)}]$ above which the radiation will focus over a distance $x_* = kL_yL_z/2\sqrt{\alpha}\,(P/P_{cr})^{1/2}$. Referring to the parameters of the TMX project /1/, i.e. $f = \omega/2\pi = 200$ GHz, pulse duration $\tau_p \approx 50$ nsec, repetition rate $f_R \approx 5$ kHz, peak pulse power $P \approx 8$ GW, typical transverse spot dimension $h \approx 4$cm, $\overline{n} \approx 2.5\times10^{14}$ cm^{-3}, $\overline{T}_e \approx 1$ kev, $B \approx 7$ T, we obtain $P_{cr} \approx 0.13$ GW and $x_* \approx 12$ cm. The typical time of relaxation of the non linear perturbation can be estimated from the eq.(2) as $\tau_{rel} \simeq L_z/V_S \approx 10^{-7}$ sec.; since $\tau_{rel} > \tau_p$, during a single pulse the steady state cannot be reached and the self-effects have to be studied in a dynamical framework.

To simplify the system (1),(2), we assume that the typical non linear velocity $V_{NL} \gg V_S$, that is, we neglect the second term in the eq.(2). It is then convenient to pass to a reference frame which moves, with the group velocity of the wave $1/\nu$, in the x direction: $\sigma = x$, $\tau = t - \nu x$. Furthermore, introducing the following dimensionless variables:

$$z/z_o \longrightarrow z\,;\quad y/z_o \longrightarrow y\,;\quad \sigma/2Kz_o^2 \longrightarrow \sigma\,;$$

$$\mathcal{E}z_o\left(\frac{c}{8P}\right)^{1/2} \longrightarrow \mathcal{E}\,;\quad t\,\frac{e\omega_{pe}}{z_o\omega}\left(\frac{2P}{Mmc^3}\right)^{1/2} \longrightarrow t\,;\quad \frac{\delta n}{n_o}\,\frac{z_o^2\omega_{pe}^2}{c^2} \longrightarrow n$$

we finally obtain the equations:

$$-i\frac{\partial \mathcal{E}}{\partial \sigma} + \frac{\partial^2 \mathcal{E}}{\partial y^2} + \alpha\frac{\partial^2 \mathcal{E}}{\partial z^2} - n\mathcal{E} = 0\,, \tag{3}$$

$$\frac{\partial^2 n}{\partial \tau^2} = \nabla_\perp^2 |\mathcal{E}|^2\,. \tag{4}$$

P_o and z_o are the power and the size of the beam at the plasma boundary, respectively. We will supplement the eqs.(3),(4) with the following boundary and initial conditions: at the initial time $\tau = 0$, there is no density perturbation $(n(\underline{r}, o) = 0, \partial n/\partial\tau|(\underline{r}, o) = 0)$ and the incident radiation pattern in the plasma is determined only from the boundary distribution $\mathcal{E}(\sigma = 0, y, z)$. We then assume that this distribution is kept constant for $\tau > 0$.

3. Formation of the "focus"

We can describe the self-focusing of the radiation in the plasma, using the so called "aberrationless approach"; we assume that the amplitude of the electric field and the density perturbation can be written in the form:

$$\mathcal{E} = \frac{1}{(a\,b)^{1/2}} \cdot \exp\left(-\frac{z^2}{a^2} - \frac{y^2}{b^2} - i\varrho z^2 - i\beta y^2 + i\mu\right) \tag{5}$$

$$n = n_o \cdot \exp\left(-\frac{z^2}{f^2} - \frac{y^2}{g^2}\right). \tag{6}$$

If we limit our analysis to the central part of the beam, we can expand the expressions (5),(6) near the centre z=y=0; when the approximated expressions for $\mathcal{E}$ and n are substituted in the eqs.(3),(4), we obtain a set of ordinary differential equations for a, b, $F=-n_o/f^2$, $G=-n_o/g^2$ as functions of σ and τ only. These equations have been numerically solved, for $\delta=0$, with boundary conditions $a(\sigma=0)=1$, $b(\sigma=0)=1$; the evolution of the beam parameters shows the self-focusing of the radiation and the formation of a singularity which moves towards the source; the time of focus formation is $\tau_F \approx 2.5$ and it appears at $\sigma_F \approx 0.22$.

4. Self similar structure of the perturbation

The linear analysis of the stability of a homogeneous spatial distribution of the elctric field, with respect to a modulation of its amplitude at the plasma boundary, has been performed in ref.3; it is shown that the amplitude of the modulation increases exponentially in time and space along the direction x of propagation of the beam. If the boundary field distribution is sufficiently smooth, without small scale bumps, the beam structure evolves contracting as a whole. Starting from this consideration one looks for self similar solutions of the eqs.(3),(4). The general form of these solutions is:

$$\mathcal{E} = \frac{A(\eta,\zeta)}{\xi} \exp\left[-\frac{i\mu z^2}{4\xi} - \frac{i\mu y^2}{4\xi} + \frac{i\sigma}{(\tau_o - \tau)\xi}\right] \tag{7}$$

$$n = \frac{N(\eta,\zeta)}{\xi^2} \tag{8}$$

$$\xi = \tau_o - \tau - \mu\sigma\,,\quad \eta = y/\xi\,,\quad \zeta = z/\xi\,,\quad \mu = \text{const.} \tag{9}$$

We see that both $\mathcal{E}$ and n have a singularity at $\sigma_F = (\tau_o - \tau)/\mu$, moving towards the source with the velocity $1/\mu = U_F$. To determine the spatial structure of the self similar functions A and N, we have solved the system /3/:

$$\frac{\partial^2 A}{\partial \zeta^2} + \frac{\partial^2 A}{\partial \eta^2} - NA + A = 0 \tag{10}$$

$$6N + 6\zeta\frac{\partial N}{\partial \zeta} + \zeta^2\frac{\partial^2 N}{\partial \zeta^2} + 6\eta\frac{\partial N}{\partial \eta} + \eta^2\frac{\partial^2 N}{\partial \eta^2} + 2\zeta\eta\frac{\partial^2 N}{\partial \zeta\,\partial \eta} = \frac{\partial^2 (A^2)}{\partial \zeta^2}\,. \tag{11}$$

The eq. (11) has been integrated over characteristics, passing to the variables: $s = \zeta$, $K = \eta/\zeta$,

$$N(s,K) = \frac{1}{s^3}\int_0^s ds' \int_0^{s'} ds''\, s'' \left[\frac{\partial^2 (A^2)}{\partial \zeta^2}\right]_{(s'',K)} \tag{12}$$

where K = const. "labels" an arbitrary characteristic.

The full structure of the basic localized mode has been computed from

eqs.(10),(12) using the method of the stabilizing multiplicator /4/. The resulting distributions $A(\zeta,\eta)$ and $N(\zeta,\eta)$ are shown in Fig. 1 for $\delta=0$. Going back to the original dimensionless variables, one sees that the resulting asymptotic behaviour $n \propto 1/z^2$ of the density perturbation survives as a "trace", after the transit of the focus through each section σ = const, and then relaxes slowly over characteristic sound times.

5. Conclusions

The present analysis has shown that the dynamical treatment of the self-focusing of high power pulsed radiation leads to the formation of a singularity in the amplitude of the electric field which locally depletes the plasma density. From the aberrationless approach we can estimate that the focus appears at $x_F \approx 60$ cm in a time $t_F \approx 10$ nsec, that is well inside the FEL pulse; then the focus moves towards the source with a (phase) velocity $U_F \approx 10^{11}$ cm/sec which slows down approaching the source. This means that during the single FEL pulse the focus appears inside the plasma and the physical picture is determined entirely by the effect of the dynamical self-focusing.

Aknowledgments

This work has been performed on the basis of the scientific cooperation agreement between the Soviet Academy of Science and the Italian National Council of Research (CNR). The authors wish to thank the CRE, EUR/ENEA Ass., Frascati, where part of the work has been carried out.

References

/1/ K.I.Thomassen, "FEL Experiments in Alcator-C", LLNL, Livermore, USA, LLL-PROP-00202, 1986;

/2/ A.G.Litvak in "Reviews of Plasma Physics", vol.10,p. 293, Consultants Bureau, New York,1986;

/3/ M.Lontano, A.M.Sergeev, "Dynamical Self-Focusing of the High-Power FEL Radiation in a Magnetized Plasma", Istituto di Fisica del Plasma, EUR-ENEA-CNR Ass., Report FP 88/1, 1988;

/4/ V.I.Petviashvili, Sov. Journal Plasma Phys.,54, 1064,(1981).

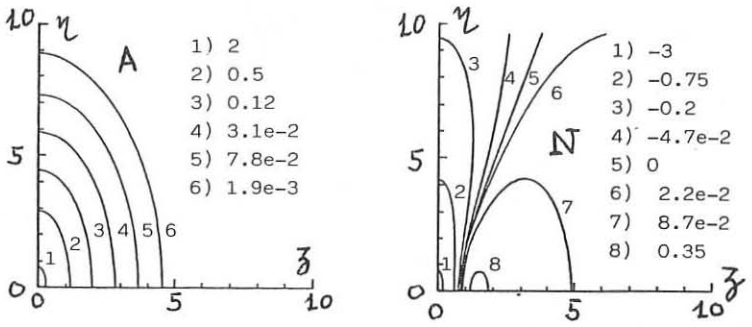

Fig.1 Level lines of A (a) and N (b) in the ζ,η-plane, for $\delta=0$. The values of the levels are indicated on the right.

SURFACE WAVES IN A TWO–ION SPECIES PLASMA WITH FINITE EDGE DENSITY

A. B. Murphy

Max–Planck–Institut für Plasmaphysik, EURATOM Association,
D–8046 Garching, Federal Republic of Germany.

1. INTRODUCTION

Interest in Alfvén surface waves has been stimulated in recent years by experimental studies of the Alfvén wave heating scheme. This scheme relies on mode conversion of the compressional Alfvén wave, generated by an external antenna, to the torsional Alfvén wave, at a resonance surface inside the plasma. The only compressional wave modes that propagate at sufficiently low frequencies are those poloidally asymmetric ($m \neq 0$) modes known as surface waves. Surface waves are also relevant to the ion cyclotron heating scheme, as they may be parasitically excited by antennas designed to couple to those 'cut–off' modes of the compressional wave which do not propagate above a certain non–zero frequency [1,2].

The behaviour of Alfvén surface waves has been investigated theoretically in both single–ion [3–8] and two–ion species [9–11] plasmas. All these studies assumed the plasma to be separated from a conducting wall by an insulating or vacuum gap. Cross and Murphy [12] showed that the surface wave spectrum in a single–ion species plasma is significantly affected when this gap is replaced by a region of low density plasma. The present paper extends this work to the case of a two–ion species plasma. The results are relevant to Alfvén wave heating of a plasma containing impurity species and to ion cyclotron minority and mode conversion heating.

2. PLASMA MODEL

I consider a cylindrical plasma of uniform electron density n_a and radius a, surrounded concentrically by plasma of uniform electron density $n_b < n_a$ and a conducting wall at radius d. A uniform magnetic field $\vec{B} = B_0\vec{z}$ exists in the region $0 < r < d$. I consider small amplitude perturbations varying as $\exp[i(k_\parallel z + m\theta - \omega t)]$, and adopt a cold plasma approximation, ignoring finite electron mass and displacement current, but including the Hall term in Ohm's law.

The wave b_z component in each region of uniform density satisfies the equation

$$\frac{\partial^2 b_z}{\partial r^2} + \frac{1}{r}\frac{\partial b_z}{\partial r} + (k_\perp^2 - \frac{m^2}{r^2})b_z = 0 \qquad (1)$$

where

$$k_\perp^2 = (F^2 - G^2)/F, \qquad F = A - k_\parallel^2,$$

$$A = \frac{\Omega_1^2}{(1-\Omega_1^2)}\frac{\omega_{p1}^2}{c^2} + \frac{\Omega_2^2}{(1-\Omega_2^2)}\frac{\omega_{p2}^2}{c^2}, \quad G = \frac{\Omega_1^3}{(1-\Omega_1^2)}\frac{\omega_{p1}^2}{c^2} + \frac{\Omega_2^3}{(1-\Omega_2^2)}\frac{\omega_{p2}^2}{c^2},$$

and $\Omega_j = \omega/\omega_{cj}$, ω is the wave frequency, $\omega_{cj} = B_0 Z_j e/m_j$ is the cyclotron frequency and $\omega_{pj}^2 = n_j(Z_j)^2/(m_j\epsilon_0)$ the plasma frequency of the ion species j of mass m_j, charge $Z_j e$ and number density n_j.

Dispersion relations were obtained by numerical integration of (1) from $r = 0$ to $r = d$, using appropriate boundary conditions at $r = d$ and $r = a$. It is noted that when a plasma is in contact with a conducting wall, the radial component of plasma velocity must be zero at the wall. This precludes the existence of surface wave modes in a cold plasma without a vacuum gap adjacent to the wall. Since the gap can be vanishingly narrow, results are given for zero gap width. These results represent the limiting case as the gap width approaches zero, in an analogous manner to the single–ion species case discussed in [12].

3. RESULTS

Representative dispersion relations are shown in Figure 1 for parameters typical of a small research tokamak, assuming $d = 0.12$ m, $a/d = 0.8$, $n_a = 1 \times 10^{19}$ m^{-3}. A plasma comprising equal proportions of hydrogen and deuterium is treated in order to make the dispersion curves clear. The figure shows, for $m = +1$ and $m = -1$, the effect of replacing a vacuum layer in the region $a < r < d$ by a low density plasma, i.e., of increasing n_b/n_a from 0 to 0.1. For $m > 0$ modes, the main effect is to introduce a cut–off and resonance near the cyclotron frequency of each ion species, thus giving a dispersion relation with three branches instead of the original one. These are labelled, in order of increasing frequency, S (surface wave), CO1 (cut–off branch 1) and CO2. S and CO1 merge respectively with the locii of the Alfvén resonance and the ion–ion hybrid resonance in the edge plasma (also shown in the figure) as $\omega \to \omega_{cD}$ and $\omega \to \omega_{cH}$ respectively. Note also that the surface wave spectrum crosses the central plasma ion–ion hybrid resonance via a mode crossing in both the presence and absence of a vacuum layer. This effect was examined in detail in [9].

The introduction of a finite density edge plasma has little effect on the dispersion relations of the $m < 0$ modes that are present in a plasma surrounded by a vacuum layer. However, a new mode (labelled CO2) now propagates, at frequencies just below ω_{cH}.

4. DISCUSSION

It is reasonable to question the relevance of the dispersion relations presented above to realistic plasma density profiles. It was shown in [12] that, in a single–ion species parabolic plasma with a finite edge density, a cut–off occurs at around the ion cyclotron frequency in the $m = +1$ dispersion relation, corresponding to the result obtained for a step profile plasma. Although a similar calculation has not yet been attempted for a two–ion species plasma, it may be assumed that a similar correspondence will be found.

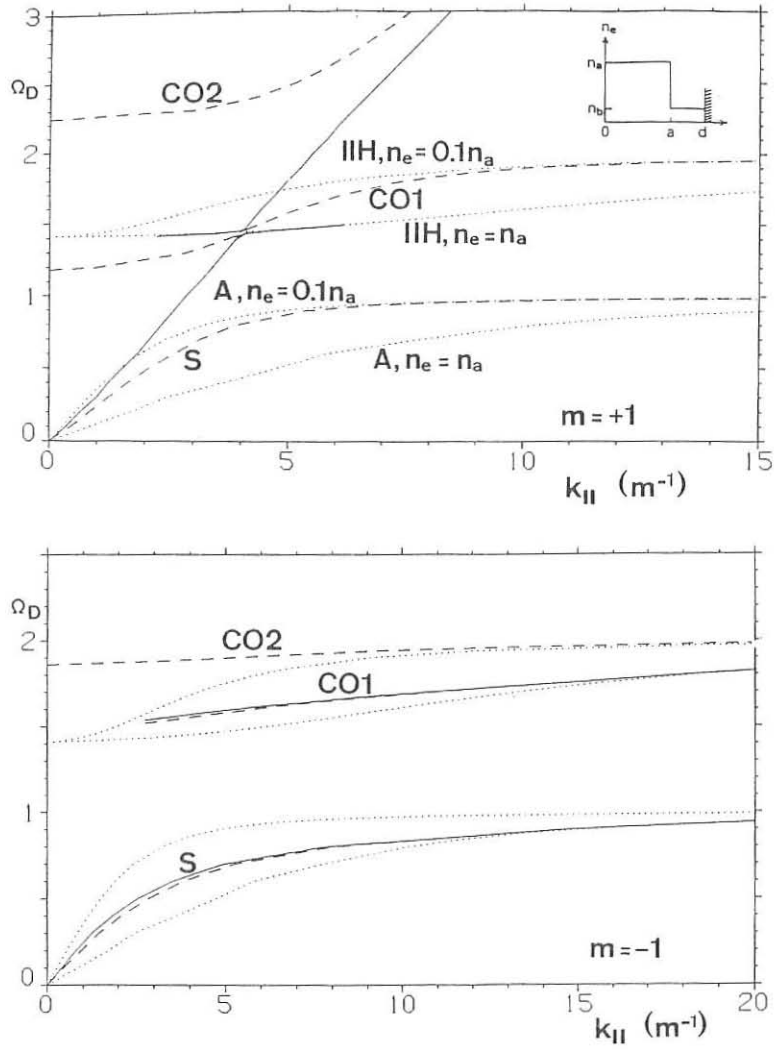

Figure 1.—Dispersion relations of the $m = +1$ and $m = -1$ compressional Alfvén wave in a step density profile plasma (see inset) consisting of equal parts deuterium and hydrogen with $d = 0.12$ m, $a/d = 0.8$, $n_a = 1 \times 10^{19}$ m^{-3}, and $n_b/n_a = 0$ (unbroken lines) and 0.1 (dashed lines). The locii of the Alfvén (A) and ion–ion hybrid (IIH) resonance frequencies at densities n_a and $0.1n_a$ are also shown (dotted lines).

In the case of plasmas of somewhat larger minor radius and density, the higher radial mode number cut–off branches (which do not propagate in the frequency range shown in Figure 1) can propagate at frequencies down to or below the cyclotron frequencies of one or both ion species. These are the modes of interest for 'fast wave' ion-cyclotron heating. The effect on the surface wave spectrum of introducing a finite density edge plasma remains the same, so the results given in this paper are relevant to ion cyclotron minority and mode conversion heating of larger devices. The existence of low $k_{||}$ surface wave modes at $\omega \approx \omega_{cH}$ could be associated with the relatively high impurity levels observed to be produced by antennas which excite a wave spectrum centred around $k_{||} = 0$ [13].

The cyclotron frequencies of impurity ions can be a small fraction of that of the majority species, and thus of the order of the wave frequency in Alfvén wave heating. This means that the alterations to the surface wave dispersion relation effected by the presence of a finite density edge plasma, particularly the introduction of a cut–off and resonance near the lower ion cyclotron frequency in the $m > 0$ case, are relevant to the Alfvén wave heating scheme. As the coupling efficiency of an antenna array to the Alfvén resonance surfaces inside the plasma depends critically on the efficiency of excitation of the surface waves present, it is clear that the presence of a finite density edge plasma should be considered in Alfvén wave heating calculations.

REFERENCES

[1] Messiaen A. M. *et al.* in *Heating in Toroidal Plasmas* (Proc. 4th Int. Symp., Rome, 1984) (ISPP, Varenna, 1984) Vol. 1, p. 315.

[2] Van Nieuwenhove R. *et al.* in *Europhysics Conf. Abs. 11D* (Proc. 14th Eur. Conf. Contr. Fusion and Plasma Phys., Madrid, 1987) (EPS, 1987) Part 3, p. 928.

[3] Paoloni F. J. *Phys. Fluids* **18** (1975), 640.

[4] Cramer N. F. and Donnelly I. J. *Plasma Phys.* **25** (1983), 703.

[5] Collins G. A., Cramer N. F. and Donnelly I. J. *Plasma Phys. Contr. Fusion* **26** (1984), 273.

[6] Appert K., Vaclavik J. and Villard L. *Phys. Fluids* **27** (1984), 432.

[7] Donnelly I. J. and Cramer N. F. *Plasma Phys. Contr. Fusion* **26** (1984), 769.

[8] Cramer N. F. and Donnelly I. J. *Plasma Phys. Contr. Fusion* **26** (1984), 1285.

[9] Cramer N. F. and Yung C.–M. *Plasma Phys. Contr. Fusion* **28** (1986), 1043.

[10] Akiyama H., Hagler M. O. and Kristiansen M. *IEEE Trans. Plasma Science* **13** (1985), 125.

[11] Appert K., Vaclavik J. and Villard L. in *Europhysics Conf. Abs. 7D* (Proc. 11th Eur. Conf. Contr. Fusion and Plasma Phys., Aachen, 1983) (EPS, 1983) Part 1, p. 305.

[12] Cross R. C. and Murphy A. B. *Plasma Phys. Contr. Fusion* **28** (1986), 597.

[13] Bureš M. *et al. Plasma Phys. Contr. Fusion* **30** (1988), 149.

Current Drive and Profile Control

LOWER HYBRID CURRENT DRIVE EFFICIENCY IN ASDEX

F. Leuterer, F. Söldner
Max-Planck-Institut für Plasmaphysik, Garching, Germany
K. Yoshioka, T. Okazaki
Energy Research Laboratory, Hitachi Ltd., Hitachi, Japan
N. Fujisawa
Japan Atomic Energy Research Institute, Naka-gun, Ibaraki-ken, Japan

The ASDEX lower hybrid current drive experiments at 1.3 GHz have been re-evaluated in view of a new analytic model for the current drive efficiency in the presence of a dc electric field /1/. This model is based on a perturbation solution of the adjoint problem to the Fokker Planck equation and includes the effects of a dc electric field and of a finite width of the wave spectrum. The current drive efficiency I_{RF}/P_{RF}, normalized to its value $(I_{RF}/P_{RF})_o$ at zero electric field, is then given by

$$\eta/\eta_o = \frac{I_{RF}/P_{RF}}{(I_{RF}/P_{RF})_o} = \frac{\ln((1 - X_1)/(1 - X_2))}{X_2 - X_1} \qquad (1)$$

where $X_{1,2} = \alpha E_N u_{1,2}^2$ with $\alpha = 12/(Z+7)$, $E_N = E/E_{Dr}$, $u = v_{ph}/v_{th}$, $E_{Dr} = m_e v_{th} \nu_o/e$ and $\nu_o = n_e e^4 \ln\Lambda/2\pi \varepsilon_o^2 m^2 v_{th}^3$. The indices correspond to the limits v_{ph1} and v_{ph2} of the wave phase velocity spectrum. The normalized efficiency, equ. (1), is shown in Fig. 1 for various values of $(X_2/X_1)^{1/2}$, i.e. the width of the spectrum. The efficiency is seen to depend mainly on X_2, corresponding to the high phase velocity boundary of the spectrum. Its dependence on X_1 is rather weak.

For the limiting situation of a very broad spectrum, $X_2/X_1 \to \infty$, equ. (1) becomes nearly independent of X_1 and can be approximated as

$$\eta/\eta_o = - \ln |1-X_2|/X_2 \ . \qquad (2)$$

In the opposite situation of a narrow spectrum with $X_1 = X_2 = X$ we get

$$\eta/\eta_o = 1/(1-X). \qquad (3)$$

In the ASDEX-experiments the plasma current I_p was feedback controlled. The measured quantities are the net RF power P_{RF}, the line averaged electron density n_e, and the rate of change of the primary current I_{OH} in the

OH-transformer which is necessary to maintain a constant plasma current. $I'_{OH,OH}$ is its value just before the application of the RF-power, $I'_{OH,RF}$ its value during applied RF-power. Their ratio is shown in Fig. 2 as a function of RF-power for different densities. From Thomson scattering we obtained the variation of the central electron temperature T_{eo} as a function of P_{RF} and n_e, shown in Fig. 3. Using a measured electron density profile we determined the accessibility condition, $N_{\parallel acc}$, to the central region of the plasma by means of a raytracing code.

The plasma current can be written as the sum of an inductively driven current, for which we assume Spitzer conductivity, and an RF-driven current,

$$I_p = I_{Ind} + I_{RF} \cdot \tag{4}$$

From our measurements the RF-driven current can be determined as

$$I_{RF} = I_p \left[1-(I'_{OH,RF}/I'_{OH,OH})\cdot(T_{e,RF}/T_{e,OH})^{1.5}\right] . \tag{5}$$

The temperature correction in this equation takes care of the variation of the Spitzer conductivity due to additional bulk electron heating by the RF-power, which is obtained from Fig. 3. The quantity X_2 is calculated from

$$X_2 = \alpha\, E_N\, u_{acc}^2 = 580 \cdot \alpha\, E/(N_{\parallel acc}^2\, n_e) \tag{6}$$

in the units V/m, 10^{12} cm^{-3}, with $E = -M\, I'_{OH,RF}/2\pi R$ and $M = 80$ µH for ASDEX. For the current drive efficiency at zero electric field we use our old experimental results of reference /2/

$$(I_{RF}/P_{RF})_o = a\cdot\mu\cdot g/n_e , \tag{7}$$

where μ describes the fraction of accessible power, g is the theoretical dependence of the efficiency changing with $N_{\parallel acc}$, and a is a numerical fit parameter good up to densities of $n_e \approx 1\cdot10^{13}$ cm^{-3}.

In Fig. 4 we show the resulting experimental current drive efficiencies. For the determination of X_2 we took $Z = 3$. Comparing Figs. 1 and 4 we find a reasonable agreement. We should, however, not forget that the above model assumes homogeneous profiles for both current density and power absorption, complete power absorption by the fast electrons and that the central value calculated for v_{phacc} is the right value to substitute for $v_{ph\,2}$.

We may also compare our results in the form of the conversion efficiency P_{el}/P_{RF} as defined by N. Fisch and C. Karney, /3/, where for our situation

$P_{el} = - M I'_{OH,RF} I_{RF}$. Taking the theoretical zero electric field efficiency

$$\eta_o = \beta(u_2^2-u_1^2)/\ln(u_2/u_1) \ , \qquad (8)$$

where $\beta = 4/(Z+5)$, the conversion efficiency becomes

$$\frac{P_{el}}{P_{RF}} = -E \frac{I_{RF}}{P_{RF}} = -E_N \frac{\eta}{\eta_o} \eta_o = \frac{2\beta}{\alpha} \cdot \frac{\ln|(1-X_2)/(1-X_1)|}{\ln(X_2/X_1)} \qquad (9)$$

This is shown as the solid lines in Fig. 5 as a function $X_2^{1/2} = (\alpha/2)^{1/2} \cdot u_{R2}$ with $u_R = v_{ph}/v_R$ and $v_R = v_{th}/(2\ E_N)^{1/2}$. We have confirmed that for the case of a localized spectrum, $X_2/X_1 = 1$, and for $Z = 1$, equ. (9) agrees very well with the numerical result of N. Fisch and C. Karney, /3/, except for the factor $2\beta/\alpha$ which is only close to, but not exactly unity. We see from Fig. 5 that the conversion efficiency is significantly degrated with increasing spectrum width X_2/X_1.

In Fig. 5 we have also plotted $P_{el}/P_{RF} = -M I'_{OH,RF} I_{RF}/P_{RF}$ for our experimental points from Fig. 4. Taking $Z = 3$ these points fit to curves in the range $(X_2/X_1)^{1/2} = 16$ to 32. This seems very high. However, we note that the empirical fit factor a in the steady state current drive efficiency is about a factor of two lower than estimated from theory /2/. If we include an absorption coefficient of ≈ 0.5, as was done in the evaluation of the PLT experiments, /4/, the points would fit to curves around $(X_2/X_1)^{1/2} \approx 4$, which seems much more realistic.

References:

/1/ K. Yoshioka, T. Okazaki, F. Leuterer, N. Fujisawa, Physics of Fluids, to be published (April 1988)

/2/ F. Leuterer, F. Söldner, D. Eckhartt et al. Plasma Phys. and Contr. Fus. 27, 1399 (1985)

/3/ C. Karney, N. Fisch, Phys. Fluids 29, 180 (1986)

/4/ C. Karney, N. Fisch, F. Jobes, Phys.Rev. A 32, 2554 (1985)

Figures:

1. Normalized current drive efficiency as a function of electric field.
2. Normalized primary current rate of change as function of the RF-power.
3. Central electron temprature with and without RF-current drive.
4. Experimental current drive efficiency.
5. Efficiency for conversion of RF-power into electromagnetic energy.

Fig. 1

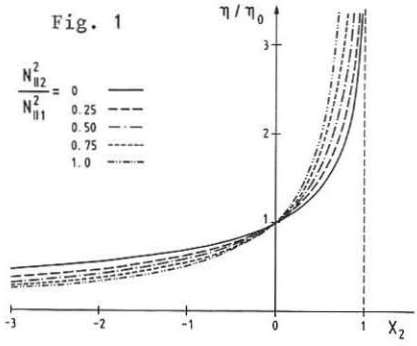

Fig. 3

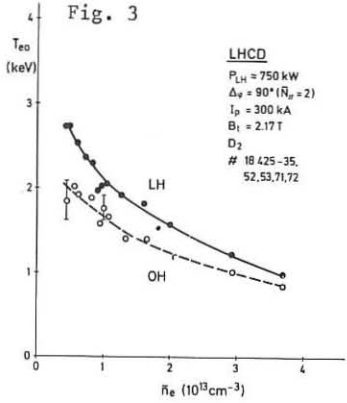

Fig. 4

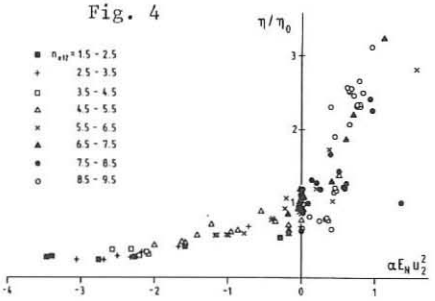

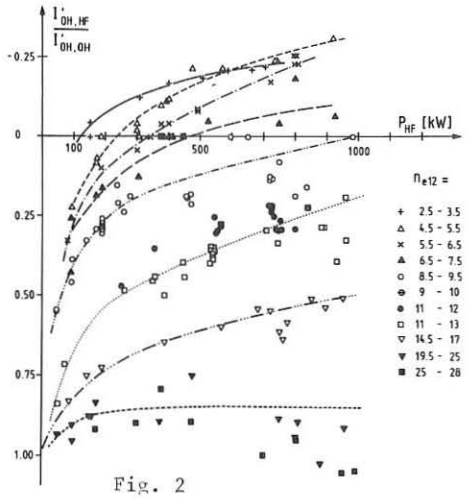

Fig. 2

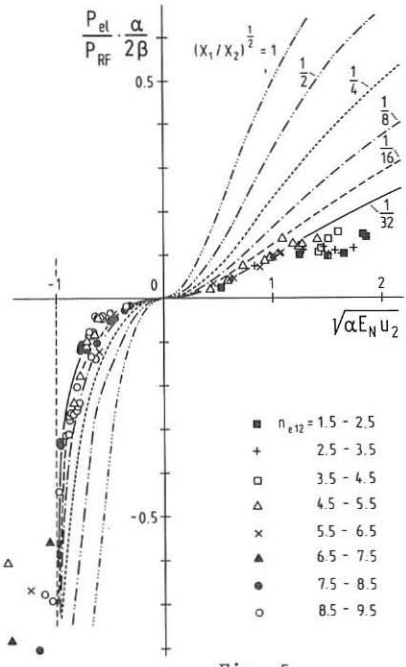

Fig. 5

EVALUATION OF THE CURRENT PROFILE IN L.H.C.D. TOKOMAKS

G. BRIFFOD. IRF-DRF - C.E.N.G. - 85 X GRENOBLE CEDEX (FRANCE)

I. LOOP VOLTAGE BEHAVIOUR AND SATURATION OF THE R.F. ABSORBED POWER

The current density driven by L.H. waves, j_{RF}, is related to the R.F. absorbed power per unit volume, p_{abs}, by the relation $j_{RF} = \eta\, p_{abs}$. Averaging over the plasma, the total current can be expressed as :

$I_{RF} = \eta_F\, P_{abs}$ (1) with $\eta_F = 83.2/(5 + Z)\; n\, R\, N_{//}^2$ (2)

The theory of the current drive efficiency has been worked out in great details by N. FISCH [1] and in a weakly relativistic case and for a narrow wave spectrum η_F takes the simplified form given by (2). As in steady state L.H.C.D. tokomaks, P_{abs} cannot be easily measured, I_{RF} is generally estimated from the drop of the loop voltage, ΔV, due to the application of the R.F. power, P_{RF}.

$V_P = R_P\, I_P \qquad V = R\,[I_P - I_{RF}] \qquad I_{RF} = I_p[1 - RV/R_P V_P] \sim I_P\, \Delta V/V_P$ (3)

As a consequence of (1) and (3), if the applied and absorbed powers are proportional $P_{abs} \propto P_{RF}$, I_{RF} and $\Delta V/V_p$ should scale linearly with P_{RF}. This is not verified experimentally as it can be seen on fig. 1 which shows the variation of $\Delta V/V_p$ as a function of P_{RF} measured on PLT [2] with a narrow wave spectrum (16.w.g.grill) and for the operating conditions given on table I. The observed saturation of $\Delta V/V_p$ corresponds to a continuous decrease of the current drive efficiency. The ratio of the experimental efficiency $\eta_{EXP} = I_{RF}/P_{RF}$ to the theoretical one (2) for $Z = 3$ is plotted on fig. 1. The efficiency improvement at low R.F. power can be explained by the presence of a D.C. electric field, $E = V/2\pi R$ which gives rise to an additional current [1]. But as P_{RF} increases, the ratio η_{EXP}/η_F, even corrected by the coupler directivity becomes much smaller than one whereas this model predicts an efficiency improvement up to $\Delta V/V_p = 1$.

One explanation to this efficiency loss proposed by J.M. RAX [3] is based on the assumptions : (i) at low RF power, the absorbed and

TABLE I

	PLT	PETULA	ASDEX	ALCATOR
$\bar{n}(10^{13})$	1	1	0.6	4
B_ϕ(T)	3	2.8	2.2	8
I_p(KA)	.500	.145	.300	.205
Z	3	3	3	2
α	0.65	0.5	0.65	0.22
N_ϕ	1.5	1.7	2	1.5
f(GHz)	2.45	3.7	1.3	4.6

Fig.1

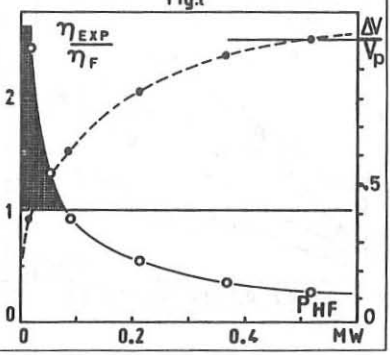

injected powers scale linearly $P_{abs} = P_{IN}$; (ii) at high power P_{abs} goes towards a limiting value P^*, corresponding to the maximum R.F. power which can be absorbed by a given plasma. With these assumptions the relations (1) and (2) become :

$$I_{RF} = \eta\, P_{abs} = \eta \frac{P_{IN}\, P^*}{P_{IN} + P^*} \quad (5) \text{ and } \quad \frac{P_{RF}}{I_p\, \Delta V/V_p} = \frac{1}{\alpha\, \eta} + \frac{P_{RF}}{\eta\, P^*} \quad (6)$$

where P_{RF} is the power launched by the coupler, α the coupler directivity and $P_{IN} = \alpha\, P_{RF}$ the fraction of the R.F. power used to drive the current. The fig. 3 shows the variation of the ratio $P_{RF}[I_p\, \Delta V/V_p]^{-1}$ as a function of P_{RF} for steady state L.H.C.D. discharges performed on ALCATOR [4] ASDEX [5] PETULA [6] PLT [2] for the operating conditions given in table I. This figure puts into evidence several important points (i) the ratio $P_{RF}[I_p\, \Delta V/V_p]^{-1}$ scales linearly with P_{RF} for the 4 discharges as predicted by (6) ; (ii) the slope $[\eta\, P^*]^{-1}$ is different for each discharge ; (iii) the loop voltage $\Delta V/V_p$ and P_{ECE} the total E.C.E. radiated power exhibit the same linear scaling for PETULA [7]. The plot of $\eta\, P^*$ as a function of I_p, shown on fig. 4, fits very well with the scaling law $\eta\, P^* = 1.2\, I_p$.

II. GLOBAL AND LOCAL MODELISATION OF THE R.F. CURRENT

To drive a steady state current, I_{RF}, the injected wave has to balance the power lost due to collisions, which can in a first estimate be evaluated as $P_d = m < n_R > c^2\, N_{/\!/}^{-2}\, \nu$ vol. (8). Where $< n_R >$ is the average resonant electron density, $c/N_{/\!/}$ the phase velocity of the wave, ν the Coulomb collisions between the resonant electrons and the bulk plasma, vol. the plasma volume. For $\Delta V/V_p = 1$, the plasma current, I_p, is entirely sustained by the resonant electrons. For this condition, $< n_R >$ can be deduced from $I_{RF} = I_p = e < n_R > c\, N_{/\!/}^{-1}\, \pi\, a^2$ and P_d writes

$$P_d(W) = 3.2\ 10^{-3}\ I_p(A)\ n(10^{13}) N_{/\!/}^2\ R(m)\ \mathrm{Log}\ \Lambda \quad (9)$$

In steady state L.H.C.D. discharges, the maximum R.F. current which is driven is of the order of I_p. As a consequence the value of P_d given by (9) can be considered to be close to the maximum R.F. power dissipated

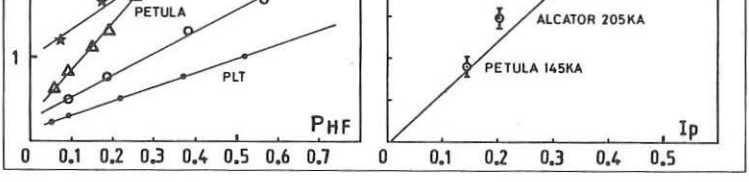

via the collisions and will be used in the following instead of P^*. With this relation $P^* = P_d$ and using the FISCH's expression (2) for the current drive efficiency, the R.F. current can be expressed as

$$I_{RF} = \eta\, P_{abs} = K_0\, \eta_F\, P_d\, \frac{\alpha\, P_{RF}}{\alpha\, P_{RF} + P_d} \qquad (10)$$

K_0 is a fitting factor, $\eta = K_0\, \eta_F$, which in a first approximation does not take into account explicitly the effect of the D.C. electric field. In this relation the product $K_0\eta_F P_d$ has the same plasma current dependence as the experimental scaling law $\eta P^* = 1.2\ I_P$. The equality between the two expressions, $K_0\eta_F P_d = 1.2\ I_P$, gives the value of K_0 to be used for the computation of I_{RF} ($K_0 = 2.4$ for $Z = 3$). The variation of I_{RF} as a function of P_{RF} computed from (10) is shown of fig. 5 for PLT, ASDEX and ALCATOR. It can be seen that these curves agree very well with the experimental values deduced from $I_{RF} = I_P\, \Delta V/V_P$.

However for these 4 discharges the accessibility condition is satisfied, $N_{acc}(o) < < N_{/\!/}>$, and the wave can penetrate up to the plasma center. But when the plasma density increases, its penetration is limited by the local accessibility condition $N_{acc}(r) = N_{/\!/}$. The injected R.F. power at a given radius and the R.F. current are then given by :

$$P_{IN} = \alpha P_{RF} - \alpha_R(r) P_{RF} - \int_a^r p_{abs}\, dV \quad (11) \qquad j_{RF} = K_0 \eta_L p_d \frac{p_{in}}{p_{in} + p_d} \quad (12) \qquad I_{RF} = \int_a^r j_{RF}\, dS \quad (13)$$

in these expressions $\alpha_R(r)P_{RF}$ is the non accessible part of the wave power sprectrum $P(N_{/\!/})$, $\eta_L = \eta_F\, 2\pi R$ is the local FISCH's current drive efficiency, $p_d = p^*$ the power per unit volume dissipated by collisions and K_0 the fitting factor which is assumed to be constant over the radius (E = Cte). A schematic representation of the radial R.F. power balance (11), displayed on fig.6, shows the main features of this model (i) in the outer part of the plasma, n and p_d are small whereas the injected power is very high. p_{abs} and j_{RF} saturate, $j_{RF} = K_0\eta_L p_d$ (ii) as the wave propagate, n, p_d and α_R increase and the R.F. current saturation is progressively reduced (iii) beyond a given radius p_{in} is smaller than p_d and j_{RF} becomes proportionnal to p_{in}. The radial

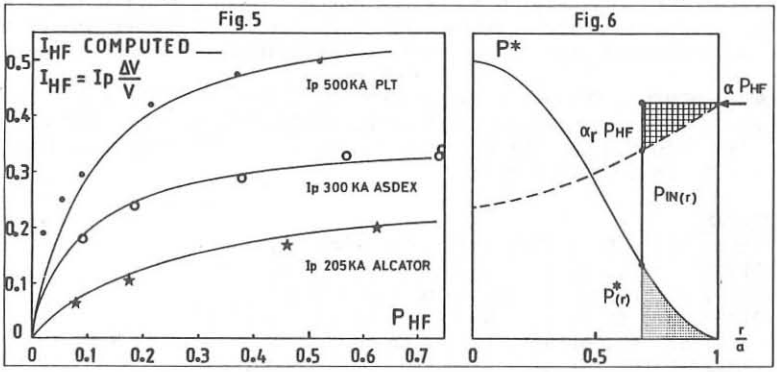

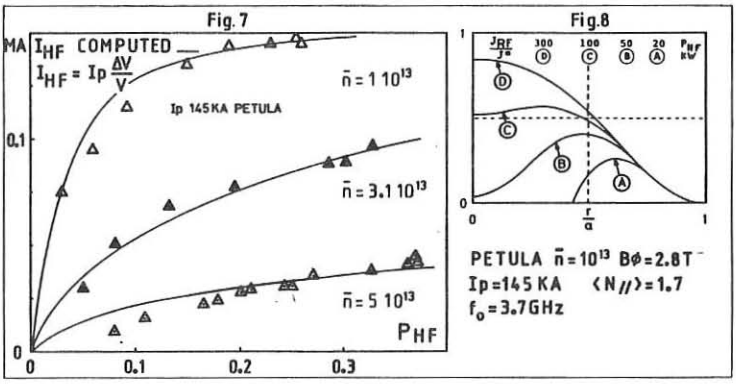

extension of the current, $\Delta r = a - r_0$, is given by $P_{IN} = 0$ in the relation (11). In a first approximation, r_0 can be evaluated by :

$$P_{IN} = \alpha P_{HF} - \alpha_R(r_0)\, P_{HF} - \int_a^{r_0} p_d \, dV = 0 \qquad (14)$$

As the R.F. power level increases, r_0 goes to 0 and at high power, $P_{RF} \gg P_d$, j_{RF} saturates everywhere, and peaks at the plasma center as seen on fig. 8. Using the approximate expression (14), and the following assumptions $p_d = p^*, n_R = n_R(0)\,[1 - r^2/a^2]^\nu$, $P(N_{//}) \propto N_{//}$ inside the main lobe of the wave spectrum, yield the following relation for the current density

$$\frac{j_{RF}(r)}{j^*(0)} = [1 - r^2/a^2]^\nu \left[1 - \frac{P_d(0)}{\alpha P_{RF}} \, 2\Delta N_{//} \, \frac{[1 - r^2/a^2]^{\nu+2}}{\langle N_{//} \rangle + \Delta N_{//} - [1 + n/B^2]^{1/2} - [n/B^2]^{1/2}} \right] \qquad (15)$$

where $2\Delta N_{//}$ is the wave spectrum width. The variation of I_{RF} versus P_{RF}, computed from (15) and (13), for different densities is shown on fig. 7 for the PETULA plasma parameters and is compared to the experimental results of ref. [6]. Fig. 8 shows the current radial profile for 4 R.F. powers. Due to space limitations more detailled comparison of this model with experimental results will be presented elsewhere.

ACKNOWLEGDMENTS : This work was performed under EURATOM - C.E.A. - JET contract. The author wants to thank C. GORMEZANO, J. JACQUINOT and the L.H. JET TEAM for usefull discussions and J. STEVENS for providing him with P.L.T. loop voltage data.

REFERENCES

[1] FISCH, N.J., Rev. Mod. Phys., 59 (1987) 175
[2] STEVENS, J.E., et al., 28th APS Meet. Nov. 1986
[3] RAX, J.M., Phys. Fluids, to be published
[4] TAKASE, Y., et al., J. Nucl. Fusion 53 (1987) 53
[5] STEINMETZ, K., et al., 11th AIEA Conf., KYOTO, Japan, Nov. 1986
[6] GORMEZANO, C., et al., 13th EPS Conf., SCHLIERSEE, F.R.G., 1986
[7] GIRARD, A., et al., 13th EPS Conf. SCHLIERSEE, F.R.G., 1986.

LOWER HYBRID WAVE STOCHASTICITY IN TOKAMAKS: A UNIVERSAL MECHANISM FOR BRIDGING THE $n_{\|}$ SPECTRAL GAP

D Moreau*, J M Rax*, A Samain*

JET Joint Undertaking, Abingdon, Oxfordshire, OX14 3EA, England
* From EUR-CEA Assoc, CEN Cadarache, 13108 St Paul lez Durance, France

Abstract

A global approach to the problem of LHCD is being attempted. For typical tokamak aspect ratios the propagation over long trajectories is stochastic and we describe the dynamics of the wave in the random phase approximation (RPA).

Motivation for a Global Approach to LHCD

Up to now, combined ray-tracing and Fokker-Planck codes have provided a fairly good description of LHCD if the waves are followed after one or a few reflections at the plasma edge and if the suprathermal electrons are allowed to diffuse towards the plasma core before slowing down[1]. In fact, because the absorption is based on the resonant interaction between the waves and the fast electrons the plasma is generally transparent to the highest phase velocity waves which are launched. This is usually referred to as the problem of the LH spectral gap.

If the wave is decomposed on the usual $\exp(-j\omega t + jn\phi + jm\theta)$ harmonic cylindrical basis, the local wave vector is given by:

$$k_{\|}(r) = (n + \frac{m}{q(r)})/R \qquad (1)$$

where $q(r)$ is the cylindrical safety factor. Under the condition $n\varepsilon >> 1$, where ε is the inverse aspect ratio of the tokamak, ray-tracing predicts a large increase in the poloidal mode number m which entails a significant upshift of the wave vector $k_{\|}$. However there are some drawbacks in using the geometrical optics for waves which are propagating over multiple passes through the plasma column. Such an approach is unable to take into account the spreading of wavepackets and therefore applies only during a characteristic correlation time of the wave. In our work we show how, due to toroidal effects, a stochastic instability appears[2], which leads to an exponential divergence of the rays and to the destruction of the correlations. The long time dynamics of the wave energy U(m) will be described as a random walk in m space[3]. Then the solution of the associated master equation can predict the steady state distribution U(m) and, via (1), the local and spectral power and current deposition, which are the crucial parameters for profile control experiments.

Resonant Toroidal Couplings

Our starting point is a modal analysis of the electric field $\bar{E}$ on a cylindrical basis:

$$\bar{E}(\bar{r},\omega) = \sum_{l,m,n} a_{lmn}(\omega)\ \bar{E}_{lmn}(\bar{r}) \qquad (2)$$

where l,m,n are the radial, poloidal and toroidal mode numbers related by the unperturbed cylindrical dispersion relation $D(\omega,l,m,n) = 0$. Fig 1 shows such a dispersion curve (f = 3.7 GHz, n = const) for the electrostatic branch and typical JET parameters. Toroidal effects induce couplings between the (l,m,n) modes and Maxwell equations can be written:

$$\frac{d}{dt} a_{lmn}(t) = - j\omega_{lmn}\ a_{lmn}(t) - j \sum_{l'm'n} V_{lmn}^{l'm'n'}\ a_{l'm'n'}(t) \qquad (3)$$

where $V_{lmn}^{l'm'n'}$'s are matrix elements of the toroidal perturbation, ie proportional to $\varepsilon^{|m-m'|}$. We are thus led to consider a system of coupled oscillators.

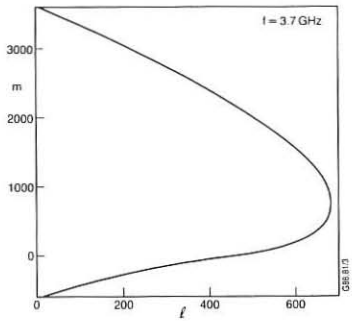

Fig 1: Dispersion Curve

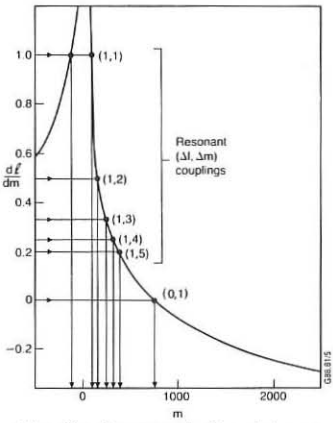

Fig 2: Resonant Couplings

Because the perturbation is stationary, toroidal couplings will be resonant when they couple modes which lie on the unperturbed dispersion curve, ie which correspond to the same eigenfrequency ($\omega_{l'm'n'} = \omega_{lmn}$). This will occur when the vector ($\Delta l = l-l'$, $\Delta m = m-m'$) is tangent to the dispersion curve, ie when the slope of the curve is rational:

$$\left(\frac{\partial l}{\partial m}\right)_{\omega} = \frac{\Delta l}{\Delta m} = \text{rational number} \qquad (4)$$

Fig 2 displays this set of resonances. We expect the dynamics of system (3) to be dominated by the resonant couplings and we are therefore tempted to apply the random phase approximation and to write a master equation for the wave energy $U(m) \propto a_{lmn} \cdot a_{lmn}^{*}$ with n = const and $l = l(\omega,n,m)$:

$$\frac{dU(m)}{dt} = \sum_{m'} P(m' \to m)\ U(m') - \sum_{m'} P(m \to m')\ U(m) \qquad (5)$$

If the transitions took place in a continuum of states, the transition probabilities $P(m \rightleftarrows m')$ would be proportional to $|V^{lmn}_{l'm'n'}|^2$. So we must find out how to compute the resonant matrix elements. A second conceptual question also arises: under which conditions is the random phase approximation justified and what is the connection between $P(m \rightleftarrows m')$ and $V^{lmn}_{l'm'n'}$ in the actual problem?

Wave Stochasticity and Criterion for Random Phase Approximation (RPA)

To make progress concerning these questions, we go back to the standard ray-tracing and express it in terms of canonical action-angle variables of the cylindrical geometry, using the hamiltonian character of ray equations. Poincaré surface of section plots in the (θ,m) plane are shown in Figs 3, 4 and 5 for various increasing inverse aspect ratios.

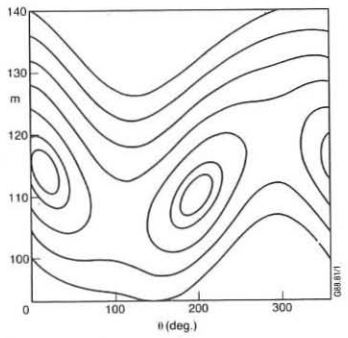

Fig 3: $r = r_o$ surface of section ($\varepsilon = 0.015$)

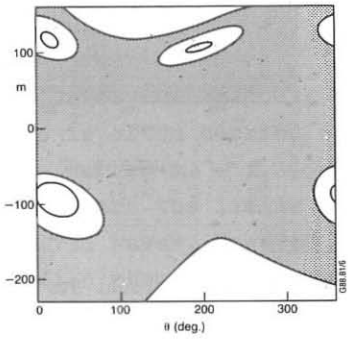

Fig 4: $r = r_o$ surface of section ($\varepsilon = 0.05$)

In Fig 3, ε is chosen sufficiently small (1.5×10^{-2}) to exhibit the island structure of phase space. The link between the ray and wave approaches yields the following relationship between the island width and the corresponding resonant matrix element:

$$\Delta m_{island} = 4\, \Delta m_{coupling} \cdot \left[\frac{2\left|V^{lmn}_{l'm'n'}\right|}{\omega''_{res}} \right]^{1/2} \qquad (6)$$

where ω''_{res} contains second derivatives of the dispersion relation. A successful check of this relation is shown in Fig 6 where we plotted the island width vs ε for various resonances and thus verified that $V^{lmn}_{l'm'n'}$ is proportional to $\varepsilon^{|m-m'|}$. For large values of ε, island overlapping leads to global stochasticity as shown in Fig 4 ($\varepsilon = 5 \times 10^{-2}$) and in Fig 5 ($\varepsilon = 0.3$). In the stochastic regime, it can be argued that the correlations are sufficiently weak to justify the use of the RPA in system(3), thus leading to (5). $P(m \rightleftarrows m')$ may then be deduced from quasi-linear theory ($P(m \rightleftarrows m') \cdot \Delta m^2_{coupling} \simeq \omega_{bounce} \cdot \Delta m^2_{island}$), which means that the diffusion of m scales as:

$$P(m \rightleftarrows m') \simeq \left|V^{lmn}_{l'm'n'}\right| \cdot \frac{\Delta m_{island}}{\Delta m_{coupling}} \qquad (7)$$

To which extent the onset of global stochasticity is sufficient for applying the RPA on the "quantum" description of the mode couplings(3) is a fundamental question which will be the subject of future work.

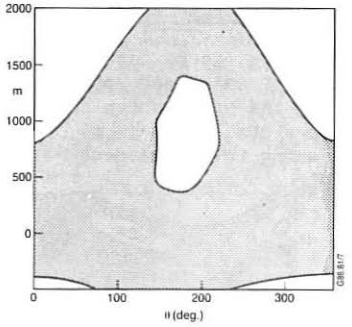

Fig 5: $r = r_o$ surface of section ($\varepsilon = 0.3$)

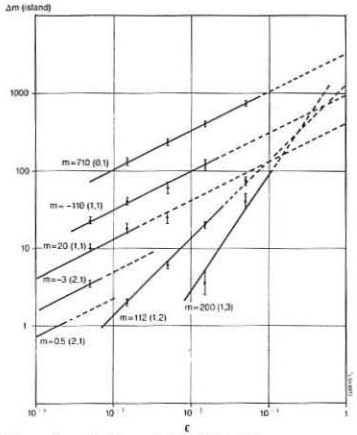

Fig 6: Island Width Versus ε

Conclusion

We propose a global stochastic description of lower hybrid wave propagation and power deposition in tokamaks. When the absorption rate $\gamma(m)$ of each unperturbed mode is included as a sink in system(5) a steady state solution can be found in the presence of a source at $m \sim 0$. Fig 7 shows that the absorbed power spectrum can be much broader and even very distinct from the launched spectrum when the so-called "spectral gap" has to be bridged by means of the stochastic diffusion. Finally, each $\gamma(m)$ has a radial distribution from which the total power deposition and driven current profiles are calculated.

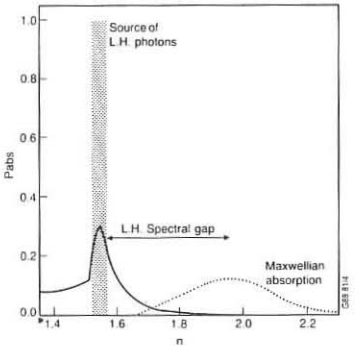

Fig 7: Thermal (...) and Non-thermal (—) absorption

References

1) P.Bonoli, 7th Topical conf. on Appl. of RF Power to Plasmas, Kissimmee p.85 (1987)
2) J.M.Wersinger, E.Ott and J.M.Finn, Phys. Fluids 21 (1978) 2263
3) S.V.Neudachin, V.V.Parail, G.V. Pereverzev, R.V.Shurygin, 12th Eur. conf. on Cont'l Fus. and Plasma Phys., Budapest, Part II p.212 (1985)

CURRENT DRIVE BY LH WAVES WITH THE WIDE SPECTRUM

V.S.Belikov, Ya.I.Kolesnichenko, I.S.Plotnik

Institute for Nuclear Research, Ukrainian SSR
Academy of Sciences, Kiev, USSR

ABSTRACT. The theory which is in agreement with the 2D-numerical calculations is presented for the case of current drive by lower hybrid waves with the wide spectrum.

The theoretical study of a plasma current driven by the travelling waves with $\omega << \omega_{Be}$ (ω is the wave frequency, ω_{Be} the electron gyrofrequency) in tokamaks is often carried out in assumption that the wave spectrum is narrow $x_2 - x_1 << 1$, $x = \omega/(k_{\parallel} v_e)$, $v_e = (T_e/m_e)^{1/2}$, x_1 and x_2 are the limits of the normalized phase velocities of excited waves. However the condition $x_2 - x_1 << 1$ is hardly satisfied when the wave phase velocities are high, $x >> 1$, especially in the case of a plasma with low temperature.

To obtain the expressions for the current density J and for the absorbed power density P one should solve the 2D-kinetic equation for the electron distribution function f. It may be done in different ways. In so-called "one-dimensional approach" $f(\underline{v})$ is represented in the form $f(\underline{v}) = f_M(v_\perp) f(v_{\parallel})$ where $v_\perp$ and $v_{\parallel}$ are the perpendicular and longitudinal particle velocities correspondingly, f_M the Maxwellian function / 1 /. In "quasi-one-dimensional approach" $f(\underline{v}) = f_M(v_\perp) f_1(v_\perp, v_{\parallel})$, f_1 being function which depends on $v_\perp$ weakly / 2 /. In the Green's function method $f(\underline{v}) = f_M(\underline{v})(1 + h(\underline{v}))$ with $h(\underline{v})$ and derivative $\partial(f_M h)/\partial v_{\parallel}$ being small / 3, 1 /. It is clear that the last method is not applicable for the case of strong quasi-linear distortion of the electron distribution ($D^{QL} >> D^C$, D^{QL} is the quasi-linear diffusion coefficient, D^C the collisional

diffusion coefficient / 2 /) i.e. it is not applicable to the case which is characterized by the largest two-dimensional distortion of $f(\underline{v})$ even when the wave spectrum is narrow.

Quasi-one-dimensional approach allows to investigate both the regime with $D^{QL} >> D^{C}$ and $D^{QL} << D^{C}$. Its results coinsides with the results of one-dimensional theory in the case of $D^{QL} >> D^{C}$ that means that one-dimensional theory holds only for this case. But quasi-one-dimensional theory is developed for the narrow wave spectrum and its application for description of currents driven by the wide wave spectrum is not justified. But to know what error it results to the comparison with the results of the numerical 2D calculations is necessary.

At first assuming that $D^{QL} >> D^{C}$ and the current is driven by LH waves with narrow spectrum we present the expressions for J and P which differs with the known ones in one-dimensional theory due to more accurate description of the collisional effects:

$$P = P_0 p(x_1, x_2), \quad J = J_0 j(x_1, Z) \qquad (1)$$

where

$$p(x_1, x_2) = 1 - (3(x_1^{-2} - x_2^{-2}) - \frac{45}{4}(x_1^{-4} - x_2^{-4}) + 35(x_1^{-6} - x_2^{-6}))/\ln(x_2/x_1) \quad \text{for} \quad x_1 \gtrsim 3 \qquad (2)$$

$j(x_1, Z)$ is obtained in Ref./ 5 /, P_0 is power found with using the rough expression for D^{C} ($D^{C} \sim x^{-3}$):

$$P_0 = 2.2\ 10^{8} \frac{L\ n_{20}^2(m^{-3})}{T_e^{1/2}(keV)} (Z + 2) e^{-x_1^2/2} \ln(x_2/x_1) \quad W \cdot m^{-3} \qquad (3)$$

$n_{20} = n_e/10^{20}$, L is the Coulomb logarithm, Z is the ion charge state, J_0 is the current obtained without taking into account

of the distribution function distortion beyond of the resonant region / 1 /. Equations (2), (3) results in the following current drive efficiency:

$$\frac{J}{P} = \frac{0.77\ T_e(\mathrm{keV})}{n_{20}(m^{-3})}\,\eta(x_1, x_2, Z) \qquad A\cdot m\cdot W^{-1} \qquad (4)$$

where

$$\eta(x_1, x_2, Z) = \frac{(x_2^2 - x_1^2)j(x_1, Z)}{4(Z + 2)p(x_1, x_2)\ln(x_2/x_1)} \qquad (5)$$

Let us compare the magnitude of η given by Eq.(5) with that one obtained in 2D numerical calculations. As an example we take $x_1 = 3$, $x_2 = 5$, $Z = 1$. Then Eq.(5) yields $\eta = 5.33$. Numerical calculations carried out in Ref./ 4 / results in $\eta = 6.55$. However, in those calculations the scattering function in the electron collision term assumed to be Maxwellian therefore the magnitude of η obtained in Ref./ 4 / should be multiplied by $j(x_1, Z)$ what yields $\eta = 10$. Thus, one may conclude that in the considered case 1D efficiency is about a factor 1.9 smaller than 2D result.

We now obtain more accurate expression for P. To do it we take into account that in the plateau region the electron distribution over the transverse velocities may be described by the temperature $T_\perp$ which exceeds the bulk electron temperature / 6 /. Then

$$P = P_0\frac{Z + 1 + T_\perp/T_e}{(Z + 2)T_\perp/T_e} \qquad (6)$$

$$\eta = \frac{(x_2^2 - x_1^2)j(x_1, Z)T_\perp/T_e}{4(Z + 1 + T_\perp/T_e)p(x_1, x_2)\ln(x_2/x_1)} \qquad (7)$$

Substituting in Eq.(6)

$$\frac{T_\perp}{T_e} = x_1^2 \frac{((1+d)^{7/3} - 1)/7 - d/3}{1 + 2d/3 + (1+d)^{1/3}}, \qquad d = \frac{x_2 - x_1}{x_1} \qquad (8)$$

we find $\eta = 10.3$. Thus Eq.(7) is in agreement with 2D result.

Let us proceed to regime with $D^{QL} \ll D^C$. In this regime $f(\underline{v})$ is disturbed weakly. Therefore in the case of wide wave spectrum the number of electrons at the right hand side of the resonant region is small as compared with the corresponding number near x_1. For this reason the current drive efficiency is mainly determined by waves with $x \sim x_1$. It enables to use expression obtained for the narrow spectrum assuming $x = x_1$:

$$\eta(x, Z) = \frac{2x^2}{Z + 5}\Bigg|_{x = x_1} \qquad (9)$$

Two-dimensional numerical calculations are carried out for $D^{QL} \ll D^C$ and $x_2 - x_1 = 1$ in Ref./ 7 /. They confirms what is said. It becomes clear if one take into account that $\langle x^2 \rangle$ introduced in Ref./ 7 / by means of expression

$$\langle x^2 \rangle = \int_{x_1}^{x_2} dx x^2 f_M(x) \Big/ \int_{x_1}^{x_2} dx f_M(x) \qquad (10)$$

is x_1^2 for the wide spectrum.

REFERENCES

1. Fisch N.J. Rev.Mod.Phys. 59 (1987) 175.
2. Belikov V.S., Kolesnichenko Ya.I., Plotnik I.S. Nucl. Fusion 22 (1982) 1559.
3. Hirshman S.P. Phys.Fluids 23 (1980) 1238.
4. Karney C.F., Fisch N.J. Phys.Fluids 22 (1979) 1817.
5. Belikov V.S., Kolesnichenko Ya.I., Plotnik I.S. Fiz.plazmy 8 (1982) 229.
6. Fuchs V., et al. Phys.Fluids 28 (1985) 3619.
7. Karney C.F.F., Fisch N.J. Nucl.Fusion 21 (1981) 1549.

NUMERICAL SIMULATION OF CURRENT DRIVE BY LOWER-HYBRID WAVES IN T-7 TOKAMAK

S.V.Neudatchin, G.V.Pereverzev

I.V.Kurchatov Institute of Atomic Energy, Moscow, USSR

An analysis of the experiments on current drive by lower hybrid waves in T-7 tokamak /1-3/ is given in the paper. Specific features of these experiments is in a comparatively-low plasma density, high electron temperature and in the presence of a residual electric field. Under these conditions the introduction of auxiliary lower hybrid power produces a condition for driving a fan-instability /4/ which, in its turn, reduces the lower-hybrid current. The calculations done with due regard for the fan-instability effect on current drive have shown a reasonable agreement with the experimental results.

The numerical simulation of current drive has been done in the following way. First, according to the generally-accepted technique /5,6/, a spectrum of a three-waveguide grill at the plasma edge in the T-7 tokamak is calculated. This spectrum includes a noticeable fraction of effectively - decelerated waves that provides an effective interaction of lower hybrid waves with electrons and an almost-complete absorption of wave energies per pass along the radius. The spectrum deformation in the process of wave propagation in this case is mainly provided by absorption and the role of toroidal effects is insignificant. Therefore we have used the wave energy transport equation in the cylindrical approximation /7/. Then, at given density and temperature profiles and at a given loop voltage on each magnetic surface a one-dimensional kinetic equation is solved /8/ When the found function of electron distribution, f_e, satisfies the condition for the fan instability drive at some value of $v_{e\parallel}^*$

$$\frac{\omega_{pe}\, v_{e\parallel}^* \sqrt{\pi}}{\nu_{ei}\, n}\left[v_{e\parallel}^* \frac{\partial f_e}{\partial v_{e\parallel}} + \frac{\omega_{pe}}{\omega_{Be}} f_e \Big/ v_{e\parallel} = v_{e\parallel}^*\left(1+\frac{\omega_{pe}}{\omega_{Be}}\right)\right] - 1 > 0 \qquad (1)$$

it is assumed that this instability limits the length of a plateau by the condition $v_{e\parallel}^{max} \le v_{e\parallel}^*(1+\omega_{Be}/\omega_{pe})$. The driven current magnitude, j_{LH}, is reduced, respectively.

An example of LH-current density calculations, $j_{LH}(r)$, and its modifications under the fan-instability effect are given in

Fig.1-2. An electron distribution function at two points along the radius at the T-7 plasma parameters is given in Fig.1. The distribution function at the residual loop voltage corresponding to the experiment, U_ℓ=0.2V, neglecting the fan-instability effect, is shown with a dashed line. Solid curves represent shapes of distribution function at a stage of quasi-linear fan-instability relaxation. One can see that the instability development considerably reduces the LH-current magnitude. A shape of the distribution function for a zero electric field (dashed-dotted line) is given in Fig.1 for comparison. It is interesting to note that in this case the fan-instability drive condition is not satisfied, and the current density, j_{LH}, turns out to be higher than that in the presence of a finite loop voltage. This dependence is illustrated in Fig.2. For a calculated modification given here an increase in the loop voltage from 0V to 0.2V reduces the LH-current magnitude from 82 kA to 63kA.

The fan instability development can also change the linear dependence of LH-current magnitude, I_{LH}, on the deposited LH-power, P_{LH}. From Fig.3 one can see that the fan-instability virtually limits I_{LH} at a certain level weakly-dependent on V_ℓ and on P_{LH}.

The fan-instability effect is reduced, when one uses more decelerated spectra providing a high but shorter plateau on the distribution function. From Fig.4 one can see that the instability effectively reduces I_{LH} at $\Delta\Phi=3\pi/4$ (spectrum maximum at $N_{II\ max}=3.5$) but it does not emerge at all at the symmetric spectrum with $\Delta\Phi=\pi$ ($N_{II\ max}=5$).

From the criterion (1) it follows that $v_{e\parallel}^{max}/v_{e\parallel}^{*} \leq (1+\omega_{Be}/\omega_{pe})$, i.e. with a rise in B_Z, $v_{e\parallel}^{max}/v_{e\parallel}^{*}$ also rises that makes the fan-instability development difficult The calculated values of I_{LH}, I_{LH}^{*} vs loop voltate, V_ℓ, at $T_e(0)$=2.5 (curves 2,2*) and $T_e(0)$=4 keV under ECRH and LH (curve I) are given in Fig.5. The experimental data are within a shadowed region. In this case, B_Z=2.3T (in comparison with B_Z=1.5T, Fig.1-3), and the fan-instability effect is not great. From Figs.4,5 one can see that the calculated current

about twoce exceeds the experiment.

In conclusion, our statements are as follows. In the paper we have calculated the LH-current dependence on the plasma and waveguide set parameters in T-7. It is shown that under experimental conditions on T-7 the fan-instability can a few times reduce the LH-current magnitude, effectively affecting the LH-current dependence on the electric field and the LH-power.The calculated values of LH-current ar 1-3 times higher than the experimental ones.

References

1. Alikaev V.V.,et al. In: Pl.Phys. and Contr. Nucl. Fus.Res. Baltimore, 1982, IAEA, Vienna, 1983, v. 2, p. 153.
2. Alikaev V.V., et al. Fizika Plasmy, 1985, v. 11, p. 53.
3. Alikaev V.V., et al. In: Pl.Phys. and Contr. Nucl. Fus., Res., Kyoto, 1986, IAEA, Vienna, 1987, v. 1, p. 533.
4. Pardil V.V., Pogutse O.P. Voprosy teorii plasmy, 1982, issue 11, p. 5.
5. Brambilla M. Nucl. Fus., 1976, v. 16, p. 47.
6. Baranov Yu.F., Shcherbinin O.N. Fizika Plasmy, 1977, v. 3, p. 246.
7. Parail V.V., Pereverzev G.V. Fizika Plasmy, 1983, v.9, p. 586.
8. Dnestrovskii Yu.N., Krasheninnikov S.N., Parail V.V., Pereverzev G.V. In: Pl. Phys. and Contr. Nucl. Fus. Res., Baltimore, 1982, IAEA, Vienna, 1983, v. 1, p. 189.

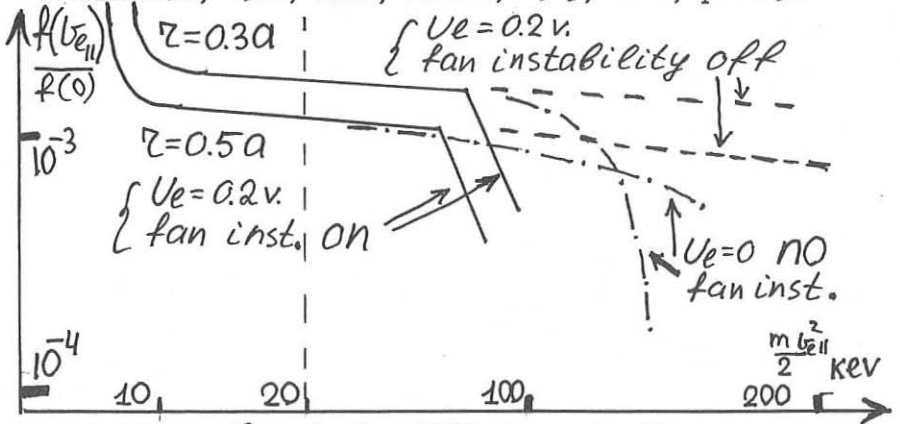

Fig 1. $\bar{n} = 6 \cdot 10^{12} cm^{-3}$, $B_{\parallel} = 1.5 T$., $Z_{eff} = 3$, $T_e(r) = 1400(1 - \frac{r^2}{a^2})^{1.5}$ $P_{LH} = 150$ kwt, $\Delta\Phi = 0.6\pi$

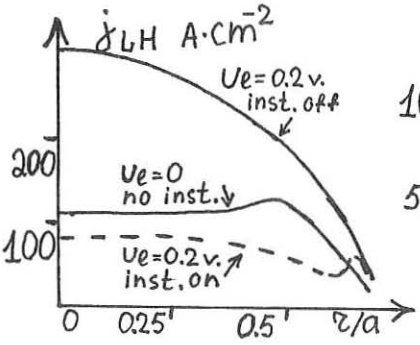

Fig. 2. $j_{LH}(r)$ profiles, parameters are the same as in Fig.1.

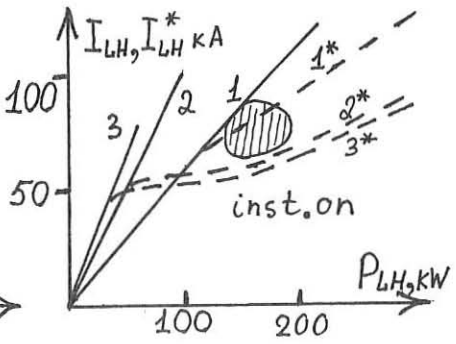

Fig. 3. I_{LH}, I^*_{LH} (with fan instability effect) vs power P_{LH} curves 1,2,3 and 1*,2*,3* - I_{LH} and I^*_{LH} at U_{loop}=0;0.3; 0.6 V, $\bar{n}$ = 8 10^{12} cm^{-3}, other parameters as in Fig.1, ▨ - exp. with U_l 0.3 V.

Fig. 4. I_{LH}, I^*_{LH} vs. U_{loop} at the decelerated spectra $\Delta\Phi = 3\pi/4$ (1,1*), and $\Delta\Phi = \pi$ (2, no inst.). 1, 2 - exp. P_{LH}=100kW, $\bar{n}$=6·10^{12}, $T_e(0)$=1000eV, B =1.9T.

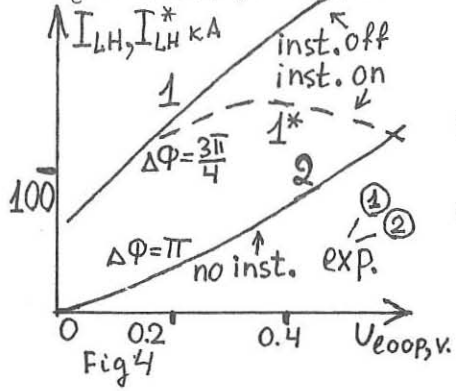

Fig 4

Fig. 5. I_{LH}, I^*_{LH} vs. U_l. Curves 1 - $T_e(r)$=4000(1-r^2/a^2)$^{2.5}$eV Z_{eff}=5. Curves 2,2* - $T_e(r)$= 2500 (1-r^2/a^2)^2, Z_{eff}=3. in both cases $\bar{n}$=8·10^{12}, B = 2.3T., P_{LH}=180 kW, $\Delta\Phi = \pi/2$, ① , ② - exp.

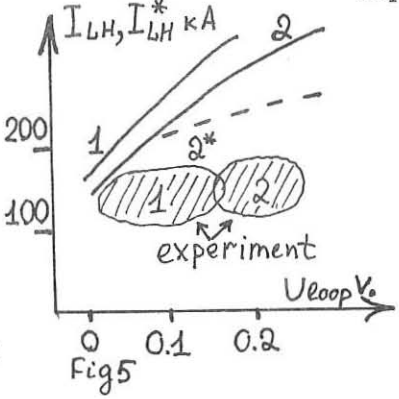

Fig5

Ray tracing studies for the lower hybrid experiments in JET

A. Moreira, V. Bhatnagar *, J. P. Bizarro *, C. Gormezano *
S. Knowlton *, and J.T. Mendonça *

Centro de Electrodinâmica - Instituto Superior Técnico
1096 Lisboa, Portugal
** JET Joint Undertaking, Abingdon, OX14 3EA, UK.*

Abstract. Lower hybrid current drive for current profile control in JET experiments will commence next year. A narrow spectrum of lower hybrid waves will be excited by a phased waveguide array antenna with partially adjustable phasing. The localization and the amount of RF driven current depends in part on the paths followed by the waves within the plasma. The propagation of lower hybrid waves in JET is studied by ray tracing. In this study we have used the ray tracing code developed in Brussels[1] which accurately models the D-shaped geometry of the magnetic flux surfaces appropriate for JET. Our work includes a study of the influence on the ray trajectories *i)* of the D-shape parameters, namely, ellipticity, Shafranov shift and triangularity, for various discharge conditions for typical JET parameters, and *ii)* poloidal extent of the antenna. Our results *i)* indicate that the Shafranov shift strongly influences the ray trajectory and *ii)* show that a bundle of rays launched with the same initial $n_{\parallel}$ over the poloidal extent of the grill face will diverge after the closest approach to the plasma centre.

The main goal of the current profile control program on JET is to significantly broaden the current drive profile so that high central temperatures can be maintained by eliminating the sawtooth instability. Among the methods currently in progress aiming at such a goal is the lower hybrid current drive. The JET LHCD system will couple up to 10 MW RF power at 3.7 GHz through a 384 waveguide array (32 per row). By proper phasing of the array, a narrow $n_{\parallel}$ spectrum of $\Delta n_{\parallel} \simeq 0.3$ is launched, with the peak $n_{\parallel}$ variable between 1.4 and 2.1. Previous LHCD experiments and theoretical work have shown that the launched wave spectrum is modified within the plasma, with the result that wave propagation and absorption are significantly different than that expected from a simple slab model treatment of propagation. LH ray tracing codes in fully toroidal geometry are used

to realistically model LH wave propagation[1-4]. Several toroidal ray tracing codes for performing LH ray path calculations are in use at JET; the code used in this study is the Brussels ray tracing code[1] modified for use in the lower hybrid range of frequencies. The ray tracing results are in excellent agreement with those obtained with the Bonoli-Englade code. The Brussels code models the plasma equilibrium with analytic representations of the D-shaped JET magnetic geometry and analytic profiles corresponding to measured data. The D-shape parameters are the ellipticity, the Shafranov shift of the magnetic axis and the triangularity. The present study aims at assessing the influence of the D-shaped geometry on the ray trajectories.

The density and temperature profiles were modelled as

$$N_s(\rho) = (N_{so} - N_{se}) \times [1 - (\frac{\rho}{a_p})^2]^{\beta_{Ns}} + N_{se} \tag{1}$$

$$T_s(\rho) = (T_{so} - T_{se}) \times [1 - (\frac{\rho}{a_p})^2]^{\beta_{Ts}} + T_{se} \tag{2}$$

where $(\ )_o$ and $(\ )_e$ are values in the plasma centre and at the edge, respectively. s refers to the different species (electrons, Deuterium, minor ion species), ρ labels the minor radius in the equatorial plane of a flux surface, and a_p is the plasma minor radius on the outer mid-plane. The plasma current density profile is taken as

$$j(\rho) = j_o \times [1 - (\frac{\rho}{a_p})^2]^{\beta_j} \tag{3}$$

All the calculations shown in the following figures were obtained for a pure electron - Deuterium plasma with the following parameters: toroidal magnetic field strength $B_T = 3.4\,\mathrm{T}$, major radius $R_o = 2.96\,\mathrm{m}$, minor radius $a_p = 1.19\,\mathrm{m}$ total plasma current $I_p = 3\,\mathrm{MA}$, $N_{eo} = N_{Do} = 4 \times 10^{13}\,\mathrm{m}^{-3}$, $N_{ee} = N_{De} = 5 \times 10^{12}\,\mathrm{m}^{-3}$, $T_{eo} = T_{Do} = 10\,\mathrm{keV}$, $T_{ee} = T_{De} = 300\,\mathrm{eV}$, $\beta_{Ne} = 1$, $\beta_{Te} = \beta_{TD} = 2$, $\beta_j = 3$. The poloidal length of the antenna is approximately 0.8 m and a set of 5 rays of a given value of $n_\parallel$ is launched along the poloidal extent. Because the variations in $n_\parallel$ and poloidal wave number arise from poloidal asymmetries, waves launched from different poloidal locations can be expected to undergo different trajectories. The following figures represent poloidal projections of ray trajectories for rays starting at different positions in the poloidal plane in front of the antenna. The rays

are followed for their first pass through the plasma until they reach the plasma boundary.

The influence of the Shafranov shift on the ray trajectories is shown in Figs.1-3. We take $n_{\parallel} = 1.8$, ellipticity $k = 1.5$, triangularity $\delta = 0.05$, central shift $\Delta = 0.1$ m in Fig.1, $\Delta = 0.2$ m in Fig.2 and $\Delta = 0.3$ m in Fig.3. We note that as Δ increases the radial penetration of the lower hybrid waves becames poorer. Also, one can observe that the rays starting with negative poloidal angle (below the mid-plane) do not penetrate as well as those starting above the equatorial plane due to a stronger down shift of the $n_{\parallel}$ of the wave. For larger values of the Shafranov shift (Figs. 2-3), waves launched from the bottom of the grill are predicted, for these parameters, to undergo a radial reflection. This feature has also been observed for a scan of the ellipticity, although the average radial penetration is not degraded with increasing ellipticity. The triangularity parameter is found to be the least important shape parameter of all (only unrealistic values would imply large variations of the ray paths).

The accessibility of the wave is improved with increasing $n_{\parallel}$. In Fig.4 the D-shape parameters are the same as in Fig.1 but a different value of $n_{\parallel} = 2$ is taken. The higher value of $n_{\parallel}$ leads to a deeper penetration in the plasma, as expected.

In this initial study of LH ray tracing in a realistic model of the JET equilibrium, we have investigated the gross behavior of the plasma shape parameters on the propagation of the lower hybrid waves. For values of $n_{\parallel}$ representative of the launched $n_{\parallel}$ spectrum, we find that the waves do not propagate inside $r/a_p \simeq 0.5$ on their first pass suggesting that an off-axis RF current will indeed be generated if the wave is absorbed. Among the D-shape parameters the Shafranov shift of the magnetic flux surfaces seems to be the most influential. An increasing Shafranov shift leads to reduced accessibility and reduced penetration.

References

1 - D. Van Easter, V.P. Bhatnagar and R. Koch, *Plasma Phys. and Controlled Fusion*, **27**, 1015 (1981).

2 - D. W. Ignat, Phys. Fluids, **24**, 1110 (1981).

3 - M. Brambilla and A. Cardinalli, *Plasma Phys.*, **24**, 1187 (1982).

4 - P. Bonoli and R. C. Englade, Phys. Fluids, **29**, 2937 (1986).

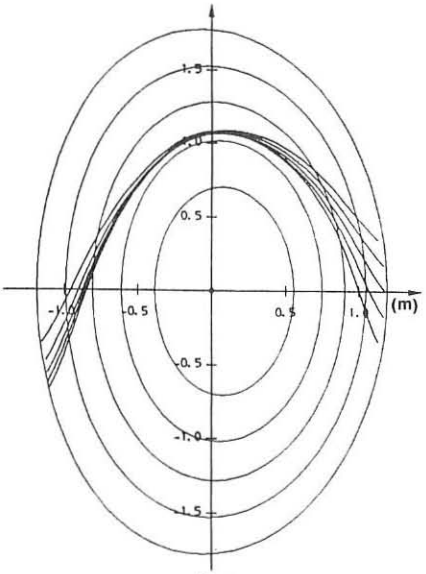

Fig.1

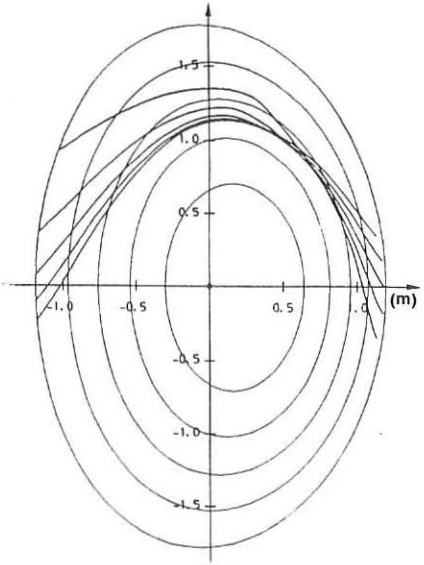

Fig.2

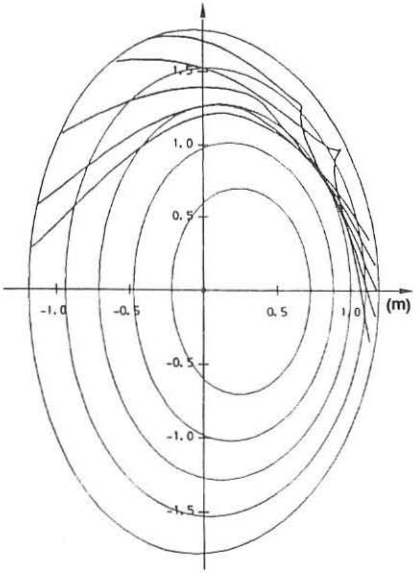

Fig.3

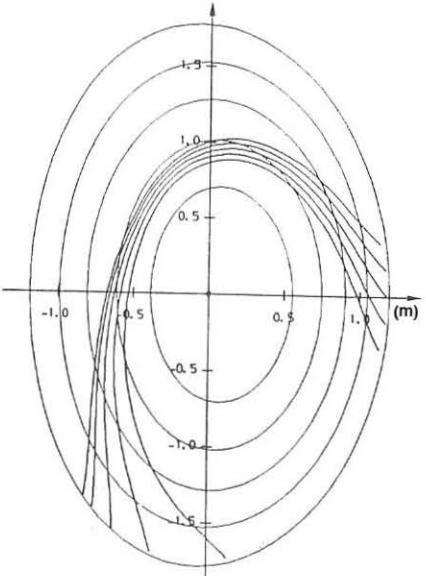

Fig.4

PROPAGATION AND ABSORPTION OF LH WAVES IN THE PRESENCE OF MHD TURBULENCE

E. Barbato, A. Cardinali, F. Romanelli

Associazione EURATOM-ENEA sulla Fusione, Centro Ricerche Energia Frascati, C.P. 65 - 00044 - Frascati, Rome, Italy

INTRODUCTION

In order to explain the results of the current drive (CD) [1,2]and heating experiments in tokamaks [3] with lower hybrid (LH) waves in the framework of quasi-linear theory, a broadening of the launched $n_\parallel$ spectrum must be invoked in most cases. Several broadening mechanisms have been proposed in the last few years relying on linear or non linear theory; however it is still an open question which is the physical process underlying this phenomenon. The possibility of controlling the deposition and the current density profile from the outside relies on the solution of this problem. In this respect it can be useful to determine the plasma parameters which play a major role.

Here we investigate both analytically and numerically the $n_\parallel$ broadening induced by toroidal effects when multiple passes of the rays are considered [4]. In order to estimate the driven current provided by such a broadening a power deposition calculation is carried out. The role of the magnetic island m = 1 on wave propagation is considered also.

$n_\parallel$-UPSHIFT AND ABSORPTION

According to the analysis of Ref [5], beyond a boundary layer of thickness r_0, the parallel refractive index is given by

$$n_\parallel(r,\theta) = \bar{n}_\parallel(r) + \tilde{n}(r,\theta) \tag{1}$$

with $\tilde{n} < \bar{n}_\parallel$ and

$$\bar{n}_\parallel(r) = \bar{n}_\parallel + \left(\bar{n}_\parallel(r_0) - n_{\parallel 0}\right) q(r_0)/q(r) + 0(\varepsilon^2) \tag{2}$$

where q is the safety factor, $\varepsilon = a/R_0$ is the inverse aspect ratio, $n_{\parallel 0} = c/\omega\, n_\phi/R_0$, and n_ϕ the toroidal wave number.

At the first transit $\tilde{n}_\parallel^{(0)}(r_0)$ is given by Eq. (27) of Ref [4]. It can be shown that, at each edge reflection, $\tilde{n}_\parallel(r_0)$ changes by an amount $2\varepsilon n_{\parallel 0}/q(r_0)\times C_0(\theta_k)$, where θ_k is the poloidal angle at the k^{th} reflection,while $C_0(\theta_k)$, which is given by Eq.(26) of Ref [5], approximatively reads:

$$C_0(\theta_k) = 3^{2/3}\,\Gamma(2/3)\,\frac{q^{5/3}(a)}{\varepsilon^{2/3}\,\nu_0^{1/3}}\left|1 - \frac{q(0)}{q(a)}\right|^2 \cos(\theta_k + \pi/3) \tag{3}$$

$$\nu_0 = \omega_{pe}^2(0)/\omega^2$$

so that:

$$\bar{n}_{\parallel}^{(k)}(r_0) = \bar{n}_{\parallel}^{(0)}(r_0) + \frac{2\varepsilon n_{\parallel 0}}{q(r_0)}\,\frac{q^{5/3}(a)}{\varepsilon^{2/3}\,\nu_0^{1/3}}\left|1 - \frac{q(0)}{q(a)}\right|^2 \cdot \sum_k \cos(\theta_k + \pi/3) \tag{4}$$

We can say naively that, at each transit through the boundary layer, $\bar{n}_{\parallel}(r_0)$ takes a kick. The sign of the kick depends on θ_k and the intensity relates essentially to q(a) and to the peaking factor q(a)/q(0). If a net positive value $\bar{n}_{\parallel}(r_0)$-$n_{\parallel 0}$) is built up through these kicks, during one or more reflections, then ($\bar{n}_{\parallel}(r)$-$n_{\parallel 0}$) will benefit by the same increment (see Eq.2) amplified by the factor $q(r_0)/q(r)$. Furthermore, in order to have a positive non negligible kick, the poloidal angle must fall near the bottom of the cross section.

An analysis, performed with a toroidal ray tracing code, qualitatively confirms these results, even though the analytical calculation presented so far applies only marginally to low density plasmas peculiar of CD experiments.

In Fig. 1a two rays are shown belonging to the same $n_{\parallel}(a) = 2$; the difference between these two rays is due to a difference in q(0) and a slight difference in n(0). The other plasma parameters are fixed to the following values: a = 40 cm, R_0 = 168 cm, B_0 = 22 kG, q(a) = 3.5, $\hat{T}$ = 2.7 keV, which refers to the Asdex CD experiment at 1.3 Ghz where typically a current of 300 kA was driven by 350÷400 kW of injected power [1]. Figure 1b shows the corresponding $n_{\parallel}$ behaviour as a function of the radial position of the ray. In both cases, after a bottom reflection $n_{\parallel}$ suffers an upshift which is larger at lower q(0).

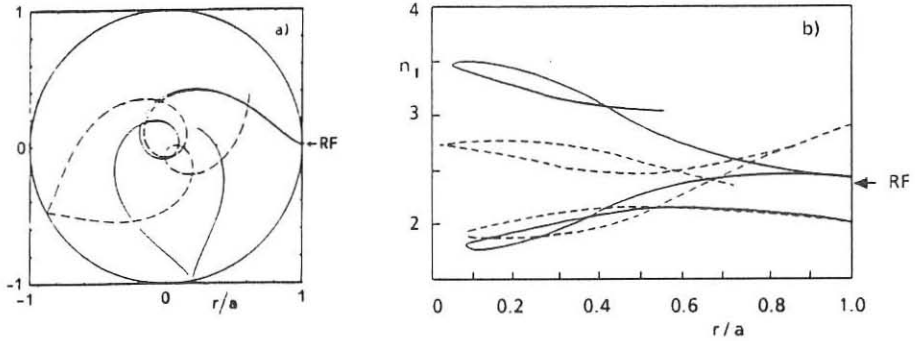

Fig. 1 - a) Projection on the cross section of two rays belonging to the same $n_{\parallel}(a) = 2$. The solid line refers to q(0) = 0.7, n(0) = 7×10^{12} cm^{-3}, the dashed line to q(0) = 1, n(0) = 8×10^{12} cm^{-3}. b) Corresponding behaviour of $n_{\parallel}$ along the rays. After a near bottom reflection both rays show a $n_{\parallel}$ upshift which is larger at lower q(0)

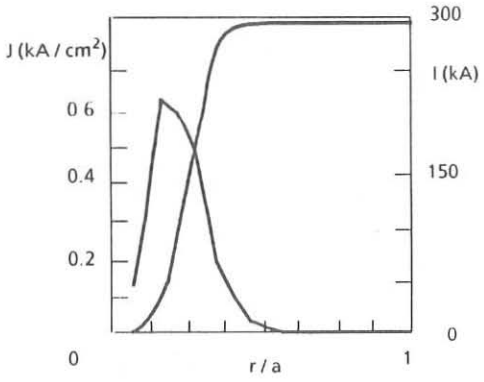

Fig. 2 - Current density profile and total driven current for a typical Asdex plasma relevant to the experiment at 1.3 GHz (n(0) = 8×10^{12}, P_{RF} = 375 kW). The original spectrum has been broadened up to $n_\parallel = 5.5$

An extensive analysis performed for the two cases q(0) = 1 and q(0) = 0.7 shows that the whole launched spectrum (which is peaked around $n_\parallel = 2$ and extending up to a value of 2.5) broadens, after many reflections, up to a value of 3.5÷4 in the first case and of 5.5÷6 in the second case.

In order to give an estimate of the power absorption and of the driven current in these two cases, use has been made of a deposition code [6]. Figure 2 shows the current density profile and the total driven current when the launched spectrum is smoothly broadened up to a value of 5.5 with 30% of the total power transferred from low $n_\parallel$ to high $n_\parallel$. 300 kW are absorbed by the electrons, while the remaining power (75 kW) is collisionally damped or lost for lack of accessibility.

A broadening of the original spectrum up to a value of 4, estimated in the other case (q(0) = 1), does not provide the prescribed value (300 kA) of the driven current.

THE ROLE OF THE m = 1 ISLAND

When q(0) < 1, a magnetic island m = 1 can affect the wave propagation.

The ray tracing code has been extended to include MHD perturbations [7], in order to evaluate this effect. Preliminary results can be summarized in this way: all the effects are expected to be proportional to the fourth power of the island amplitude normalized to a characteristic length which is of the order of the minor radius a; $n_\parallel$ suffers an upshift when the ray meets the island at the O-point. When multiple passes are considered an appreciable effect is expected if the ray goes through the O-point many times. That, however seems to be a very special situation. Figure 3 shows the $n_\parallel$ variations along the ray in the case of an island of amplitude 0.4, localized at r/a =0.5. The peak density and temperature are 5×10^{12} cm^{-3} and 1.7 keV respectively, the launched $n_\parallel$ is 3 and the other plasma parameters are the same of Fig. 1, with q(0) = 0.7. To infer the effect of the island the curve of Fig. 3 has to be compared with the curve reported in Fig. 4 and obtained in absence of the island.

CONCLUSIONS

An analytical estimate is given of the $n_\parallel$ variation induced by toroidal effects when multiple passes are considered. It is found that the most important parameters in determining the $n_\parallel$ variations are the q(a) value and the peaking factor q(a)/q(0). Numerical calculations confirm these results.

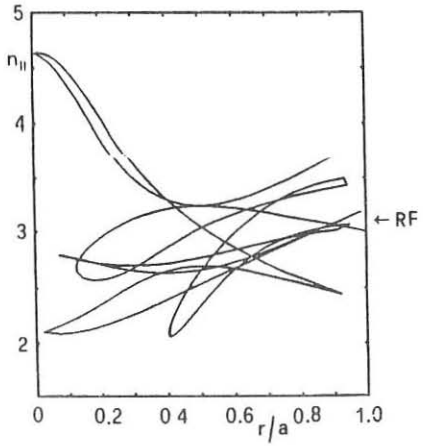

Fig. 3 - $n_{\parallel}$ behaviour along the trajectory when a m = 1 island of amplitude 0.4 a is present

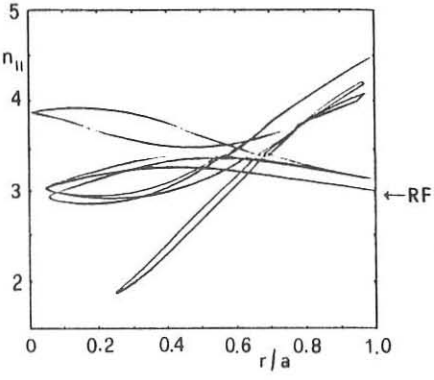

Fig. 4 - $n_{\parallel}$ behaviour along the trajectory for the same parameters of Fig. 3 but in absence of the island

It is shown that in presence of MHD turbulence $n_{\parallel}$ upshifts if the ray goes through the O-point. An appreciable enhancement of $n_{\parallel}$ could take place if the ray met the island at the O-point many times.

References

[1] F. Leuterer et al., Plasma Phys. Controlled Fusion, 27,1399(1985)
[2] S. Bernabei et al., *Proc. 11th Conf. on Plasma Physics and Controlled Fusion*, IAEA, Kyoto, 13-20/11/86, paper CN47-FII/1 (1986)
[3] F. Alladio et al., *Proc. 12th Europ. Conf. on Controlled Fusion and Plasma Phys.*, Budapest, 2-6/9/85, vol. 28, IA, p. 179 (1986)
[4] P.T. Bonoli, R.C. Englade, Phys. Fluids, 29,2937(1986)
[5] A. Cardinali, F. Romanelli, Phys. Fluids, 29, 810(1986)
[6] E. Barbato, V. Zanza, *Proc. 13th Europ. Conf. on Controlled Fusion and Plasma Phys.*, Schliersee, 14-18/4/86, vol II, p.449 (1986)
[7] F. Romanelli, A. Cardinali, R. Bartiromo, *Proc. 14th Europ. Conf. on Controlled Fusion and Plasma Phys.*, Madrid, 22-26/6/87, vol III,p. 903 (1987)

Multijunction Grill and Its Application on Lower Hybrid Current Drive Experiments

Jiang Tong-Wen, Liu Yu-Xiu,
Wu Gui-Ping, Zhang Xue-Lei

Institute of Plasma Physics,
Academia Sinica, Hefei,China

ABSTRACT

We have developed a new kind of lower hybrid wave launching structure-multijunction grill. In this new launcher the PF power is divided by means of an E-plane of rectangle waveguid and the phase difference of adjacent waveguides is obtained by a suitable length of the dielectric Teflon inserted into corresponding waveguides. Lower hybrid current drive experiments have been succesfully performed in HT-6M Tokamak with this multijunction grill. A driven efficiency η_{CD} up to 0.55 ($10^{13}cm^{-3}$.m.KA/KW) has been obtained. The influence of LHCD on MHD behaviour of plasma has been clearly observed too, though the RF power coupled to plasma is very low.

INTRUDUCTION

The phased waveguide array (i.e. the conventional grill) is the most promising antenna in the LH experiments. Such systems have already proven to be effective in prescent tokamaks. To date, RF power in the megawatt range have been launched into the plasma by means of grills containing up to a network of 4×8 waveguides.

Multimegawatt experiments have been considered for a few large devices. The launchers used for three devices contain hundreds of waveguides, leading to very cumbersome RF systems. In order to alleviate the constraints of such launchers, it has been proposed to use a new type of grill-the multijunction grill. In this new grill, an E-plane is used as a power divider, and the phase difference of the adjacent waveguides is obtained by exchanging the WG wavelength of the corresponding waveguides, allowing the proper (N_{11}) spectrum to be launched. Therefore the structure of this new grill is simplified largely. We have developed a new four-junction grill, its phase shifter is obtained by means of a suitable length of the Teflon inserted in the corresponding waveguides. The phasing between adjacent waveguides is 90°. This new type of grill was successfully used in LHCD experiments on the HT-6M tokamak.

PRINCIPLE OF THE MULTIJUNCTION GRILL

As shown in Fig.1, a multijuction grill is obtained by dividing the main waveguid into a given number (N) of secondary waveguids by means of metallic walls that are parallel to the main wavguide wall. It is well known that, the distribution of electromagnetic field for H_{10} mode in the

rectangular waveguide is given by

$$E_y = -\frac{\omega\pi}{a}\sin(\frac{\pi x}{a})e^{j(\omega t - \alpha z)}$$

$$H_x = \frac{\alpha}{\mu}\cdot\frac{\pi}{a}\sin(\frac{\pi x}{a})e^{j(\omega t - \alpha z)}$$

$$H_z = -j\frac{\pi^2}{\mu a^2}\cos(\frac{\pi x}{a})e^{j(\omega t - \alpha z)}$$

$$E_x = E_z = H_y = 0$$

It is easy to know, the inserted metallic walls, which is parallel to the main waveguide wall,does not influence the former distribution of the field. The transmitted power density is uniform along the direction of the WG narrow wall, therefore, the power divider has become very simple.

A two-dimensional numerical study of the theory of a multijunction grill indicates: the wave reflections between the grill mouth and the E-junction plane allow a self-adaptation when the travelling waves are excited with an adequate phasing between the secondary waveguides. This feature is available for LHCD experiments.

The phasing in the multijunction grill can be made by the different ways, for example:

(a). Reducing the height of the waveguides.

The suitable phasing is obtained by reducing the height of the waveguides with suitable length of the reduced-height section. Step transformers at each end of the reduced-height section allow a good matching to be obtained. This way had been used in the Petula-B tokamak in France.

(b). Inserted suitable dielectric.

As shown in Fig.2, the phasing is obtained by a suitable length of the dielectric inserted in the corresponding waveguides. The phasing in the inserted-dielectric section is given by

$$\Delta\phi = \left[\frac{\sqrt{\varepsilon_r-(\frac{\lambda_o}{2a})^2}}{\sqrt{1-(\frac{\lambda_o}{2a})^2}} - 1\right]\cdot\frac{L}{\lambda_g}\cdot 360^\circ$$

where λ_g is the WG wavelength in the vacuum, ε_r is the relative dielectric constant. We have developed a four-junction grill by means of this way, its phasing is 90°.

STRUCTURE OF THE FOUR-JUNCTION GRILL

As shown in Fig.2, the new grill consist of power divider-shifter, vacuum seal Teflon, coupler and bellows. The sizes of the grill section have been chosen as follows: the total outsize is $188\times62mm^2$, the inside sizes of each secondary waveguide are a=184mm and b=13mm, the wall thickness d=2mm, the period of the grill Δ=b+d=15mm. The Teflon has been chosen as inserted dielectric for shifter, its permittivity ε_r=2 at F=915MHZ. The 90° phasing is obtained by means of a suitable length (0, 11.4cm, 22.8cm, 34.2cm) of the Teflon inserted in the corresponding waveguides, the error of the phasing $d\phi < \pm 2°$. The total RF Penetration is 85%. The bellow allows the

coupler to adjust distance between coupler and plasma edge in ± 10mm. Calculation shows that in the case of $\Delta\phi = \pi/2$ a broad spectrum up to N_{11}=10 with a peak at N_{11}=5 has been obtained.

LHCD EXPERIMENTS

LHCD experiments with a multijunction grill have been performed successfully in the HT-6M tokamak. Its main parameters are the follows: major radius R=65cm, minor radius r=20cm, toroid field B_t < 15KG and plasma current I_p < 150KA. In this experiment they are B_t=6≅11KG, I_p=40≅70KA and $\bar{n}_e$= $2\cong 6\times 10^{12}cm^{-3}$.

The lower hybrid RF system consists of a magnetron power source(F=915 MHZ,P=30kw, τ=30ms), a waveguide transmission line and a multijunction grill. This system is much simpler than the conventional system.

The low density ohmic discharges are very reproducible in the HT-6M, so we can compare the discharges without and with LHW power successfully to obtain the effects of the RF power. When the RF power P_{rf} is superposed on the ohmically heated plasma, the loop voltage V_L decreases drastically, while the plasma current I_p increases only slightly. The decrement of the voltage ΔV_L is proportional to P_{rf}. The Fig.3 shows the changing singal of V_L, I_p and $\bar{n}_e$ with RF power. The maximum RF-driven current I_{rf}=25KA estimated from $I_{rf}=I_p\ |\Delta V_L|/V_L$ have achieved in present experiments with P_{rf}=10KW at $\bar{n}_e=3.5\times 10^{12}cm^{-3}$, B_t=11KG. The current drive efficiency defined by $\eta_{CD}=\bar{n}_e \cdot R\cdot I_{rf}/P_{rf}(10^{13}cm^{-3}\cdot m\cdot KA/KW)$ is near 0.55.

Generally, the electron line average density $\bar{n}_e$ does not change with RF power, but the perturbances are always observed during RF application. The electron density profile monitored by using a seven-channel infra-red laser beam in the LHCD case seems little more peaked than in the purely ohmic discharge.

In the cases of purely ohmic discharge, the m=2 and m=3 oscillation modes has been often observed, but they are strongly suppressed when RF is turned on, despite the RF power coupled to plasma is only P_{rf}=10KW (Fig.4).

The saw-tooth oscillation in the plasma centre has obvious change at LHCD, as shown in Fig.5, the oscillatory period becomes longer and its amplitude is larger with more RF power.

FIGURE CAPTIONS

Fig.1. Schematic diagram of the principle of a multijunction grill
Fig.2. A four-junction grill antenna
Fig.3. Evolntion of loop voltage, plasma current and electron density.
Fig.4. m=2 and m=3 oscillation modes without (a) and with (b) RF
Fig.5. Lower hybrid wave influences the feature of the saw-tooth oscillation.

REFERENCES

[1]. Petula Group EUR 7424 EN P343
[2]. T.Imai et al., EUR 7424 EN P377

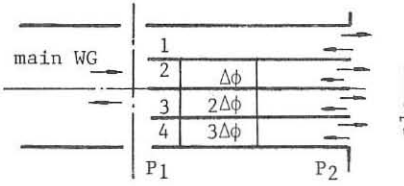

Fig.1

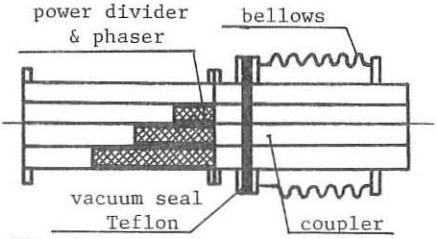

Fig. 2

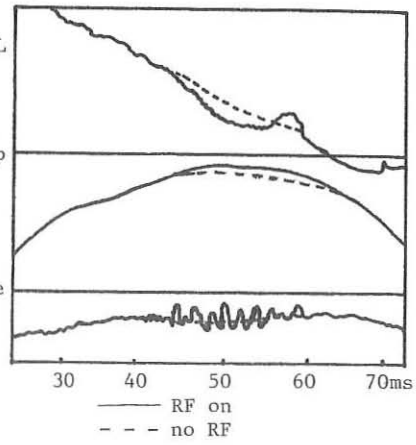

Fig.3

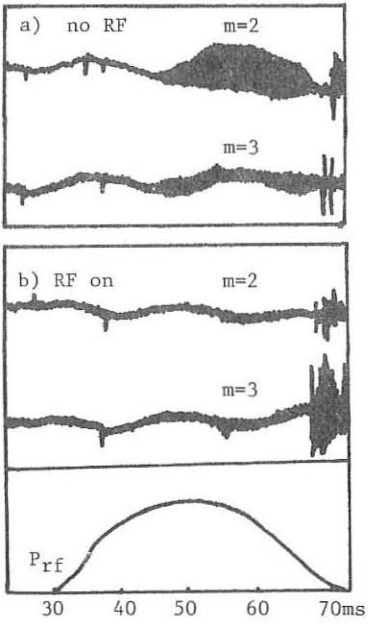

Fig.4

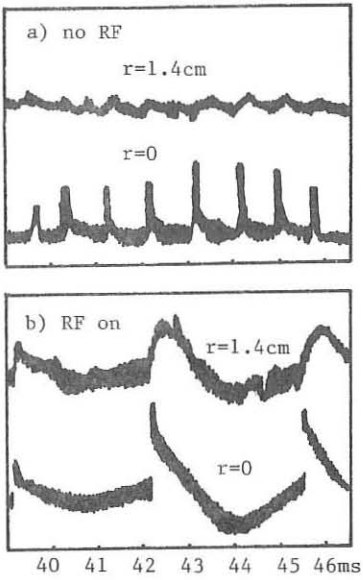

Fig.5

ELECTRICAL FIELD EFFECT ON ALFVEN DRIVING CURRENTS.

I.F.Potapenko (M.V.Keldish Institute of Applied Mathematics of AS, Moscow, USSR), A.G.Elfimov, V.P.Sidorov (I.N.Vekua Institute of Physics and Technology, Sukhumi, USSR).

1. A problem of driving current sustainment by means of travelling waves is essential in realizing a steady-state tokamak. Within the Alfven frequency range this problem has been analyzed with electrical field effects disregarded by a number of authors /1-3/. As it is known, electrical field influence on a lower hybrid driving current is fairly essential /4/. In the present paper we have studied effects of a quasistationary inductive electrical field ($E = \gamma E_{Dz}$) parallel to the constant magnetic field on electron distribution function evolution the driving current being sustained by a narrow packet of travelling Alfven waves with a phase velocity $v_\phi / v_T = C_A \lesssim 1$. Alfven wave effects on the electron distribution function due to Landau damping have been taken into account in a quasilinear approximation with a constant diffusion coefficient $\mathcal{D}$ which differs from zero over the region $|C_A - v_z| \leq C_A \Delta/2$ where Δ is the wave packet width. We do not discuss problems of current sustainment under the conditions where the effect of tokamak bounced particles upon the driving current is considerable /2,4/ for $v_\phi < v_{Te}\sqrt{2/R}$.

A drift-kinetic equation with a nonlinear integral of Landau (Fokker-Plank) electron-electron collisions has been solved /5/, the equation being twodimensional in the velocity space:

$$\frac{\partial f_e}{\partial t} = \frac{\partial}{\partial v_z}\left(\mathcal{D}\frac{\partial f_e}{\partial v_z}\right) - \frac{eE}{m}\frac{\partial f_e}{\partial v_z} + \check{S}t^{e\alpha} f_\alpha \qquad (1)$$

The electron-ion collision integral has been linearized due to taking a Maxwell shape for the ion distribution function.

It should be noted that in order to compute Eq.(1), wholly conservative schemes have been used which most adequately expose the evolution of main macroscopic plasma characteristics.

2. First, we shall consider electron behaviour in a field of the Alfven wave packet with the quasistationary electrical field absent ($\gamma = 0$). The quasilinear term effect upon the electron distribution at the initial stage is most powerful within the phase-space region $v_z \simeq C_A$ where $\mathcal{D} \neq 0$. Then, diffusion takes place into other regions of the space and a typical distribution of a perturbed function ($\delta f_e \simeq f/f_M - 1$) evolves which is defined by departure from the Maxwell function. Fig.1 shows the structure of these pertubation. Within the region of $v_z < C_A$, a characteristic drop in the distribution function is observed which is due to the particle flow transported

into the region of $v_z > c_A$ as a result of the quasilinear term effect. In other directions $\mu = v_z/|v| = 0; -1$ whithin the region of $|v| > c_A$, a relative surplus of particles is also observed due to a perpendicular collisional particle flow emerging from the region of $v_z > c_A$. As a result of the quasilinear effect, the energy and pulse transition from the wave packet to the electrons takes place which results in heating plasma slowly and forming a quasistationary driving current (see Fig.2a) during the period of several electron-ion collisions ($\sim 3\text{-}5\tau_{ei}$). Here, it should be taken into account that fast particles become wholly maxwellized during longer times $\tau \gg \tau_{ei}$. Due to this fact and also as a result of the norming chosen, remains at a considerable value for (see Fig.1).

3. While considering the influence of an electrical field which is small in comparison with that of Dreiser ($\gamma \ll 1$) upon the Alfven driving current, it should be borne in mind (see Fig.1) that the electron distribution function is initially distorted by a quasilinear addend. Then, as it was already mentioned in Item 2, the $v > v_{Te}$ region becomes more enriched with electrons in comparison with the Maxwell distribution. In such a case, even a small electrical field (γ = 0,005) more intensely influences these electrons due to the fact that they are close to the critical velocity $v_{cr} = 1/\sqrt{\gamma}$. While in the beginning of simultaneous acting of the electrical field and the Alfven packet in Eq.(1), the total current density is aqual to the sum of currents ($j_\Sigma = j_D + j_E$) for their separate action (see Fig.2). The nonlinear current enhancement effect [6] (induced conductivity) is observed at the quasistationary stage. In this case, the total current density exceeds ($j_\Sigma > j_D + j_E$) the sum of currents for the terms (D and E) separately acting. The induced conductivity effect becomes stronger on increasing C_A, D and γ.

For the case of reversely directed field ($\gamma < 0$) at the current rise stage, the total current density is equal to the difference of the currents ($j_\Sigma = j_D - j_E$). Then, j_Σ becomes saturated, begins to decrease in size and even changes its sign due to nonlinear enhancement in j_E as a result of the electron distribution function distorted by the quasilinear term.

The driving current generation efficiency which is equal to the ratio of the current to power j_Σ/P_Σ with no electrical field present (γ = 0) is in qualitative agreement with the results of Ref./1/ (see Fig.3a). With the electrical field applied ($\gamma > 0$), the driving current generation efficiency grows for small and high values of phase velocities ($v_\varphi \ll v_{Te}$ and $v_\varphi \gg v_{Te}$), and for small values of D it tends to reach the current generation efficiency with a single electrical field $j/p = 1/\gamma$. For higher values of D, the total current generation efficiency decreases, approaching to that of generated by the wave field only, remaining 1,4-1,6 times higher

than the wave field generated one as a result of the induced conductivity.

4. The induced conductivity effects may be used at the current rise stage in tokamaks for saving volt-seconds efficiently in an inductor and elongating the quasistationary discharge stage.

The driving current reversal effect due to the reverse electrical field should be taken into consideration while developing concepts of inductor recharging for tokamaks if recharging time is higher than 50-100

REFERENCES

1. Fish N.J. and Karney Ch.F.F. Phys. Fluids, 1981, v. 24, p.27.
2. Cordey J.G., Eldington T., Start D.F.H. Plasma Phys., 1982, 24, p.73.
3. Elfimov A.G., Kirov A.G., Sidorov V.P. in "High-Frequency Plasma Heating" Institute of Applied Physics of AS USSR, Gorky, 1983.
4. Dnestrovsky Yu.N., Parail V.V. et al. Contr. Pap. 12Europ. Conf. Contr. Fusion and Plasma Phys., Budapest, 1985, p.2, p.200.
5. Elfimov A.G., Potapenko I.F., Sidorov V.P. Preprint 164, pub. by M.V. Keldysh Inst. of Applied Mathematics, Moscow, 1987.
6. Fish N.J. Phys. Fluids, 1985, v.28, p.245.

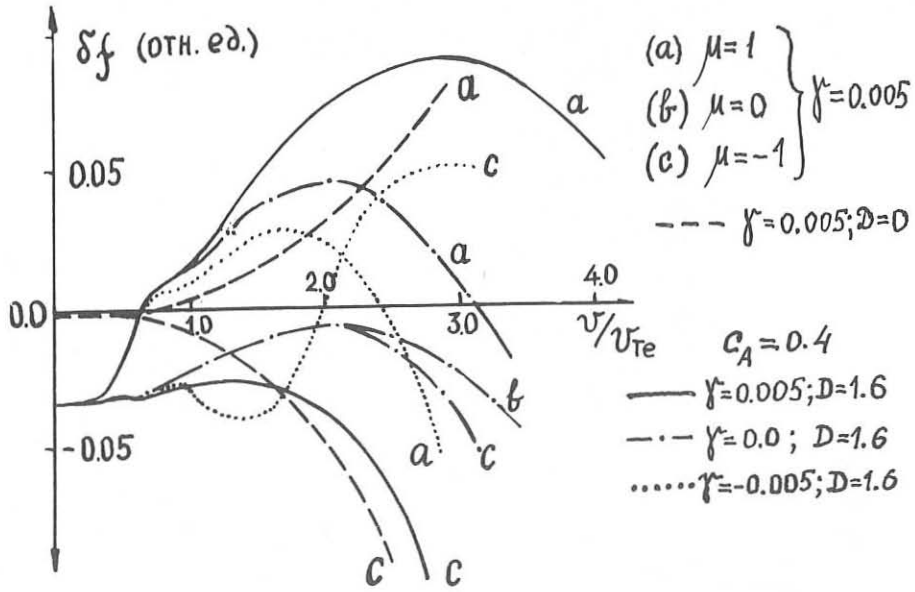

Fig.1. Distribution function distortion under the effect of quasilinear wave packet and direct electrical field.
Fig.2. Current evolution via time.

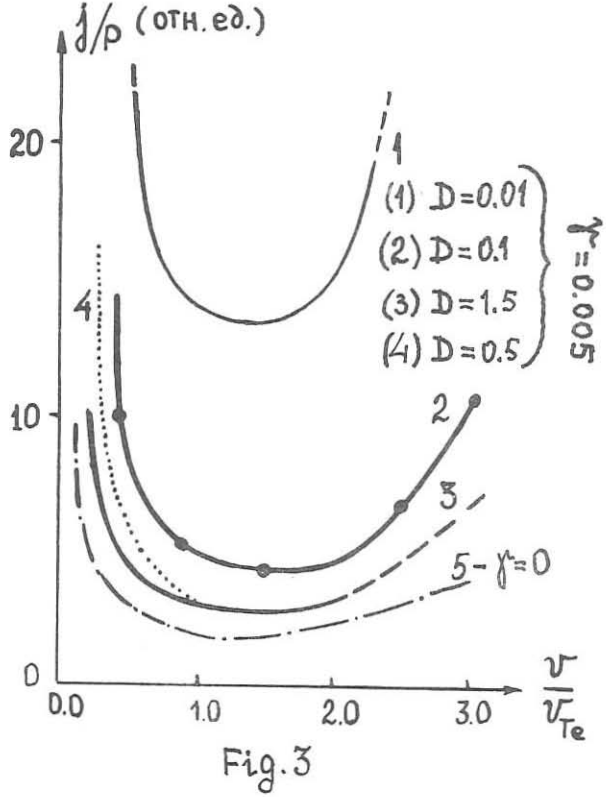

Fig.3

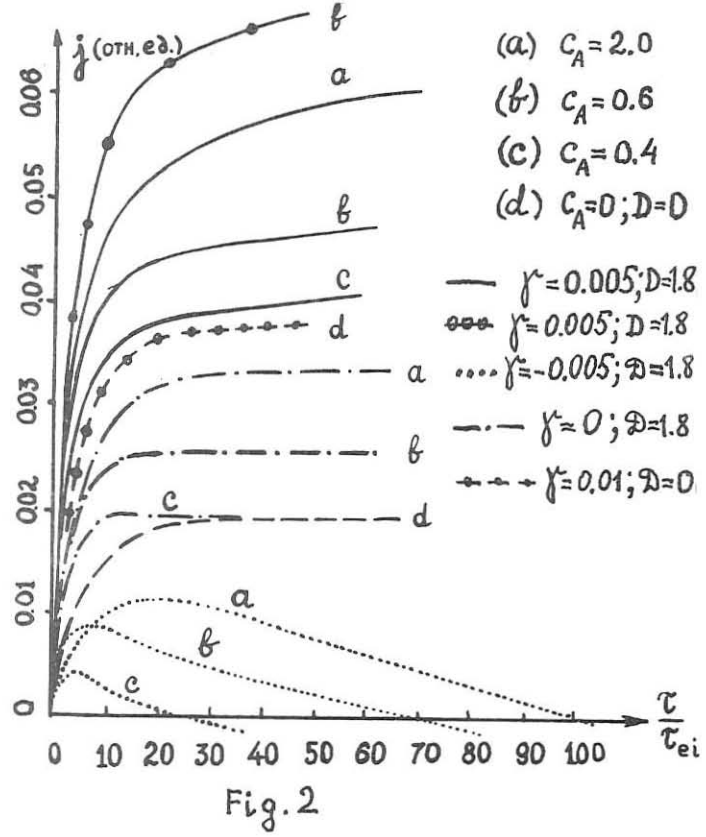

Fig.2

Fig.3. Driving current generation efficiency.

ALFVEN WAVE HEATING AND ITS EFFECT ON THE TOKAMAK CURRENT PROFILE

T. Dudok de Wit, A. A. Howling, B. Joye and J. B. Lister

Centre de Recherches en Physique des Plasmas
Association Euratom - Confédération Suisse
E.P.F.L., LAUSANNE (Switzerland)

The aim of this paper is to interpret the effect of Alfvén Wave Heating (AWH) on the current, density and temperature profiles of the TCA Tokamak plasma. AWH is accompanied by significant increases in line-averaged density $\overline{n_e}$ and $(\beta_p + l_i/2)$ [1], where $(\beta_p + l_i/2)$ is deduced from the equilibrium values of plasma current and vertical field (after correcting for the vertical field penetration L/R time of 1.1 ms for the vacuum vessel). For given plasma conditions, the value of $(\beta_p + l_i/2)$ does not depend sensitively on the exact major radius of the plasma (determined by using different position feedback methods which controlled the magnetic axis or the outermost flux surface). We therefore have confidence in the accuracy of the $(\beta_p + l_i/2)$ measurement.

In the absence of a reliable diamagnetic loop measurement for β_{perp}, the contributions of β_p and l_i must be separately evaluated and it is here that different interpretations may arise. In what follows, we present the observations which support the hypothesis of current profile (l_i) changes and discuss how these conjectured changes might be induced by AWH. We then compare this scenario with one in which increases in plasma energy (β_p) are presumed to account for the increase in $(\beta_p + l_i/2)$, in order to determine whether β_p, l_i, or a combination of both are responsible for these changes.

Current Profile Changes. Strong evidence for the effect of AWH on the current profile comes from the changes in amplitude of the Mirnov activity (associated with a modification of the current density gradient near the q=2 surface) closely linked with the appearance of AW thresholds in the plasma which can, in extreme cases, lead to spectral-related disruptions [2]. Further evidence includes changes in sawtooth frequency [3], and the phenomenon of hysteresis in which the loading of the global resonances (or Discrete Alfvén Wave DAW) is observed to depend on $(\beta_p + l_i/2)$ changes, while a 1-D kinetic code predicts that the DAW loading does depend on l_i [4]. We have considered two schemes in which AWH could be changing the current profile:

Heating at the AW resonance surfaces. Firstly, it was proposed that the dissipation of the Kinetic Alfvén Wave (KAW), excited at its AW resonance surface, may locally heat the plasma hence causing a current profile modification. However, there is no X-ray flux response coincidental with the passage of the resonance surfaces as they move outwards during the AW-induced density rise, and ($\beta_p + l_i/2$) tends to decrease instead of increase when a new resonance layer appears near the centre of the plasma. RF power modulation experiments demonstrate that there is in fact evidence for indirect AWH and that this energy is deposited at the q=1 surface [5]. The model of current profile modification due directly to resonance surface heating is therefore inadequate.

Current Drive by AWH. Secondly, it has been suggested that the KAW drives current by electron Landau damping, the required asymmetry for driving a net current with a symmetric antenna being due to the plasma gyrotropy. Parallel or anti-parallel current drive associated with resonance surfaces near the edge would then strongly influence the ohmic current density profile. This model was tested by separately driving travelling waves with toroidal mode number n=+1 and n=-1. Direct antenna voltage measurements were used to estimate the ratio of AW power in each direction. Using phase shift circuits in the individual AW generator final stages, a power ratio of better than 1000 was obtained for n=+/- 1 waves. The spectral purity obtained was confirmed by the change in wavefields, the lifting of the degeneracy in the (n,m) = (+1,+1) and (-1,-1) DAWs, and detailed observations of the density fluctuations due to the KAW [6]. The macroscopic parameters of the plasma however were unaltered; the ($\beta_p + l_i/2$) trace differed between the n=+1 and n=-1 cases only briefly after the appearance of the DAW threshold, and even then by less than by 0.04. This result is comparable to the change in l_i obtained with a semi-analytical model which assumes that current is driven at the AW resonance surface by transfer of momentum to non-trapped electrons. This experiment would seem to definitively deny the influence of direct AW current drive, although it might be claimed that higher-n travelling waves (which cannot be produced with the four pairs of antennae on TCA) could possibly drive current.

Changes in the Plasma Energy Content. Since it is difficult to positively measure a current profile change, a simple analysis of ($\beta_p + l_i/2$) was performed on plasmas in different conditions for which the following assumptions were made:

a) the plasma energy remains constant; or

b) the current profile remains unaltered.

The solid lines in Fig.1 represent an AWH discharge, the dashed lines refer to an ohmic discharge and will be explained afterwards. An increase in ($\beta_p + l_i/2$) is always observed at the onset of the RF pulse. The range of values of β_p represented by the shaded area were calculated assuming that the electron and ion temperatures did not change (giving the lower line), and assuming that the ion temperature increased linearly with the AWH-induced density

rise (giving the upper β_p trace). The range of β_p in the figure is therefore due to the density change and the reasonably-expected variation in ion temperature [7] due to increased electron-ion power transfer. The observed transient broadening of the density profile [8] and the peaking of the temperature profiles each have a relatively small effect which tend to cancel, thus leaving the value of β_p unaltered.

Figure 1a) shows the range of values of l_i calculated from the $(\beta_p + l_i/2)$ trace and the calculated β_p trace, ie assuming that no electron heating occurs. Note that an initial peaking in the current profile is predicted.

Figure 1b) shows the range of values of T_e (normalised to the initial ohmic value) necessary to account for the measured $(\beta_p + l_i/2)$ on the assumption that l_i does not change from its ohmic value. A rise and fall of the electron temperature is always predicted.

These two figures thus represent the two possible extremes of current profile change with no electron heating (Fig 1a) and electron heating with constant current density profile (Fig 1b).

The heavy dashed line in Fig 1b is a Thomson scattering measurement of T_e on axis. We note that the trend in T_e is similar, although the observed temperature change is not sufficiently large to explain the $(\beta_p + l_i/2)$ variation in terms of the fixed current profile model. It is clear that only a compromise between the two extreme models can explain the $(\beta_p + l_i/2)$ and T_e measurements, ie simultaneous changes in both the electron temperature and the current profile are necessary to account for the large increase in $(\beta_p + l_i/2)$. If l_i were assumed not to change, an astonishingly high AW heating efficiency would be deduced.

In order to check that temperature and profile changes are not simply due to the AWH-induced density rise, the parameters of an ohmic gas-puffing shot, with a similar initial density rise, are superimposed with dashed lines. Small changes in l_i or T_e, according to the model used, also occur, but clearly the AWH causes significantly larger increases. This general behaviour was consistently reproduced for a wide range of plasma currents.

Conclusions. AWH does not appear to be significantly influencing the current density profile by direct heating associated with resonance surfaces, or by current drive by the Kinetic Alfvén Wave. However, a comparison with gas-puffing shots (which can reproduce the initial rate of density rise) indicates that AWH does lead to electron temperature heating and some current profile peaking at the onset of RF heating, and that both of these must be included before the increase in $(\beta_p + l_i/2)$ can be explained.The mechanism by which these changes occur remains to be explained - it may involve a change in confinement. This mechanism would also have to account for the observed spectral-related phenomena. The installation of full antenna screens, to investigate the possible elimination of the AWH-induced density rise [9], and experiments with prolonged plasma pulses in which steady-state condtions could be achieved, will provide many answers to the questions of heating and profile changes during AWH.

Acknowledgements. We wish to thank the TCA team for its technical support. This work was partially supported by the Fonds National Suisse de la Recherche Scientifique.

References.

[1] JOYE B. et al - paper presented at this conference.
[2] APPERT K. et al - (Invited paper) Intl. Conf. Pl. Phys. Kiev, USSR April (1987)
[3] BESSON G. et al Pl. Phys. and Contr. Fus. 28 1291 (1986)
[4] BORG G. G. et al - paper presented at this conference.
[5] JOYE B. et al 'Dynamical plasma response to additional heating.' Accepted for publication in Pl. Phys. and Contr. Fus. (1988)
[6] BEHN R. et al Pl. Phys. and Contr. Fus. 29 75 (1987)
[7] De CHAMBRIER A. et al - to be submitted to Pl. Phys. and Contr. Fus.
[8] COLLINS G. A. et al 12th Eur. Conf. Contr. Fus. and Pl. Phys. Budapest 2 248 (1985)
[9] BALLICO M. J. et al - submitted to Pl. Phys. and Contr. Nuc. Fus

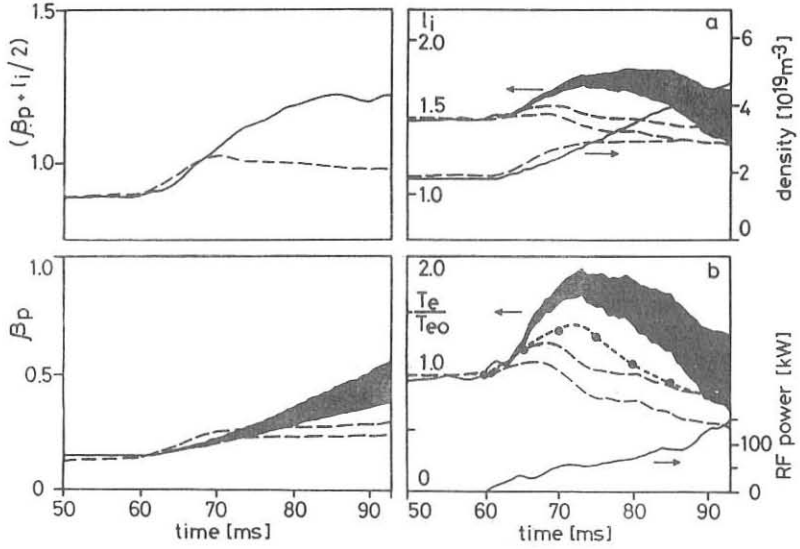

Figure 1 Measured (β_p+ l_i /2) trace and estimated β_p range allowing for T_i increases, with the consequent variations in:
a) l_i (assuming no change in T_e) and b) T_e (assuming no profile changes). Solid lines: Alfvén Heated plasma, dashed lines: gas-puffing into an ohmic plasma
- - ● - - $T_e(0)$ from Thomson scattering. Plasma current = 120kA

CURRENT DRIVE BY ICRF WAVES IN TOKAMAKS

Vdovin V.L.

I.V.Kurchatov Institute of Atomic Energy, Moscow, USSR

Abstract. Analitical and numerical analisis of CD by ICRF FMS and IB waves in tokamak-reactor like INTOR in selfconsistent "multiloop antenna-plasma-FP equation-current"cylindrical plasma model has been done.

The FMSW CD efficiency is $\gamma=\bar{n}I(MA)R(m)/P(MW) \cong 0.25\text{-}0.35$ for Cherenkov and TTMP mechanisms. The FMSW and IBW minority ($\omega=\omega_{ci}$, i=H, He-3, alfas) CD efficiencies are small and not interesting for reactor applications. The FMSW absorption by α - particles is insignificant under conditions $\omega/k_{\parallel} \geq v_{Te}$ and $\omega \neq n\omega_{c\alpha}$.

1. CD by FMS waves. The 5-loops antenna ($\Delta\varphi=\pi/2$) located outside ofthe torus launches FMSW to INTOR plasma with parabolic profiles [1]. The reflected waves, kinetic, quasilinear (Q-L) effects and antenna-plasma coupling are taken into account [1,2]. The Q-L diffusion coefficient (DC) for 1-D FP equation has been taken as

$$D_{rf} = \frac{e^2}{2m^2 v_{Te}^2} \sum_n \frac{\Delta_n \cdot \hat{\theta}_n \hat{\theta}_n^*}{(\omega - k_{zn} v_{\parallel})^2 + \Delta_n^2}$$

where (extension of $\hat{\theta}_n \hat{\theta}_n^*$ for cylindrical geometry)

$$\hat{\theta}_n \hat{\theta}_n^* = \sum_n |E_{zn}|^2 + 2\left(\frac{v_\perp}{v_{ph,n}}\right)^2 \rho_e^2 \left\{\left(\frac{1}{r}\frac{\partial E_r^*}{\partial \varphi} - \frac{\partial E_\varphi}{\partial r}\right) \times \hat{L}\left(\frac{1}{r}\frac{\partial E_r}{\partial \varphi} - \frac{\partial E_\varphi}{\partial r}\right)\right\} - \left(\frac{v_\perp}{v_{ph,n}}\right)\rho_e \left\{-E_z^* \frac{\partial E_\varphi}{\partial r} + E_\varphi^* \frac{\partial E_z}{\partial r} + \frac{E_z^*}{r}\frac{\partial E_\varphi}{\partial \varphi} - \frac{E_r^*}{r}\frac{\partial E_z}{\partial \varphi}\right\}$$

and $\vec{E}$-electrical field, $v_{ph,n}=R\omega/n$ (n=1,2,..) and $\rho_e = v_{Te}/\omega_{ce}$, $\hat{L}$ - 2-order differencial operator. Here, as a first step, $\hat{L}=-1$ was chosen (Δ_n is given in [2,1]).

The current profile induced by FMSW with f=106 MHz ($\omega \geq 2\omega_{cD}$) is

and for f=40 MHz - on Fig. 1b

shown on Fig.1a (R=4.9 m, ā=1.52 m, exciting current at r=s=1.6 m flows; the chamber radius is b=1.7 m; 5 loops have wideness D=0.16 m and 0.6 m, distancies between loops are 0.33 and 0.99 m for a and b; T_{e0}=40 keV, $n_{e0}=3\times10^{20}$ m^{-3}). The CD efficiencies (CDE) are $\gamma\cong0.3$ A/W/m^2, CD profiles are center peacked. The dependeces of γ vs. plasma and antenna parameters are given in [1].

2. The FMSW absorption by α-particles one can obtain by analising the dispersion relation

$$n_\perp^2\left\{\frac{3n_{||}^2\epsilon_{22}}{n_{||}^2-\epsilon_{||}}\cdot\frac{\hat{\epsilon}_{23}}{\epsilon_{33}}+\left(\epsilon_{||}+n_{||}^2-\frac{\epsilon_{12}^2}{n_{||}^2-\epsilon_{||}}\right)\epsilon_{33}^{-1}+1-\delta\hat{\epsilon}_{||}-n_{||}^2\frac{\epsilon_{23}^2}{\epsilon_{33}}\right\}+\frac{(\epsilon_{||}-n_{||}^2)^2+\epsilon_{12}^2}{n_{||}^2-\epsilon_{||}}=0$$

where ϵ_{ij} and $\delta\hat{\epsilon}_{11}$ are permittivity tensor components, quantity $n_\perp^2$ from $\delta\hat{\epsilon}_{11}$ and $\hat{\epsilon}_{23}$ is extended. So alfas/electrons Im $k_\perp$ ratio is

$$\frac{Im\,k_\perp^{(\alpha)}}{Im\,k_\perp^{(e)}}=\frac{2n_\alpha}{n_e}\,\frac{\xi_\alpha}{\xi_e}\,\frac{\frac{T_\alpha}{T_e}CX^2+2\frac{T_e}{T_\alpha}(B+X^2)}{CX^2+B}\,exp\left(-\xi_\alpha^2+\xi_e^2\right)$$

where $\xi_\alpha=\omega/k_{||}V_\alpha$, $\xi_e=\omega/k_{||}V_{Te}$, $B=\epsilon_{||}+n_{||}^2-\epsilon_{22}^2/(n_{||}^2-\epsilon_{11})$, $C=\omega_{pe}^4/\omega_{Be}^2k_{||}^2c^2$, $X^2=(1+\xi_e\,$ Re $Z(\xi_e))$, $Z(\xi_e)$-plasma dispersion function. One can see that under condition $\omega/k_{||}v_{Te}\gg1$ $Im(k_\perp^{(\alpha)})/Im(k_\perp^{(e)})\ll1$ [1]. Consequently for FMSW with high phase velocity ($\omega/k_{||}\gg v_{Te}>v_\alpha$) at $\omega\leq\omega_{CD}$-particle absorption is small and waves are absorbed at plasma center on electrons ($\omega\neq n\omega_{ci}$). The similar result has been obtained in [3] for frequencies $\omega\ll\omega_{ci}$.

3. Minority FMS and IBW investigation by numerical solution of 2-D FP equation was done in order to obtain quantitative results in asymetrical ion minority scheme suggested by N.Fisch [4]. The Q-L DC was chosen as

$$\mathcal{D}_{rf}^{ql}=\bar{\mathcal{D}}_{rf}(u,\theta)\,exp\left(-(u\cos\theta-u_{||}^0)^2/\Delta u^2\right)/\pi^{1/2}\Delta u$$

where $u_{||}^0=(1-4)v_{||}/v_T'$, $\Delta u=\Delta v_{||}/v_T'$(prime-minority species). The ion Bernstein (IB) wave ray tracing results show that significant amount of wave energy by minority ions with $v_{||}=(3-4)v_T'$ is absorbed. For FMSW the velocity range is greater: $v_{||}=(1-4)v_T'$. The IBW Q-L diffusion coefficient depends on $v_\perp$ and $k_\perp$

$$\overline{D}_{rf}^{IBW} = \zeta J_\ell^2(K_\perp v_\perp/\omega_c')/(K_\perp v_\perp/\omega_c')^2 \qquad (*)$$

where ζ is T.Stix parameter ($\zeta \sim |E_+|^2$), J_ℓ-Bessel function (for FW $D_{rf}^{FW} = \langle P_{rf} \rangle / 2nm'$). The results for hydrogen and He-3 minorities with FMSW in Table 1 are given. The local CDE is small :~2 A·cm/W for He-3 and~10 A·cm/W for H. These results are worser than that obtained in [5]. It is due to fact that minority drift velocity $v_{dr} = \int v_{||} f(v_{||}, v_\perp) dv_{||}$ is small: $v_{dr} = (0.05\text{-}0.1)v_T'$. The calculations have shown that CDE falls with increasing of RF power.

The minority CDE possible to increase making use IB waves, namely the peculiarities of their DC (*) , bounding wave-ion interaction to large perpendicular velocities ($J_\ell(k_\perp v_\perp/\omega_c') = 0$). So minority ions do not pushed strongly in perpendicular direction, where they interact mainly with electrons so pitch-angle scattering is absent. Related He-3 distribution function is shown on Fig.2, and localization over lower energies is seen. The CDE increases slightly (Table 2). The CDE for INTOR parameters with IBW is lower 4 A·cm/W in plasma with He-3 and lower 7 A·cm/W for D minority at $P_{rf} = 1\text{-}2$ W/cm^3. Again these efficiencies are not interesting for a reactor.

The analagous calculations for IBW interacting with α-particles have given [1]: ~ 20 A·cm/W at $P_{rf} \sim 2$ W/cm (for a reactor J=200-400 A/cm^2 are nesessary), again small CD efficiency.

Thus in ICR frequencies range (and lower) only FMS waves interecting directly with electrons, having good penetration to plasma center and negligible α-particles absorption, are main candidat for noninductive current drive in reactor.

REFERENCIES

1. V.L.Vdovin, USSR Contr. to 15 session of Phase IIA Part 3 of INTOR workshop (July 1987, Vienna), group C
2. Y.Kishimoto et al, Japan Contr. to ibid., group C
3. K.L.Wong et al, Nucl. Fusion 30,(1987) 834
4. N.J.Fisch, Nucl. Fusion 21,(1981) 15
5. V.V.Mahajan et al, Phys. Fluids 30 (1987) 2101

Table 1

Minority FMSW	n_e 10^{20} m^{-3}	T keV	Vph/Vt	<Prf> W/cm^3	Jrf A/cm^2	Vdr/Vt	Jrf/Prf A·cm/W	ε=r/R
H^+	1	30	2	0.4	1.38		3.45	0.1
H^+	1	30	3	0.1	0.176		1.76	0.1
H^+	1	20	4	0.5	5.8	8.5 10	11.6	0.1

Table 2

IBW								
He-3	1	40	2	2.2	2.47	1.37 10	1.12	0
He-3	1	40	2.5	2.2	3.71	2.0 10	1.7	0
He-3	1	40	4	2.2	7.16	4.0 10	3.25	0
He-3	1	40	1.5	2.2	1.52	0.84 10	0.69	0
He-3	1	20	3	1.1	1.53		1.4	0

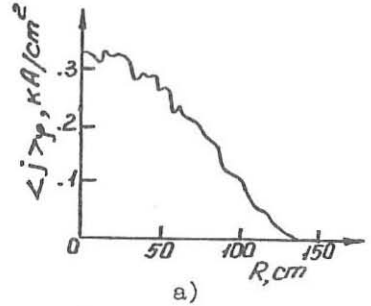

a)

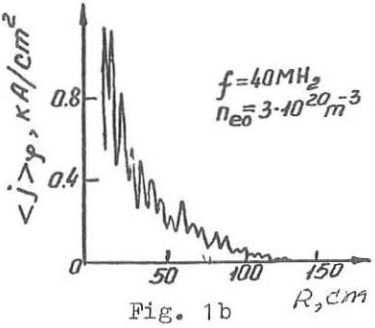

Fig. 1b

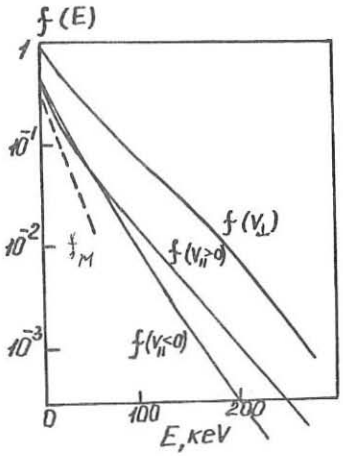

Fig.2 He-3 distribution function (5%) in T-plasma, IB wave. T=20 keV, n=10^{20} m^{-3}, $\langle v_{ph}\rangle = 3v_T'$, $\Delta v_{ph} = 2v_T'$, $\langle P_{rf}\rangle$=1.1 W/cm^3, ε=0, Z=1, $\langle E\rangle_{rf}$=50.4 keV, t=t_{sp}/3 I=1.53 A/cm^2.

ELECTRON CYCLOTRON CURRENT DRIVE EXPERIMENTS IN THE WT-3 TOKAMAK

H. Tanaka, K. Ogura, A. Ando[a], S. Ide, M. Iida, K. Iwamura, A. Yamazaki, T. Itoh, M. Iwamasa, K. Hanada, M. Nakamura[b], T. Maekawa, Y. Terumichi and S. Tanaka

Department of Physics, Faculty of Science,
Kyoto University, Kyoto 606, Japan

A series of rf (lower hybrid and electron cyclotron) current drive experiments has been carried out in the WT-2[1-3] and the WT-3[4,5] tokamaks. In this paper, we report experiments on the electron cyclotron current drive at the second harmonic ($2\Omega_e$ ECCD) in WT-3 (R_0 = 65, a = 20 cm and $B_t(0) \leq 1.75$ T). The plasma current I_p up to 25 kA is sustained or ramped up by the $2\Omega_e$ EC wave alone after the Ohmic heating (OH) power is shut down. The hard x-ray pulse height analysis has been performed in the line of sight parallel or antiparallel to I_p. The velocity distribution function of the high energy tail electrons is asymmetric in the toroidal direction. The $2\Omega_e$ EC wave is mainly absorbed by the tail and the $2\Omega_e$ EC-driven current is generated by enhancement of asymmetric distribution of the tail.

A Vlasov antenna is used to convert a microwave from a gyrotron ($\omega/2\pi$ = 56 GHz, $P_{EC} \leq 200$ kW, $\tau \leq 100$ ms and TE_{02} mode) to a linearly polarized one. The wave is launched from the low field side of the torus in X-mode, angled at 60° or 120° to the toroidal field (antiparallel or parallel to I_p respectively). To obtain information on anisotropy of the velocity distribution function of the high energy tail electrons, a NaI scintillator has been installed to view the plasma through two lead apertures at an angle θ to the magnetic axis in the equatorial plane. The angle θ is changed from 0° to 90°. When the direction of I_p is inverted, the angle θ is changed from 90° to 180°.

In Fig. 1, the typical waveforms of a $2\Omega_e$ ECCD plasma are shown (the $2\Omega_e$ ECR layer is located at $r(2\Omega_e) = R(2\Omega_e) - R_0 = 6$ cm). The target plasma (line-averaged electron density $\bar{n}_e \simeq 2 \times 10^{12}$ cm^{-3}, temperature $T_e \simeq$ 200 eV) is produced by OH. After the OH power is turned off, the OH current disappears within 50 ms (dotted curves). When the EC pulse (48kW, 75ms) is injected (full curves), a constant plasma current I_p = 16 kA continues to flow for 70 ms with loop voltage $V_L = 0$. The strong emissions of soft and hard x-ray I_{sx}(2.5keV), I_{hx}(35keV) and microwave I_μ(70GHz) from the high energy tail electrons appears. Bulk electron temperature and density in the ECCD plasma are nearly the same as those in the OH plasma and kept almost constant during the EC pulse. The radial position of their peaks is at r ≃ 0 cm. As the injected microwave power P_{EC} increases, the $2\Omega_e$ EC-driven current I_p changes from ramp-down to flat-top, then to ramp-up (Fig. 2). Correspondingly I_{sx}(1.7keV) emitted from the high

energy tail electrons increases, while $I_{sx}(0.2keV)$ emitted from the bulk electrons does not change. These results show that the EC wave selectively heats the high energy tail electrons, which are carrying the plasma current.

Hard x-ray pulse height analysis has been performed in the $2\Omega_e$ ECCD plasma (P_{EC} = 65 kW, I_p = 20 kA, $n_e \simeq 2 \times 10^{12}$ cm^{-3}). Hard X-ray spectra during ECCD in forward (θ = 20°), perpendicular (θ = 90°) and backward (θ = 117°) directions are shown in Fig. 3 (a). The 'equivalent temperatures' are 90, 70 and 60 keV, respectively. This means that the velocity distribution of the high energy tail electrons is asymmetric in the toroidal direction and the temperature and density are higher in the forward direction.

In Fig. 3 (b) the hard x-ray spectrum measured in the OH plasma at θ = 90° is shown with that in the ECCD plasma. Hard x-ray up to 200 keV is observed in the initial OH plasma, implying that the high energy tail electrons are present. When P_{EC} is injected, photon count increases more than five times and hard x-ray up to 400 keV appears. As shown in Fig. 4, for low filling-gas pressure, p = (0.5 ∿ 1.2) × 10^{-2} Pa, non thermal emissions I_μ(70GHz) and I_{hx}(35keV) appear in the OH plasma and flat-top discharges are formed when P_{EC} is injected. For p > 1.4 × 10^{-2} Pa, these emissions are weak and I_p decreases with time even if P_{EC} is injected. These results show that the presence of the high energy tail electrons in the initial OH plasma is necessary for formation of the $2\Omega_e$ ECCD plasma.

The flat-top or ramp-up discharges are obtained when the $2\Omega_e$ ECR layer is near the center of the vessel, $r(2\Omega_e)$ = 0 ∿ 10 cm. There is no remarkable difference when the wave is injected in the opposite direction (Fig. 5). Numerical calculations on $2\Omega_e$ EC absorption have been made using a code which includes the Doppler and the relativistic effects of the high energy tail electrons. The radial profiles are assumed as follows: for the bulk electrons $n_{eb}(r) = n_{eb0}(1-r^2/a^2)^{\alpha nb}$, $T_{eb}(r) = T_{eb0}(1-r^2/a^2)^{\alpha tb}$ and for the high energy tail electrons $n_{eh}(r) = n_{eh0}(1-r^2/a^2)^{\alpha nh}$, $T_{eh}(r) = T_{eh0}(1-r^2/a^2)^{\alpha th}$ in accordance with the experimental data. A non-relativistic Maxwellian distribution of the bulk electrons and a relativistic 'three-temperature distribution' of the high energy tail electrons f_{eh} are used.

$$f_{eh}(p_\perp, p_{//}) = A_N \exp(-\mu_\perp \gamma_\perp - \mu_{//} \gamma_{//})$$

where $\gamma_\perp^2 = 1 + (p_\perp/m_e c)^2$, $\gamma_{//}^2 = 1 + (p_{//}/m_e c)^2$, $\mu_\perp = m_e c^2/T_\perp$, $\mu_{//} = m_e c^2/T_{//F}$ ($p_{//}>0$), $m_e c^2/T_{//B}$ ($p_{//}<0$), assuming $T_{//F}$ = 90 keV, $T_{//B}$ = 60 keV and $T_\perp$ = 70 keV. Single-pass absorption at $2\Omega_e$ is rather weak (∿0.35) and 0.73 of its amount is due to the high energy tail electrons (Figs. 6 (b) ∿ (d)). The low single-pass absorption and the multi-reflection on the wall result in that the $2\Omega_e$ EC heating effect does not depend strongly on the direction of waves.

In summary, when P_{EC} is injected into a plasma after the OH power is turned off, the plasma current is sustained or ramped up by P_{EC} alone. The angular dependence of hard x-ray spectra with respect to the magnetic field indicates the anisotropic velocity distribution of the high energy tail electrons, whose forward parallel temperature is about 90 keV. The ray tracing reveals that the wave is mainly absorbed by these high energy tail

electrons. The $2\Omega_e$ EC driven-current is generated by an asymmetric $2\Omega_e$ heating of the high energy tail electrons existing in the initial OH plasma.

Acknowledgements : We wish to thank the other member of WT-3. This work is partly supported by a Grant-in-Aid for Science and Culture in Japan.

(a) Institute of Plasma Physics, Nagoya University, Nagoya 464, Japan
(b) Osaka Institute of Technology, Osaka, Japan

References:
(1) M. Nakamura et al., Phys. Rev. Lett. 47 (1981) 1902.
(2) S. Kubo et al., Phys. Rev. Lett. 50 (1983) 1994.
(3) A. Ando et al., Phys. Rev. Lett. 56 (1986) 2180.
(4) S. Tanaka et al., in Proc. 11 th Intern. Conf. Plasma Phys. and Contr. Nucl. Fusion Res., Kyoto, 1986 IAEA-CN-47/F-II-6.
(5) H. Tanaka et al., Phys. Rev. Lett. (to be published)

Fig. 1

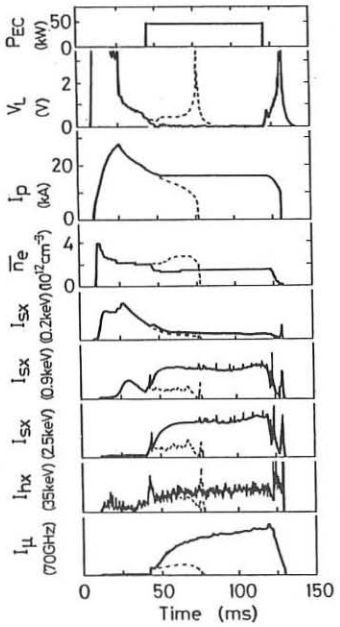

Fig. 2

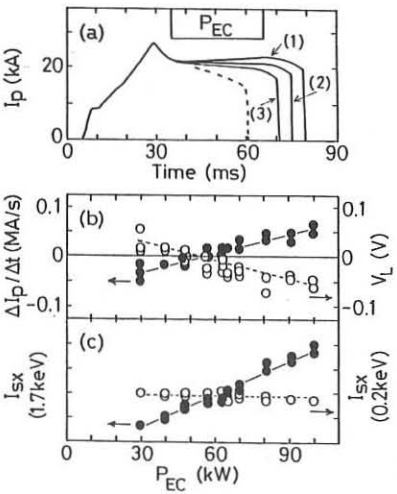

Fig. 1 The waveforms of a long flat-top ECCD discharge (full curves) and a OH discharge without P_{EC} (dotted curves).
Fig. 2 (a) ramp-up, flat-top and ramp-down discharges for P_{EC} = (1) 100 kW, (2) 57 kW and (3) 30 kW. (b) ramp-up rate $\Delta I_p/\Delta t$ (•) and loop voltage V_L (o), (c) soft x-ray emission I_{sx}(1.7keV) (•) and I_{sx}(0.2keV) (o) as functions of P_{EC}.

Fig. 3

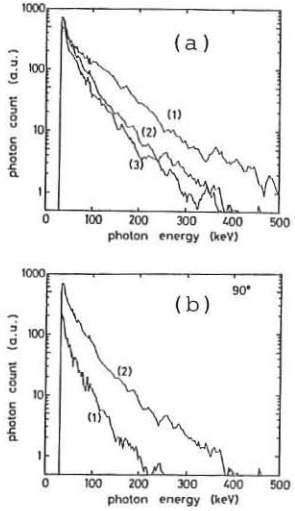

Fig. 4

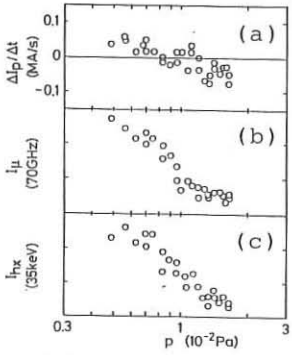

Fig. 5

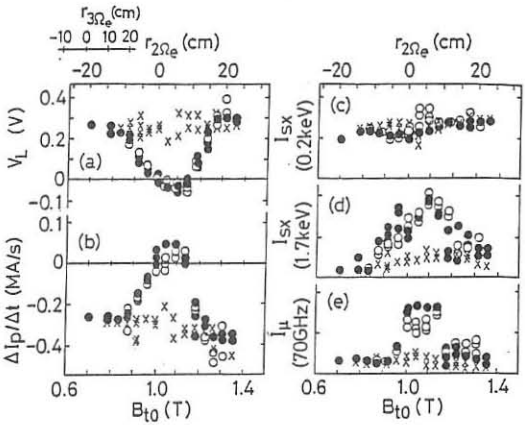

Fig. 6

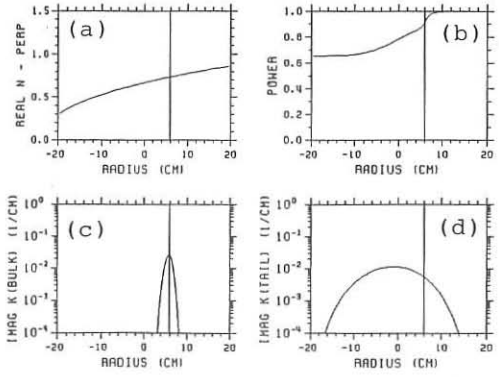

Fig. 1 (a) Hard x-ray spectra in the $2\Omega_e$ ECCD plasma, curve (1) θ = 20°, (2) θ = 90°, (3) θ = 117°, and (b) those at θ = 90° in (1) the OH plasma, (2) the $2\Omega e$ ECCD plasma.

Fig. 4 (a) $\Delta I_p/\Delta t$, (b) ECE I_μ(70 GHz) and (c) I_{hx}(35keV) as functions of filling-gas pressure.

Fig. 5 (a) V_L, (b) $\Delta I_p/\Delta t$, (c) Isx(0.2keV), (d) Isx(1.7keV) and (e) I_μ(70GHz) as functions of $B_t(0)$ or the position of the $2\Omega_e$ ECR layer $r(2\Omega_e)$. Solid circles are for EC injection antiparallel to I_p, open circles for parallel one and crosses for the OH plasma.

Fig. 6 Results of the ray tracing at $B_t(0)$ = 1.09 T. (a) The real part of $N_\perp$, (b) the wave power, the imaginary part of k for bulk electrons (c) and high energy electrons (d) along the ray (projections on a cross section of the plasma column).

ELECTRON CYCLOTRON CURRENT DRIVE: THEORETICAL CONSIDERATIONS

M. Bornatici[a] and M. Pieruccini[b]

a) Physics Department, University of Ferrara, Ferrara, Italy;
b) Physics Department, University of Milano, Milano, Italy.

On the basis of an asymptotic analysis of the absorbed power and the wave-induced current, a Fisch-type formula for the electron cyclotron current-drive efficiency is obtained and discussed. The case of upshifted frequencies is considered in some detail.

Introduction. On the basis of the standard quasi-linear theory of the (relativistic) wave-particle interaction one can write the absorbed power density and the corresponding wave-induced current density around the n-th harmonic of the electron cyclotron frequency as[1]

$$\{P^{(n)}, J^{(n)}\} = -2\pi m^2 c \int d\gamma\, d\bar{p}_{||}\, \gamma D\, \delta(\gamma\omega - \omega N_{||}\bar{p}_{||} - n\omega_c)\quad \mathcal{L}(f)\{1, \mathcal{L}(\chi/mc^2)\} \qquad (1)$$

$\mathcal{L} \equiv \partial/\partial\gamma + N_{||}\,\partial/\partial\bar{p}_{||}$; χ is the response function $(=(-ec/v)\,\bar{p}_{||}\,G(\gamma)$; $\nu \equiv \omega_p^2\, e^2\, \ln\Lambda/(mc^3))$; D has to do with a scalar energy diffusion coefficient and to lowest order in the finite Larmor radius effects is

$$\gamma D = \pi\, (ec/2^n n!)^2\, (n\omega_c/\omega)^2\, \frac{1}{N_\perp^2}\, (\omega N_\perp/\omega_c)^{2n}\, \bar{p}_\perp^{2n}\, |E_{eff}|^2 \qquad (2)$$

with $|E_{eff}|^2 = |E_x - iE_y + (\omega/n\omega_c)N_\perp\,\bar{p}_{||}\,E_z|^2$, the external magnetic field being $\underline{B}_o = B_o\,\hat{z}$.

By performing the $\bar{p}_{||}$-integration in (1) by means of the δ-function, one, in particular, obtains for the (normalized) current-drive (CD) efficiency $\hat{\eta} = (J/(-en_o c))/(P/\nu n_o mc^2)$

$$\hat{\eta}^{(n)} = \frac{\int_{\gamma_-}^{\gamma_+} d\gamma\, [\bar{p}_\perp(\gamma)]^{2n}\, \mathcal{L}(f)\, \mathcal{L}(\bar{p}_{||}\, G(\gamma))\Big|_{\bar{p}_{||}=\bar{p}_{||}(\gamma)}}{\int_{\gamma_-}^{\gamma_+} d\gamma\, [\bar{p}_\perp(\gamma)]^{2n}\, \mathcal{L}(f)} \qquad (3)$$

$[\bar{p}_\perp(\gamma)]^2 = \gamma^2 - 1 - [\bar{p}_{||}(\gamma)]^2$ and $\bar{p}_{||}(\gamma) = (1/N_{||})(\gamma - n\omega_c/\omega)$ are the resonant perpendicular and parallel momentum; the limits of the γ-integration for the case of $N_{||}^2 < 1$ are

$$\gamma_\pm = (1-N_{||}^2)^{-1}\, \{n\omega_c/\omega \pm [N_{||}^2(N_{||}^2 - 1 + (n\omega_c/\omega)^2)]^{1/2}\}, \qquad N_{||}^2 - 1 + (n\omega_c/\omega)^2 > 0 \qquad (4)$$

In getting (3), the relativistic corrections in the wave polarization have been neglected, i.e., $E_{eff} \approx E_x - iE_y + (\omega/n\omega_c)(N_\perp/N_{||})(1 - n\omega_c/\omega)E_z$, with the result that, in this approximation

the CD efficiency (3) is independent of the polarization.[2]

In order to carry out explicitly the γ-integration in (3), it is assumed that $\mathcal{L}(f) \sim e^{-\mu(\gamma-1)}$, $\mu = mc^2/T_h$ ($\gg 1$), i.e., the distribution function of the resonant (current-carrying) electrons is a (relativistic) Maxwellian with an effective temperature T_h. In this case the denominator of (3) and, thus, the absorbed power can be evaluated in terms of the modified Bessel functions of the 1.st kind of order equal to an integer plus one-half and argument $z=(\mu/2)(\gamma_+ - \gamma_-)$. On the other hand, with the response function in the nonrelativistic limit, for which $G=(2\sqrt{2}/(5+z))(\gamma-1)^{3/2}$, the numerator of (3) and, thus, the driven current density can be expressed in terms of differences of incomplete gamma functions of order equal to an integer plus one-half, whose argument is either the maximum or the minimum resonant energy (normalized to T_h), i.e., $\varepsilon_{M,m} = \mu(\gamma_\pm - 1)$. These expressions are, in general, somewhat cumbersome and the relevant physics can be conveniently displayed by an asymptotic study.

Asymptotic analysis. Two significant asymptotic limits of the CD efficiency (3) are connected with the width of the range of the resonant energies, i.e., the range of the γ-integration in (3),

$$z \equiv \frac{\mu}{2}(\gamma_+ - \gamma_-) = \frac{\mu N_{||}^2}{1-N_{||}^2}\left(1+\frac{1}{N_{||}^2}[(n\omega_c/\omega)^2 - 1]\right)^{1/2} \qquad (5)$$

The corresponding asymptotic expressions for the two integrals in (3) are given in the following table for frequencies around the fundamental.

Asymptotic expressions for the two integrals occurring in the CD efficiency (1), $\omega \approx \omega_c$	
$\int_{\gamma_-}^{\gamma_+} d\gamma\, [\bar{p}_\perp(\gamma)]^2\, e^{-\mu(\gamma-1)}$	$\int_{\gamma_-}^{\gamma_+} d\gamma\, [\bar{p}_\perp(\gamma)]^2\, e^{-\mu(\gamma-1)}\, \mathcal{L}\,(\bar{p}_{||}\, G(\gamma))\Big\vert_{\bar{p}_{||}=\bar{p}_{||}(\gamma)}$
$\frac{1-N_{||}^2}{\mu^3 N_{||}^2}\, e^{-\mu(\gamma_- -1)} \times \begin{cases} \mu(\gamma_+ - \gamma_-),\ z=(\mu/2)(\gamma_+ - \gamma_-) \gg 1 \\ [\mu(\gamma_+ - \gamma_-)]^3/6,\ z \ll 1 \end{cases}$	$\frac{1-N_{||}^2}{\mu^3 N_{||}^2}\, \mathcal{L}\,(\bar{p}_{||}\, G(\gamma))\Big\vert_{\substack{\bar{p}_{||}=\bar{p}_{||}(\gamma) \\ \gamma=\gamma_-}}\, e^{-\mu(\gamma_- -1)} \times \begin{cases} \mu(\gamma_+ - \gamma_-),\ z \gg 1 \text{ and } \mu(\gamma_- -1) \gg 1 \\ [\mu(\gamma_+ - \gamma_-)]^3/6,\ z \ll 1 \end{cases}$

Note that the asymptotic expression for the current for $z \gg 1$ is subject to the further condition $\mu(\gamma_- -1) \gg 1$. The CD efficiency (3) corresponding to the asymptotic expressions thus obtained is[2]

$$\hat{\eta} = \mathcal{L}\,(\bar{p}_{||}\, G(\gamma))_{\bar{p}_{||}=\bar{p}_{||}(\gamma);\ \gamma=\gamma_-} = \left[\frac{1}{N_{||}}(\gamma - \omega_c/\omega)\ dG/d\gamma + N_{||}\, G(\gamma)\right]_{\gamma=\gamma_-} \qquad (6)$$

with γ_- the minimum resonant energy defined in (4). Note that the "intrinsic efficiency" $\eta = \mathcal{L}(\bar{p}_{||}\, G(\gamma))$, with $\bar{p}_{||}$ and γ independent variables, is just Fisch's result,[3] obtained by evaluating the contribution of individual electrons on the basis of collisionality considerations only, i.e., without any reference to the actual absorption process that is needed in order to drive the current. The physics brought out by (6), and not contained in Fisch's result, consists in accounting for the constraints arising from the (relativistic) resonance condition, namely, $\bar{p}_{||} = (1/N_{||})(\gamma - n\omega_c/\omega)$ and the three variables $N_{||}$, ω_c/ω and $\gamma=\gamma_-$ related by (4), so that (6) yields the CD efficiency as a function of only two independent variables, e.g., $\hat{\eta}=\hat{\eta}(\gamma_-, \omega_c/\omega)$. Formally, the Fisch-type result (6) is simply the ratio of the two integrands, i.e., the ratio between the spectral (with respect to γ) current density and the spectral absorbed power, evaluated at the minimum resonant energy. This occurs whenever the relevant part of current carrying electrons is concentrated around the minimum energy. In this way the CD efficiency does not depend on the distribution function of the resonant electrons (hence, no temperature-dependence appears in (6)).

For a given ω_c/ω, one can make use of (4) to express $N_{||}$ (>0) as a function of γ_-, i.e., $N_{||}^2 = (\gamma_- - n\omega_c/\omega)^2\ (\gamma_-^2 - 1)^{-1}$, and write (6) as

$$\hat{\eta}(\gamma_-, \omega_c/\omega) = [\mathrm{sgn}(\gamma - \omega_c/\omega)(\gamma^2 - 1)^{1/2}\ \ dG/d\gamma + \frac{|\gamma - \omega_c/\omega|}{(\gamma^2 - 1)^{1/2}}\ G(\gamma)]_{\gamma=\gamma_-} \qquad (7)$$

From (7) it appears that for upshifted ($\omega>\omega_c$) frequencies the CD efficiency is higher than for downshifted frequencies ($\omega<\omega_c$); in particular, for $\omega_c/\omega > \gamma_-$ (>1), the two terms on the right-hand-side of (7) tend to cancel each other. Note, however, that this effect is appreciable only at relativistic energies, while at low energies this "up- down-shift" effect shows up only if the contribution from the resonant electrons with energy higher than the minimum is accounted for. For moderately relativistic energies, efficiency (7) is an increasing function of energy,[3] so that to maximize it one should choose γ_- as high as possible. For the specific case of upshifted frequencies and $N_{||}^2 < 1$, the maximum of the minimum resonant energy is $\gamma_- = \gamma_+ = \omega/\omega_c$, which occurs for $1 - N_{||}^2 = (\omega_c/\omega)^2$. The corresponding maximum CD efficiency is

$$\hat{\eta}(\gamma_- = \omega/\omega_c>1) \equiv \hat{\eta}_{max} = [(\omega/\omega_c)^2 - 1]^{1/2}\ \ (dG/d\gamma + \frac{\omega_c}{\omega}\ G(\gamma))_{\gamma=\omega/\omega_c} \qquad (8)$$

It has to be noted that the maximum value (8) is limited by the upper bound on the maximum minimum resonant energy $\gamma = \omega/\omega_c < 1.22$ connected with the harmonic overlap with the second harmonic.[4]

In conclusion, the asymptotic analysis presented here can be extended to account for polarization as well as trapping effects on the CD efficiency.

Acknowledgements. This work has been performed with financial support from the Ministero della Pubblica Istruzione of Italy. Part of the work of one of the authors (M. P.) has been performed at the FOM-Instituut voor Plasmafysica, Rijnhuizen, Nieuwegein, The Netherlands, with financial support from Euratom.

References.

1. T. M. Antonsen and B. Hui, IEEE Trans. Plasma Sci. **PS-12**, 118 (1984).
2. R. H. Cohen, Phys. Fluids **30**, 2442 (1987).
3. N. J. Fisch, Phys. Rev. A **24**, 3245 (1981).
4. G. R. Smith, R. H. Cohen and T. K. Mau, Phys. Fluids **30**, 3633 (1987).

OPTIMIZING CURRENT DRIVE BY ELECTRON CYCLOTRON WAVES IN THE PRESENCE OF TRAPPED PARTICLES

G. Giruzzi

Association EURATOM-FOM, FOM Instituut voor Plasmafysica
"Rijnhuizen", Nieuwegein, The Netherlands

1. Introduction. Current drive by electron cyclotron (EC) waves is a possible candidate for operating a steady state tokamak reactor. In this method [1], a net toroidal current is generated by a heating process which is essentially perpendicular to the toroidal direction. In the limit of a homogeneous magnetic field configuration, this process is, in principle, almost as efficient as a direct parallel heating [1], but in a toroidal system electron trapping imposes a stringent limit to its efficiency [2]. This effect is particularly important in the case of wave absorption at downshifted frequency ($\omega < \omega_c$, ω and ω_c being the wave and the EC frequency, respectively), and at high wave power levels. In this work, two methods for minimizing this deleterious effect are investigated: i) moving the absorption region to the inboard side of the magnetic surfaces; ii) combining EC and lower hybrid (LH) waves. In order to evaluate the current drive efficiency for realistic wave power levels, the time-dependent bounce-averaged quasilinear/Fokker-Planck equation [3] is solved by means of a 2-D Fokker-Planck code [4]. The case of the extraordinary (x) mode absorbed at $\omega < \omega_c$ is considered in detail, both for low and high wave power. It is shown that, in this case, moving the absorption region is rather ineffective in enhancing the current drive efficiency, because of the interplay of quasilinear and toroidal effects for high wave power. On the other hand, combination with LH waves can be quite efficient in minimizing the negative impact of electron trapping.

2. Poloidal and power dependence of the current drive efficiency. The bounce-averaged quasilinear/Fokker-Planck equation which governs the time evolution of the electron distribution function f in momentum space is discussed elsewhere [3,4]. The basic features of the interaction between electrons and EC waves in toroidal geometry are contained in the resonance condition

$$\gamma - \frac{\omega_c(\chi)}{\omega} - \frac{N_{||} u_{||0}}{\mu^{1/2}} \left[1 - \frac{u_{\perp 0}^2}{u_{||0}^2} \left(\frac{B(\chi)}{B(0)} - 1 \right) \right]^{1/2} = 0 \, . \qquad (1)$$

where $\gamma = (1+u^2/\mu)^{1/2}$, $\vec{u}$ is the electron momentum normalized to $(mT_e)^{1/2}$, $\mu = mc^2/T_e$; m, T_e are the electron mass and temperature, respectively, c is the speed of light, $N_{||}$ is the parallel refractive index, B is the tokamak magnetic field, χ is the poloidal angle corresponding to the location of wave absorption, and $u_{||0}$, $u_{\perp 0}$ are, respectively, the parallel and perpendicular components of $\vec{u}$ at the location $\chi = 0$ (equatorial plane, at the low-field side). Equation (1) states that for given values of ω_c/ω and $N_{||}$ the wave is resonant with particles having a larger (smaller) value of $u_{||0}$ ($u_{\perp 0}$) as χ moves from 0 to π (low-field side to high-field side). Therefore, the current drive efficiency (which is proportional to $u_{||}^2$) should increase when the resonance moves to the high-field side [2]. Moreover, the spread $\Delta N_{||}$ of the wave beam in $N_{||}$ determines a spread of the resonance in momentum space, via Eq. (1), which yields

$$\Delta u_{||0} \propto \Delta N_{||} / |u_{||0}| \, , \qquad \Delta u_{\perp 0} \propto u_{\perp 0} \Delta N_{||} \, . \qquad (2)$$

Thus, both $\Delta u_{||0}$ and $\Delta u_{\perp 0}$ decrease for χ increasing from 0 to π. As shown in the following, this also affects the current drive efficiency, especially for high wave power.

The following parameters are considered: R=225 cm, a=70 cm, $B=B_0/[1+(r/R)\cos\chi]$, B_0= 4.5 T, $n_e(0)=5\times10^{13}$ cm^{-3}, $T_e(0)$=3 keV, $\omega/2\pi$=100 GHz, ψ = arsin $N_{||}$ = -45°, $\Delta\psi \approx 7°$, where a, R are the tokamak radii, r is a radial coordinate in the poloidal plane, $\Delta\psi$ is the spread of the wave beam in the toroidal direction. For these parameters, an x-wave injected from a top location is completely absorbed in the first transit [5]; the power absorption peaks at r ≈ 30 cm, where $\omega_c/\omega \approx 1.2$, $N_{||} \approx -0.75$ and $\Delta N_{||} \approx 0.09$. These local values are kept constant in the following examples, but χ is varied, in order to investigate the role of toroidal effects in the resonance. Specifically, the cases $\chi = 0, \pi/2$, and π are considered and compared to the results obtained in the homogemeous limit, for wave power P_0 = 1 MW and P_0 = 10 kW, respectively. The electron distribution

function f at steady-state, for P_0 = 1 MW, is shown in Figs. 1, 2; f is represented by the parallel distribution $f_{||}(u_{||0}) = 2\pi \int du_{\perp 0} u_{\perp 0} f$ and the perpendicular temperature $T_\perp(u_{||0}) = (2\pi T_e/f_{||}) \int du_{\perp 0}(u_{\perp 0}^3/2) f$. Fig. 2 shows that the perpendicular stretching of f is strongly limited by the presence of trapped electrons; moreover, the widths of the deformations in $T_\perp$ reflect the poloidal dependence of the resonance width [Eq. (2)]. Consequently, the parallel deformations of f are also affected (Fig. 1), as well as the current drive efficiency. The latter is defined as $\eta = J/(2\pi RP)$ (where J is the current density and P the absorbed wave power density); it is shown for low and high wave power in table I. It results that: i) η is weakly power-dependent in the homogeneous limit, but strongly power-dependent in toroidal geometry; ii) the poloidal dependence of η follows that of $u_{||0}$ for low wave power (i.e., η increases monotonically with χ), but for high wave power it is affected also by the behaviour of $\Delta u_{||0}$, $\Delta u_{\perp 0}$: the inboard location no longer yields the best efficiency. This shows that the physics of the current drive process is governed by the interplay of quasilinear and toroidal effects, hence, even qualitative conclusions drawn from the linear and homogeneous-field theories may be questionable. However, the efficiencies presented in table I for the high wave power case are very low, which shows that moving the poloidal location of wave absorption is rather ineffective for current drive optimization.

3. Combining EC and LH waves. Current drive by EC waves at downshifted frequency can be much more efficient in the presence of LH waves, as demonstrated in Ref. 5, in the limit of a homogeneous magnetic field configuration. In toroidal geometry, this point needs reconsideration, and it is now investigated by adding to the quasilinear/Fokker-Planck equation a bounce-averaged term describing the parallel diffusion due to LH waves [5]. The case $\chi = \pi/2$ of Sec. 2 is considered, for P_0 = 1 MW, but in the presence of a flat parallel tail in the range $3.6 \lesssim u_{||0} \lesssim 7$. Note that the resonant $u_{||0}$ for the x-wave packet at r = 30 cm is close to the lower end of this tail. The resulting distribution function is shown in Figs. 3,4, without (dashed line) and with (solid line) EC waves. Although the EC wave power is transferred to low-energy electrons ($u_{||0} \approx$ 3.5), the population of the whole tail is enhanced, because of the parallel diffusion due to the LH waves (Fig. 1). Since the high-energy part of the tail is not populated by a direct interaction with the EC waves, but via this cross effect [5] only, its perpendicular energy does not increase significantly (Fig. 2), hence the negative effects of electron trapping are minimized. Because of these two beneficial effects, the efficiency of the additional current driven by the EC waves is much larger than in the absence of LH waves, i.e., η = 75.2 A/kW, instead of 10.8 A/kW. This proves the effectiveness of combining parallel to perpendicular diffusion in order to minimize the deleterious effects of electron trapping on the efficiency of current drive by EC waves.

Aknowledgements. Useful discussions with Prof. F. Engelmann are gratefully aknowledged. This work was performed under the Euratom-FOM association agreement, with financial support from ZWO and Euratom.

REFERENCES

[1] FISCH, N.J., BOOZER, A.H., Phys. Rev. Lett. **45** (1980) 720.

[2] CHAN, V.S., et al., Nucl. Fusion **22** (1982) 787; START, D.F.H., et al., Plasma Phys. **25** (1983) 447; COHEN, R.H., Phys. Fluids **30** (1987) 2442; GIRUZZI, G., Nucl. Fusion **27** (1987) 1934.

[3] KERBEL, G.D., Mc COY, M.G., Phys. Fluids **28** (1985) 3629; O'BRIEN, M.R., et al., Nucl. Fusion **26** (1986) 1625; YOSHIOKA, K., ANTONSEN, T.M., Nucl. Fusion **26** (1986) 839.

[4] GIRUZZI, G., Phys. Fluids, to be published (Euratom-FOM Report 87/049).

[5] FIDONE, I., et al., Nucl. Fusion **27** (1987) 579.

Table I : η (A/kW)

P_0 (MW)	homogeneous	$\chi = 0$	$\chi = \pi/2$	$\chi = \pi$
10^{-2}	50.3	27.5	33.5	34.5
1	37.9	5.8	10.8	6.3

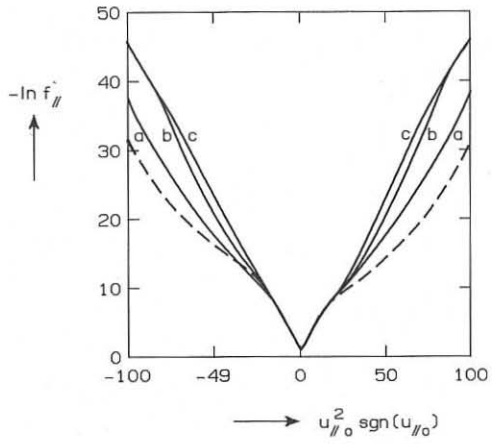

Fig. 1 : $-ln(f_{||})$ vs $u^2_{||0}sign(u_{||0})$, for the homogeneous (dashed line) and the toroidal case (solid lines). $P_0 = 1$ MW.
a) $\chi = 0$
b) $\chi = \pi/2$
c) $\chi = \pi$.

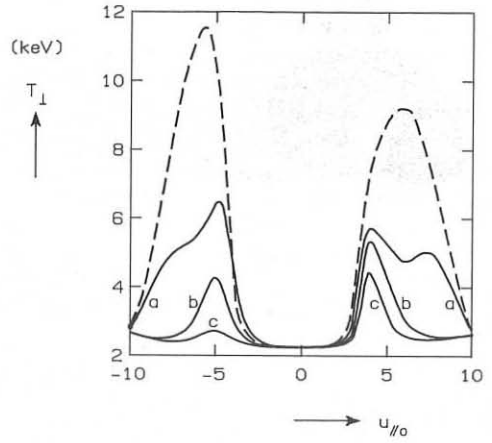

Fig. 2 : Perpendicular temperature in keV vs $u_{||0}$, for the homogeneous (dashed line) and the toroidal case (solid lines). $P_0 = 1$ MW.
a) $\chi = 0$
b) $\chi = \pi/2$
c) $\chi = \pi$.

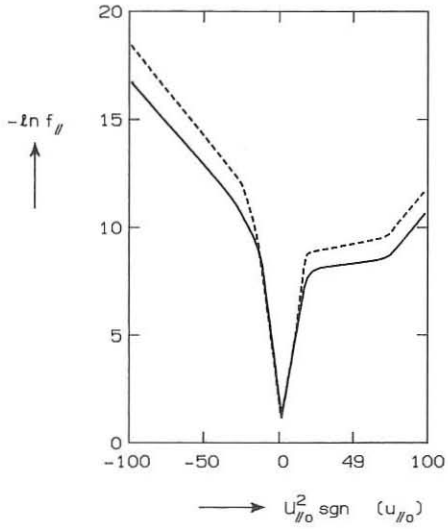

Fig.3 : $-ln(f_{||})$ vs $u^2_{||0}sign(u_{||0})$, with LH waves alone (dashed line) and with the addition of EC waves, for P_0 = 1 MW (solid line). $\chi = \pi/2$.

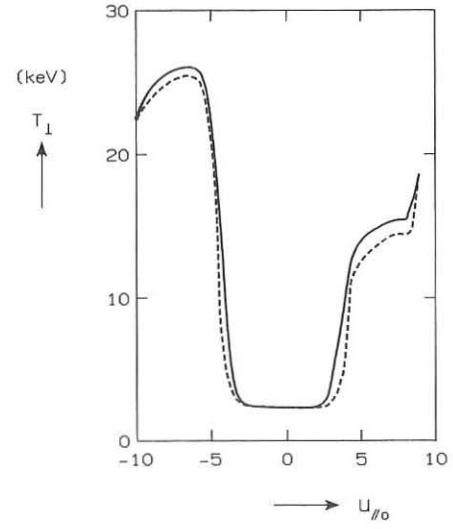

Fig.4 : Perpendicular temperature in keV vs $u_{||0}$, with LH waves alone (dashed line) and with the addition of EC waves, for P_0 = 1 MW (solid line). $\chi = \pi/2$.

PROPAGATION, ABSORPTION AND CURRENT GENERATION BY EC WAVES IN THE LH CURRENT DRIVE REGIME

D. Farina, S. Finardi

Istituto di Fisica del Plasma, CNR
Associazione EURATOM-ENEA-CNR, Milano, Italy

Introduction

The interaction of electron cyclotron (EC) waves with a plasma where the current is driven by lower hybrid (LH) waves has been studied. This problem is of interest when combined injection of the two waves is considered in order to increase the LH current drive (CD) efficiency or to modify the current density profile and control the MHD instabilities. Moreover, it can be useful for the analysis of the emission spectra (ECE) in a LHCD plasma. Previous analyses /1-2/ have been performed in the down shifted resonance scheme, i.e., when the EC wave frequency ω is lower than the classical electron cyclotron frequency $\Omega = eB/mc$, along the EC ray trajectory. In this condition the EC wave is absorbed by the suprathermal electrons of the LH tail, which are the only particles resonating with the wave. In this work the full relativistic dispersion relation has been solved to describe the resonant interaction of electrons belonging to the suprathermal tail and to the thermal bulk. The present analysis allows to investigate the transition between the thermal resonant scheme (when tha classical resonance condition $\omega = \Omega$ is verified inside the plasma) and the up shifted or the down shifted resonance scheme (when $\omega = \Omega$ is verified at the periphery of the plasma or outside).

Outline of the analysis

When the EC injected power is lower than the LH power, it is possible to analyze the interaction of the EC waves with the plasma in the framework of the linear theory. In this case at the steady state, we assume that the unperturbed electron distribution results from the balance between the collisional and the quasi linear diffusion in momentum space due to the LH waves only. Following the 1D analysis

performed by Fisch /3/, the electron distribution function reads:

$$f = C\, f_m(v_\perp)\, \exp - \int_0^{w} dw\; w/(1 + w^3 D(w)/(2 + Z))$$

where $w = v_\parallel / v_t$, f_m is a Maxwellian function and D is the LH quasi linear diffusion coefficient, which is non zero in the LH resonant region $v_1 < v_\parallel < v_2$. In the limit of large diffusion this function turns to be constant with respect to the parallel component of the velocity in the resonant region and Maxwellian outside. This model exhibits the main features of the complete solution except for the value of the perpendicular temperature of the tail (here assumed equal to the bulk temperature).

The relativistic dielectric tensor for the EC waves has been evaluated for the assumed model distribution function. The hermitian part of the dielectric tensor has been reduced to an integral over only one variable in momentum space, while for the anti hermitian part an analytical expression has been given. The full dispersion relation has been solved for frequency around the first cyclotron harmonic. Note that, since the EC wave absorption for the first harmonic is not due to Larmor radius effects (as it happens for higher harmonics), the assumption about the perpendicular temperature of the tail does not affect significantly the results. The computation of the EC driven current is performed following the adjoint method /4/.

Results

The behaviour of the solution N of the dispersion relation shows different features depending on the value of the propagation angle (or of the parallel component of the refractive index $N_\parallel$) and on the following plasma parameters: plasma density and temperature, suprathermal electron density and location and width of the LH resonant region in velocity space (v_1, v_2). Following the experimental results on LHCD /5/, we assume suprathermal plasma densities of order 1% of the plasma density. In case of quasi perpendicular propagation (Fig.1a), the thermal interaction is well separate from the suprathermal, the latter occuring always for $Y = \Omega/\omega > 1$. This effect is still more evident when the EC power is injected into the plasma in the same direction of the LH driven current ($N_\parallel < 0$), the EC wave-plasma interaction taking place for a very large range of magnetic field (or wave frequency) (Fig.1). when the EC wave propagates in the opposite direction of the current ($N_\parallel > 0$), the resonant absorption occurs in the same Ω/ω range of the thermal plasma but with larger values and different profiles. Depending on the plasma parameters and on the value of $N_\parallel$, the plot can show two

maxima (Fig.2), the former for $(1 - N_{\parallel}^2)^{1/2} < Y < 1$, due to the suprathermal electrons, and the latter corresponding to the thermal maximum. The larger values occurs when simultaneous interaction of thermal electrons and highly energetic electrons takes place. This effect is illustrated in Fig.3, where the resonance curve $\gamma = Y + N_{\parallel} v_{\parallel}/c$ is shown for different values of the ratio Y in momentum space together with the level curves of the distribution function. Significant modifications of the real part of the refractive index are also found, affecting the values of the resonance and cut-off frequencies.

The analysis has been applied to the injection of 140 GHz r.f. power into the FTU tokamak. The total absorbed power and the power absorbed by the tail are shown in Fig.3 for both OM and XM, for high field side injection and a magnetic field at the plasma centre $B_o = 6$ T (the classical resonance condition is verified at about half radius). In this condition the EC wave resonates along its trajectory first with the suprathermal electrons and then with the thermal bulk. Referring to the previous observations about Figs.2,3 we note that, in general, the mentioned separation of the absorbed power is meaningful only when $N_{\parallel} \lesssim v_1/c$. Large values of absorbed power has been found; a suitable choice of the injection angles and of the plasma parameters can allow to deposite the r.f. power to the chosen electron population.

References

/1/ I. Fidone et al., Phys. Fluids **27**, 2468 (1984);

/2/ D. Farina et al., Plasma Phys. and Contr. Fusion, in press (1988);

/3/ C. F. F. Karney and N. J. Fisch, Phys. Fluids **22**, 1817 (1979);

/4/ C. F. F. Karney and N. J. Fisch, Phys. Fluids **28**, 116 (1985);

/5/ R. Bartiromo et al., Nucl. Fusion **26**, 1106 (1986).

Figure Captions

Fig.1: Imaginary part of the perpendicular refractive index $N_{\perp}$ for OM and XM vs the ratio $Y = \Omega/\omega$ for $N_{\parallel} = -0.4$, $\omega_p^2/\omega^2 = 0.5$, $T_e = 2$ keV, $v_1/c = 0.2$, $v_2/c = 0.7$. The light curve correspond to a Maxwellian plasma;

Fig.2: Same as in Fig.1 but for $N_{\parallel} = 0.4$;

Fig.3: Level curves of the distribution function and resonance curves for different values of Y; a) $N_{\parallel} = -0.4$, b) $N_{\parallel} = 0.4$;

Fig.4: OM and XM total absorbed power and power absorbed by the tail P_t vs $N_{\parallel}$, for FTU ($B_o = 6$ T, $n_e = 1.2 \times 10^{14}$ cm^{-3}, $T_e = 2$ keV).

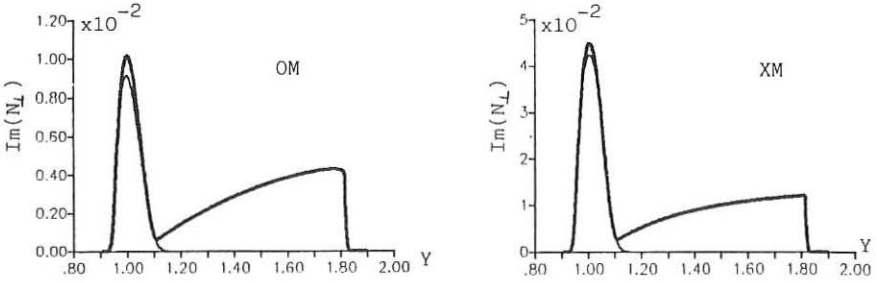

Figure 1

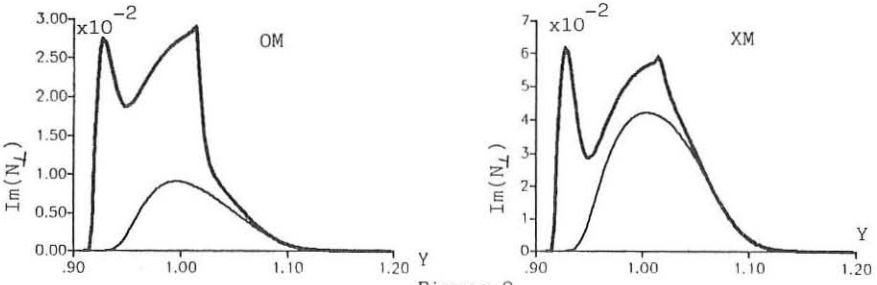

Figure 2

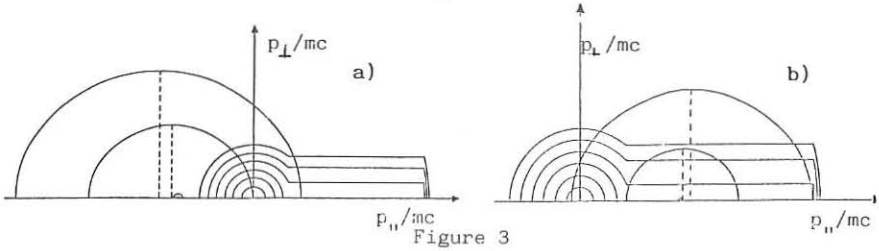

Figure 3

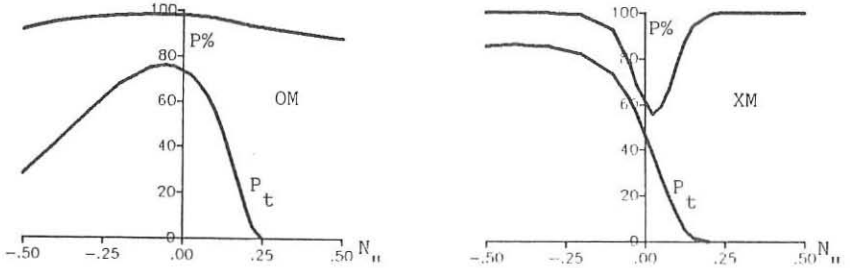

Figure 4

CURRENT DRIVE IN TOKAMAK PLASMAS BY BEATING OF HIGH FREQUENCY WAVES

J.A.Heikkinen, S.J.Karttunen and R.R.E.Salomaa[1]

Technical Research Centre of Finland, Nuclear Engineering Laboratory, P.O.B. 169, SF-00181 Helsinki, Finland

1. INTRODUCTION

Large amplitude longitudinal plasma waves (plasmons) can be excited by beating of two intense electromagnetic (EM) waves whose frequency difference equals to the plasma frequency ω_p. Beat-waves (BW) have several applications like plasma heating, particle acceleration, diagnostics and current drive [1]. The beat-wave current drive offers some advantages over other rf-methods. High frequency EM pump waves ($\omega_{1,0} >> \omega_p, \Omega$, where Ω is the electron gyrofrequency) have good access into the plasma which provides excellent possibilities to localize the generation region and to control the current profile. The phase velocity of the beat-plasmon is close to the speed of light c for collinear pump waves so that very energetic, weakly collisional electrons are generated. The current induced by the fast electrons decays slowly and it can be easily sustained. Furthermore, the beat-wave method does not suffer from density limitations and the entrance aperture requirements are rather modest which make it suitable to compact tokamaks, too.

The main difficulty is that at present there exist no pulsed high power EM-sources at wavelengths 50-200μm, which would be ideal for beat-wave current drive in tokamak plasmas. However, the progress in free electron laser (FEL) technology is rapid which gives hopes that a FEL, meeting the requirements of current drive, can be constructed.

2. PLASMON EXCITATION

We assume a simple geometry where the EM pump waves $\mathbf{E}_1(\mathbf{k}_1, \omega_1)$ and $\mathbf{E}_0(\mathbf{k}_0, \omega_0)$ propagate exactly along the external magnetic field $\mathbf{B}_{ext}$. If the pump frequencies are high ($\omega_{1,0} >> \omega_p, \Omega$), the coupled envelope equations for the electric fields are [2]

$$(\partial_t + c\partial_z)E_m = M(E^* E_{m+1} - E E_{m-1}), \tag{1}$$

$$(\partial_t + \nu_{ei} + i\delta - i\Delta|E|^2)E = (\omega_p/\omega_1)M \sum_m E_m E^*_{m-1}. \tag{2}$$

Eq. (1) describes the behaviour of the EM pump modes (m = 1,0) and their cascading to higher order modes (m = $-1,\pm2,\ldots$), and Eq.(2) determines the plasmon evolution. Eqs. (1)-(2) are well satisfied as long as $|m| << \omega_1/\omega_p$. The coupling coefficient is $M = q_e k/4m_e\omega_1$, where $k=k_1-k_0$ is the wave number of the plasmon and q_e and m_e are the elementary charge and the electron mass, respectively. The nonlinear term $\Delta|E|^2$ [$\Delta = (\sqrt{3}q_e/4m_e c\sqrt{\omega_p})^2$] is the relativistic frequency shift [3], which saturates the growth of the plasmon amplitude E, if the collisional damping ν_{ei} and the linear detuning $\delta = [\omega_p^2 - (\omega_1 - \omega_0)^2]/2(\omega_1 - \omega_0)$ are small. The spatial derivative is neglected in Eq. (1) because the group velocity of the plasmon is low [$v_g = 3(v_e/c)v_e$ where v_e is the electron thermal velocity].

Equations (1)-(2) can be solved analytically in the limit of small linear damping [2], which is the case in the multi-keV tokamak plasma ($\nu_{ei} << \omega_p$). The evolution of the EM-cascade is given in terms of Bessel functions. The plasmon solution is periodic (expressable with elliptic integrals) with a maximum E_{max} and a period t_{per} [2]

$$E_{max} = (16v_1 v_0/3c^2)^{1/3} m_e \omega_p c/q_e , \qquad (3)$$

$$t_{per} = 17.0\times(v_1 v_0/c^2)^{-2/3}\omega_p^{-1} . \qquad (4)$$

$v_{1,0} = q_e|E_{1,0}|/m_e\omega_{1,0}$ are the electron quiver velocities. Behind the EM-pulse a plasmon wake is formed ($v_g << c$), which decays at least as $\exp(-\nu_{ei}t)$. If the collision frequency ν_{ei} is low, the plasmon is absorbed by nonlinear wave-particle interactions. These transfer the wave momentum to very fast electrons ($v_{ph} \approx c$) which is an optimal situation regarding current drive.

The optimum length of the EM-pulse is $t_p = t_{per}/2$ so that E_{max} is just reached by the end of the pump pulse. To obtain plasmon amplitudes high enough, the intensity parameter $I\lambda^2$ (I is the pump intensity and λ is the pump wavelength) must exceed the value $10^{14}\,Wcm^{-2}\mu m^2$. The corresponding pulse length is in the nanosecond range according to (4).

3. CURRENT GENERATION

The local current density can be easily obtained from the momentum conservation between the plasmon and plasma electrons

$$j_{max} = q_e \varepsilon_0 k|E|^2/2m_e\omega_p . \qquad (5)$$

To find the total current, j_{max} must be multiplied by the beam area A and by a volume factor $L/2\pi R$, where L is the length of the plasmon and R is the major radius (see Fig.1). The plasmon length L is determined by the pump depletion [2], i.e.,

$$L = 2m_e c^2(\omega_1/\omega_p)^2/q_e|E| . \qquad (6)$$

In the presence of EM-cascading the depletion length L and energy conversion from the pumps to the beat-plasmon are much larger than in the pure three-wave case where the Manley-Rowe relations predict a very weak conversion for $\omega_1/\omega_p >> 1$. Energy conversion can be further increased by a proper detuning δ so that cascading towards lower frequencies is preferred [4].

At typical tokamak densities the depletion length (6) may vary from several meters to a few centimeters with pump wavelengths 10-300μm. For a given density, the wavelengths of the EM-waves should be chosen such that the depletion length is comparable with R. Then the beat-wave conversion is completed in a single pass. Otherwise the EM pump pulses have to be circulated with complicated mirror systems.

The fast electron current, generated by a single pulse, decays at rate ν_{ee} which is proportional to $n_e \varepsilon^{-3/2}$, where ε is the fast electron energy. To sustain the current, the pulse repetition rate must be of the order of ν_{ee}. This fixes the average pump power $P = W_L \nu_{ee}$, where W_L is the pulse energy of the EM pump. Total power need of the BW current drive is P/η where η is the efficiency of the EM-source (CO_2 laser or FEL).

4. PARAMETER STUDIES AND DISCUSSION

The fast electron energy ε is a key parameter regarding the feasibility of the beat-wave current drive. In principle, a fairly large number of very energetic electrons are produced by the beat-waves due to their high phase velocity and large amplitude. The energy corresponding to the phase velocity is in MeV-range so that an assumption of ε=500keV is reasonable. If it turns out that the fast electron energies remain well below 500keV the power requirements to sustain the current are substantially enhanced.

Some examples of current drive parameters are given in Table. Problems with a CO_2 laser are the enormous power need for MA currents and the long depletion length at $\lambda = 10\mu$m. Situation is better at longer wavelengths. For $\lambda \geq 200\mu$m, however, the current density remains fairly low, which leads to large beam diameters, if several MA currents are aimed at. Thus the useful wavelength range lies around 100μm.

The feasibility of the beat-wave current drive improves considerably, if bootstrap amplification of the current occurs. The amplification of a seed current may be as high as 10-20 [5]. Thus, beat-wave driven seed currents of a few hundred kA would suffice. The power need in the FEL case is reduced to few MW, and in the CO_2 case to 20-50 MW. The beat-wave method applies well to the bootstrap seeding, because the beat current can be driven locally and its magnitude and diameter are easily varied to optimize the bootstrap amplification.

Plasma density [10^{14} cm^{-3}]	10	1.0	1.0
Toroidal field [T]	10	5	5
Major radius [m]	2	5	5
Pump wavelength λ_1 [μm]	10.0	200	100
Pump wavelength λ_0 [μm]	10.1	213	103
Pump intensity [10^{10} W/cm^2]	100	1.0	4.0
Pulse length [ns]	2.7	2.9	3.1
Depletion length [m]	51	2.3	9.8
Plasmon field [MV/m]	224	122	116
Total current density [kA/cm^2]	53	0.29	1.1
$J_{tot}Rn_e/P$ [10^{13} Am/cm^{3}W]	4.6	5.8	5.0

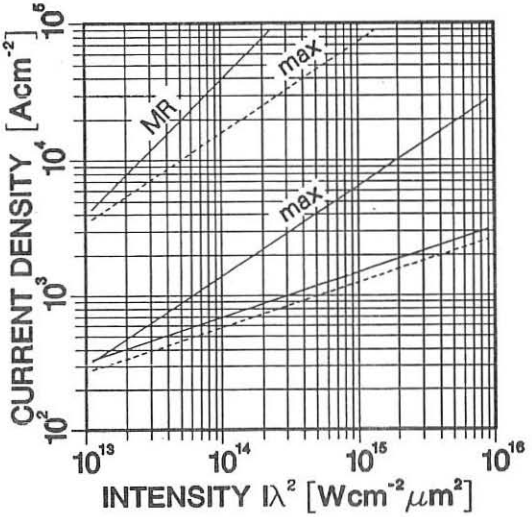

Fig.1 Current densities with 100μm FEL; Parameters B_{ext}, R and n_e are 5T, 5m, 10^{14} cm^{-3} (solid); 10T, 2m, 10^{15} cm^{-3} (dashed). Upper (max) curves are the local values, Eq.(5), and lower curves give the total current densities. Small corrections due to magnetic field B_{ext} are included.

[1] B.I.Cohen, Comments Plasma Phys.Contr.Fusion 8,197(1984)
[2] S.J.Karttunen & R.R.E.Salomaa, Phys.Rev.Lett.56,604(1986) and IEEE Trans.Plasma Sci. PS-15,134(1987).
[3] M.N.Rosenbluth & C.S.Liu, Phys.Rev.Lett.29,701(1972).
[4] B.I.Cohen et al., Phys.Rev.Lett.29,581(1972).
[5] R.J.Bickerton et al., Nature Phys.Sci.229,110(1971).

1) Helsinki University of Technology, SF-02150 Espoo, Finland

Effect of Electron Spatial Diffusion on Current Drive

Y.Kishimoto, T.Takizuka, M.Yamagiwa, S.I.Itoh†, and K.Itoh††

Japan Atomic Energy Research Institute, Naka Fusion Research Establishment, Naka, Ibaraki 311-01

† Institute for Fusion Theory, Hiroshima University, Hiroshima 730

†† Plasma Physics Labolatory, Kyoto University, Uji, Kyoto 611, Japan

Introduction

Recently, RF current-drive is considered to be a method to controll the radial shape of the plasma current density. In that case, the radiation spectrum of the RF wave is one of the controllable parameters in the experiment. However, the spatial profile of the driven current and the current-drive efficiency are affected by the diffusion of electrons not only in the velocity space but also in the real space. The local analysis shows that the spatial loss of the tail electrons reduces the current-drive efficiency owing to the suppression of the tail generation [Ref.1,2].

In this papaer, we extend the local analysis to the nonlocal one which describes the spatial diffusion of the RF-induced tail electrons in the radial direction. The radial profile of the driven current and the power partitions are obtained by solving a Fokker-Planck equation which includes the one spatial dimension.

Basic Equation

We solve the electron Fokker-Planck equation which takes account of the spatial diffusion of fast electrons,

$$\frac{\partial f}{\partial t} = \nu_e(x)\frac{\partial}{\partial v_z}\left[\hat{D}_C\left(\frac{v_z}{v_e}\right)\left\{\frac{\partial f}{\partial v_z}v_e^2 + v_z f\right\}\right] + \frac{\partial}{\partial v_z}D_W\frac{\partial f}{\partial v_z} + L(f,v_z,x) + S(v_z,x) \quad (1)$$

where $\nu_e(x)=n_e(x)e^4\ln\Lambda/2\pi\varepsilon_0^2m^{1/2}T_e(x)^{3/2}$ the local electron collision frequency, $v_e(x)=\sqrt{T_e(x)/m}$ the local electron thermal velocity, D_C the collisional diffusion coefficient [Ref.3], D_W the RF diffusion coefficient. $L(f)$ expresses the spatial diffusion of electron and $S(v_z,x)$ is the particle source term which is determined so as to conserve the local plasma density.

As for the mechanism of the spatial diffusion, we adopt the stochastic magnetic field fluctuation model given by $L(f)=(\partial/\partial x)v_z D_s(\partial f/\partial x)$ in the slab geometry. Here, D_s is the spatial diffusion coefficient expressed by $D_s \sim \pi R_{eff}\langle\tilde{b}^2\rangle$, where $R_{eff} \sim \pi R_0$ (R_0 : major radius) is the auto-correlation length of the magnetic field and $\tilde{b}=\tilde{B}/B_0$ is the amplitude of the magnetic perturbation. The density and the temperature profiles in the collision operator are chosen as $n_e(x)=(n_{e0}-\hat{n}_e)(1-x^2/a^2)+\hat{n}_e$ and $T_e(x)=(T_{e0}-\hat{T}_e)\exp(-3x^2/a^2)+\hat{T}_e$, where $\hat{n}_e$ and $\hat{T}_e$ are the density and temperature at the plasma surface and a is the minor radius.

Equation (1) is solved in (x,v_z)-plain for $-a\leq x\leq a$ with the boundary condition, $f(x=\pm a,v_z)=f_M(x=\pm a,v_z)$, which simulates the particle and momentum sink at the plasma surface. Here, f_M is the local Maxwellian distribution.

Numerical Results and Discussions

In the following calculation, we introduce the diffusion coefficient normalized by the central quantities, i.e. $\hat{D}_w=D_w/v_{e0}^2\nu_{e0}$ and $\hat{D}_s=D_s/a^2\nu_{e0}$. We also choose the edge values as $\hat{n}_e=0.1n_{e0}$ and $\hat{T}_e=0.1T_{e0}$.

Figures 1(a) and (b) illustrate the logarithmic contour plots of the electron distribution function $f(x,u=v_z/v_e)$ in the phase space at the steady state for (a) $\hat{D}_s=10^{-6}$($\tilde{b}=1.4\times10^{-5}$) and (b) $\hat{D}_s=10^{-4}$($\tilde{b}=1.4\times10^{-4}$). The magnetic fluctuation $\tilde{b}$ is estimated by using the JFT-2M machine size with T_{e0}=1keV. In these calculation, $\hat{D}_w=0.4$ is chosen for $3\leq u\leq 8$ ($D_w=0$ for otherwise) and $\hat{D}_w$ and $\hat{D}_s$ are taken to be spatially uniform. It is found in Fig.1(b) that the tail electrons are transported towards the plasma boundary and hence the population of the tail component increases.

The spatial profile of the power partition is shown in Figs.2(a) and (b) corresponding to Fig.1 (P_w : power absorbed from the RF wave, P_c : power transfered by the collisional process, P_L : power transfered by the spatial diffusion, P_s : power supplied by the particle source term). In the case of small $\hat{D}_s$, the relation $P_w \sim -P_c$ is obtained in the steady state as seen in Fig.2(a). With an increase of $\hat{D}_s$, the absorbed power is partially removed from the central region (i.e. P_L becomes negative for $0 \lesssim x/a \lesssim 0.3$). This power is transfered to the off-center region (i.e. P_L becomes positive for $0.3 \lesssim x/a \lesssim 1.0$) through the spatial diffusion and deposited to the bulk

plasma through the collisional power transfer where the relation $P_L \sim -P_c$ is satisfied. Thus the nonlocal power deposition is observed during the current-drive.

The current profiles are shown in Figs.3(a) and (b) corresponding to Fig.1. The broadening of the current profile is seen in Fig.3(b) with an increase of $\hat{D}_s$ although the total current and the global current-drive efficiency do not change so much ($\overline{J}/\overline{P}_w = \int J(x)dx / \int P_w(x)dx$ = 0.97A.m/W for $\hat{D}_s=10^{-6}$(Fig.3(a)) and $\overline{J}/\overline{P}_w$= 0.10A.m/W for $\hat{D}_s=10^{-4}$(Fig.3(b))).

Figure 4 shows the dependence of the global current-drive efficiency $\overline{J}/\overline{P}_w$ on the spatial diffusion coefficient $\hat{D}_s$ for the different values of $\hat{D}_w$. It is found that the global efficieny remains almost constant value up to around the critical value $\hat{D}_s = 2\times10^{-4}$ although the current profile becomes broader. Exceeding this critical value, the global efficiency rapidly decreases because the tail component of the distribution escapes from the plasma boundary. This effect of the spatial diffusion strongly depends on the machine size through the dependence od $\hat{D}_s \propto a^{-2}$ for the given magnetic fluctuation level.

Acknowledgements

The authors would like to thank Drs. A.Fukuyama of Okayama University and T.Yamamoto of Japan Atomic Energy Research Institute for valuable discussions and comments.

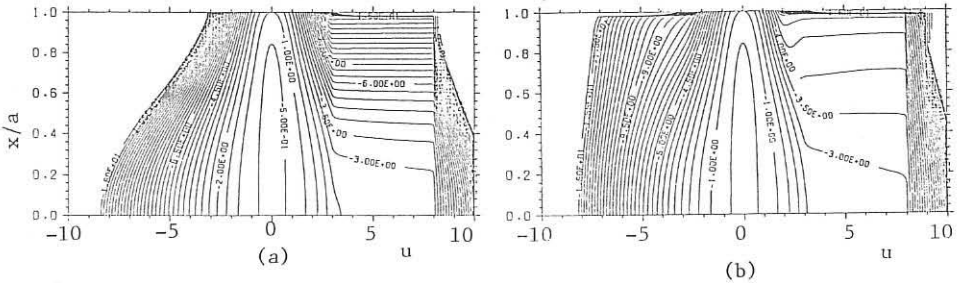

Fig.1 Logarithmic contour plots of electron distribution in the phase space at the steady state for (a) $\hat{D}_s=10^{-6}$ and (b) $\hat{D}_s=10^{-4}$ cases.

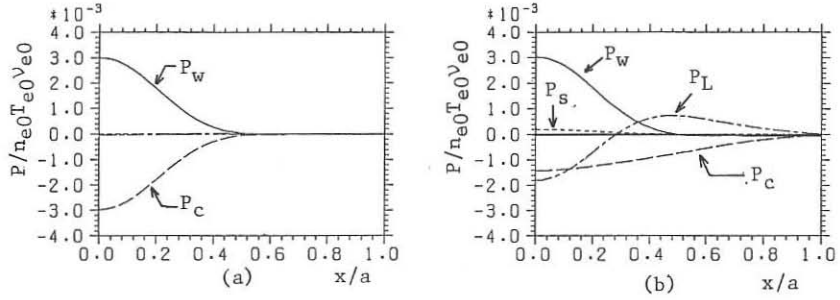

Fig.2 Spatial structure of power density for (a) $\hat{D}_s=10^{-6}$ and (b) $\hat{D}_s=10^{-4}$.

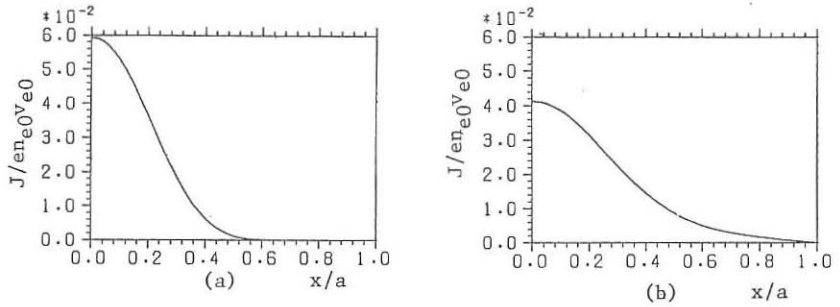

Fig.3 Spatial structure of driven current for (a) $\hat{D}_s=10^{-6}$ and (b) $\hat{D}_s=10^{-4}$.

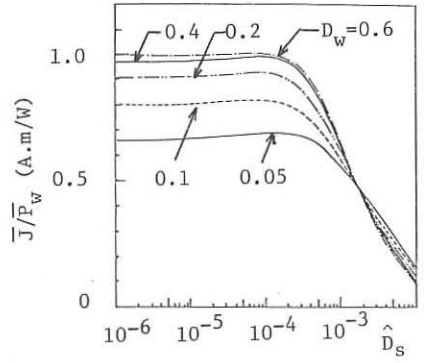

Fig.4 Dependence of global current-drive efficiency $\overline{J}/\overline{P}_w$ on $\hat{D}_s$ for various values of $\hat{D}_w$.

References

[1] S.I.Itoh and K.Itoh, in 11th international Conference on Plasma Physics and Controlled Nuclear Fusion Research (IAEA, Kyoto, 1986), paper IAEA-CN-47/E-111-5.

[2] S.C.Luckhardt, Nucl. Fusion, 27 1914(1987).

[3] Y.Kishimoto, K.Hamamatsu, A.Fukuyama, S.I.Itoh and K.Itoh, Nucl. Fusion, 27, 549(1987).

COMPUTATION OF SELF-CONSISTENT 2-D MHD WITH NEUTRAL-BEAM AND BOOTSTRAP CURRENTS IN ELONGATED PLASMAS*

R. S. Devoto
Lawrence Livermore National Laboratory, P.O. Box 5511,
Livermore, CA 94550 USA

K. Tani, M. Azumi
Japan Atomic Energy Research Institute, Naka-machi, Naka-gun,
Ibaraki-ken JAPAN

INTRODUCTION

The observation of substantial current drive from neutral beam injection (NBI) in TFTR, JET and DIII-D has led to renewed interest in a steady state, non-inductively driven tokamak. The discovery of apparently considerable neoclassical (bootstrap) current in TFTR [1], makes a steady state device even more attractive since the bootstrap portion of the current could be obtained without additional power input. Motivated by these results, we have developed a code, ACCOME, which self-consistently computes the 2-D MHD equilibrium with the current driven by neutral beams, bootstrap and the electric field. In this paper we first describe some details of the code in the next section and in the subsequent section show some applications to DIII-D and to a possible ITER design.

DESCRIPTION OF CALCULATION PROCEDURE

In order to obtain an MHD solution which is consistent with the driven current, we must solve the Grad-Shavranov equation simultaneously with the solution for the beam deposition of fast ions and the bootstrap current. A direct simultaneous solution is impractical, however, since the deposition of the neutral beam can only be computed for a known density distribution which depends on the contours of poloidal flux. We thus choose to use an iterative procedure. From the geometric properties of the desired solution, i.e., plasma elongation, κ, triangularity, δ, major radius, R_o, minor radius, a, and plasma current, I_p, we set up a Solov'ev model equilibrium. We assume thermal density and temperature profiles of the form n, T α $(1 - \psi)^{\alpha_j}$ where the exponent α_j may be different for temperature and density. The deposition of the neutral beam on these flux surfaces and the fast ion distribution function is computed as fully described in Ref. 2. Neutral beams of elliptical cross section are assumed; deposition is computed with a Monte Carlo technique. The fast ion distribution function is found with the aid of the bounce-average eigenfunction analysis of Cordey [3]. The eigenfunctions are obtained numerically, in contrast to Cordey [3], who obtained an approximate analytic solution. The solution is corrected for energy diffusion of fast ions to speeds above the injection speed with the method of Gaffey [4]. The fast-ion current is obtained from the usual moment of the distribution function. In addition, we compute the pressure

*Work performed under the auspices of the U.S. Departmernt of Energy by Lawrence Livermore National Laboratory under Contract W-7405-ENG-48.

due to the fast ions and, in the case of a D-T plasma, the pressure from the fast alpha particles. The partial cancelling current of the neo-classical electrons is found on each flux surface from the results of Start and Cordey [5].

The neoclassical bootstrap current is computed from the banana-plateau expressions of Hinton and Hazeltine [6]. The multi-ion plasma is replaced with a single ion of charge Z_{eff}.

The above computations yield the flux-surface averaged current, $\langle j_{||} B\rangle/B_o$, on each flux surface, where B_o is the reference toroidal field at the geometric major radius. The pressure function $p(\psi)$ is also known. Note that we assume isotropic pressures even though the fast-ion pressure is clearly anisotropic. From these quantities and the old values of $f = R B_t$ and $\langle B^2\rangle$ we can compute new values of the function $ff' = -\mu_o (f^2 p' + f \langle j_{||} B\rangle) / \langle B^2\rangle$ and use it to solve the Grad-Shavranov equation, $\Delta^*\psi = R^2\nabla(R^{-2}\nabla\psi) = -\mu_o R^2 p' - ff'$.

A free boundary solution with appropriately placed poloidal coils is obtained with the SELENE code described in [7]. Following this step, we iterate through the computation of the currents and then the MHD until the solution has converged. Typically 5-10 iterations are necessary to obtain converged current profiles.

APPLICATIONS

We have applied this code to current drive by NBI in DIII-D [8]. The experiments were carried out with 70 keV H beams injected into an He plasma. Beams with two different aimings were used-one at 63° to the centerline of the plasma and one at 46° to the centerline. 340 kA of driven current was sustained with a total injection power of 11 MW. We have simulated this experiment with the ACCOME code using densities and temperatures deemed representative of the plasma: $T_{eo} = T_{io} = 2$ keV, $n_{eo} = 2.5 \times 10^{19}$ m^{-3}, and $Z_{eff} = 5$. The density profile was taken as fairly flat with $\alpha_n = 0.5$ and the temperature more peaked with $\alpha_T = 1.0$. Z_{eff} was assumed flat over the cross section. The power fraction of the beams in full, 1/2- and 1/3-energy components was taken as 0.53, 0.30, and 0.17, respectively. The power was split evenly between the two beam aimings.

The calculations were carried out in a mode which fixes the total plasma current at 340 kA, computes the beam-driven and bootstrap current and then adjusts the electric field to obtain sufficient additional Ohmic current to reach the desired total current. Neoclassical resistivity is assumed. The computed total current components were NB: 240 kA, BS: 51 kA and OH: 47 kA. It is probable that there is also a residual Ohmic component in the experiment since the L/R time is somewhat longer than the experimental duration.

As a second application, we considered current drive by neutral beams and bootstrap in a projected ITER design. Parameters for this design as well as some output from the current-drive calculations are collected in Table I.

Table I. Parameters for a projected ITER design.

R_o, m	4.0	a, m	1.4
κ	2.3	δ	0.25
B_o, T	5.0	I_p, MA	14
E_{beam}, MeV	1.5,1.5,0.8	R_{tan}, m	4.2, 4.6, 4.9
P_{beam}, MW	15, 21, 8	I_{bs}/I_p	0.40
$\langle n_e \rangle$, $10^{20} m^{-3}$	0.7	$\langle T_e \rangle$, keV	17
α_n	1.0	α_T	0.5
Z_{eff}	1.5	β_{pth}	0.55

As indicated in Table I, three NB injectors with different tangency radii were used. The beam footprint had a total height of 1.4 m and a total width of 0.6 m. The inner two beams had an energy of 1.5 MeV in order to obtain sufficient penetration to the plasma core. The required energy is determined by including the effect of multi-step ionization [9] on the stopping cross sections. This process is predicted to enhance the cross section by a factor of about 1.6 over the cross section for ionization of ground state atoms in the energy range around 1.5 MeV.

For these calculations, the total plasma current is fixed, and the code adjusts the NB power to obtain this current. This adjustment is done dynamically during the iterations, since the bootstrap current will vary as the NB current changes. A plot of the toroidal current density in the z = 0 plane is shown in Fig. 1. We see some structure from the three beams. A final plot in Fig. 2 shows the safety factor, q_ψ, vs. $\bar{\psi}$. We see that q_ψ remains above unity over the plasma cross section and rises to a value above 3 near the edge. For this case, the current drive figure of merit, $\eta = \langle n_{e20} \rangle I R_o / P$ for the neutral-beam-driven current alone is 0.58 A / W-m^2. Including the extra current from bootstrap effects raises the figure of merit to 0.96.

REFERENCES

1. M. C. Zarnstorff, et al., Phys. Rev. Lett. (to be published).
2. K. Tani, M. Suzuki, S. Yamamoto, J. Azumi, "On the Analysis of Beam Driven Current in a Tokamak," JAERI-M 88-042 (1988).
3. J. G. Cordey, Nuc. Fusion 16, 499 (1976).
4. J. D. Gaffey, J. Plasma Phys. 16, 499 (1976).
5. D. F. H. Start, J. G. Cordey, Phys. Fluids 23, 1477 (1980).
6. F. L. Hinton, R. D. Hazeltine, Rev. Mod. Phys. 48, 239 (1976).

7. M. Azumi, G. Kurita, Proc. 4th Int. Symp. Computing Methods in App. Science and Engineering (Paris, 1979) 335.
8. T. Simonen, et al., "DIII-D Neutral Beam Current Drive Studies," Bulletin APS 32, 1900 (1987); M. Matsuoka, private communication (1987).
9. C. D. Boley, R. K. Janev, D. E. Post, Phys. Rev. Lett. 52, 534 (1984); A. S. Schlachter, private communication (1988).

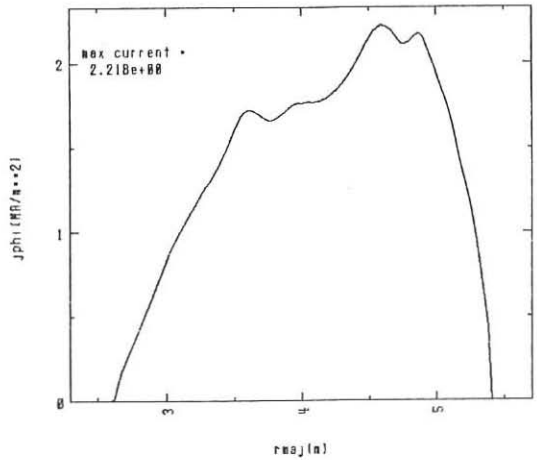

Figure 1. Toroidal current density (MA/m²) vs. major radius (m).

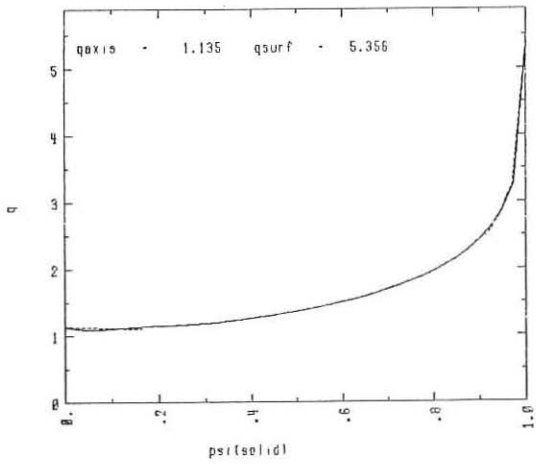

Figure 2. Safety factor q_ψ vs. $\bar{\psi}$.

Neutral Beam Injection Heating

G

PROFILES OF TOROIDAL PLASMA ROTATION

N C Hawkes[1], M von Hellermann, A Boileau[2], L Horton[3], E Källne[4], N J Peacock[1], J Ramette[5], and D Stork.

JET Joint Undertaking, Abingdon, Oxon, UK. [1] Culham Laboratory, Abingdon, Oxon, UK. [2] NRS-ENERGIE, CP1020, Varennes, Quebec, Canada J0l 2P0. [3] Fusion Energy Division, ORNL, Oak Ridge, Tennessee, USA. [4] Royal Institute of Technology, S10044 Stockholm, Sweden. [5] CEA Saclay, France.

INTRODUCTION

Strong toroidal rotation ($\omega_\phi \leq 10^5$ rads sec^{-1}) in Neutral Beam Heated (NBH) discharges in JET has been previously reported [1]. Recently the multi-chordal visible charge exchange recombination spectroscopy (CXRS) diagnostic has produced radial profiles of the toroidal velocities of dominant light impurities (carbon and oxygen). These are compared with X-ray spectroscopy and an estimate of plasma viscosity obtained.

INSTRUMENTATION

The spectroscopic sight-lines which will eventually be applicable to rotation measurements on JET are shown schematically in figure 1. An X-ray crystal spectrometer [2] viewed radiation from a NiXXVII resonance line, determining the central (major radius ~ 2.7-3.5 m) toroidal angular velocity via Doppler shift determination. The CXRS diagnostic [3] measures the Doppler shifted light from excited C^{6+} and O^{8+} ions resulting from charge-exchange collisions of the Neutral Beams with the fully-stripped impurity ions in the plasma. This diagnostic has 8 lines of sight across the plasma giving a toroidal rotation profile at points defined by the intersection of the chords and the neutral beams. In addition an XUV diagnostic [4] was occasionally used to make measurements on the lower ionisation states of nickel.

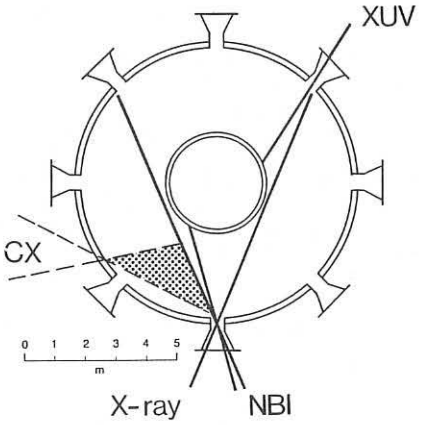

Fig.1: Schematic showing instruments on JET. NBI denotes the two banks of neutral beams, CX the 8 lines-of-sight of the charge exchange diagnostic, X-ray and XUV denote the sight lines of these two spectrometers.

RESULTS

Figure 2 shows an example of the time history of the rotation velocities derived from Doppler-shift measurements on the rotating C^{6+}* ions at different major radii. The discharge shown is one in which the H-mode was achieved during NBH in a single-null X-point discharge and the start of the H-mode is indicated by the drop in the edge H_α recycling. The rotation profile shapes show little change in time indicating that the velocity profile is established across the whole plasma radius rapidly (< 500 ms) after the start of injection. This is a similar timescale to the acceleration of the plasma to equilibrium speed.

The contrast to the plasma behaviour observed with ICRF heating is shown in figure 3. The CXRS diagnostic is not available when NBH is not applied to the discharge but rotation of the nickel lines measured by the X-ray and XUV diagnostics is shown. It is not possible to determine the unshifted (stationary plasma) position of any line with sufficient provision to ascribe absolute rotation velocities to the shifts observed. Previous measurements of rotating MHD modes on JET [1] and their correlation with the central NiXXVII Doppler-shift have shown that Ohmic plasmas prior to NBH are normally rotating slowly (~ 0.6 - 0.8 10^4 rads sec^{-1}) in the direction counter to the plasma current. ICRF can be seen to increase the counter rotation. This is consistent with previous observations [1] that ICRF slows down the NBH-induced plasma rotation during combined heating discharges.

Figure 4(a) shows an example from a shot similar to that of figure 2, of a rotation profile time history obtained from the CXRS diagnostic. The central measurement of rotation from the NiXXVII line agrees within errors with that of the CXRS for the near-axis rotation. The data in figure 4(b) show how the rotational profile develops through the period of the 'monster sawtooth' (figure 4(c)) developed in a JET H-mode discharge. A sawtoothing action of the central rotational velocity is evident which is similar to previous observations on the NiXXVII line [1] in L-mode discharges. The rotational profile appears to broaden during the JET H-mode. If a parabolic function is fitted through these rotational profiles a γ_ϕ value from 1 to 2 is normally obtained although the function is not a particularly good fit. At present the position of peak rotation appears to be shifted by ~ 10-15 cm with respect to the electron temperature maximum determined by the JET LIDAR Thompson scattering diagnostic [5]. The origin of the shift is under investigation but does not affect relative profile shapes.

VISCOSITY

A calculation has been made of the viscosity profile using the CXRS data and assuming that the momentum loss is governed by a diffusion type equation

$$\frac{\delta p}{\delta t} = - \text{div}\ \Gamma_p + S(r) = 0 \text{ (steady state)} \qquad (1)$$

with $$\Gamma_p = - \chi\ \text{grad}\ p \qquad (2)$$

where $p(r)$ = $mv(r)$ is the plasma momentum
χ = diffusivity of momentum (viscosity)
$S(r)$ = field line averaged momentum source rate from the beams

For simplicity linear momentum in the outer semi-minor radius (not affected by the sawtooth) is considered and the rotational velocity of all ion species is assumed equal. This is valid to within a few per cent at the electron temperatures under consideration. $S(r)$ is available for JET from a neutral particle deposition code PENCIL [6], which also calculated the number of fast ions in trapped orbits and hence not contributing to the force balance. In solving (1) and (2) the momentum and source profiles have been approximated by low order polynomials. The calculated viscosity profile ($\chi(r)$) is shown in figure 5. Also shown as a sensitivity analysis is the difference which a shift of ~ 10-15 cm in the velocity profile would bring to the $\chi(r)$ calculation. $\chi(r)$ decreases monotonically with radius due to the momentum deposition profile being peaked near the axis and a near linear fall of momentum with minor radius. The viscosity derived is comparable to the diffusion coefficient of 1 m^{-2} s^{-1} assumed for impurities on JET. A global momentum time of ~ 0.66 secs is derived from integration of the stored momentum. This compares with an energy confinement time in this H-mode ~ 0.9 secs.

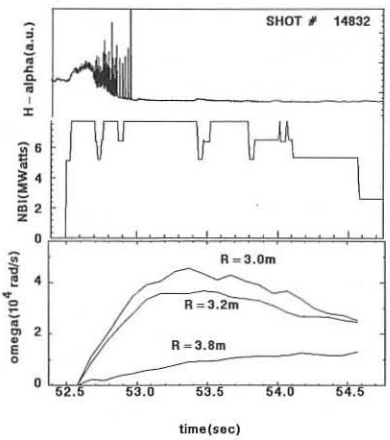

Fig.2: Time histories of the rotational velocities at 3 different radii in response to NB heating at the start of an H-mode discharge.

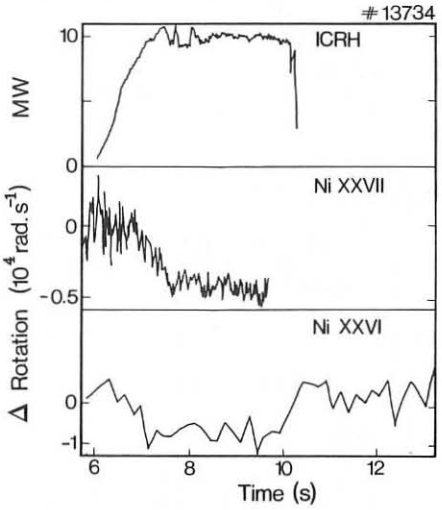

Fig.3: Rotation seen with the X-ray (NiXXVII) and XUV (NiXXVI) instruments during RF heating.

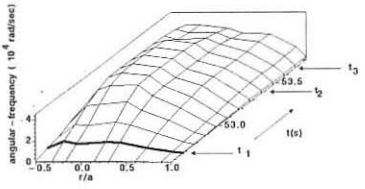

(a)

Fig.4: Rotational profile time development (a),(b) during an H-mode discharge showing the effect of the monster sawtooth as seen by the electron temperature diagnostic (c).

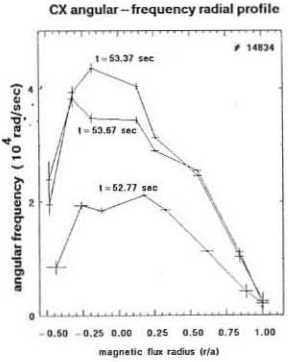

(b)

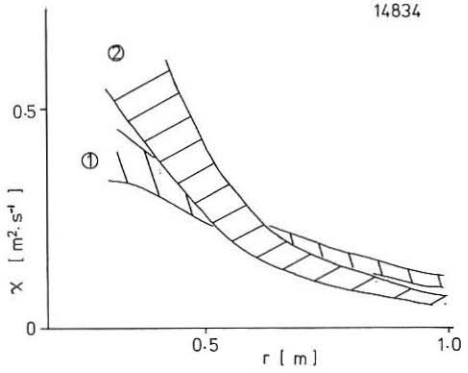

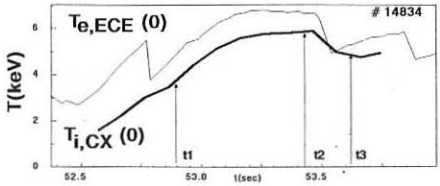

Fig.5: Derived viscosity profile at 2 times within an H-mode period (1) at the sawtooth peak (2) at the sawtooth crash. Hatched areas indicate the effect of the ± 8 cm error in radial measurement from the CXRS diagnostic.

CONCLUSIONS

Rotation profiles of light elements from the CXRS diagnostic can now be produced during NBH. Agreement exists between the central values and those obtained from the X-ray lines of nickel. The X-ray and XUV diagnostics are capable of detecting differences in toroidal rotation between ohmic and ICRF heating phases.

Using data from the CXRS diagnostic a viscosity profile has been derived.

References

[1] Stork D. et al, 14th Euro. Conf. on Cont. Fus. and Plasma Phys., Madrid (1987). Europhys. Conf. Abstracts 11D,I,306.
[2] Bartiromo R. et al, submitted to Rev Sci Instrum.
[3] Boileau A. et al, JET report JET-P(87)44.
[4] Schwob J.L., Wouters A.W. and Suckewer S., Rev Sci Instrum 59 (1987) 1601.
[5] Gowers C. et al, 14th Euro. Conf. on Cont. Fus. and Plasma Phys., Madrid (1987), ref [1], 1236.
[6] Stubberfield P.M. and Watkins M.L., JET Internal Report DPA(06)/87.

TRANSPORT STUDIES OF HIGH DENSITY OHMICALLY HEATED PLASMAS AND HIGH POWER NEUTRAL BEAM HEATED PLASMAS ON JT-60

T.HIRAYAMA, K. SHIMIZU, H. SHIRAI, M. KIKUCHI,
N. HOSOGANE, H. YOSHIDA and JT-60 Team

Naka Fusion Research Establishment
Japan Atomic Energy Research Institute
Naka-machi, Naka-gun, Ibaraki-ken, Japan

1.Introduction

Particle and energy transport characteristics have been studied in ohmic- and neutral beam-heated plasmas in JT-60, using the one-dimensional transport code SCOOP/LIBRARY[1]. The experiments were carried out in hydrogen plasmas with R_0=3.04m,a=0.8~0.9m,B_t=4.5T,I_p=1.0~2.0MA, and beam heating power of 20MW. Clean plasmas with effective charge number of Z_{eff}=1~2 and flat density profiles were obtained both for ohmic-heated, divertor and limiter discharges. The confinement analysis on those plasmas shows that the gross energy confinement time becomes saturated with ~400ms at the density of $\bar{n}_e$~4×10$^{19}m^{-3}$ and is weakly dependent on the plasma density and the plasma current above this threshold density. The neutral beam heating degrades the energy confinement with heating power as L-mode discharges but the dependence of the confinement time on the plasma density and the plasma current is still weak as the one in ohmic discharges. Numerical simulation studies have been performed based on the drift wave turbulence model [2]. Graphite limiters, armor and divertor plates were installed for high current operation in April and May, 1987. High ion temperatures above 10KeV were obtained hydrogen beam heating of 20MW onto a hydrogen plasma at 1.0~2.0MA,4.5T. The limiter operation and the low density $\bar{n}_e \leqq 1.5\times10^{19}m^{-3}$ (before heating) were required in order to obtain the hot ion mode.

2.Ohmic-Heated Plasmas

Flat density profiles showing $n_e(0)/\langle n_e\rangle$=1.1~1.2 were realized for the electron density grater than 4×10$^{19}m^{-3}$, in diverted plasmas. Although peaked profiles like a parabolic shape were founded in limiter discharges at the low density less than 2×10$^{19}m^{-3}$, the peaked profiles become to be broader as increasing the density and there is no difference in the shape of density profile between both discharges of the limiter and the divertor. The characteristics of the density profiles are satisfactorily simulated with no anomalous inward particle flux. The differences in cold neutral energies i.e. E_0=5eV for divertor discharges and E_0=30eV for limiter discharges, could be responsible for the difference in density profiles at the low density.

The central electron temperature rapidly decreases from ~3KeV to ~2KeV as the density increases to around 2~3×10$^{19}m^{-3}$ and gradually

decreases to 1.0~1.5KeV for $\bar{n}_e \geqq 4\times10^{19}m^{-3}$. These low electron temperatures bring on $Z_{eff}<1$ in the data analysis with employing the trapped electron correction factors [3] to the plasma resistivity (Fig.1). These results strongly suggest that the electrical resistivity has the Spitzer-type dependence and the correction factor should be small. A small power density of joule heating on axis due to the low resistivity as well as low Z_{eff} causes relative low electron temperatures.

The confinement analysis shows that the gross energy confinement time of the ohmically heated plasma becomes saturated with ~400ms at the density of $\bar{n}_e\sim4\times10^{19}m^{-3}$ and is weakly dependent on the plasma density and the plasma current above this threshold density. The saturation of the energy confinement time is caused by the increase of the ion energy loss channel. The combination of the neoclassical ion heat diffusivity with enhancement factor of 3 and the electron heat diffusivity $\chi_e=5\times10^{19}/n_eq$, employing the Spitzer resistivity, well reproduces the saturation and the profile of electron temperatures over the wide density region ($\bar{n}_e=2\sim8\times10^{19}m^{-3}$) (Fig.2). On the other hand, apart from the empirical transport, numerical simulation based on the drift wave turbulence model has been studied. This model results in the underestimation of the plasma temperature in the low density because of too strong dependence of thermal conductivities on the electron temperature, though the numerical results show good agreements with experimental data in the medium density range ($\bar{n}_e\geqq4\times10^{19}m^{-3}$).

3.Neutral Beam-Heated Plasmas

High ion temperatures above 10KeV were obtained at $I_p=1.0\sim2.0MA$ and $B_T=4.5T$ using hydrogen neutral beam heating of 20MW onto a hydrogen plasma. The limiter operation and the low density $\bar{n}_e\leqq1.5\times10^{19}m^{-3}$ (before heating) were required in order to obtain the hot ion mode. Figure 3 shows the typical example of high T_i discharge with $I_p=1.0MA$ (shot no. E3962). NBI heating of 20MW started at 6.55 sec and, at the end of the 0.5sec beam pulse, the electron density increased from an initial value of $\bar{n}_e=0.8\times10^{19}$ to $2.8\times10^{19}m^{-3}$. The central ion temperature T_i^{AB} measured by active beam probe [4] increased from an initial value of ~3KeV up to 11KeV. The measurements of Doppler broadening of TiXXII line also shows the high ion temperature of 8KeV. Both measurements of ion temperatures are consistent with each other, taking into account of the density profile of Titanium ions calculated by the impurity transport code. Values of effective charge number Z_{eff} were evaluated to be 4 to 7.

These high T_i discharges have been studied steadily and unsteadily by using the one dimensional transport code including the orbit-following Monte Carlo NBI code. Steady state analysis of power balance [5] shows that the high electron temperatures raised by the increased power deposition to electrons due to high Z_{eff} is responsible for the high ion temperature, together with the reduction of ion density. High electron temperature reduces the equipartition loss in the ion power balance. Reasonable agreements both of ion temperature and total stored energy between calculations and experimental results are obtained. Time evolutional simulations of ion temperature have also carried out by using the experimental data of electron temperature and electron density. Figure 3 shows simulation results for $Z_{eff}=5.0$, where oxygen is assumed to be the impurity ion and Z_{eff} is taken to be constant in time and space. In the

initial phase of neutral beam injection, the reduction of ion density due to high Z_{eff} decreases the charge exchange loss in the central region and causes the rapid increase of ion temperature, which is consistent with the measurements of Doppler broadening of TiXXII and magnetic probes. On the other hands, in the case of low Z_{eff}, the increase of ion temperature is slow, although the ion temperature in the steady state is almost same as in the case of high Z_{eff}. In the quasi-steady state, the convection loss is dominant in the ion power balance and the ion temperature is insensitive to Z_{eff} for fixed electron temperature. It was also found that the depletion of thermal ion density due to NBI fast ions is important for the temporal evolution of ion temperature in the low density plasma, especially in the initial phase of NBI heating.

Acknowledgement

The authers would like to express their appreciations to Drs. S. Mori and K. Tomabechi for their continued encouragement and support.

References

[1] Hirayama, T. et al., JAERI-M 88-043 (1988)
[2] Shirai, H. et al., JAERI-M 87-029 (1987)
[3] Hirshman, S.P., Hawryluk, R.J., Birge, B., PPPL-1326 (1977)
[4] Tobita, K. et al., to be published in Nuclear Fusion
[5] Hosogane, N. et al., JAERI-M 87-178 (1987). submited to Nuclear Fusion.

Figure Captions

Fig.1 The resistive Z_{eff} from Spitzer resistivity (a : Z_{eff}^{SP}) and from the neoclassical resistivity with trapping correction (b : Z_{eff}^{NC}) versus the line averaged electron density.

Fig.2 The profiles of elecrtron temperature, ion temperature, electron density and safety factor calculated by using the empirical electron heat diffusivity $\chi_e=5\times10^{19}/n_e q$, the ion neoclassical heat diffusivity with enhacementy factor of 3 and Spitzer resistivity. Open circles show the electron temperatures measured by Thompson scattering.

Fig.3 Typical example of high T_i discharges. T_i^{AB} and T_i^{TiXXII} are ion temperatures measured by the active beam and the Doppler broadening of T_iXXII, respectively, and T_{e0}^{TS} is the electron temperature at the magnetic axis measured by Thompson scattering. NBI heating starts at t=6.55sec.

Fig.4 Results of transport simulation by using experimental data of electron temperature and line averaged electron density, and Z_{eff}=5, which is assumed to be constant in time and space. Neoclassical ion thermal diffusivity with enhancement factor of 1 is used in the simulation. W_e, W_i and W_b are calculated stored energies of electrons, thermal ions and beam ions, respectively.

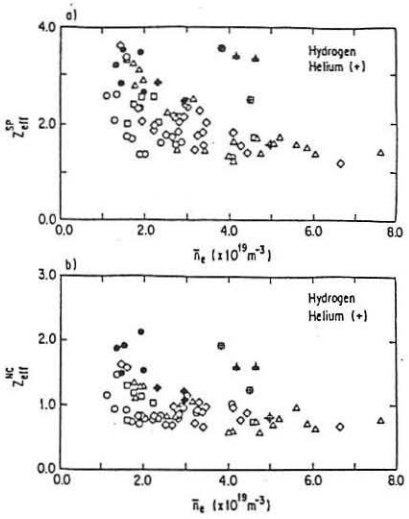

Fig. 1

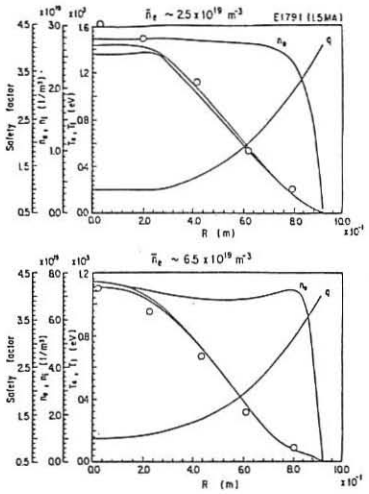

Fig. 2

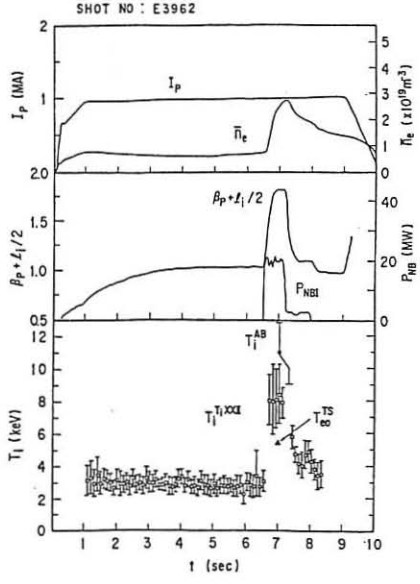

Fig. 3

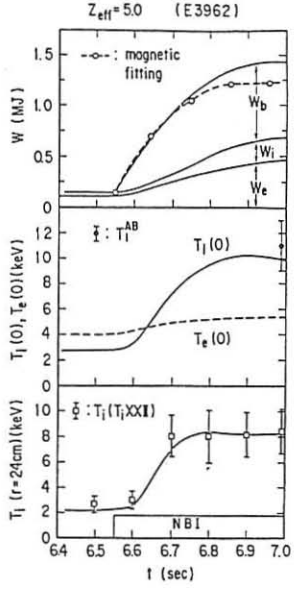

Fig. 4

MASS LOSS WITH PELLET REFUELLING ON ASDEX DURING NEUTRAL INJECTION HEATING

A.Carlson, K.Buechl, O.Gehre, M.Kaufmann, R.S.Lang, L.L.Lengyel, J.Neuhauser, V.Mertens, W.Sandmann, ASDEX TEAM, PELLET TEAM, NI TEAM

IPP Garching, EURATOM Association, Fed. Rep. of Germany

I. INTRODUCTION

Shortly after injection of a pellet into an ASDEX discharge (1) with neutral injection heating, a large quantity of plasma is lost by some mechanism much faster than that normally active. The measured increase of particles in the target plasma (with about 1 msec time resolution) corresponds to only about half the measured number of particles in the pellet. Other measurements verify that the pellet particles do indeed penetrate deep into the target. The nature of the plasma cloud produced by the pellet is understood in general, but the further interaction of the cloud with the target plasma can be very complex. Two mechanisms to account for the observed loss are proposed: an outward drift due to toroidal geometry and finite resistance, or transport from instabilities driven by the large pressure and density gradients or the corresponding large current perturbation.

The geometry of pellet injection on ASDEX (major radius R = 165 cm, minor radius a = 40 cm) is shown in Fig. 1. Hydrogen or deuterium pellets are injected radially inward in the equatorial plane. The pellet mass is deposited radially as neutral gas over a distance $\delta_{rad} = 10 - 30$ cm. The neutral gas expands poloidally (and toroidally) to a thickness of $\delta_{pol} = 1 - 2$ cm before it is ionized. Thereafter, the plasma cloud expands mainly along field lines with the acoustic speed, so that the length δ_{tor} increases with time. The cloud streches once around the torus ($\delta_{tor} = 2\pi R$) after a time interval of about 0.1 msec. Thermal equilibration occurs on a time scale of about 0.3 msec. The pellet cloud has a particle content less than or comparable to that of the target plasma, but is geometrically much more compact. Since energy is transferred to the cloud with the thermal speed of the target electrons, but the cloud expands only with its own acoustic speed, the pellet cloud acts as an energy sponge, resulting in beta, as well as density, one to two orders of magnitude larger than that of the surrounding plasma. Beta should remain roughly constant between ionization and the attainment of thermal equilibrium, the effects of expansion and heat flux approximately cancelling.

II. EXPERIMENTAL OBSERVATIONS The number of electrons in the ASDEX plasma at 1 msec intervals is determined using a four-chord FIR interferometer. The accuracy of these measurements is verified and improved by comparison with Thomson scattering profiles and lithium beam measurements of the edge density. The number of atoms in each pellet is measured in flight using a resonant microwave cavity. The

fueling efficiency η is defined as the step increase in the target electron content divided by the pellet atom content. For ohmically-heated (OH) discharges, $\eta_{OH} = 100\%$ with an accuracy of $\pm 10\%$, that is, all the pellet mass can be found in the target plasma after the injection. For neutral-injection-heated (NI) discharges (1.3 MW, L-mode), $\eta_{NI} = 50\%$. (η during other heating methods has not yet been investigated.) The interferometer and pellet mass signals are plotted for one ASDEX disharge in Fig. 2. Note that the jumps in the interferometer signal are about twice as large during the OH phases at the beginning and end of the discharge, than they are during NI, although the pellets all have about the same mass.

The simplest explanation, that only half the pellet mass penetrates the plasma in the NI case, the rest being ablated already in the scrape-off layer, is contradicted by observations of H_α light. Photodiode measurements (shown in Fig.3) and photographs show ablation primarily 5 to 20 cm inside the separatrix, not in the scrape-off-layer, for NI as well as OH. We are thus forced to the conclusion that a large quantity of plasma, corresponding to half the pellet mass or up to half the target plasma, is lost over a radial distance of around 10 cm in a time less than 1 msec. This corresponds to a diffusion constant greater than $10^5 \mathrm{cm}^2/\mathrm{sec}$, which is one to two orders of magnitude larger than that found in ASDEX under normal conditions (e.g. between pellets), so that a different and much more effective particle transport mechanism must be involved.

Measurements of the plasma energy show a step-like decrease at the time of each pellet injection during NI. Assuming that it is distributed evenly among the electrons and ions lost, this energy difference corresponds to a temperature of around 140 eV. This relatively low temperature, roughly twice the temperature at the separatrix, indicates that the energy loss is mostly convective and that the particles lost probably come from the pellet cloud (although a significant fraction of the target plasma might have such a low temperature after giving up its heat to the pellet). Furthermore, the small energy loss indicates that the particles are lost perpendicular to the magnetic field, since a parallel loss mechanism (such as ergodization of the flux surfaces) would certainly result in large conductive energy losses.

Various diagnostics of the plasma edge and divertor chamber show elevated signals after injection of a pellet. The signals rise rapidly and then decay with a divertor time constant of 3–5 msec. The short rise time of the signals (< 0.1 msec for the Langmuir probes) is further evidence that the loss occurs very rapidly.

III. CANDIDATE LOSS MECHANISMS

An estimate of the initial ideal MHD perturbation produced by the cloud indicates a global $n = 1$ displacement with an amplitude of a fraction of a millimeter only. The simplest dissipative mechanism that could explain the rapid loss is the torus drift of the localized finite beta cloud in resistive MHD. The gradient and curvature of the toroidal magnetic field result in vertical drift currents within the pellet cloud. These currents must return through the target plasma, whose finite conductivity results in a voltage difference, and therefore a vertical electric field, across the pellet cloud. The electric field causes the cloud to drift outward so that some fraction of it is lost. The loss continues until the pellet cloud has distributed itself poloidally, at which time the net outward drift stops. The total currents involved are of the order of several tens of kiloamperes. Order of magnitude estimates of the E×B drift velocity easily yield

values above the 10^5 cm/sec required to produce substantial losses within the 0.2 msec available. This shows that non-turbulent resistive loss could be significant, so that this mechanism deserves more careful consideration. However, it is not clear that this model will be able to satisfactorily explain the observed difference between NI and OH discharges.

A second candidate mechanism is loss due to resistive instabilities of various kinds. Tearing, driven by the large currents related to the pellet perturbation, and ballooning, driven by the pressure gradients at the edge of the cloud, are commonly discussed, but a quantitative assessment of the expected anomalous transport is not available. We note, however, that the fact that the pressure profiles before pellet injection are much closer to the ideal ballooning limit during NI than during OH could possibly provide an explanation for the difference in mass loss for the two cases.

The clarification of the mechanism responsible for the rapid loss of plasma during pellet refuelling will aid the design of pellet systems for future experiments, but more important, it may help our general understanding of particle transport processes in tokamaks.

References

(1) Kaufmann, et al.,"Pellet Injection with Improved Confinement in ASDEX", to be published in Nucl. Fusion. See also contributions from V. Mertens and from L.L. Lengyel, this conference.

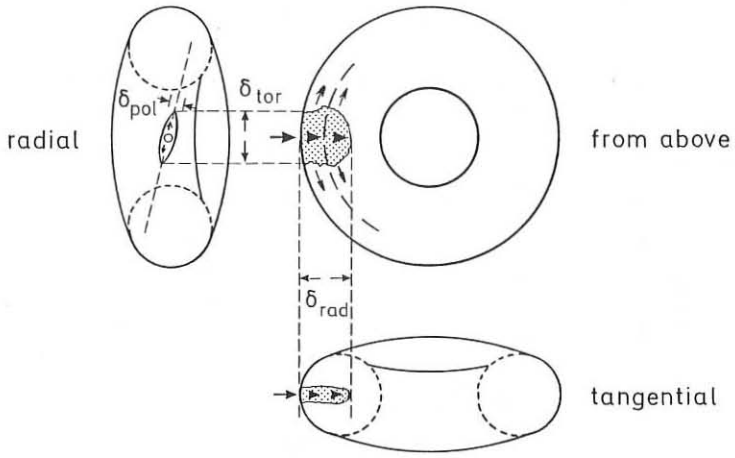

Fig. 1: Geometry of pellet injection. Three views of ASDEX, showing the path of the injected pellet (large arrows) and the expansion of the pellet cloud (small arrows) along field lines (broken line).

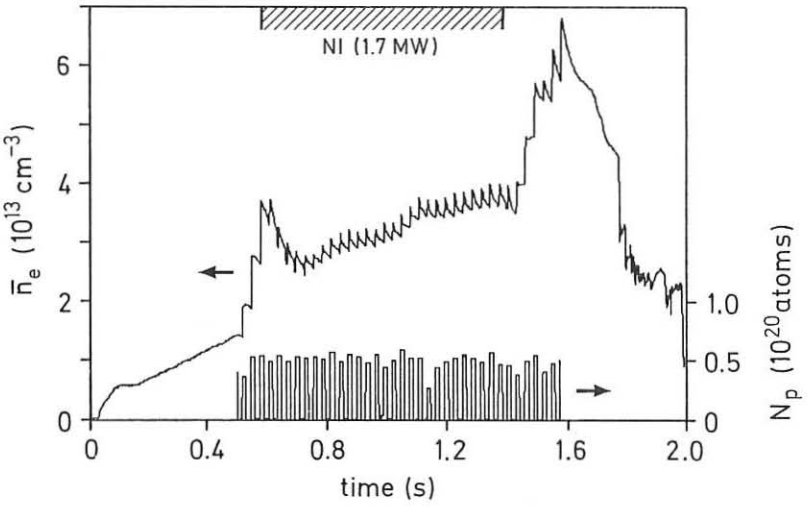

Fig. 2: Interferometre and pellet mass signals for ASDEX discharge 18913. The jump in density during ohmic heating (the first three and the last five pellets) is about twice as large as during neutral injection heating, although the pellet mass is constant.

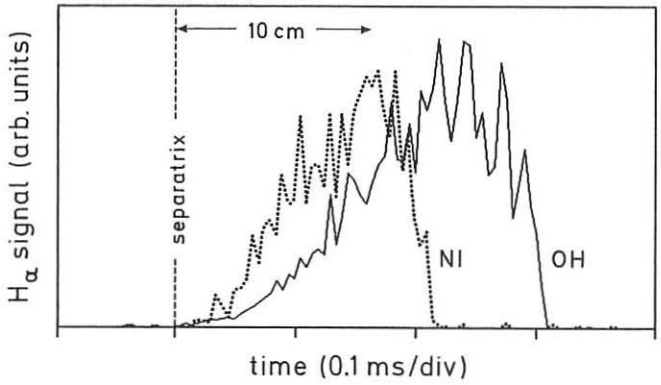

Fig. 3: Photodiode measurements of H_α light for the second and ninth pellets of ASDEX discharge 18913. The second pellet, injected in the OH phase, penetrated 18 cm (distance = (620 m/sec) $\times$ time); the ninth pellet, injected during NI, penetrated 13 cm.

CURRENT DRIVE AND HEATING SYSTEMS BASED ON HIGH-ENERGY (1- TO 3-MeV) NEGATIVE ION BEAMS*

W. R. Becraft,† M. A. Akerman, H. H. Haselton, B. D. Murphy, D. C. Lousteau, P. M. Ryan, J. H. Whealton, G. E. McMichael,‡ A. Schempp**

Oak Ridge National Laboratory, P.O. Box Y, Oak Ridge, Tennessee 37831, U.S.A.

Next-generation fusion devices based on the tokamak confinement concept are expected to emphasize steady-state operation. Such future reactors may include designs like the International Thermonuclear Experimental Reactor (ITER) and the International Tokamak Reactor (INTOR). Effective means of non-inductive plasma current drive would therefore be necessary.

This paper describes a concept for a current drive system based on negative ions with beam energy > 1 MeV. Preliminary physics calculations show that the core current necessary for stability enhancement can best be achieved by beams with energy ranging from 1 to 4 MeV. Further study and experiments will better define the optimum energy. Work under way at Oak Ridge National Laboratory (ORNL) and at collaborating institutes in Canada and the Federal Republic of Germany is defining a system, its elements, a configuration and operational scenarios deemed appropriate for such devices as ITER and other future steady-state tokamaks, and the requisite research and development to provide such a system.

The beam system under study comprises a negative ion source, low-energy beam transport, a radio-frequency quadrupole (RFQ) accelerator (4-rod concept), funnels (if needed) for beam combining, a plasma neutralizer, ion dumps for non-neutralized particles, and the necessary auxiliary elements such as a vacuum system. The system to be described is a 35-MW (11.6-A, 3-MeV) unit with a neutralized beam ~9 cm in diameter that offers beam-machine interface ease. The status of each element is discussed and indications of needed experiments and development are presented.

A summary of the physics needs and assumptions is given; this aspect will be treated in more detail in other papers.

The fusion concept being emphasized throughout the world as the leading candidate for an eventual power reactor is the tokamak confinement scheme. The tokamak devices built to date are pulsed devices. Maintenance of a plasma current will be required for steady-state operation. The plasma current must be maintained noninductively in that any inductive approach requires a varying magnetic field with a limited swing. Both particle and wave approaches to noninductive current drive have been studied and tested to small extents [1-4]. The expanding worldwide research to achieve the required plasma current drive is focusing on neutral beams as the most promising concept for the next generation of ignition devices [5]. Two aspects of using neutral beams to create the plasma current that support the potential selection of this technique for reactors are (1) the relative credibility of beams for driving current that derives from experimental evidence and (2) the ability of beams to penetrate to the plasma center and drive the required core current.

Simple analysis of beam current drive penetration shows that beam energies of >1 MeV will be required in tokamak configurations such as ITER with $R_0 = 4.5$ m and demonstration reactors with $R_0 \sim 6$ m.

*Research sponsored by the Office of Fusion Energy, U.S. Department of Energy, under contract DE-AC05-84OR1400 with Martin Marietta Energy Systems, Inc.
†Consultant, Grumman Space Systems, P.O. Box 3056, Oak Ridge, TN 37831.
‡Chalk River Nuclear Laboratories, Ontario, Canada KOJ 1JO.
**Institut für Angewandte Physik der Universtät Frankfurt, D-6000 Frankfurt am Main, Federal Republic of Germany.

The main issue that has deterred consideration of high-energy (>1-MeV) deuterium beams in the past has been the lack of an adequate technology base, although the idea for this application was proposed several years [6]. During recent years, much has been accomplished in the beam acceleration technology necessary for these high-energy beams. For example, the continuing negative ion source developments are resulting in characteristics that are near-scalable. RFQ accelerators have been successfully operated under very challenging conditions. The operation of RFQs at, e.g., Los Alamos National Laboratory (LANL) and the Chalk River Nuclear Laboratories (CRNL) has provided a valuable experimental database from which scaling to the higher currents but much lower brightness plasmas and lower current density beams acceptable for current drive systems can be done with some confidence.

Design concepts for neutral beam current drive systems have been developed at ORNL, in collaboration with CRNL [7], using the rf accelerator technology base that has expanded so rapidly in recent years. In addition to the substantial and growing database for the RFQ accelerator, a significant advantage accrues from the fact that its driving power is rf in the ion cyclotron range of frequencies (ICRF) for tokamaks, a very available and economical power source. Present accelerator theory appears adequate to design such devices, and experience at other laboratories with heavy ion accelerators at similar frequencies and light ion accelerators operating near their space-charge limits lends confidence to the predictions of rf properties and accelerator efficiencies calculated for the system described below.

The RFQ design is based on the 4-rod RFQ concept advanced by Schempp [8], along with McMichael and Hutcheon et al., which is particularly suitable for high-current designs. Conceptual designs for RFQs with an output current of 3.7 A have already been done and are under further study. Energy efficiencies of 60% for room-temperature RFQs are already obtainable, even though efficiency has been of secondary interest to date because of the very short pulse and extremely low duty factor of present applications. As a consequence, no serious effort has been made to date to reduce the losses. A development program is being initiated to study the potential of raising the RFQ room-temperature efficiency to as much over 80%, as seems feasible from a cost payoff basis.

Several different forms of rf accelerators have been considered: in particular, the MEQALAC, drift tube linear accelerators (linacs), and RFQs. Only the RFQ can simultaneously provide continuous gentle bunching and strong focusing. It is an ideal matching device between a continuously operating ion source and the discrete beam bunches needed for rf accelerators. It is this development that makes possible the efficient acceleration of very intense beams from low energies. Only four electrodes are required in the entire RFQ system, which consists of a matching section, an adiabatic buncher, and the accelerator with continuous radial focusing throughout.

The system proposed by ORNL is shown conceptually in Fig. 1. It comprises the negative ion source, a low-energy beam transport system to match the beam to the RFQ, the RFQ, a plasma neutralizer, and an ion dump. The higher efficiency (80-85%) plasma neutralizer is used in the design, because the very small diameter (7 cm) of the beam exiting the RFQ permits the maintenance of the neutralizing plasma with an insignificant plasma generating rf energy (~400 kW). Beam systems with large cross sections, such as those in present fusion appications, would have prohibitively large particle losses from the neutralizer ends, and the resulting required plasma generating power would offset the plasma neutralizer efficiency gain.

A variation of the system is shown in Fig. 2, where four of the systems in Fig. 1 are combined with beam funnels to produce a 35-MW beam. This configuration uses four beam lines feeding one plasma neutralizer and ion dump. This arrangement requires efficient two-beam to one-beam funnels and results in a high-power, small-diameter beam and an easy interface with the tokamak.

It is apparent from a cursory study of this system that, in addition to relying only on scaling of presently developed concepts, it has many attractive features for tokamak application:

Very small diameter beam	- Small tokamak ports - Reduced volume near tokamak - Reduced neutron backstreaming
Beam is bent before neutralizer	- No neutron backstreaming to sensitive beam components - More machine interface flexibility
Low beam divergence (~1 m-rad)	- Can use 10- to 20-m drift tube after neutralizer - Can place key equipment farther from the machine, behind shield - Easier hands-on maintenance can result

The cost of the rf accelerated beam should be quite competitive with other rf and beam concepts that may be considered for current drive.

The key issues to be addressed in pursuing the desired development of this system include those related to the physics of high-energy beams, the system and component designs and technology development necessary to meet the core current drive needs, and the planning and execution of experiments on present and future fusion devices that will help guide the evolution and application of high-energy neutral beams for current drive, plasma heating, and possibly alpha diagnostics.

The following summary statements are offered:

- A plasma current drive mechanism is required to extrapolate present tokamak physics and technology into a reactor regime.
- Core plasma current drive is essential in achieving the required current profile for stability.
- Available (credible) current drive options are limited.
- Preliminary scoping studies indicate that high-energy (1- to 3-MeV) neutral beams, coupled with some LH, provide a validated physics and technology option that appears to be a good candidate for current drive in a reactor.
- Optimal tokamak and neutral beam parameters must be determined and pursued.
- Related programs may be important; neutral beam heating, alpha particle diagnostics, high-Z current drive, and experimental tests on confinement devices (e.g., ATF).

It seems likely that a reactor-like tokamak can be made steady-state with 1- to 3-MeV beams to provide core plasma current drive.

References

[1] M.C. Zarnstorff, M.G. Bell, M. Bitter, R.J. Goldston, et al., "Driven Currents in TFTR," presented at the 14th European Conference on Controlled Fusion and Plasma Physics, Madrid, June 22-26, 1987.

[2] D.C. Robinson, M. Cox, T. Edlington, B. Lloyd, M. O'Brien, et al., "ECRH Current Drive Experiments on CLEO," presented at the 14th European Conference on Controlled Fusion and Plasma Physics, Madrid, June 22-26, 1987.

[3] S. Knowlton, C. Gormezano, D. Moreau, R.J. Anderson, et al., "Plasma Current Profile Control in JET by Lower Hybrid Current Drive," presented at the 14th European Conference on Controlled Fusion and Plasma Physics, Madrid, June 22-26, 1987.

[4] H. Hamnén, C. Challis, J.G. Cordey, D. Campbell, M. Cox, et al., "Neutral Beam Current Drive Studies at JET," presented at the 14th European Conference on Controlled Fusion and Plasma Physics, Madrid, June 22-26, 1987.

[5] Meeting of the Ignition Physics Steering Group Subcommittee on Current Drive Meeting, S. Bernabei, Chairman, Princeton Plasma Physics Laboratory, September 3–4, 1987.
[6] L. R. Grisham, D. E. Post, D. R. Mikkelsen, and H. P. Eubank, "Plasma Heating With Multi-MeV Neutral Atom Beams," Nuclear Technology/Fusion 2, 199 (1982).
[7] G. E. McMichael, private communication, 1987.
[8] A. Schempp, H. Deitinghoff, M. Ferch, P. Junior, H. Klein, "Four Rod λ RFQ for Light Ion Acceleration," Nucl. Instrum. Methods B10/11, 831 (1985).

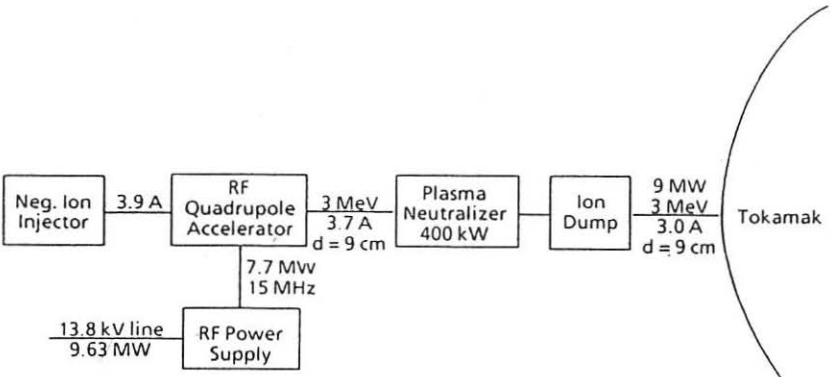

Figure 1. High-energy rf accelerated beam module (9 MW): "basic building block."

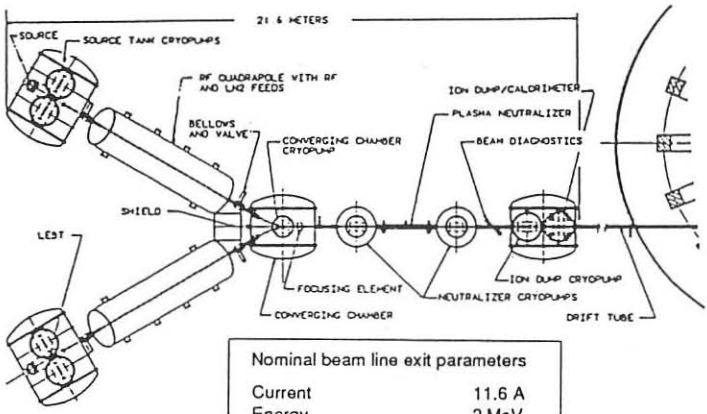

Nominal beam line exit parameters	
Current	11.6 A
Energy	3 MeV
Radius, beam	4.5 cm
Length	22 m
Power	35 MW
Efficiency	38–60 %

Figure 2. RF accelerated 3-MeV neutral beam system

FIRST EXPERIMENTAL RESULTS OF ENERGY RECOVERY ON THE TORE SUPRA NEUTRAL BEAM INJECTOR PROTOTYPE

M.Fumelli, F.Jequier and J.Paméla

Association EURATOM-CEA, CEN Cadarache, 13108 St-Paul lez Durance, France

ABSTRACT: A neutral injector with Energy Recovery has been designed and tested. A new type of electrode, the STEM, has been developed for this injector in view of electron suppression and trapping. A first series of experiments were made with H, D and He beams, up to 60 keV, 12 A, 0.5 s duration. The recovery of the unneutralized part of the beam has been clearly demonstrated. The decelerated ion collector potential was as low as 0.05 Vbeam. At least 90% of the full energy residual ions are collected.

INTRODUCTION

Tore Supra will be equipped with 6 neutral injectors (D^-, 40 A, 100 keV each) of a completely new type based on the concept of the energy recovery of the unneutralized fraction of the beam. In a conventional neutral beam injector, these residual energetic ions are magnetically deflected and dumped at full power on actively cooled targets. In the "energy recovery" scheme[1], also called direct conversion[2], these ions are electrostatically decelerated and collected at low energy on a device ("recovery electrode") whose potential Vr is near that of the ion source. This improves the injector power efficiency and reduces heat load problems of ion dumps. We present here the main features of the Tore Supra neutral injector prototype and the first experimental results.

INJECTOR DESIGN - STEM ELECTRODE PRINCIPLE

The design of the energy recovery system (ERS) was based on a computer study[3]. The whole injection line was conceived with constant care of the specific problems of energy recovery. The principal elements are (fig. 1):

1) Grounded source: the ion source is grounded[1-4], the neutralizer being held at the accelerating negative high voltage Vbeam. With this disposition, the recovery electrode is near to ground potential (slightly negative). This reduces problems arising with the collection of particles resulting from ionization processes and simplifies the electrical circuit.

2) Neutralizer gas pumping: a chamber with baffles is placed at the end of the neutralizer in order to reduce ionization in the suppressor region.

3) Suppressor electrodes (STEM): these electrodes are placed on beam sides, at the entrance of the ion decelerating gap of the ERS. They are negatively biased (Vs) with respect to the neutralizer, creating an electrical potential barrier which blocks the neutralizer plasma electrons. Secondary electron emission by ion impact on the suppressor must be

minimized because it reduces the ERS efficiency[3]. Therefore we developed a composite electrode that we named STEM (for Suppression and Trapping of Electrons by Multi-plate device), conceived to trap electrostatically at least 50% of these electrons. It is made of two electrically isolated sets of copper plates mounted in alternation: this allows the application of a trapping potential between plates (Vp).

4) Narrow beam: in Fontenay-aux-roses[4-5], we have developed a very narrow beam system (6.5 x 120 cm at the extraction plane) in view of the energy recovery. This reason of this choice is that Vs varies roughly as the 4/3rd power of beam transverse dimension[3], and therefore broad beams are not suited for energy recovery.

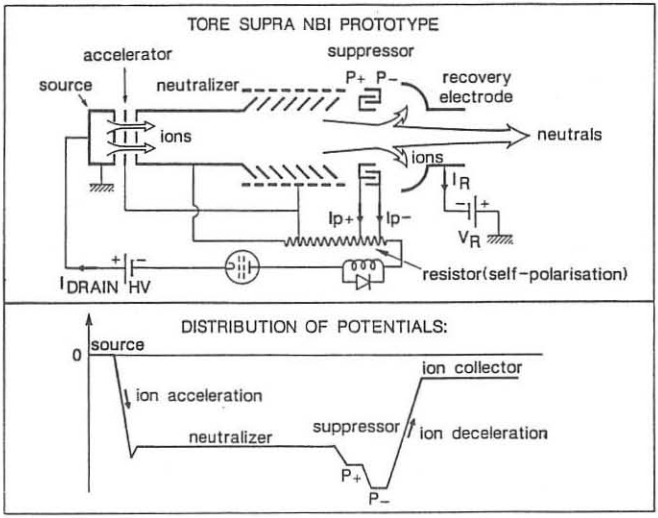

Figure 1: Schematic view of the prototype injector equiped with the ERS and distribution of potentials on the different components. The difference with a classical injector is that the residual ion current is not drained from the HV generator but at the lower potential Vr; thereby one can really speak of "Energy Recovery".

EXPERIMENTAL RESULTS:

This series of experiments was made with He, H and D beams of characteristics up to 60 keV, 12 A and 0.5 s duration. The main results are:

1) the effect of energy recovery is unambiguously demonstrated (see figures 2 and 3). A value Vr ≈ 0.05 Vbeam is sufficient for the recovery of the residual ions, in agreement with the numerical calculations[3]. As expected from beam neutralization calculations, the recovered current decreases when the neutralizer target thickness is increased (see figure 4).

2) the value of Vs required to stop neutralizer electrons is clearly defined by the experiment as shown on figure 5. The measured suppression tension (≈ -10 kV in the case of figure 5) is found to be in agreement with the numerical calculations[3].

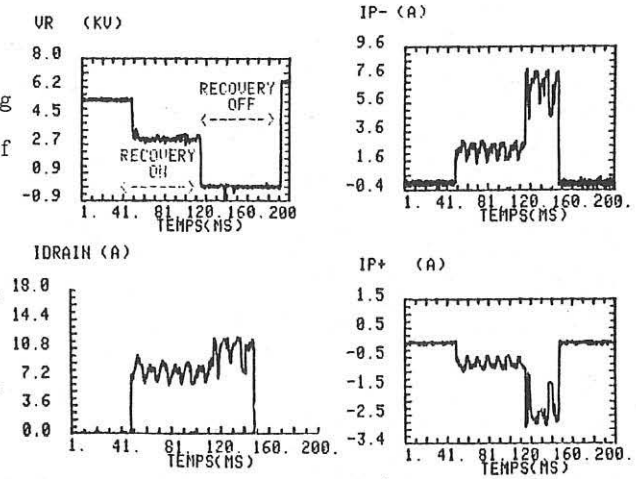

Figure 2: Four electrical signals recorded during an Helium shot at 50 keV. At the beginnig of the shot Vr = -3 kV. After 80 msec, Vr is set to zero: Idrain, Ip+ and Ip- (defined in figure 1) raise significantly. This is expected when the residual ions are no longer collected and fall on the suppressor plates.

Figure 3: Idrain and Ir are plotted versus Vr (30 shots, He, 50 keV, perveance matched). A significant raise of Idrain is observed when Vr=0. This corresponds to the recovered current amplified by a factor $(1+\varepsilon\gamma)\approx 3$, due to secondary electron emission (see text). The negative value of Ir when Vr=0 is due to the collection of these electrons by the recovery electrode.

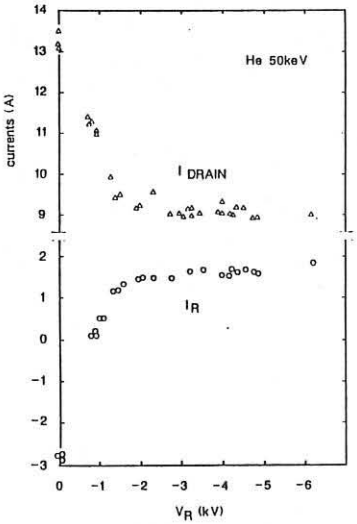

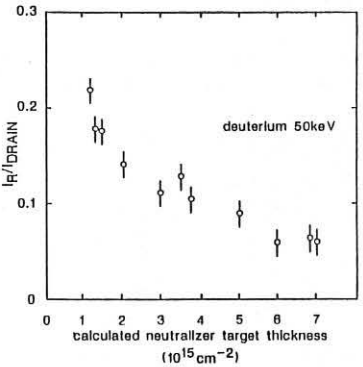

Figure 4 Ir normalized to Idrain decreases when the neutralizer target thickness increases, as expected from neutralization calculations.

3) figure 6 demonstrates the efficiency of the secondary electron trapping by application of the polarization Vp between suppressor plates. γ being the secondary electron emission coefficient and ε the electron escaping probability from suppressor (when Vp = 0, ε = 1), the ratio of

currents without and with polarization yields a measurement of $(1+\gamma)/(1+\varepsilon\gamma)$. γ and ε have been deduced from this type of measurements combined with calorimetry on both sets of suppressor plates.

At 50 keV, we measured $\gamma = 6 \pm 1$ in helium and $\gamma = 4 \pm 1.3$ in hydrogen. When a polarisation $Vp \approx 0.25$ Vs is applied, we measured $\varepsilon \approx 0.45$ in helium and hydrogen at 50 keV (i.e. electron trapping efficiency above 50%).

4) We measured a very high collection efficiency (≈90%) of the unneutralized full energy beam particles. In this first experiment, half of this gain was lost due to secondary electrons emitted from the suppressor. An important fraction of these electrons is probably due to bombardment by spurious energetic particles (direct beam interception, aberrated trajectories). We will try to reduce this interception in the next experiments (improvement of collimation in front of the STEM) and thereby further increase the overall ERS efficiency.

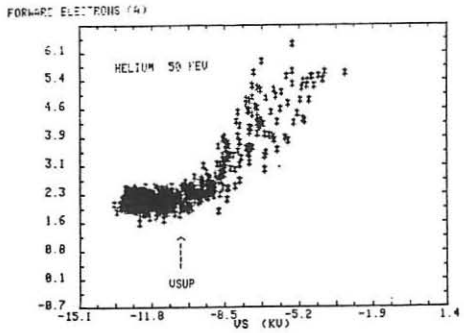

Figure 5: electron current in the forward direction decreases when the (absolute) value of Vs raises, until an electrostatic barrier is created ($|Vs| > 10$ kV). This plot was recorded during a single 50 keV Helium shot, Vs being varied by means of a capacitor.

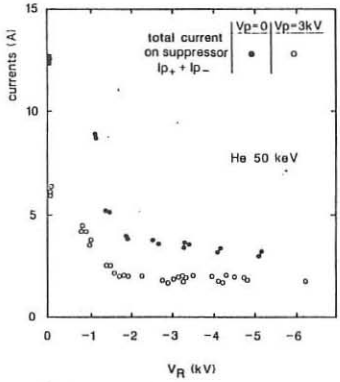

Figure 6: the net suppressor current is plotted versus Vr for two series of He beams at 50 keV, perveance matched. The first series (30 shots, open points) was made with a polarization $Vp \approx 3$ kV. The second series (18 shots, dark points) was made without polarization ($Vp = 0$).

The authors wish to thank G.Delogu, J.Godaert, P.Van Coillie, R.Yattou, P.Heister and J.Prévitali for their valuable technical support.

References:

1) M.Fumelli, Nuclear Instr. and Methods 118 (1974), 337-342.
2) R.W.Moir, Top. Meeting on the Tech. of Nucl. Fus., San Diego (1974)
3) J.Paméla, EURATOM-CEA, EUR-FC-1322 (january 1987).
4) M.Fumelli, F.Bottiglioni, F.Jequier and J.Paméla, First results from the Tore Supra prototype injector, SOFT conference, Avignon (september 1986)
5) M.Fumelli, F.Jequier and F.Bottiglioni, the Tore Supra ion source, SOFT conference, Avignon (september 1986).

TRANSPORT IN AN ERGODIC MAGNETIC FIELD WITH AMBIPOLAR ELECTRIC FIELD EFFECTS

W. Feneberg* and M. A. Hellberg†

*Max-Planck-Institut für Plasmaphysik,
EURATOM Association, D-8046 Garching, Fed. Rep. of Germany

† Plasma Physics Research Institute,
University of Natal, Durban, South Africa

INTRODUCTION

Stochastic magnetic fields may be applied to tokamak edges to establish an ergodic divertor [1] or they may arise spontaneously due to instabilities. In addition, they may play an important role in the H-mode, since Neuhauser, *et al* [2] have recently shown that asymmetries in the deposition profiles on ASDEX divertor plates may be explained by imperfectly installed multipole windings leading to a stochastic magnetic layer just inside the separatrix.

Transport in a stochastic magnetic field has been investigated in a number of earlier papers based on the quasilinear theory [3,4], resulting in the well known diffusion coefficient of Rechester and Rosenbluth [3] for the case of a steady-state perturbation field. Thyagaraja, *et al* [5], using a simplified Fokker-Planck equation, considered a fluctuating stochastic magnetic field and found a large increase of the transport in the long mean free path regime.

In this paper we use the drift kinetic equation, including the effect of the electric field, together with the Krook (or BGK) collision model [6], which conserves particles, momentum and energy. We consider a fluctuating stochastic magnetic field. It should be noted that even for a time-independent applied perturbation, a frequency arises through the azimuthal electron drift $V_E = -(\nabla\phi \times \vec{B})/B^2$.

In agreement with previous theory we find that only modes that are in resonance with the unperturbed magnetic surfaces contribute to the transport, but with a coefficient that is larger by a factor $\gamma = 2\lambda_e/Rq$ than that derived from quasilinear theory (here λ_e is the electron mean free path, R the torus major radius and q the safety factor). In particular we find that inclusion of momentum conservation in like-particle collisions plays a significant role. Using a simpler collision model that conserves only particle number, we also obtain an estimate for the width of the resonant layer. We find that transport occurs in the range

$$0 \leq \left|(m - nq)\right| \leq \left(\frac{\lambda_e}{rq}\right)^{-1}\left(\frac{\omega}{\nu}\right)^{1/2}$$

Here m and n are the poloidal and toroidal winding numbers, and ω and ν the fluctuation and collision frequency, respectively.

We also present a self-consistent solution for the radial electric field based on a model in which the radial electron transport is anomalous due to motion along the stochastic field lines and the ion transport is neoclassical. Although there is no detailed flux balance, overall ambipolarity yields a relation between the radial electric field and the poloidal rotation velocity. Radial ion momentum balance and toroidal momentum balance of the whole fluid enables one then to solve for the electric field, as well as the poloidal and toroidal rotation velocities. It is found that the neoclassical perpendicular ion current produces a toroidal rotation in the Co-direction, of approximately $V_{i,\phi} = -P'/en_eB_\theta$, where P' is the total radial pressure gradient and B_θ the poloidal magnetic field.

COLLISIONAL TRANSPORT EQUATIONS

We consider cylindrical flux surfaces perturbed by a weak stochastic magnetic field with radial component b_r, which we expand as

$$b_r = \sum\sum\sum b_{\omega,m,n}(r) exp(i(\omega t + m\theta - n\phi)). \tag{1}$$

The particle flux perpendicular to the unperturbed flux surfaces is given by

$$\Gamma_r = < b_r \int f v_\parallel d^3v >, \tag{2}$$

where $< .. >$ represents a time-average over the magnetic surfaces, i.e. over θ, ϕ and t, and f is the total distribution function.

To find f we solve the drift kinetic equation for the electrons in the rotating system, given by V_E. We use the cylindrical approximation, neglecting the $\vec{B} \times \nabla B$ drift,

$$\frac{\partial f}{\partial t} + v_\parallel \hat{B}.\nabla f - \frac{q}{m}(\hat{B}.\nabla\phi)\frac{\partial f}{\partial v_\parallel} = \nu_{e,e}(f^M_{e,e} - f) + \nu_{e,i}(f^M_{e,i} - f). \tag{3}$$

The Maxwellian $f^M_{e,e}$ has the self-consistent values of density n_e, drift $\vec{u_e}$ and temperature T_e of the total (perturbed) distribution, i.e.

$$f^M_{e,e} = n_e \left(\frac{m_e}{2\pi T_e}\right)^{\frac{3}{2}} exp\left[-\left\{\frac{m_e}{2T_e}\left(\left(v_\parallel - u_\parallel\right)^2 + 2\mu B\right)\right\}\right]. \tag{4}$$

Here μ is the magnetic moment. We see that particle number, momentum and energy are conserved in like-particle collisions [6]. For electron-ion collisions we conserve particles and energy, but momentum transfer is allowed, representing electron-ion friction.

The distribution function is expanded, $f = f_0 + f_1$, with f_0 a Maxwellian in the unperturbed magnetic field and f_1 being represented by a series similar to that for b_r, eqn. (1). The resultant radial particle flux (eqn. (2)) has been calculated for resonant modes, i.e those for which the parallel wave number $k_\parallel = \frac{m-nq}{Rq} = 0$. It may be written as

$$\Gamma_r = -2\frac{\lambda_e}{Rq}\frac{v_{e,th}}{T_e} D_M \left(P'_e - en_e\phi'_0\right). \tag{5}$$

Here D_M has the form of a magnetic diffusion coefficient

$$D_M = Rq \sum\sum\sum b_{\omega,m,n} b^*_{\omega,m,n} A(k_\parallel), \tag{6}$$

where b^* represents the complex conjugate and $A(k_\parallel)$ is a form factor which describes the resonance width.

Using the simplified Krook model conserving only particles (as in [5]), and expanding in the parameter $\epsilon = v_{e,th} k_\parallel / \nu << 1$, we find

$$A^{-1}(k_\parallel) = 1 + \frac{v^4_{e,th} k^4_\parallel}{\nu^2 \omega^2},$$

from which one may deduce a resonance width

$$0 \leq \left| \frac{v_{eth} k_\parallel}{\nu} \right| \leq \left(\frac{\omega}{\nu} \right)^{1/2}$$

This value is small enough to lie within the expansion range, and is considerably smaller than that given in [4].

Evaluating the radial thermal flux

$$Q_r = < b_r \frac{m}{2} \int \left(\left[v_\parallel - u_\parallel \right]^2 + 2\mu B \right) \left(v_\parallel - u_\parallel \right) f d^3 v >, \tag{7}$$

we find that

$$Q_r = -\frac{5}{2} \left(\frac{\lambda_e}{Rq} \right) v_{e,th} n_e D_M \frac{\partial T_e}{\partial r}. \tag{8}$$

Momentum conservation in the collision term, which is neglected, for instance, in [4] and [5], yields a factor 2 in the electron particle flux and 2.5 in the electron thermal flux, but causes the ion transport to vanish, even for $k_\parallel = 0$.

ELECTRIC FIELD EFFECTS

Because of the difference between the electron and ion thermal velocities, particle flow in an ergodic magnetic field is not automatically ambipolar and a radial electric field is set up to restore ambipolarity. We investigate here a model proposed by Stringer [7], in which we consider the above anomalous electron transport arising from the braided magnetic field, and neoclassical ions .

Equating the neoclassical ion flux [8] and the anomalous electron flux (eqn. 5), one finds that the radial electric field adjusts itself to the value of the poloidal rotation. For a self-consistent calculation, however, one needs two further equations. These are the equation for radial ion motion

$$\phi'_0 + V_{i,\phi} B_\theta - V_{i,\theta} B_\phi = -\frac{P'_i}{e n_i}, \tag{9}$$

(with $V_{i,\phi}$ the toroidal ion rotation velocity) and the toroidal momentum balance for the whole fluid

$$m_i n_i \nu_i V_{i,\phi} = m_i \omega_i f_p \Gamma_i + M_\phi \tag{10}$$

(with ν_i a phenomenological drag frequency to describe the momentum sink, M_ϕ a momentum source and $f_p = B_\theta / B_\phi$). The three unknowns $\phi_0', V_{i,\phi}$ and $V_{i,\theta}$ can be found from the ambipolar transport condition and these two equations.

The term with Γ_i occurs in a stochastic magnetic field, as transport is not locally ambipolar and the component parallel to the field lines cannot contribute to the $\vec{j} \times \vec{B}$ forces. Thus Γ_i can be replaced by the parallel electron flux $\Gamma_{e,\parallel}$. As the $\vec{j} \times \vec{B}$ force is a large quantity, the electric field is restricted to the value

$$e n_e \phi_0' - P_e' \sim 0. \tag{11}$$

M_ϕ is typically too small to control the toroidal rotation, which thus follows purely from radial momentum balance (9) and neoclassical rotation (10),

$$V_{i,\phi} = -\frac{P'}{e n_e B_\theta} - \frac{T_i}{e B_\theta} \cdot \frac{\partial (\ln n_i T_i^{-\gamma})}{\partial r} \tag{12}$$

(where $P = P_e + P_i$ is the total pressure).

This rotation velocity can be considered an indicator of the presence of a stochastic magnetic field and reaches values large enough to be measured - for ASDEX in the H-mode a value of about 5×10^4 m/s may be estimated.

Acknowledgements

Valuable discussions with D.Pfirsch have led to the use of the Krook collision model. This research was supported in part by the Foundation for Research Development.

References

[1] W. Engelhardt and W.Feneberg *J. Nucl. Mat.* **76,77**, 518 (1978)

[2] J.Neuhauser, et al. *Amer. Phys. Soc. Plasma Phys. Div. meeting*, Paper 5V18, San Diego (1987)

[3] A.B.Rechester, M.N.Rosenbluth *Phys. Rev. Lett.* **40**, 38 (1978)

[4] T.Yamagishi, D.K.Bhadra *Plasma Phys. & Contr. Fus.* **25**, 1415 (1983)

[5] A.Thyagaraja, I.L.Robertson, F.A.Haas *Plasma Phys. & Contr. Fus.* **27**, 1217 (1985)

[6] P.C.Clemmow, J.P.Dougherty *Electrodynamics of Particles and Plasmas* Addison-Wesley, London (1969)

[7] T.E.Stringer *private communication*

[8] L.M.Kovrizhnyk *Nucl. Fus. Suppl.* **12**, 33 (1972)

LARGE AREA - 4 cm HOLLOW ANODE ION SOURCE

V. Miljević

The Boris Kidrič Institute-Vinča, The Institute for Atomic Physics,
P.O.B. 522, 11001 Belgrade, Yugoslavia

Neutral beam injection heating is a promising method of heating magnetically confined plasma /1,2/. Different types of both the positive and negative ion sources for neutral beam applications have been developed /3,4/.

In this paper a new type of an ion source producing uniform, dense and quiescent plasma with high percentage of atomic species is presented.

The ion source is essentially a tandem discharge consisting of a hollow anode discharge (HAD), as the source of both the high energy electrons and atomic hydrogen (predissociation method) /5-10/, and a standard reflex or PIG discharge, as a plasma source, supplying ions to the extraction electrodes /11,12/. They are separated by a hollow anode.

Fig.1. shows a sketch of a 4 cm grid diameter tandem ion source. It consists of a concave cathode (CC), and a hollow anode (HA), representing hollow anode diode, cylindrical anode (CA) and target cathode (TC). Axial magnetic field is applied by MC1 and MC2 source coils. Thus, the PIG discharge chamber is enclosed by the hollow anode flange, cylindrical anode and target cathode.

The hollow anode is represented by a disk (made of aluminum alloy) with the aperture in the center 0.5 mm dia. The upper side of the disk, facing the cathode, is insulated by a thin ceramic layer deposited by a plasma arc thus making only inner surface of the anode aperture conductive. Details of the hollow anode are shown in /6,7/. Teflon insulator (TI) enables the hollow anode to be in the center of the concave cathode curve and knife-edge seal. The operating gas, controlled by a needle valve, enters from the cathode side, through a heat sink (HS), and is pumped away through the hollow anode aperture and PIG chamber by a standard high vacuum system. Technical hydrogen was used.

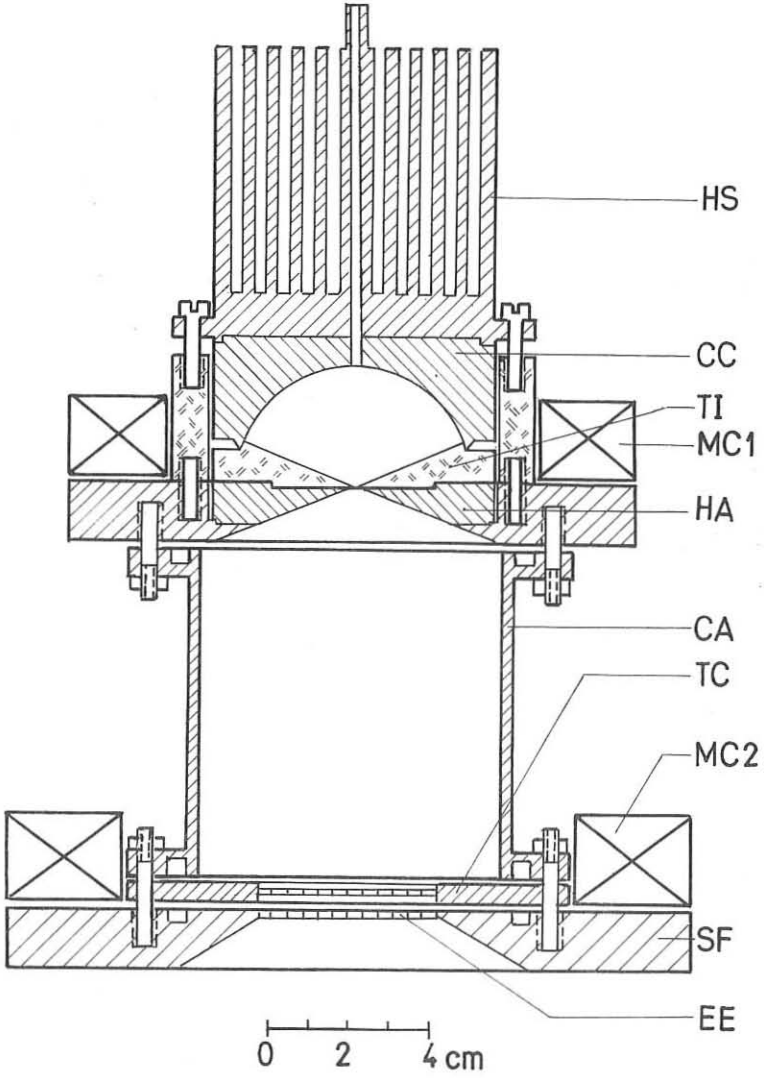

Fig.1. 4 cm hollow anode ion source: HS - heat sink, CC - concave cathode, TI - teflon insulator, HA - hollow anode, MC1, MC2 - magnetic coils, CA - cylindrical anode, TC - target cathode, EE - extraction electrode, SF - source flange.

In the hollow anode discharge the concave cathode focuses electrons toward the hollow anode placed in the center of the curvature, providing a high density of high-energy electrons in the hollow anode aperture. In this way the probability of ionization and excitation of the gas while passing through the aperture is increased. That is why HAD is rather inhomogeneous discharge with maximum both the electron density and temperature concentrated in the small volume of the hollow anode aperture /6,7/. Outside the hollow anode discharge, through the hollow anode aperture, an intensive electron beam (without additional acceleration) is obtained /8,9/. The intensity and the energy of the electron beam depend on the hollow anode diameter, the discharge voltage and current, and the gas pressure. By decreasing the diameter the brightness of the beam is increased. The electron beam current practically equals the discharge current /6,10/.

The hollow anode discharge is a very stable discharge and transition into an arc or spark is not observed.

Optical spectrum of the hydrogen hollow anode discharge consists of essentially all Balmer lines. It shows that in the hollow anode aperture a high degree of dissociation and ionization take place. Spectral lines of the cathode or anode material have not been found in the spectrum regardless of the mass of the operating gas /5,6/.

The high energy electrons from the HAD accelerated by a double layer through the hollow anode aperture into the downstream discharge chamber are constrained by the magnetic field and osscilate between hollow anode and target cathode. In this way a filamentless low voltage PIG (or reflex) discharge produces high purity atomic hydrogen plasma enclosed by the hollow anode, cylindrical anode and target cathode.

The ions so created are formed into an ion beam by the extraction electrode (EE).

Typical operating conditions of the hollow anode tandem ion source are:

- hollow anode hydrogen discharge pressure is of the order of 10^{-1} mbar (typically $3\text{-}5\cdot10^{-1}$ mbar). In this case pressure in the vacuum chamber is about $5\cdot10^{-5}$ mbar. The pressure in the PIG discharge chamber has not been measured.

- hollow anode discharge current is I_H = 60-80 mA at U_H = 250 V
- PIG discharge current is I_p = 200 mA at U_H = 280 V
- magnetic field at the axis of the PIG cylindrical anode is about B = 50-60 G.

For the above mentioned operating conditions a hydrogen ion beam exceeding 10 mA at 1.5 kV is obtained. No ion beam optimization work has been done so far.

In order to improve plasma characteristics it is planned to add multipole line cusp confining field around the PIG chamber.

The hollow anode tandem ion source can produce high purity ion beam with good gas and power efficiency. As the pressure in the vacuum chamber is low, for many applications of this source differential pumping is not necessary.

Further work is in progress.

REFERENCES:

/1/ F.H.Coensgen, W.F.Cummins, G. Gormezano, B.G.Logan, A.W.Molvik, W.E. Nexsen, T.C.Simonen, B.W.Stallard, and W.C.Turner, Phys.Rev.Lett. 37,143(1976).
/2/ L.D.Stewart, A.H.Boozer, H.P.Eubank, R.J.Goldston, D.L.Jasseby, D.R. Mikkelsen, D.E.Post, B.Prichard, J.A.Schmidt, and C.E.Singer, in Proc. of the See.Int.Symp. on the Production and Neutralization of Negative Hydrogen Ions and Beams (Brookhaven National Laboratory, Upton, NY, 1980), p.321.
/3/ Y.Okumura, H.Horiiki, and K.Mizuhashi, Rev.Sci.Instrum. 55,1(1984).
/4/ L.R.York, R.K.Stevens,Jr., K.N.Leung, and K.W.Ehlers, Rev.Sci.Instrum. 55.681(1984).
/5/ V.Miljević, Appl.Opt. 23,1598(1984).
/6/ V.Miljević, Rev.Sci,Instrum. 55.931(1984).
/7/ V.Miljević, IEEE Trans. on Nucl.Science, NS-32, No 5, 1757(1985).
/8/ V.Miljević, XVIII ICPIG, Int.Conf. on Phen. in Ionized Gases, Swansea, (1987), p.768.
/9/ V.Miljević, J.Appl.Phys. to be published (1988).
/10/ V.Miljević, unpublished.
/11/ W.L.Stirling, C.C.Tasai, and P.M.Ryan, Rev.Sci.Instrum. 48,533(1977).
/12/ C.C.Tasai, W.L.Stirling, and P.M.Ryan, Rev.Sci.Instrum. 48,651(1977).

DETERMINATION OF VIBRATIONAL AND ROTATIONAL STATE POPULATION IN HYDROGEN BY DISSOCIATIVE ELECTRON ATTACHMENT

I. Čadež, R.I. Hall, M. Landau, F. Pichou, D. Popović and C. Schermann

*Groupe de Spectroscopie par Impact Electronique et Ionuque, Université Pierre et Marie Curie, 4 Place Jussieu T12-E5, Paris 5, FRANCE
and
+Laboratory for Atomic Collision Physics, Institute of Physics, P.O.Box 57, 11001 Belgrade, YUGOSLAVIA

The potential importance of negative ion beams for formation of high energy neutral beams for heating and current drive for fusion plasmas is well recognized and the ion sources for this purpose are quickly developing (1),(2). Efficient production of hydrogen negative ions in volume sources is achieved by dissociative electron attachment (DEA) to vibrationally and rotationally excited hydrogen molecules (3). Excited molecules and low energy electrons are produced in the specific low pressure plasma. The knowledge of mechanisms for vibrational and rotational excitation and deexcitation has fundamental role for designing and modeling these sources (4). Also, the corresponding diagnostic techniques for determinantion of vibrational and rotational state population are very important for the development of volume ion sources as well as for the study of other hydrogen plasmas.

New diagnostic technique for determination of hydrogen and deuterium vibrational and rotational state population under the conditions similar to those in volume negative ion sources and some results of its application are described in this contribution. This technique is based on detection of low energy H^- resulting from DEA. The high sensitivity is achieved due to the exceptionally strong increase of cross section with the internal nuclear motion excitation for the case of the 4 eV DEA process in hydrogen (5).

The experimental setup is schematically shown in Fig. 1. The electron beam of variable energy is produced by electron gun comprising an electrostatic 127 deg. energy filter and

corresponding electron optics. The gas molecules to be analysed are effusing from the gas cell and are crossed at right angle by electron beam. Perpendicularyto the electron beam directon the quadrupole mass filter is mounted together with a simple entrance ion optics. The negative ions created by DEA in the interaction region are focused, filtered from other negatively charged particles by quadrupole mass filter and detected by an off-axis channel electron multiplier. The stainless steel gas cell used in this experiment is also schematically shown in Fig. 1. The tungsten filament is mounted in the cell and when resistively heated it is a source of electrons and hydrogen atoms. By appropriate voltage biasing the discharge in the gas cell can be generated between the filament and the grounded wall. The gas cell is shielded by mu-metal and its wall is cooled by air or water. The pressure in the gas cell was varied in the range between few μbar to about one mbar.

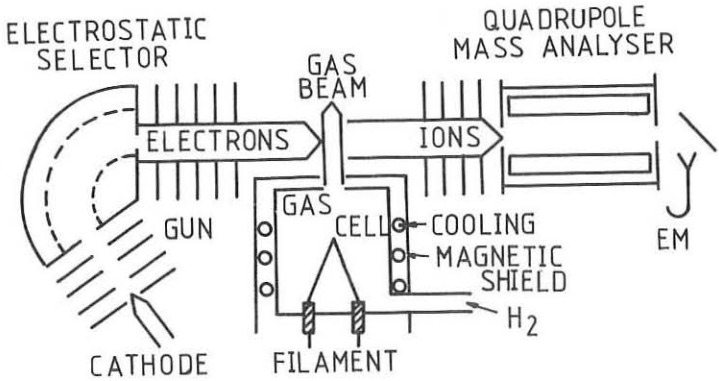

Figure 1

The information on the vibrational excitation is obtained by scanning the low energy H^- current vs. electron energy. One example of the H^- yield spectrum in the range of the 4 eV process is shown in Fig. 2. In the case with no appreciable population of higher vibrational states (at room temperature) only the peak at about 4 eV appears resulting from DA to v=0 molecules. The narrow peak is obtained by appropriate tunning of ion optics so that detection efficiency for low energy ions is enhanced. Target molecule excitation results in lower thresholds for DEA and therefore ions at lower energies appear. The relative state distribution can be obtained by deviding the relative peak hights from such spectra by the available theoretical relative peak DEA cross-sections (6), (7). The spectrum from Fig. 2 was obtained with the hydrogen pressure of 0.07 mbar, tungsten filament heated to about 2700K

and without discharge in the gas cell. The relative vibrational state distribution for this case is nearly Boltzmanian with vibrational temperature about 3000 K. This high vibrational excitation is produced by recombination of H atoms formed by thermo-dissociation on the hot filament and H atoms adsorbed on the wall (8). This finding is very important for modeling and developing negative ion sources. Recently, an attempt to use this mechanism for creation of the pre-excited hydrogen molecules in the volume ion source was reported (9).

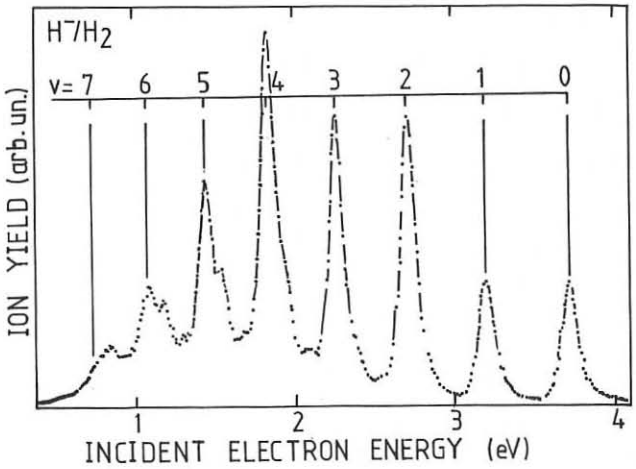

Figure 2.

The experiments performed with the discharge generated between the filament and the cell wall showed relative population increase predominantly for the lower vibrational states when compared to the dicharge "off" case (but with filament "on") (10). Although this finding can not be generalized to the discharges in the volume sources because of different discharge conditions as well as because of the extraction effects present in our experiment, it stimulates further efforts for the study of vibrational population determination under the discharge conditions.

For spectra with almost pure vibrational excitation as the one from Fig. 2, the spectrum analysis is simple, but when the rotational states are appreciably excited as well, appropriate deconvolution is necessary in order to get correct relative state populations.

The dependence of the 14 eV DA process on the vibrational and rotational excitation was studied as well. The experimentally determined near threshold DEA cross-section for

v=1, 2, 3 state of hydrogen molecule is 3.6, 4.5 and <2 times biger than that for v=0 state. This dependence is not so spectacular as for the 4 eV process due to the longer life-time of the negative ion state. The model analysis of these results gave the information on the corresponding negative ion curve for hydrogen and deuterium. The data on the 14 eV process are of importance for diagnostics of the low vibrational states especially for deuterium as the cross-sections for the 4 eV process are very small for this molecule.

R e f e r e n c e s

1. Proceedings of the Fourth International Symposium on Production and Neutralization of Negative Ions and Beams, AIP Conference Proceedings No. 158, J. G. Alessi, Ed., Brookhaven, NY, (1986)
2. Proceedings of the Third European Workshop on the Production and Application of Light Negative Ions, H. J. Hopman, Ed., FOM-Institute, Amsterdam, The Netherlands, to be published, (1988)
3. M. Bacal, Physica Scripta, T2/2, p467, (1982)
4. J. R. Hiskes, in (1), p2, (1986)
5. M. Allan and S. F. Wong, Phys.Rev.Lett., 41, p1791, (1978)
6. J. P. Gauyacq, J.Phys.B., 18, p1859, (1985)
7. J. M. Wadehra, Phys.Rev.A, 29, p106, (1984)
8. R. I. Hall, I. Čadež, M. Landau, F. Pichou and C. Schermann, Phys.Rev.Lett., 60, p337, 1988
9. K.N. Leung, S.R. Walther and W. B. Kunkel, in (2),(1988)
10. I.Čadež, R.I.Hall, M.Landau, F.Pichou and C.Schermann, in (2), (1988)

ELECTRODINAMIC ACCELERATORS USE FOR HIGH TEMPERATURE PLASMA PRODUCTION

N.I.Archipov, A.M.Zhitlukhin, V.M.Safronov, V.V.Sidnev, Yu.V.Skvortsov

I.V.Kurchatov Institute of Atomic Energy, Moscow, USSR

Modern electrodynamic accelerators are able to generate plasma streams with a density of $n = 10^{15} - 10^{16}$ cm^{-3}, a temperature of Te ~ 100eV, Ti ≤ 1000ev, a directed velocity of up to $V = 10^{2}$ cm/s and a total energy above W=100kJ. Such plasma sources are interesting for thermonuklear research and might be used for a hot plasma creation in open systems. In this case it is needed to slow down plasma stream and to convert its kinetic energy into the thermal energy of the stationary plasma.

The possibility of the stream energy thermalisation by means of the plasma collision with the material target, the magnetic barrier and the counterstreaming plasma is studied in this work. It should be noted also that investigation of the collisionless plasma streams with $\beta \sim 1$ has its own physical interest.

Experiments were carried out at the MK-200 device consisted of two plasma guns with pulsed gas admission (hydrogen, deuterium). Guns are fed from two 1150 μF capacitor banks. The operating voltage U_c is varied from 15 to 30 kV. The discharge current attains a peak value in ~ 6,5 μs. On leaving the gun plasma stream is transported along 30 cm diameter metallic liner with the longitudinal magnetic field up to B_z=20 kG. So the plasma streams are isolated from the liner walls by the magnetic field.

A set of diagnostic tools such as Mach - Zehnder interferometer, magnetic probes, pressure detectors, Thomson - scattering apparatus (λ =6943 Å), neutron and X - ray detectors, ca-

lorimeters are used for plasma parameters measuring.

1. Interaction with the material target.

In this experiment the only regime is used (U_c= 15kV, B_c= 7,2 kG). Targets (plastic, metal) are placed at a distance of 100 cm from the gun muzzle. Parameters of the plasma stream leading - edge are as follows: velocity of V= $3,8*10^7$ cm/s, density of n =$8*10^{15}$ cm^{-3}, diameter of D=9cm, temperature of T_i+T_e =250 eV, T_e/T_i =0,1-0,2. Longitudinal magnetic field is almost absent ($B << B$) in the leading - edge of the plasma stream.

It is found that plasma - target interaction is accompanied by the shock wave formation. Shock front propogates upsteam and causes relaxation of the kinetic stream energy. The plasma pressure behind the shock is of P=$8*10^{18}$ eV*cm^{-3} and corresponds to the stagnation pressure (taking into account the plasma radial expansion and the magnetic energy increase). It confirms the complete thermalization of the plasma directed energy. The "stationary" plasma life-time does not exceed τ =5-7μ s. Fast cooling is caused by the thermal contact of plasma with the coil material target. This is the principal shortcoming of such thermalization method.

2. Interaction with the magnetic barrier.

Magnetic barrier solenoid (50 cm in length) is placed at 200 cm from the gun and generates the mirror magnetic field up to Bm =20kG. Plasma streams are transported in a longitudinal magnetic field of B =6.4kG from the gun to the magnetic barrier. Plasma stream parameters are the following: n =(2-3)*10^{15} cm^{-3}, V =(4-5)*10^7 cm/s, T = T_i + T_e =0.7keV, D =11cm, total energy of W =35kJ, internal magnetic field Bi << Bo. At the mirror ratio of k = Bm/Bo =3, ($Bm^2/8\pi \approx \rho V^2/2$) the energy of the plasma stream penetrating through the magnetic barrier

does not exceed 50% of the total stream energy. Plasma is partially reflected and thermalized by the mirror magnetic field. Plasma with $n = (3-3.5)*10^{15}$ cm^{-3}, T =1.3keV, D =15cm is produced in front of the barrier. The deuterium plasma is the neutron source ($N = 10^9$ neutrons per shot). The plasma life-time is of $\tau = 15\mu$s.

There are two essential shortcomings of this thermalization method. In the first place, a great magnetic field is needed for effective energy relaxation. Secondly, magnetic field penetrates rapidly into the hot plasma. The penetrating time is significantly less the Bohm diffusion time. This fact indicates that well-developed turbulence seems to arise.

3. Collision of two plasma streams.

Plasma guns are placed at a distance of 700cm opposite each other and are joined by a liner with homogeneous longitudinal magnetic field up to 16kG. Plasma streams with $n = (1-5)*10^{15}$ cm^{-3}, $V = (4-8)*10^7$ cm/s, Te =10-100eV, Ti =100-1000eV, Bi << Bo collide in the central section of the liner.

The complete thermalization of the plasma kinetic energy resulting in the creation of the stationary high temperature plasma takes place independently on the gun s regime and the magnetic field strength. At Vo =30kV, Bo =16kG, a plasma column of 200 cm in length with $n = 4*10^{15}$ cm^{-3}, Ti =2-2.5keV, Te =200-300eV, W =70kJ, $\beta \sim 1$ is produced. A maximum neutron yield $5*10^{10}$ neutrons per shot is achieved.

Transverse diffusion coefficient of the hot plasma does not exceed $D_\perp = (1/5-1/10)Db$, where Db = ckT/16eB. It should be noted that with increased magnetic field a value of $D_\perp$ reduses more sharply than $\sim 1/B$. It is very likely that $D_\perp$ will be significantly less Db at a greater magnetic field.

Plasma life-time is of $\tau = 20-25\mu$s and exceeds the time of the longitudinal spread at the thermal velocity

τ_{th} = L/2V ≈ 2 μs. It is explained by the effect of the plasma stream tailes on the hot plasma expansion.

Conclusion.

The plasma stream interaction with the material target, the magnetic mirror and the counterstreaming plasma is accompained by a formation of the shock wave which causes kinetic energy thermalization. This result is not obvious in advance because the ion mean free path calculated for directed particle energy $\lambda_i = 5*10^{12} \varepsilon^2/n$ and the ion collision time τ_i in any case are much larger than a width of shock front d < 20cm and its formation time τ =1-2 μs. It confirms the collisionless turbulent nature of the shock wave. It isn't known what plasma instability is responsible for the shock front formation. Additional experiments are needed. Nevertheless the data obtained permit to use powerfull electrodynamic accelerators for high temperature plasma production.

Diagnostics H

SCATTERING OF MILLIMETRE-SUBMILLIMETRE WAVES FROM THE TORTUS TOKAMAK PLASMA

M.D.Bowden, G.F.Brand, I.S.Falconer, P.W.Fekete, B.W.James and K.J.Moore

School of Physics, University of Sydney, N.S.W., 2006, Australia

INTRODUCTION

A submillimetre molecular vapour laser and a tunable gyrotron have been used as sources of millimetre-submillimetre radiation in a series of plasma scattering experiments on Sydney University's TORTUS tokamak.

Two experiments are described here. The first studied the density fluctuations associated with Mirnov oscillations. The second studied the kinetic Alfven waves which appear when an Alfven wave is launched into the plasma to heat it.

The suitability of the two sources for scattering is discussed.

THE SOURCES AND THE SCATTERING SYSTEM

The plasma is a hydrogen plasma in the small TORTUS tokamak [1] whose dimensions and typical operating conditions are major radius = 0.44 m, minor radius = 0.10 m, B_ϕ = 0.85 T, I_ϕ = 18 kA and pulse duration $\approx$ 15 ms.

The submillimetre laser is a formic acid vapour laser, optically pumped with a CO_2 laser, which delivers 10 mW at 433 μm. The experimental arrangement is shown in Fig. 1. The laser beam is focused to a beam waist in the equatorial plane. The design of the optical system permits the minor radius at which the beam passes through the plasma to be easily selected.

After passing through the plasma, the laser beam is focused onto a Schottky diode detector.

The gyrotron, GYROTRON III [2], can deliver tens of watts of power and is tunable over the frequency range 75 to 330 GHz (4 to 0.9 mm). It is tuned by raising the magnetic field of the 12 T superconducting magnet. One cavity resonance after another is excited, the adjacent strong cavity resonances being approximately 10 GHz apart. The experimental arrangement is shown in Fig. 2. The quasi-optical (Vlasov) antenna converts the high-order waveguide modes into a well-collimated, linearly-polarized beam. This beam is intercepted by a second waveguide and the beam that subsequently emerges from the other end is, to a good approximation, gaussian. After passing through the plasma, the signal is detected by a diode detector.

A magnetic probe at the edge of the plasma picks up poloidal magnetic field fluctuations.

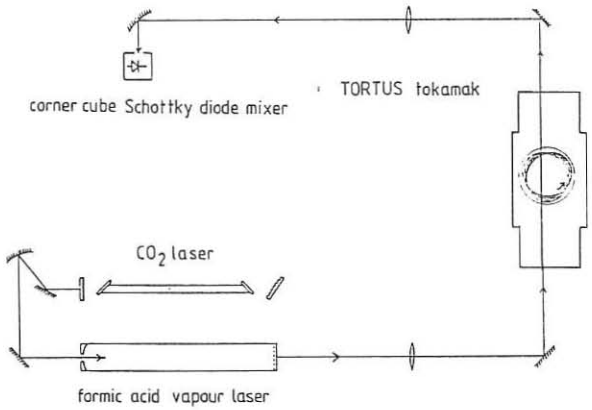

Fig. 1 Scattering experiment with the submillimetre laser.

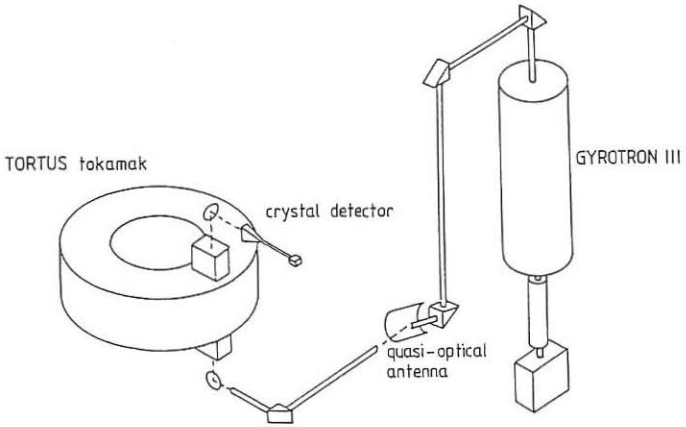

Fig. 2 Scattering experiment with the gyrotron.

MIRNOV OSCILLATIONS

In both the submillimetre laser and gyrotron experiments, the signals from the detector and the magnetic probe are amplified with a broadband amplifier. Data taken over a 2 ms window during the lifetime of the plasma is then fourier-analysed to obtain power spectra. Typical results are shown in Fig. 3.

The oscillation revealed by the magnetic probe is due to rotating magnetic island structures which can develop on rational surfaces in tokamaks. The peak in the detector spectrum is due to scattering from perturbations associated with these structures.

The scattered signal is largest when the beam passes through the

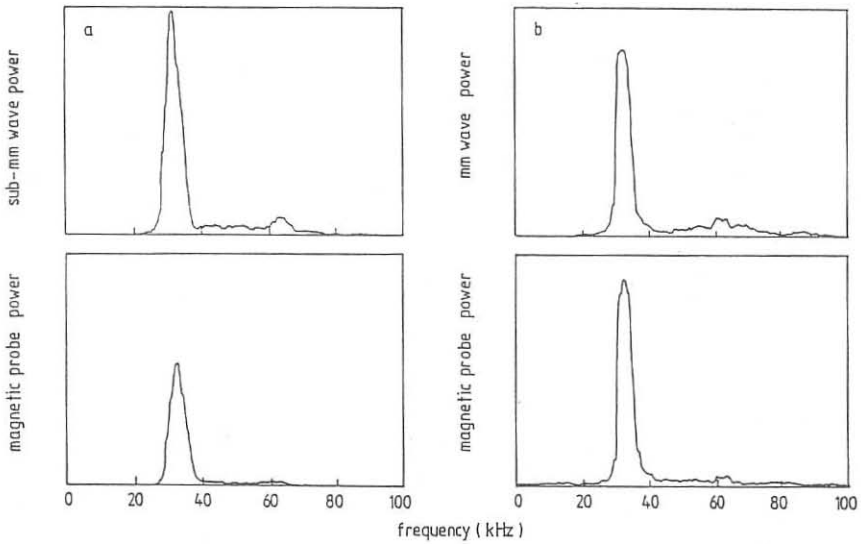

Fig. 3 Millimetre-submillimetre wave and magnetic probe power spectra. (a) Using the submillimetre laser, and (b) using the gyrotron operating at 175 GHz.

equatorial plane at approximately 0.7 of the minor radius when more of the rational surface lies within the beam and the effective scattering volume is a maximum.

KINETIC ALFVEN WAVES

This diagnostic is at present being applied to a compressional Alfven wave heating experiment on the TORTUS tokamak in which 60 kW of rf power at 5 MHz is launched into the plasma [3]. Mode conversion to the kinetic Alfven wave is expected to occur at the Alfven resonance layer [4] and we investigate the scattering from the density perturbations of this wave.

The signal from the detector is amplified with a narrow-band amplifier tuned to 5 MHz. The scattered signal is small and is revealed only when the results of many shots are averaged. This investigation is continuing.

DISCUSSION

The gyrotron has the advantage of much higher power and tunability. However, because the wavelength of the submillimetre laser is smaller, it can provide a narrower beam. This means that it can give better spatial resolution and, more importantly, there are no complications due to aperturing of the beam by the tokamak ports.

The conditions on the wavenumber k (= $2\pi/\lambda$) for far-forward scattering are similar for the two sources. The requirement that the centre of the scattered beam lies within the (1/e maximum intensity) radius of the incident beam gives the condition on the perpendicular part, $k_{\perp}$. For the submillimetre laser where the radius at the waist is 4.2 mm,

$k_\perp$ must be less than 430 m^{-1}.

In the case of the gyrotron, the radius of the beam at the mouth of the waveguide is 13.2 mm and, if aperturing is ignored since the narrow dimension of the tokamak port is perpendicular to the scattering plane, $k_\perp$ must be less than 940 m^{-1} for all wavelengths.

For the Mirnov oscillation experiment $k_\perp < 40\ m^{-1}$ and the condition is easily satisfied.

$k_\perp$ for the kinetic Alfven waves depends on all the plasma parameters, the frequency and toroidal wavenumber of the waves being launched. Fig. 4 shows $k_\perp$ for a plasma with a parabolic density profile ($n_0 = 1x10^{19}$, $2x10^{19}\ m^{-3}$), a parabolic-squared temperature profile (T_{max} = 100 ev, T_{min} = 20 ev), a uniform magnetic field (0.75 T) and a wave frequency of 5 MHz, calculated according to the dispersion equation

$$k_\perp^2 a^2 = \omega^2 - \Omega^2(1 - \omega^2/k_\parallel^2 V_A^2).$$

It can be seen that there are a wide range of conditions such that $k_\perp$ satisfies our requirements for far-forward scattering.

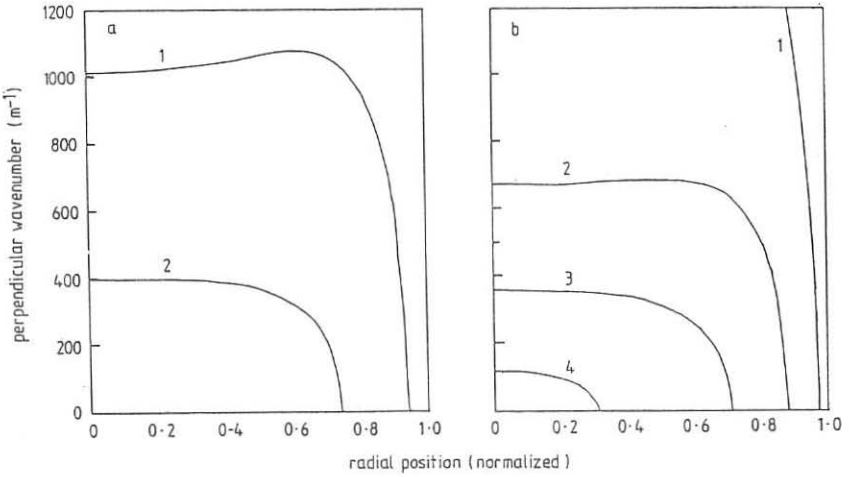

Fig.4 $k_\perp$ vs. radial position. The parameter is n the toroidal mode number. (a) $n_0 = 1x10^{19}\ m^{-3}$, (b) $n_0 = 2x10^{19}\ m^{-3}$.

REFERENCES

[1] CROSS R.C., JAMES B.W., KIRBIE H.C., LEHANE J.A. and SIMPSOM S.W. Atomic Energy in Australia 24 2 (1981).

[2] BRAND G.F. "Tunable Gyrotrons" in INFRARED and MILLIMETER WAVES (ed. K.J. Button, Academic Press) Vol. 14, pp 371-408 (1985).

[3] BALLICO M.J., BRENNAN M.H., CROSS R.C., LEHANE J.A. and SAWLEY M.L. in the proceedings of this conference.

[4] DONNELLY I.J., CLANCY B.E. and CRAMER N.F. J. Plasma Phys 34 227-246 (1985) and 35 95-106 (1986).

A MICROWAVE REFLECTOMETER FOR THE TJ-II FLEXIBLE HELIAC

A. P. Navarro, E. Anabitarte , C. Alejaldre and F. Castejón

Asociación **EURATOM / CIEMAT**, 28040 Madrid, SPAIN

INTRODUCTION

Microwave reflectometers have demonstrated their capability to determine electron density radial profiles in tokamaks (1, 2). Remarkable characteristics make them very suitable for this application : they can use only one channel reducing drastically the requirements in access to the plasma and, by using fast enough swept power supplies for the microwave source, (in the current state of the art, sweeping times are in the order of 1 ms), it is possible to obtain several n_e profiles in a single discharge. Besides, by keeping the microwave beam frequency constant, it is possible to study n_e fluctuations at the radial position where the reflection, for that particular frequency, takes place. Changing the frequency, the radial profile of these fluctuations can be deduced (3).

This diagnostic technique is based in the measurement of the phase difference between the incident and the reflected waves, at the layer where n_e reaches the cutoff condition. This phase change is given by (4):

$$\Delta\Phi = 4\pi\frac{f_0}{c}\int_a^{r_c}\sqrt{\varepsilon}\cdot dr - \frac{\pi}{2} \qquad [1]$$

where f_0 is the incident wave frequency and ε its propagation index in the plasma.

The radial position of the cutoff layer, r_c, is deduced from the measurement of $\Delta\Phi$, and n_e can be obtained from the fact that wave frequency (f_0) equals the cutoff value at this radial position:

$$f_0 = f_{pe} \qquad [2] \qquad O-mode \qquad f_0 = \frac{1}{2}\left(f_{ce} + \sqrt{f_{ce}^2 + 4f_{pe}^2}\right) \qquad [3] \qquad X-mode$$

where f_{pe} and f_{ce} are the plasma and cyclotron frequencies, respectively.

In this paper microwave reflectometry in stellarator is studied in detail for the first time by its application to the TJ-II flexible heliac (5). The effect from the characteristic magnetic structure of this device on the propagation of the two possible modes ,O and X, of the reflectometer have been studied, deducing the most adequate angles for beam launching. Estimations for the achievable spatial resolution are presented and ray tracing calculations (6) have been used to determine the antenna requirements.

Electron density fluctuation measurements with this technique in TJ-II have been also considered, deducing a model for data analysis and estimations for the achievable spatial resolution and sensitivity.

TJ-II n_e PROFILE DETERMINATION

A cylindrical model for TJ-II with the center at the hard core has been used to simulate its magnetic structure (7):

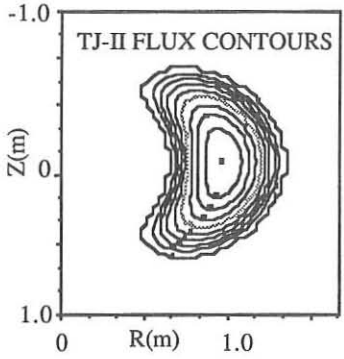

$$B_v^r = \left(a_1 I'_1\left(\frac{r}{R_0}\right) + b_1 K'_1\left(\frac{r}{R_0}\right)\right)\cdot \sin\left(\theta - \frac{z}{R_0}\right) \quad [4]$$

$$B_v^\theta = \frac{\mu_0 I}{2\pi r} + \frac{R_0}{r}\left(a_1 I_1\left(\frac{r}{R_0}\right) + b_1 K_1\left(\frac{r}{R_0}\right)\right)\cdot \cos\left(\theta - \frac{z}{R_0}\right)$$

$$B_v^z = B_0 - \left(a_1 I_1\left(\frac{r}{R_0}\right) + b_1 K_1\left(\frac{r}{R_0}\right)\right)\cdot \cos\left(\theta - \frac{z}{R_0}\right) \quad [6]$$

$$\psi_v = \frac{B_0 r^2}{2R_0} - \frac{\mu_0 I}{2\pi}\ln r - \left(a_1 r I'_1\left(\frac{r}{R_0}\right) + b_1 r K'_1\left(\frac{r}{R_0}\right)\right)\cdot \cos\left(\theta - \frac{z}{R_0}\right) \quad [7]$$

Fig.1-TJ-II Flux contours.

where B^r, B^θ and B^z are the magnetic field components and ψ the helical flux, for vacuum. Fig.1 shows the TJ-II magnetic structure deduced with this model. Electron density can be deduced by assuming it constant on flux surfaces:

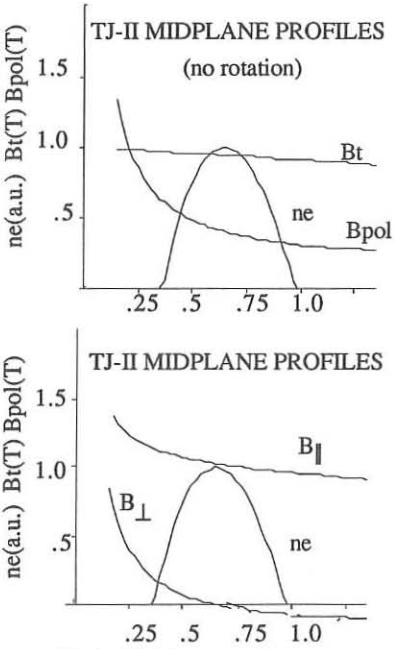

Fig.2- Midplane profiles

$$n_e = n_{e0}\left(1 - \psi(\rho)/\psi(\rho_0)^{\alpha_1}\right)^{\alpha_2} \quad [8]$$

Fig.2-a presents the equatorial midplane profiles for ne and the toroidal and poloidal components of the magnetic field . The poloidal component is comparable to the toroidal one, due to the high current in the hard-core of the device, making difficult to separate O and X modes in the microwave propagation.This mixed-mode propagation could be very useful to determine local values of magnetic field profiles along the propagation line providing, if the adequate theory for data analysis is developed, radial profiles for induced currents in the plasma. Nevertheless, to preserve mode purity the waveguide can be rotated to align it with the direction of the transverse field, Fig. 2-b presents the same magnitudes than 2-a for a 23^0 rotation. In this situation the perpendicular field can be neglected

Using this set-up, the cutoff frequencies for the O and the X mode, propagating in the equatorial midplane, have been calculated assuming parabolic profiles with different central densities, (Fig.3).

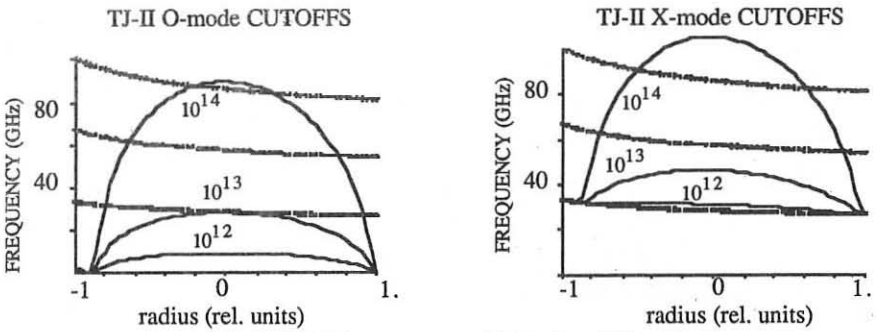

Fig.3.- TJ-II frequency cutoffs for O and X modes

These results show that the standard instrumentation used in tokamak reflectometry can be applied to TJ-II, covering the full operational space of the device, and the effect from cyclotron absorption is very localized.

Spatial resolution for these measurements have been calculated assuming it as the length of the reflection layer, given by (4):

$$\Delta = \left(\frac{\lambda}{2\pi \left(\frac{d\varepsilon}{dr} \right)^{-0.5}} \right)^{2/3}$$

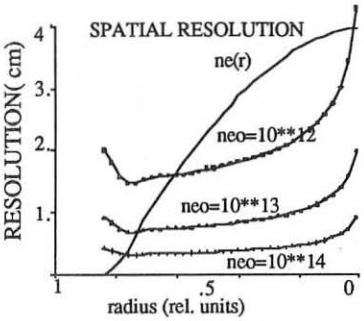

Results are presented in the Fig. 4 for the three central densities considered (10^{12}, 10^{13} and 10^{14} cm^{-3}) and parabolic profile. Resolution improves with density gradients and, so with its central value, and it is always better than 2 cm.

Fig.4 Spatial resolution

n_e FLUCTUATION ANALYSIS

Density fluctuations can be also analyzed by keeping frequency constant in the reflectometer. Changing the frequency in steps during the discharge plateau, it would be possible to determine the fluctuation radial profile. Simulation of the reflectometer signal,using expression [1], have been addressed for density perturbations of the type:

$$\delta_n = A_n \exp\left(- \left| \frac{r - r_s}{\lambda_s} \right| \right) \exp(-i\omega t)$$

where A_n, r_s, λ_s and ω are the perturbation amplitude, radial location, radial width and frequency, respectively.

Simulation results are presented at Fig.6 for a single mode and a multiple mode perturbation. Main conclusion is that reflectometry can detect the existing perturbations, determining location and relative amplitude.

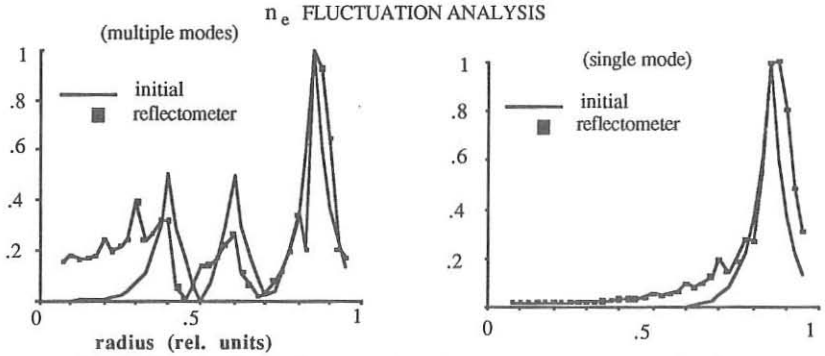

Fig.6.- Density fluctuation reconstruction from reflectometer signals.

RAY TRACING CALCULATION

The ray-tracing code RAYS[6,7] has been used to follow a single ray propagating at 28 GHz into a plasma characteristic of TJ-II and with central density changing from 0.9 to 2.0 x 10^{13} cm^{-3}.It is shown that antenna diameters of the order of 5 cm. will be able to pick-up the return signal for central densities in excess of 1.2x 10^{13} cm^{-3}

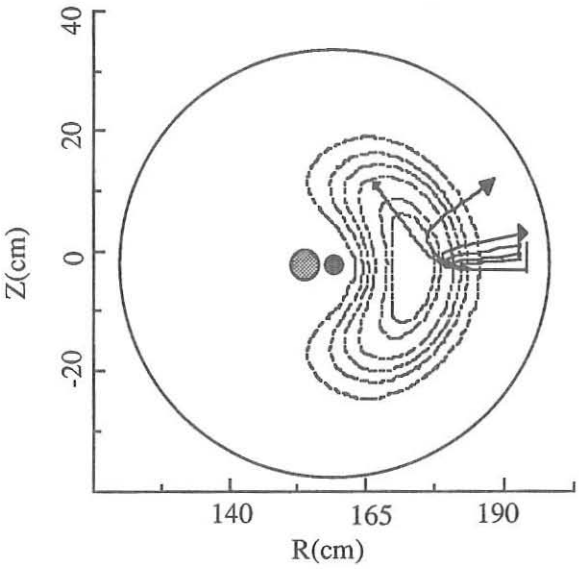

REFERENCES

1.-Simonet, F., Rev. Sci. Instrum. 56, 664, 1985
2.-Bottolier-Curtet, H. and Ichtchenko, G., Rev. Sci. Instrum. 58, 539, 1987
3.-Anabitarte, E. et al. Bull. Am. Phys. Soc.,32, 1938,1987
4.-Cavallo, A. and Cano, R. Report EUR-CEA-FC 1137, 1982
5.-Guasp J., et al., Controlled Fusion and Plasma Physics (Proc. 12th Europ.Conf. Budapest, 1985), Vol. 1, European Physical Society 441, 1985
6.-C. Alejaldre et al. This conference
7.-Batchelor, D.B. et al. RAYS: A Geometrical Optics Code for EBT, Oak Ridge National Lab., Rep. ORNL/ TM-6844 , 1982
8.-Harris, J.H., et al., Nucl. Fusion 25, 623 ,1985

INVESTIGATIONS ON ECRH VIA 140 GHZ COLLECTIVE SCATTERING IN A TOKAMAK PLASMA

U.Tartari and M.Lontano

Istituto di Fisica del Plasma, CNR-ENEA-EURATOM Association
Milano (Italy)

1 - INTRODUCTION

Recent developments in gyrotron technology have made available high-power, millimeter wavelength sources with stable frequency output and long pulse, narrow linewidth capability. Besides opening the way to ECRH experiments at high density and high magnetic field, these developments enlarge the perspective for plasma diagnostics /1/. Collective Thomson scattering (CTS) will be extensively applicable to tokamaks both in ohmic and r.f. heated conditions.

Within the wide class of plasma "perturbations" open to CTS investigation, ECRH plays a preminent role. Basic effects of ECW propagation and absorption, as collective oscillations, may be directly verified by this technique.

Although no definite theory of CTS in ECR heated plasmas is available up to now to support quantitative estimates, signal levels due to conversion of an externally injected extraordinary mode (XM) into electron Bernstein modes (driven BM: DBM), as predicted by full-wave theory, may be reasonably expected to be strong, so allowing measurement even in non optimized conditions. A similar experiment is planned on Text /2/ with a 245 GHz laser source.

A second CTS feature is potentially of interest for ECRH investigations. The spectral density function for CTS at high frequency being $S(r,\underline{k},\omega) = 1/|\varepsilon(r,\underline{k},\omega)|^2$, where ε is the dielectric function of the magnetized plasma /3/, a resonant feature is expected at the local upper-hybrid frequency $\omega_{uh}(r)$ where $\varepsilon(\omega_{uh}) \cong 0$. This feature, which is due to spontaneous Bernstein waves (SBM), is not specific of the heated phase and then the associated scattered signal levels and S/N may be estimated from scattering theory. By numerical simulations, the sensitivity of the SBM resonances to ECRH-induced local variations of n_e (density drop) and T_e (bulk heating), and to suprathermal tails has been positively verified /4/. The effect of these last may be discriminated against local bulk heating by comparison with ECE data.

Preliminary feasibility evaluations of ECRH studies via CTS are reported here with reference to the tokamak Thor II (R_o = 52 cm, a = 19 cm), where a 28 GHz (200 kW, 10 msec) ECRH system is available and implementation of a 140 GHz (200 kW, 100 msec) gyrotron is being considered for the near future.

Although not exclusive, CTS+ECRH experiments in small size, low field (1 T) tokamaks are encouraged by reduced beam spread and a favourable frequency condition ($\omega / \Omega_e = 5$) leading to low cyclotron-harmonic noise in the measure.

The following effects will be considered for measurement on Thor II: (a) ECRH induced microturbulence; (b) 28 GHz driven wave-activity (DBM); (c) $\omega_{UH}(r)$ resonant feature (SBM).

2 - EXPERIMENTAL SET-UP

The XM at the cyclotron frequency (28 GHz) will be injected from the high field side. The 140 GHz wave will be top-launched and radial scanning will be ensured by a rotating parabolic mirror. Several receivers are needed to meet the different goals: (a) a homodyne detection chain to provide down-conversion of the high-level microturbulent spectrum before signal processing by a transient digitizer; (b) a first heterodyne chain, with automatic frequency control, IF amplification and a spectrum analyzer, to detect DBMs at 28 GHz; (c) a second heterodyne chain to detect the low-level resonant SBMs. In contrast to (b), this last chain must operate at maximum sensitivity and thus cryogenic cooling will be used for the mixer and IF-amplifier sections. A set of local oscillators and IF amplifiers will be required in (c) to cover the whole frequency range spanned by the $\omega_{UH}(r)$ resonance ($\Delta\nu \cong 20$ GHz) at 1 GHz steps.

3 - SENSITIVITY AND NOISE

Either of the two scattering bands (left: L, right: R), determined by 1) the selection rules for $\underline{k}$ and ω, and 2) the phase velocity of the fluctuation waves, may be used in principle for coherent detection. In the SBM case, if isotropic emission is assumed, both scattering bands are effectively available. In the DBM case where the wave is backward, in contrast, only the R band is compatible with the scattering geometry. The selected band is down-converted in all cases to ensure the $\nu_{IF} < 10$ GHz required for low-noise amplification.

Plasma and system noise have been estimated for representative Thor II plasma parameters compatible with XM injection ($n_{eo} = 1.5\times10^{13}$ cm^{-3}, $T_{eo} = 200\div400$ eV, standard profiles, and $r = a/2$ when required). The more critical case of SBM detection in the L band has been considered for testing the sensitivity achievable. For a $T_{SA} = 7\times10^5$ K equivalent noise contribution from the spectrum analyzer, $G = 10^3$ IF amplifier gain, and $C = 0.25$ mixer conversion factor, a total noise temperature at the input of the equivalent noise-free receiving system of $T_{Syst} = 3.5\times10^3$ K is obtained at $r = a/2$.

Cyclotron harmonic noise at the corresponding local upper-hybrid frequency, $\nu_{UH} = 37$ GHz, comes from 3rd harmonic. Multiple reflections and polarization scrambling at the walls have been taken into account in a slab model, with

scrambling coefficients p = 0.15 (change) and q = 0.7 (conservation). Only ordinary mode (OM) emission needs to be considered since operation in this mode optimizes the scattered signal and a single mode receiving antenna may be used. Fig.1 shows that 3rd harmonic plasma noise is at most comparable to system noise. For the representative point we get $T_{rad}^{(OM)} \simeq 1.5\times10^3$K. System-noise-limited operation should therefore be allowed in Thor II conditions.

The spectral density function integrated over linewidth,

$$S_o(k) = \frac{2\pi}{\alpha^2} \cdot \frac{\omega_{pe}^2/\Omega_e^2}{1+\omega_{pe}^2/\Omega_e^2} \quad ,$$

where $\alpha = 1/k\lambda_D$ is the scattering parameter, has been divided by the number of spectral resolution intervals (3 MHz) included in the estimated resonance linewidth ($\sim$30 MHz). The $L_s\Delta\Omega$ (length of the scattering volume times collection solid angle) factor in the relationship between scattered power P and S /3/ is estimated from the coherent and k-resolution conditions, conservatively taking a resolution factor of 5. The S/N given in Fig.2 for three electron temperatures is for P = 100 kW and is normalized to $\Delta\nu_{IF}$ = 1 GHz and $T_n = 10^3$K. The effective average S/N is of order 10^3 for $\Delta\nu_{IF}$ = 3 MHz and a $T_n = (3.5+1.5)\times10^3$K total noise. Fig.3 shows that the average S/N is almost constant in the temperature range of interest for Thor II and that it strongly decreases with increasing electron temperature in plasma-noise limited systems covering the same range of plasma parameters.

4 - WAVE-VECTOR MATCHING

For CTS at large frequency off-sets the matched fluctuation wave-numbers and angles are frequency dependent (non-Bragg regime). Wave-numbers ranging up to 50 cm^{-1} in the L band and up to 60 cm^{-1} in the R band can be matched by varying the scattering geometry. The corresponding angles between the incident and the fluctuation wave-vector range from 30° to 60° (L band) and to 100° (R band) respectively. Inspection of the dispersion relation relevant to BMs in perpendicular propagation, on the other hand, shows that larger wave-numbers (up to more than 100 cm^{-1}) than those matched by the scattering apparatus are displayed by the BMs.

Wave-number matching in the SBM case is not a problem, however, since $k_\perp$ coupling must be ensured near the local upper-hybrid point (vertical branch of the dispersion relation), where a large range of low $k_\perp$ values is crossed in a short radial interval. In the DBM case in contrast $k_\perp$ matching in principle is possible only in a limited region near the 28 GHz upper-hybrid layer. Due to the relatively high power levels at which mode conversion is expected, however, monitoring of the DBM should not be too critical

even with partial mismatching. Finally, matching to the electrostatic component of the residual XM, if any, should be not critical since wave-numbers here are low.

5 - CONCLUSIONS

Good S/N should be attainable in CTS+ECRH experiments on Thor II due to the very low cyclotron harmonic plasma noise. Criticality of wave-number matching for the DBMs does not seem to preclude monitoring of these waves. Detailed information on the ECRH absorption mechanisms, local plasma parameters, suprathermal content, and on microturbolence developped during ECRH should therefore be obtainable by CTS at 140 GHz.

REFERENCES

/1/ - Woskow P.,et al., Rev.Sci.Instr.,56,914,(1985).

/2/ - Peebles W.A., et al., Rev.Sci.Instr.,57,1980,(1986).

/3/ - Sheffield J.,"Plasma scattering of electromagnetic radiation", Academic Press,N.Y.,(1975).

/4/ - Lontano M. and Tartari U.,"Simulations of upper hybrid resonances in collective scattering at 140 GHz", IFP Rep.88-7,(1988).

FIG.1: 3rd harmonic radiation temperature (K) vs radial position r/a.

FIG.2: Normalized average S/N vs radial position r/a.

FIG.3:(1) receiver limited, (2) plasma limited, (3) total S/N vs central electron temperature (eV).

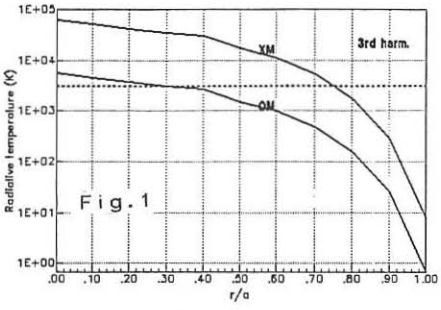

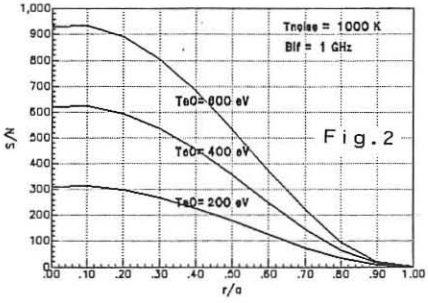

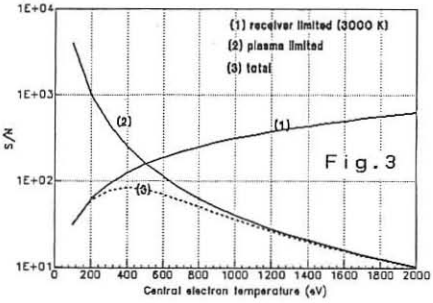

where j_{isot} is the emissivity connected with the isotropic part f(p) of the distribution, and A accounts for the anisotropy. For the specific case in which f(p) is a relativistic Maxwellian, one obtains[5] (in the limit of tenuous plasma)

$$j_{isot}^{(X,O)}/j_o = \frac{a(\mu)\ \mu^{3/2}}{4\sqrt{\pi}\ (1+T^2_{(X,o)})\sin^2\theta}\quad (\gamma_o{}^2-1)^{3/2}\ (1-\tilde{\beta}_o{}^2)^{1/2}\ \ Z_o{}^{2n_o}\ \ e^{-\mu(\gamma_o-1)}\cdot$$
$$\cdot\ \{[(1-\tilde{\beta}_o{}^2)^{1/2}+\frac{T_{(X,o)}}{\gamma_o}\cos\theta]^2+\beta_o{}^2\ h^2\ \gamma_o{}^2\ T^2_{(X,O)}\} \qquad (4)$$

whereas the anisotropy factor A is

$$A=\frac{\mathrm{erf}(x_+)+\mathrm{erf}(x_-)}{2\cos\psi_o},\qquad x_\pm=\frac{\cos\psi_o\pm\beta_o\cos\theta}{[2(\sigma^2+h^2)]^{1/2}} \qquad (5)$$

and

$a(\mu)\equiv(\pi/2\mu)^{1/2}\ e^{-\mu}/K_2(\mu)$; $\mu\equiv mc^2/T$; $\gamma_o{}^2\equiv 1+(2\bar{\omega}/\mu)[1+(9\bar{\omega}/2\mu)\sin^2\theta]^{-1/3}$; $\bar{\omega}\equiv\omega/\omega_c$;
$\beta_o{}^2\equiv 1-1/\gamma_o{}^2$; $\tilde{\beta}_o\equiv\beta_o\cos\theta$; $n_o\equiv\bar{\omega}\ \gamma_o(1-\tilde{\beta}_o{}^2)$; $h\equiv(1-\tilde{\beta}_o{}^2)^{3/4}/(2\bar{\omega})^{1/2}$;
$Z_o\equiv z_o\ e^{(1-z_o^2)^{1/2}}/[1+(1-z_o{}^2)^{1/2}]$; $z_o\equiv\beta_o\ \sin\theta/(1-\tilde{\beta}_o{}^2)^{1/2}$;
$T_{(O)}\equiv\mathrm{sgn}(\cos\theta)\ [a+(1+a^2)^{1/2}]=-T_{(X)}{}^{-1}$; $a\equiv\sin^2\theta/2\bar{\omega}|\cos\theta|$.

A different approximation to j_{isot} can be obtained by noting that, when the isotropic part of the distribution is Maxwellian, Kirchhoff's law holds so that $j_{isot}=N_r{}^2(\omega^2T/8\pi^3c^2)\alpha_{isot}$, where α_{isot} is the corresponding absorption coefficient. α_{isot} can be evaluated by making use of the integral representation (with no harmonic expansion) of the dielectric tensor (the second of Trubnikov's formulae) and carrying out the relevant 1D-integration by the saddle point technique. One thus finds[1]

$$j_{isot}^{(X,O)}/j_o=\frac{2\,a(\mu)}{27\sqrt{\pi}}\quad \mu^{3/2}\ \chi\ \{1,\frac{1}{\sqrt{R_o}}-2\ \mathrm{cotg}^2\theta\ (\sin\theta/\chi)^{2/3}\}\ \ e^{\mu-\sqrt{R_o}} \qquad (6)$$

where

$$\sqrt{R_o}\equiv\mu\ (\chi/\sin\theta)^{1/3}\ \{1+\frac{9-10\cos^2\theta}{20\sin^2\theta}\ (\sin\theta/\chi)^{2/3}\},\qquad \chi\equiv 9\bar{\omega}/2\mu\quad (\gg 1)$$

which is appreciably simpler than (4) (the first (second) term in the curly brackets in (6) refers to the X (O) mode).

For propagation perpendicular to the magnetic field, both (4) and (6) yield[1]

$$j_{isot}^{(X,O)}(\omega,90°)/j_o=\frac{2\,a(\mu)}{27\sqrt{\pi}}\ \ \mu^{3/2}\ \chi\ \{1,\frac{1}{\mu\ \chi^{1/3}}\}\ \ e^{-\mu(\chi^{1/3}-1+9/20\chi^{1/3})} \qquad (7)$$

whereas the anisotropy factor (5) reduces to $(\cos\psi_o)^{-1}$.

Numerical analysis. The accuracy of approximations (4)-(6) has been tested by comparison with the exact values. The frequency dependence of the (normalized) emissivity of the X-mode is shown in Fig. 1a for a Maxwellian distribution, for a propagation angle $\theta=60°$ and varying temperature. The exact spectrum (solid line) is shown together with the approximated results from (4) (dashed line) and (6) (double-dashed line). It appears that both approximate formulas (4) and (6) are accurate at (and below) 100 keV, for which approximation (4) is somewhat better than (6), the accuracy tending to become worse at higher temperatures. For a more quantitative comparison we have evaluated the error Δ of a chosen approximation with respect to the exact value, i.e., $\Delta\equiv(j_a-j)/j$, j_a denoting the emissivity corresponding to either approximation (4) or (6). The relative error corresponding to Fig. 1a is shown in Fig. 1b, from which, in particular, it appears that i) for T=100 keV, the error connected with approximation (4) is <5% over most of the continuous part of the spectrum; ii) for T=300 keV, approximation (6) is better than (4) in the frequency-range $\omega/\omega_c\gtrsim 7$, the corresponding error being $\lesssim$20%; more generally, approximation (6) is adequate at frequencies that are the higher

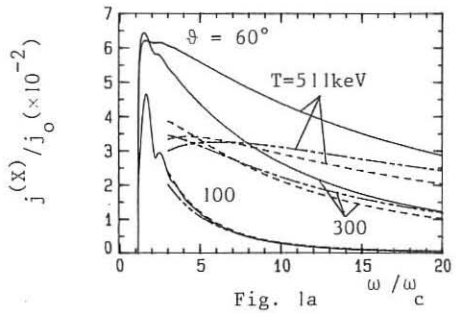

Fig. 1a

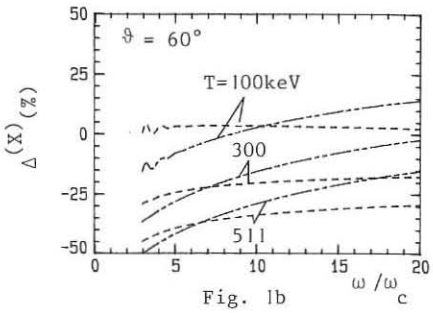

Fig. 1b

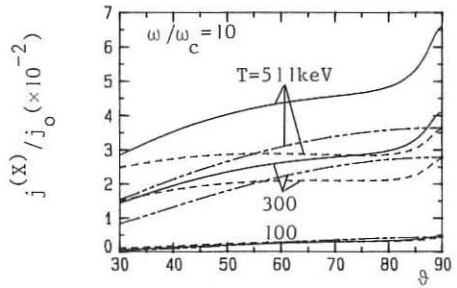

Fig. 2a

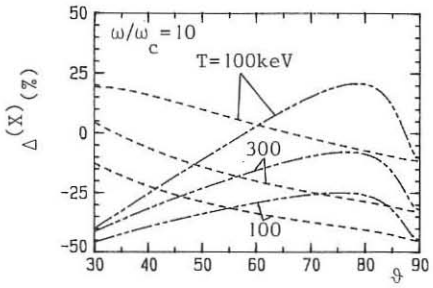

Fig. 2b

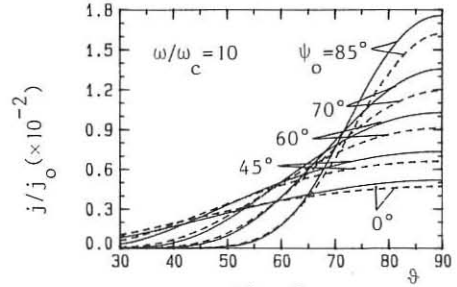

Fig. 3a

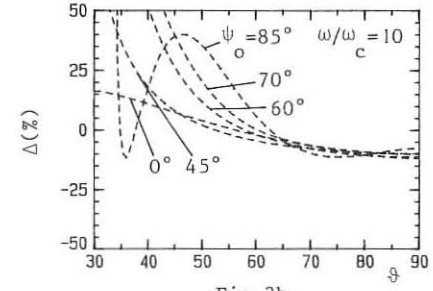

Fig.3b

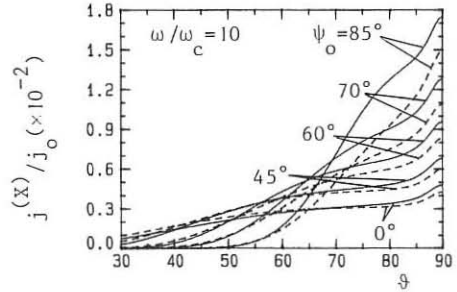

Fig. 3c

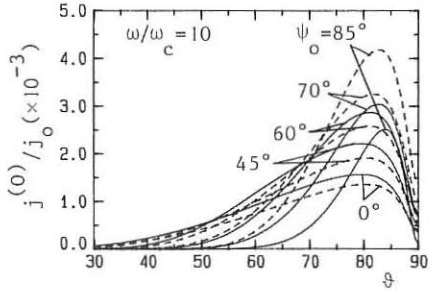

Fig. 3d

REFLECTOMETRY ON JET

R Prentice, P Cripwell*, A E Costley, J A Fessey, J C M de Haas+, A E Hubbard, C A J Hugenholtz+, T Oyevaar, M Paume°, A J Putter+, A C C Sips+ and K Slavin

JET Joint Undertaking, Abingdon, Oxfordshire, OX14 3EA, UK
* On attachment from Imperial College of Science and Technology, London
+ FOM Instituut voor Plasmafysica, Rijnhuizen, Nieuwegein, Netherlands
° CEA Cadarache, St Paul lez Durance, France

INTRODUCTION

The reflectometry work on JET has two components. One is the development of a multichannel instrument to probe the plasma along a major radius with radiation propagating in the ordinary (o) mode (E ∥ B) [1]. This system is currently being installed and commissioned and preliminary results have been obtained with four of the probing channels. In addition, exploratory experimental work with radiation propagating in the extra ordinary (e) mode (E ⊥ B) is in progress. We report on both aspects of the work in this paper.

THE MULTICHANNEL O-MODE REFLECTOMETER

The o-mode instrument, shown in Fig. 1, has 12 discrete frequencies distributed over the 18-80 GHz band, enabling electron densities in the range 0.4-8 x 10^{19} m^{-3} to be probed. This instrument employs specially developed combiner and separator systems [2], antennas [3] and sensitive phased locked heterodyne detection systems [4]. The antennas are mounted within a port on the JET vacuum vessel and a special, oversized waveguide run, employing reduced height E-plane bends, transmits the radiation from the sources and returns the signals to the detectors sited outside the biological shield in the diagnostic hall.

The instrument has two modes of operation: narrow band swept and fixed frequency. When the frequency of each source is swept, at rates up to 5 kHz, the radial positions of the different critical density layers, ie. the density profile, can be determined. When the frequencies are held constant, the magnitude and direction of movement of the critical density layers can be determined with a spatial resolution of a few mm. This mode of operation should be well suited to studies of fluctuations and density changes. The two modes of operation can be interleaved during a plasma pulse.

Signals from three different detection systems are available from each channel [4]: a period detector which measures the difference in group delay between the arms of the reflectometer, a fringe counter which measures phase changes and a coherent detector which includes amplitude variations as well as phase changes, this being equivalent to homodyne detection.

The instrument is currently in the final stages of installation and commissioning but preliminary results have been obtained using the 18, 24,

34 and 39 GHz channels. Fig. 2 shows four coherent detector signals (bandwidth 0-250 Hz) from the reflectometer together with the line integrated density from a transmission interferometer operating at 2 mm wavelength. The effects of plasma sawteeth on the signals are clearly visible. The positions of the critical density layers for the four frequencies have been obtained using density profiles from the FIR interferometer. The general delay observed between the 34 and 24 GHz channels can be used to deduce a particle diffusion coefficient [6,7], the value of which is typically $\sim 0.4\ m^2 s^{-1}$. On the time scale displayed no general delay can be resolved between the 24 and 18 GHz channels since the critical density layers are close together. The 39 GHz signal has a different appearance because its critical density lies inside the mixing radius for the sawtooth collapse.

The effect which an 'H' mode plasma has on the coherent detector and fringe counter signals can be seen in Fig. 3, where the H-alpha signal is also displayed. It will be noted that both the H-alpha and coherent detector signals show a marked reduction in the level of fluctuations during the 'H' mode period. Close examination also shows that small, periodic spikes on the H-alpha signal are correlated with sharp transitions in the reflectometer signals. Over the duration of the 'H' mode, both fringe counter traces show a total movement of about 20 mm. Results from the SXR diagnostic indicate that this movement is likely to be due to a general broadening of the density profile.

These preliminary results show that the basic microwave operation of the system is satisfactory and give encouragement for full system operation.

E-MODE REFLECTOMETRY

Reflectometry using radiation propagating in the extraordinary mode reflecting at the upper cut-off layer F_{uc}, has advantages for some applications over reflectometry using the ordinary mode. The profiles of $F_{uc}(R)$ mean that the inner half of the density profile is often accessible. The wavelength of the probing radiation is smaller and the spatial resolution, a function of the wavelength, is improved. Further, simultaneous measurements in both polarisations can give information on the magnetic field. To exploit these possibilities, a provisional e-mode instrument has recently been constructed on JET.

The reflectometer is set up in a Michelson configuration and can cover either the range 50-75 GHz or 75-110 GHz. The source is a remotely controllable Backward Wave Oscillator. The output frequency can be varied in discrete steps so that a number of different radial positions may be investigated during a single plasma pulse.

The e-mode instrument has measured sawtooth density pulses (Fig. 4) which have also been measured simultaneously by the o-mode system. By comparing the timing of the pulse peaks on the two reflectometers, the total magnetic field at the reflecting radius of the e-mode wave can be determined. The accuracy of the derived value is limited chiefly by the uncertainty of $n_e(R)$. While the present uncertainty in the determination of B_p is large (±50%), it is anticipated that it can be significantly when density profiles from the multichannel o-mode instrument become available.

Frequency spectra of the signals due to density fluctuations up to 40

kHz have also been obtained with the e-mode instrument, with critical radii varied from pulse to pulse. The system is being upgraded, as shown in Fig. 5, to include a second, fixed-frequency source. Waves at the two frequencies will be separated using a dual band-pass filter. It will then be possible for the first time to correlate signals with closely spaced input frequencies ($\Delta F \geq 1$ GHz), in order to study the radial localization of the reflectometer measurements, as well as the radial correlation length of density fluctuations.

REFERENCES

[1] R. Prentice, A.E. Costley, J.A. Fessey and A.E. Hubbard. Course and Workshop on Basic and Advanced Diagnostic Techniques for Fusion Plasmas. Varenna, Italy, September 1986. EU 19797, Vol 2, p451.

[2] F. Mederios and N. Williams. 12th International Conference on Infrared and Millimeter Waves. Orlando, Florida, USA, December 1987.

[3] F. Mederios and N. Williams. 17th European Microwave Conference. Rome, Italy, September 1987, p201.

[4] C.A.J. Hugenholtz and A.J. Putter. Rijnhuizen Report 86-170. FOM-Instituut voor Plasmafysica, Nieuwegein, Netherlands.

[5] A.E. Hubbard, A.E. Costley and C.W. Gowers. J. Phys. E:Sci. Instrum. 20, 423 (1986).

[6] A.E. Hubbard, D. Ward and T.E. Stringer. 13th European Conference on Controlled Fusion and Plasma Heating. Schliersee, April 1986. Vol 10C, Part 1, p232.

[7] A. Gondhalekar, D. Campbell, A. Cheetham, A. Edwards, J. de Haas, A.E. Hubbard, J. O'Rourke, P. Thomas and M. Watkins. This conference.

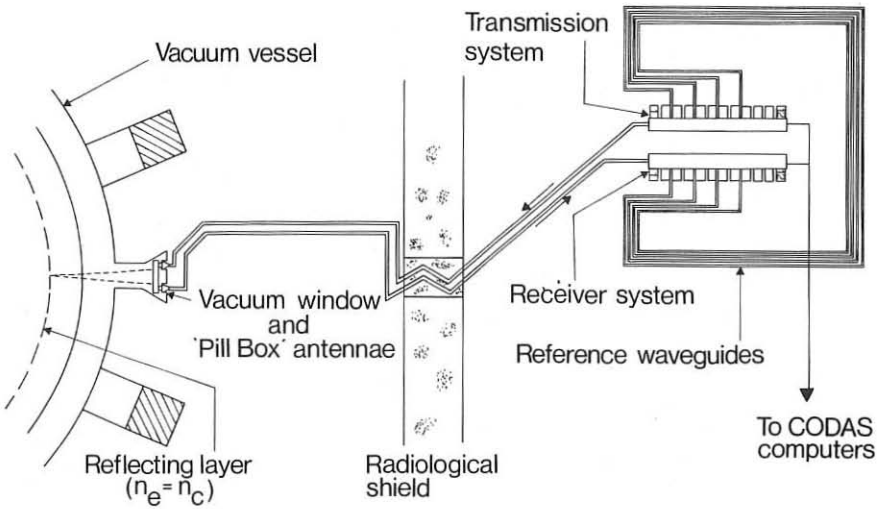

Fig. 1 Schematic of the JET multichannel reflectometer system

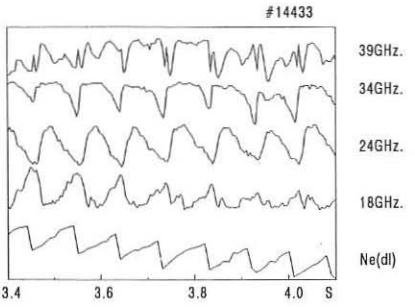

Fig. 2: Sawtooth activity monitored by the coherent detectors and the 2 mm interferometer.

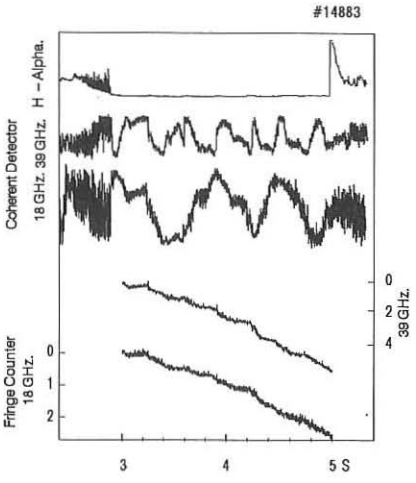

Fig. 3: Coherent detectors, fringe counters and H-alpha signals during an 'H' mode plasma.

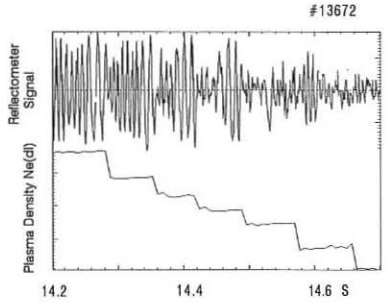

Fig. 4: Sawteeth monitored by the e-mode system working at 40 GHz. Absorption by the second harmonic of the electron cyclotron resonance occurs at 14.64 s.

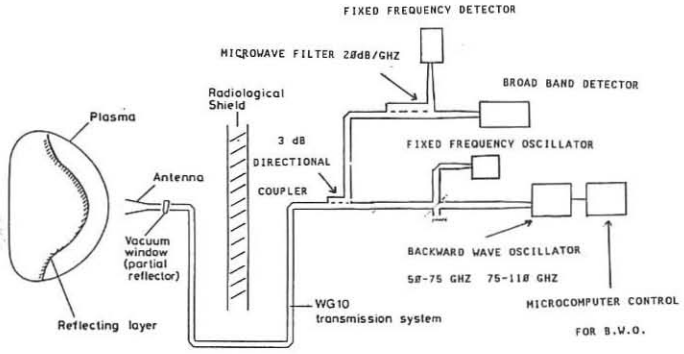

Fig. 5: Schematic of instrument for studies of density fluctuations.

INTEGRATED ELECTRON TEMPERATURE AND DENSITY MEASUREMENTS ON JET

D V Bartlett, D J Campbell, A E Costley, N Gottardi, C W Gowers, K Hirsch[1], S E Kissel, P Nielsen, S Nowak, J O'Rourke, H Salzmann[1]

JET Joint Undertaking, Abingdon, Oxon, OX14 3EA, U K
[1] Universität Stuttgart, 7000 Stuttgart 80, F R G

INTRODUCTION

The plasma electron parameters on JET are measured by three independent diagnostics: LIDAR–Thomson scattering (T_e and n_e), electron cyclotron emission (T_e) and FIR interferometry (n_e). Up to the present, data from these three diagnostics have in the main been treated independently. However, by combining the measurements in a systematic way, it is possible to obtain $n_e(R)$ and $T_e(R)$ with improved precision and reliability. In addition, some new diagnostic possibilities arise.

In this paper, the results of a systematic comparison of the diagnostics over an approximately six month period are presented. The benefits of this comparison are discussed.

MEASUREMENT SYSTEMS

The combination of LIDAR (Light Detection and Ranging) and Thomson scattering techniques yields a new method for obtaining T_e and n_e spatial profiles on large plasma devices, and has been applied for the first time at JET [1]. The system time resolves the spectrum backscattered from a short (300 ps) ruby laser pulse which is directed across the equatorial diameter of the plasma. By using the time of flight principle, it measures the profiles with a resolution of $\approx$ 12 cm (fixed by the pulse duration and the detection bandwidth, 700 MHz) at 2 s intervals throughout the lifetime of the discharge. The uncertainty in the LIDAR measurements is predominantly statistical and results in an uncertainty in T_e of $\approx$ 5%. The shape of the density profile measured with the LIDAR system is known to an accuracy of $\approx$ 5%, whereas the absolute level of the density is subject to a systematic calibration uncertainty of $\approx$ 30%.

The principles by which electron temperature is determined from electron cyclotron emission (ECE) measurements are well known [2]. The electron temperature is measured as a function of radiation frequency, and a frequency to space transformation is carried out using the measured toroidal magnetic field with a correction applied for the internal fields. The principal ECE system on JET is a Michelson interferometer which views the plasma along a sightline parallel to the major radius, 0.13 m below the plasma mid–plane. This instrument has a spatial resolution (both along and perpendicular to the line of sight) of 0.15 m and a temporal resolution of 15 ms. Other ECE instruments provide T_e measurements with space and time resolutions of 0.02 m and 10 μs respectively. Systematic errors dominate the ECE measurements and lead to $\approx$ 10% absolute uncertainty in T_e.

The JET far–infrared interferometer [3] measures the line–integrated electron density along a number of chords through the plasma using the 195 μm radiation from a DCN laser. In the measurements reported here, data from the six vertical chords has been used. The time resolution of the instrument, $\approx$ 100 μs, is determined by the fringe modulation frequency (100 kHz) and the line–integrated density resolution, $\approx 5 \times 10^{17}$ m^{-2}, is set by the minimum detectable phase shift ($\approx$ .05 fringe). The density distribution must be inferred by a generalized Abel inversion of the chordal data, and this can lead to uncertainties in local values of density of up to $\approx$ 10%.

Figure 1 shows the poloidal cross–section of JET, with the viewing directions of the three diagnostics.

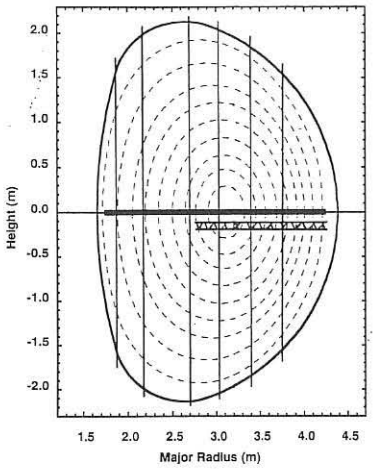

Figure 1: Schematic showing the viewing directions of the three diagnostics in the JET poloidal cross–section. The fine lines are the six vertical interferometer channels, the thick line is the LIDAR sightline, and the hatched zone the region of ECE measurements.

DENSITY COMPARISONS

Direct comparisons of individual measurements have been carried out for a wide range of plasma conditions. Figure 2 shows interferometer and LIDAR results for widely varying profile shapes.

The LIDAR measurement of $n_e(R)$ is essentially localized. On the other hand, the Abel inversion of the interferometer data must assume that the density is constant on the magnetic flux surfaces. The good agreement obtained confirms the validity of the assumptions in the Abel inversion, notably that the flux surfaces correspond to contours of constant density. Moreover, the detail observed when higher order polynomials are used in the inversion routine is shown by these comparisons to be real.

The shape of the density profile measured with the LIDAR is known to an accuracy $\approx$ 5% whereas the absolute level is subject to systematic calibration uncertainty $\approx$ 30%. By normalizing the line integral calculated from the LIDAR profile to that measured directly by the interferometer, it is possible to improve significantly the absolute level of LIDAR density profiles. A systematic comparison of the ratios of the line integrals (without normalization of the LIDAR) over a period of $\approx$ 6 months, figure 3, shows a small decrease in the LIDAR values compared to the interferometer. This may be due to a carbon deposit on the vacuum windows.

Events which produce rapid density changes, such as pellet injection, can cause errors in the interferometer's fringe counters. With multiple pellet injection, it is not possible to reconstruct the density evolution using only the interferometer data and working back from the decay at the end of the discharge. However, recovery of the full time evolution is frequently possible by comparing the interferometer and LIDAR data.

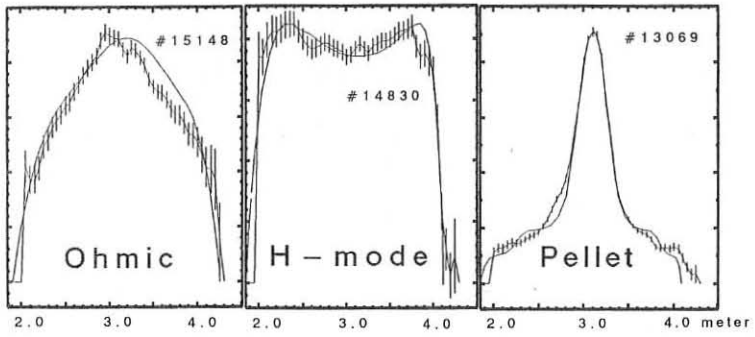

Figure 2: Density profiles of widely varying shapes measured by the interferometer and LIDAR. The LIDAR profile has been normalized to the interferometer data independently for each case.

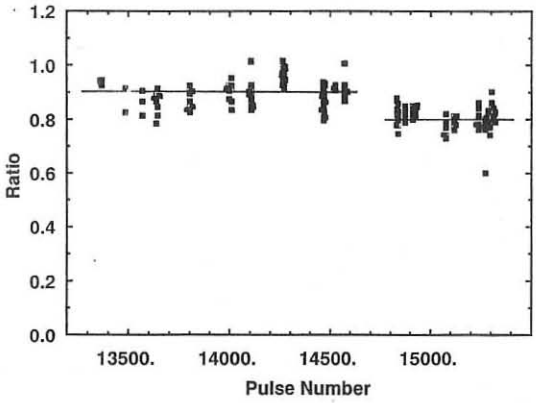

Figure 3: Ratio of the line integral density calculated from LIDAR profiles to the measured interferometer value for plasma pulses spread over a 6 month period. The ratio was initially constant at ≈ 0.9, but decreases to ≈ 0.8 in the last 2 month period.

TEMPERATURE COMPARISONS

Both the ECE and LIDAR provide localized temperature measurements, with similar spatial resolution. However, since the nature of the errors is quite different for the two diagnostics, a detailed comparison of data averaged over many JET pulses should allow the systematic uncertainties in the ECE temperatures to be evaluated, and the full time resolution of the ECE instruments to be exploited. Comparison of the measurements made by the two systems over a wide temperature range (for example, figure 4) show generally good linearity, but with a consistent difference in absolute

level of 10 to 20%. The source of this difference is being investigated. If it is a systematic error in the ECE spectral calibration, this can be removed by normalization against the LIDAR. The apparent shift between the two high temperature profiles of figure 5 suggests an error in the calculation of the plasma internal magnetic fields under these conditions. A systematic study is in progress to see if the ECE/LIDAR comparisons can be used to derive the local magnetic field in the plasma.

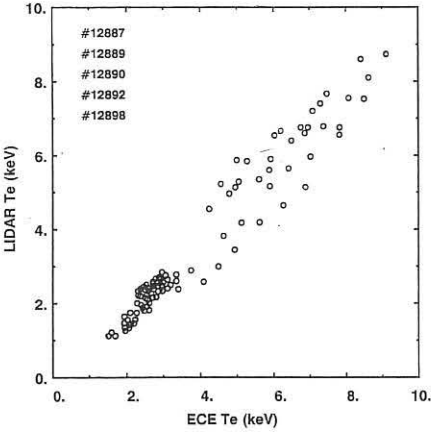

Figure 4: Comparison of T_e measured by LIDAR and ECE on a series of pulses with strong additional heating. The ECE values are $\approx$ 0.9 those of the LIDAR.

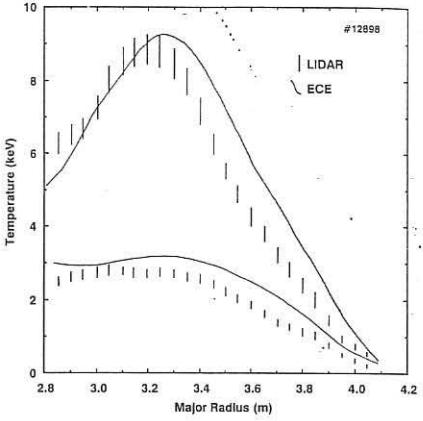

Figure 5: Comparison of LIDAR and ECE profiles at low T_e and high T_e (additional heating) on the same plasma pulse.

SUMMARY

The comparisons which have been made show that considerable benefit can be expected from integration of data from the three diagnostic systems. These benefits fall into three categories:
(i) Reduction of systematic errors. In each comparison, one diagnostic suffers more from systematic errors than the other (LIDAR measurements of n_e, ECE T_e measurements). (ii) Detection (and possibly correction) of measurements perturbed by adverse plasma conditions. (iii) New measurement possibilities. Comparisons between ECE and LIDAR may provide information about the accuracy of calculations of the plasma internal magnetic fields.

The pellet shot reported in this paper was obtained using a multi–pellet injector provided by ORNL under a JET–USDOE Agreement.

[1] H Salzmann et al, Nuclear Fusion, **27**, 1925 (1987)
[2] A E Costley et al, Proc. of EC–4 The 4th Intl. Workshop on ECE and ECRH (Rome, March 1984)
[3] D Veron, in Workshop on Diagnostics for Fusion Reactor Conditions Varenna 1982, EUR 8351–II EN, Page 283 (Permagon, 1983).

MEASUREMENTS OF DENSITY FLUCTUATIONS USING A HOMODYNE SMALL ANGLE SCATTERING TECHNIQUE WITH A SIMPLIFIED WAVE VECTOR SELECTION

O.Küttel

University of Fribourg, Department of Physics,
Pérolles, 1700 Fribourg, Switzerland

1. Introduction

Small-angle CO_2 laser scattering has widely been used for the investigation of density fluctuations in plasma (Philipona, 1987; Slusher and Surko, 1980; van Andel et al., 1987). The method allows a simultaneous determination of the wave vector K and the frequency ω of the fluctuation and therefore the determination of the spectral density function $S(K,\omega)$. Though the calculation of a dispersion relation is possible. The antenna theorem of Siegman which requires an alignment of local oscillator and scattered signal beam within a solid angle $\Omega \geq \lambda^2/A$ (A=surface of the detector), the complex optical path in many scattering experiments as well as the request to choose different scattering angles without lengthy alignments are crucial points of this method.

The object of this paper is to present a new method to produce the local oscillator beam. In this set-up a separate local oscillator beam is no longer necessary which represents a great advantage over many scattering experiments. This method was tested sucessfully for the investigation of density fluctuations in a He plasma. Firs results are presented.

2. Basic principle and optical lay-out

The local oscillator is produced with a beamsplitter which lies just behind the plasma vessel in the main laser beam (Fig. 1). One part of the beam which contains the scattered and frequency shifted radiation is reflected and directed onto the cooled GeHg detector. The beamsplitter angle is controlled by two microprocessor step motors in the two directions X and Y. The transmitted part of the beam crosses the beamsplitter a second time by the help of mirror M1 and M2 in the LO triangle at an angle of 90 degrees to the incoming beam, now insensitive to a beamsplitter displacement and is superimposed to the scattered radiation onto the detector, where it serves as the local oscillator. With an attenuator in the LO triangle the LO power is limited to 80 mW. Changing the scattering angle leaves the local oscillator position unchanged and therefore the requirement of Siegman's theorem is fulfilled for any angle.

Fig. 2 shows the arrangement of the optical lay-out (Philipona, 1987). A CO_2 laser beam (λ_0=10.6μm, P_0=20W) crosses the plasma column and is focused on the beam dump at a distance of 12m in front of the detector. The beam radius in the scattering center is w=0.9cm. A spatial filter in front of the detector cleans the scattered beam from possible stray light of the main beam.

The signal is detected with a cooled GeHg detector (20°K) and analyzed with an analog spectrum analyzer (Küttel and Philipona, 1988). The optical system is tested and calibrated by Rayleigh scattering from ultrasonic waves produced with a little tweeter near the plasma boundary.

This optical system is very suitable for measurements with a detector array. A slit or a cylindrical lens in the LO part of the optical system produces a diffraction pattern which is unaffected by the angular displacement of the beamsplitter and covers all elements of the detector.

3. Measurements and Discussion

Density fluctuations are measured in a magnetized He plasma which is produced in pulses of 2ms with 50Hz repetition rate by microwave discharge. The plasma column with a radius of 4cm is contained in a vacuum vessel with a He gas filling pressure of p=5mTorr and an axial magnetic field of 1-3kG. The mean electron density and temperature is $\bar{n}_e = 3 \cdot 10^{18} m^{-3}$ and $\bar{T}_e = 5eV$, respectively. Previous measurements have shown strong turbulences at the edge of the plasma (Philipona and Küttel, 1988). The appearance of strong density fluctuations in the density gradient $\tilde{n}/n \leq 30\%$ suggested the idea of drift instabilities. Microturbulences are investigated for different magnetic fields B_0 in the range 1-3kG. Fig. 3 provides four frequency spectra of poloidal turbulences for different scattering angles. All spectra are characterized by a prominent peak around 60kHz which decreases in amplitude with increasing frequency. The peak frequency scales linearly with the magnetic field B_0, $\omega(\text{peak}) \sim B_0^1$, in the investigated range 1-3kG. A single wave vector is associated with a broad range of frequency $\Delta\omega \sim \omega$.

The mean wave vector of the poloidal fluctuation $\bar{k}_\Theta$ shows no significant scaling with the magnetic field and is $\bar{k}_\Theta = 3\text{-}4 cm^{-1}$ with a k-resolution $\Delta k = 2 cm^{-1}$. The results obey quite well to the "mixing-length" argument describing the scaling of the fluctuations: $\tilde{n}/n \leq 1/\bar{k}_\Theta L_n$ where $L_n = (1/n \cdot dn/dr)^{-1}$ is the gradient length of the density (Liewer, 1985). Fig. 4 shows this relationship. All other possible scalings fit the data less well than the scaling $(\bar{k}_\Theta \cdot L_n)^{-1}$.

4. Conclusion

The presented small angle scattering technique is an improved method to measure density fluctuations. The major advantages are the easy way to align local and scattered beam, the quick wave vector selection and the fact to use no separate local oscillator beam.
Although the investigation of the turbulences in a linear plasma machine has yet not been terminated, first results show striking similarities to microturbulences in tokamaks. Maybe, this is an indication that microturbulences are not only driven by tokamak specific causes.

Acknowledgements

D. Aeby is gratefully acknowledged for technical assistance and for elaborating the software. This work is supported by the Swiss National Science Foundation.

References

Liewer P.C. (1985) Nucl. Fusion **25**, 543
Küttel O. and Philipona R. (1988) accepted for publication in Appl. Optics
Philipona R. (1987) Rev. Sci. Insturm. **58**, 1572
Philipona R. and Küttel O. (1988) submitted for publication in Plasma Phys. Contr. Fusion
Slusher R.E. and Surko C.M. (1980) Physics Fluids **23**, 472
Van Andel H.W.H., Boileau A., Von Hellermann M. (1987) Plasma Phys. Contr. Fusion **29**, 49

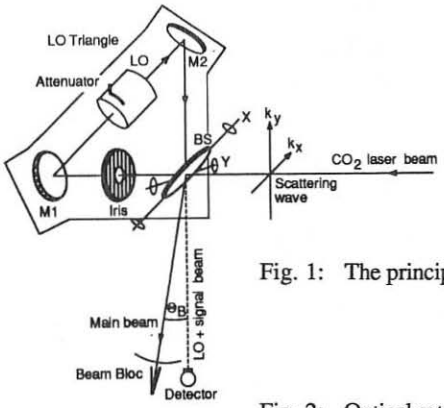

Fig. 1: The principle of the method

Fig. 2: Optical set-up

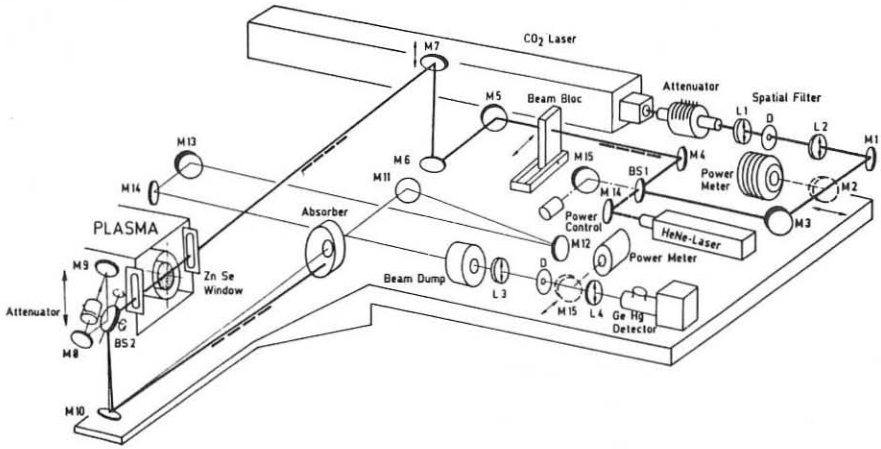

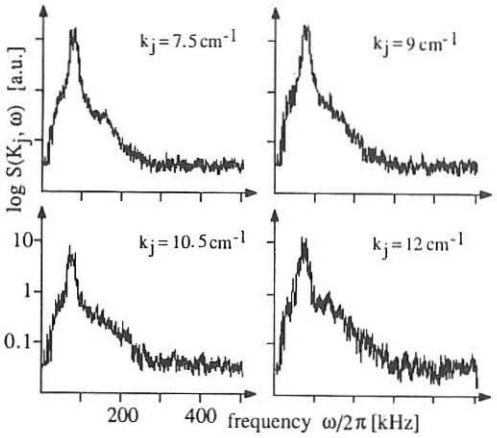

Fig. 3: Frequency spectra for different scattering angles. $B_O = 2.5kG$

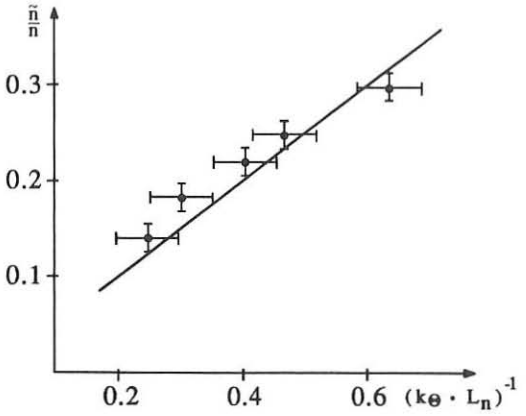

Fig. 4: Amplitude of the density fluctuations versus $(\bar{k}\theta \cdot L_n)^{-1}$

The solid line corresponds to $\frac{\tilde{n}}{n} = \frac{1}{2}(\bar{k}\theta \cdot L_n)^{-1}$

A MICROWAVE REFLECTOMETRIC SYSTEM FOR THE ASDEX TOKAMAK

M. Manso, F. Serra, J. Mata, J. Barroso, J. Comprido, C. Teixeira,
P. Caetano, P. Luz, A. Monteiro, A, Silva, J.Mendonça
Instituto Superior Técnico, 1096 Lisboa Codex, Portugal

J. Neves, J. Pereira, S. Ramos, A. Almeida, L. Cupido, P. Marques
Universidade de Aveiro, Aveiro, Portugal

1. General Introduction

A reflectometric system is being developed to measure density profiles and density fluctuations on the ASDEX tokamak.

Density profiles will be obtained with broad band swept frequency operation using the ordinary mode; the position and density of a plasma layer will be obtained through the phase change the wave undergoes after the reflection on the layer where the wave frequency equals the local (cut-off) plasma frequency. The system has been designed for the range 18 - 60 GHz, so electron densities from ~ 4×10^{12} cm^{-3} to 4.5×10^{13} cm^{-3} can be measured, both on low-field and high-field sides of the plasma column.

Electron density fluctuations will be studied with fixed frequency operation. For large-scale coherent oscillations (e.g. MHD and related sawtooth activity) the interpretation of the measurements will rely on the spectral analysis of the reflected signal: a main spectral line at the injected frequency and several harmonics Doppler shifted by the frequency of the fluctuations and its multiples; both the localization of the reflecting layer and the amplitude of the fluctuations will be obtained from the measurements of a particular value of a phase shift externally added to the reflected signal which reduces to zero the even (or the odd) harmonics of the spectrum, as described in /1/. For small-scale, either coherent (case of Lower Hybrid-induced) or incoherent (drift turbulence) density fluctuations, the scattering effects on the incident wave from all regions between the plasma edge and the reflecting layer must be taken into account /2, 3/; a theoretical model is under development /1/, in order to interpretate reflectometric measurements of the scattered energy flux, which will exhibit the contribution of different ranges of wave vectors along the propagation path.

Here, we describe the experimental set-up of the reflectometric system, which is now in its early stage of comissioning, and make some remarks on the expected measurements of density profiles on ASDEX.

2. Experimental apparatus

The reflectometric system for ASDEX includes three identical reflectometers in the ranges 18 - 26.5 GHz, 26.5 - 40 GHz, 40 - 60 GHz, (respectively standard K, Ka and U bands). Each one has two measuring channels corresponding to antennae in inner and outer positions placed in a toroidal cross section of the machine (Fig.1).

The basic configuration of one reflectometer is shown in Fig.2.

Microwave sources shall be YIG oscillators for the K and Ka bands and a BWO oscillator for the U-band. All sources have fast frequency sweeping (~100 μs- 5 ms). Oversized waveguides shall be used in the upperband in order to overcome losses.

Reflectometers are of one antenna type as this configuration needs less access to the plasma. Six antennae are to be installed inside the tokamak, two per frequency band, as shown schematically in Fig. 1. The short distance between the antennas and the relevant plasma layers, together with spatial constraints, suggest the use of focussed hog-horn antennae, consisting of a feeding horn attached to an ellipsoidal reflector. Good spatial resolution (across the beam) is foreseen: ~ 8cm, 5cm and 3cm, respectively for the K, Ka and U bands; also small beam widths of the main lobe are expected (at 3 dB): respectively ~ 20°, 10° and 5°.

The detection is homodynic and uses high sensitivity broadband detectors with an IF bandwidth of ~ 1 MHz.

The microwave circuits can have two configurations, depending on the position of the switch A (Fig.2), suitable respectively for density profile measurements and for fluctuations measurements. The configurations can be changed during one shot.

(i) Density profile measurements

In this case, switch A is in the open position and arm 1 is excluded from the circuit. The reference signal is obtained from the reflection of the incident wave in a movable screw placed at the mouth of the antenna. This eliminates the phase errors due to different paths of propagation of the reference and of the signal reflected from the plasma; these errors could become very significant as the waveguide paths inside the tokamak are rather long (1-2 m), and the total waveguide lengths could have large variations due to temperature changes.

The reflected signals propagate through a directional coupler, placed inside the machine in order to avoid contributions coming from the reflections at the microwave window.

Standard sweeping times will be ~ 2ms; times as low as 100-200 μs are envisaged whenever we shall study the time evolution of the profile due to density fluctuations, caused namely by sawtooth activity.

(ii) Density fluctuations measurements

When measuring large-scale fluctuations, a variable phase shift (from 0 to π) must be added to the reference signal during the measuring time, so the signal reflected at the mouth of the antennae can no longer be used; the screw is removed , switch A is closed and the reference comes from the signal sampled by the directional coupler in arm 1.

The measurements must be performed in times $\lesssim$ 1 ms and fast, electronically controlled broadband phase shifters would be required. As this is a non-available component for the relevant frequency bands (and its development would be a very time-consuming task) an alternative solution has been studied. The reflected signals are down frequency converted to the X-band (8 to 12.4 GHz), thus enabling the use of standard broadband controlled phase shifters for the X-band (Fig.3); due

to the balanced configuration phase/frequency deviations of the local oscillator shall not produce phase errors. This solution can be extended to density profile measurements.

3. Interpretation of reflectometric measurements on ASDEX

ASDEX is a tokamak with major radius R = 165cm, minor plasma radius a=40cm and toroidal magnetic field $B \leq 2.8$ T /4/

In order to discuss the validity and to test the numerical methods of calculating density profiles from reflectometric data, we analysed typical density profiles recently obtained through interferometric and Thomson scattering methods (as the one in Fig.4(a), approximated by an analytical function for best fitting with the data (Söldner, private communication, IPP Garching, 1987)). By comparing the inhomogeneity scale length with the wavelength of the probing wave, one concludes that the WKB approximation for the wave propagation seems to hold down until close to the limiter ($ne \lesssim 0.3 \times 10^{13}$ cm^{-3}, so $F \lesssim 16$ GHz), so the total phase delay $\phi(F)$ can be easily analitically inverted for the case of the O-mode in order to find the position of the reflecting layer .

For each frequency sweep, the acquisition system will store N values of wave frequencies (Fi) at all 2π phase shifts, $\phi(Fi)$; from Fi and $\phi(Fi)$ the position X(Fi) of the density layer n(Fi) will be obtained, and therefore the density profile at N points. Several numerical treatments can be used in order to obtain the profile, aiming to optimizing either the accuracy of the result or the calculation time. Simonet (private communication, 1987) has suggested two basic methods: an iteratif one, based on the values $\phi(F)$, the other using directly X(F) values. Those methods were tested for several ASDEX profiles (as the one of Fig.4 (a)), which gave the data for their numerical reconstruction. The results suggest the convenience of using the direct method, with the most accurate scheme of interpolation (trapezoidal, Fig. 4 (b)); a reduction of 70% in the calculation time is obtained in comparison with the most accurate scheme of the iterative method. At the plasma edge, the differences between the given profile and the ones obtained from numerical reconstruction are significant; it will be necessary to accurately determine the initial conditions for the profiles, whose slopes in this region strongly differs from theoretical parabolic profiles (Fig.4 (d)).

The phase shifts as a function of the wave frequency have been theoretically evaluated from typical ASDEX profiles data, and the beat frequencies (fB) for each reflectometer were therefore estimated. For standard sweep times (~ 2 ms) , $fB < 25$ kHz, and therefore sampling rates with period $\lesssim 2\,\mu s$ will ensure measurements with good accuracy (5%); considering sweep times as low as 100 μs, the same accuracy will imply sample periods of ~ 200 ns, corresponding to sampling rates of 5 MHz.

References

/1/ M. Manso, F. Serra, and J. Mendonça, Energy Independence Conf. on Plasma Physics and Controlled Fusion, Rio de Janeiro (1987)
/2/ F. Simonet, Ph.D. Thesis, Univ. Nancy I (1986)
/3/ A. Hubbard, Ph.D. Thesis, Univ. London (1987)
/4/ ASDEX Group, Report IPP III/47 (1978)

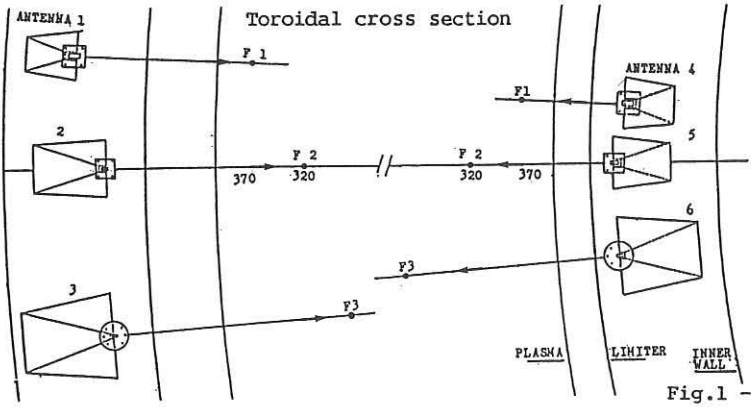

Fig.1 - Installation of the antennae

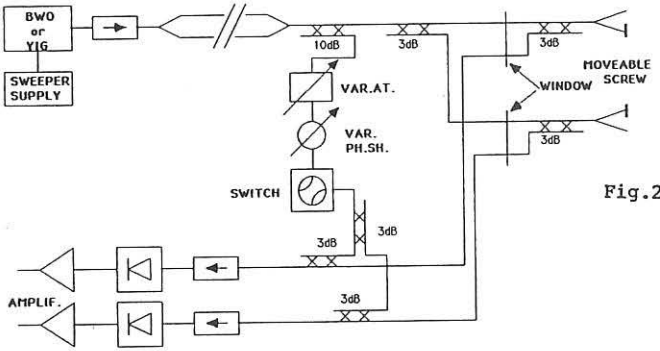

Fig.2 - Schematic of the ASDEX reflectometer

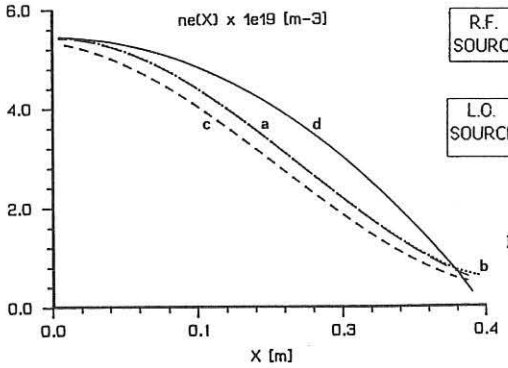

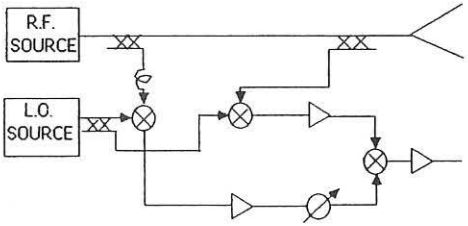

Fig.3 - Down frequency conversion

Fig.4 - a) ASDEX density profile, with $\bar{n}e = 2.9 \times 10^{19}\ m^{-3}$; b)c) Estimated profiles using direct numerical methods, respectively with trapezoidal, and one-point interpolation schemes; d) Theoretical parabolic profile.

SENSITIVITY OF TRANSIENT SYNCHROTRON RADIATION TO TOKAMAK PLASMA PARAMETERS

Arnold H. Kritz† and Nathaniel J. Fisch‡

† Department of Physics, Hunter College/CUNY, New York, NY 10021

‡ Princeton Plasma Physics Laboratory, Princeton University, Princeton, NJ 08543

Brief, but intense, resonant wave heating of high energy electrons can produce in tokamaks a transient synchrotron radiation response that is distinguishable from the steady background radiation. The radiation response, a two-dimensional pattern in frequency-time space, is highly sensitive to the details of both the heating pulse and the plasma parameters. For example, the radiation associated with the wave-heating of high-energy electrons tends to be at lower frequency and to decay more slowly than radiation associated with the heating of low-energy electrons. More precise details of the radiation pattern, however, are governed by, e.g., the plasma density, the effective ion charge state or the observation angle with respect to the magnetic field.

Given a description of a physical process, it may be possible to deduce from data representing the process, the parameters that govern the process. Here, quite gross characteristics of the radiation response can be used to deduce the heating and plasma parameters. By gross characteristics, we mean those that reflect primarily the two-dimensional shape of the radiation response and are largely insensitive to noise or calibration errors. It turns out, in fact, that the gross characteristics of the radiation are sufficient to allow simultaneous deduction of several heating and plasma parameters of interest. Thus, we are not limited to the case where only one parameter is considered unknown.

In this work we restrict ourselves to the steady-state plasma (no dc electric field), and we identify the plasma properties that can be reliably extracted through observation of the transient radiation. The theory of the incremental radiation response, including the Green's function for efficiently calculating the radiation response, has been described in Ref. 1. Here, we examine the sensitivity of the response to specific parameters of interest.

An example of such a radiation response is shown in Fig. 1. Here the incremental radiation of ordinary polarization, plotted as a function of frequency and time, results from electrons initially with about 130 keV of parallel energy. This initial condition corresponds to the temporary increment in energetic electrons that would result from the stimulus of brief but intense rf heating. Because of particle conservation, a temporary decrement in somewhat lower energy electrons must accompany the temporary increase in energetic electrons. There is an incremental radiation response to this

decrement too, but for simplicity of presentation, we consider here only the positive part of the incremental radiation, as though energetic electrons were just put there.

In Fig. 1a, the radiation is viewed at an angle of 12° with respect to the magnetic field (i.e., $\theta = 12°$), while in Fig. 1b, the radiation is viewed at $-12°$. An object of this work is to see, for example, whether by observing the radiation response only, we could deduce this angle. To the extent that the radiation response depends sensitively upon the viewing angle, we have hopes of uncovering this parameter. Deducing the angle of observation informs on the direction of the magnetic field, or, equivalently, the q-profile. Other parameters of interest that shall be considered here include the ion charge state, and, if not known, the details of the stimulus itself.

In the case of Fig. 1, it is evident that if it were only a matter of distinguishing 12° in the viewing angle, our task would be quite simple. However, more fine discriminations are of interest, and, moreover, it may be necessary to deduce several parameters simultaneously. In this report we show that this can be done, even in the presence of noise. The property of this diagnostic that we exploit in particular is the very many data points that comprise the radiation response. Taking data in both time and frequency makes available perhaps several hundred data points, so that the signal can be extracted effectively from the noise. In considering the effects of noise, we assume here, for simplicity, that the noise is gaussian and uncorrelated. With this model for noise, we then calculate the conditional probability that parameters of interest have certain values, given the noisy data.

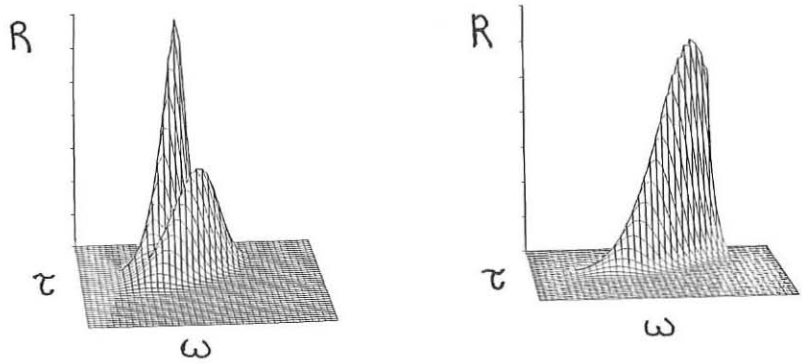

Figure 1. Transient O-mode radiation vs. ω and τ; in a) $\theta = 12°$ and in b) $\theta = -12°$.

Consider for example Fig. 2a. Suppose that all plasma parameters are known, but we do not know the q-profile, i.e., we do not know θ. Suppose also that, whereas we are able to impose a stimulus narrow in velocity space, we do not know precisely the energy of the affected electrons. Further, to evaluate this technique as a diagnostic, we simulate experimental data by corrupting the theoretically computed values with gaussian uncorrelated noise. In Fig 2a, we plot the joint probability of θ and u_0 given

the noisy data as a function of θ and u_0. Here the noise is 30% of the maximum signal and 1600 data points are used. Note that, despite the noise, the angle of observation θ is inferred to within a degree and the stimulus location is inferred to within 5%. By *inferred*, we mean here that marginal probability of θ given the data (i.e., summed over all possible stimulus locations) is finite only for θ lying within a narrow range. In Fig 2b, we raise the noise to 120% of the maximum signal. Here the velocity-space location of the stimulus is inferred about as well, and the angle of observation θ, while more uncertain, is still inferred to about a degree. In Fig. 3, we plot the marginal probability of θ versus θ for several levels of noise. Note that in the limit of infinite noise the marginal probability becomes flat as a function of θ, which is what we have taken as our *a priori* probability.

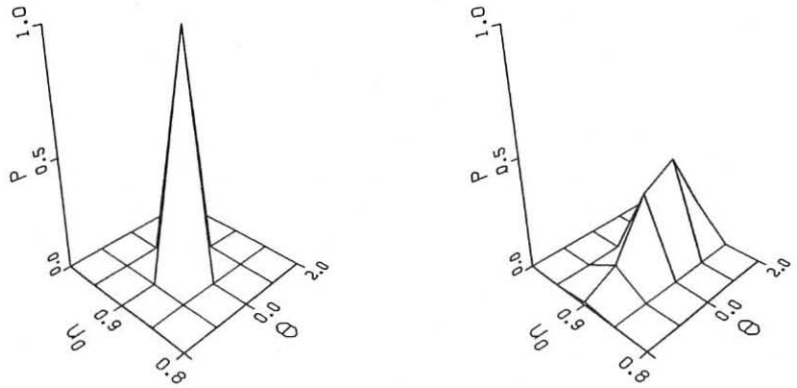

Figure 2. Joint probability $P(\theta, u_0 \,|\, \text{data})$ when a) the noise level is 30% and *b*), 120%.

In Table 2, we take as unknown not only θ, but also the stimulus width in velocity space and the ion charge state Z_{eff}. The table illustrates the degree to which we can deduce simultaneously these three parameters. The result of this exercise is that we realize that the radiation response varies in rather different ways with these parameters, so that the chances of inferring any one of the parameters would not be diminished severely by a lack precise knowledge of the other parameters.

In general, to the extent that the radiation response depends sensitively upon any particular parameter, we have hopes of uncovering that parameter. On the other hand, to the extent that the radiation response is insensitive to any particular parameter, we then have hopes of ignoring that parameter.

The radiation that we expect to measure is about 1/100 of the background radiation. For a maxwellian plasma with temperature, density and magnetic field of 5 keV, $10^{14}\,\text{cm}^{-3}$ and 4 T, the background radiation in the perpendicular direction is approximately 4 milliwatts/(unit solid angle–cm)^3 when the frequency interval is 1 GHz. The time duration of the radiation response is a slowing-down time of a resonant electron, which typically might be 10's of milliseconds.

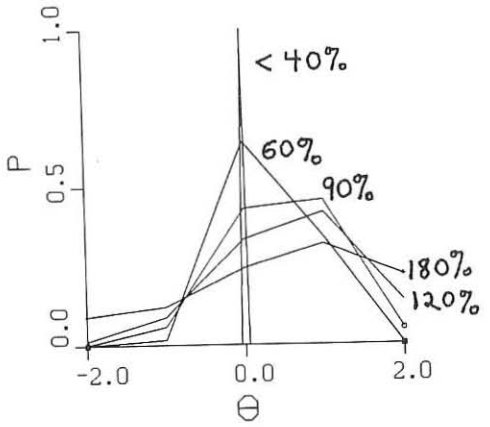

Figure 3. Dependence of $P(\theta)$ on noise level.

	$P_M[38\%]$	$P_M[76\%]$
$\theta = -2.0°$	0.00	0.00
$\theta = -1.0°$	0.00	0.02
$\theta = 0.0°$	0.96	0.46
$\theta = 1.0°$	0.04	0.51
$\theta = 2.0°$	0.00	0.00
$Z_{\text{eff}} = 1$	0.97	0.77
$Z_{\text{eff}} = 2$	0.03	0.23
$\Delta u = 0.05$	1.00	1.00
$\Delta u = 0.10$	0.00	0.00

Table 1.

The results presented assume that 1600 noise-uncorrelated data points are available. The effective noise level decreases roughly as the square root of the number of data points. In practice, the noise levels that we are simulating here are actually quite high, so fewer data points should not be a great problem. Only near the cyclotron harmonics might it be difficult to distinguish the incremental radiation from a high level of background radiation. In any event, the resolution of the viewing angle is more likely limited by the optical system (to about 1° or 2°) rather than by the level of noise or other uncertainties in plasma parameters. To the extent that the angle θ is resolvable, information concerning the local value of q becomes available.

In summary, we have proposed an invasive method for extracting information on plasma parameters from synchrotron radiation. The approach relies on detailed and sure knowledge of the behavior of fast electrons in a steady-state plasma. While certainly there are a number of practical matters to sort out, it appears that inferences might be drawn reliably concerning macroscopic plasma parameters, such as the ion charge state or the current profile, which are difficult to deduce through other means.

This work was supported by United States Department of Energy under contracts DE–FG02–84–ER5–3187 and DE–AC02–76–CHO3073.

---

[1] N. J. Fisch, *Inverse Problem for Incremental Synchrotron Radiation*, to appear in Plasma Phys. and Controlled Nuclear Fusion, 1988.

POLARIZATION CHANGE OF ELECTROMAGNETIC WAVES PASSING THROUGH TOROIDAL SHEARED PLASMAS

A.Airoldi, A.Orefice, G.Ramponi

Istituto di Fisica del Plasma, Associazione Euratom-Enea-Cnr
Via Bassini 15, 20133 Milano (Italy)

The polarization change of an e.m. wave passing through a magnetized plasma turns out to be of renewed interest because of the possibility, offered by polarimetry measurements in the infrared range of frequencies, of determining the current density profile in a tokamak plasma /1/. Because of the magnetic shear, acting as a coupling parameter between the characteristic modes in Maxwell equations, the fraction of energy in each mode is not a constant, and a non-WKB treatment is necessary in order to describe the evolution of the wave polarization.

In the present work we consider e.m. waves injected into a toroidal inhomogeneous plasma with their wave vector $\mathbf{k}$ contained in a poloidal plane φ = const. In our approximation the wave is assumed to remain basically transversal all along its trajectory, with $\mathbf{k}$ pointing in the propagation direction. The trajectory, in its turn, is assumed to be basically straight, thus allowing to define a coordinate system (φ, $\mathbf{k}$, α), with $\alpha = \varphi \times \mathbf{k}$, where $E_k = 0$, being $\mathbf{E}$ the (real) wave electric field.

The (real) electric vector of a plane wave shall describe, in general, an ellipse which, in the plane (φ ,α), takes the form

$$\begin{aligned} E_{\alpha} &= a_1 \cos\delta + a_2 \sin\delta \\ E_{\alpha}^{\varphi} &= a_3 \cos\delta + a_4 \sin\delta \end{aligned} \qquad (1)$$

with $\delta = -\omega t$.

The plasma region crossed by such a wave is decomposed into elementary slabs, such that in each slab the plasma may be assumed to be homogeneous. Therefore entering each slab the wave splits into extraordinary (X) and ordinary (O) waves, which recompose when they get out and evolve because of the phase difference $d\Phi$ piled up in ds. This is seen to be described by a first order differential equation of the form:

$$d\mathbf{a}/ds = -(k_x - k_o)\,\mathbf{U}(s) \qquad (2)$$

where $\mathbf{a} = (a_1, a_2, a_3, a_4)$ are the coefficients which completely identify the polarization ellipse all along the wave trajectory, k_x and k_o are the wavenumbers of the "local" X and O modes, and $\mathbf{U}$ is a set /2/ of four functions of the plasma parameters.
Solutions of eq. 2 are shown here for different plasma parameters.

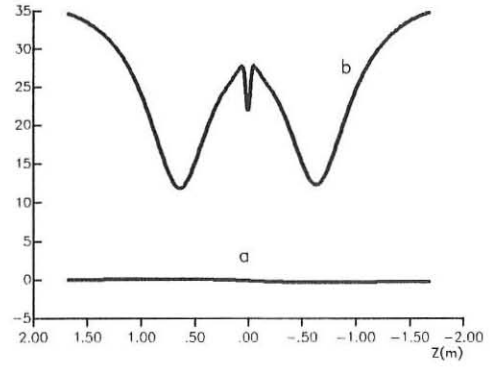

Fig.1 - Rotation angle $\Delta\beta$ (curve a) in degrees and percentual energy contained in the X mode (curve b) along the vertical trajectory passing in R = 3.08 m for a JET D-shaped equilibrium case, corresponding to B_t = 2.2 T, q(0) = .9, q(a) = 5.4, $n(0) = 4 \times 10^{13}$ cm^{-3}

In Fig. 1 the rotation angle $\Delta\beta$ for a wave which initially is linearly polarized with E oscillating along the toroidal direction (β = 0), and the fraction of energy (in percent) contained in the X mode are shown along a vertical trajectory at $R = R_o$, in the case of a JET typical equilibrium and λ = 195 μm. It is evident that, while the wave doesn't rotate in this case (the longitudinal component of the magnetic field is zero all along the trajectory), there is a continous exchange of energy between the X and O component of the wave.
In Fig.2 we plot both the rotation angle $\Delta\beta$ and the quantity P_t/P_o, i.e. the power which is transferred into the direction perpendicular to the initial one, at various radial positions R, for the same parameters as in Fig.1. In the case shown there is complete agreement between our results and those obtained by the analytical expression of DeMarco-Segre /3/. A variation of the q(0) value, i.e. of the current density profile near the center, induces a variation of the $\Delta\beta$ profile, as shown in Fig. 3, where the slope of the $\Delta\beta$ curve at the plasma center is plotted versus q(0). This fact confirms that it is possible to get information about the q(r) profile, if the density profile is

known with sufficient accuracy. Fig.3 refers to a JET-like circular equilibrium case, which allows an analytical continuous dependence on q(0).

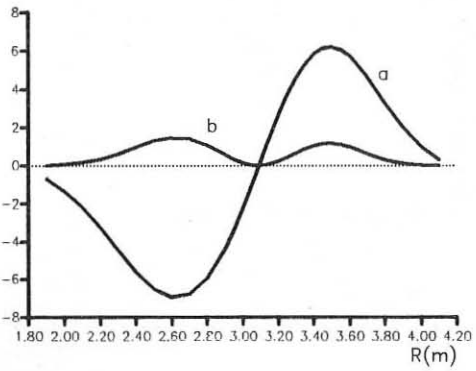

Fig.2 - Rotation angle $\Delta\beta$ in degrees (curve a) and percentual energy transferred in perpendicular direction (curve b) for different radial positions for the same equilibrium conditions of Fig.1.

In the case of different plasma parameters (FTU-like , i.e. $n(0) = 5x10^{14}$ cm^{-3} , $B_t = 7$ T, $q(0) = 0.8$, $q(a) = 3.5$) and for $\lambda = 195$ μ a sensible difference exists between our results for $\Delta\beta$ and those predicted by the DMS analytical expression, as shown in Fig.4. This fact is to be ascribed not only to the total value of the phase difference $\Delta\Phi$, but also to the fact that, in the case shown, the effect of the component of the magnetic field transverse to the trajectory is not negligible with respect to that due to the longitudinal one. In this case, in fact, the polarization change is not uniquely due to the rotation angle, but also to the ellipticity change.

Work done under JET Contract JT6/9004

REFERENCES

/1/ Soltwisch H., Rev. Sci. Instruments 57,1939 (1986)
/2/ Airoldi A., Orefice A., Ramponi G., submitted to Nuovo Cimento
/3/ DeMarco F., Segre S., Plasma Physics 14, 245 (1972)

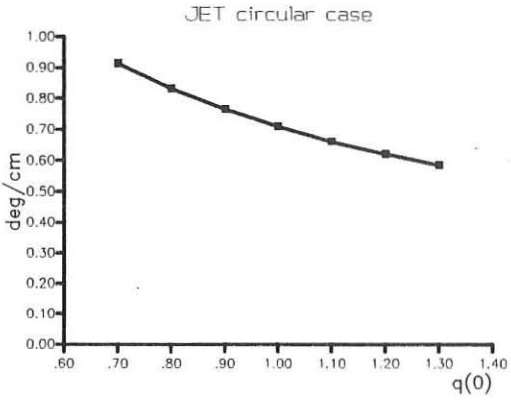

Fig.3 - Slope of $\Delta\beta$ in the central zone of the plasma vs. the value of safety factor.

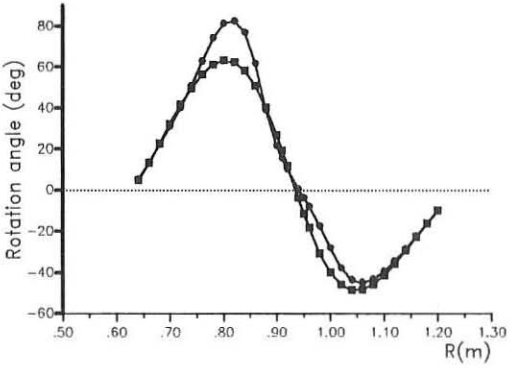

Fig.4 - Rotation angle $\Delta\beta$ in degrees (dot marks) according to the present formulation and to DMS evaluation (square marks) for different radial positions in a FTU-like plasma.

Ion Cyclotron Emission Measurements On JET

P. Schild[a] and G.A. Cottrell

JET Joint Undertaking, Abingdon, Oxon OX14 3EA, United Kingdom

[a] *Permanent address : Lab. Phys. des Plasmas , Grenoble University, France*

Introduction

A JET ICRH antenna has been used in reception mode to monitor the time and frequency-resolved ion cyclotron emission (ICE) from deuterium 6 MA ohmically heated plasmas with antenna configuration in dipole phasing. The ICE spectrum is compared with a computed thermal spectrum for harmonics from 1 to 5 . It shows the characteristic harmonically related superthermal peaks[1,2]. These observations reveal that the superthermal emission is modulated in time and is correlated with inverted sawteeth and with the H-α signal located near the plasma edge.

ICE Spectrum

The antenna was used to monitor the ICE from 10 MHz to 100 MHz. The signal is detected using a spectrum analyser, which provides about six spectra per pulse. Previous experiments[2,4], made with the same equipement, suggest that the ion temperature could possibly be measured by analogy with the technique of electron cyclotron emission (ECE). However, the superthermal emission for deuterium ohmic cases masks the thermal emission, and is influenced by the fusion products of the D-D reactions [3].

To study the effects of these superthermal ions on the spectrum, we need to calculate the thermal level. To compute this, we have used a code based on Black Body radiation[5]. In this frequency range and ion temperature level (typically $T_i \approx 2\ KeV$ for ohmic pulses), we have $h\nu/kT \ll 1$, and can take the Rayleigh–Jeans law to get the thermal intensity. To take into account that the waves, before being received by the antenna, may make many reflections within the vacuum vessel, (in the optically thin limit), we include a slab model for these in the code. We use the formula :

$$I(\omega,T_i) = \frac{N^2\omega^2}{8\pi^3 c^2} kT_i \cdot (1 - e^{-\tau}) \qquad (1)$$

where N is the refractive index of the medium, defined by $N \sim \omega_{pi}/\omega_{ci}$, and the subscript i stands for the ion majority species, and τ is the total optical depth for the plasma at frequency $\omega/2\pi$. We calculate τ from the dielectric tensor for a cold plasma , including a small perturbation to take into account that the plasma is warm[8]. We also include the effects of finite larmor radius and non relativistics particles. Having solved the dispersion relation, we may use previous results[6,7] from ECE theory and calculate the optical depth. We also assume the ion temperature profile and the ion density profile to be parabolic. We then compute the thermal emission from the first to the fifth ion cyclotron harmonic for the ion majority species. We do not compute for harmonics greater than five, because these fall outside of our frequency range.

We calibrate the ICE signal by taking into account the coupling resistance of the antenna over our frequency range. This gives us a function with which we obtain the ICE power in front of the antenna

We now compare this calculated Black Body emission with a ICE spectrum from a 6 MA discharge with deuterium majority (figure 1).

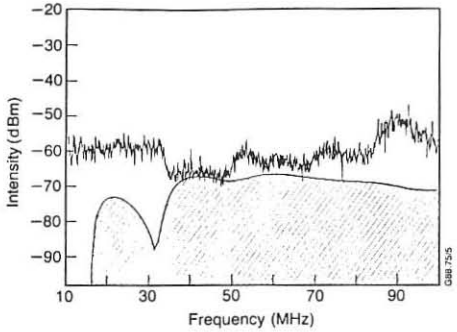

Fig. 1 : Comparison between the ICE spectrum and the computed thermal emission ($B_0 = 2.18\ T$). The hached region represents the thermal emission.

It can be seen that the computed spectrum explains some of the underlying features of the experimental spectrum. However, below a frequency around 40 MHz, the thermal emission is not the main source of the emission. This is due to the weak absorption of the fundamental of deuterium $\omega = \omega_{cD}$ below 21 MHz. It can also be seen that our computation reproduces the ICE spectrum in the range 40–50 MHz, suggesting that the thermal spectrum of the bulk ions is visible in this interval.

We know that the observed peaks are linked with the presence of fusion products of D-D reactions[2] ; T, ^{3}He, H^+ . The peaks A to F on figure 2 can be related to the cyclotron harmonics

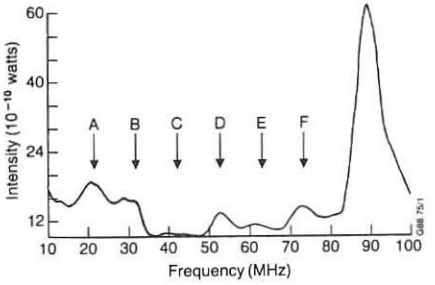

Fig. 2 : The peaks A to F are harmonics of T,^{3}He,H^+ for a magnetic field of 2.1 Tesla. The ICE spectrum is smoothed by a gaussian to improve the signal-to-noise ratio.

of the three particles. These are linked respectively by the following relations: peaks A to F are the cyclotron harmonics 2 to 7 of T; peaks A, C, E are the cyclotron harmonics 1 to 3 of ^{3}He; peaks B and E are the cyclotron harmonics 1 and 2 of H^+. In order to obtain the correspondence between them, we take the value 2.1 Tesla for the magnetic field. This means that the emission which produces the peaks is near the plasma edge. The last observation provides support to the interpretation[2] that the superthermal ICE is generated by fusion products near the pickup antenna.

Time Resolved Measurements.

We have observed the time-resolved emission of peak D with a sampling rate of 1 kHz. When the 6 MA current flat top is reached, inverted sawteeth are observed on the ICE emission. Comparison with a soft X-Ray signal from the plasma edge (figure 3) shows a good correlation between the two, which indicates it originates near the edge. We also compare the ICE signal with an H–α signal. It is also well correlated (figure 4). The ICE signal can be to delayed with respect to the soft X-Ray signal. The $q = 1$ surface is at radius $R \approx 3.7\ m$. So the ICE signal originates outside this surface. As the H–α emission originates from a region close to the limiter, the correlation with the ICE signal indicates further that the ICE emission is coming from the plasma edge. This localisation of the emission clearly must be taken into account in future models of the ICE spectrum.

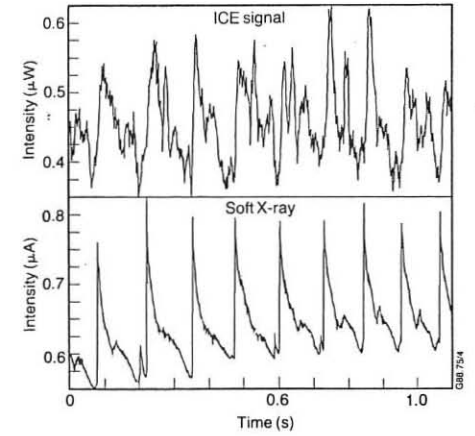

Fig. 3 : Time-resolved soft X-Ray ($R \approx 3.7\ m$) and ICE signals are compared, during the current flat top.

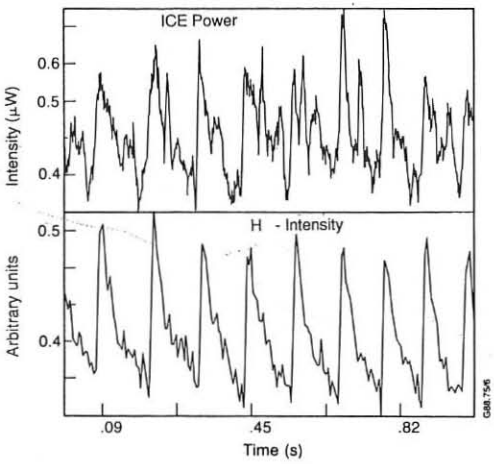

Fig. 4 : Time-resolved H_α signal are compared with ICE, during the current flat top.

Discussion and Conclusion.

Comparison between the ICE and the computed thermal emission spectrum reveals where the superthermal component of the emission is dominant. The nonthermal emission peaks can be interpretated in terms of the ion cyclotron harmonics of fusion products of the D-D reaction. It is possible to match the observed and calculated ICE harmonics peaks if the field is taken to be that value near the boundary ($R = 4.2\ m$) of the plasma, suggesting that the origin of the emission is near the plasma edge. Taking the time-resolved emission of one of these peaks, we find the ICE signal shows inverted sawteeth. These two observations give support to the interpretation that the superthermal emission originates from the plasma edge. near the pickup antenna.

The coincidence of the inverted sawteeth of ICE and H–α signals in time gives strong support to the interpretation of the ICE as originating from the outside part of the plasma, in the near field region of the ICRH antenna. It is possible that deeply trapped fusion products, born in the central part of the discharge, can make large orbit excursion in the outer part of the plasma. These particles may suffer collective velocity-space instabilities which can drive unstable waves in this region.

Acknowledgement.

It is a pleasure to thank Dr. A. Edwards for the help to use the Soft X-Ray data and M. Brandon for experimental assistance.

References

[1] G.A. Cottrell et al, Proc. 13th Europ. Conf. on Controlled Fusion and Plasma Physics,Schliersee, W. Germany, Vol. II,37(1986)

[2] G.A. Cottrell, R. O. Dendy, Phys. Rev. Lett. **60** ,33(1988)

[3] W.H.M. Clark ,Proc 4th Inter. Symp. on Heating in Toroidal Plasma, Rome, Italy, Vol. I, 385–391(1984)

[4] G.A. Cottrell, Proc. Workshop on Application of RF Waves to Tokamak Plasma, Varenna, Vol. II,710–716(1985)

[5] Bekefi, Radiation Process in Plasma (1966)

[6] Bornatici et al, Plasma Physics, **23** ,1127(1981)

[7] Engelman et al, Nucl. Fus., **13** , 497(1973)

[8] Shkarofski , Physics of Fluids, **9** , 561(1966)

RADIAL DECAY OF BROADBAND MAGNETIC FLUCTUATIONS IN ASDEX

L. Giannone, E. Holzhauer* and J. Gernhardt

Max Planck Institut für Plamsaphysik,
Garching, F. R. G.

* Institut für Plasmaforschung,
Universität Stuttgart, F.R.G

1. INTRODUCTION

A new magnetic probe system, consisting of coils mounted on a pneumatically driven manipulator, has been installed on ASDEX. The manipulator may be scanned through a distance of 8 cm in the radial direction within 150 ms. This system then possesses the capability of obtaining measurements of the radial decay of broadband magnetic fluctuations at a single poloidal location /1/. Other experiments have used coils positioned at different poloidal locations and measured the radial decay by plotting the fluctuation amplitude as a function of the radial position of each coil /2,3/.Measurements of magnetic fluctuation amplitude during L and H transitions were previously made by coils located at a distance of 14 cm from the separatrix /4/. The new coils may be moved to within 4 cm of the separatrix.

2. EXPERIMENT

The radial, poloidal and toroidal components of the fluctuating magnetic field may be detected simultaneously. A passive high pass filter is used to attenuate the dominant coherent magnetic fluctuations due to Mirnov oscillations. The signal is amplified with a gain of 200 and monitored by an analogue-to-digital converter, a spectrum analyser or a frequency comb. The frequency comb contains a splitter and a set of 8 bandpass filters. This allows the RMS amplitude of the probe signal at 8 frequencies in the range 30 kHz to 1 MHz to be measured simultaneously.

The signal-to-noise ratio at distance of 4 cm from the separatrix is greater than 20 dB up to a frequency of 1 MHz for the radial and poloidal components in Ohmic discharges. At low frequencies the toroidal component is smaller than the poloidal and radial components, while at higher frequencies they are of comparable magnitude. In ASDEX, the measured poloidal field contains a component generated by switching noise on the

multipole and vertical field coils. Radial profiles of the fluctuation amplitude of the radial component were therefore studied.

The radial decay of broadband magnetic fluctuations was measured by scanning the coils through a distance of 8 cm. The probe starts 12 cm away from the separatrix, moves to within 4 cm of the separatrix and returns (see Fig. 1). The closest distance to the separatrix was determined by observed increases in the hard x-ray flux, which resulted from runaway electron collisions with the probe. Ohmically heated and neutral beam heated plasmas with various values of magnetic field and plasma current have been studied.

The poloidal mode number, m, has been inferred from the radial decay of the magnetic fluctuation amplitude, since in a current free region the amplitude decreases as $r^{-(m+1)}$ in cylindrical geometry /2,3/. This implicitly assumes that the conducting wall is positioned at an infinite distance from the plasma and that the toroidal wavelength is infinite ($k_z = 0$). A plot of the logarithm of the amplitude versus the logarithm of the minor radial positon was used to find m. The decay of magnetic fluctuation amplitude in the presence of a conducting wall at a finite distance from the plasma with $k_z \neq 0$ has been considered /5/. The expected radial decay for a single mode may be expressed in terms of modified Bessel functions. With the conducting wall on ASDEX at r = 61 cm and the separatrix at r = 40 cm, it was found that the m number was overestimated, when the effect of the conducting wall and finite k_z were ignored.

Modes with the lowest m predominate when a number of modes with different m are unstable, because of the strong dependence of the radial decay on m. From these measurements of the radial decay of broadband magnetic fluctuations, it is found that $m \leq 8$ on ASDEX. This value is consistent with those observed in other experiments /1-3/.

3. THEORY

The identification of the plasma instability responsible for the generation of broadband magnetic fluctuations and the extent to which magnetic fluctuations cause anomalous electon transport are important topics in fusion research. It has been suggested that broadband magnetic fluctuations are due to microtearing modes /2,6/. These modes are high m temperature gradient driven tearing modes.

Calculations concerning the linear instability of microtearing modes in ASDEX, show that modes with $m \leq 10$ may be unstable for typical discharge conditions /7/. In Ohmic discharges the unstable modes are located at radial positions

inside of half the plasma minor radius, while in neutral beam heated plasmas the most unstable modes are located closer to the plasma boundary (see Fig. 3). This result suggests that the enhanced magnetic fluctuation level measured in neutral beam heated plasmas /4/ may be partly due to a change in the position of the unstable modes, and this should be taken into account in those experiments considering the scaling of the inverse of confinement time, τ_E^{-1}, with broadband magnetic fluctuation amplitude /8/.

4. CONCLUSION

For ASDEX plasma parameters, experimental observations and theoretical calculations suggest that the microtearing mode remains as a candidate for the plasma instability which is responsible for the generation of the broadband magnetic fluctuations.

Further work is required to apply a more sophisticated theory which describes the non-linear and toroidal coupling of different modes and the saturation of each mode to the experiment. In the linear theory each mode generates fluctuations at a frequency determined by the plasma parameters. A broadband spectrum is produced as a result of the non-linear and toroidal coupling of modes that are located at different radial positions within the plasma.

/1/ F. Ryter, A. Pochelon and F. Hoffmann,
14th European Conference on Controlled Fusion and Plasma Physics, Madrid, Vol. I, 265, 1987.

/2/ N. Ohyabu et al.,
Phys. Rev. Lett., 58, 120, 1987

/3/ M. Malacarne et al.,
JET Report, JET-P(87) 22.

/4/ G. Dodel, E.Holzhauer and J.Massig,
14th European Conference on Controlled Fusion and Plasma Physics, Madrid, Vol. I, 249, 1987.

/5/ G.Bateman,
"MHD Instabilities", p.111,
MIT Press, 1978.

/6/ J.F. Drake and Y.C. Lee,
Phys. Fluids, 20, 1347, 1977.

/7/ L.Giannone,
"Linear stability of microtearing modes in ASDEX",
IPP Report, IPP III-125, 1987.

/8/ M. Malacarne and P.A. Duperrex,
JET Report, JET-P(87) 26.

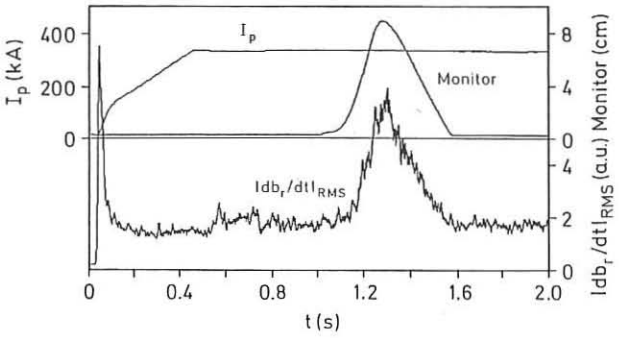

Fig. 1

Fig. 1 The movement of the manipulator is monitored and the radial profile of the RMS amplitude of $\delta b_r/dt$ is measured at f = 82 kHz in an Ohmic discharge with B = 1.85 T and I_p = 320 kA. The bandpass filter has $\Delta f/f$ = 0.1.

Fig. 2 Radial decay of broadband magnetic fluctuation amplitude as a function of frequency for an Ohmic discharge. A plot of the logarithm of the amplitude versus the logarithm of the minor radial position yields the poloidal mode number, m. The presence of the conducting wall needs to be taken into account.

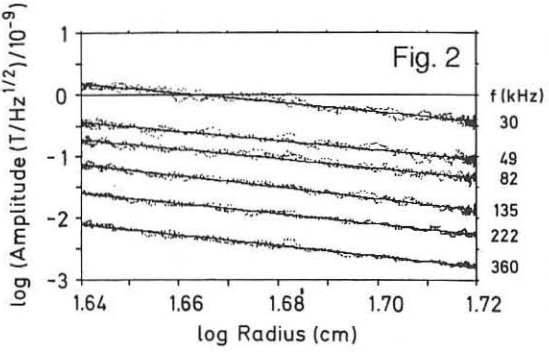

Fig. 3
Microtearing mode stability in a plasma with B = 1.85 T and I_p = 320 kA. The imaginary part of the eigenvalue, δ, versus normalised radius for an Ohmic discharge is plotted in Fig. 3(a) and for a discharge with neutral beam injection in Fig. 3(b). The mode is unstable when $\delta > 0$.

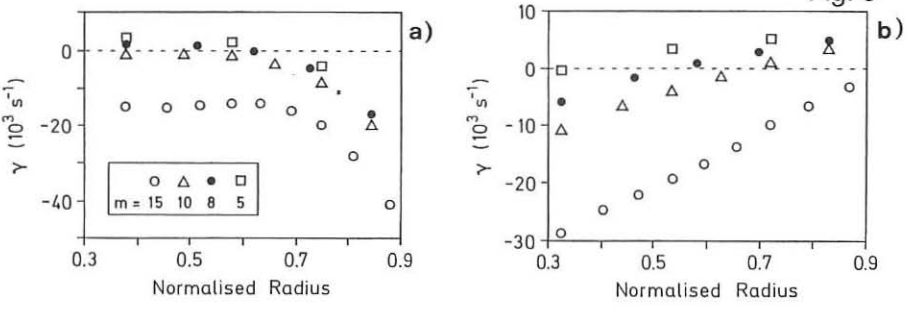

VERSATILE TECHNIQUE OF FINDING A LOCAL DYNAMIC VALUE OF ELECTRON HEAT CONDUCTION COEFFICIENT, χ_e^{HP} FROM EXPERIMENTAL DATA

Neudatchin S.V.

I.V.Kurchatov Institute of Atomic Energy, Moscow, USSR

A new versatile technique of finding χ_e^{HP} from experiments by heat pulse propagation is proposed. The basis for a new technique is a numerical solution to the heat conduction equation for an electron temperature perturbation $\tilde{T}_e(r,t)$. The equation is solved for a piece of the radius, where the real experimental signals, $\tilde{T}_e^{exp}(r,t)$, from the left-hand side point and from the right-hand side one out of three successive points of measuring $\tilde{T}_e(r,t)$ are taken as the left-hand side boundary and the right hand side boundary conditions for $\tilde{T}_e(r,t)$. The quantity χ_e^{HP} is chosen from the coincidence between the calculation and the experiment at the intermediate point of measuring $\tilde{T}_e(r,t)$. It is shown that the technique is applicable to the finding of χ_e^{HP} from the heat wave due to sawtooth oscillations, on the one hand, and due to ECRH, on the other. In difference from other techniques, this versatile technique determines χ_e^{HP} from a combined heat wave due to on-axis ECRH under strong saw-teeth. An instantaneous determination of χ_e^{HP} just after a shot in tokamak is possible.

Some analytical methods of finding χ_e^{HP} are widely used for tokamaks, but these methods depend on the way of producing a perturbation in the electron temperature $\tilde{T}_e(r,t)$. Using the method /4/, one can find an average value of χ_e^{HP} within the region between the saw-teeth oscillation radius, r_0, and a point of measuring $\tilde{T}_e(r,t)$. The method /1/ is applicable to local ECRH.

Let us consider the transport equation, $\tilde{T}_e(r,t)$, on the background of a stationary profile, $T_{e0}(r)$. Designating $T_e = T_{e0} + \tilde{T}_e$, $\chi_e = \chi_{e0} + \tilde{\chi}_e$ etc. and assuming $\tilde{n}_e/n_{e0} \ll \tilde{T}_e/T_{e0}$

$\frac{3}{2} n_0 \frac{\partial \tilde{T}_e}{\partial t} = \frac{1}{r}\frac{\partial}{\partial r}\left[r n_0 (\chi_{e0} + \tilde{\chi}_e + \tilde{\chi}_e \nabla T_{e0}/\nabla \tilde{T}_e)\nabla \tilde{T}_e\right] + \tilde{Q} =$

$= \frac{1}{r}\frac{\partial}{\partial r}\left[r n_0 \chi_e^{HP} \nabla \tilde{T}_e\right] + \tilde{Q}$, $\chi_e^{HP} = \chi_{e0} + \tilde{\chi}_e + \tilde{\chi}_e \nabla T_{e0}/\nabla \tilde{T}_e$ (1)

In /2/ it has been shown that $\chi_e^{HP} = \chi_{e0} + (\partial \chi_e/\partial \nabla T_e)\cdot \nabla T_{e0}$ at $\chi_e = \chi_e(\nabla T_e)$, $\nabla \tilde{T}_e \ll \nabla T_e$. The calculation of $\tilde{T}_e(r,t)$-evolution at $\chi_e(\nabla T_e)$ has been done, using the complete transport code in the same paper /2/. The calculation shows that the $\tilde{T}(r,t)$ evolution is diffusive (χ_e^{HP}=const(t)) at $\chi_e = \chi_e(\nabla T_e)$ and similar to that in TFTR /6/. Therefore, finding χ_e^{HP} by some, "dynamic "technique, one can find the quantity $\partial \chi_e/\partial \nabla T_e$ that is important for understanding a physical cause for anomalous electron transport.

Let us describe the proposed technique in detail. Let us have $T(r,t)$ measured at three successive points along the radius, r_1, r_2, r_3 located outside the zone, where the temperature perturbation source acts (i.e. $\tilde{Q}$ =0). The points should be located not far from each other, $r/a \lesssim 0.1$, that usually takes place in the experiments (in JET there are forty points of measuring $\tilde{T}_e(r,t)$ and 38 sets of three successive points, respectively). Let us solve Eq.(1) in a range $r_1 \leq r \leq r_3$, i.e. in the range, the left-hand side boundary and the right-hand side boundary coincide with the left-hand side point and with the right-hand side point of measuring $\tilde{T}_e(r,t)$. As we have already discussed, let us consider the $\tilde{T}_e(r,t)$ - propagation upon a stationary background. Therefore, an initial condition for $\tilde{T}_e(r,t)$ is $\tilde{T}_e(r,0)=0$ at t=0 (t=0 is the start up of the source functioning, $\tilde{T}_e(r,t)$). Let us assume the experimental signals, $\tilde{T}_e^{exp}(r_1,t)$ and $\tilde{T}_e^{exp}(r_3,t)$, to be the left-hand side and the right-hand side boundary conditions for Eq.(1). Presetting various values of χ_e^{HP}=const $(r,t) = \chi$, we calculate the behaviour of $\tilde{T}_e^{cal}$ (χ, r, t) at an intermediate point, r_2 from the numerical solution to Eq.(1). The quantity χ_e^{HP} is found from a minimum deviation of the calculation for an intermediate point, $\min\left[\int_0^t / \tilde{T}_e^{cal}(\chi,\right.$

$,r_2,t)-\tilde{T}_e^{exp}(r_2,t)/^{1\div2}dt]$, from the experiment. The value of χ_e^{HP} obtained is almost local, i.e. an average within the range $r_1 \leq r \leq r_3$, $(r_1 \div r_3) \ll a$. Moreover, any changes in χ_e or in heat sources or sinks on the left and on the right from the range $(r_1 \div r_3)$ will not affect χ_e^{HP}. One can also find a radial dependence, $\chi_e^{HP}(r)$, e.g. searching within the class of solutions $\chi_e^{HP}=\alpha_n r^n m$ n=0,1,2,3, finding α_n for each n as described above. As for a radial dependence, it is determined from the absolute minimum of the quantity $\int_0^t /\tilde{T}_e^{calc.}(\alpha_n r^n, r_2, t)-\tilde{T}_e^{exp.}(r_2,t)/^{1\div2} dt$ When one knows the error bars in the measurements of $\tilde{T}_e(r,t)$, it is easy to estimate the error bars in determination of χ_e^{HP}

Three points of measuring $\tilde{T}_e(r,t)$ are not alwais present in the experiment. Let us have only two points of measuring $\tilde{T}_e$ r,t , r_1 and r_2. Then assuming the boundary condition to be on the liner, r=a, instead of the right-hand side boundary condition, i.e. $\tilde{T}_e(a,t)=0$, one can solve Eq.(1) in the range $r_1 \leq r \leq a$. Then one can determine χ_e^{HP} in the same way as at three points of measurement.

Let us verify the technique by some examples now. Let us determine χ_e^{HP} from a heat wave under saw-tooth oscillations. The most complicated case is as follows: enhanced rate of $\tilde{T}_e(r,t)$ - evolution in the vicinity to the zone r_0, when $\chi_e^{HP}/\chi_{e_{OH}}^{PB}$ =4-6. $\tilde{T}_e$ (r,t) - evolution in T-10 is given in Figs. 1-2 /3/ . The dashed line 2 corresponds to the calculation with a complete transport code at $\chi_e=\chi_e(\nabla T_e)$ /2/ when $\chi_0+(\partial\chi_e/\partial\nabla T_e)\cdot\nabla T_{e_0}=4\cdot10^3 cm^2 s^{-1}$ The result obtained by the proposed technique: $\chi_e^{HP}=7\times10^3 cm^2 s^{-1}$ at Δt=3 ms ($5-9\times10^3$ at 10% error in $\tilde{T}_{e_{max}}(r_2 t)$; 6.4×10^3 at Δt= 1.5 ms ($5.3-8\times10^3$); 6×10^3 at Δt=0.75 ms ($5-7\times10^3$). The dashed-dotted line 3 corresponds to our technique at Δt=1.5 ms, χ_e^{HP}= 6.4×10^3. One can see that our technique allows one to choose a time interval with the best "resolving power" of the method (with a minimal spread in χ_e^{HP} due to error bars of the measurements). Now, let us consider the combined heat wave due to on-axis ECRH

and strong saw-tooth oscillations.A "quasi-experimental" $\widetilde{T}_e(r, t)$-evolution at three points along the radius,determined from the calculation by the complete transport code /7/ ,is shown in Fig.3.In the calculation by the transport code P^{*}_{ECRH}=1 MW, $\bar{n}$ =3.5x10^{13}, J_p=340 kA, B_z=3T, χ_e =2χ_e^{MM} from the T-II scaling law /5/ ,i.e. $\chi_e \sim \sqrt{Te}/n$, $\chi_{e0}(r)$=5x10^3÷10x10^{3}cm^{2}s^{-1} at 11 cm$\leq r\leq$ 18 cm, at t=0, and $\chi_e(r)$=6.3-11x10^3 at t=10 ms. Using the proposed technique,one obtains χ_e^{HP}=8x10^3 at the optimum Δ t=8 ms (χ_e^{HP}=7.2-9x10^3 within the error bars ±6 eV).One can see that it is very close to the real values of χ_e (r_2).

The calculation by the proposed technique at χ_e^{HP}=8x10^{3}cm^{2}s^{-1} and at Δt=8ms is given in Fig.3 with a dashed line.

Thus,the serviceability of a new,versatile technique for finding the local value of χ_e^{HP} from the experimental data is given in the paper. The technique is applicable to an automatic express-processing of experimental data immediately after the shot in tokamak or stellarator.

References

1. Dnestrovskij,Yu.N.,Neudatchin,S.V.Preprint IAE,1986,4301/6
2. Neudatchin,S.V.VANT.Fusion,Series 1986,issue 3,p.42 (in Russian)
3. Bagdasaroc,A.A.,Vasin,N.L.,Esipchuk,Yu.V.,Neudatchin,S.V.et. al.Fizika plasmy,1987, v.13, N 8, p. 899.
4. Callen,J.D.,Jans,G.L.-Phys.Rev.Lett.,1977,v.38,p.391.
5. Vlasenkov,V.S.et al.,In:Plasma Ph.and Cont.Nucl.Fus.Res.-Vienna,IAEA,1977, v.1,p.85.
6. Frednicson,E.D.,Callen,I.D.,Colchin R.I.et al.,1986,PPPL-2255.
7. Dnestrovskij,Yu.N.,Kostomarov,D.P.Numerical simulation of Plasmas,1986,Springer,Verlag.

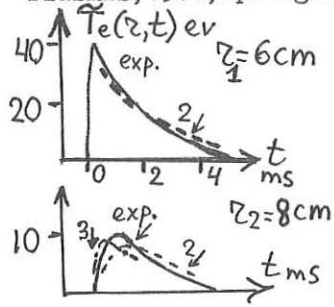

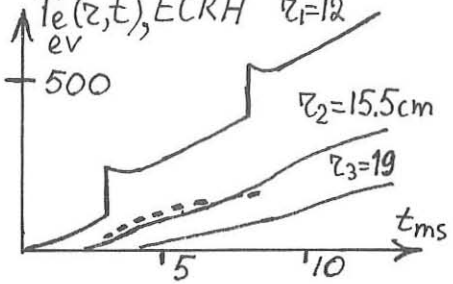

PLASMA SHEATH STRUCTURE IN THE PF-150 PLASMA-FOCUS DEVICE

A. Kasperczuk, R. Miklaszewski, M. Paduch, K. Tomaszewski, Z. Wereszczyński

Institute of Plasma Physics and Laser Microfusion
P. O. Box 49, 00-908 Warsaw, Poland

The paper deals with investigating the structure of plasma sheath during the collapse phase in the PF-150 plasma-focus device by means of a set of optical diagnostics. The main idea of the investigations is to describe properties of strong shock waves generated by means of current discharge in deuterium (D_2). Theoretical papers published so far do not describe sufficiently processes following strong shock waves [1, 2]. They usually deal with one-dimensional models, in which only a part of essential physical phenomena is included. Thus, there is necessary to carry out detailed experimental investigation of the plasma-focus in order to understand the accompanying phenomena better and to achieve more complete data for their simulation. Precise determination of the plasma sheath structure requires simultaneous using of many diagnostics allowing to measure the distributions of plasma

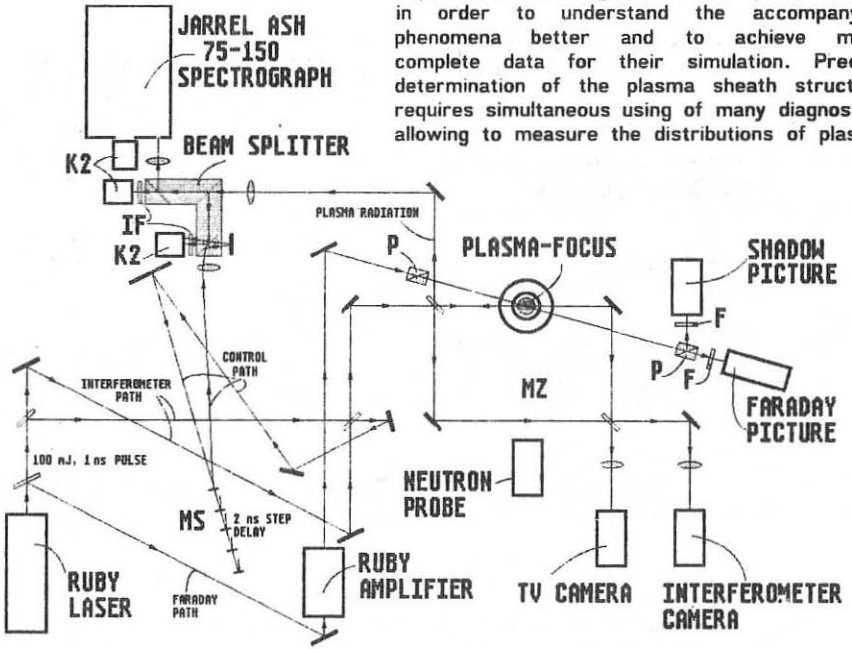

Fig. 1. *Scheme of the experimental system. The descriptions means as follows:* ***K2*** *- image converter,* ***IF*** *- interference filter,* ***MS*** *- mirrors of synchronizing line,* ***F*** *- glass filter,* ***P*** *- polarizer,* ***MZ*** *- Mach-Zehnder interferometer*

density, plasma temperature and magnetic field inside the sheath. That is why the fine synchronized system of optical diagnostics was built, consisting of laser interferometry, fast frame photography, time- and space-resolved spectroscopy in the visible range, and the Faraday rotation technique [3, 4, 5]. Moreover, there were developed some helpful methods of readout and analysis of recorded data. The scheme of the experimental system is shown in Fig. 1.

Because of the high speed of the phenomena being investigated, the pictures of plasma achieved from all diagnostics should be taken in the same moments with the time jitter not greater than 1 ns. Thus, it was built a special system of electronic synchronization (with accuracy of 5 ns) and the electrooptical system of synchronization control (accuracy not lower than 1 ns) which are shown in Fig. 2. Using the output radiation of the laser oscillator to fire the laser-triggered spark-gaps we achieve that the moment of laser pulse generation is connected to the moment of electrooptical camera triggering. The length of optical compensating line is matched in such way that the camera records light emitted from plasma in the moment when the laser probe beam passes through the discharge chamber.

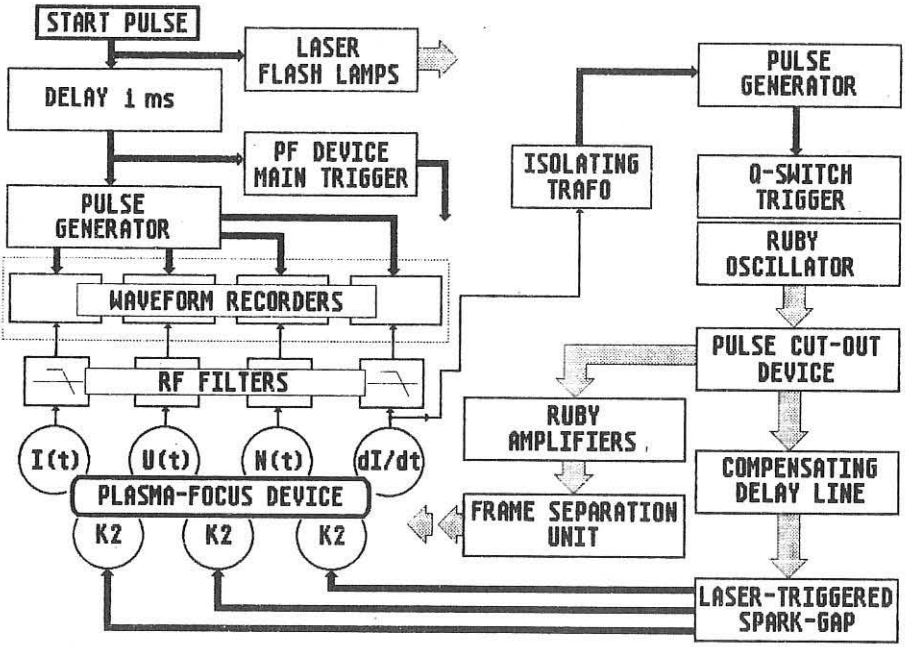

Fig. 2. *Scheme of diagnostic system synchronization.*

The synchronization control is realized as follows: laser beams corresponding to two interferometric frames are additionally directed towards special optical line consisting of a set of beam splitters MS. These beams, after reflecting from each of splitter fall onto the image converter in the electrooptical camera where they are

recorded as a series of light spot used as time markers. The distances between succeding splitters are matched in such way that the consecutive spots appear on the photocathode surface every 2 ns. Because the exposure time in both the electrooptical camera and the interferometer is 1 ns, recording one of the light marker (or two adjacent ones) by camera informs about diagnostics timing with the accuracy better than 1 ns within the range from -6 to +12 ns (see Fig. 3).

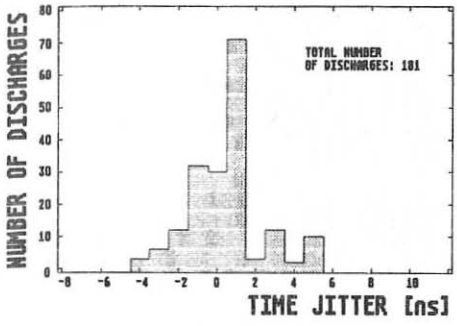

Fig. 3. *Spread of diagnostics timing.*

Determination of the electron temperature distribution within the plasma sheath is a new element in comparison with measurements previously described in papers [3], [4] and [5]. The basis of the method used here is the registration of plasma density profile $n_e(r)$ simultaneously with the plasma radiation intensity profile $\mathfrak{I}(r)$ for the wavelength range in which the strong line emission does not occure. The window of $\Delta\lambda$ = 60 Å centered at 5930 Å was chosen by experimental investigation of time- and space-resolved spectra of plasma radiation. In this window the continous radiation is dominant (***free-free*** and ***free-bound*** transitions only).

Considering the electron density spatial distribution $n_e(r)$ and the plasma radiation one $\mathfrak{I}(r)$ we introduce the parameter $n_e^2/\mathfrak{I}$ as a function of radius r. Actual relation between this parameter and the electron temperature of plasma T_e depends on the type of radiation emitted. Total emission coefficient ε_{tot} within the observed spectral range is the sum of two terms:

$$\varepsilon_{tot} = \varepsilon_{ff} + \varepsilon_{fb}$$

The exact formula for ε_{tot} given in paper [6] may be in the temperature range of interest (i.e. 1 ... 100 eV) quite well approximated as:

$$\varepsilon_{tot} = n_e^2 \frac{3.51}{\ln T_e - \ln 2.61}$$

Hence, we can derive the value of electron temperature within the plasma sheath if the values of ε_{tot} and n_e are known from experiment, using formula:

$$T_e = 2.61 \exp\left(3.51 \frac{n_e^2}{\varepsilon_{tot}}\right)$$

Actually, we measure the value of intensity $\mathfrak{I}(r)$ instead of emission coefficient ε_{tot}, but these physical quantities are the same within the accuracy of constant factor,

depending on experimental conditions only (geometry of experiment, optical system transmission, camera sensitivity etc.). The constant factor should be determined from additional measurement of the electron temperature at least in one point within observed area, for example from the ratio of continous radiation intensities registered by means of two cameras wieving different spectral windows.

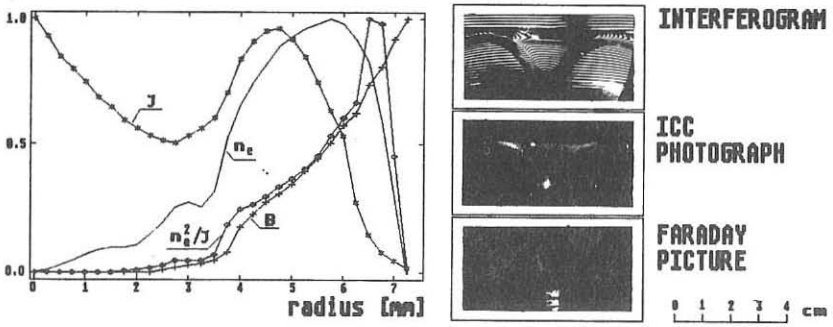

Fig. 4. *An example of experimental results. The plots are normalized relating to their maxima (B_{max}= 12 T, n_{emax}= 2.2·10^{18} cm^{-3}, J and n_e^2/J curves are in arbitrary units).*

The investigation presented in this paper are a part of a wider program which aims of determining the causes of unrepeteability of neutron yield in succeding plasma-focus discharges, and also the saturation effect observed on the plot of neutron yield vs energy stored in condenser bank for the energies of 200 - 300 kJ. The essential part of this program is to investigate a connection between the neutron emission and the plasma sheath structure during collapse phase. Joining together the precisely synchronized interferometer, electrooptical camera and polarimeter we are able to achieve spatial distributions of electron density, visible light emission and magnetic field in plasma sheath. Integral neutron yield registered in each discharge allows to find its connections with above parameters. As an example are given the plots on Fig. 4 showing the registered structure of plasma sheath.

References:

1. Ya. B. Zel'dovich, Yu. R. Raizer; Physics of Shock Waves and High-Temperature Phenomena, Academic Press, London 1966.
2. L. Bilbao, M. Kelly, H. Bruzzone; Phys. Fluids, **29**, p. 4180 (1986).
3. S. Czekaj, S. Denus, A. Kasperczuk, R. Miklaszewski, M. Paduch, T. Pisarczyk, Z. Wereszczyński; Proceedings of 4th International Workshop on Plasma focus and Z-Pinch Research, p. 124, Warsaw 1985.
4. S. Denus, A. Kasperczuk, R. Miklaszewski, M. Paduch, T. Pisarczyk, Z. Wereszczyński; IPPLM Report, No. 5, 1986.
5. S. Czekaj, S. Denus, A. Kasperczuk, R. Miklaszewski, M. Paduch, S. Śledziński, K. Tomaszewski, Z. Wereszczyński; 9th European Conf. on Controlled Nucl. Fus. and Plasma Phys., Aachen 1983, paper O-23.
6. W. Lochte-Holdgreven, ed.; Plasma Diagnostics, North-Holland, Amsterdam 1968.

TWO-DIMENSIONAL OPTICAL TOMOGRAPHY OF IMPURITIES IN THE FT-2 TOKAMAK

B.V.Kuteev, +A.D.Lebedev, I.E.Sakharov, S.P.Sivko,
A.E.Soldatov, S.N.Ushakov

M.I.Kalinin Polytechnical Institute, Leningrad, USSR
+A.F.Ioffe Institute of Physics and Technology, Leningrad

The impurities profiles information plays important role in the considerations of transport phenomena in tokamaks.

Various experimental data being obtained so far on several tokamaks such as JET, PDX, ASDEX prove that phenomena concerning impurities behaviour (transport, entry mechanism and so on) are essentially non one-dimensional in their nature /1,2,3/.

The large amount of unique information on the impurities spatial profiles can be obtained from spectroscopical experiments. This diagnostic enables us in principle to treat ion species separatelly. However, the experiments used so far were either one-projectional or multy-projectional but without ion species separation.

This paper deals with two-projectional tomography spectroscopical experiments on the FT-2 tokamak with selection of different ion species such as oxigen and carbon in various states of ionisation aswell as neutral hydrogen.

The small FT-2 tokamak (the major radius R = 55 cm and the limiter a = 8 cm) was operating in the regime with central chord average density $N_e = 2 \times 10^{13}$ cm^{-3}, toroidal magnetic field B_t = 21 kGs, total plasma current J_p = 30 kA, electron and ion temperatures T_e = 400 eV, T_i = 140 eV.

Figure 1 presents the general design of collecting the impurities radiation. The spectral lines selection was performed

by means of the MDR-2 the grating monochromators. The line spatial distribution profiles were obtained using slotted rotating disks with a scan time of 1.5 ms.

Local emissivity profiles were obtained using numerical reconstruction methods. The local distributions were constrained to the class of functions

$$f(r,\beta)=f_0(r)+f_1(r)\times\mathrm{Cos}(\beta)+f_2(r)\times\mathrm{Sin}(\beta)+f_3(r)\times\mathrm{Cos}(2\beta),$$

where (r,β) denotes polar coordinates and $f_i(r)$ were represented with polynoms of even powers of r.

The profiles reconstructed can be subdivided into the three classes approximately. The first class presents profiles with near uniform emission distribution in one narrow ring located on the periphery of the discharge (see Fig.2). Such types of profiles were observed usually for ion species in suffitiently high ionisation states (C^{V},O^{V}). The second class has the strong asymmetry in one or both projections. Such distributions were typical for peripheral ions lines (C^{iii},O^{ii},O^{iii}). And finally, the third class presents profiles consisted of both uniform distributed narrow ring and sharp peak located on the inner side of the plasma column. These are typical for O^{iv} ions and Hß (see Fig.3).

The strong asymmetry in the peripheral ions emissivity can be explained in the terms of the additional localized source of impurities that can appear on the periphery of the discharge when the plasma column kisses the wall.

The angular symmetry of the profiles typical for ion species in the high ionisation states speaks of the transport phenomena important role in the formation of such distributions.

The third class profiles can take place due to either the closeness of the different chemical elements spectral lines (like Ne^{i} for O^{iv} e.g.) or some MARFE-like instability.

The experimental setup enabled us to consider the time evolution of the emissivity profiles. In the number of cases we observed its transformation that can be interpreted as source

displacement (see Fig.4). The angular motion of such type was as far as 90° sometimes.

The research being performed tells us that the second projection in the tomography presents the better possibility to interpret data obtained in the simple cases especially.

Finally we'd like to mention the difficulties encountered in the third class profiles reconstruction . The formal procedure described above leads sometimes to appearance of the artifitial peculiarities in the central part of the discharge that seem to have nothing to do with the rerum natura. Its presence means that the functional class used in the reconstruction algorithm is not quite adequate to the physical subject. To avoid these difficulties one should use either alternative functional classes or additional projections.

References

1. J.O'Rurke,D.Campbell,B.Denne et al. Poloidally asymmetric edge phenomena in JET // 12th European conference on controlled fusion and plasma physics. - Budapest,1985,-part 1. - p.155-158.
2. W.Feneberg,M.Kornherr,P.Smeulders et al. Poloidal asymmetric impurity radiation in ASDEX in the presence of neutral injection // ibid.,p.299-302.
3. K.Brau,S.Suckewer. Vertical poloidal asymmetry of low-Z element radiation in the PDX tokamak // Nuclear Fusion - 1983.-v.23.-n.12.-p.1657-1668.
4. V.N.Budnikov,V.V.Djachenko,L.A.Esipov et al. Lower hybrid ion heating in the FT-2 tokamak. // This conference.

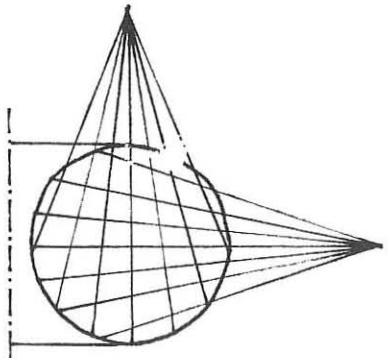

Fig. 1

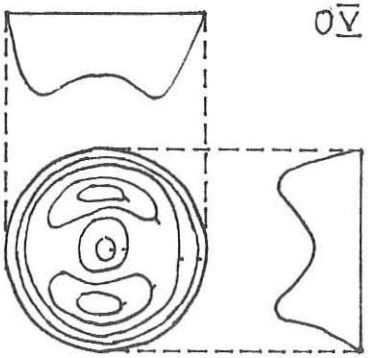

Fig. 2

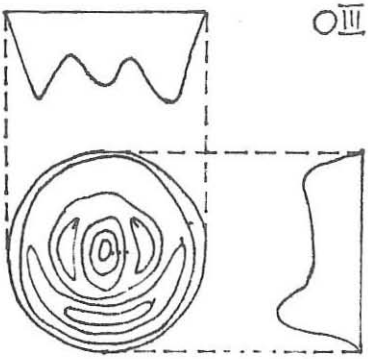

Fig. 3

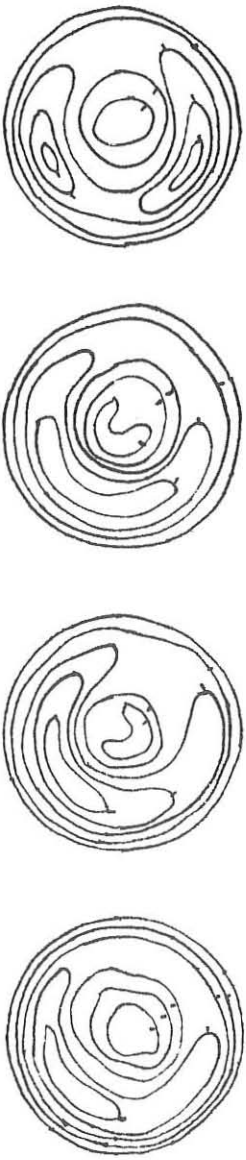

Fig. 4 "Cinema"

THE APPLICABILITY OF RUTHERFORD SCATTERING FOR T_i-MEASUREMENTS AT MEDIUM- AND LARGE-SIZED EXPERIMENTS

E.P. Barbian, A.A.E. van Blokland, A.J.H. Donné and H.W. van der Ven

Association Euratom-FOM, FOM-Instituut voor Plasmafysica, Rijnhuizen, P.O. Box 1207, 3430 BE Nieuwegein, The Netherlands

Introduction

Fast and mono-energetic helium atoms (20-30 keV) are transmitted through the core of the plasma and become elastically scattered by unshielded Coulomb interaction with the nuclei of randomly moving plasma ions. The conservation of momentum and energy at single encounters determine the energy distribution of the scattered fast neutrals when observed at small scattering angles ($\sim 7^0$).

The method can be considered to be especially useful for observation of the bulk distribution of the ions. No special pre-assumption concerning a maxwellian-shaped distribution has to be used and no interpretational efforts on transport losses between interaction volume and detector are necessary. The beam intensity should be large enough to allow for a sufficient number of scattered particles falling on the detector within a desired time-interval which defines the time resolution.

Application of the method

The Rutherford scattering diagnostic has been applied at the T-4 tokamak in 1978 [1], using an 8 keV He-beam of 10 A/m^2 and in a pilot experiment at the JFT-2 tokamak [2]. Earlier development on the diagnostic has also been performed at the Rijnhuizen laboratory [3] leading to the use of a high-resolution time-of-flight analyser for the observation of slowing-down spectra of neutral heating beams in ASDEX [4]. Recently, a scattering diagnostic was put into operation at JT-60 [5,6] utilizing a 200 keV helium beam for the large-sized plasma. Extensive feasibility studies at FOM Rijnhuizen [7,8] concentrated on the influence of plasma impurities on the measurement and results were taken for parameter optimization for application of Rutherford scattering at TEXTOR. A joint project between FOM Rijnhuizen and KFA Jülich (FRG) has been started in 1987 to implement the diagnostic at the TEXTOR tokamak.

The general applicability of the beam-scattering diagnostic for medium-sized and large experiments beyond the parameter sets, existing at present time, will be discussed in the contribution. The estimates are supported by a comparison with an example of JT-60 data and are also extended to even higher probing beam energies of 300-500 keV which are suitable values for large fusion devices.

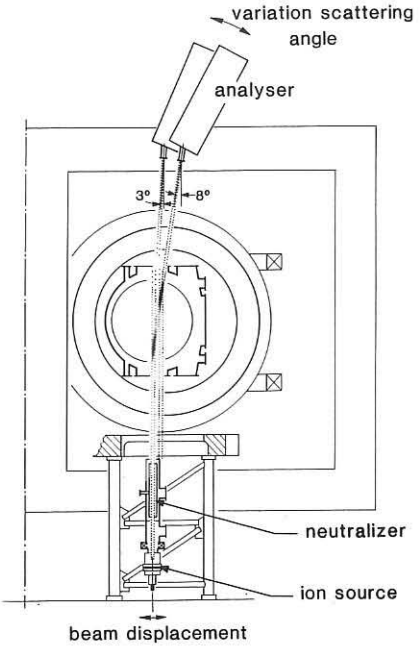

Fig. 1. The scattering experiment at TEXTOR (liner diameter ≈ 100 cm) is composed of the vertically positioned ion source for up to 30 keV and 50 mA helium beam, a gas neutralizer cel (efficiency ~ 40%) and a time-of-flight single particle analyser at a scattering angle α, to be chosen between 3^0 and 8^0. The image shows scattering in the poloidal plane. By turning the analyser by 90^0, observations can also become possible in axial (toroidal) direction. The remotely controlled lateral movement of the source axis provides a point-to-point shift of the scattering volume.

Experimental data projection

Time-of-flight analyser:
64 channels, 1000 counts per sample
Time resolution : 2 ms
Continuance : 5 s
Spatial resolution: 2 cm (radial) and 20 cm (vertical)
Data processing : CAMAC technique and local VAX-station
Expected T_i-values: 0.5 to 5 keV
Instrumental error: 20 eV equivalent.

Theoretical consideration

For probing species with energies $E_b \gg T_i$ and small-angle scattering which implies small impact parameters ($b < 0.05\ a_o$, a_o indicating the Bohr radius) one can write the energy distribution of the particles received at the detector in accordance with [9].

The energy distribution observed with a solid angle $\partial\Omega$ is given by

$$\frac{\partial^2\Gamma(E)}{\partial E\partial\Omega} = C(E_b)\eta(E_b)Jn_pV\frac{1}{E_b^3}\left(\frac{E}{T}\right)^{1/2}\frac{7.3}{\sin^5\theta}\frac{Z_p^2 Z_b^2}{\sqrt{\gamma}}\times\exp\left(\frac{-[E-E_b(1-\gamma\sin^2\theta]^2}{4\gamma E_b T\sin^2\theta}\right), \quad (1)$$

with θ, the scattering angle; γ, the mass ratio of beam and plasma particles; E_b, the beam energy (eV); E, the energy of a detected neutral particle (eV); J, the equivalent neutral beam intensity (A m^{-2}); n_p, the local ion density in the scattering volume (m^{-3}); V, the scattering volume (m^3); Z_p, Z_b, the nuclear-charge numbers of plasma and beam particles; $\eta(E_b)$, the energy-dependent attenuation of the beam in the plasma; and $C(E_b)$, the survival probability, which takes into account the electron-loss processes which occur simultaneously with the scattering collision. The dimension of the factor 7.3 in Eq. (1) is ($kg^2\ m^6\ C^{-3}\ s^{-4}$).

The ion temperature value can be deduced from the width of the nearly gaussian-shaped distribution using

$$\Delta E_{FWHM} \approx 4(\ln 2)^{1/2}\sin\theta\ (\gamma E_b T_i)^{1/2}. \quad (2)$$

For calculating the distribution one takes into account the energy-dependent attenuation of the beam $\eta(E_b)$ and a competing electron loss $C(E_b)$ process at the instant of the scattering. The survival probability $C(E_b)$ for the scattered neutral is well above 80% for encounters of energetic helium atoms with protons and only 2% for scattering on C^{6+} or O^{8+} [7]. Despite the square dependence on the nuclear charge number Z_p in Eq. (1), the superimposed contribution from impurities (Fig. 2) for standard parameters of TEXTOR (E_b = 5 keV/amu) are very small.

The contribution of impurities in the case of JT-60, however, is quite appearing. The relatively higher beam energy (47.5 keV/amu) has again a small impact on the electron loss probability in collision with highly charged impurities, which is also about 98% (2% survive). However, strong changes appear for the loss probability for collision with the main plasma component H^+ itself. Mainly due to one electron capture an unfavourable loss of 75% has to be taken into account. For JT-60 parameters and an 8% oxygen component which corresponds with reported Z_{eff} values, there is great similarity (Fig. 3) between calculated (dotted line) [10] and experimental values [5,6].

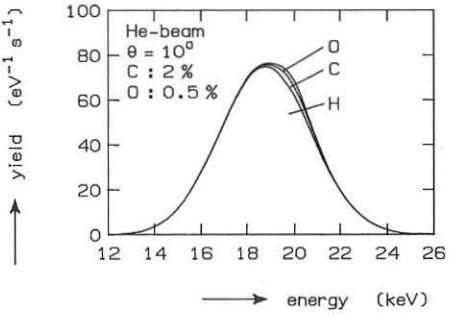

Fig. 2.

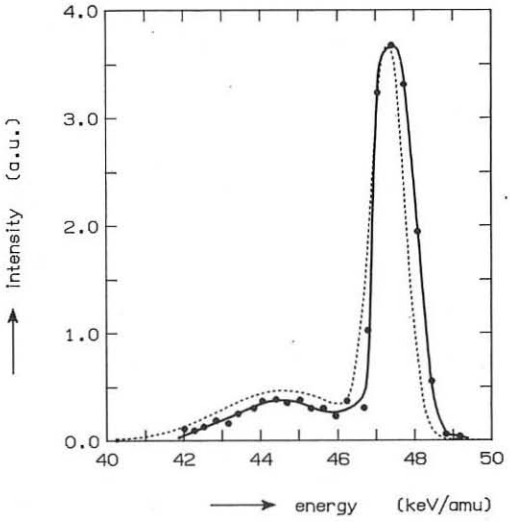

Fig. 3.

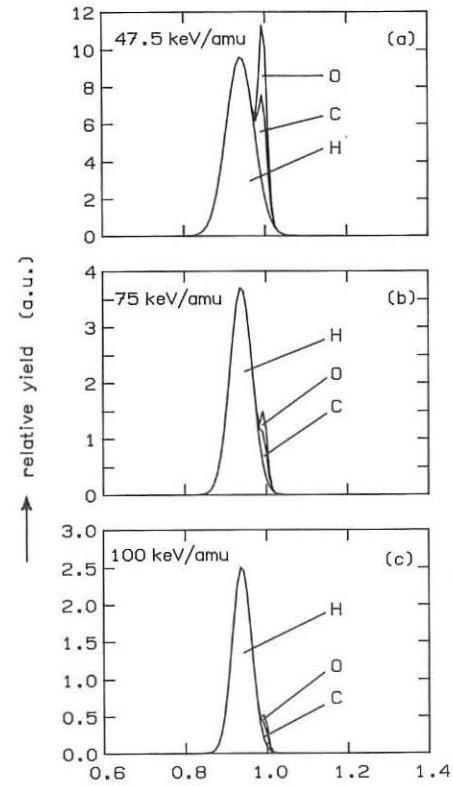

Fig. 4.

Taking again JT-60 parameters as being representative for large experiments and using impurity values of 2% C and 1% O, the calculations were extended to 75 and 100 keV/amu, keeping T_i at 1.9 keV and α at 7^0. The beam attenuation is weakly energy-dependent and the total yield is slightly smaller for higher energies.

Conclusion

The choice of higher beam energies compared to the somewhat unfavourable regime near 50 keV improves strongly the main distribution in relation to that of the impurity satellite (Fig. 4). The contribution from high Z-atoms is also small at low beam energies (< 10 keV/amu) and due to a higher yield this is a comfortable situation. High T_i-values (> 10 keV) necessitate the use of much higher beam energies. No limitations from the impurity component appear to limit the potentiality of the beam diagnostic for application at large fusion devices.

Acknowledgement

This work was performed under the Euratom-FOM association agreement with financial support from NWO and Euratom.

References

[1] E.L. Berezovskii, A.I. Kislyakov, S.Ya. Petrov, G.V. Roslyakov, Sov. J. Plasma Phys. **6** (1980) 760.
[2] H.Takeuchi et al., Jpn. J. Appl. Phys. **22** (1983) 1717.
[3] G.J.H. Notermans, H.W. van der Ven, H.J.B.M. Brocken, Rijnhuizen Report 82-140 (1982).
[4] G.H.J. Notermans, Rijnhuizen Reports 84-155 and 84-157 (1984).
[5] K. Tobita, Y. Kusama, M. Nemoto, H. Takeuchi, T. Itoh, Y. Tsukahara, Bull. Am. Phys. Soc. **32** (1987) 1768.
[6] K. Tobita et al., submitted to Nucl. Fusion, 1988.
[7] A.J.H. Donné, E.P. Barbian and H.W. van der Ven, J. Appl. Phys. **62** (1987) 3130.
[8] E.P. Barbian, A.A.E. van Blokland, A.J.H. Donné and H.W. van der Ven, Bull. Am. Phys. Soc. **32** (1987) 1774.
[9] V.G. Abramov, V.V. Afrosimov, J.P. Gladkovskij, A.I. Kislyakov and V.I. Perel', Sov. Phys. - Tech. Phys. **16** (1972) 1520.
[10] A.J.H. Donné, F.J. de Heer, R.E. Olson, J. Appl. Phys., to be published.

APPLICATIONS OF RESONANT MULTIPHOTON IONIZATION OF ATOMS TO FUSION PLASMA RESEARCH

F. L. Tabares

Association EURATOM/CIEMAT, 20040 MADRID, SPAIN

INTRODUCTION

Although Resonant Multiphoton Ionization (RMPI) techniques have been extensively used ,under different names, in many fields of physics and chemistry[1] and it has been successfully used in weakly ionized plasmas for H_2,H and metastable H_2 detection [2],the difficulties associated to the detection of the ions formed by RMPI within a fusion plasma make this technique not very suitable as a non perturbative plasma diagnostic.

In the present work a new method for single shot, in situ velocity distribution measurements based on RMPI in combination with Laser Induced Fluorescence (LIF) , of relevance for impurity flux determinations in fusion plasma research is proposed, altogether with some others experiments in the plasma edge.

VELOCITY DISTIBUTIONS MEASUREMENTS OF NEUTRAL IMPURITIES

Velocity distributions of neutrals are important not only for the evaluation of impurity fluxes but also to determine the mechanism responsible for their ejection. The continuous character of the flow of sputtered particles and the imposibily to chop it make time of flight (TOF) techniques not applicable to in situ velocity measurements in fusion plasma experiments so that Doppler shifted excitation in LIF detection of neutrals is the only method extensively used until now for this purpose[3]. In general these measurements require many, reproductible , plasma discharges and new methods based on fast scanning of the dye laser frecuency during a single discharge have been proposed as alternative[4] .In any case velocity resolution has to be gained on expenses of the signal versus noise ratio and correction for the laser power at each wavelength is always needed due to the low saturation parameter attained under these conditions.

One possible way for in situ chopping of the continuous flow of neutral impurities is by laser ionization of all the atoms present in the detection volume ,so that a negative going pulse of several nanoseconds of duration can be produced in the detection signal (impact excitation or LIF signal) . If the monitoring signal is the LIF

In order to completely ionize all the atoms in the sampling volume one needs to choose the right splitting of the excimer power into direct (ionizing) beam and pumping one. That in principle will depend on the particular atomic system under consideration, but a simple calculation based on the rate equations for a three level system plus ionization [1] shows that if, for example, one starts with a 0.5 Jul/pulse XeCl laser and a ratio 1:1 between the power used to pump the dye laser and that of the ionizing beam, so that a modest 50 uJul/pulse UV radiation is obtained after frecuency doubling ,still high enough to saturate the resonant transition (S=150 for Be,S=100 for Fe,focussing in 2x2mm^2), ionization will take place to a 100% in a time shorter than the laser pulse (15 to 20 nsec), even if the excimer radiation is focussed in an area several times larger ,thus minimizing alignment problems.

Sampling of the LIF signal in a relevant time scale could be achieved by optically delaying successive reflections of the probing laser or by using a long pulse dye laser (several hundred nanoseconds) and crossing the excimer at the beginning of the pulse, thus obtaining a continuous LIF signal. In this configuration, however, two lasers are required and synchronization problems must be solved, although due to the short time required by the TOF experiment (see below) that should not be difficult

MODEL CALCULATION

The time evolution predicted by Eq. 1 is not directly applicable to extended sources as one has in limiter experiments. Convolution over all the emitter area and the different paths across the sampling volume depending on geometry, as well as attenuation through the plasma edge has to be taken into account.

Figure 1 shows the results of the calculation for a Be bar limiter, as mounted in the tokamak Unitor [5], where a 0.6 cm diameter hole is used to look at the scattering volume, a prism of 2x2x4 mm placed at 1 cm from the limiter in this simulation. Plasma edge temperature and density profiles as well as ionization and excitation rate constants are the same as in Ref 6 . No contribution to the refilling of the hole due to CX or electron recombination is considered as they are expected to be slow to effectively compete with the direct flux of sputtered atoms in the relevant time scale . A cosine distribution for sputtered particles is assumed.

As it can be seen in Fig 1a, discrimination between sputtering (Thompson model) and thermal distributions should be obvious even in a short time after the ionizing pulse (t=0). A factor of two in the binding energy will be also distinguishable after several tens of nanosecond. Fig 1b shows the velocity distributions for these two cases (Eb= 3.32 eV and 1.66 eV respectively) as they would be measured by Doppler shift in the same geometry and plasma edge conditions.

intensity under saturation conditions no correction for the sampling laser intensity is required and good signal to noise ratio is expected in one single plasma discharge.

RMPI-TOF EXPERIMENT

The proposed experiment consist on crossing two laser beams (the ionizing and probing ones) in the scattering volume and to record the time evolution of the LIF signal after complete ionization has taken place. After the detection volume has been depleted of neutral atoms by the RMPI process an spatial hole in terms of neutral density is formed. As the sputtered atoms start to fill it, the density in the observation volume will continuously increase and therefore the LIF signal when used as a density diagnostic,i.e. bandwith greater than the Doppler profile.

Assuming a well collimated atomic beam with a given velocity distribution f(v) and a scattering volume with dimension parallel to the travelling direction l the density after a given time after ionization is given by :

$$n(t)=n(0)x\left[t/l\int_0^{l/t} f(v)\,vdv + \int_{l/t}^{\infty} f(v)dv\right] \qquad (1)$$

where n(0) stands for the density of neutrals before ionization takes place.

The accurancy of the velocity distribution obtained with method will be limited by that of the scattering volume dimensions and its resolution by the dimensions themselves and the minimum sampling interval,ultimately limited by the lifetime of the excited level,providing that ionization takes place in a large extend during the ionizing pulse.

The most appealing way to carry out the experiment would be by using the same experimental set-up as for LIF detection. This in many instances consists of a dye laser pumped by an excimer one,typically XeCl at 308 nm, so that one has a 4.03 eV high power photon source readily available . This photon energy combined with that of the pumping photon is able to bring all the neutral atoms to the ionization continuum in most of the metals typically monitored in limiter experiments. Table 1 shows some of them:

TABLE 1

ATOM	EXCITATION,nm (eV)	IONIZATION(eV)
Fe(I)	302.0 (4.11)	3.79
Cr(I)	425.4 (2.92)	3.85
Ti(I)	293.3 (4.23)	2.61
Be(I)	234.9 (5.28)	4.04

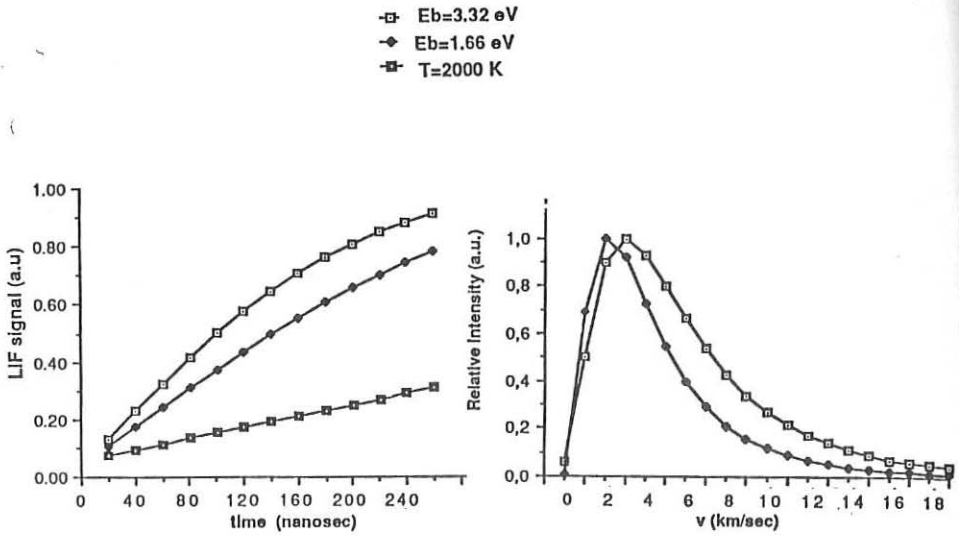

Fig.1a: Calculated time evolution of the LIF signal

Fig.1b: Convoluted velocity distributions

OTHER EXPERIMENTS

The good spatial and temporal resolution of laser diagnostics could be used in the RMPI experiments to probe the plasma edge. Although no detailed calculations have been performed yet,the screening properties of the plasma edge could,in principle , be tested without perturbing other plasma parameters in combination with neutral atomic beam diagnostics,among others.

REFERENCES

1. Laser Analitycal Spectrometry,V. S. Letokhov ed.,Adam Hilger, Bristol (1986)

2. J.H.M. Bonnie, E.H.A. Grannema and H.JHopman, Rev.Sci Instrum. 58, (1987) ,1353

3. A.Elbern, E, Hintz and B. Schweer, J. Nucl. Mat. 76&77,(1978),143

4. M. Maeda *et al.* ,J. Nucl. Mat. 111&112, (1982), 95

5. J. Hackman and J. Uhlenbusch, Nucl, Fusion. 24,(1984) 640

6. M. Bessenrodt-Weberpals *et al* ,Proceedings of the 14th European Conference on Controlled Fusion and Plasma Physics,Madrid ,1987,p.710

HIGHRESOLVED TIME MEASUREMENT OF THE LIGHT DENSITY DISTRIBUTION FROM THE TEXTOR MAIN LIMITER CROSS-SECTION

I. Lakicevic, Institute of Physics, Beograd, Yugoslavia
Z. Mucha, Institute of Fundamental and Technological Research, Warshaw Poland
E. Hintz and U. Samm, Institut für Plasmaphysik, KfA Jülich GmbH, Ass. EURATOM, Fed. Rep. of Germany
J. Uhlenbusch, Physikalisches Institut II, Universität Düsseldorf, Fed. Rep. of Germany

Introduction

For investigation of the time development of very fast processes during discharges in tokamak TEXTOR we have used a 16 mm camera. On the basis of the very flexible TEXTOR limiter configuration and the very high time resolution (up to 50 μs) it was possible to investigate different instabilities up to a few KHz. A special experimental arrangement has been used for the measurement of the poloidal rotation velocity of the plasma. These measurements are very useful for investigation of the dynamics of disruptions. Unfortunately, quantitative evaluations are very limited.

Experimental arrangement

TEXTOR is a tokamak [1] with a major radius of 175 cm and a minor radius of typically 46 cm. The TEXTOR limiter system consists of three poloidal limiters movable along the minor radius within 45-55 cm, located in the same poloidal cross-section and covering about 30 % of the minor circumference (Fig. 1). The limiter segments are made of graphite with a radius of curvature in toroidal direction of 5 cm (inner) and 1.2 cm (upper, outer, lower).

Discharges in TEXTOR can be produced with a maximum plasma current of 500 KA and a maximum toroidal magnetic field of 2.6 T. The typical operating conditions are: 340 KA and 2 T, the flat top of the plasma current about 1 s, peak density $3.5 \cdot 10^{13}$ cm^{-3}, peak electron temperature 1.3 KeV and the discharge duration up to 3 s.

For the camera measurements an experimental arrangement on TEXTOR has been set up as shown in Fig. 2. We have used a 16 mm HYCAM camera with rotating prism, moving film, highest speed of 18 000 frame/s and maximum streak resolution of 150 μs/cm. After some additions to the camera, it was possible to make high speed frames as well as streak photographs. In the case of frame photographs, plasma light from the whole area of the main limiter cross-section has been photographed, whereas for the case of the streak photographs, entrance slit of the camera was imaged in front of one of the existing limiters. The films were analysed by using a photo-densitometer and the video copies of these films were analysed by using a video image processing system.

Results and discussion

The frame photographs show that both plasma ignition and termination take place at the inner side. During the current ramp-up phase a very fast rotation of bright, island shaped areas in the wall region is observed. The plasma light emission (H_α) comes from the limiter region and very strong pulsations of the plasma light emission exist during the additional heating. From these photographs we have evaluated the H_α-emission profiles at different limiters (see Fig. 3) which are in anti-phase with the temperature oscillations of the sawtooth instability with a frequency of 14-15.7 ms. During typical disruption discharges, many consecutive plasma-wall contacts, occuring mainly at the inner side, were observed. During the contacts, very strong H_α-radiation, arizing predominantly from the inner wall region was observed; however, between the contacts this radiation spread over almost the entire plasma volume. From these photographs it is seen that very strong and irregular pulsation of the H_α-radiation exists.

The oblique lines on the streak photographs shown in Fig. 4 arize due to the rotation of the bright island shaped areas mentioned above. From the slope of these lines, the poloidal rotation velocity of the plasma and the corresponding frequency (see Fig. 5) are evaluated. From figure 5 one can see a very strong fluctuation of the plasma poloidal rotation velocity during the current ramp-up phase, followed by the plateau of about 0.9 km/s after the plasma position control system has been switched on, and again a small increase.

In order to make a theoretical comparison one can use the following formula [2] for the poloidal rotation velocity of the different species of the plasma:

$$v_{\theta_s} = -\frac{T}{eB_\phi}\left\{\left(\frac{\partial n}{\partial r}\frac{1}{n} - \frac{1}{Z_s}\frac{\partial n_s}{\partial r}\frac{1}{n_s}\right) + \left(K - \frac{1}{Z_s}\right)\frac{\partial T}{\partial r}\frac{1}{T}\right\},$$

where all quantities have the standard notation. For measured temperature gradients on TEXTOR [3,4] $\partial T/\partial r = -10$ eV/cm and for hydrogen plasma one gets:

$$v_{\theta_H} = \begin{cases} 0.75 \text{ km/s}, & K = 2.3 \quad [5] \\ 1.05 \text{ km/s}, & K = 3.1 \quad [2] \end{cases}$$

which is in a very good agreement with the measured value of (0.9 ± 0.1)km/s. The measured value agrees very well with new calculations [6].

From the streak photographs we have also evaluated an oscillation of $\nu_1 = 1.86$ KHz during the plateau of the poloidal rotation of the plasma as well as an oscillation of $\nu_2 = 0.92$ KHz, 180 ms after the beginning of the discharge (see Fig. 6).

The plateau of the poloidal rotation velocity of the plasma of 0.9 km/s is equivalent to the frequency of $\nu = 306.5$ Hz. The ratio $\nu_1/\nu = 6.08$ is approximately equal to the value of $q = 5.94$ for the measured $I_p(r)$ profiles at $r = 48.8$ cm.

Using streak photographs we have determined the direction of the plasma poloidal rotation. The plasma rotates in the same direction as the poloidal magnetic field: it is counterclockwise in the poloidal cross-section shown in Fig. 1.

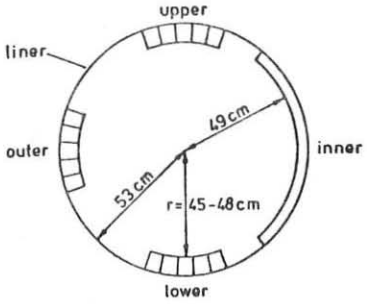

FIG. 1

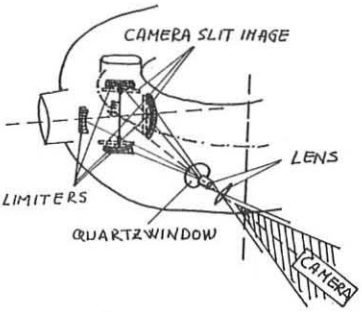

FIG. 2

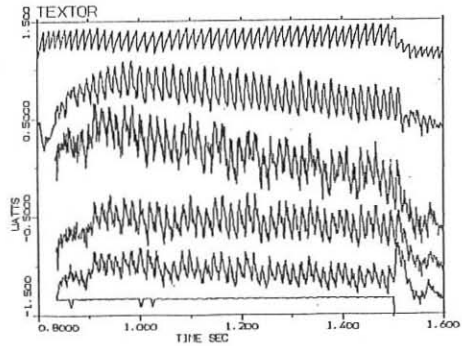

SH.NO. 24066
TEMPERATURE IN CENTER

D_α AT UPPER LIMITER

CAMERA SIGNAL AT LOWER LIMITER
CAMERA SIGNAL AT UPPER LIMITER
CAMERA SIGNAL AT INNER LIMITER
ICRH

FIG. 3

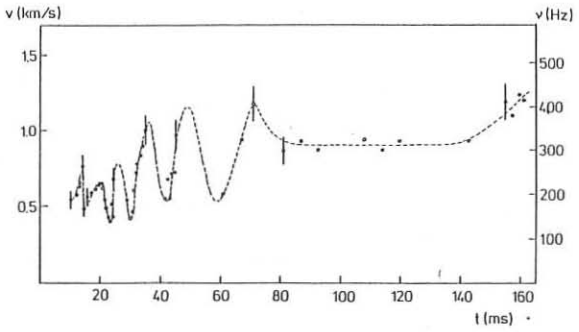

FIG. 5

FIG. 4

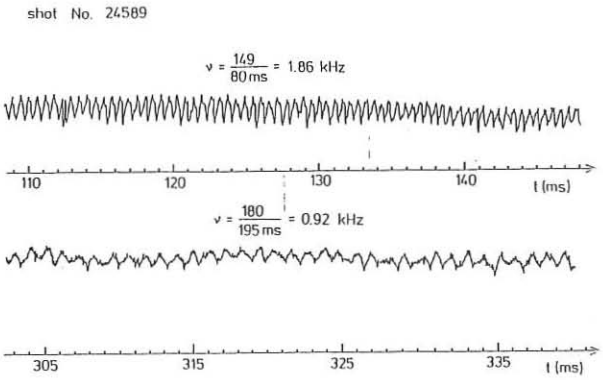

FIG. 6

Conclusions

From the camera measurements on the tokamak TEXTOR we have drawn the following conclusions:

1. According to the relation $\int H_{\alpha_L} \sim \sqrt{T_e(0)}$, $n_e(0)$ and our measurements it follows:
   1.1. sawtooth instability is poloidally symmetric,
   1.2. symmetric and synchronized within $t \lesssim 0.5$ ms, and
   1.3. its period is 14-15.7 ms.

2. m = 6 mode was observed during the current ramp-up phase:
   2.1. plasma poloidal rotation velocity (0.9 km/s) has been measured during the current ramp-up phase (m = 6 mode),
   2.2. plasma poloidal rotation frequency (306.5 Hz) has been measured (it agrees with m = 6 mode rotating at v = 0.9 km/s), and
   2.3. measured values are in a very good agreement with other measurements and theoretical predictions for typical TEXTOR Te-gradients.

3. Two high frequency instabilities have been measured:
   3.1. fluctuation of 1.86 KHz for a time of almost 70 ms after the plasma position control system has been switched on, and
   3.2. fluctuation of 0.92 KHz, 180 ms after the beginning of the discharge.

References

1. H. Solwitsch et al., Plasma Phys. Controlled Fusion, 26 (1984) 23
2. M.G. Bell, Nuclear Fusion, 19 (1979) 33
3. Y.T. Lie et al., Proc. Int. Conf. Plas. Phys., Lausanne 2 (1984) 320
4. A. Pospieszyk and G.G. Ross, Proc. 14th Europ. Conf. Controlled Fus. Plas. Phys., Madrid 110 (1987) 1280
5. K.T. Tsang and E.A. Frieman, Phys. Fluids, 19 (1976) 747
6. H. Gerhauser and H.A. Claaßen, Report Jül-2125 (1978)

MEASUREMENTS OF X-RAY RADIATION FROM PLASMA BY A PHOTOELECTRON METHOD

Yu.V.Gott, V.A.Shurygin
I.V.Kurchatov Institute of Atomic Energy, Moscow, USSR

The energy distribution of electrons emitted from a target radiated by X-rays from hot plasma allows one to determine the plasma electron temperature T_e [1] , and to study the behavior of impurities [2] .

The thermal X-ray continuum [3]

$$I_\gamma(E_\gamma) \sim \frac{1}{\sqrt{T_e}} \exp(-E_\gamma / T_e) \qquad (1)$$

is converted into a photoemission spectrum

$$I_e(E_e) = \sum_i f_i(E_{\gamma i}) I_\gamma(E_{\gamma i}) \qquad (2)$$

where

$$E_{\gamma i} = E_e + E_i \,, \qquad (3)$$

$$f_i(E_{\gamma i}) = B\, \tau_i(E_{\gamma i}) R(E_e) \,, \qquad (4)$$

$E_{\gamma i}$ - is the energy of photons, E_e is the energy of photoelectrons, E_i is the binding energy in the ith atomic shell, $f_i(E_{\gamma i})$ is the conversion efficiency of the target in photoelectron spectrometer (PhES), $\tau_i(E_{\gamma i})$ is the photoionization cross-section in the i th shell, $R(E_e)$ is the effective photoelectron penetration range, B is constant. Substituting (1),(3) and (4) into (2) we get

$$I_e(E_e) \sim \frac{1}{\sqrt{T_e}} \exp(-E_e / T_e)\, \Phi(E_e, T_e) \qquad (5)$$

where

$$\Phi(E_e, T_e) = BR \sum_i \tau_i \cdot \exp(-E_i / T_e) \qquad (6)$$

is the factor representing conversion of the X-ray continuum into the photoelectron one. From (5) one can see that plasma temperature T_e can be determined from the slope of photoelectron spectrum as well as from X-ray continuum (1). Indeed,

$$T_{exp} = -\left[\frac{\partial}{\partial E_e} \ln I_e(E_e)\right]^{-1} = -\left[-\frac{1}{T_e} + \frac{\partial}{\partial E_e} \ln \Phi(E_e, T_e)\right]^{-1}. \qquad (7)$$

Hence $T_{exp} = T_e$, if

$$\left|\frac{\partial}{\partial E_e} \ln \Phi(E_e, T_e)\right| \ll \frac{1}{T_e} \qquad (8)$$

The calculations according to Eqs.(5)-(8) show that the plasma electron temperature is determined from a part of photoelectron spectrum with $E_e > (2\text{-}3)T_e$ with an accuracy of not worse than 15%.

One channel PhES-modification is described in [1]. The continuum measurements by the five channel PhES are presented. The foils made of carbon, silver, bismuth 150-400Å thick, were used as targets.

Photoelectron spectra from a carbonic target obtained on the T-13 tokamak [4] in the regime with the following parameters: plasma current 30 kA, plasma density 10^{-13}cm^{-3}, minor radius 6,5 cm, major radius 41 cm, discharge duration 20 ms, are shown in Fig.1. The spectra were registered for 8-10 shots in the facility. The spectrum 1 is measured in the time interval from the 11-th to the 12-th ms, i.e. during the dischar-

ge current plateau, the spectrum 2 - from the 3-d ms up to the 6-th ms. The values of T_e obtained coincide with the data found by filter method and by Spitzer's plasma conductivity relation.

A photoelectron spectrum from a bismuth target obtained in the OGRA-4 mirror trap [5] with a magnetic field of baseball configuration and with a maximal plasma density $5.10^{12}cm^{-3}$ produced with a gyrotron (100 kW) and by neutral beam injection (300 kW) is shown in Fig.2. The spectra measurements were performed during 20 ms after injection for 10-15 shots in the facility. From the photoelectron spectrum given in Fig.2 one can see that the plasma electron energy distribution in the facility is not a Maxwellian one that is confirmed by the Thomson scattering technique.

Thus, it has experimentally been shown that the photoelectron method allows one to register the X-ray spectra from plasma, beginning from 50 eV, to determine temperature T_e, beginning from 30 eV, to register the line-radiation of impurities. In difference from the pulse-height analyzer (PHA) system [3], PhES has no loading limitations. Therefore, for the same time interval under operating conditions of a TFTR-like facility one can register 10^4-10^5 times greater number of photons than in PHA method. PhES has a weak sensitivity to hard X-rays and to neutron irradiation that gives an opportunity to use it at the facilities with reactor parameters in the experiments with D-D and D-T plasmas.

The authors are thankful to the T-13 and OGRA-4 teams for their assistance in the experiments.

References

1. Gott Yu.V. et al., Nucl. Instrum. Meth., 214 (1983) 463.
2. Afrosimov V.V. et al., Fiz. Plazmy 5(1979) 987.
3. S. Von Goeler, Diagnostics for Fusion Experiments (Pergamon Press, New York, 1979) 79.
4. Abramov A.V. et al., Fiz. Plazmy 11 (1985) 505.
5. Panov D.A., Int.School of Plasma Physics, Varenna, Italy, 2(1983) 409.

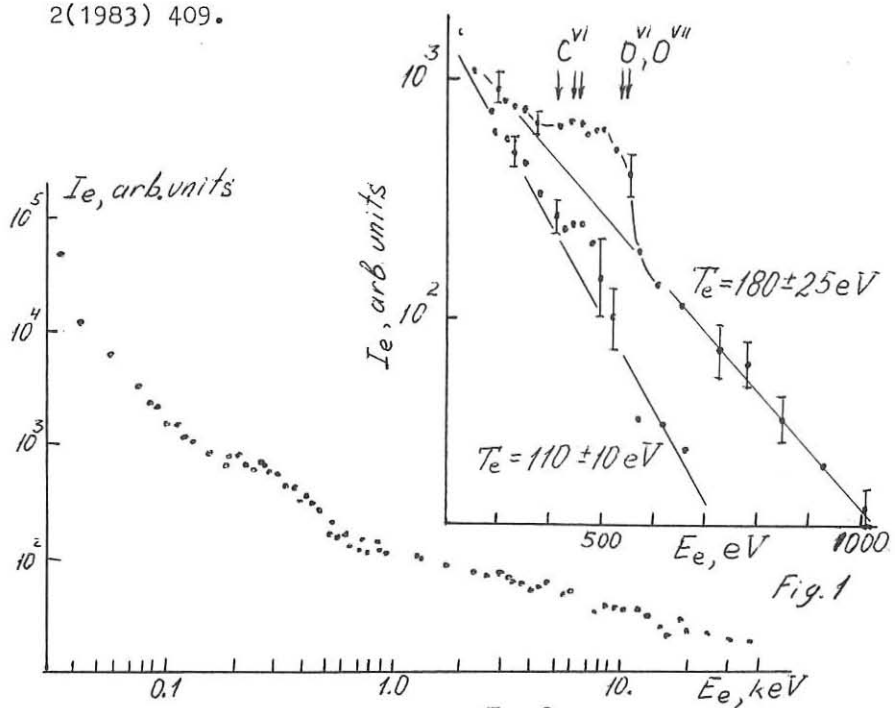

Fig. 1

Fig. 2.

RESULTS ON JET PLASMA AND IMPURITY BEHAVIOUR BASED ON MEASUREMENTS OF RADIAL PROFILES IN THE SOFT X-RAY REGION

H.W.Morsi, K.Behringer, B.Denne, E.Källne[a], G.Rupprecht[b], U.Schumacher[c]

JET Joint Undertaking, Abingdon, Oxon, U.K.
[a] Physics I, Royal Inst. of Technology, Stockholm, Sweden
[b] Now at European Southern Observatory (ESO), Garching, FRG
[c] MPI für Plasmaphysik, Association EURATOM-IPP, Garching, FRG

Abstract
First measurements of spatial profiles of the emission lines of different nickel ionisation stages were carried out at JET by means of the spatial scan double crystal monochromator. These profiles are compared with results of transport simulations, by which the calculated ionisation balance is verified. The measurements, furthermore, give the emission shells presently used for ion temperature measurements using X-ray line profiles.

1. Introduction

The measurements of the spatial and temporal distributions of impurities in magnetically confined high temperature plasmas are important for the investigations of impurity behaviour and radiation power losses. For electron temperatures of several keV the line radiation is emitted predominantly in the soft X-ray region. Therefore X-ray spectroscopy over a wide wavelength range (from about 0.1 nm to 2.5 nm) with continuous spatial scanning across the minor plasma radius is important both for studying the emission shells to understand the ionisation equilibrium and the impurity transport and for emission layer measurements in diagnostics like ion temperature measurements from X-ray line Doppler profiles.

For this purpose a double crystal monochromator [1], capable of continuous spatial scanning of X-ray spectral lines across the plasma minor radius, has recently come into operation at JET. The double crystal system allows effective shielding against neutrons and hard X-rays from the plasma.

2. The spatially scanning double crystal monochromator

A scheme (not to scale) of this double crystal monochromator is shown in Fig. 1. The two plane crystals simultaneously have to fulfill the Bragg condition $n\lambda = 2d \cdot sin\ \Theta$ (with λ the wavelength, 2d the lattice constant, Θ the Bragg angle and n an integer) within a relatively small angular margin. The crystal reflectivity has to be high and constant across the crystal surface to obtain high photon throughput of the monochromator [2]. The spectral resolution of the device is determined by the angular acceptance of the X-ray collimator and the rocking curve width of crystal 2.

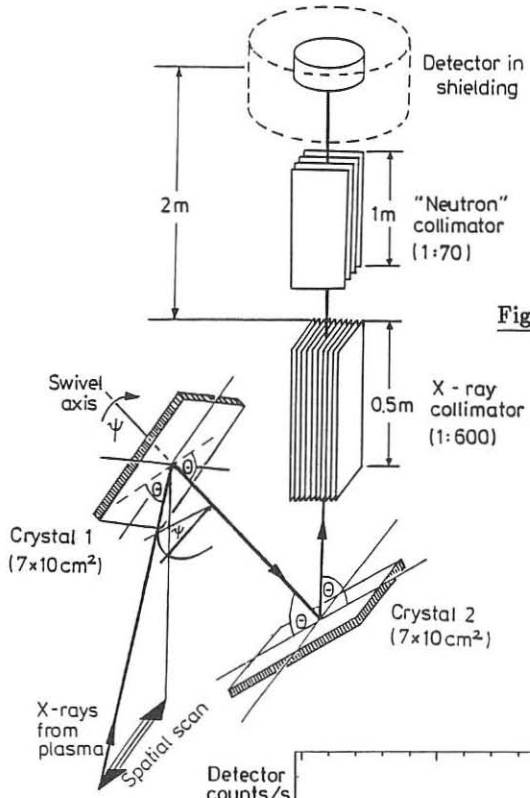

Fig. 1 Schematic of the spatial scan double crystal monochromator

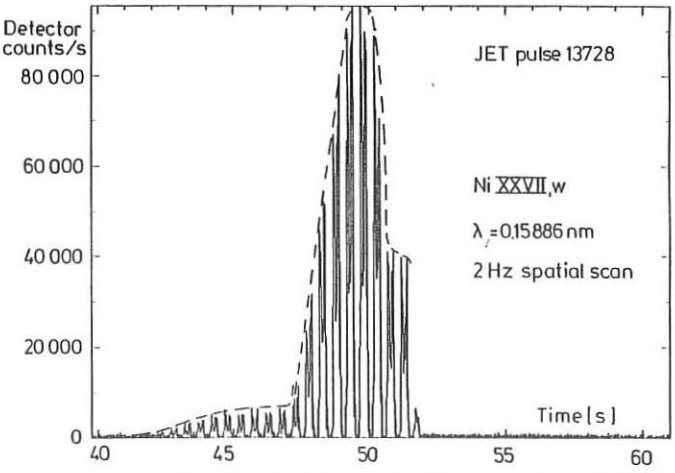

Fig. 2 Example of the count rate versus time for the helium-like resonance line of nickel spatially scanned with 2 Hz

The swivelling of crystal 1 by an angle ψ around the optical axis between the two crystals enables a continuous spatial scanning of the plasma. The detector is a large-area multiwire proportional counter [3]in a shielding block on top of the instrument. A "neutron" collimator is used for the reduction of the neutron and hard X-ray flux from the plasma for background count rate limitation. The neutron collimator, moreover, has to limit the acceptance angle in the non-dispersive direction for crystal 2, in order to obtain a smooth photon throughput as function of swivel angle as well as to define the spatial resolution of the instrument. Details of the properties and the tests of the monochromator as well as the measurements of the relative sensitivity of the instrument using a calibrated large-area X-ray source are described in [4].

For the first measurements LiF(220) crystals (2d = 0.2848 nm) were used allowing the wavelength range from 0.113 nm to about 0.203 nm to be covered with most of the hydrogen- and helium-like transitions of medium-Z impurities (like Ni). For the longer wavelengths of the oxygen lines KAP(001) crystals (2d = 2.6579 nm) will be used.

3. First results of spatially resolved X-ray line emission from JET

First measurements of the emission shells of several nickel ionisation stages were performed at JET by means of the spatial scan double crystal monochromator. The radial profiles are quite different for lines of different ionisation stages: The profiles of the lower stages are nearly flat, while those of the hydrogen- and helium-like transitions are peaked around the plasma center.

An example of the detector count rate for the helium-like resonance line (w) of nickel $1s^2\ ^1S_o - 1s2p\ ^1P_1$ taken at 2 Hz scan frequency is plotted in Fig. 2. The peaks just follow the time dependence of the line intensity (as obtained from the high-resolution X-ray spectrometer KX1 at JET, dotted line). Examples of the relative intensity distributions of the hydrogen-like nickel line Ly α_2 ($1s^2S_{1/2}$-$2p^2P_{1/2}$) and the helium-like w line are given in Fig. 3 versus radius R in the JET midplane. Abel inversion of these profiles gives the relative emission coefficients of these lines versus the distance (R - R_o) from the plasma center R_o, plotted in Fig. 4 (solid lines).

The radial profiles of these two nickel lines were also simulated using the impurity transport code [5]with the actual radial distributions of electron temperature T_e and density n_e as well as the atomic physics and transport data input. These simulated emission coefficient radial distributions are added into Fig. 4 as dotted lines. The agreement of measured and simulated profiles is satisfactory within the error bars of the plasma parameters and the assumptions underlying the analysis.

Acknowledgements

The authors are grateful to Drs. C. Andelfinger, W. Engelhardt and H. Röhr for many fruitful discussions and to J. Fink, R. Lobel, H. Schäfer, H.-B. Schilling, G. Schmitt, G. Snelling and B. Viaccoz for continuous support.

References

[1] W.Engelhardt, J.Fink, G.Fußmann, H.Krause, H.-B. Schilling, U. Schumacher, MPI für Plasmaphysik, Report IPP 1/212, IPP III/81, Garching 1982; C.Andelfinger, J.Fink, G.Fußmann, H.Krause, H.Röhr, H.-B. Schilling, U.Schumacher, P.Becker, H.Siegert, H. Belzig, A.Berghausen, R.Veigel, H.Zech, Report IPP 1/226, Garching, 1984

[2] U.Schumacher, Nucl.Instr.and Meth. A251, 564 (1986) and A259, 538 (1987)

[3] G.Rupprecht, JET-Report, to be published

[4] J.Fink, H.W.Morsi, H.Röhr, U.Schumacher, Report IPP 1/240 (1987); H.W.Morsi, H.Röhr,U.Schumacher, Z.Naturforsch. 42a, 1051 (1987); and to be published

[5] K.Behringer, JET-Report JET-R(87)08 (1987)

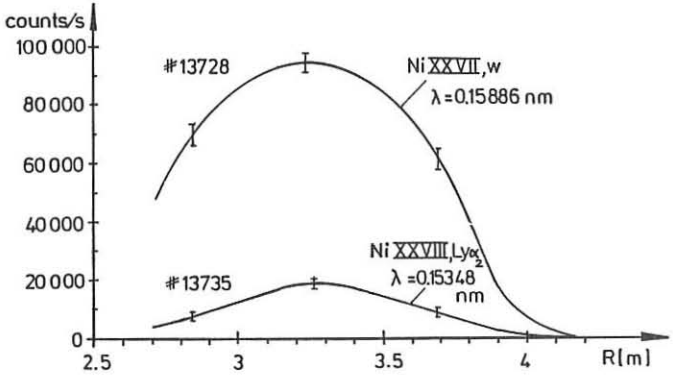

Fig. 3 Relative intensity distributions of nickel hydrogen-like Lyα_2 and helium-like resonance line w versus radius R in the JET midplane

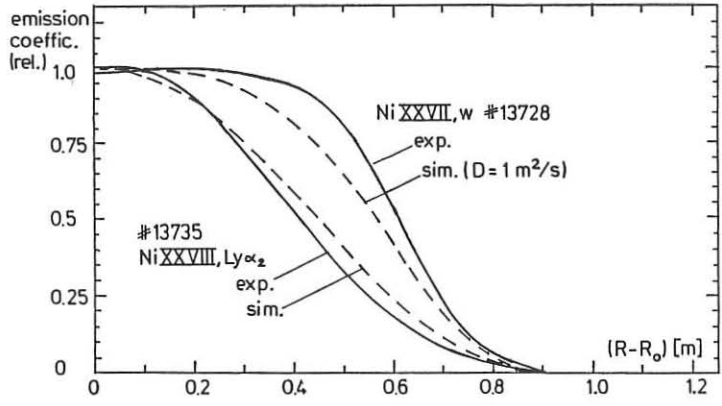

Fig. 4 The radial distribution of the emission coefficients of the nickel lines of Fig.3.

HIGH RESOLUTION SPARSE CHANNEL TOMOGRAPHY FOR SLOWLY VARYING ROTATING SXR PROFILES

Hermann Krause, Manfred Kornherr, ASDEX Team, NI Team

IPP Garching, EURATOM Association, Fed. Rep. of Germany

Abstract: A tomographic reconstruction algorithm is presented which allows to reconstruct rotating plasma soft X-ray profiles. The method utilises the fact that the Fourier spectrum of the measured line integrals shows distinct spectral lines of finite width each of which is caused predominantly by one single poloidal harmonic mode. The reconstruction now uses a best-fit method to get for each line the corresponding poloidal harmonic modes. The sum of all modes then is the SXR profile in high poloidal resolution. The nonperfect periodicity of the plasma rotation results in Fourier spectrum lines of finite width. Since the best-fit can be performed for each relevant frequency deviations from periodicity are fully taken into account.

Tokamak plasmas are typically observed by SXR pin-hole cameras the chords of which view the plasma in the same poloidal plane. Tomographic reconstruction methods which do not use plasma rotation [1] then permit a poloidal resolution which depends directly on the number of pin-hole cameras available. For each camera with chords which span across a full plasma diameter one single poloidal harmonic mode can be determined in amplitude and phase. The radial resolution depends on the distance of the camera chords in the plasma. For the typical case of two cameras thus the M=0 and the M=1 poloidal harmonics can be reconstructed.

If plasma rotation is used a virtually unlimited poloidal resolution is possible even with few cameras. Previous efforts [2] to use plasma rotation required a precise knowledge about the phase angle of the rotating feature as a function of time. This could, in practice, only be determined from inspection of the signals in cases where one single mode with its phase-coupled harmonics was found rotating. Several independently rotating features could thus not be treated.

The new method, in contrast, does not require an explicit information about phase angles. To demonstrate the method a numerical experiment has been conducted. For the geometry of the ASDEX experiment and its two SXR cameras an artificial rotating SXR profile (cf. fig. 1) is assumed. This profile shows on an unvarying base a rotating feature which is predominantly a M=1 mode. For a time interval of 1.6 ms the line integrals of 58 chords are calculated by numerical integration. 400 samples at a sampling frequency of 250 kHz are simulated. The rotation frequency is 10 kHz initially and speeds up by 5 percent during the interval. The amplitude of the rotating peak on the base profile grows from zero to a maximum value within the sampling window.

Thus the simulated plasma rotation is nonperiodic due to an unstable rotation speed and an unstable mode amplitude.

Figure 2 shows for a typical chord the calculated line integral (top) and the Fourier spectrum of the signal (bottom). The signal clearly shows the growing mode amplitude. The spectrum is calculated using a standard FFT program the result of which is a discrete spectrum i.e. amplitude and phase are determined for discrete frequencies which span the range from 0 to half the sampling frequency in steps of f_0 given by the inverse of the time window width.

As expected the approximately periodic signal results in distinct lines of finite width. E.g. the line near 10 kHz is caused by the M=1 poloidal harmonic, the other lines by the poloidal harmonics M=2,3,4,..., M=0 is centered at small frequencies. Fourier analysis has thus isolated the individual poloidal harmonics from each other.

For tomographic inversion now the plasma profile is represented in polar coordinates as a sum of poloidal harmonics which rotate in both directions at all discrete frequencies (cf. (1)). The radial dependence of the individual cos- and sin-terms is given by a sum over suitable functions. Chosen are modified Zernicke polynomials (cf. (2)). The profile represented is thus determined by the coefficients $A^c_{i\ell m}$ and $A^s_{i\ell m}$ which have to be found by a best-fit to the measurements.

$$\epsilon(r,\Theta,t) = \sum_{i=-I}^{I}\sum_{\ell=0}^{L}\sum_{m=0}^{M}\left(A^c_{i\ell m}\cdot\rho_{\ell m}(r)\cdot\cos(m\Theta-2\pi i f_0 t) + A^s_{i\ell m}\cdot\rho_{\ell m}(r)\cdot\sin(m\Theta-2\pi i f_0 t)\right) \tag{1}$$

$$\rho_{\ell m}(r) = (1-r^2)^2\cdot\sum_{s=0}^{\ell}\frac{(-1)^s\cdot(m+2\ell-s)!\cdot r^{m+2\ell-2s}}{s!\cdot(m+\ell-s)!\cdot(\ell-s)!} \tag{2}$$

The determination of the coefficients splits naturally into separate best-fit problems, one for each discrete frequency since an observed Fourier amplitude at the discrete frequency $i\cdot f_0$ can only be caused by poloidal harmonics which rotate at $i\cdot f_0$ and $-i\cdot f_0$ (cf. (1)). The best-fit is performed to the cos- and sin-amplitudes of the observed Fourier spectrum rather than the observed line integrals directly. The best-fit is a standard linear least-square fit. The fit problem is defined by a matrix whose elements describe the response of one measured channel, i.e. the cos- and sin-amplitudes of the Fourier spectrum at a single discrete frequency due to each of the poloidal harmonic modes with one single radial function at unit intensity. The matrix elements are calculated by numerical integration. Considerable savings are possible since matrix elements are independent of the discrete frequency. Again, the number of cameras determines how many poloidal harmonics with both directions of rotation can be fitted to the measured cos- and sin-amplitude at a discrete frequency.

It is thus necessary to define frequency windows around the observed lines in the Fourier spectra and to assign one poloidal harmonic to each window. In case of window overlap there are discrete frequencies for which two ore more modes are assigned. These cases

can still be treated if the number of cameras is larger or equal to the number of modes assigned to a discrete frequency. The process of window setting and mode assignment is a manual input to the process. Obviously window setting is uncritical for narrow lines and difficult for lines which are wider than the line separation. Since line width is determined by deviations from a perfect rigid rotation and line width tends to increase with the higher harmonics there is a practical trade-off between achievable poloidal resolution and how fast the profile of the rotating plasma evolves or how fast the rotation frequency changes.

Figure 3 shows a reconstructed profile to be compared with fig. 1 for the simulated example based on windows 0 to 5 kHz for M=0 and 7 kHz to 15kHz for M=1. The poloidal resolution is thus chosen to be the same as can be achieved with codes that do not utilise plasma rotation. Obviously poloidal structures are considerably smoothed out. Fig. 4 then gives a reconstruction based on M=0 to M=8 with suitable windows defined. Here poloidal resolution is drastically improved.

Figure 5 shows a measured signal of an ASDEX discharge and its Fourier spectrum. The signal is sampled at 250 kHz and shows obvious changes in the signal form during the selected time window. Only 29 channels in two cameras were used for the measurement. The spectrum line near 10 kHz is caused by the M=1 poloidal harmonic and smaller contributions of M=2 to M=5 are visible. A reconstruction with suitable windows defined based on M=0 to M=5 is given in fig. 6.

[1] R. S. Granetz et al., Nucl. Fusion, **25**, p.727, (1985)
[2] P. Smeulders, IPP-Report 2/252 1983 and Nucl. Fusion **23**, p. 529 (1983).

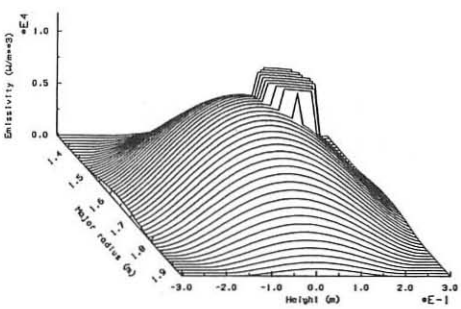

Fig. 1: Simulated SXR profile with rotating peak for t=1.4 ms.

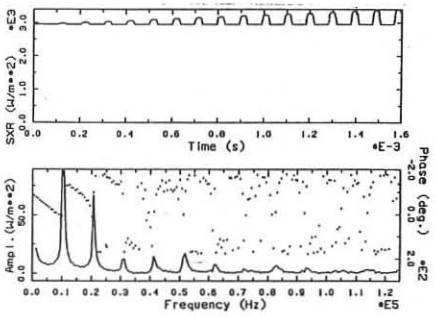

Fig. 2: Calculated SXR line intensity (top) for the rotating profile of fig. 1. Fourier spectrum (bottom) and phases (dotted) of the signal.

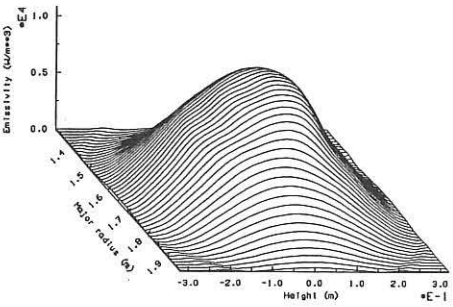

Fig. 3: Reconstruction of the rotating profile of fig. 1 based on M=0 and M=1 for t=1.4 ms.

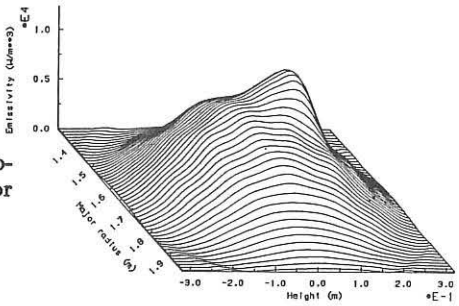

Fig. 4: Reconstruction of the rotating profile of fig. 1 based on M=0 to M=8 for t=1.4 ms.

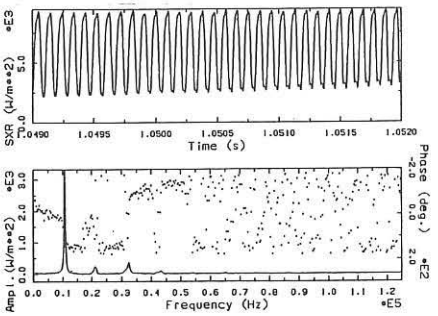

Fig. 5: ASDEX measured SXR signal and Fourier spectrum thereof.

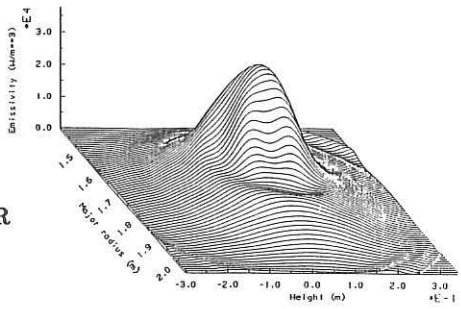

Fig. 6: Reconstruction of an ASDEX SXR profile based on M=0 to M=5.

COLLECTIVE THOMSON SCATTERING FOR ALPHA PARTICLES DIAGNOSTICS IN TOKAMAKS

F.P. Orsitto, P. Buratti

Associazione EURATOM-ENEA sulla Fusione, Centro Ricerche Energia Frascati, C.P. 65 - 00044 - Frascati, Rome, Italy

INTRODUCTION

In general the light scattered at a given angle by thermal plasmas exhibits a Doppler broadened spectrum with respect to the incident probe frequency.

Analyzing the form factor it turns out that the parameters important for the design of a scattering experiment are: a) the Salpeter parameter α; b) the angle ϕ between the K_s scattering wavevector and the plane perpendicular to the magnetic field.

The parameters α and ϕ must be optimized in order to have a scattering form factor dominated by alpha particles and unaffected by magnetic field effects.

In this paper we examine the effects of the magnetic field on the scattering form factor using an analytical model besides a full numerical computation. In Sec. 2 the analytical model is used in order to obtain expressions for the conditions to be fulfilled in order to avoid the effects of the magnetic field and to have a scattering dominated by alpha particles rather than by electrons. In Sec. 3 the role of the lower hybrid resonance is analyzed. In Sec. 4 the power requirements and signal to noise ratio are calculated for CO_2 ($\lambda_0 = 10.6\times10^{-6}$ m) sources and numerical examples are given for the conditions expected for D-T operation on JET.

2. THE FORM FACTOR FOR THE MAGNETIZED PLASMAS

The dynamic form factor $S(k, \omega)$ depends on the velocity distribution of each particle species through the polarizabilities H_j (where j = e, D, T, α); these are expressed as series of lines spaced by respective cyclotron frequencies ω_{cj}. The width of each line is given by the Doppler broadening along the momentum K_s, $\omega_i = K_s \cdot v_i$ [1]. It is easy verify that all the parameters relevant to the scattering form factor only depend on the Salpeter parameter α and on the angle ϕ. In this section we will show that the choice of α and ϕ is linked to the following considerations:

i) the angle ϕ is chosen in order to minimize the effects of the electronic frequency roll-off. As we will see, examining the electronic polarizability He, the angle ϕ must be:

$$\sin\phi \gg v_\alpha / v_{the}$$

ii) the Salpeter parameter α is decided following the constraint that the ratio between the alpha signal and the electron background $R_{\alpha\ell}$ must be greater than 2.

For the purpose of examining more deeply the form factor we discuss briefly the electron and ion polarizability He,i, and we will derive the value of $R_{\alpha\ell}$ as function of α and ϕ.

2.1 - Electron polarizability He

The electron polarizability He is a sum on harmonics of the electron cyclotron frequencies. Because this spacing is so large in respect to all the frequencies we are interested in ($\omega \ll \omega_{c\ell}$) it is possible to evaluate He using only the n = 0 harmonic [1].

In this paper we are interested to the alpha feature which is regulated by the ratio between the electron polarizability He and the plasma dielectric function $\varepsilon = 1 - He - Hi - H\alpha$. We want the electron respons He uniform in the range of the alpha feature, i.e. $\omega \sim \omega_\alpha \sim K_s v_\alpha$. By an inspection of He [1] we conclude that in order to maintain $He \sim \alpha^2 \sim$ constant, we must choose the geometry in such a way that:

$$\sin\phi \gg v_\alpha / v_{the} \tag{1}$$

In the limit opposit to (1) we have that $He \sim 1$, so the electron polarizability is depressed by a factor α^{-2}.

2.2 - The ion polarizability Hi

It is well known that the ions are weakly magnetized: in fact the parameter $\varepsilon_i = \omega_{ci}/\omega_i$ (where ω_i is the thermal ion bandwidth), which measure the ion magnetization, is much less than 1.

We know that the polarizability is made by a sum of lines spaced by the ion cyclotron frequency (ω_{ci}), whose width is $\sim \omega_i \sin\phi$. So the condition $1 > \sim \sin\phi \gg \varepsilon_i$ guarantee that the feature characteristics of the presence of the magnetic field will disappear.

We can assume that the magnetic field effects could be absent in the alpha particle polarizability and that also for the distribution function [1] we can assume the unmagnetized form. In the calculation of the alpha form factor must be retained the magnetic field dependence in $|He|^2$ and in $|\varepsilon|^2$.

2.3. - The ratio between the alpha and electron feature

One of the main points in the design of an alpha particles collective scattering experiment is the determination of the ratio of the electron to the alpha feature by an appropriate choice of the α and ϕ parameters. If we suppose that the alpha particles are thermalized at a temperature T_α, the ratio $R_{\alpha\ell}$ is given by [1,3]:

$$R_{\alpha\ell} = \frac{|H_e|^2 \dfrac{n_\alpha}{n_e} \dfrac{e^{-(\omega/\omega_\alpha)^2}}{\omega_\alpha}}{\left| |1 - Hi|^2 \sum_n X_n\left((K_{s\perp}\rho_e)^2\right) e^{-x_{ne}^2}/\omega_e \sin\phi \right|}, \qquad X_n(y) = e^{-y} I_n(y), \qquad x_{ne} = \frac{\omega_{ce} - \omega}{\omega_e \sin\phi}$$

a good approximation for the electron distribution function (in the denominator) is to use the n = 0 harmonic because $\omega_\alpha \ll \omega_{ce}$, so we obtain to the leading order in α and taking the ions unmagnetized (i.e. $\sin\phi \gg \varepsilon_i$):

$$R_{\alpha\ell}(\omega \sim \omega_\alpha) \sim 2.7\, \alpha^4 \frac{n_\alpha}{n_e} \frac{v_{the}}{v_\alpha} \sin\phi$$

The value of $R_{\alpha\ell}$ is regulated by the product $\alpha^4 \sin\phi$, so the condition $R_{\alpha\ell} > = 2$ implies that:

$$\alpha^4 \sin\phi \geq 0.74 \frac{n_e}{n_a} \frac{v_a}{v_{the}} \qquad (2)$$

Now we evaluate the right hand side of (2) in the two regimes hypotesized as relevant for the JET in the D-T phase: the hot ions (HI) and the H regimes [2]. The plasma parameters are as follows:

$$\text{HI}: T_e = 10\,\text{keV},\ n_e = 2\times10^{13}\,\text{cm}^{-3},\ n_a = 10^{12}\,\text{cm}^{-3}$$

$$\text{H}\ : T_e = 10\,\text{keV},\ n_e = 10^{14}\,\text{cm}^{-3},\ n_a = 2\times10^{11}\,\text{cm}^{-3}$$

Using a value of $v_a \sim 1.3\times10^9$ cm/s we obtain:

$$\alpha^4 \sin\phi \geq \begin{matrix} 3.2 & \text{HI} \\ 81.4 & \text{H} \end{matrix}$$

with $\sin\phi \gg 0.22 = v_a/v_{the}$ ($\phi \gg 13°$) and $\alpha > 1$.

3. THE RESONANCE ROLE IN THE FORM FACTOR

The enhancement of the scattering cross section due to the lower hybrid resonance has been discussed in Ref. [3], where the electronic response He has been taken as unmagnetized. This led to an overestimation of the resonance role in the alpha form factor, and a closer inspection to the nature of the resonance shows that its effect can never be very strong.

An inspection of the plasma dielectric function shows that the lower hybrid resonance occurs for angular ranges ($\phi \ll \omega_a/\omega_e$) where the electronic roll-off is operating and the electronic polarizability is depressed by a factor of α^{-2}. The resonance is then enhanced because the electron response decrease in the roll-off region; and we find that only for $\phi \ll \omega_a/5\omega_e$ (i.e. $\phi \ll 0.7°$) the lower hybrid resonance is dominated by the alpha particles. This probably rules out the use of the resonance in the alpha particles scattering experiments.

4. CALCULATIONS OF THE SCATTERED SIGNAL AND SIGNAL TO NOISE RATIO

The mean scattered powers (P_s) per unit frequency at a given K_s on the alpha particles spectrum $\omega_a \sim K_s v_a$ is given by:

$$\bar{P}_s = 2\pi n_a L\Omega r_e^2 P_0/\omega_a \quad [\text{W/Hz}] \qquad (3)$$

where P_0 is the incident power (Watt) on the area transverse to the beam. The factor $L\Omega$ is the product of the scattering volume characteristic length times the collection solid angle. It depends on the incident wavelength and the scattering angle, because the waist into the plasma (w_0) is constrained to amount at several fluctuation wavelength, in order to obtain a spectrum well resolved. Furthermore the collection

solid angle is determined by the nature of the coherent detection [4], i.e. $\Omega = \lambda_0^2/\pi w_0^2$. This means that the value of $L\Omega$ must be of the order:

$$L\Omega = \frac{2w_0}{\sin\theta}\,\lambda_0^2/\pi w_0^2 = 2\lambda_0/[r\pi\cos\theta/2]$$

where θ is the scattering angle and r is the number of fluctuation wavelength present in a beam waist: typically $r >= 5$. At moment we must consider concretely two sources as candidate for such experiments: the CO_2 laser and the gyrotron [7]; here we give some analysis on CO_2 laser.

The CO_2 laser source was previously studied [5] as a candidate for the alpha particle experiment. Looking at $R_{\alpha\ell}$ value we observe that (for CO_2 laser) the geometry must be chosen which minimize the α parameter, in order to realize a scattering angle useful to separate easily the main and the scattered beam. The minimization of the α-parameter forces the choice of an azimuthal angle $\phi \sim 90°$ (i.e. $k = k_{\parallel}$) and in the two regime considered, the scattering angle is $\theta = 0.44°$ for HI and the H corresponding at two values of α of 1.34 for HI and 3.0 for the H-regime. Using formula (3) we can calculate the nominal power which is neaded in order to obtain a predetection signal to noise ratio (P_s/NEP) of 1, when a NEP $\sim 3\times10^{-19}$ W/Hz is supposed uniform on a bandwidth of 9 GHz (which is the alpha bandwidth). Furthermore, if we include a realistic value for the heretodyne efficiency $\eta_H \sim 10\%$, we evaluate the power neaded in the order of gigawatts, ~ 2.6 GW for HI, and 13 GW for H. The time pulsewidth of the CO_2 laser of 1.5 microseconds is easily obtained with standard methods, but lasers of pulsedwidth of 5 μs and 10 μs have been realized long time ago [6]. It turns out that, for JET hot ion mode, a laser with energy of ~ 4 kJ in 1.5 μs could give a S/N ~ 20 postdetection signal to noise ratio ($S/N = [P_s/(P_s+NEP)]\sqrt{B_\iota}$) on a 1 GHz channel (the total bandwidth is ~ 9 GHz), if a NEP ~ 3×10^{-19} W/Hz uniform on this bandwidth and an heterodyne efficiency of 10% is assumed. The scattering angle should be 0.44°, at $\alpha_{MIN} \sim 1.34$; the waist into the plasma must be ~ 0.7 cm and $L\Omega \sim 1.35\ 10^{-4}$ cm.

REFERENCES

[1] E.E. Salpeter, Phys. Rev., **122**, 1663 (1961)
[2] The JET Team, Report JET-P(87)37
[3] L. Vahala et al., Nucl. Fusion, **26**, 51 (1986)
[4] E. Holzauer et al., Plasma Phys., **20**, 867 (1978)
[5] D.P. Hutchinson et al. Rev. Sci. Instrum., **56**, 1075 (1985)
[6] L. Bartolini et al., Int. J. Infrared Millimiter Waves, **4**, 185 (1983);
A. Semet et al., ibidem p. 231;
T.R. Lawrence et al., *Meeting of IRIS Specialty Group on Active Systems*, Monterey, 5-7/11/85, CA
[7] P.P. Woskov, Report MIT PFC/RR-87-16 (1987)

CURRENT PROFILE DETERMINATION VIA POLARIMETRY IN HIGH DENSITY, HIGH FIELD TOKAMAKS

M. Nagatsu, W.A. Peebles and N.C. Luhmann, Jr.

Institute for Plasma and Fusion Research,

University of California, Los Angeles, CA 90024

INTRODUCTION

Measurement of the current profile in tokamak devices is of great importance in understanding plasma stability and transport phenomena. A variety of methods have been proposed to measure the current profile. Cano et al. on the ST tokamak demonstrated the possibility of measuring the local poloidal field using upper hybrid layer harmonic generation[1]. Forrest et al., on the DITE tokamak, performed a q profile measurement using Thomson scattering techniques[2]. Recently using a Li beam and tunable dye laser, West et al. have performed q measurements on TEXT[3]. The application of Faraday rotation techniques to determine current profile has been pioneered by Soltwisch on the TEXTOR device where the profile has been measured as a function of time[4].

The purpose of the present work is twofold. First, the establishment of a routine polarimetric measurement of the current profile on the TEXT device allows, for the first time, a comparison with an independent technique-the Li beam measurements of West et al. It also allows extension of the measurement to higher densities and fields, as well as the study of the modification of current profile during ECRH. Second, the possibility of measuring the current profile on the MTX device is relevant to future ignition devices such as CIT. It is also important to the MTX device itself especially during current drive experiments. It is therefore intended to investigate the possiblitiy of measuring both the Faraday rotation and elliptization of the incident electromagnetic wave in order to more accurately compensate for the expected large elliptization at submillimeter wavelengths on devices such as MTX and CIT.

PROPOSED POLARIMETRY SYSTEM

The proposed multichannel interferometry/polarimetry system is shown in Fig. 1. Parabolic cylindrical mirrors are used to expand the probe and reference beams in one dimension to view the entire plasma cross section. The two beams are combined and detected using a linear array of corner cube GaAs Schottky barrier diode mixers[5]. The wires of the beam splitting polarizers are oriented at 45° to the incident beams.

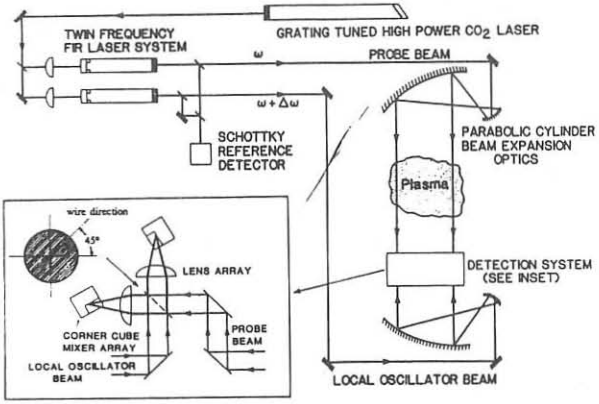

Figure 1 Schematic of the multichannel far-infrared interferometry/polarimetry system.

The transmitted beam through the plasma suffers changes in its polarization state through Faraday rotation Ψ_p and elliptization ε_p. These are given by[6]

$$\Psi_p = \frac{1}{2}\tan^{-1}(s_2/s_1) \tag{1}$$

$$\varepsilon_p = |s_3|/(1+\sqrt{1-s_3^2}) \tag{2}$$

where s_1, s_2 and s_3 are the Stokes parameters whose evolution for an electromagnetic wave propagating in the z-direction is given by

$$\frac{d\vec{s}(z)}{dz} = \vec{\Omega}(z)\times\vec{s}(z) \tag{3}$$

where

$$\vec{\Omega}(z) = \frac{\omega}{c}(\mu_1-\mu_2)\vec{s}_{c_2} \tag{4}$$

and ω is the wave frequency, μ_1 and μ_2 are the refractive indices of the slow and fast waves and $\vec{s}_{c_2}$ is the polarization vector of the fast wave.

If we assume that ω is much larger than both the electron plasma frequency, ω_{pe}, and cyclotron frequency ω_{ce}, the Faraday rotation angle Ψ_p reduces to the familiar expression[7]

$$\Psi_p = 1.5\times10^{-20}\lambda^2\int_0^L n_e(z)B_{pl}(z)dz \tag{5}$$

where Ψ_p is in units of degrees, wavelength λ in μm, electron density n_e in cm^{-3} and poloidal field component parallel to the probing beam B_{pl} in kG. As for the ellipticity ε_p, it scales with λ^5 when the incident beam is launched perpendicular to the toroidal field with either O-mode or X-mode. However, it should be noted that as ω_{pe}, ω_{ce}, approach ω these simple wavelength scalings are no longer satisfied.

In our detection scheme, the polarization change due to the plasma yields two mixer output signals whose amplitude ratio is given by

$$R = \sqrt{\frac{1+\varepsilon_p^2-(1-\varepsilon_p^2)\sin2\Psi_p}{1+\varepsilon_p^2+(1-\varepsilon_p^2)\sin2\Psi_p}} \simeq \cot\left(\Psi_p+\frac{\pi}{4}\right) \text{ when } \varepsilon_p \ll 1 \tag{6}$$

In addition, there is a phase difference between equivalent detectors given by

$$\Delta\phi = \tan^{-1}\left[\varepsilon_p\tan(\Psi_p+\pi/4)\right] - \tan^{-1}\left[\varepsilon_p\tan(\Psi_p-\pi/4)\right] \tag{7}$$

This assumes an ideal wire polarizer. In principle, therefore, measurement of the amplitude ratio and phase difference, allow us to independently evaluate the Faraday rotation Ψ_p and ellipticity ε_p. It should be noted that the amplitude ratio is very insensitive to ellipticity compared to the scheme discussed in Ref. 4. However, the required accuracy of the measurement of R is greater due to the dependence on $(\Psi_p+\frac{\pi}{4})$.

LABORATORY TESTS

We have tested the principle of the proposed polarimetry/interferometry system in the laboratory. First, the amplitude ratio measurement has been performed by using a wire polarizer (1000 lines/inch) to simulate the effect of the plasma. The radiation transmitted through the polarizer is rotated by an amount equal to the rotation angle of the polarizer. In Fig. 2 (a), the experimental results of the amplitude ratio are plotted versus polarizer rotation angle together with the theoretical prediction of eq. (6) with $\varepsilon_p = 0$. The measured rotation angles inverted from the amplitude ratio are also plotted in Fig. 2(b), which agree with theory within an error of 3%. Second, the ellipticity measurement has been performed by rotating a quartz plate, which introduces a known ellipticity and rotation angle to the electromagnetic wave. The experimental results are shown in Fig. 3 where phase difference $\Delta\phi$ is plotted as a function of the quartz rotation angle and compared with theoretical prediction. The results show excellent agreement between theory and experiment.

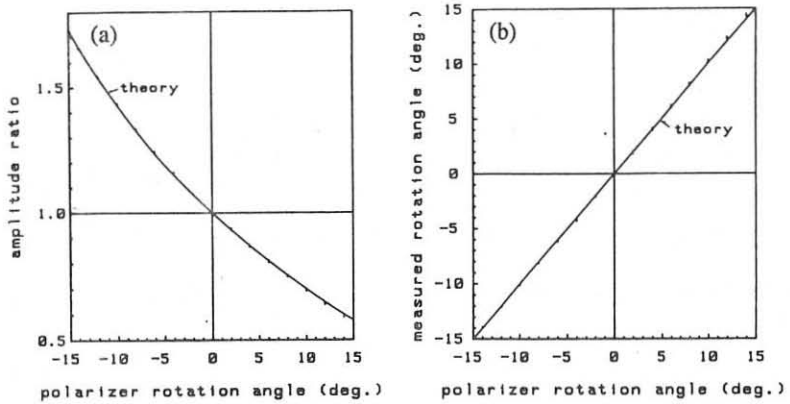

Figure 2 Experimental results of (a) amplitude ratio between two equivalent mixer outputs and (b) measured rotation angle versus the polarizer rotation angle. Solid curves indicate theoretical prediction using equation (6) with $\varepsilon_p = 0$.

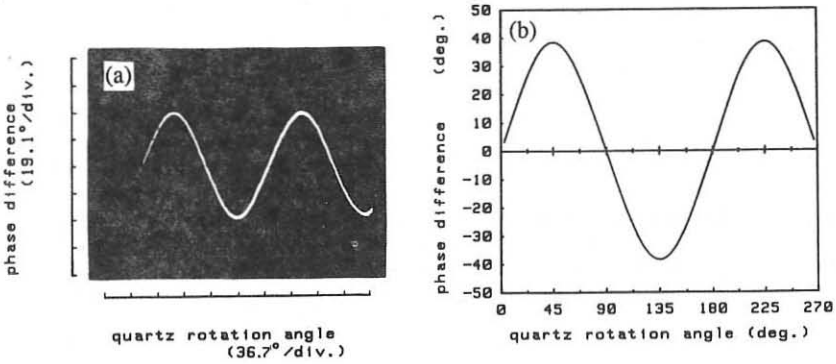

Figure 3 (a) Experimental results illustrating the phase difference between two equivalent mixer outputs versus the quartz rotation angle and (b) theoretical prediction using equation (7).

TEXT POLARIMETRY

Initially a nine channel polarimeter system will be installed to obtain the central q-value in a low density (n_e~$1\times10^{13}cm^{-3}$) and low current (250 kA) plasma and compare it with the previous experimental results of West et al.[3] In Fig. 4, calculations of the rotation angle and ellipticity are shown for wavelength of 1.22 mm, assuming parabolic profiles for electron density and current density with $n_e = 1\times10^{13}cm^{-3}$, $I_p = 250$ kA and $B_t = 15$ kG.

For other plasma discharge conditions, it is intended to optimize the Faraday rotation by altering the laser operating wavelength. For example, at $n_e = 5\times10^{13}cm^{-3}$, $I_p = 400$kA and $B_t = 28$ kG, the rotation angle Ψ_p and ellipticity ε_p are $\Psi_p \sim 10^o$ and $\varepsilon_p \sim 0.035$ for $\lambda = 496$ μm. Operation at $\lambda = 1.22$ mm would produce excessive elliptization. If this initial central q measurement is successful, then the polarimetry system would be extended to 29 channels (1.5 cm channel spacing) to improve the inversion accuracy.

MTX POLARIMETRY

Figure 5 indicates the problems associated with a measurement of the current profile on MTX. The elliptization is larger by an order magnitude than that in TEXT even though we use a 185μm laser. Clearly, a combination of iterative data analysis and measurement of elliptization will be necessary if polarimetry measurements are to be

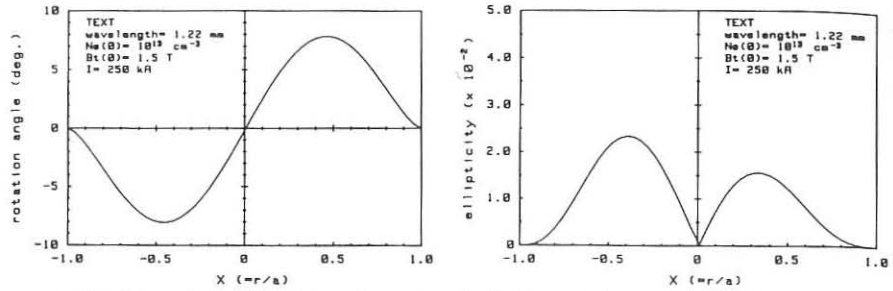

Figure 4 Calculation results of Faraday rotation angle and elliptization at the wavelength of λ = 1.22 mm in the TEXT tokamak.

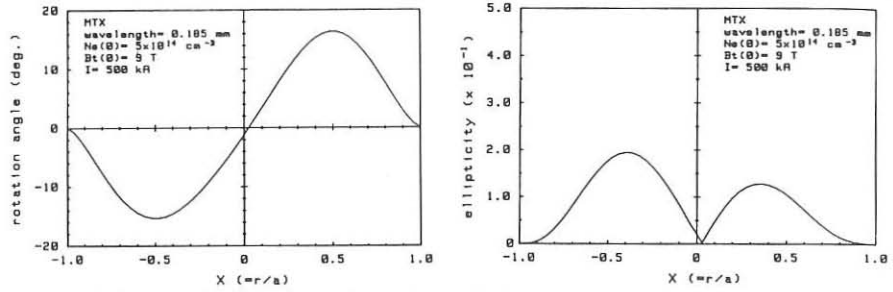

Figure 5 Calculation results of Faraday rotation angle and elliptization at the wavelength of λ = 185 μm in the MTX tokamak.

utilized on MTX. The experimental results of the laboratory tests illustrate the possibility of measuring both the Faraday rotation angle and elliptization of the incident electromagnetic wave and make the proposed polarimeter attractive, especially for application to high density, high field plasmas where elliptization effects are large. In this situation, it is often found that the Faraday rotation angle cannot be described by eq.(5). The implication on the usual inversion procedures will be discussed.

CONCLUSION

The feasibility of polarimetry measurements on both TEXT and MTX has been examined. A nine channel system will be installed on TEXT to measure the central q-value in a low density plasma. Future modifications to this system will include a 29 channel detector array to allow full current profile measurement during a single discharge.

ACKNOWLEDGEMENT

This work supported by U.S. DOE Contract # DE-FG03-86ER53225.

REFERENCES

1. R. Cano, I. Fidone and J.C. Hosea, Phys. Fluids 18 1183 (1975).
2. M.J. Forrest, P.G. Carolen and N.J. Peacock, Nature, 271 718 (1978).
3. P. West, D.M. Thomas, J.S. deGrassie and S.B. Zheng, Phys. Res. Lett. 58, 2758 (1987).
4. H. Soltwisch, Rev. Sci. Instrum. 57 1939 (1986).
5. W.A. Peebles, R.L. Savage, Jr., D.L. Brower, S.K. Kim. T. Lehecka, J. Howard, E.J. Doyle and N.C. Luhmann, Jr., Int. J. Infrared and Millimeter Waves, 8 1355 (1987).
6. S.E. Segre, Plasma Phys. 20 295 (1978).
7. D. DeMarco and S.E. Segre, Plasma Phys. 14 245 (1972).

ION TEMPERATURE DETERMINATION FROM NEUTRON RATE DURING NEUTRAL INJECTION IN ASDEX

K. Hübner, R. Bätzner
Institut für Angewandte Physik, Universität Heidelberg, D-6900 Heidelberg
B. Bomba, H. Rapp, W. Herrmann, H. Murmann, A. Eberhagen, H.-U. Fahrbach, O. Gehre, R. Preis, H. Röhr, K.-H. Steuer, O. Vollmer
Max-Planck-Institut für Plasmaphysik, EURATOM Association, D-8046 Garching

Neutron rate measurements are very often used to determine the ion temperature in ohmic discharges. We have developed software (NR code) which extends this method to neutral beam injection heating (D^0 in D plasma) by introducing a model for neutron production by fast ions. Our software is fully modular however, so that it can also be used for all kinds of thermonuclear plasmas and in future, also for non-thermonuclear neutron production, which may arise RF-heated discharges.

Relaxation time model

The local neutron rate in a plasma is simply given by

$$Q_{ab} = n_a n_b \langle\sigma v\rangle_{ab} = n_a n_b \iint \sigma_{ab} f_a(v_a) f_b(v_b)\, dv_a dv_b. \qquad (1)$$

n_a, n_b, f_a, f_b, v_a, v_b are, respectively, the densities, distribution functions, and velocities of the two reacting ion species, σ_{ab} is the corresponding cross-section, and $\langle\sigma v\rangle_{ab}$ is the reactivity of this process. For the distribution function we use the following ansatz:

$$n f = n_0 f_0 + n_1 f_1 + n_2 f_2 + n_3 f_3, \qquad (2)$$

where the index 0 denotes the background plasma, and the indices 1, 2, and 3 the deuterons injected with full (45 keV), half, and one-third energy, respectively. For the ASDEX plasma parameters we can use a Maxwellian for f_0. We have to distinguish the following contributions to the neutron rate in the case of D^0 injection in D plasma

$$\begin{aligned} Q_{DD} = {} & \tfrac{1}{2} n_0^2 \langle\sigma v\rangle_{00} + \alpha_1 n_1^2 \langle\sigma v\rangle_{11} + \alpha_2 n_2^2 \langle\sigma v\rangle_{22} + \alpha_3 n_3^2 \langle\sigma v\rangle_{33} \\ & + n_0 n_1 \langle\sigma v\rangle_{01} + n_0 n_2 \langle\sigma v\rangle_{02} + n_0 n_3 \langle\sigma v\rangle_{03} \\ & + \alpha_{12} n_1 n_2 \langle\sigma v\rangle_{12} + \alpha_{13} n_1 n_3 \langle\sigma v\rangle_{13} + \alpha_{23} n_2 n_3 \langle\sigma v\rangle_{23}. \end{aligned} \qquad (3)$$

The first term describes the thermonuclear production in the bulk plasma, and the terms in the second row are the beam-target reactions for the three injection energies. The remaining terms describe the different beam-beam reactions, their coefficients α taking into account possible injection in opposite directions.

As we shall see, for the ASDEX plasma the main contributions are due to the beam-target and the thermonuclear production. Because the distribution function of the bulk plasma is isotropic, the beam-target production only depends on the energy of the injected deuterons and not on their pitch angle. We can therefore use the energy distribution function for the fast deuterons, which is simply calculated from the classical relaxation of the particle energy W:

$$dW/dt = - W/\tau_W, \qquad (4)$$

where τ_W is the energy relaxation time. The resulting distribution functions are

$$n_i f_i(W) = \frac{\dot{N}_i D_i(r)}{n} \frac{n\tau_{W_j}}{W_i}, \quad i = 1, 2, 3. \tag{5}$$

Here n is the electron density, $\dot{N}_i$ are the numbers of deuterons injected per second, and $D_i(r)$ their deposition profile. The energy relaxation parameter $n\tau_W$ is a function of only the electron temperature and the energy itself.

Interpretation of neutron rate

The emission profiles for the different contributions in eq. 3 to the neutron rate and thus the volume-integrated neutron rate itself are completely determined with the geometric data of the plasma, the electron density and temperature profiles n(r) and $T_e(r)$, the profile $Z_{eff}(r)$, the deposition profile D(r) of the injected deuterons, and the plasma deuteron density and temperature profiles $n_D(r)$ and $T_D(r)$. The emission profiles for the different contributions in eq. 3 to the neutron rate and thus the volume-integrated neutron rate itself are completely determined. The densities of electrons n, deuterons n_D, and protons n_H are related by

$$\frac{Z_x - Z_{eff}}{Z_x - 1} = \frac{n_D}{n}\left(1 + \frac{n_H}{n_D}\right), \tag{6}$$

where Z_x is the charge of the dominant impurity. In a deuterium plasma without protons, n_D could therefore be determined from Z_{eff}, and thus the ion temperature T_D from the measured neutron rate Q_{DD}. If there is any information about the shape of the ion temperauture profile, the neutron emission profile $D_{DD}(r)$ can also be deduced. For plasmas with a mixture of protons and deuterons, as with H^0 injection in D plasma, one of the two parameters T_D and n_D/n_H can always be calculated from the neutron rate if the other is known.

Structure of the NR software

To take care of all these possibilities, our software has a fully modular structure. The scheme is shown in Fig. 1; firstly, the software DATA FILES reads all input data. It is thus easy to adapt changes in the ASDEX data files or to introduce new data which become accessible with the development of new diagnostics. An example of the last is the new $Z_{eff}(r)$ measurement from visible bremsstrahlung which is now availiable at ASDEX.

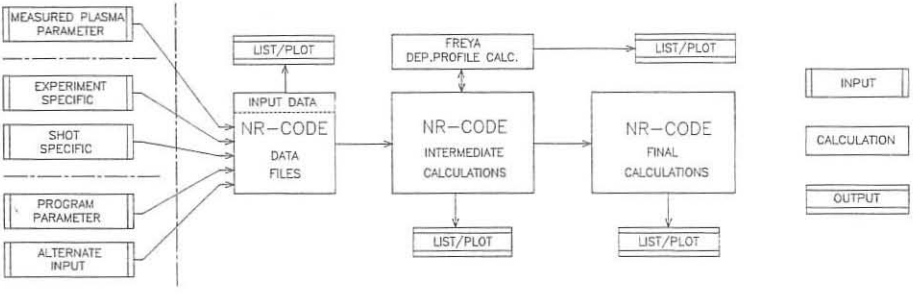

Fig.1: Software scheme

Secondly, the reactivities and the distribution functions are determined in INTERMEDIATE CALCULATIONS and the input data for FREYA code calculation of the deposition profile D(r) are prepared. In the FINAL CALCULATIONS one of the parameters Q_{DD}, T_D, and n_D can always be calculated, the other two being taken as ALTERNATE INPUTS. The software thus allows not only determination of the ion temperature or density, but also prediction of neutron rates and therefore detailed studies of the influence of relevant plasma parameters on the neutron rate.

By this modular structure all components of eq. 3 can be separately discussed. Furthermore, if this becomes advisable, it would be easy to change the model for neutron production by fast ions and use, in particular, more sophisticated distribution functions, even for the target plasma. Last but not least, the flexibility of the software allows us to treat, besides D^0 injection, not only ohmic discharges but also H^0 injection in deuterium plasmas and ICR and LH heating. For most of these cases the hydrogen content of the plasma is the main problem.

D^0 injection in deuterium plasma

As an example of the treatment of D^0 injection in deuterium plasma, we consider two discharges, one with a high ion temperature of about 3.5 keV (#17061, injection: 4.15 MW, 1.1 - 1.4 sec) and another with a relatively low ion temperature of about 2.0 keV (#16910, injection: 3.1 MW, 1.1 - 1.5 sec). Figure 2 shows for both discharges the time development of the neutron rate Q and the central electron temperature, as well as the time-dependent central deuteron temperature calculated from Q. Table 1 gives for discharge #17061 for some times the components Q_{00}, Q_{01}, Q_{02} (the indices correspond to those in equation 3) and the ratio T_D/T_e, calculated for a content of 10% protons.

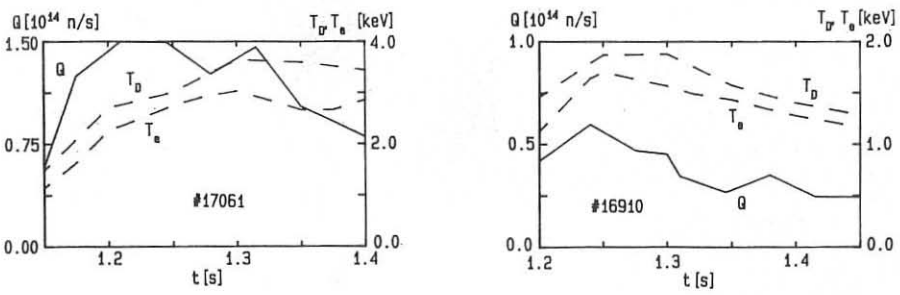

Fig. 2: Neutron rate (Q), electron (T_e) and deuteron (T_D) temperatures

The dominant neutron production is due to the full energy beam reactions with the target plasma Q_{01}. The half-energy beam (Q_{02}) contributes about 10% of Q_{01}. At the beginning of the injection this is appreciably higher than the thermonuclear production Q_{00}. But during injection the temperatures increase, causing an increase in the beam-target reactions (owing to T_e and T_D) as well as in Q_{00}. At the maximum of the neutron rate Q_{00} is about twice Q_{02}. The scatter in the results for T_D/T_e reflects the uncertainty of the temperature determination.

TABLE 1

time [sec]	Q_{00}	Q_{01}	Q_{02}	T_D/T_e
	[10^{13} neutrons/sec]			
1.15	0.036	4.41	0.35	1.30
1.20	0.72	10.5	1.03	1.20
1.25	2.07	12.9	1.29	1.10
1.30	2.32	8.31	0.91	1.20
1.35	1.14	7.36	0.83	1.35
1.40	0.39	6.60	0.68	1.20

Table 2 gives the different particle densities $n_i = \int n_i f_i dW$ on the plasma axis. They are of the same order for all components of the beam, but about one order of magnitude smaller for the beams than for the target plasma.

Table 2 Deuteron densities on axis at maximum neutron production

	n_0	n_1	n_2	n_3	
#17061	4.16	0.64	0.45	0.16	10^{13} deuterons/cm^3
#16910	3.37	0.45	0.17	0.12	10^{13} deuterons/cm^3

Table 3 gives for discharge #16910 at 1.3 sec all components of eq. 3, for injection of the total power in one direction and for the hypothetical case of balanced injection with half the power in each beam. Here, owing to the low ion temperature the thermonuclear production is of the same order as the production by the one-third energy beam component, which itself amounts to only 1.5% of the beam production. The production by reactions between the beam particles clearly shows a dependence on the relative velocity, as is to be expected. But owing to the small densities in the beams compared with the target plasma the beam-beam productions are smaller than the one-third energy beam-target production, even in the hypothetical case of balanced injection, and so it is always negligible.

Table 3

	neutron rate [neutrons/sec] unidirectional inj.	balanced inj.
Q_{00}	7.99×10^{11}	7.99×10^{11}
Q_{01}	4.39×10^{13}	4.39×10^{13}
Q_{02}	3.71×10^{12}	3.71×10^{12}
Q_{03}	7.39×10^{11}	7.39×10^{11}
Q_{11}	7.35×10^{7}	1.44×10^{11}
Q_{12}	1.47×10^{8}	8.20×10^{10}
Q_{13}	1.86×10^{8}	2.94×10^{10}
Q_{22}	7.18×10^{5}	3.19×10^{10}
Q_{23}	6.42×10^{5}	8.54×10^{9}
Q_{33}	7.39×10^{3}	2.12×10^{9}

H^0 injection in deuterium plasma

As an example of the treatment of H^0 injection in deuterium plasma we consider the discharge #21502 (1.35 MW, 1.0 - 3.0 sec). In this case we have only the thermonuclear production Q_{00}. Figure 4 shows the measured neutron rate and the ratio n_D/n_H from CX measurements. Figure 5 gives the deuteron temperature calculated with our software and, for comparision, the electron temperature from ECE measurements. Here again we find $T_D/T_e \approx 1.2$. The decrease in the neutron rate is caused by the small decrease in the ion temperature.

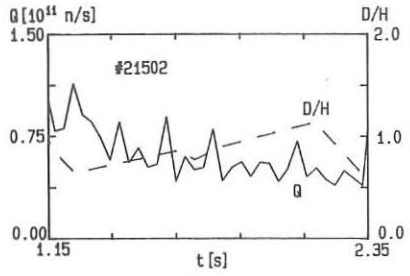

Fig. 4. Neutron rate and n_D/n_H for discharge #21502

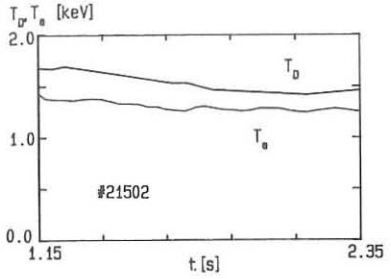

Fig. 5: Ion and electron temperature for discharge #21502

SEPARATE MEASUREMENT OF PARTICLE AND RADIATION LOSSES BY USING TIME-OF-FLIGHT TYPE NEUTRAL PARTICLE ENERGY ANALYZER

F.Tsuboi, S.Adachi, K.Hattori, M.Ichimura, M.Inutake, T.Kondoh, A.Mase, Y.Nakashima, N.Yamaguchi, K.Yatsu and S.Miyoshi

Plasma Research Center, University of Tsukuba,
Tsukuba, Ibaraki 305, Japan

ABSTRACT

The method which can measure the energy losses due to charge-exchange neutrals and radiations separately is presented. The reduction of the radiation loss after ECR discharge cleaning in the tandem mirror GAMMA 10 is clearly observed.

INTRODUCTION

In order to study and improve the plasma confinement, it is very important to clarify the main energy-loss-channel from the confined plasma. A bolometric method has been widely used in many plasma confinement devices to measure the total energy flux emitted from the plasma. It is easy to omit the particle flux, but difficult to separate the radiation flux from the particle flux, completely. A new method for the separation of the energy losses due to neutral particles and radiations by using the difference of their time-of-flights has been developed[1] . The ratio of the particle loss to the radiation loss from the same plasma volume to the same solid angle is easily obtained by this method. The absolute values of each loss power could be evaluated by taking account of the total loss power measured by the conventional bolometer. This new method is applied for evaluating the effect of the ECR discharge cleaning (ECR-DC) on the tandem mirror GAMMA 10[2] . The ratios of the particle loss to the radiation loss before and after ECR-DC are measured and the significant reduction of the radiation loss after ECR-DC is clearly observed.

EXPERIMENTAL APPARATUS

Figure 1 shows a schematic drawing of the time-of-flight type neutral particle energy analyzer system, TOF, which consists of a chopper system, a flight tube and a Daly type detector. Hydrogen atoms,

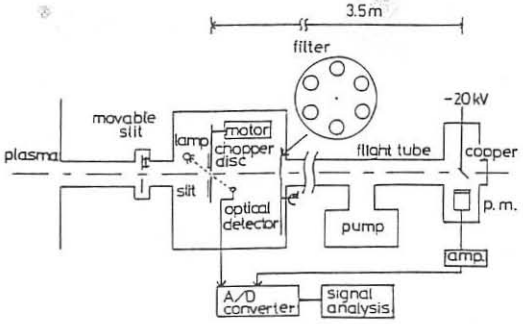

Fig.1 The schematic drawing of TOF system

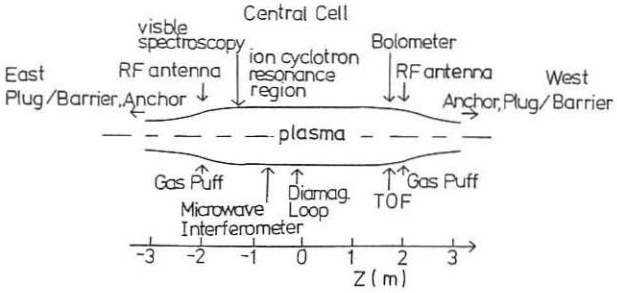

Fig.2 The experimental arrangement in the central cell of GAMMA 10

H^0 and photons are emitted from the plasma and chopped by a rotating disk with slits and travel 3.5m in the flight tube. Due to the difference of their time-of-flights, the signals of the neutrals and photons can be detected separately. The time resolution of this system is a few microseconds. The energy distribution of particles is estimated from their time-of-flight profile. The energy distribution of photons is estimated by use of several filters which have different energy windows for the transmission of photons.

GAMMA 10 is an axisymmetrized tandem mirror with thermal barriers. In the central cell, ions are heated by ICRF. In the present experiment, the ion cyclotron resonance layers exist near the central cell midplane. TOF system and the bolometer are set near the ICRF antenna as shown in Fig.2. The wall conditioning of the central cell had been done only by the pulsed discharges (< 60msec) with the density of 3×10^{12} cm^{-3} in every 12 min. Recently a steady state ECR discharge cleaning with lower density of 2×10^{10} cm^{-3} has been applied for 30 hours[3]. The effects of ECR-DC appear clearly in the detector signals.

RESULTS AND DISCUSSION

Figure 3(a) shows the typical detector signals before ECR-DC with no filters in the flight pass. When a slit opens, the signal of photons from the plasma is detected immediately and then signals of particles appear with the delay time determined by their time-of-flights. There are 24 slits of 0.02cm width and 1.0cm length at 7.5 cm radius on the chopper disc which rotates at the rate of about 40000 rev/min. Then the signals of photons and particles are obtained in every 100μsec. By dividing the time-of-flight spectrum of particles into every 1.6μsec, we can estimate the energy distribution by taking account of the secondary emission coefficient of the copper target[4] as shown in Fig.4(a). On the other hand, the energy distribution of photons is obtained by changing filters which can transmit photons in different energy ranges. By considering the transmission coefficient and the photo-electric yield

of the copper[5),(6)], we can obtain the energy distribution of photons as shown in Fig.5(a). The radiation is strong in the VUV region as indicated in the figure. From the visible spectroscopic measurement, it is expected that the strong line emissions due to light impurities, C and O, lie in this region. This system has no sensitivity for photons with energy less than 10eV due to the abrupt reduction of the photo-electric yield. By using the bolometer with LiF window which transmits the photons in the energy region lower than 12 eV, we confirmed the radiation in this energy region has less contribution to the total power loss from the plasma. The ratio of the particle loss to the radiation loss calculated from Fig.4(a) and Fig.5(a) becomes about 12.

The typical detector signals obtained after ECR-DC is shown in Fig.3(b), when the plasma density is almost the same as the density before ECR-DC. It is clearly observed that the peak height of the photon signal becomes remarkably small compared with that of particle signals. Figures 4(b) and 5(b) are the energy distribution of particles and photons after ECR-DC, respectively. The total loss power measured by the bolometer is almost the same in both cases before and after ECR-DC. Then, the ordinates of Figs.4(b) and 5(b) are normalized as the values of the total loss power calculated from the both energy distributions before and after ECR-DC become equal. The ratio of the particle loss to the radiation loss after ECR-DC becomes about 75. It can be calculated from Figs.5(a) and 5(b) that the radiation loss is reduced to about 1/6 after ECR-DC. This fact agrees qualitatively with the reduction of the line intensities of the light impurities measured by the spectroscopic measurement.

SUMMARY

The new method has been developed for evaluating the energy losses due to neutral particles and radiations separately by using the differences of their time-of-flights. The effects of ECR discharge cleaning in the tandem mirror GAMMA 10 are studied by this method. It is clearly observed that the energy loss due to radiations is reduced to about 1/6 after ECR-DC.

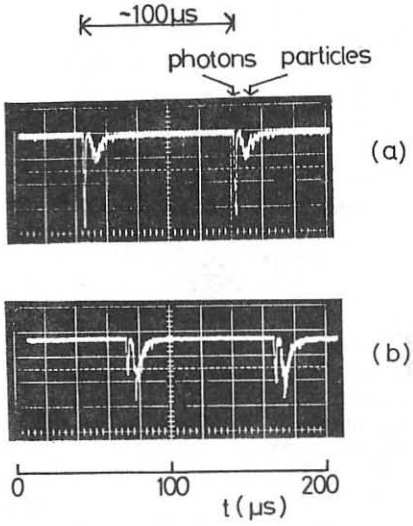

Fig.3 The typical signals before (a) and after (b) ECR-DC

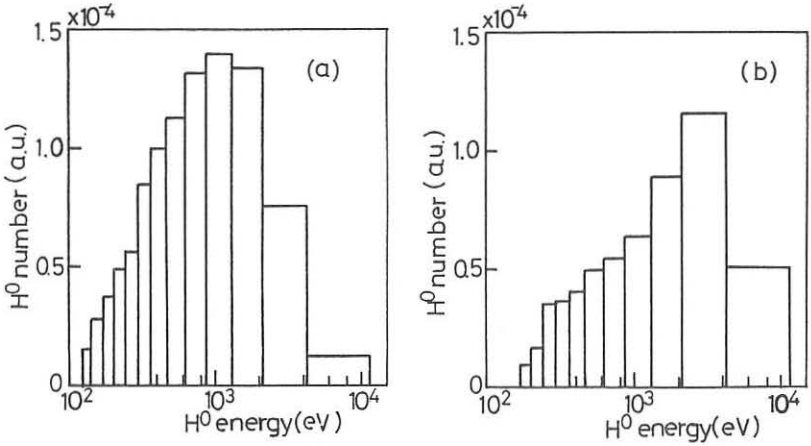

Fig.4 The energy distributions of H^0 before (a) and after (b) ECR-DC

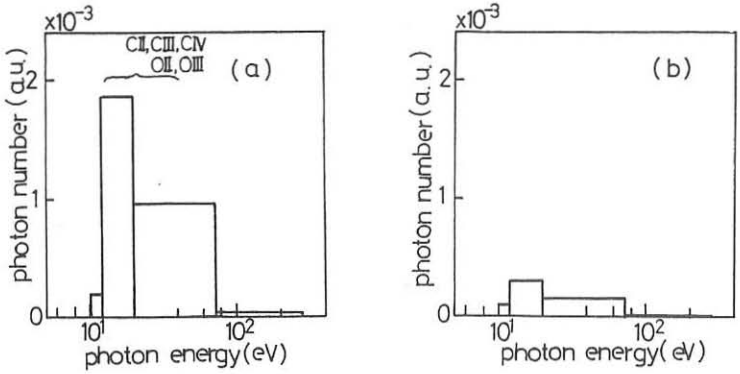

Fig.5 The energy distributions of photons before (a) and after (b) ECR-DC

REFERENCES
(1) F.Tsuboi et al., to be published
(2) M.Inutake et al., Phys.Rev.Lett. 55,939(1985)
(3) Y.Nakashima et al., to be published in J.Nucl.Mater.
(4) A.I.Kislyakov, J.Stockel and K.Jakubka, Sov.Phys.Tech.Phys. 20,986(1975)
(5) R.B.Cairns and J.A.R.Samson, J.Opt.Soc.America 56,1568(1966)
(6) R.H.Day, P.Lee, E.B.Saloman and D.J.Nagel, J.Appl.Phys. 52,6965(1981)

INVESTIGATION OF SLOWING-DOWN AND THERMALIZED ALPHA PARTICLES BY CHARGE EXCHANGE RECOMBINATION SPECTROSCOPY - A FEASIBILITY STUDY

Manfred von Hellermann, Hugh Summers, Alain Boileau *)

JET Joint Undertaking, Abingdon UK
*) INRS Energie, Varennes, Canada

Motivated by the expectation of achieving significant alpha particle production in the approaching fusion conditions of JET, JT60 and TFTR tokamaks, a range of alpha particle diagnostics have been under study in recent years [1]. One class is based on exploiting the charge exchange reaction through use of appropriate diagnostic or heating neutral beams. Single charge transfer with the associated excitation of recombination radiation can be used as a spectroscopic method for the measurement of alpha particle density and velocity distribution function. The charge capture and subsequent cascading and redistribution gives emission in the HeII n=4-3 (4686 A) line which can be transferred either by quartz fibres or by a mirror relay system to remote spectroscopic equipment beyond the biological shield.

For significant charge exchange the relative velocity of alpha particle and of injected neutral (hydrogen or deuterium) must be within a band of approximately 100 keV/amu which is defined by the fall of the effective charge exchange rate at higher relative velocities.

Visible charge exchange recombination spectroscopy of **thermal** ionized plasma particles, including helium, using the neutral heating beams is well established on JET [2]. The study presented here investigates the scope of information which may be achieved using the existing heating beam capability with upgrading to E_{beam}=140 keV at 0.7MWatt per beam on **slowing-down alpha particles** with energies $kT_i < E_{alpha} < 3.5$ MeV. Clearly the study must also be concerned with the CXRS spectral features associated with the background thermal helium at relatively higher ion temperatures than achieved at present and the merging of the cooling and thermal helium velocity distribution function.

For future JET operation with input powers up to 40 Mwatts of Ohmic and auxiliary heating it is expected to achieve, in particular during hot-ion modes [3] with low to moderate electron densities , alpha particle power levels of approximately 5 MWatts. For slowing down times in the order of 1 to 2 sec and an assumed main alpha particle production within a volume of roughly 50 m^3 we may expect alpha particle densities in the plasma centre between 10^{17} m^{-3} and 10^{18} m^{-3}.

For the geometry of the JET heating beams and the CXRS multichord viewing line system (cf. [4]) we can calculate from a known energy dependence of the effective excitation rate (Fig.1) and a slowing-down velocity distribution function (Fig.2) the expected recombination

spectra. An example of a theoretical spectrum consisting of the superposition of the contributions of thermalized and slowing-down alpha particles as well as the continuum background radiation is shown in Fig.3. The absolute photon fluxes are based on the extrapolated neutral beam data and an attenuation code used for the present low-Z impurity density calculations [2]. The spectrum representing the slowing-down alphas covers a spectral width in the order of 150A. The shape and Doppler shift depend on slowing-down parameters as well as the observation geometry and neutral beam energy.

The detection limit of the highest alpha particle energies contributing to the observed spectrum is demonstrated in a semilogarithmic plot (Fig.3b) where the continuum level and its associated noise level correspond to the actual observed levels of the current CXRS system. In order to discriminate the broad low-level slowing-down spectrum from the background continuum level two alternatives are being considered. One is active beam modulation and the other is the use of an additional passive viewing line which does not intersect the beams. The latter provides a simultaneously measured background spectrum.
Fig.4 shows an example of 2 actual JET spectra gained during NB injection in a deuterium plasma with a ^{3}He minority (2 to 5% of the electron density) typical for RF plasma heating. In this example the NB pulse was applied 2 sec after the RF pulse. Both viewing lines are fed into the multi-chord CXRS system enabling a subtraction of two spectra using one spectrometer and one 2-dim detection system. The residual of the subtraction is the CX Doppler broadened spectrum (representing in this example the plasma centre ion temperature of 4.3 keV) and the rms noise level of the continuum. A remaining small cold constituent, presenting approximately 10% of the total intensity, is supposed to be due to a non perfect toroidal symmetry in plasma boundary emmission.

Conclusion

A measurement of an alpha particle density radial profile in the quoted density range appears to be feasible. The reconstruction of a velocity distribution function in the energy range below 0.5 MeV in the plasma centre should be possible using either a passive viewing line for a simulataneous background subtraction or alternatively an active beam modulation technique. In the forthcoming JET operation period with combined NB and ICRH heating the high energy tails of helium minority velocity distribution function will be investigated.

[1] Workshop on Alpha Particle Diagostics, JET 1986, TFTR 1987
[2] A.Boileau et al. ,JET Report JET-P(87)44
[3] G.F. Cordey et al. ,JET Report JET-P(86)38
[4] see S.Corti et al, this conference

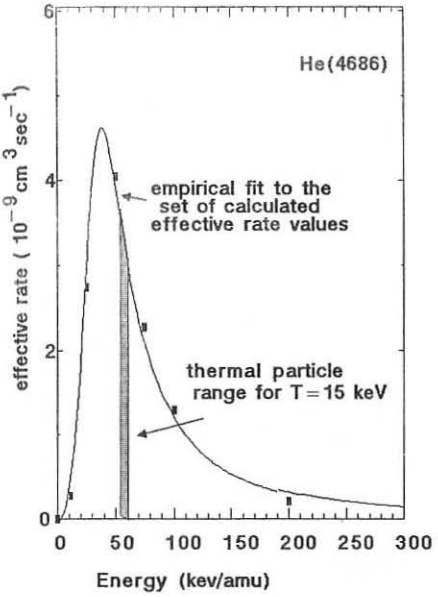

Fig.1 Effective excitation rate

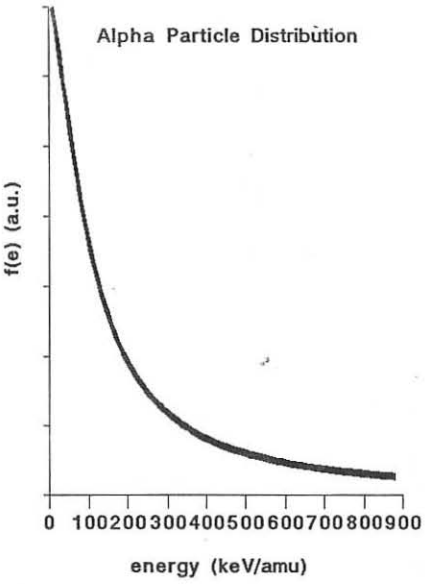

Fig.2 Alpha particle distribution function

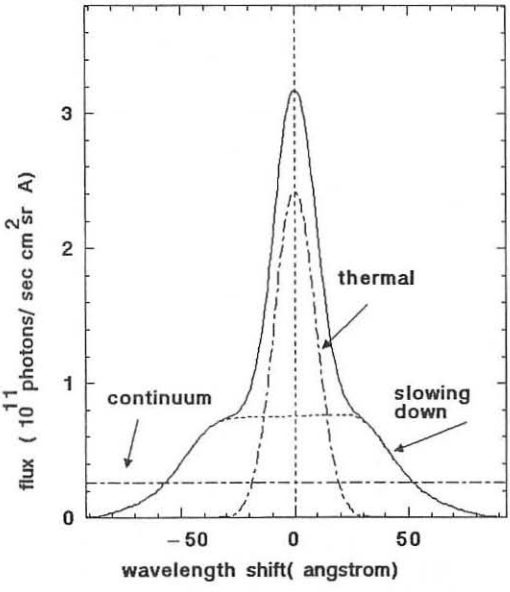

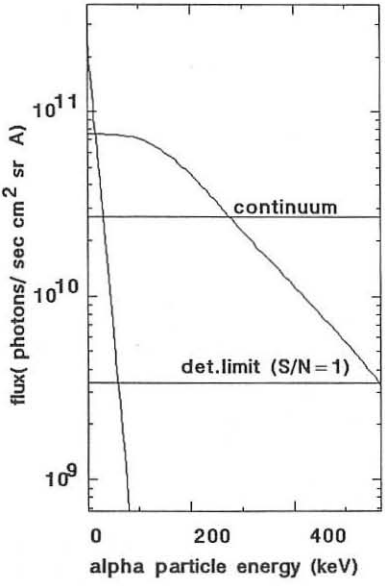

Fig.3 Thermal and slowing down spectrum for E=60keV/amu, P=5MWatt
n(alpha)=10**18 m**-3, n(electron)=5*10**19 m**-3

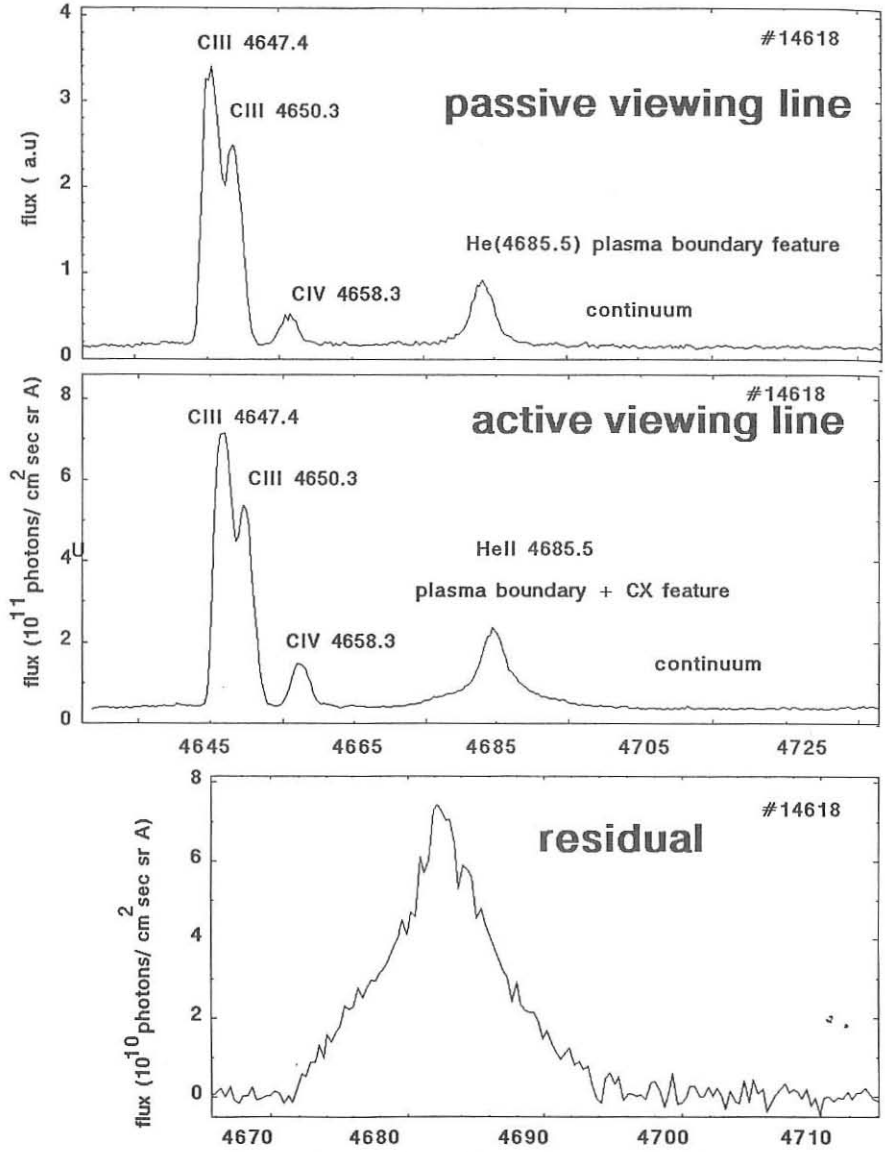

Fig.4 Background subtraction using a passive viewing line. The helium minority density is approximately 5*10**17 m**-3. The background noise level is less than 5*10**9 photons/cm**2 sec sr A. The residual contains a CX component of 4.3keV and a cold boundary feature of 0.18 keV.

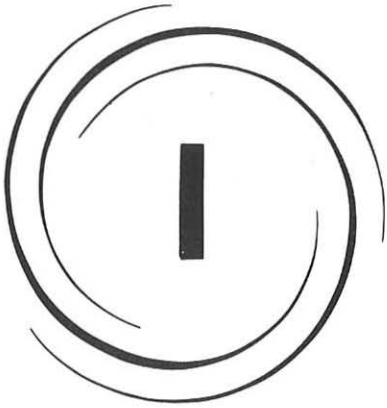

Basic Collisionless Plasma Physics

I

LINEAR AND NONLINEAR COUPLED ALFVÉN-VARMA MODES IN INHOMOGENEOUS PLASMAS

P. K. Shukla and L. Stenflo[a)]

Fakultät für Physik und Astronomie
Ruhr-Universität Bochum
D-4630 Bochum, F. R. Germany

a) Department of Plasma Physics
Umeå University, Sweden

More than two decades ago, Varma [1] discovered a low-frequency (compared to the ion gyrofrequency) flute-like electrostatic ion drift mode that can be driven unstable due to the magnetic field gradient in nonuniform plasmas. The Varma mode is derived on the basis of hydrodynamic equations including an equation of state in the form of the conservation of the magnetic moment of the two-dimensional ion fluid [2]. This new mode seems to have been observed in many laboratory experiments [3]. It has been suggested that the Varma mode can account for catastrophic plasma losses in mirror devices.

In view of the growing importance of the Varma mode in connection with mirror reactors, it is desirable to find the relation between this mode and some of the existing modes in nonuniform magnetized plasmas. In this paper, we have achieved this goal by incorporating the electromagnetic effects in Varma's theory. It has been found that the Varma mode is linearly coupled with the Alfvén wave. The instability of coupled Alfvén-Varma modes is analyzed. Linearly unstable coupled Alfvén-Varma modes attain finite amplitude and start interacting nonlinearily. In order to describe such an interaction, we have derived a set of nonlinear coupled equations. It is shown that nonlinearly coupled Alfvén-Varma modes self-organize in the form of dipolar vortices. Condition under which the latter arise is given.

Consider a weakly inhomogeneous electron-ion plasma immersed in an external magnetic field $B_o\hat{z}$. The density and magnetic field gradients are assumed to be along the x axis. We are concerned with the instability of this equilibrium against low-frequency (compared to the ion-gyrofrequency $\omega_{ci} = q_i B_o/m_i$) electromagnetic perturbations in a plasma relevant to mirror reactors in which $T_i >> T_e$. This situation arises during the

neutral beam injection experiments. We consider two-dimensional ion and three-dimensional electron motions. Then, in the guiding center approximation (viz., $\partial_t \ll \omega_{ci}$), the appropriate expressions for the perpendicular components of the ion and electron velocities are

$$\vec{v}_{i\perp} = \vec{v}_E + \frac{m_i}{q_i B_o^2}\left(\partial_t + \vec{v}_{i\perp}\cdot\nabla\right)\vec{E}_\perp + \frac{\mu_i}{q_i B_o^2}\vec{B}_o \times \nabla B_o - \frac{1}{q_i n_i}\nabla \times \left(n_i \mu_i \frac{\vec{B}_o}{B_o}\right), \quad (1)$$

and

$$\vec{v}_{e\perp} = \vec{v}_E + v_{ez}\vec{B}_\perp / B_o, \quad (2)$$

where q_i and m_i are the charge and mass of the ions, $\vec{v}_E = \vec{E} \times \vec{B}_o / B_o^2$, μ_i $(= p_{i\perp}/n_i B_o)$ is the ion magnetic moment, v_{ez} is the parallel electron velocity, and the electric and magnetic fields are given by

$$\vec{E} = -\nabla\phi - \frac{1}{c}\hat{z}\,\partial_t A_\parallel,$$

and

$$\vec{B}_\perp = \nabla A_\parallel \times \hat{z},$$

where ϕ is the scalar potential and $A_\parallel$ is the parallel component of the vector potential. The perpendicular component of the vector potential is set to be zero. This ammounts to neglecting the compressional magnetic field perturbations and is consistent with the low-β $(m_e/m_i \ll \beta \ll 1)$ approximation.

Inserting (1) and (2) into the ion continuity, the conservation of the charge density under the quasi-neutral approximation ($n_i = n_e = n$), the ion energy equation, and the parallel component of Ohm's law, we obtain letting $n = n_o(x) + n_1$ $(n_1 \ll n_o)$ and $\mu_i = \mu_{io}(x) + \mu_1$ $(\mu_1 \ll \mu_{io})$:

$$d_t\left(\frac{n_1}{n_o} - \frac{1}{\omega_{ci} B_o}\nabla_\perp^2\phi\right) + \frac{1}{B_o}\hat{z}\times\nabla\phi\cdot\nabla\left(\ln n_o - \ln B_o\right) + \vec{v}_D\cdot\nabla\frac{\mu_1}{\mu_o} = 0, \quad (3)$$

$$\vec{v}_D\cdot\nabla\left(\frac{n_1}{n_o} + \frac{\mu_1}{\mu_{io}}\right) - \frac{1}{\omega_{ci} B_o}\left(d_t\nabla_\perp^2\phi + v_A^2 d_z \nabla_\perp^2 A_\parallel\right) = 0, \quad (4)$$

$$d_t \mu_1 + (\mu_{i0}/B_0)\, \nabla\phi \times \hat{z} \cdot \nabla B_0 = 0, \tag{5}$$

$$\partial_t A_{\parallel} + d_z \phi = 0 . \tag{6}$$

In deriving (4), we have made use of the parallel component of Ampere's law

$$v_{e\parallel} = (e \mu_0 n)^{-1} \nabla_\perp^2 A_{\parallel} .$$

Furthermore, $\vec{v}_D = \mu_{i0} \vec{B}_0 \times \nabla B_0 / q_i B_0^2$, $d_t = \partial_t + (\vec{v}_D + \vec{v}_E)\cdot\nabla$, $d_z = \partial_z + (\vec{B}_\perp / B_0)\cdot\nabla$ and v_A is the Alfvén speed.

Neglecting the nonlinear terms, we can Fourier transform (3)-(6). We then find four linear algebraic equations, the combination of which leads to the dispersion relation

$$1 = \frac{k_z^2 v_A^2}{\omega^2} - \left[\frac{(\varkappa_n/\varkappa_B)-1}{\omega} - \frac{1}{\omega-\omega_*}\right] \frac{\omega_* \omega_{ci}}{\omega-\omega_*} \frac{k_y \varkappa_B}{k_\perp^2} , \tag{7}$$

where $\varkappa_B = d_x \ln B_0(x)$, $\varkappa_n = d_x \ln n_0(x)$, $\omega_* = k_y \varkappa_B \mu_{i0}/q_i \equiv k_y v_{Dy}$.

Two comments are in order. First, for $k_z = 0$, Eq. (7) is identical to Varma's dispersion relation in the high density regime. Secondly, in the absence of the magnetic field gradient, Eq. (7) yields $\omega = \pm k_z v_A$, which is the dispersion relation of Alfvén waves. Clearly, electromagnetic effects cause a coupling between the Alfvén and Varma modes. It can easily be shown that when $\omega \approx \omega_* \approx k_z v_A$, Eq. (7) admits an instability supported primarily by the magnetic field gradient. The growth rate of that instability is

$$\mathrm{Im}\ \omega \approx (\omega_{ci}\, \omega_*^2\, k_y \varkappa_B / k_\perp^2)^{1/3} . \tag{8}$$

We now present a particular class of nonlinear solutions to (3)-(6). We assume that all functions depend on the variables x and $\xi = y + \alpha z - ut$, where α and u are constants. It can then be shown that in the new stationary frame, combination of (3)-(6) yields a nonlinear partial differential equation

$$\mathcal{L}\left[\frac{M\omega_{ci}}{u(1-M)}\left(\frac{\varkappa_B}{1-M}+\varkappa_B-\varkappa_n\right)\phi + \left(1-\frac{\alpha^2 v_A^2}{u^2}\right)\nabla_\perp^2\phi\right]=0, \tag{9}$$

where $\mathcal{L} = \partial_\xi - (uB_o)^{-1}(\partial_x\phi\,\partial_\xi - \partial_\xi\phi\,\partial_x)$ and $M = v_{Dy}/u$. Equation (9) is satisfied by the ansatz

$$\nabla_\perp^2\phi = C_1\phi + C_2 x, \tag{10}$$

provided that the constants C_1 and C_2 are related by

$$\frac{M\omega_{ci}}{(1-M)u}\left(\frac{\varkappa_B}{1-M}+\varkappa_B-\varkappa_n\right)+\left(1-\frac{\alpha^2 v_A^2}{u^2}\right)\left(C_1+\frac{C_2}{uB_o}\right)=0. \tag{11}$$

The dipolar vortex solutions of (10) can be constructed in the usual manner. In the outer region, we have $C_2=0$ and the localization requires that

$$M\omega_{ci}\left[\varkappa_n-\varkappa_B-\varkappa_B/(1-M)\right]/u(1-M)(1-\alpha^2 v_A^2/u^2) > 0.$$

To summarize, we have investigated linear and nonlinear properties of coupled Alfvén-Varma modes in an inhomogeneous magnetic field. It is found that the coupled Alfvén-Varma modes can be driven unstable by the gradient of the external magnetic field in an inhomogeneous plasma. Furthermore, it has been shown that nonlinearly interacting Alfvén-Varma modes self-organize in the form of dipolar vortices. The latter may decide anomalous transport properties of mirror reactors.

This research was supported by the Deutsche Forschungsgemeinschaft through the Sonderforschungsbereich 162 "Plasmaphysik Bochum/Jülich" Teilprojekt L5.

REFERENCES

[1] R. K. Varma, Nucl. Fusion 7, 57 (1967).

[2] R. K. Varma, in Modern Plasma Physics, IAEA, Vienna (1981), p. 147.

[3] Arsenin et al., Sov. J. Plasma Phys. 13, 87 (1987).

NUMERICAL SIMULATION OF THE EVOLUTION OF FLUTE VORTICES

V.P.Pavlenko, V.I.Petviashvili, V.B.Taranov
Institute for Nuclear Research Academy of Sciences of the Ukrainian SSR, Kiev, U.S.S.R.

In a nonuniform magnetized plasma the buoyant force can arise if there is an unfavorable curvature of the magnetic field lines. The plasma convection which is similar to the convection of a fluid in the gravitational field is coused by this force. The linear analysis shows that the unstable perturbations arise that have in this case the form of "tongues" which are strongly elongated along the external magnetic field - so called flute modes [1]. The main nonlinear effect associated with the development of the flute instability is the "twisting" of these "tongues" by the external magnetic field. It can be expected as the qualitative analysis shows that the evolution of flute instability will be terminated in a random set of localized two dimensional vortices. The further investigation of properties of the flute instability needs the application of numerical methods. In the present article the time evolution of flute vortices of different type is investigated numerically.

To describe the dynamics of the flute perturbations we use the equations obtained in [2]. In dimensionless variables with normalizing on space (K_0) and temporal ($K_0 U$)

scales of vortex (u is the velocity of vortex) the equations have the form

$$\frac{\partial}{\partial t}\nabla^2\phi + (1+\alpha)\frac{\partial}{\partial y}(n-\nabla^2\phi) = \tag{1}$$

$$= J(\nabla^2\phi, \phi) + \alpha\, div\, J(\nabla\phi, n)$$

$$\frac{\partial n}{\partial t} + \frac{\partial}{\partial y}(\phi - n) = J(n, \phi) \tag{2}$$

here $J(a,b) = \frac{\partial a}{\partial x}\frac{\partial b}{\partial y} - \frac{\partial a}{\partial y}\frac{\partial b}{\partial x}$, $\alpha = \frac{v^*}{u}$, $n = \frac{\kappa_0}{\varkappa}\tilde{n}$,

$$\phi = \frac{\kappa_0 c}{u B_0}\tilde{\phi}, \quad \kappa_0^2 = \frac{v_0 \varkappa \Omega_i}{u(u+v^*)} > 0$$

v^*, v_0 are velocities of the diamagnetic and gravitational drifts correspondingly, Ω_i is ion cyclotron frequency, $\varkappa^{-1}$ is the characteristical scale of the plasma nonuniformity. The equations (1),(2) have been solved by the Lax - Wendroff method /alternating directions/ on the 64 x 64 grid with periodic boundary conditions. To invert the Laplace operator we have used the fast Fourier transformation on x variable and periodic running on y variable. The correctness of results is checked on the base of integrals of motion

$$I_1 = \int n\, dx\, dy, \quad I_2 = \int \nabla^2\phi\, dx\, dy \tag{3}$$

$$I_3 = \int \left\{ (\nabla \Phi)^2 - (1+\alpha) n^2 \right\} dx\, dy$$

The equations (1),(2) have the stationary solution in the form of dipole vortex of flute type [2]:

$$\Phi(r,\varphi) = \frac{K_1(r)}{K_1(r_0)} r_0 \cos\varphi, \quad r \geq r_0$$

$$\Phi(r,\varphi) = \left[(1+\kappa^2)\frac{r}{r_0} - \frac{J_1(\kappa r)}{J_1(\kappa r_0)} \right] \frac{r_0}{\kappa^2} \cos\varphi, \quad r \leq r_0 \qquad (4)$$

$$n = \Phi$$

The parameters κ and r_0 obey the dispersion relation for the dipole vortex

$$\frac{J_2(\kappa r_0)}{J_1(\kappa r_0)} = -\kappa \frac{K_2(r_0)}{K_1(r_0)}$$

We have considered the following initial conditions:

a) the shape of the dipole vortex type which is close to the stationary solution (4);

b) the solitary monopole vortex;

c) two dimensional periodic system of vortices in the form of the standing wave. The temporal evolution of these perturbations is considered in $\alpha \ll 1$ limit. The obtained results are as follows:

a) the numerical results have shown that the shape

which is close to the dipole vortex has the life time $t \simeq 5,5$. We note that in our scales the inverce increment of the linear flute instability in this case is $t = \gamma_L \simeq 4$;

b) the solitary monopole vortex is chosen with Gauss shape with amplitude corresponding to the linear level. We have seen the enhancement of the vortex amplitude with increment of the linear flute instability. In the final stage at the time $t \simeq 3$ the long wavelength structure of the dipole vortex type has been observed;

c) the temporal evolution of the initial perturbation in the form of the standing wave is also investigated starting from the level of amplitude corresponding to the linear stage. Here as well as in the case of monopole vortex the generation of harmonics on the nonlinear stage ($t \gtrsim 1,5$) have been observed. These harmonics are increasing with increment close to the linear flute instability increment.

So, in the limit $\alpha \ll 1$ we can conclude that in all cases considered the linear stage of the flute instability is succeded by the nonlinear one and the increase of perturbations of the potential and density continued.

References.

1. B.B.Kadomtsev,"Kollektivnya javlenija v plasme", Nauka, Moskva, 1976.

2. V.P.Pavlenko, V.I.Petviashvili, Sov.J. Plasma Phys. 9, 603, Sept.-Oct. 1983.

ELECTROSTATIC ION CYCLOTRON WAVES IN A STEADY-STATE TOROIDAL PLASMA

A.Fasoli, M.Fontanesi, A.Galassi, C.Longari, E.Sindoni
Dipartimento di Fisica dell'Università degli Studi di Milano
Via Celoria 16, 20133 Milano, ITALY

Introduction

THORELLO is a steady-state toroidal plasma suitable for basic collisionless plasma physics researches [1]. The combined possibilities to operate in different discharge regimes and to perform space-resolved cw measurements make particularly interesting the study of plasma waves interaction. An interferometric method allows the experimental reconstruction of the Electrostatic Ion Cyclotron Waves dispersion relation. In addition, by comparing experimental data with theoretical curves, the order of magnitude of the ion temperature can be obtained.

1. Experimental set-up and discharge parameters

The vacuum chamber has circular cross-section and is made of stainless-steel to achieve very low rate of outgassing. Minor and major radii are 9 cm and 40 cm respectively.
Low ultimate pressure and good purity conditions are obtained by operating high density cleaning discharges. The toroidal field magnet consists of four bunches of 14 coils each; the maximum steady-state toroidal magnetic field on the axis is about 2 kG. The plasma is produced in different neutral gases (H_2, He, Ar, Ne) by hot filament electron emission and acceleration by bias voltage.
Electronic density and temperature are measured by electrostatic Langmuir probes. These probes can scan the plasma cross-section radially on different toroidal positions at three poloidal angles. Apart from a hot electron region near the filament the plasma can be considered homogeneous and nearly maxwellian. In order to operate with uniform radial profiles of electron density and temperature a small vertical magnetic field ($\sim$ 5 G) produced by Helmoltz coils has been superimposed. A lay-out of the device is shown in fig.1.
The possibility to operate in different discharge regimes is shown in fig.2 and 3, where electron density and temperature are reported versus neutral gas pressure and filament current respectively. Profiles of T_e and n_e are shown in fig.4.

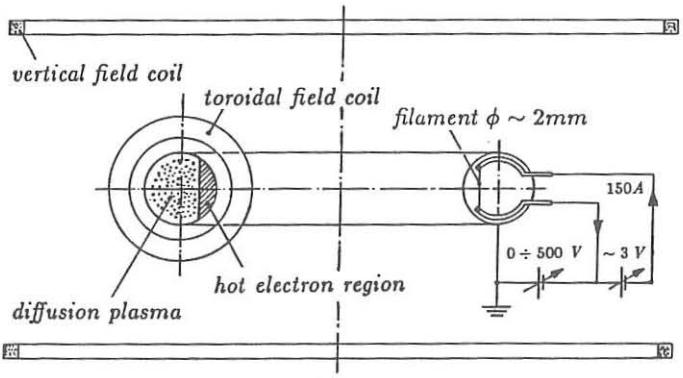

Fig.1

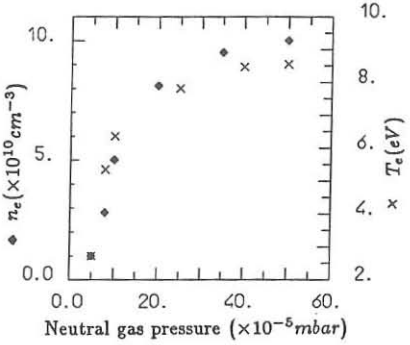

Fig.2

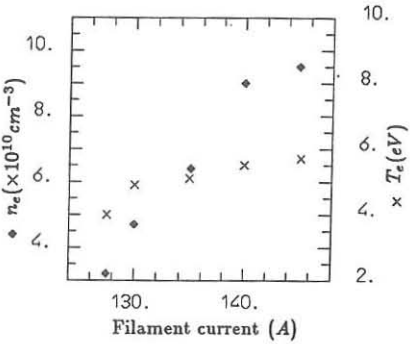

Fig.3

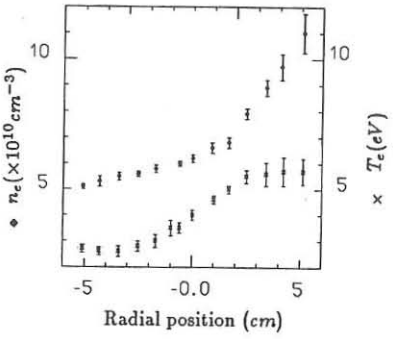

Fig.4

Fig.1: lay-out of *THORELLO*.

Fig.2,3: Electron density and temperature in H_2 vs. neutral gas pressure (2) and filament current (3) measured by Langmuir probes in the centre of plasma column.

Fig.4: Radial profiles of n_e and T_e in hydrogen plasma (positive values of position refer to the high field side).

2. Excitation and detection of electrostatic ion cyclotron waves.

Electrostatic ion cyclotron waves propagation has been studied in hydrogen plasma in the central region of the *THORELLO* plasma column. A numerical analysis of electrostatic dispersion equation [2] in the range of ion cyclotron frequency for transverse propagation, i.e. for values of $k_{\|}$ in the range

$$\frac{\Omega_i}{v_{t_e}} \ll k_{\|} \ll \frac{\Omega_i}{v_{t_i}} \tag{2.1}$$

shows the existence of two different branches (see fig.5) in each low–order harmonic band. The two branches are characterized by small, but finite, values of the imaginary part of perpendicular wavenumber, except for narrow regions across each harmonic resonance; according to Schmitt we will call these modes Neutralized Ion Bernstein Waves, NIBW [3].

Experimental observation of NIBW has been carried out on *THORELLO* by a continuous–wave interferometer. Wave excitation is achieved through an electrostatic antenna consisting of two thin metallic blades fed by a low power RF signal and phased 180° apart, installed at the plasma center. The size of the two blades and their distance is selected to guarantee a $k_{\|}$ spectrum peaked near $1cm^{-1}$, in order to satisfy condition (2.1) for our discharge parameters. A fraction of the signal is used as reference in a mixer (LO port).

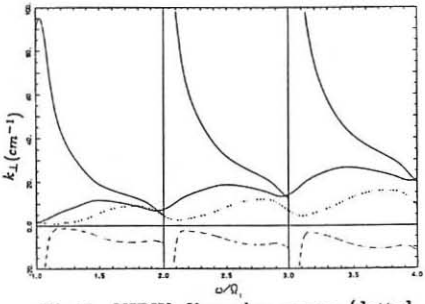

Fig.5: NIBW dispersion curves (dotted lines represent imaginary parts of the branches).

A T–probe, passing through the antennas perpendicularly to the magnetic field, is used to detect the wave; the signal from the plasma is then sent to the RF port of the mixer. The mixer output, after filtering in order to suppress time–dependent terms, is sent to the y–channel of a digital oscilloscope, while a voltage proportional to the probe distance from antenna drives the x–channel. By probe scanning of the experimental region we obtain an interferometric trace of the type shown in fig.6. Apart from a strong non–propagating disturbance in proximity of the antennas, whose non–linear origin is confirmed by a pronounced dependence on RF perturbation amplitude, the interferograms show the expected oscillating behaviour. Perpendicular wavelenghts are obtained by measuring the distance between a maximum and a minimum of the sinusoidal trace, for any operating frequency [4].

Backward modes and high–frequency ($> 2\Omega_i$) forward modes exhibit perpendicular wavenumber too large to be excited by electrostatic plane antennas and to be observed by finite spatial resolution detection system. Due to this limitation, the experimental reconstruction of the dispersion relation has been possible, in hydrogen plasma, for the

forward branch only in the first two harmonic bands. Comparison of experimental data with numerical curves computed for the *THORELLO* plasma parameters has shown some discrepancy, that we ascribed to the assumption of a fixed value for $k_{\|}$. An analytical method applied to the integral of normal modes pointed out that plasma dynamics, via the dispersion relation $k_{\perp}(k_{\|})$, can favour the detection of particular $k_{\|}$ modes at a distance from antenna much greater than one wavelenght. The $k_{\|}$ values of interest correspond to stationary points of the function $Rek_{\perp}(k_{\|})$, while the antenna spectrum and the exponential coefficient containing $Imk_{\perp}$ act as *weights* on different terms.
The agreement between experimental data and theoretical curves, generated by this model for an ion temperature of $0.1eV$ ($n_e = 2 \times 10^9 cm^{-3}$, $T_e = 1eV$), is shown in fig.7.

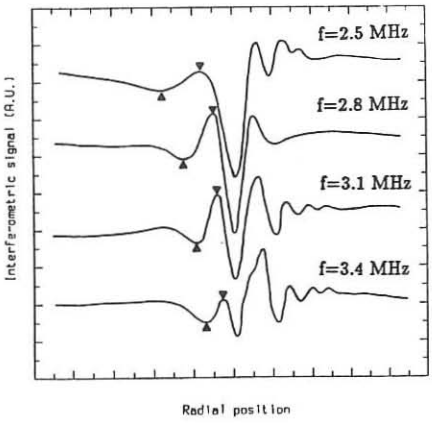

Fig.6

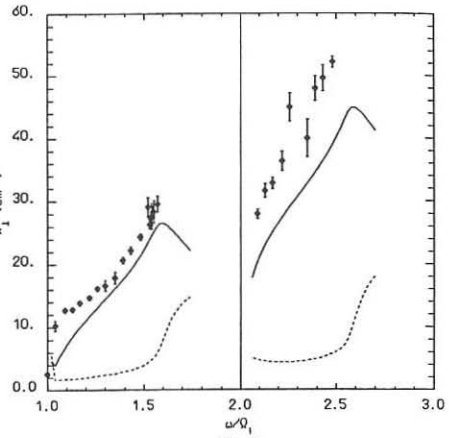

Fig.7

Conclusions.

The possibility of exciting and detecting ion cyclotron electrostatic modes predicted by warm plasma theoretical models has been verified. The good agreement between experimental results and numerical curves suggests the use of the dispersion relation of these waves as a diagnostic tool for the evaluation of ion temperature in the peculiar *THORELLO* plasma conditions.

* * *

The authors would like to thank C.Maroli and V.Petrillo for helpful discussions and suggestions, and G.Carbone for his valuable technical assistance.

References.

[1]–G.Agosti, et al., *Il Nuovo Cimento*, 9 D, 1 (1987).
[2]–A.Fasoli, A.Galassi, C.Longari, C.Maroli, V.Petrillo, *this conference.*
[3]–J.P.M.Schmitt, *Phys. Rev. Lett.*, **31**, 982 (1973).
[4]–J.Goree, M.Ono, K.L.Wong, *Phys. Fluids*, **28**, 2845 (1985).

ELECTROSTATIC DISPERSION RELATION IN THE ION CYCLOTRON REGIME

A.Fasoli, A.Galassi, C.Longari
Dipartimento di Fisica dell'Università degli Studi di Milano (ITALY)

C.Maroli, V.Petrillo
Istituto di Fisica del Plasma ENEA–CNR–EURATOM, Milano (ITALY)

The classic electrostatic dispersion relation has been analysed in the ion cyclotron regime for low density and low temperature magnetized plasmas, in connection with experiments on small size toroidal devices, aimed to produce and detect longitudinal waves in this range of frequency[1],[2].

The dispersion relation has the following form:

$$k_\perp^2 + k_\parallel^2 + \sum_\sigma \frac{\omega_{p\sigma}^2}{v_{t\sigma}^2}[1 + z_\sigma B(\lambda_\sigma, z_\sigma, \alpha_\sigma)] = 0 \qquad (1)$$

where $\underline{k}$ is the wave vector, $z_\sigma = \frac{\omega}{\sqrt{2}k_\parallel v_{t\sigma}}$, $\lambda_\sigma = \frac{k_\perp^2 v_{t\sigma}^2}{\Omega_{c\sigma}^2}$, $\alpha_\sigma = \frac{\omega}{\sqrt{2}k_\parallel v_{t\sigma}}$ and $\Omega_{c\sigma}$, $\omega_{p\sigma}$ and $v_{t\sigma} = \sqrt{\frac{T_\sigma}{m_\sigma}}$ are respectively the cyclotron and the plasma frequencies and the thermal velocity of the species σ.

The function B is defined as:

$$B(\lambda, z, \alpha) = \sum_{n=-\infty}^{+\infty} e^{-\lambda} I_n(\lambda) Z(z - n\alpha)$$

Since we are considering a boundary value problem, the dispersion relation is solved to give the complex values of $k_\perp$ as functions of real ω and $k_\parallel$ for fixed values of the other parameters.

The range of frequency considered is in the neighbourhood of the ion cyclotron frequency and its first harmonics. A hydrogen plasma is considered; the plasma density

ranges from 10^9 to $10^{11} cm^{-3}$ and temperatures of the order of a few eV are assumed for both electrons and ions. Oblique propagation is investigated, $k_{\|}$ being varied from 10^{-2} to $1 cm^{-1}$.

In fig.1, a plot of the numerical solution of equation (1) is shown, with emphasis on those roots presenting immediate physical interest. In fact, the dispersion relation (1) has infinite roots, due to its trascendental character, but, among all these, a forward branch and a backward branch (ion Bernstein wave) can be recognized near each harmonic, these two branches being characterized by relatively low values of the imaginary part of $k_{\perp}$.

Both real and imaginary parts of the perpendicular component of the forward wave vector present slight oscillations with period $\frac{2\pi}{\Omega_{ci}}$ superimposed on a roughly linear increase with ω. The backward branches are described with more details in Fig.2. Between the n^{th} and the $(n+1)^{th}$ harmonic, only one substantially real backward mode exists, which becomes strongly damped in going towards $\omega = n\Omega_{ci}$.

For $\omega \simeq n\Omega_{ci}$, the Bernstein wave converts into a virtual mode ($|\mathrm{Im}k_{\perp}| \simeq \mathrm{Re}k_{\perp}$), while for $\omega > (n+1)\Omega_{ci}$ it becomes evanescent ($\mathrm{Re}k_{\perp} \ll \mathrm{Im}k_{\perp}$).

As regards the possibility of conversion between the forward and the backward branches, the present analysis provides results different from those obtained in ref. [3]. In fact, as can be seen in Fig.1, the coincidence of the roots does not exactly occur. Nevertheless, in a certain range of frequency (for instance, around $\omega \simeq 1.5\Omega_{ci}$ in the first harmonic region) the real parts of $k_{\perp}$ for the two modes approach one another in correspondence to relatively low values of $\mathrm{Im}k_{\perp}$. In this condition, a partial transformation of the forward wave into the backward one may, therefore, take place. This convergence of the two roots appears to be more pronounced between Ω_{ci} and $2\Omega_{ci}$ and for increasing electron temperatures. As regards the role of the electron component of the gas, agreement with ref. [3] has been found; the electrons do not influence the dynamics of the backward branch, while they affect the behaviour of the forward root.

An analytical study of dispersion (1) has been performed, which accounts for the behaviour of the roots.

As regards the backward roots, when $\mathrm{Re}k_\perp \gg |\mathrm{Im}k_\perp|$, and $\lambda_i \gg 1$, the Bessel functions can be represented by the asymptotic expressions $I_n(\lambda) \sim \frac{e^\lambda}{\sqrt{2\pi\lambda}}[1+O(\frac{1}{\lambda})]$, so that, near each harmonic

$$k_\perp \sim [-\frac{\omega_{pi}^2 \Omega_{ci}\omega}{2\pi k_\parallel v_{ti}^4} Z(z_i - n\alpha_i)]^{\frac{1}{3}}$$

In particular, the approximate value of $k_\perp$ at $\omega = n\Omega_{ci}$ can be obtained:

$$k_\perp(\omega = n\omega_{ci}) = e^{-i\frac{\pi}{6}} \frac{n\omega_{pi}^2 \Omega_{ci}^2}{2v_{ti}^4 k_\parallel}$$

which is in good agreement with the numerical data, especially when $n > 2$.

For the flat, strongly damped part of the Bernstein branches at the left of each harmonic $\omega = n\Omega_{ci}$, $\mathrm{Re}k_\perp < |\mathrm{Im}k_\perp|$, so $\lambda_i = \chi - i\epsilon$ with $\epsilon \gg \chi$. In this condition,

$$I_n(\lambda_i) \sim \frac{e^{\lambda_i}}{\sqrt{2\pi\lambda_i}}[1+O(\frac{1}{\lambda_i})] + \frac{e^{-\lambda_i - i(n+\frac{1}{2})\pi}}{\sqrt{2\pi\lambda_i}}[1+O(\frac{1}{\lambda_i})]$$

and therefore the dispersion relation can be simplified in the form

$$\tan(2\epsilon - \frac{\pi}{4}) \sim (\frac{\omega_{pi}}{\Omega_{ci}})^2 [\frac{1}{\epsilon} - \frac{n\Omega_{ci}}{2v_{ti}k_\parallel \epsilon^{\frac{3}{2}}}]$$

from which an estimate of ϵ for the various virtual waves can be deduced.

It can be noted that the difference between the imaginary parts ϵ of λ_i for two contiguous virtual roots is roughly $\frac{\pi}{2}$, so that, for instance, in the range of frequencies $\omega < \Omega_{ci}$, nine strongly damped waves of this type exist in addition to those two virtual roots represented in Fig.2.

References

[1]–J.Goree, M.Ono, K.L.Wong, *Phys. Fluids*, **28**, 2845 (1985).

[2]–A.Fasoli, M.Fontanesi, A.Galassi, C.Longari, E.Sindoni, ***this conference.***

[3]–J.P.M.Schmitt, *Phys. Rev. Lett.*, **31**, 982 (1973).

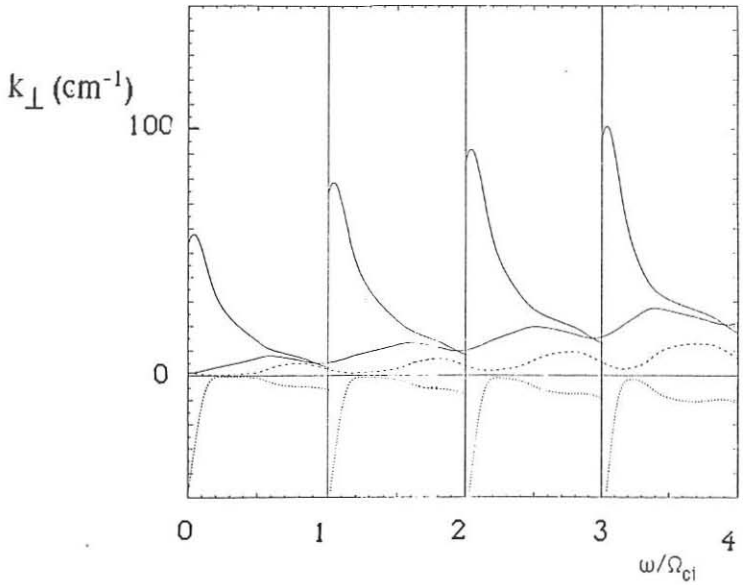

Fig 1: Forward and backward branches for n_e=2 10^9 cm^{-3}, T_e=10eV, T_i =1 eV, $k_{||}$ = 1 cm^{-1}. The dotted and the dashed curves are respectively the imaginary parts of $k_\perp$ for the backward and for the forward branch.

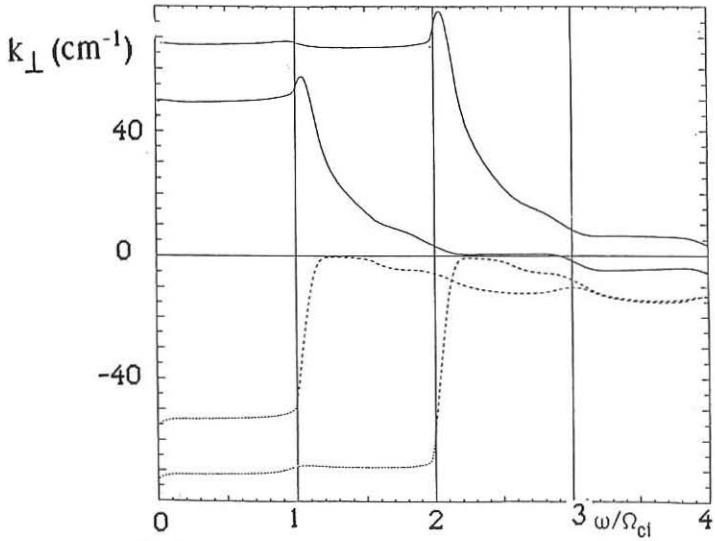

Fig 2: Backward roots for the same parameters of Fig. 1.

EICI PROPERTIES AS A FUNCTION OF THE CURRENT CHANNEL DIAMETER

Eldridge van Niekerk and Peter Krumm

Plasma Physics Research Institute, Dept. of Physics,
University of Natal, Durban 4001, South Africa.

INTRODUCTION

The electrostatic ion cyclotron instability (EICI), first observed by D'Angelo and Motley [1] in a Q-machine plasma, was theoretically explained by Drummond and Rosenbluth [2] in terms of an infinite, collisionless plasma model with a drifting Maxwellian electron distribution. It is destabilized in laboratory plasmas by drawing an electron current to a small electrode (the "button" or "disc") immersed in a magnetized plasma, thus apparently providing the drifting electron population required by the Drummond-Rosenbluth theory. However, the critical button size needed for the instability to be observed (button diameter $D \leq 6\rho_i$ = ion gyroradius) and the dependence of the frequency of the destabilized waves on the magnetic field in the vicinity of the button have focussed attention on aspects of the instability obviously not covered by the theory of Drummond and Rosenbluth. Schrittwieser [3] investigated the effect of varying the button size by using a segmented annular ring structure and found that at large diameters ($D \geq 6\rho_i$) the instability is modulated by a low frequency potential relaxation instability. Moving the button along the axis of an inhomogeneous field, Cartier et al [4] observed a filamental quenching of the instability at button diameters $D \sim \rho_i$.

By using a continuously adjustable iris in front of a biased collector we have investigated the properties of the EICI as a function of the button diameter in the range $\rho_i \leq D \leq 30\rho_i$. We confirm the filamental quenching at small button diameters (for uniform B) and the low frequency modulation at large diameters. In addition we observe a sharp frequency shift ($\Delta f \sim 15\%$) at large button diameters which has not been reported previously. Alternative mechanisms for the destabilization of EIC-waves have been suggested [5], [6] in order to account for obsevations not covered by the Drummond - Rosenbluth theory. We believe that the frequency shift observed in our experiments may indicate that there are, indeed, different mechanisms involved in the destabiliztion of ion cyclotron waves. In this paper we report measurements on the frequency, amplitude and radial phase of the EICI in an attempt to demarcate different driving mechanisms of the instability.

EXPERIMENTAL ARRANGEMENT

The experiment was performed in a Q-machine, schematically depicted in fig. 1. Ion cyclotron waves were destabilized by drawing an electron current to the endplate of a potassium plasma column of diameter 6 cm, length 1 m, density $n_e = 10^9 \sim 10^{10}$ cm^{-3}, $T_e = T_i = 0.2eV$, immersed in a magnetic field B = 1 - 3 kG. An aperture of variable size, using a 16 segment iris, was kept floating immediately in front of the biased end plate. This method of destabilizing EIC-waves corresponds to the conventional button arrangement, but with the advantage of allowing the effective button diameter to be varied continuously over the range D$\sim$ 3-50 mm. The end plate was electrically heated to prevent alkaline contamination. Wave frequency and amplitude measurements were recorded by feeding the button signal $g_2(t)$ (see fig. 1) into a digital oscilloscope/microcomputer system. For radial amplitude and phase measurements the signal $g_1(t)$ from a movable probe, located 50 cm from the hot plate, was used.

RESULTS

Initially the wave frequency decreases slightly with an increase in button diameter, as is depicted in fig. 2. However, at D $\sim$ 15 mm a sudden jump in the frequency occurs, accompanied by a drop of at least an order of magnitude in the button signal amplitude. Fig. 3 shows that the button diameter, at which the frequency shift occurs, decreases with increasing magnetic field strength, and is of the order of $10\rho_i$. Fig. 4 shows that for small button diameters (D = 10 mm) no frequency jump occurs when the button bias is varied, while for D = 20 mm both high and low frequency modes can be seen. Fig.5 shows the radial phase variation for a 14 mm and 30 mm diameter button. The smaller button shows the sharp π phase change characteristic of a standing wave whilst for the larger button there are indications of a wave travelling away from the edge of the current channel.

DISCUSSION

The initial decrease in frequency with increasing button diameter shown in fig. 2 (3 mm $\leq$ D $\leq$ 15 mm) is best explained by the Drummond- Rosenbluth theory, if the wavelength is understood to be set by the button diameter, D = $\lambda/2$. The frequency jump at D = 15 mm, however, cannot be accounted for by the Drummond-Rosenbluth theory. On the other hand, the theory of Ganguli et al [6] does allow for higher frequencies to be driven by a perpendicular electric field, $E_\perp$. Fig. 4, which shows that for a given button diameter the frequency jump depends on the button bias (threshold for $E_\perp$) may give credence to this interpretation. For the smaller button diameters the peak amplitude for the m = 1 mode was found to correspond to $k_\perp\rho_i = 1.1$, in agreement with the Drummond- Rosenbluth theory which predicts a maximum growth rate for $k_\perp\rho_i \sim 1$. Finally the phase measurements shown in fig. 5 indicate, for the larger button diameter, a travelling wave originating at the edge of the current channel. As any radial electric field would be expected to be localized in this region (an assumption well supported by radial potential profile measurements) this wave could

well be driven by a perpendicular electric field, $E_\perp$.

CONCLUSION

We have observed a significant frequency jump ($\Delta f \sim 15\%$) as the button diameter is increased. Measurements on the low frequency mode seem to indicate that it is destabilized by an electron drift, hence driven by a parallel electric field ($E_\parallel$). The higher frequency mode cannot be explained along these lines but may be understood as the perpendicular electric field mode ($E_\perp$) described by Ganguli et al [6].

ACKNOWLEDGEMENTS

We wish to thank Dr. M. Alport for his helpful suggestions, in particular concerning the carrying out of the phase measurements.

REFERENCES

[1] D'Angelo N. and Motley R.W. *Phys. Fluids* **5**, 633 (1962)
[2] Drummond W.E. and Rosenbluth M.N. *Phys. Fluids* **5**, 1507 (1962)
[3] Schrittwieser R. *Phys. Fluids* **26**, 2250 (1983)
[4] Cartier S.L., D'Angelo N., Krumm P.H. and Merlino R.L. *Phys. Fluids* **28**, 432 (1985)
[5] Hatakeyama R., Muto F. and Sato N. *Jap. J. Applied Phys.* **24**, L285 (1985)
[6] Ganguli G., Lee Y.C. and Palmadesso P. *Phys. Fluids* **28**, 761 (1985)

FIGURES

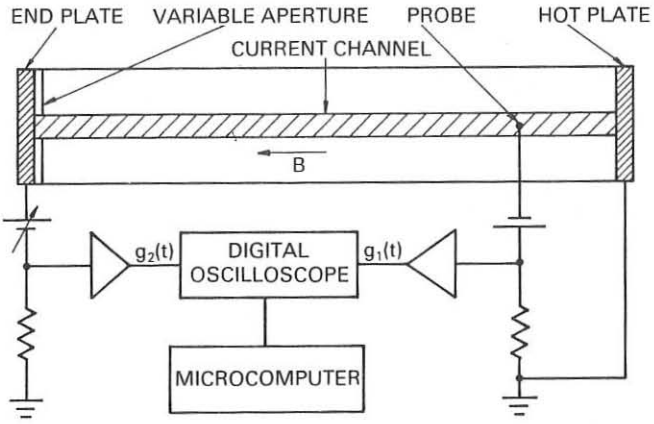

Fig. 1: Schematic diagram of experimental arrangement.

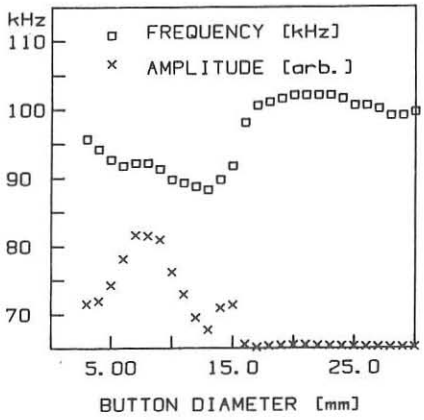

Fig. 2: Frequency and amplitude of EIC-waves as a function of button diameter. B = 2.2kG, V_B = -1.0V

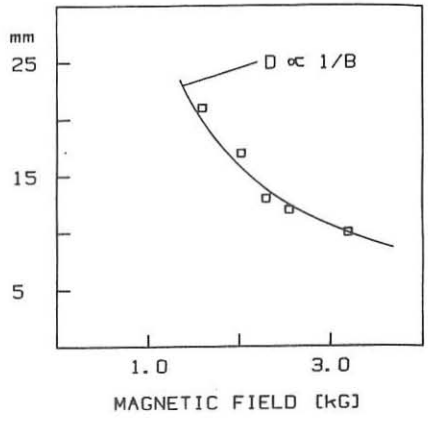

Fig. 3: Button diameter at frequency jump versus magnetic field. V_B = -1.0V

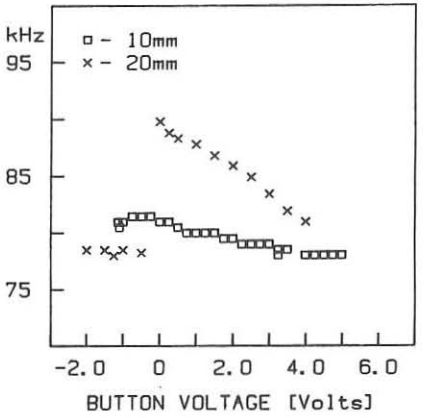

Fig. 4: Wave frequency versus button voltage for two different button diameters.

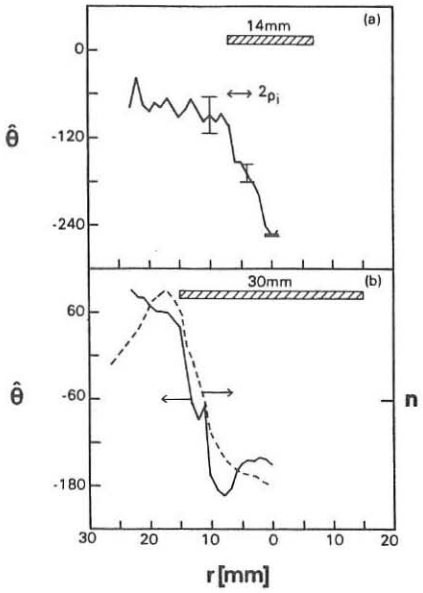

Fig. 5: Radial variation of phase ($\hat{\Theta}$) for (a) 14mm (b) 30mm diameter buttons.

ONSET OF CHAOTIC DIFFUSION IN DYNAMICAL GUIDING CENTERS SYSTEMS WITH MORE THAN 2 ELECTROSTATIC WAVES

R. NAKACH, J.H. MISGUICH

Association EURATOM-CEA sur la Fusion, CEN de CADARACHE,
13108 Saint-Paul-lez-Durance Cedex (France)

In order to understand guiding center diffusion across a straight magnetic field in presence of perpendicular electrostatic turbulence, several numerical studies have been performed previously, either *i)* with few [1] or *ii)* with many electrostatic waves [2], with reasonable agreement with theory [3]. For such non-autonomous Hamiltonian systems in two dimensions, the physical space is also the phase space.

An observed feature of the numerical models with many waves is the existence of a threshold in the value of the turbulence amplitude for the onset of large scale stochastic motion. Here we focus our attention on the mechanism responsible for the onset of chaos in a restricted number of waves, and on the conditions for the existence of a threshold.

We consider an electrostatic potential including three plane waves in two dimensions. The drift motion of the guiding centers is governed by $\dot{\vec{x}} = \frac{c}{B^2} \vec{E} \wedge \vec{B}$. Explicitly the equation of motion reads:

$$\begin{pmatrix} \dot{x} \\ \dot{y} \end{pmatrix} = \frac{c}{B} \sum_{i=1}^{3}{}' a_i \begin{pmatrix} -k_i^y \\ k_i^x \end{pmatrix} \cos \xi_i(x,y,t) \qquad (1)$$

where $\xi_i(x,y,t) \equiv k_i^x x + k_i^y y - \omega_i t + \theta_i$.

Let us consider the variables ξ_1 and ξ_2, corresponding to the dominant waves, as two independent variables. Expressing x and y in terms of ξ_1 and ξ_2 and t, normalizing the time to the frequency ω of the waves ($\tau \equiv \omega t$, with $\omega \equiv \omega_1 = \omega_2 = \omega_3$), leads to the following equations of motion in these phase variables, valid for a specific orientation of the three wave-vectors:

$$\dot{\xi}_1 = -1 - e_2 \cos \xi_2 + e_3 \cos (\xi_1 - \xi_2 + \tau) \qquad (2)$$

$$\dot{\xi}_2 = -1 + e_1 \cos \xi_1 + e_3 \cos (\xi_1 - \xi_2 + \tau), \qquad (3)$$

Here, e_1 are the normalized amplitudes of the different waves, including also a dependence on the orthogonality of pairs of wave-vectors.

The equations (2) and (3) can be derived from the following Hamiltonian in which the variables ξ_1 and ξ_2 are canonically conjugated:

$$\mathcal{H}(\xi_1, \xi_2, \tau) = \xi_2 - \xi_1 + e_1 \sin \xi_1 + e_2 \sin \xi_2 + e_3 \sin (\xi_1 - \xi_2 + \tau) \quad (4)$$

In the case of two electrostatic waves, the Hamiltonian (4) in which we set $e_3 = 0$, is obviously an exact invariant of motion, and therefore the motion is completely integrable. Two fundamentally different cases are found according to the values of the normalized amplitudes e_1 and e_2 with respect to 1.

It is clear, from the equations of motion (2) and (3) with $e_3 = 0$, that no stationary singular point can exist if $e_2 < 1$, and $e_1 < 1$, which implies that no closed periodic orbits can exist, and therefore no separatrix. For this case we have obtained an analytical solution of the equations of motion (2) and (3) in a parametric form[5], based on the fact that the Hamiltonian (4) (with $e_3 = 0$) appears as a generalization of the celebrated Kepler equation[4] of astronomy to two variables.

The salient feature (for large amplitudes with $e_1 > 1$ and $e_2 > 1$) is the appearance of stationary points (elliptic or hyperbolic points), which obviously correspond to stationary phases of the waves and thus to resonances of the guiding centers with these waves (x and y coordinates moving along straight lines with constant velocities). Explicit results are given in Ref.[5].

Numerical simulations have been performed, using the surface of section method, to solve Eqs.(2) and (3) with arbitrary amplitudes, in order to study the influence of the third wave.

First of all, let us consider the case $e_1 = e_2 < 1$, in search of the amplitude of the third wave necessary to lead to large scale stochastization of the trajectories. For $e_1 = e_2 = 0.9$, in Fig. 1 we show the solutions of the equations of motion in which the third perturbation wave has an amplitude $e_3 = 0.1$. In this case the phase space (which is periodic in two angles) appears to be divided in two symetric domains, well separated by a S-shaped phase curve which will be revealed to be very strongly resistent to the pertubation. In each area, some surfaces are already destroyed.

Moreover, an important phase curve, exact solution of Eqs. (2) and (3) takes the form of a straight line $\xi_2 = \xi_1 \pm \pi \pmod{2\pi}$ when $e_1 = e_2 \equiv e$,

for any value of e_3. This curve plays a role similar to the median S-shaped curve; these two resistent curves separate the phase space in two disconnected areas.

In **Fig. 2** we exhibit the structure of the existing separatrices surrounding the two resistent curves, for lower values of the amplitudes ($e_1 = e_2 = 0.2$, $e_3 = 0.18$) insuring a non-stochastic motion. We observe the existence of ascending and descending "boulevards" filled with phase curves, around the straight line and the S-shaped curve, respectively. These "boulevards" are limited by the separatrices and become tangent in two hyperbolic points. The important phenomenon is that these two points collapse on the point ($\xi_1 = 0$, $\xi_2 = \pi$) when $e_3 = e$, connecting the straight line with the S-shaped curve: this seems to be the mechanism responsible for the beginning of the filling of the whole phase space by a stochastic sea. For higher values of the amplitude e, this *threshold for large scale stochasticity* appears already for a lower value of the perturbation.

The conclusions of this study can be summarized as follows. The guiding center system in two electrostatic waves is completely integrable, invariant curves in phase space are topologically different according to the values of the amplitudes with respect to one. For amplitudes less than one, an exact analytical solution has been obtained [5]. In three electrostatic waves, *chaos* appears for a lower value of the perturbation e_3 when the amplitudes of the basic two waves are larger. The stucture of the phase space is determined by domains delimited by two important resistent phase curves (a straight line and a median S-shaped curve surrounded by phase curves forming "boulevards"). When the amplitude of the perturbation reaches the amplitude of the basic two waves, these "boulevards" become infinitely thin, allowing for a connection between different domains. This phenomenon seems to be the mechanism responsible for the beginning of the large-scale stochasticity.

For a k^{-3} spectrum with many waves, as studied in Ref. 2, one can conjecture that the threshold for large-scale stochasticity would actually vanish in the limit of a *continuum spectrum*. This can be understood from the fact that for each couple $e_1 = e_2$ one almost always find a perturbation of equal or larger value of e_3 (which depends on the amplitude of the third wave *and* on the orthogonality of the wave-vectors).

1. R.G. KLEVA, J.F. DRAKE: Phys. of Fluids 27, 1686 (1984).
2. M. PETTINI, A. VULPIANI, J.H. MISGUICH, R. BALESCU, M. DE LEENER, J. ORBAN: EUR-CEA-FC report 1271 (1986), to appear in Phys. Rev. A.
3. J.H. MISGUICH, R. BALESCU, H.L. PECSELI, T. MIKKELSEN, S.E. LARSEN and QIU XIAOMING: EUR-CEA-FC report 1252 (1985); Plasma Phys. Control. Fusion 29, 825 (1987).
4. G.N. WATSON: p.551 in *A treatise on the Theory of the Bessel Functions*, Cambridge, University Press (1962).
5. R. NAKACH, J. MISGUICH: EUR-CEA-FC report 1339 (1988).

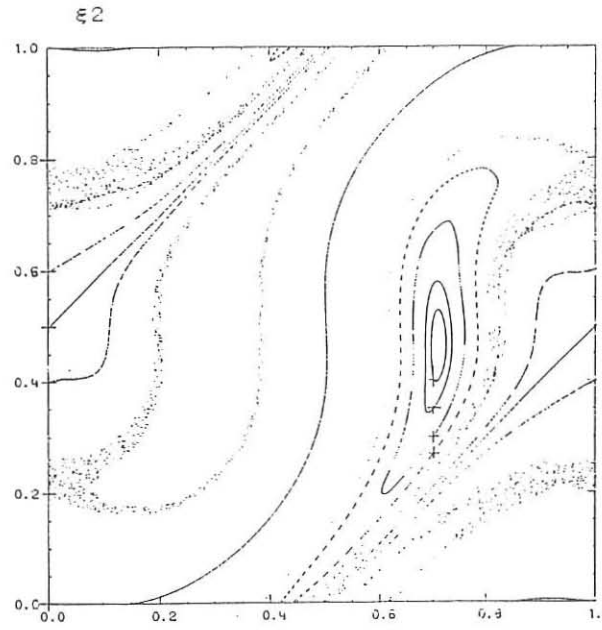

Fig.1:

Poincaré section over 1000 periods of 10 trajectories. The amplitudes are $e_1 = e_2 = 0.9$ and $e_3 = 0.1$.

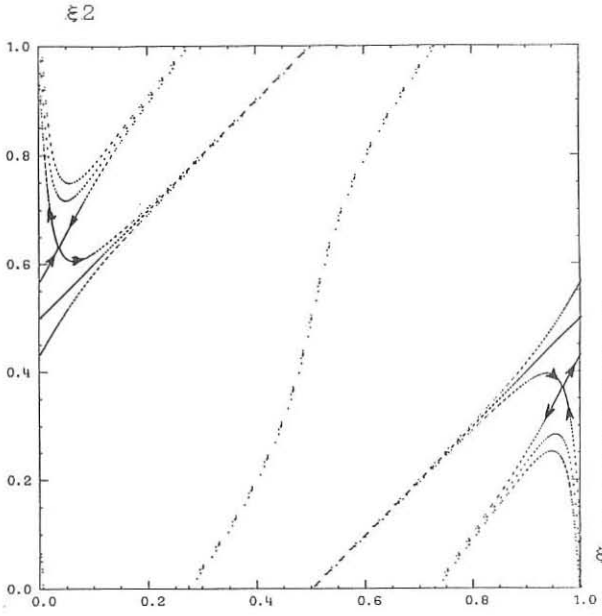

Fig.2:

Poincaré section over 1000 periods, for $e_1 = e_2 = 0.2$ and $e_3 = 0.18$, of 4 trajectories: the S-shaped curve, the straight line and the two separatrices.

NEGATIVE ENERGY WAVES IN THE FRAMEWORK OF VLASOV-MAXWELL THEORY

Dieter Pfirsch

Max-Planck-Institut fuer Plasmaphysik
EURATOM Associaton, D-8046 Garching

Linear negative energy waves are of interest in the context of nonlinear and dissipative instabilities /1/, /2/. They might also have a bearing on, for example, problems of anomalous transport. This paper presents conditions for the existence of negative energy waves derived via a variational formulation of the Vlasov-Maxwell theory /3/, /4/, /5/.

Noether's theorem is used to obtain a second-order energy expression in the perturbations which is the wave energy. Using localized perturbations, it can be shown for any equilibrium that negative energy waves exist if for at least one particle species ν

$$\vec{k} \cdot \vec{v}\, \vec{k} \cdot \frac{\partial f_\nu^{(0)}}{\partial \vec{v}} > 0 \tag{1}$$

holds for some $\vec{v}$ and $\vec{x}$ and for some directions $\vec{k}$ /5/. This generalizes a result recently obtained by Morrison for homogeneous isotropic plasmas /2/. Here $f_\nu^{(0)}(\vec{x}, \vec{v})$ is the unperturbed distribution function for species ν in a frame of reference in which the total energy of the equilibrium is smallest.

Since the Vlasov theory becomes invalid for length scales smaller than the Debye length, the question is to what degree it is necessary to localize the perturbations. For a homogeneous plasma with $\vec{B}_0 = 0$ no localization is necessary. For general inhomogeneous systems with $\vec{B}_0 \neq 0$ the localization needed should be similar to that for general homogeneous magnetized plasmas, which are therefore investigated in this paper. $\vec{B}^{(0)}$ and $\vec{A}^{(0)}$ are taken as

$$\vec{B}^{(0)} = (0,\, 0,\, B^{(0)}) \quad , \quad \vec{A}^{(0)} = (0,\, B^{(0)}\, x\, ,\, 0)\, . \tag{2}$$

For $\vec{B}^{(0)} = 0$ the minimum is obtained for a vanishing perturbation $\vec{A}^{(s)}$ of the vector potential, which is a possible choice in the sense of an initial condition /5/. In this paper

$$\vec{A}^{(s)} \equiv 0 \tag{3}$$

is also chosen for $\vec{B}^{(0)} \neq 0$, which, however, might no longer correspond to the minimum of $E^{(2)}$ and therefore overestinate the necessary localization.

With eqs. (2) and (3) the second-order wave energy becomes

$$E^{(2)} = \sum_\nu \frac{1}{4m_\nu} \int d^3x\, d^3v\, f_\nu^{(0)} \left\{ \left| \frac{\partial F_\nu^{(s)}}{\partial \vec{x}} - \omega_\nu \frac{\partial F_\nu^{(s)}}{\partial v_y} \vec{e}_x \right|^2 + \right.$$

$$+ \vec{v} \cdot \left[\left(\frac{\partial F_\nu^{(s)}}{\partial \vec{x}} - \omega_\nu \frac{\partial F_\nu^{(s)}}{\partial v_y} \vec{e}_x \right) \nabla \cdot \frac{\partial F_\nu^{(s)*}}{\partial \vec{v}} + \text{conj. compl.} \right] +$$

$$\left. + \frac{1}{16\pi} \int d^3x \left| \vec{E}^{(s)} \right|^2 \right. , \qquad (4)$$

$\omega_\nu = e_\nu B^{(0)}/(m_\nu c)$,
$\vec{e}_x$ is the unit vector in the x-direction ,
$\vec{E}^{(s)}$ is the complex amplitude of the electric field perturbation and
$F_\nu^{(s)} = F_\nu^{(s)}(\vec{x}, \vec{v}, t)$ is a generating function for the perturbation of the particle positions and velocities (in eq.(4) $|F_\nu^{(s)}|^2$ is chosen $\sim \delta(v_x)$ which is possible because of $f_\nu^{(0)} = f_\nu^{(0)}(v_x^2 + v_y^2, v_z)$) :

$$\vec{x}_\nu^{(s)} = \frac{1}{m_\nu} \frac{\partial F_\nu^{(s)}}{\partial \vec{v}} , \quad \vec{v}_\nu^{(s)} = - \frac{1}{m_\nu} \left(\frac{\partial F_\nu^{(s)}}{\partial \vec{x}} - \omega_\nu \frac{\partial F_\nu^{(s)}}{\partial v_y} \vec{e}_x \right) . \qquad (5)$$

The electric field energy can be made equal to zero, being a bilinear expression of phase space integrals involving linearly the functions $F_\nu^{(s)}$, without influencing the particle contributions to $E^{(2)}$. With

$$F_\nu^{(s)} \sim e^{i\, \vec{k} \cdot \vec{x}} ,$$

relation (4) becomes

$$E^{(2)} = V \sum_\nu \frac{1}{4m_\nu} \int d^3v \left[- \left| F_\nu^{(s)} \right|^2 \vec{k} \cdot \vec{v}\, \vec{k} \cdot \frac{\partial f_\nu^{(0)}}{\partial \vec{v}} + \right.$$

$$+ i\, \omega_\nu\, k_x\, f_\nu^{(0)}\, F_\nu^{(s)*} \frac{\partial F_\nu^{(s)}}{\partial v_y} +$$

$$+ i\, \omega_\nu\, v_x \left(\vec{k} \cdot \frac{\partial f_\nu^{(0)}}{\partial \vec{v}}\, F_\nu^{(s)} \frac{\partial F_\nu^{(s)*}}{\partial v_y} - \frac{\partial f_\nu^{(0)}}{\partial v_y}\, F_\nu^{(s)}\, \vec{k} \cdot \frac{\partial F_\nu^{(s)*}}{\partial \vec{v}} \right) +$$

$$\left. + \omega_\nu^2\, f_\nu^{(0)} \left| \frac{\partial F_\nu^{(s)}}{\partial v_y} \right|^2 \right] . \qquad (6)$$

V is a large periodicity volume. $|\vec{k}| -> \infty$ again yields the general condition (1). On the other hand

$$\vec{k} \parallel \vec{B}^{(0)} \quad , \quad \frac{\partial F_\nu^{(s)}}{\partial v_y} = 0 \quad , \quad v_z \frac{\partial}{\partial v_z} \int f_\nu^{(0)}(\, v_y^2\, ,\, v_z)\, dv_y > 0 \qquad (7)$$

allows $E^{(2)} < 0$ without any restriction on $|\vec{k}|$.

In general, one will have conditions between (1) and (7). This is qualitatively similar to perpendicular wave propagation, which is treated here more explicitly.
For this case eq. (6) becomes with $\vec{k} = (0, k, 0)$

$$E^{(2)} = V \sum_{\nu} \frac{1}{4m_\nu} \int d^3v \left(\omega_\nu^2 \, f_\nu^{(0)} \left| \frac{\partial F_\nu^{(s)}}{\partial v_y} \right|^2 - \left| F_\nu^{(s)} \right|^2 k^2 \, v_y \, \frac{\partial f_\nu^{(0)}}{\partial v_y} \right) . \tag{8}$$

From eq. (8) it follows that

$$k \, \frac{\partial F_\nu^{(s)}}{\partial v_y} \not\equiv 0 \tag{9}$$

is necessary for $E^{(2)} < 0$. Minimization of $E^{(2)}$ under the constraint

$$V \sum_{\nu} \frac{1}{4m_\nu} \int d^3v \, \omega_\nu^2 \, f_\nu^{(0)} \left| \frac{\partial F_\nu^{(s)}}{\partial v_y} \right|^2 = 1 \tag{10}$$

with a Lagrange parameter $\frac{1}{\lambda} - 1$ yields for the minimum of $E^{(2)}$

$$E^{(2)} = 1 - \frac{1}{\lambda} . \tag{11}$$

This is negative for $0 < \lambda < 1$. With the dimensionless quantities

$$\hat{v}_y = \frac{v_y}{v_{th\ \nu}} , \quad \lambda \, k^2 \, v_{th\ \nu}^2 \, / \, \omega_\nu^2 = \lambda \, k^2 \, r_{g\nu}^2 = \Lambda , \tag{12}$$

the corresponding Hermitian eigenvalue problem is

$$\Lambda \, \hat{v}_y \, \frac{\partial f_\nu^{(0)}}{\partial \hat{v}_y} \, F_\nu^{(s)} + \frac{\partial}{\partial \hat{v}_y} \left(f_\nu^{(0)} \, \frac{\partial F_\nu^{(s)}}{\partial \hat{v}_y} \right) = 0 . \tag{13}$$

Negative $E^{(2)}$ are associated with

$$k^2 r_{g\nu}^2 = \frac{\Lambda}{\lambda} > \Lambda > 0 . \tag{14}$$

The smallest k and therefore the least localization corresponds to the smallest eigenvalue Λ .
$\Lambda > 0$ requires that $f_\nu^{(0)}$ have a minimum with respect to $\hat{v}_\perp = \sqrt{\hat{v}_x^2 + \hat{v}_y^2}$. The minimum wave vector is then qualitatively given by

$$k_{min}^2 \, r_{g\nu}^2 \sim \frac{1}{\Delta \hat{v}_y \, \hat{V}_y} \, \frac{\frac{1}{2}(f_\nu^{max} + f_\nu^{min})}{f_\nu^{max} - f_\nu^{min}} , \tag{15}$$

f_ν^{max} : the maximum of $f_\nu^{(0)}$, f_ν^{min} : its relative minimum in $\Delta\hat{v}_y$,
$\Delta\hat{v}_y$: distance between the maximum and the minimum of $f_\nu^{(0)}$,
$\hat{V}_y$: velocity somewhere between the maximum and the minimum of $f_\nu^{(0)}$.
A numerical solution of the eigenvalue problem (13), (10) was obtained for

$$f_\nu^{(0)}(v_\perp^2,\, v_z) \;=\; \frac{\sqrt{1\;-\;\alpha/\beta}^{\,-3}}{(2\pi)^{3/2}\; v_{th}^3}\; e^{-\frac{1}{2}\,(1\,-\alpha/\beta)^{-1}\;\hat{v}_z^2}\;\left(e^{-\frac{1}{2}\hat{v}_\perp^2}\;-\;\alpha\, e^{-\frac{1}{2}\beta\hat{v}_\perp^2}\right),$$

$$0 \le \alpha < 1 \quad , \quad \beta > 1 \,. \tag{16}$$

$f_\nu^{(0)}$ has a minimum with respect to $v_\perp$ for $\alpha\beta > 1$. At the same time the system is linearly stable for

$$\alpha = \beta^{-\epsilon} \quad , \quad \frac{1}{2} \le \epsilon < 1 \,. \tag{17}$$

α and ϵ were chosen in the range

$$0.5 \le \alpha \le 0.9 \quad , \quad 0.1 \le \epsilon \le 0.9 \,. \tag{18}$$

For this range the numerically obtained values for

$$k_{min} r_g \;=\; \sqrt{\Lambda_{min}}$$

can be approximated by

$$k_{min} r_g \;=\; 1.13\, \sqrt{\frac{F\;+\;1}{2\; H_{max}\; (F-1)}}\,, \tag{19}$$

with

$$H_{max} \;=\; \frac{1}{2}\,\hat{v}_{y\;max}^2 \;=\; \frac{ln\;\alpha\;\beta}{\beta\;-\;1} \quad , \quad F \;=\; f_{max}/f_{min}\,,$$

$$f_{max} \;=\; f_\nu^{(0)}(v_{y\;max}^2,\, v_z) \qquad , f_{min} \;=\; f_\nu^{(0)}(0,\, v_z)\,.$$

Equation (19) agrees with the general relation (15). In the unstable parameter regime $k_{min} r_g$ is not much larger than 1, in the stable regime it is between 10 and 60, but there is no relation to the Debye length. The corresponding negative energy waves therefore do not necessarily contradict the range of validity of the Vlasov equation.

/1/ P.J. Morrison, S. Eliezer, Phys. Rev. A, **33**, 4205 (1986)
/2/ P.J. Morrison, Z.Naturforsch. **42a**, 1115 (1987)
P.J. Morrison, M. Kotschenreuther Institute for Fusion Studies, Report IFSR 280 (1988), Austin, TX, USA
/3/ D. Pfirsch, Z.Naturforsch. **39a**, 1, (1984)
/4/ D. Pfirsch, P.J. Morrison, Phys.Rev. A, **32**, 1714 (1985)
/5/ P.J. Morrison, D. Pfirsch, Institute for Fusion Studies, Report IFSR 313 (1988), Austin, TX, USA, to be submitted to Phys. Rev. A

NONLINEAR GENERATION OF LARGE-SCALE MAGNETIC FIELDS IN PLASMAS

A.G.Sitenko, P.P.Sosenko

Institute for Theoretical Physics, Academy of Science of the Ukrainian SSR, Kiev (USSR)

Recent laser plasma studies [1-4] have revealed a new plasma eigenmode, namely, magnetic electron oscillations, which may result in magnetic field generation and in variation of transport coefficients. Linear generation mechanisms were investigated in [3,4], while the importance of nonlinear effect was stressed in [5,6], where the reduced nonlinear equations for the magnetic electron mode were derived.

In the present paper the nonlinear mechanism of large-scale magnetic field generation via the double cascade of magnetic electron oscillations is established within the context of the generalized model [5,6]. This phenomenon result in the formation of zonal electron flows. The decay instability increment is calculated.

The system of model equations for the nonlinear magnetic electron waves may be derived from the equations of state and transport equations for electrons and ions [5,6], and it may be cast into the form

$$\partial_t(1-d^2\Delta)B-\frac{c}{4\pi en_o}\vec{z}\vec{\nabla}B\times\vec{\nabla}d^2\Delta B-\langle\vec{z}\vec{\nabla}B\times\vec{\nabla}d^2\Delta B\rangle-\frac{1}{2}\vec{z}\vec{\nabla}\ln n_o\times$$

$$\vec{\nabla}(B^2-\langle B^2\rangle)+\frac{4\pi}{n_o}\vec{z}\vec{\nabla}p_h\times\vec{\nabla}(n_o+n_1)=0, \qquad (1)$$

$$\partial_t p_h+\frac{c}{4\pi en_o}n_o^{\gamma}\vec{z}\vec{\nabla}\frac{P}{n_o^{\gamma}}\times\vec{\nabla}B+\vec{z}\vec{\nabla}p_h\times\vec{\nabla}B-\langle\vec{z}\vec{\nabla}p_h\times\vec{\nabla}B\rangle+$$

$$+(\gamma-1)T_o\vec{z}\vec{\nabla}B\times\vec{\nabla}n_1=0, \qquad (2)$$

$$(\partial_t^2-c_s^2\Delta)n_1=-(e_i/4\pi em_i)\langle(1/2)B^2+d^2\vec{\nabla}\vec{\nabla}:$$

$$(\vec{\nabla}B\times\vec{z})(\vec{\nabla}B\times\vec{z})\rangle=0, \qquad (3)$$

where $\vec{B}=B\vec{z}$ is a magnetic field vector, directed along z-axes, and transverse motions in the plane (x,y) are considered,

p_0 is a pressure of perturbation, brackets denote averaging over the period magnetic oscillations, n_1 is a low frequency perturbation of the ion density due to the ponderomotive force effect. e,m,n_o and T_o are the charge, the mass, unperturbed density and temperature of electrons, $d \equiv c/\Omega_e$, c is a light velocity, Ω_e is a plasma frequency. e_i and m_i are the charge and the mass of ions, c_s is an ion-sound velocity, $\gamma=5/3$.

Let us consider weakly nonlinear wave motions of infinite plasmas. Then a closed nonlinear equation for the space-time Fourier transform B_k of the magnetic field ($k=\vec{k},\omega$) can be easily derived from[4](1)-(3):

$$\varepsilon(k)B_k + \sum_{1+2=k} \varkappa(1,2,)B_1B_2 + \sum_{1+2+3=k} \varkappa(1,2,3)B_1B_2B_3 = 0 \qquad (4)$$

where

$$\varepsilon(k) = 1-\Omega^2/(\omega^2(1+d^2k^2)), \qquad (5)$$

$$\Omega = (T_o|aa_n|/m)^{1/2}dk_y,$$

$$a_n = \partial_x \ln n_o, \quad a = \partial_x \ln(T_o/n_o^{\gamma-1}),$$

(it is assumed that plasma is inhomogeneous along the x-axes),

$$\varkappa(1,2)B_1B_2 \equiv [ic/8\pi e n_o \omega(1+d^2k^2)]\{\vec{z}\cdot\vec{k}_1\times\vec{k}_2(d^2(k_2^2-k_1^2)-$$

$$(\Omega/\omega)(\Omega_1/\omega_1-\Omega_2/\omega_2))-ia_nk_y(B_1B_2-\langle B_1B_2\rangle)\} \qquad (6)$$

(the brackets mean that low-frequency component of oscillations is excluded),

$$\varkappa(1,2,3)B_1B_2B_3 \equiv -\frac{d^2}{4\pi m n_o}\frac{\vec{z}\cdot\vec{k}_1\times(\vec{k}_2+\vec{k}_3)}{(1+d^2k^2)}\Big\{\frac{\vec{z}\cdot\vec{k}_2\times\vec{k}_3}{\omega(\omega_2+\omega_3)\omega_3}(B_1B_2B_3-$$

$$-B_1\langle B_2B_3\rangle-\langle B_1B_2B_3\rangle)-(e_i/e)c_s((\omega_2+\omega_3)^2-$$

$$c_s^2(\vec{k}_2+\vec{k}_3)^2)^{-1}\ (d^2(\vec{z}\cdot\vec{k}_2\times\vec{k}_3)^2+(\vec{k}_2+\vec{k}_3)^2/2)$$

$$((\gamma-1)a_nk_y/\omega-ak_{1y}/\omega_1)B_1\langle B_2B_3\rangle\Big]. \qquad (7)$$

The unperturbed state is assumed to be linearly stable, $aa_n < 0$, and Eq.(5) yields the expression for the eigenfrequency of magnetic electron waves[3]:

$$\omega_k = \Omega/\sqrt{1+d^2k^2} \qquad (8)$$

The nonlinear interaction coefficient defined in (6) has usual symmetry properties (which reflect the conservation of the energy and the momentum of the waves), which may be cast

into the convinient form:

$$\psi_k \varkappa(1,2)-\psi_1 \varkappa^*(k_1-2)-\psi_2 \varkappa^*(k_1-1)=0, \qquad (9)$$

where $\psi_k=(1+d^2k^2)\omega$, (10)

and $\psi_k=(1+d^2k^2)\Omega$. (11)

We study the stability of a monochromatic pump wave with frequency ω_o, wave vector k_o and amplitude B_o. The parametric instability dispersion equation which follows from (4):

$$1-\frac{|B_0|^2}{2}\left\{\frac{a(k_0,k,-k_0)}{\varepsilon(k)}+\frac{a(-k_0,k-2k_0,k_0)}{\varepsilon(k-2k_o)}\right\}=0 \qquad (12)$$

$a(1,2,3)\equiv\varkappa(1,2,3)-2\varkappa(1.2+3)\varkappa(2,3)/\varepsilon(2+3)$,
yields the result [6] for the decay instability increment γ_D if the decay of a magnetic electron wave into another magnetic electron wave and and an ion-sound wave is considered:

$$\gamma_D^2=\left(\frac{e}{e}\right)\frac{|B_0|^2}{64\pi n_o\sqrt{mm_i}}\frac{\vec{z}\cdot\vec{k}_0\times\vec{k}}{d^2\sqrt{1+k^2}}\,k_-(1+2(\vec{z}\cdot\vec{k}_o\times\vec{k})^2/k_-^2)$$

$$((\gamma-1)a_nk_y-ak_{oy})/(k_y\sqrt{|aa_n|}),\quad \vec{k}_-=\vec{k}_o-\vec{k} \qquad (13)$$

(dimensionless variables have been introduced: $dk\to k$, $da\to a$, $da_n\to a_n$).

Let us consider the decay of a magnetic electron wave into two magnetic electron waves. In such a case Eq.(12) yields the following expression for the instability increment γ_m^2:

$$\gamma_m^2=\frac{|B_0|^2}{64\pi n_o md^2}\,\frac{(k^2-k_0^2)(k_0^2-k^2)}{(1+k^2)(1+k_-^2)}\,\frac{\sqrt{1+k_0^2}+\sqrt{1+k^2}}{\sqrt{1+k_o^2}+\sqrt{1+k_-^2}}\left\{(\vec{z}\cdot\vec{k}_o\times\vec{k})^2\cdot\right.$$

$$\left.(1+\sqrt{1+k^2}/(\sqrt{1+k^2}+\sqrt{1+k_0^2}))^2+(a_nk_y)^2/(k_0^2-k^2)^2\right\}, \qquad (14)$$

where the symmetry properties (9) were used.

Eq.(14) yields the instability condition:

$$(k^2-k_o^2)(k_o^2-k_-^2)>0 \qquad (15)$$

i.e. the pump wave has an intermediate value of k, and the double cascade of magnetic electron waves to large and small values of k takes place. It is natural to consider this process as a mechanism of nonlinear generation of large scale magnetic fields in plasmas. The instability condition (15) can be redu-

ced to the form: $k_y(k_{oy}-k_y) > 0$ (16)

i.e.the instability results in the decrease of the wave vector projection k_y and the formation of structures, strongly prolongated along the direction perpendicular to that of the inhomogeneity. This implies the creation of zonal electron flows

We assume that $k \sim k_o \sim k_\perp$ for definiteness.Then,it follows from(13) and (14):

$$\gamma^2_m/\gamma^2_D \sim (m_i/m)^{1/2} k^5 (1+a_n^2/k^6)/(1+k^2)^{3/2} \quad (17)$$

Therefore,the nonlinear mechanism of magnetic electron waves double cascade is dominant if $k > 1$ (18)

or if $k << (m_i/m)^{1/2}(a_n)^2$ (19)

If $(m_i/m)^{1/2}(a_n)^2 << k << 1$ (20)

the nonlinear mechanism of ion-sound waves generation is dominant.

1.Jones R.D.Phys.Rev.Lett.1983,51,1269.
2.Amendt P.,Rahman H.V.,Strauss M.Phys.Rev.Lett.,1984,53,1226.
3.Yu M.Y.,Stenflo L. Phys.Fluids,1985,28,3447;Ibid.1987,30, 2298.
4.Stenflo L.,Yu M.Y.Ibid.1986,29,2335.
5.Nycander J.,Pavlenko V.P.,Stenflo L.Ibid.,1987,30,1367.
6.Stenflo L.,Shukla P.K.,Yu M.Y.Phys.Rev.,1987,A36,955.

FINITE LARMOR RADIUS EFFECTS ON PARTICLE DIFFUSION IN A TURBULENT PLASMA

F.R. Hansen , G. Knorr[1] , J.P. Lynov , H.L. Pécseli and J. Juul Rasmussen

Association EURATOM-Risø National Laboratory, DK-4000 Roskilde, Denmark

Abstract

A new representation of a finite Larmor radius plasma is proposed , which permits the transition $r_L \to \infty$ without being mathematically ill-posed. This representation has been incorporated into a 2D numerical simulation code, which is being used to investigate particle diffusion in an electrostatic, turbulent plasma.

1. Introduction

Usually, finite Larmor radius effects in an inhomogeneous electric field are taken into account by including a modifying term into the fluid equation of motion for the ions. This term is derived by analytical averaging to lowest order over the gyromotion of an ion and is proportional to r_L^2. The effect of this modifying term is that an ion at a given position, on the average, has a slightly different $\mathbf{E} \times \mathbf{B}$ drift velocity than the electrons which are subject to the same electric field. Physically, the term is small but important, since it may be the cause of charge separation, which may induce instability. However, this lowest order modifying term is valid only for variations which are gentle over the scale determined by the Larmor radius.

We propose a new representation of a finite Larmor radius plasma which can be applied to much more general types of electric field variations than the usual description.

2. Basic equations

Our finite Larmor radius equations have the following form, in which all densities are *guiding center* densities.

[1] University of Iowa, Iowa, U.S.A.

$$\frac{\partial n_i}{\partial t} + \nabla \cdot (n_i \overline{\mathbf{v}}) = 0 \tag{1}$$

$$\frac{\partial n_e}{\partial t} + \nabla \cdot (n_e \mathbf{v}) = 0 \tag{2}$$

$$\nabla^2 \phi = -(\overline{n_i} - n_e) \tag{3}$$

$$\mathbf{v} = -\nabla\phi \times \mathbf{e}_z \ , \quad \overline{\mathbf{v}} = \mathbf{G} * \mathbf{v} \ , \quad \overline{n_i} = \mathbf{G} * n_i \tag{4}$$

A constant, homogeneous magnetic field in the z-direction is assumed.

The electrons move with the zero Larmor radius drift, whereas the ions move with a drift velocity, which is averaged over their finite Larmor radius. In the Poisson equation (3) the electron particle density coincides with the guiding center density, whereas the ion particle density is obtained from the guiding center density by a filter operation. This operation is performed by the convolution integral operator $\mathbf{G}$. The same filter operation is employed in determining the modified ion guiding center drift, $\overline{\mathbf{v}}$, from the ordinary $\mathbf{E} \times \mathbf{B}$ drift velocity, $\mathbf{v}$.

The numerical scheme is based on a spectral method [1] in which the dynamical equations are solved in $\mathbf{k}$-space in order to obtain high accuracy ("infinite order") in calculating the spatial derivatives. Periodic boundaries are assumed. In $\mathbf{k}$-space the convolution operations in (4) become simple multiplications, and the Fourier transform of $\mathbf{G}$ for a Maxwellian ion velocity distribution is found to be

$$g(\mathbf{k}) = \exp(-\frac{1}{4} r_L^2 k^2) \tag{5}$$

where r_L is the average Larmor radius. The effect of this filter is that every $\mathbf{k}$-mode of the electric field and of the ion guiding center density is included when calculating the corrected quantities $\overline{\mathbf{v}}$ and $\overline{n_i}$ in (4).

We note that the form of $g(\mathbf{k})$ in (5) allows the transition $r_L \to \infty$ without being mathematically ill-posed. The consequences of this transition in Eqs. (1)–(4) are physically reasonable.

3. Numerical results

A numerical study of the influence of finite Larmor radius effects on particle diffusion in a turbulent plasma has been initiated. Preliminary results with a spectral resolution of 32×32 modes have been obtained on a VAX 8700 computer. The side length of the computational box was set equal to 1, and as initial conditions the electron and

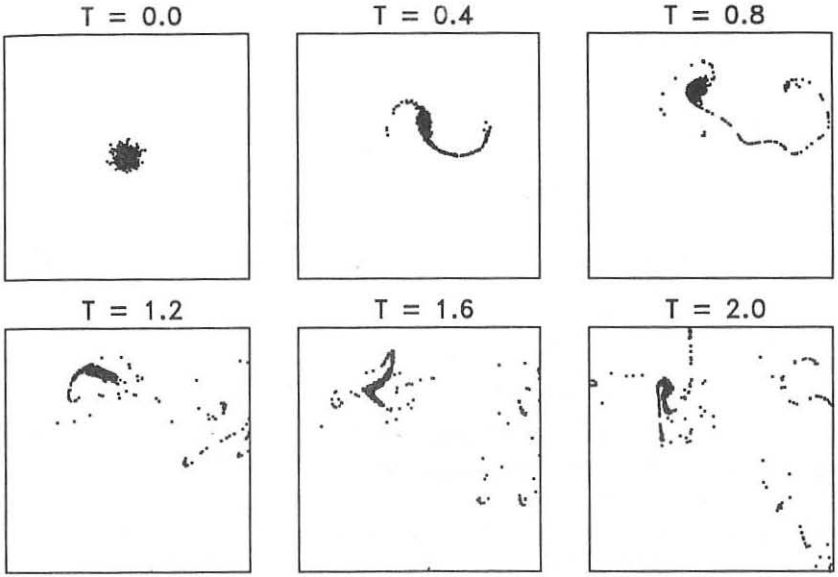

Figure 1: Positions of 500 test particles in a two-dimensional, electrostatic, turbulent plasma. The test particles trace the positions of ion guiding centers with $r_L/L = 0.05$; where L is the side length of the computational box.

ion guiding center densities were excited according to the spectrum

$$| n_{i,e}(\mathrm{k}) | = \begin{cases} \frac{k^2}{(2\pi)^2+k^2} & \text{if } k < 16\pi \\ 0 & \text{otherwise} \end{cases}$$

with random phases in the interval 0–2π for every mode. The plasma was then allowed to evolve self-consistently.

In order to study the particle diffusion in this plasma, two samples of 500 test particles tracing the motion of electron and ion guiding centers, respectively, were followed. These test particles were initially placed around the center of the computational box according to a two-dimensional random number generator with Gaussian statistics : $f(r) = (2\pi\sigma^2)^{-1} \exp(-r^2/(2\sigma^2))$. The initial value of σ was chosen to be 0.025. In Fig. 1, we show an example of the temporal evolution of the ion test particles for the case of $r_L = 0.05$.

At every time step, the two-dimensional standard variation, σ, of the electron and ion test particles was determined. Figure 2(a) shows the temporal evolution of σ_i (solid line) and σ_e (dashed line) corresponding to the example shown in Fig. 1. For

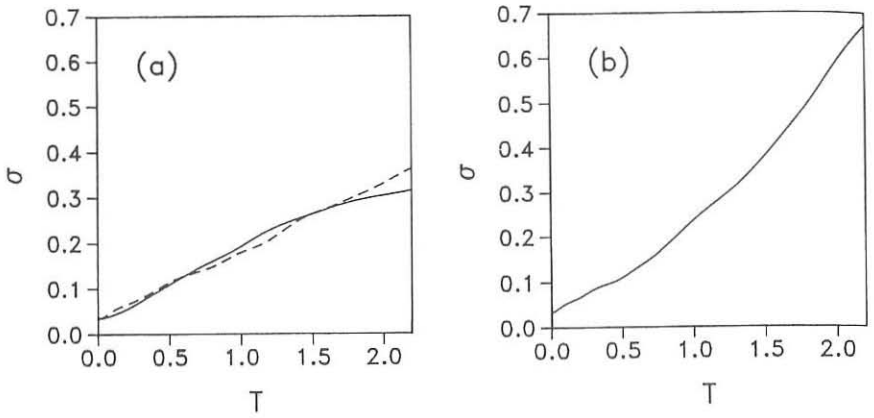

Figure 2: Temporal evolution of σ_i (solid lines) and σ_e (dashed lines) for : (a) $r_L/L = 0.05$, and (b) $r_L = 0$. Note that $\sigma_e = \sigma_i$ in case (b).

comparison we show in fig. 2(b) the evolution of $\sigma_{e,i}(t)$ for similar initial conditions but with $r_L = 0$. Note that in this case the electron and ion guiding centers have the same statistics.

By comparing figs. 2(a) and 2(b) we immediately see the influence of the finite Larmor radius modifications. Due to the filter operation described above, ions with a finite Larmor radius on the average tend to smooth out the small scale length variations of the electrical field, which cause substantial scattering of the guiding centers in a zero Larmor radius plasma.

In order to obtain more quantitative information on the particle diffusion in a turbulent plasma, we are implementing our numerical code on an Amdahl VP1100 supercomputer. This will allow us to obtain a higher spatial resolution for longer time sequences, which is essential for a detailed comparison with various analytical theories [2,3].

References

[1] Gottlieb, D. and Orszag, S.A. (1977) *Numerical Analysis of Spectral Methods: Theory and Applications*, 172 pp. S.I.A.M., Philadelphia.

[2] Taylor, J.B. and McNamara, B. (1971). Phys. Fluids **14**, 1492.

[3] Misguish, J.H., Balescu, R., Pècseli, H.L., Mikkelsen, T., Larsen, S.E. and Xiaoming, Qiu (1987), Plasma Phys. Contr. Fusion **29**, 825.

ON LARGE DEBYE DISTANCE EFFECTS IN A FULLY IONIZED PLASMA

Bo Lehnert and Jan Scheffel
Dept. of Plasma Physics and Fusion Research
The Royal Institute of Technology, S-100 44 Stockholm, Sweden

This is a study of electrostatic electron plasma oscillations. Although a classical problem, being investigated by many authors, we felt that the border between fluid-like (oscillative) and free-streaming (damped) behaviour required more detailed analysis. The information contained in this problem is by analogy useful when discussing the damping (or stabilizing) Large Larmor Radius (LLR) effect for magnetically confined plasmas. Just as the particle self-electric field becomes insufficient in limiting the particle excursions for Large Debye Distances (LDD), a large Larmor radius can allow a smearing out, or damping, of otherwise unstable distribution functions. The LLR effect on the Rayleigh-Taylor instability is presently being investigated.

We here study longitudinal electron oscillations of a homogeneous plasma, being initially disturbed at $t=0$. Quasi-neutrality is assumed. The ions are immobile with density n_0. Small perturbations are assumed, so that a linearization becomes possible[1]. We then have $f(x,t,w) = f_0(w) + f_1(x,t,w)$, where index '$_1$' denotes perturbed quantity. The equations to be solved are the Vlasov and Poisson equations

$$\frac{\partial f_1}{\partial t} + w\frac{\partial f_1}{\partial x} - \frac{e}{m_e}E_1\frac{\partial f_0}{\partial w} = 0 \qquad (1)$$

$$\frac{\partial E_1}{\partial x} = -\frac{e}{\varepsilon_0}\int_{-\infty}^{\infty} f_1\, dw \qquad (2)$$

We will here study two types of initially perturbed distribution functions: (i) $f_1(x,o,w) = exp(-w^2/u_0^2)cos(\alpha x)$ and (ii) $f_1(x,o,w)=exp(-w^2/u_0^2)\ exp(-\alpha^2x^2)$, with a thermal velocity $u_0= (kT/m_e)^{1/2}$. Of these, the first perturbation conforms to classical Landau analysis. It is a non-localized perturbation, which will generate two superimposed waves; one travelling in the $+x$ - direction and one in the $-x$ - direction. The second perturbation is localized initially. A straightforward comparison between the two cases is somewhat troublesome though, since the distributions are characterized by different $\beta\equiv\alpha\lambda_D$, where λ_D is the Debye distance. When Fourier transformed in space, we note that $F[cos(\alpha x)] \sim \delta(k-\alpha)$ and $F[exp(-\alpha^2x^2)] \sim exp(-k^2/4\alpha^2)$, i.e. whereas the k-spectrum of the non-localized perturbation contains only one component, the localized k-spectrum is more complex. The background plasma is Maxwellian; $f_0(w) = (n_0/u_0\sqrt{\pi})\ exp(-w^2/u_0^2)$. In the following $\omega_0=u_0/\sqrt{2}\lambda_D$ denotes plasma frequency.

We Fourier transform in space, but refrain from the traditional Laplace transformation in time [2], hereby avoiding the problem with poles in the associated integral. We eliminate the electric field, consequently solving the integro-differential equation (denoting $d/dt = '$)

$$g'(k,t,w) + ikwg(k,t,w) = -\frac{2i\omega_0^2}{ku_0^3\sqrt{\pi}} we^{-\frac{w^2}{u_0^2}} \int_{-\infty}^{\infty} g(k,t,w')dw' \qquad (3)$$

where

$$g(k,t,w) = \frac{1}{\sqrt{2\pi}} \int_{-\infty}^{\infty} f_1(x,t,w)e^{-ikx}dx \qquad (4)$$

From (3) it can be seen that the R.H. term can be neglected as $\beta \to \infty$ (free-streaming) and that the second term on the L.H. side becomes small as $\beta \to 0$ (fluid case). There is a subtlety with the case $\beta \to \infty$; even though the collective term becomes small for a given time as $\beta \to \infty$, one can always find a sufficiently long time for a given β when it becomes important [3]. Due to the large damping caused by free-streaming, the initial distribution has then, however, generally died out to an uninterestingly small amplitude. As the full solution $g(k,w,t)$ has been computed, we perform an inverse transformation to obtain $f_1(x,t,w)$. However we are more interested in the density perturbation $n_1(x,t) = \int f_1(x,t,w)dw$, which we plot in the Figs. The spatial scale is given as a factor q times $\lambda = 2\pi/\alpha$, the time scale by a factor γ times $1/\omega_0$.

Analytical, exact special cases are used for testing the code; in the free-streming limit ($\beta \to \infty$, moderate times) exact analytic solutions are obtainable for both the non-localized and localized density perturbation. For the initial perturbation $f_1(x,o,w) = b f_0(w) \cos \alpha x$ we find the free-streaming solutions $f_1(x,t,w) = bf_0(w)\cos\alpha(x-wt)$ and $n_1(x,t) = b\cos\alpha x \exp(-\beta^2\omega_0^2t^2/2)$. Already at $\beta = 1.5$ free-streaming damping clearly dominates the behaviour. The transition from the oscillatory, however Landau damped behaviour, is striking as β exceeds unity. For the initial perturbation $f_1(x,o,w) = bf_0(w) \exp(-\alpha^2x^2)$ the exact free-streaming solutions become $f_1(x,t,w) = bf_0(w)\exp(-\alpha^2(x-wt)^2)$ and $n_1(x,t) = b\, n_0(1+2\beta^2\omega_0^2t^2)^{-1/2} \exp(-\alpha^2x^2/(1+2\beta^2\omega_0^2t^2))$. Numerical runs give very good agreement. We will also compare our results with conventional, asymptotic Landau analysis.

Landau[4] performed a normal mode analysis to obtain the time-asymptotic behaviour of the distribution function. The perturbed electric field and particle distribution were assumed to vary as $\exp i(\omega t + \alpha x)$, where the wavenumber α was assumed real, whereas ω has both a real (oscillatory) and imaginary (damped or growing) part. This normal mode is associated with that pole of the dispersion relation which has its imaginary part in the lower, complex ω -plane and is closest to the real axis. The pole corresponds to the normal mode with the weakest damping and should therefore dominate the overall behaviour, provided the residues (amplitudes) of the other poles are comparative or smaller. A straightforward scaling of terms for small β yields that the collective term, containing the electric field, becomes comparable to the free-streaming term after a time $t_c \approx \beta/\omega_0$. This is an estimate of the time required for normal mode analysis to apply.

We note that this time increases with β. For the real (oscillatory) part of the eigenfrequency we have, classically $\omega_r^2 \approx \omega_0^2(1+3\beta^2)^{1/2}$. Damping of the perturbations corresponds to the imaginary part;

$$\mathrm{Im}\left(\frac{\omega}{\omega_p}\right) = \sqrt{\frac{\pi}{8}}\frac{1}{\beta^3}e^{-\frac{1}{2\beta^2}-\frac{3}{2}} = 0.14\frac{1}{\beta^3}e^{-\frac{1}{2\beta^2}} \qquad (5)$$

which is the expression obtained by Landau for small k. For $\beta \geq 0.5$ the Jackson[5] solution (numerical one-pole) must be used for the normal modes. In the region $\beta > 1$ single normal modes do not determine the behaviour except for times so long that the initial perturbation has practically died out. Instead the contributions from more poles of the dispersion relation must be added, so that the $exp(i\omega t)$ behaviour transforms to a more complex one, such as the free-streaming solutions given above.

Our results are the following. First, strong LDD damping for $\beta \geq 0.5$ was found for both initial distributions, see Figs 1-4. This seems to imply that the analogous effect of LLR damping would become pronounced for $kr_L \geq 0.5$, in agreement with the intuitive picture that when $r_L/\lambda \geq 1/4$ the perturbation structure cannot be fully upheld (r_L is the Larmor radius). Secondly, the Landau one-pole solution for small k is valid only for $\beta \leq 0.5$, whereas Jackson's arbitrary k, one-pole solution, is valid for larger β after longer times, see Fig.5. Thirdly, the time it takes the plasma to find these normal modes is approximately given by $t_C = \beta/\omega_0$ for not too large β. For $\beta > 1$ the initial damping has nearly died out when this occurs, see Fig.6 for $\beta = 1$. The exact free-streaming solutions show that more of the ω-spectrum has to be included in a valid normal mode analysis.

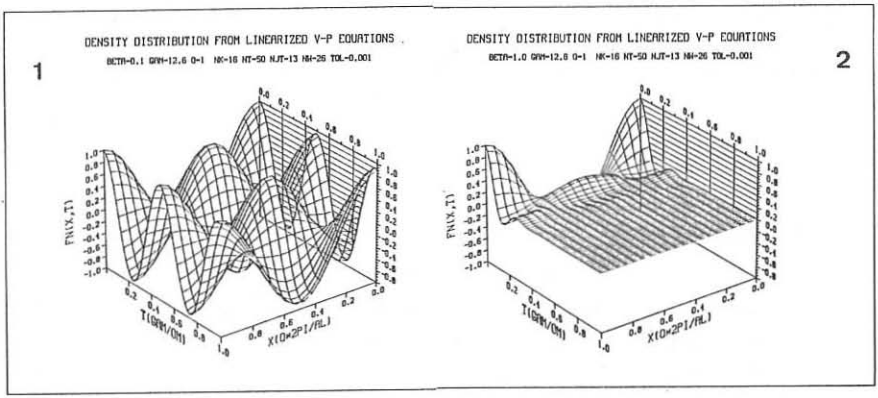

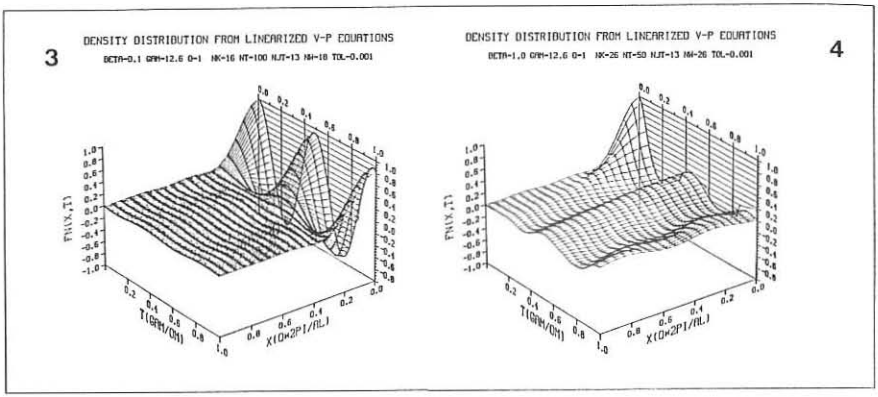

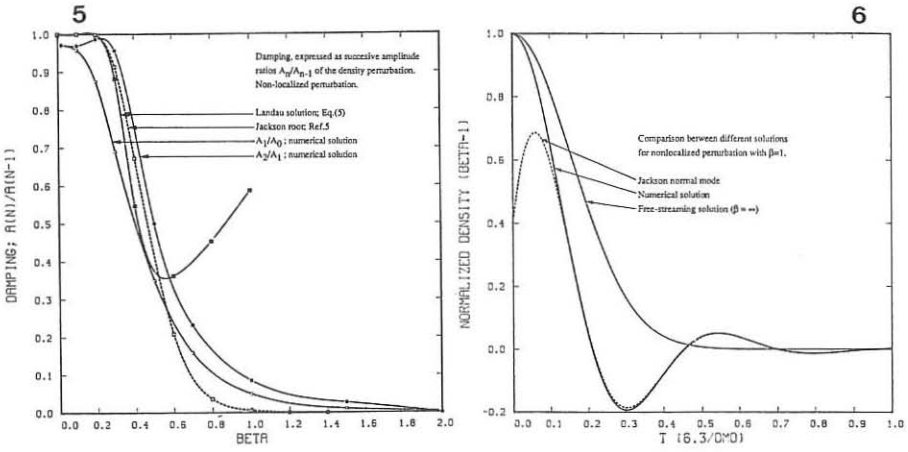

REFERENCES:

[1] Lewak, G.J., J. Plasma Phys. 3(1969)243

[2] Lehnert, B., The Royal Institute of Technology, Stockholm, TRITA-PFU-85-05

[3] Li, J. and Spies, G., Private communication

[4] Landau, L., J. Phys. 10(1946)45

[5] Jackson, J.D., J. Nucl. Energy, Part C, 1(1960)171

DISTRIBUTION FUNCTIONS OF CHARGED PARTICLES IN A TIME-DEPENDENT MAGNETIC FIELD NEAR THE CHARGED SURFACE

V.A. Kotelnikov, F.A. Nikolaev, T.A. Gurina

Moscow Aviation Institute, USSR

The development of modern plasma physics is impossible without the further detailed research of plasma's interaction with electric and magnetic fields. Maximum information can be obtained by the research conducted on the distribution functions level. In this work we consider the processes in a plasma in the vicinity of a charged surface in the presence of an external magnetic field.

Let an infinite charged cylinder with radius R_0 be put transverse to the flow of collisionless ion-electron plasma (Fig. 1). Near cylinder there exists uniform time-dependent magnetic field. The magnetic induction $B(t)$ is paralleled to the cylinder axis. The surface of the body is ideally catalitic.

The evolution processes in a plasma in the vicinity of the cylinder can be discribed by the time-dependent Vlasov-Maxwell system of equations in a four-dimensional phase space with corresponding initial and boundary conditions:

$$\frac{\partial f_\alpha}{\partial t} + V_r \frac{\partial f_\alpha}{\partial r} + \frac{V_\theta}{r}\frac{\partial f_\alpha}{\partial \theta} + \left(\frac{V_\theta^2}{r} + \frac{q_\alpha}{m_\alpha} E_r + \frac{q_\alpha}{c m_\alpha} B V_\theta\right)\frac{\partial f_\alpha}{\partial V_r} +$$

$$+ \left(\frac{q_\alpha}{m_\alpha} E_\theta - \frac{V_r V_\theta}{r} - \frac{q_\alpha}{c m_\alpha} B V_r\right)\frac{\partial f_\alpha}{\partial V_\theta} = 0, \quad \alpha = e, i, \qquad (1)$$

$$\vec{E} = -\vec{\nabla}\varphi - \frac{1}{c}\frac{\partial \vec{A}}{\partial t}, \qquad (2)$$

$$\vec{B} = \mathrm{rot}\,\vec{A}, \qquad (3)$$

$$\Delta\varphi + \frac{1}{c}\,\mathrm{div}\left(\frac{\partial \vec{A}}{\partial t}\right) = -4\pi \sum_\alpha q_\alpha \int_{-\infty}^{\infty}\int_{-\infty}^{\infty} f_\alpha(t, r, \theta, V_r, V_\theta)\, dV_r\, dV_\theta. \qquad (4)$$

In this case when Coulomb's calibration $\operatorname{div} \vec{A} = 0$ we obtain the following equations[1]:

$$E_r = -\frac{\partial \varphi}{\partial r}, \qquad E_\theta = -\frac{1}{r}\frac{\partial \varphi}{\partial \theta} - \frac{1}{c}\frac{r}{2}\frac{\partial B}{\partial t}, \tag{5}$$

$$\Delta \varphi = -4\pi \sum_\alpha q_\alpha n_\alpha(t,r,\theta). \tag{6}$$

The initial conditions:

$$\sum_\alpha q_\alpha n_\alpha \Big|_{t=0} = 0, \tag{7}$$

$$f_\alpha\Big|_{t=0} = n_{\alpha\infty}\left(\frac{m_\alpha}{2\kappa T_\alpha}\right)^{3/2}\pi^{-1}\exp\left\{-\frac{m_\alpha[(V_r+V_{\infty}\cos\theta)^2+(V_\theta-V_{\infty}\sin\theta)^2]}{2\kappa T_\alpha}\right\}. \tag{8}$$

The boundary conditions:

$$\lim_{r\to R_0^-} f_\alpha = 0, \qquad \varphi\Big|_{r=R_0} = \varphi_0, \qquad \lim_{r\to\infty}\varphi = 0. \tag{9}$$

On the present stage the computer simulation is the most efficient way to solve multidimensional kinetic problem. The numerical model gives us the chance to conduct the qualitative analysis of the phenomena and to get vast results for practice.

To solve the problem (1), (5 - 9) a discrete version of transference method of initial distribution functions along Vlasov's equations characteristics with simultaneus recalculation of electric self-field[2-3].

For that the limited support of the distribution functions is used:

$$\operatorname{supp} f_\alpha = \{(r,\theta,V_r,V_\theta):\ r\in[R_0,R_\infty],\ \theta\in[0,\pi],\ V_r\in[-V_{max}-V_{\infty}\cos\theta,\ V_{max}-V_{\infty}\cos\theta],\ V_\theta\in[-V_{max}+V_{\infty}\sin\theta,\ V_{max}+V_{\infty}\sin\theta]\}.$$

The quantity R_∞ is the conditional boundary of the excited region and V_{max} is the boundary of the cutting "tail" of Maxwell distribution. The solving of the problem was conducted with the help of partial on velocities Debye scales:

$$M_r = (\kappa T_i/4\pi e^2 n_{i\infty})^{1/2}, \quad M_v^\alpha = (2\kappa T_\alpha/m_\alpha)^{1/2}, \quad M_t = M_r/M_v^i,$$
$$M_\varphi = \kappa T_i/e, \quad M_n = n_{i\infty}, \quad M_B = c m_i/e M_t.$$

Let the magnetic induction be build up in a manner $B = B_0(1-\exp \gamma t)$, where B_0 is the moderate magnetic field ($R_L^e < R_0 < R_L^i$, R_L^e, R_L^i - Larmor's radius of the particles). Then at velocities $V_\infty = (0 - 5)\, M_v^i$ the relaxation of the distribution functions of ions (DFI) is determined by the presence of external flow[3], and the relaxation of the distribution function of electrons (DFE) is determined by the presence of magnetic field moving the electrons around the magnetic lines of force.

At a result of our calculations it has been obtained that, if $B > 0$, we got deformation of DFE in the velocity space at $r \simeq R_0$ in the direction of $V_\theta < 0$. It can be explained by the fact that electrons with $V_\theta > 0$ frequently hit the surface and are absorbed by it when spinning the line. In Fig. 2 we have plotted isolines of DFE at moment $t = 1{,}0 \cdot M_t$ for the case $B_0 = 0{,}005 \cdot M_B$, $\varphi_0 = -6 \cdot M_\varphi$, $R_0 = 3 \cdot M_r$, $\gamma = -5 \cdot M_t^{-1}$, $T_e / T_i = 1$, $m_e/m_i = 5 \cdot 10^{-4}$, $V_\infty = 0$. For electron densities which are moments by the corresponding distribution function the oscillatory profile of distribution along the radius is characterised (Fig. 3).

Hence, the numerical solution gives us the perfect picture of the relaxation of the distribution of charged particles, and the evolution of excited region near the charged surface in plasma flow for each set of determining parameters for this problem - B_0, φ_0, R_0, V_∞ .

References.

1. Landau L.D., Lifshitz E.M. The theory of field. M., Fismatgiz, 1960.
2. Alexeev B.V., Novikov V.N., TVT, (1984), 22, 814.
3. Alexeev B.V., Kotelnikov V.A., Gurina T.A. Proc. of Int, Conf. on Plasma Phys., Kiev, USSR, 1987, v. 4, p. 217.

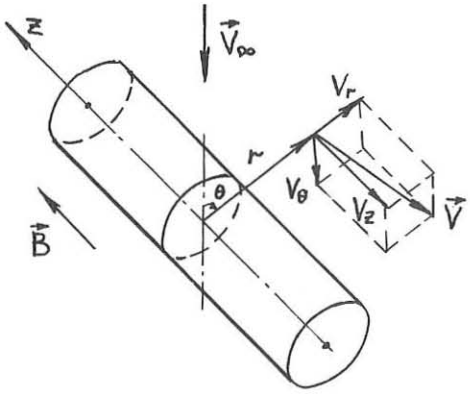

FIG. 1.

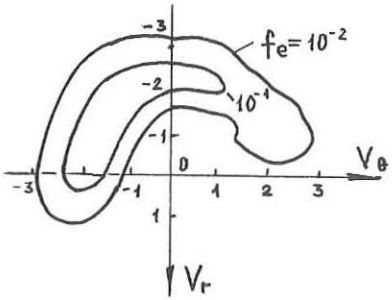

FIG. 2.

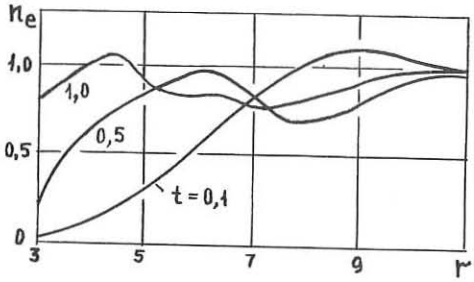

FIG. 3.

A NEW REPRESENTATION OF THE RELATIVISTIC DIELECTRIC TENSOR FOR A MAGNETIZED PLASMA

M. Bornatici and G. Chiozzi
Physics Department, University of Ferrara, Ferrara, Italy

A representation of the dielectric tensor which does not involve the sum over harmonics is obtained. The novel form can be expressed in terms of either a product of two Bessel functions whose orders are functions of momentum, or an integral over the range $(0,\pi/2)$ of combinations of $J_{0,1,2}$ with cosine functions.

Introduction. The standard form of the (relativistic) dielectric tensor ε_{ij}, relevant to electron cyclotron interaction in a magnetized plasma, involves both a double integral over the momentum variables, e.g., $p_\perp$ and $p_\parallel$, and an infinite sum over harmonics of terms each of which contains the product of two Bessel functions whose argument is a function of $p_\perp$. More specifically, in the reference frame in which $\underline{B}_o = \hat{\underline{z}} B_o$ and $\underline{k} = k_\perp \hat{\underline{x}} + k_\parallel \hat{\underline{z}}$, one has[1]

$$\varepsilon_{ij} = \delta_{ij} + 2\pi \left[\frac{\omega_p}{\omega}\right]^2 \int_0^\infty dp_\perp \int_{-\infty}^{\infty} dp_\parallel \left[\frac{p_\parallel}{\gamma} F(p_\perp, p_\parallel)\delta_{iz}\delta_{jz} + \frac{\omega}{\omega_c} U(f_o) T_{ij}(p_\perp, p_\parallel)\right] \qquad (1)$$

where $F(p_\perp,p_\parallel) \equiv p_\perp (\partial f_o/\partial p_\parallel) - p_\parallel (\partial f_o/\partial p_\perp)$, with $f_o = f_o(p_\perp, p_\parallel)$ the (gyrotropic) equilibrium distribution ($\int d^3p\, f_o = 1$), and $U(f_o) \equiv \partial f_o/\partial p_\perp + (N_\parallel/\gamma mc) F(p_\perp, p_\parallel)$. The tensor T_{ij} is given by an infinite sum over cyclotron harmonics of a quantity which contains a singular factor multiplying a dyadic tensor, namely,

$$T_{ij} \equiv \sum_n \frac{V_i^{(n)} (V_j^{(n)})^*}{\mu - n}, \quad \mu \equiv \frac{\omega}{\omega_c}(\gamma - N_\parallel p_\parallel / mc) \qquad (2)$$

with $\underline{V}^{(n)} = \underline{V}_\perp^{(n)} + \hat{\underline{z}} p_\parallel J_n$, the perpendicular (to $\underline{B}_o$) component being

$V_\perp^{(n)}=p_\perp[\hat{x}(nJ_n/b)+i\hat{y}J_n']=(p_\perp/2)[(\hat{x}+i\hat{y})J_{n-1}+(\hat{x}-i\hat{y})J_{n+1}]$, the later representation referring to a frame of reference in which the wave electric field perpendicular to $\underline{B}_o$ is $\underline{E}_\perp=(1/\sqrt{2})(E_x+iE_y,E_x-iE_y)$. In this reference frame, to be referred to as the "circular frame", the dyadic in (2) is real. Furthermore, $J_n\equiv J_n(b)$, $J_n'\equiv dJ_n/db$, with $b\equiv(\omega/\omega_c)N_\perp(p_\perp/mc)$.

The infinite number of singularities in $\underline{p}$-space arising from the factor $(\mu-n)^{-1}$ in (2) and connected with the relativistic resonance condition $\gamma-N_{||}p_{||}/mc-n\omega_c/\omega=0$ is dealt with by performing the integration along the causal contour which amounts to assuming that $N_{||}$ has a small (negative) imaginary part (ω is taken real) so that, using the Plemelj formula, $[\mu(\gamma,p_{||})-n]^{-1}=P(1/(\mu-n))-i\pi\delta(\mu-n)$, P indicating the Cauchy principal value. It follows that one can write $T_{ij}=T_{h,ij}+iT_{a,ij}$, respectively the Hermitian and anti-Hermitian part, so that, in particular, the anti-Hermitian part of the dielectric tensor (1) is

$$\varepsilon_{a,ij}=-2\pi^2\left[\frac{\omega_p}{\omega}\right]^2\int dp_\perp dp_{||}U(f_o)\sum_n V_i^{(n)}(V_j^{(n)})^*\delta(\gamma-N_{||}p_{||}/mc-n\omega_c/\omega) \qquad (3)$$

whose salient characteristic is the infinite sum over cyclotron harmonics.

Representation without expansion in harmonics. The tensor T_{ij} and, hence, the dielectric tensor ε_{ij} can be expressed in forms whose Hermitian parts do not involve the (infinite) sum over harmonics, thus being possibly more advantageous than (2).

A. Two Bessel functions representation of T_{ij}. The summation of the harmonic series appearing in (2) can be performed by means of the summation rule[2]

$$\sum_{n=-\infty}^{\infty}\frac{J_{n+p}(b)J_{n+l}(b)}{\mu-n}=\frac{\pi}{\sin[\pi(\mu+l)]}J_{\mu+p}(b)J_{-(\mu+l)}(b)\ ,\ \mathrm{Re}(p-l)\geq -1 \qquad (4)$$

With (4), the tensor (2) reduces to

$$T_{ij}=-\frac{\pi p_\perp}{\sin(\pi\mu)}\begin{bmatrix} \frac{p_\perp}{2}J_{\mu+1}J_{-(\mu+1)} & \frac{p_\perp}{2}J_{\mu+1}J_{1-\mu} & -\frac{p_{||}}{\sqrt{2}}J_{-\mu}J_{\mu+1} \\ \frac{p_\perp}{2}J_{\mu+1}J_{1-\mu} & \frac{p_\perp}{2}J_{\mu-1}J_{1-\mu} & -\frac{p_{||}}{\sqrt{2}}J_{-\mu}J_{\mu-1} \\ -\frac{p_{||}}{\sqrt{2}}J_{-\mu}J_{\mu+1} & -\frac{p_{||}}{\sqrt{2}}J_{-\mu}J_{\mu-1} & -\frac{p_{||}^2}{p_\perp}J_\mu J_{-\mu} \end{bmatrix} \qquad (5)$$

the matrix appearing in (5) being (real and) symmetric. The main features of the form (5) of the tensor T_{ij} with respect to (2) are: i) the infinite sum over harmonics is no longer present (explicitly); ii) the orders of the Bessel functions appearing in (5) are now functions of the momentun via the same variable μ ($=(\omega/\omega_c)(\gamma-N_{||}p_{||}/mc)$) that appears in the denominator $\sin(\pi\mu)$. Using (5) into the double integral over the momentum variables in (1) makes it convenient to chose μ as one of the integration variables, instead of $p_\perp$ or $p_{||}$, and split the range of the corresponding integral into symmetric intervals around each singular point μ=n (n integer), with the result that

$$\int_{-\infty}^{\infty} d\mu \frac{f(\mu)}{\sin(\pi\mu)} = \sum_{n=-\infty}^{\infty} \int_{n-1/2}^{n+1/2} d\mu \frac{f(\mu)}{\sin(\pi\mu)} = \sum_{n} \left[P\int_{n-1/2}^{n+1/2} d\mu \frac{f(\mu)}{\sin(\pi\mu)} - i(-1)^n f(n) \right] \qquad (6)$$

Since the matrix on the right-hand-side of (5) is real, the anti-Hermitian part of the dielectric tensor comes entirely from the singularities connected with $1/\sin(\pi\mu)$. Thus, from (6) one recovers the standard harmonic expansion (3) for $\varepsilon_{a,ij}$ and, hence, no real advantage is obtained by using (5) rather than (2). As for the Hermitian part of ε_{ij} instead, for every singular point n the μ-integration in (6) is over a finite range instead of being an infinite integral as in the standard harmonic expansion (2). This fact turns out to be advantageous for the numerical evaluation of $\varepsilon_{h,ij}$ at high temperatures and high frequencies[3,4] (We note that the (2,3)-element (the (1,3)-element) obtained by Weiss[3] (Tamor[4]) in the expression corresponding to (5) does not appear to be correct).

B. Integral representation of T_{ij}. Each element of matrix (5) can be expressed in integral form with a single Bessel function by using the relation[5]

$$J_\upsilon(z)J_\lambda(z)=\frac{2}{\pi}\int_0^{\pi/2} d\phi\, J_{\upsilon+\lambda}(2z\cos\phi)\cos[(\upsilon-\lambda)\phi] \ , \quad \mathrm{Re}(\upsilon+\lambda)>-1 \qquad (7)$$

Applying (7) to (5) yields the symmetric form

$$T_{ij}= -\frac{2p_\perp}{\sin(\pi\mu)}\int_0^{\pi/2}d\phi\begin{bmatrix} \frac{p_\perp}{2}J_0\cos[2(\mu+1)\phi] & \frac{p_\perp}{2}J_2\cos[2\mu\phi] & -\frac{p_\parallel}{\sqrt{2}}J_1\cos[(2\mu+1)\phi] \\ \frac{p_\perp}{2}J_2\cos(2\mu\phi) & \frac{p_\perp}{2}J_0\cos[2(\mu-1)\phi] & t_{23} \\ -\frac{p_\parallel}{\sqrt{2}}J_1\cos[(2\mu+1)\phi] & t_{23} & -\frac{p_\parallel^2}{p_\perp}J_0\cos[2\mu\phi] \end{bmatrix} \quad (8)$$

with $t_{23}\equiv-(p_\parallel/\sqrt{2})\{(2\mu/b)J_0\cos(2\mu\phi)-J_1\cos[(2\mu+1)\phi]\}$; the argument of $J_{0,1,2}$ being $2bc\cos\phi = 2(\omega/\omega_c)N_\perp(p_\perp/mc)\cos\phi$ (A representation similar to (8) has been obtained also by Shi et al.[6]). The salient characteristic of (8) is the ϕ-integral over the $(0,\pi/2)$-range of combinations of $J_{0,1,2}$ with cosine functions. As for (5) the poles connected with $\sin(\pi\mu)=0$ contribute an anti-Hermitian part to the dielectric tensor. More specifically, for $N_\parallel^2<1$ one has

$$\varepsilon_{a,ij}=4\pi\left[\frac{\omega}{p}\right]^2\sum_n(-1)^n\int_0^{\pi/2}d\phi\int_0^{p_o}dp_\perp\,\frac{p_\perp}{\Delta}\left[\gamma U(f_o)t_{ij}\right]_{\mu=n} \quad (9)$$

where t_{ij} is the integrand of the ϕ-integration in (8), $\Delta=[(1-N_\parallel^2)(p_o^2-p_\perp^2)]^{1/2}/(mc)^2$ and $p_o=[(n\omega_c/\omega)^2/(1-N_\parallel^2)-1]^{1/2}mc$.

Acknowledgements. This work has been performed with financial support from the Ministero della Pubblica Istruzione of Italy.

References

1. M.Bornatici,R.Cano,O.De Barbieri,F.Engelmann, Nucl.Fusion23,1153(1983)
2. E.A.Evangelidis, J.Math.Phys. 25,2151(1984)
3. I.Weiss, J.Comp.Phys. 61,403(1985)
4. S.Tamor, Int.Rep. SAIC-86/3081-APPAT-77
5. I.S.Gradshteyn and I.A.Ryzhik, Table of Integrals, Series and Products (Academic Press, New York, 1980)
6. B.R.Shi, J.D.Gaffey, Jr. and C.S.Wu, Phys. Fluids 29,4212(1986)

FUNDAMENTAL HARMONIC ELECTRON CYCLOTRON EMISSION FOR HOT, LOSS-CONE TYPE DISTRIBUTIONS

M. Bornatici*, U. Ruffina* and E. Westerhof‡
* Physics Department 'A. Volta', University of Pavia, Pavia, Italy
‡ Association Euratom-FOM, FOM-Instituut voor Plasmafysica 'Rijnhuizen' Nieuwegein, The Netherlands.

INTRODUCTION

Electron cyclotron emission (ECE) is an important diagnostic tool for the study of hot plasmas. ECE can be used not only to measure the electron temperature [1] but also to obtain information about non-thermal characteristics of the electron distribution function [2]. One such a non-thermal characteristic is a loss-cone anisotropy. Loss-cone anisotropy can give rise to unstable growth of electro-magnetic waves around the harmonics of the electron cyclotron resonance (see [3], for a review) and to increased emissivity of electron cyclotron waves [4]. In case of high electron temperatures, also the dispersion properties of the extraordinary (X-) mode around the fundamental electron cyclotron resonance are changed due to loss-cone anisotropy [5, 6]. For propagatiuon perpendicular to the magnetic field, these changes depend on the parameter δ which is defined by $\delta \equiv (\omega_p / \omega_c)^2 \mu$ [6], where μ is an inverse temperature parameter defined by $\mu \equiv m_e c^2/T$, and all other quantities have their usual meaning. For $\delta \gg 1$ and $\delta \ll 1$ the wave dispersion is well described by the cold-plasma limit and the tenuous-plasma limit, respectively [1]. In the intermediate regime (η of order 1) wave dispersion is significantly modified. In this regime a (near) resonance or a (near) cut-off can occur for frequencies below the fundamental electron cyclotron harmonic. This resonance and cut-off correspond to the Upper-Hybrid resonance and low-density cut-off, respectively, that are down shifted in frequency by the combined effect of high temperature and loss-cone anisotropy.

Here, the consequences of these dispersion properties for the emissivity of the fundamental harmonic X-mode are analyzed for perpendicular propagation. The emissivity, η_1^X, is calculated for two types of distribution functions having a loss-cone anisotropy in the parameter regime for which the dispersion properties were discussed previously in Refs. [6] and [7]. These distribution functions are a relativistic Dory-Guest-Harris type distribution function (subsequently referred to as DGH distribution) and modified relativistic Maxwellian distribution having a loss-cone with rounded edges (subsequently referred to as LC distribution). The DGH distribution is defined by

$$f(\bar{p}) = C_j(\mu) \, \bar{p}_\perp^{2j} \, e^{-\mu\gamma} \qquad (1)$$

where $\bar{p} \equiv p / m_e c$ is the normalized momentum, $\gamma \equiv \sqrt{1 + \bar{p}^2}$ is the relativistic mass factor, the normalization $C_j(\mu) \equiv \mu^{j+1} [4 \pi 2^j j! \, K_{j+2}(\mu)]^{-1}$, j is the loss-cone index (j = 0 corresponds to the relativistic Maxwellian), and K_ν is the modified Bessel function of order ν. For the LC distribution the definition

$$f(\bar{p}) \equiv C(\mu, \psi_{loss}, D) \frac{1}{1 + e^{\frac{|\psi| - \psi_{loss}}{D}}} e^{-\mu\gamma} \tag{2}$$

$$\text{with} \quad C(\mu, \psi_{loss}, D) \equiv \mu \left\{ 4\pi K_2(\mu) \left(1 + D \ln \frac{e^{\frac{-\psi_{loss}}{D}} + 1}{e^{\frac{1-\psi_{loss}}{D}} + 1} \right) \right\}^{-1}$$

as given in Ref. [8] is used. Here $\psi \equiv p_{\parallel}/p$ is the cosine of the pitch angle, $\psi_{loss} \equiv \cos\theta_{loss}$, where θ_{loss} is the loss-cone angle, and D is the width of the loss-cone edges. The limit D = 0 corresponds to the sharp edged loss-cone, and D = 0 and $\theta_{loss} = 0$ yields the relativistic Maxwellian.

The emissivity was calculated with the usual equation for the emissivity as derived in Ref. [9]. This equation can be written as

$$\eta = N_r^2 \frac{\omega_p^2 \omega m_e}{32\pi^3} \frac{1}{|s|} \sum_n \int \frac{d^3p}{\gamma} f(\mathbf{p}) |\mathbf{e} \cdot \mathbf{j}_n^*|^2 \delta\left(\gamma - N_{\parallel}\bar{p}_{\parallel} - \frac{n\omega_c}{\omega}\right) \tag{3}$$

where N_r is the ray-refractive index, ω_p is the plasma frequency, ω is the wave frequency, N the refractive index, **s** is the power flux in the waves normalized to $|\mathbf{E}|^2$, **E** being the electric field of the waves, **e** is the polarization vector of the electric field, and $\mathbf{j}_n$ is defined by

$$\mathbf{j}_n \equiv \left[\frac{n\bar{p}_{\perp}}{b} J_n(b) \quad ; \quad i\bar{p}_{\perp} J_n'(b) \quad ; \quad \bar{p}_{\parallel} J_n(b) \right], \qquad b \equiv \frac{\omega}{\omega_c} N \bar{p}_{\perp}, \tag{4}$$

$J_n(b)$ being the Bessel function of order n. In writing Eq. (3) we have used the identity

$$|s| = \frac{c}{4\pi} N \frac{\left|\frac{\partial}{\partial N^2}\Lambda'\right|}{\cos\beta\, \lambda_{ss}}, \tag{5}$$

where Λ' is the determinant of the hermitian part of the dispersion tensor, λ_{ss} is the trace of the adjoint of Λ', and β is the angle between **s** and the wavevector. This way, the relation of η to **s** is shown explicitly. The emissivity of the X-mode around the fundamental harmonic, η_1^X, is then obtained from Eq. (3) by evaluating only the n=1 term. The Bessel functions were approximated by their first term from the series expansion, $J_n(b) = b^n / 2^n n!$. This means that only lowest order finite Larmor radius effects were retained.

The results are presented in terms of a normalized emissivity, $\bar{\eta}_1^X$, defined by

$$\bar{\eta}_1^X \equiv \frac{\eta_1^X}{\cos\beta\, \eta_0 N_r^2}, \quad \text{with } \eta_0 \equiv \frac{\omega_p^2 \omega_c m_e}{8\pi^2 c}. \tag{6}$$

This normalized emissivity is the more relevant quantity, because in the equation of radiative transfer the emissivity occurs in the combination η_1^X / N_r^2, while the equation of radiative transfer is to be integrated along the direction of energy propagation to obtain the intensity of radiation emitted by the plasma.

RESULTS AND DISCUSSION

It is noted that the calculations of the polarization vector and of the normalized power flux ocurring in Eq. (3) require the knowledge of the dielectric tensor and the wave refractive index and, hence, the solution of the dispersion equation. The elements of the dielectric tensor were calculated either numerically or, in case of the DGH distribution, using the analytical expressions of [5]. Referring to the DGH distribution it is noted that the results obtained numerically are equal to those obtained from the analytical expressions with an accuracy of better than 1%.

The results for the DGH distribution are presented in Fig. 1a. This figure gives the normalized emissivity of the fundamental harmonic X-mode for a DGH distribution with electron density $(\omega_p / \omega_c)^2 = 0.1$, loss-cone index j = 1, and temperatures T = 10., 15., 20., 30., and 50. keV. In Fig. 1b $\bar{\eta}_1^X$ is given for a LC distribution with $(\omega_p / \omega_c)^2 = 0.1$, loss-cone angle $\theta_{loss} = 60^o$, width of the loss-cone edges D = 0.1, and temperatures T = 10., 15., 22., 33., and 50. keV. Clearly the results for the both types of distribution functions are very similar. The most striking feature in these figures are the sharp peaks at T = 20. and 30. keV for the DGH distribution and at T = 22. and 33. keV for the LC distribution. These sharp peaks are a sensitive function of the temperature and are close to maximum for the parameters chosen in Fig. 1. An explanation of the peaks can be found in the combined effects of moderately high temperatures and loss-cone anisotropy on the wave dispersion as discussed in Ref. [6] for the DGH distribution and in Ref. [7] for the DGH and the LC distribution. The peaks are associated with the occurrence of either a resonance or a cut-off for frequencies just below the fundamental electron cyclotron frequency. Both at a resonance and at a cut-off the normalized power flux in the direction parallel to the wave vector, $\cos \beta \, | \mathbf{s} |$, goes to zero. Consequently, the emissivity at those frequencies becomes large, as the normalized emissivity is inversely proportional to $\cos \beta \, | \mathbf{s} |$ (cf. Eqs. (3) and (6)). This is illustrated in Fig. 2 giving the corresponding behaviour of $\cos \beta \, | \mathbf{s} |$. It is noted that in case of a resonance it is the normalized power flux itself that goes to zero. In case of a cut-off, on the other hand, the normalized power flux in the direction parallel to the wave vector goes to zero while the power flux in the direction perpendicular to both the wave vector and the magnetic field remains finite. Thus, $\cos \beta$ goes to zero. This latter result is due to the fact that, for the cases considered here, when the real part of the wave vector has a cut-off the imaginary part of the wave vector is very large (see Ref. [6]). This causes the direction of energy propagation to become perpendicular to both the wave vector and the magnetic field.

Physically, these results can be interpreted by considering that as the energy flux in the waves goes to zero, the interaction time between the waves and the electrons will increase dramatically, which may give rise to the observed increase in the emissivity.

FIGURE CAPTIONS

Fig. 1 The normalized emissivity, $\bar{\eta}_1^X$, of the fundamental harmonic X-mode for a DGH distribution (a) with electron density $(\omega_p / \omega_c)^2 = 0.1$, loss-cone index j = 1, and temperatures T = 10., 15., 20., 30., and 50. keV, and for a LC distribution (b) with the same density, loss-cone angle $\theta_{loss} = 60^o$, width of the loss-cone edges D = 0.1, and temperatures T = 10., 15., 22., 33., and 50. keV.

Fig. 2 The normalized energy flux in the direction parallel to the wave vector, $\cos \beta | \, s \, |$, of the fundamental harmonic X-mode for both types of distribution functions (DGH (a), LC (b)) with the same parameters as in Fig. 1.

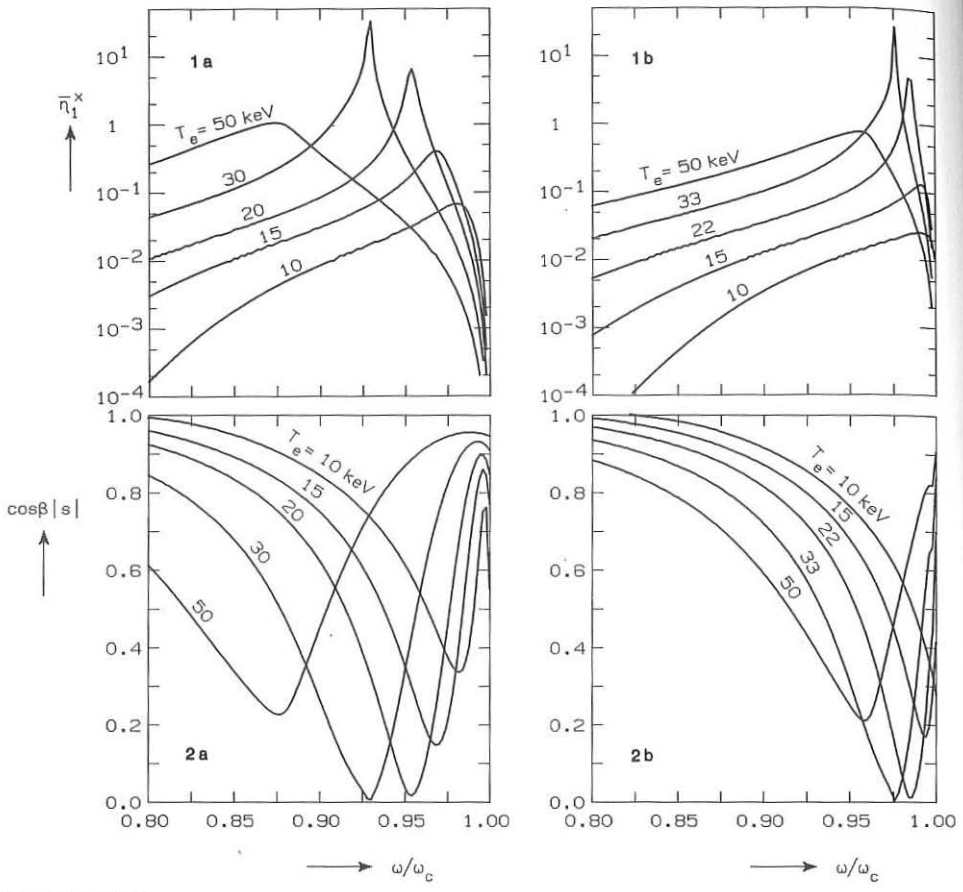

REFERENCES

[1] BORNATICI M., CANO R., DE BARBIERI O. and ENGELMANN F.(1983) Nucl. Fusion **23**, 1153.

[2] HUTCHINSON I.H. and KATO K. (1986) Nucl. Fusion **26**, 179.

[3] WU C.S. (1985) Space Science Reviews **41**, 215.

[4] BORNATICI M. and RUFFINA U. (1986) Plasma Phys. Contr. Fusion. **28**, 1589.

[5] BORNATICI M., RUFFINA U. and WESTERHOF E. (1985) in the proceedings of EC5 'Fifth International Workshop on Electron Cyclotron Emission and Electron Cyclotron Heating', 9-12 Nov. 1985, San Diego, (Report GA-A18294) p. 88.

[6] BORNATICI M. and RUFFINA U. (1988) Plasma Phys. Contr. Fusion. **30**, 113.

[7] WESTERHOF E., (1987) 'Electron cyclotron waves, transport and instabilities in hot plasmas', thesis University of Utrecht (Netherlands).

[8] LASNIER C.J. and ELLIS R.F. (1986) Phys. Rev. **A 33**, 742.

[9] FREUND H.P. and WU C.S. (1977) Phys. Fluids **20**, 963.

WAVE-WAVE INTERACTION OF HOT COLLISIONLESS PLASMA

W.H. Amein and B.F. Mohamed

Plasma Physics and Accelerators Dept., Atomic Energy Authority,
Nuclear Research Centre, Cairo, Egypt.

Interaction between oscillations in a plasma and the plasma itself or external fields applied to the plasma result in the energy exchange between oscillations of plasma and its other degrees of freedom or the external fields [1,2,3].

In the present work, we consider a plasma of hot ions and cold electrons ($T_i \gg T_e$), and the current of velocity $\vec{u}$ propagate in the Z-direction perpendicular to the external magnetic field $\vec{H}_0$, $u \ll V_T$, $\omega_{He} \gg \omega_{\vec{K}}$, $\delta_{\vec{K}} \gg \omega_{Hi}$, $|\cos\theta| \equiv |K_z/z| \ll 1$ and $\vec{K} \equiv \{K_\perp, \varphi, K_z\}$. The nonlinear scattering of the electron-sound oscillation on plasma ions is investigated. Also the matrix elements, which describes wave-wave interaction in the plasma are obtained. The condition of instability of plasma wave is calculated.

Consider that the relation (15) in ref. [1], and under the conditions of the splitting electron-sound waves on plasma ions such that:

$$\omega_{\vec{K}'} = \omega_{\vec{K}-\vec{K}'} \quad , \quad \omega_{\vec{K}''} = \omega_{\vec{K}} \quad , \quad \omega_{\vec{K}} = \omega_{\vec{K}'} + \omega_{\vec{K}''} \tag{1}$$

The condition $\frac{\omega_{K'}}{K'} = \frac{\omega_K}{K}$ cannot satified if $K' \neq K$. In fact, we can find K'_z from (1) such that:

$$|K_z| \ll |K'_z| \simeq \frac{K_\perp}{\sqrt{2}} \frac{u}{V_{T_i}} \sqrt{\frac{m_e}{m_i}} \tag{2}$$

$$\omega_{\vec{K}} = - \frac{\vec{K}\,\vec{u}}{2(2-\sqrt{2})} \tag{3}$$

The relation (3) is gives the frequency of plasma oscillation due to scattering.

The linear growth rate $\delta_L(\vec{K})$ in ref. [1], can be also obtained under the condition (1), and by substituting from (3), we have:

$$\delta_L(\vec{K}) \simeq - \frac{1}{4}\sqrt{\frac{\pi}{2}} \frac{1}{(2-\sqrt{2})^2} \cdot \frac{K u^2}{V_{T_i}} \left[2(2-\sqrt{2}) \operatorname{sign}\cos\theta + 1\right] \tag{4}$$

where $|\cos\theta| = \dfrac{u}{2 V_{T_i}(2-\sqrt{2})} \sqrt{\dfrac{m_e}{m_i}}$

From relation (4) we see that if the current velocity $\vec{u}$ in the direction of wave length $\vec{k}$ this gives $\cos\theta > 0$ and this yields to $\gamma_L < 0$ and stabilization of waves becomes, and when the current velocity $\vec{u}$ is in opposite direction of $\vec{k}$ in this case $\cos\theta < 0$ and $\gamma_L > 0$, which gives the instability of the plasma.

To find the solution of the dispersion relation (12) in ref. [1], we shall consider

$$A_{\vec{k}} = A^{(0)}_{\vec{k}} + A^{(1)}_{\vec{k}} + A^{(2)}_{\vec{k}} + \cdots \tag{5}$$

In final form, we have by an order of magnitude that:

$$\frac{\partial A^{(0)}_{\vec{k}}}{\partial t} = \gamma_L(\vec{k})\, A^{(0)}_{\vec{k}} + \frac{\alpha_{\vec{k}} |A^{(0)}_{\vec{k}}|^2}{\gamma_{\vec{k}}} A^{(0)}_{\vec{k}} \tag{6}$$

where $\alpha_{\vec{k}} \simeq V_{\vec{k},\vec{k}'} V_{\vec{k}+\vec{k}',\vec{k}''}$, are the matrix elements describes wave-wave interaction of the plasma and:

$$V_{\vec{k},\vec{k}'} V_{\vec{k}-\vec{k}',\vec{k}''} \sim \frac{e^2 \omega_{LH}^2 \, u}{m_i^2 \, V_{Ti}^5 \, \gamma_{\vec{k}}} \tag{7}$$

By substituting from (7) into (6) we have:

$$\frac{\partial A^{(0)}_{\vec{k}}}{\partial t} = 2\,\gamma_L(\vec{k})\, A^{(0)}_{\vec{k}} + A^{(0)}_{\vec{k}} \frac{|A^{(0)}_{\vec{k}}|^2 e^2 \omega_{LH}^2 \, u}{\gamma_{\vec{k}} \, m_i^2 \, V_{Ti}^5} \tag{8}$$

where $|A^{(0)}_{\vec{k}}|^2 \sim \varphi^2$, intensity of oscillations, and

$$\omega_{LH} = \omega_{Pi} \left(1 + \frac{\omega_{Pe}^2}{\omega_{He}^2}\right)^{-1/2} , \quad \omega_{He} = \frac{e\vec{H}}{mc}$$

Under the condition of strong nonlinear interaction of waves

$$\Delta\gamma \sim \gamma_{\vec{k}}$$

we have from (8), that

$$\frac{e|\varphi|}{T_i} \sim \frac{\gamma_L}{\omega_{LH}} \sqrt{\frac{V_{Ti}}{u}} \tag{9}$$

Relation (9) represent the condition of instability due to wave-wave interaction in the plasma.

References:

[1] W.H. Amein, Sh. M. Khalil, N.M. El-Siragy and S.A. El-Waraki, 1982 "INTERNATIONAL CONFERENCE ON PLASMA PHYSICS", June 9-15, 1982, Göteborg/Sweden.

[2] W.H. Amein, J.A. El-Naggar and V.L.Sizonenko; Plasma Physics, Vol. 19, pp. 651 to 661, 1977.

[3] D.B. Kadomtsev, "IN PROBLEMS OF PLASMA INSTABILITIES" 1, 1964, (in Russion).

HEATING OF THE PLASMA BY INCIDENT ELECTRON BEAM

N.G. Zaki and W.H. Amein

Plasma Physics and Acclerators Dept., Atomic Energy Authority,
Nuclear Research Centre, Cairo, Egypt.

The instabilities that arise in the interaction of charged particle beams with a plasma (electrostatic instability) are of extreme interest [1]. The stability of beam-plasma systems has been also studied by the authors in references [2,3,4].

In the present work, we consider a longitudinal one dimensional oscillations in a cold, magnetized plasma, which is inhomogeneous in density and bounded in the direction of beam motion.

From the continuity equation and the equation of motion of the plasma, we can find the perturbed plasma density takes the form:

$$n_p^{(1)} = -\frac{i}{\omega}\frac{\partial}{\partial x}\left[n_p^{(0)}(x) \cdot \frac{i e E_x}{\omega m\left(1-\frac{\omega_c^2}{\omega^2}\right)} \right] \qquad (1)$$

where $\omega_c = \frac{e H_0}{mc}$ is the Cyclotron frequency.

Let the density and the velocity of the beam have the forms:

$$N_b = n_b^{(0)} + n_b^{(1)} \; , \; n_b^{(1)} \ll n_b^{(0)} \; ; \quad \vec{v}_b = v_b^{(0)} + v_b^{(1)}(t)$$

From the continuity equation and the equation of motion of the beam, we have:

$$n_b^{(1)} = -\frac{n_b^{(0)} e}{m v_b^{(0)2}} e^{i\beta x} \cdot \int dx' \int dx'' \frac{\partial E_x}{\partial x''} e^{i\beta x''} \qquad (2)$$

where $\beta = \frac{\omega}{v_b^{(0)}}$

Substituting (1) and (2) into Poisson's equation, we have an equation for the field as:

$$\left(-i\omega + v_b^{(0)}\frac{\partial}{\partial x}\right)^2 (\beta E_x) + \omega_b^{(0)2}\left(1-\frac{\omega_c^2}{\omega^2}\right) E_x = 0 \qquad (3)$$

where: $\omega_b = \left(\frac{4\pi n_b e^2}{m}\right)^{1/2}$, $\frac{\partial n_b}{\partial x} = 0$, $v_b^{(0)} > 0$, $\frac{\partial v_b^{(0)}}{\partial x} = 0$

Introducing the variables:

$$\xi \equiv \frac{\omega}{v_b^{(\omega)}} x \quad , \quad E = \frac{\mathcal{E}}{\beta} \exp(i\xi) \tag{4}$$

where $\beta = \varepsilon - \frac{\omega_c^2}{\omega^2}$

Equation (4) is reduced to:

$$\frac{d^2\mathcal{E}}{d\xi} + \frac{\alpha}{\beta}\mathcal{E} = 0 \tag{5}$$

where: $\alpha = \frac{\omega_b}{\omega^2}\left(1 - \frac{\omega_c^2}{\omega^2}\right)$

Let us solve equation (5) in the case when the variation of $\frac{\beta}{d\beta/d\xi}$ is insignificant within the interval that is of the order of one wavelength [5]: $\left|\frac{\beta}{d\beta/d\xi}\right| \ll \sqrt{|\alpha\beta|}$

$$\mathcal{E} \approx \beta^{1/4}\left\{\mathcal{E}_+ \exp\left(i\int_0^\xi d\xi\sqrt{\frac{\alpha}{\beta}}\right) + \mathcal{E}_- \exp\left(-i\int_0^\xi d\xi\sqrt{\frac{\alpha}{\beta}}\right)\right\} \tag{6}$$

where: $\mathcal{E}_+$, $\mathcal{E}_-$ are integration constants.

Similarly, to work Amein et al. [6], we can find the solutin of the field equation (5) at the resonance point like that:

$$\mathcal{E} = 2\sqrt{a\eta}\left\{A \cdot H_1^{(1)}(2\sqrt{a\eta}) + B \cdot H_1^{(2)}(2\sqrt{a\eta})\right\} \tag{7}$$

where: $\eta = \xi - \ell + i\lambda\delta$, $a = \alpha\lambda$, $\frac{1}{\lambda} = \left.\frac{\partial R_e \varepsilon}{\partial \xi}\right|_{\xi=\ell}$,

$\delta = \frac{\nu}{\omega} \ll 1$;

ν is the collision frequency of the electrons plasma with other particles. In case of the asymptotic solution of equation (7) at $|2\sqrt{a\eta}| \gg 1$ we have the constants A and B as:

$$A = \frac{\sqrt{\pi}}{2} \cdot \frac{\exp\left(i\frac{3}{4}\pi + \int_0^\ell d\xi\sqrt{\frac{\alpha}{|\beta|}}\right)}{(\alpha^{1/4}\lambda^{1/2})}\mathcal{E}_+$$

$$B = \frac{\sqrt{\pi}}{2} \cdot \frac{\exp\left(-i\frac{3}{4}\pi - \int_0^\ell d\xi\sqrt{\frac{\alpha}{|\beta|}}\right)}{(\alpha^{1/4}\lambda^{1/2})}\mathcal{E}_- \tag{8}$$

and

$$\mathcal{E} \approx i\frac{2}{\pi}\{-A + B\} \tag{9}$$

The amount of energy absorbed by the plasma per unit time is determined by the expression:

$$S = \int dx (jE^* + j^*E) = \frac{\omega}{2\pi}\int dx\, Im\beta\, |E|^2 \tag{10}$$

where j is the density of the electric current created by plasma electrons.

Using expression (4), (8) and (9) in the right hand side of expression (10) and integrating near the point $\xi = \ell$ (the integration over the rest of the interval of variation of ξ yields a small correction) we get:

$$\frac{S}{S_b} = \frac{2}{\alpha^{1/2}} \exp 2 \int_{\ell}^{\ell} d\xi \sqrt{\frac{\alpha}{|\beta|}} \cdot \frac{W_E}{W_b} \tag{11}$$

where $S_b = n_b v_b^{(0)} m v_b^{(0)2}/2$ is the energy flux density in the unperturbed beam; W_E is the average density of electrostatic energy of the wave in the interval $\xi \longrightarrow -\infty$. Expression (11) omits the exponentially small items, proportional to the value. Obviously, expression (11) can be considered as valid provided:

$$\frac{S}{S_b} \gg 1 \tag{12}$$

The power absorbed by the plasma will be determined by expression (11). Thus, the beam, due to the resonant increase of the field in the interval $\beta \approx 0$ and the presence of static magnetic field, act as a mechanism responsible for putting power into the plasma and not only for amplification of the waves.

From relation (12), we see that: the amount of energy absorbed by the palsma per unit time S is much greater than the energy flux censity in the unperturbed beam S_b, in contrary on the unmagnetized plasma in reference [6].

References:

[1] Ya. B. Fainberg, V.I. Kurilko, and V.D. Shapiro, Sov. Phys. - Tech. Phys. 6 (1961), 459.

[2] A.I. Akhizer and Ya. B. Fainberg, Doklady Adad. Nauk SSSR 64 (1949) 555.

[3] D. Bohm and E. Gross, Phys. Rev. 75(1949) 1851; 75 (1949) 1864.

[4] D.N. Wall, P.D. Edgley and R.N. Franklin, Plasma Physics 23 (1981) 145.

[5] V.L. Ginzburg, The Propargation of Electromagnetic Waves in Plasma (Oxford, 1964).

[6] W.H. Amein, V.V. Dolgopolov, A.M. Hussein and K.E. Zayed; Plasma Physics 17 (1975) 497.

LEAKAGE OF MHD SURFACE WAVES IN STRATIFIED MEDIA

V. M.Čadež
Institute of Physics
P.O. Box 57, YU-11001, Beograd, Yugoslavia,

V. K. Okretič
Faculty of Mechanical Engineering, University of Beograd,
27. mart 80, YU-11000 Beograd, Yugoslavia.

We investigate MHD surface waves in stratified media and a possibility of their energy dissipation through the leaking mechanism, similarly to what was done earlier in the case of the high frequency electromagnetic domain /1/.

The considered basic state consists of an one-component, perfectly conductive, compressible, stationary fluid being piecewise homogeneous. There are two discontinuity planes at x=0 and x=a where the density ρ_o, the temperature T_o and the magnetic field intensity B_o change their values:

$$\rho_o, T_o, B_o = \begin{cases} \rho_{o1}, T_{o1}, B_{o1} = \text{const.}, & x<0 \quad \text{region 1} \\ \rho_{o2}, T_{o2}, B_{o2} = \text{const.}, & 0<x<a \quad \text{region 2} \\ \rho_{o3}, T_{o3}, B_{o3} = \text{const.}, & a<x \quad \text{region 3} \end{cases}$$

while the magnetic field $\vec{B}_o=(0,0,B_o)$ is oriented along the boundaries of the three regions.

All the quantities ρ_{oi}, T_{oi} and B_{oi} $(i=1,2,3)$ are mutually related through the boundary conditions of the total pressure continuity at x=0 and x=a:

$$\rho_{oj}(c_j^2 + \frac{\gamma}{2} A_j^2) = \rho_{oj+1}(c_{j+1}^2 + \frac{\gamma}{2} A_{j+1}^2) \qquad j=1,2 \qquad (2)$$

where $c_i=(\gamma R T_{oi})^{1/2}$ and $A_i=B_{oi}/(\mu_o \rho_{oi})^{1/2}$ are the sound speed and the Alfven speed respectively in the three regions.

We start from standard set of linearized MHD equations for small perturbations about the considered basic state:

$$\frac{\partial \rho}{\partial t} + \nabla\cdot(\rho_o \vec{v}) = 0, \qquad p = R(\rho_o T + \rho T_o)$$

$$\rho_o \frac{\partial \vec{v}}{\partial t} = -\nabla\left(p + \frac{\vec{B}\cdot\vec{B}}{\mu_o}\right) + \frac{1}{\mu_o}(\vec{B}_o\cdot\nabla)\vec{B} + \frac{1}{\mu_o}(\vec{B}\cdot\nabla)\vec{B}_o$$

$$\frac{\partial \vec{B}}{\partial t} = \nabla \times (\vec{v} \times \vec{B}_o), \qquad \nabla\cdot\vec{B} = 0$$

As the fluid perturbations are assumed adiabatic, the energy balance equation takes the following form:

$$\frac{\partial p}{\partial t} + \vec{v}\cdot\nabla p_o = c^2\left(\frac{\partial \rho}{\partial t} + \vec{v}\cdot\nabla\rho_o\right)$$

Since all the basic state quantities depend on x only, the solutions for perturbations ρ, v, p, and B can be expressed in terms of Fourier-Laplace transforms $f(x)\exp(-i\omega t+\ell y+kz)$.

The above set of equations now reduces to a single equation for the amplitude u(x) of the x-component velocity perturbation /2/:

$$\frac{d}{dx}\left\{\frac{\rho_o(x)\left[k^2A^2(x)-\omega^2\right]}{m_o^2(x)+\ell^2}\cdot\frac{du}{dx}\right\} - \rho_o(x)\left[k^2A^2(x)-\omega^2\right]u = 0 \qquad (3)$$

where:

$$m_o^2(x) = \frac{[k^2A^2(x)-\omega^2]\,[k^2c^2(x)-\omega^2]}{[c^2(x)+A^2(x)][k^2c_t^2(x)-\omega^2]}, \qquad c_t^2(x) = \frac{c^2(x)\,A^2(x)}{c^2(x)+A^2(x)}$$

The equation (3) can now be analytically solved for the three homogeneous regions.

One mode that follows from (3) is evidently the bulk Alfven wave $\omega^2 = k_i^2A_i^2$ for which $k_1^2A_1^2 = k_2^2A_2^2 = k_3^2A_3^2$ is valied due to the requirement that the frequency does not change across the boundaries at x=0 and x=a.

The other modes follow from solution of (3) when the relevant boundary condition is satisfied. Namely, having integrated the equation (3) across the discontinuity one gets that the expression

$$\frac{\rho_o(x)[k^2A^2(x)-\omega^2]}{m_o^2(x)+\ell^2} \cdot \frac{du}{dx} \qquad (4)$$

does not change from one region to another. This boundary condition is physically equivalent to the continuity of the total pressure perturbation at x=0 and x=a.

The solutions of equation (3) which are finite at $|x| \to \infty$ have the following form:

$$\begin{aligned} u_1(x) &= C_1 \exp(\varkappa_1 x) && x \le 0 \\ u_2(x) &= C_2 \exp(\varkappa_2 x) + C_2' \exp(-\varkappa_2 x) && 0 < x \le a \\ u_3(x) &= C_3 \exp(-\varkappa_3 x) && x > a \end{aligned} \qquad (5)$$

where $\varkappa_i = (m_{oi}^2 + \ell^2)^{1/2}$

The obtained solution vanishes as $|x| \to \infty$ if the coefficients $\varkappa_i$ are real, indicating a pure surface wave in that case.

However, if $\varkappa_1$ becomes imaginary (for m_{o1}^2 sufficiently negative) the perturbations will have a wave solution in the region 1 and, consequently, a surface wave that propagates along the boundary x=a will be partly converted to a bulk wave spreading with a constant amplitude throughout the halfspace x<0. The surface wave will thus be loosing its energy and its amplitude will be decreasing in time.

The related dispersion equation that follows from solutions (5) and the requirement that (4) does not change across the boundaries, is:

$$1 + \Omega_{23}^2 = \frac{(1 - \Omega_{12}^2)(1 - \Omega_{23}^2)}{1 + \Omega_{12}^2} \exp(-2\varkappa_2 a) \qquad (6)$$

where

$$\Omega_{ij}^2 = \frac{\rho_{oi}(k^2A_i^2 - \omega^2)(m_{oj}^2 + \ell^2)^{1/2}}{\rho_{oj}(k^2A_j^2 - \omega^2)(m_{oi}^2 + \ell^2)^{1/2}} \qquad i=1,2; \quad j=i+1$$

The exponential term on the right-hand side of (6) represents the coupling effect of the two boundaries and will be considered as a small correction to the single boundary solution /3,4/. The effect of the second boundary thus results into a complex frequency shift $\Delta\omega$ such that $|\Delta\omega| \simeq \exp(-2\varkappa_2 a)$. The consequence of this is that related surface waves at the boundary x=a become weakly dispersive and attenuated.

The phase velocity of surface waves, which follows from the dispersion relation (6), is within the interval:

$$\min(A_2, A_3) < \frac{\omega}{k} < \max(A_2, A_3).$$

Part of these waves becomes leaky if the additional criteria:

$\varkappa_1^2 = m_{o1}^2 + \ell^2 < 0$, $\varkappa_2^2 = m_{o2}^2 + \ell^2 > 0$ and $\varkappa_3^2 = m_{o3}^2 + \ell^2 > 0$

are satisfied.

To conclude, we show that it is, in principle, possible to have such a basic state configuration that allows surface waves on the boundary x=a to leak into space x<0 from the boundary at x=0. This effect has to be taken into account when the energy transports by wave propagation in structured media is considered.

References:

1. Yu. M. Aliev, O. M.Gradov, A. Yu. Kyrie, V. M. Čadež, and S.Vuković: *Phys. Rev. A*, **15**, 2120, 1977.
2. L. Chen and A. Hasegawa, *Phys. Fluids*, **17**, 1399, 1974.
3. M. Lee and B. Roberts: *Astrophys. J.* **301**, 430, 1986.
4 B. Roberts: *Solar Phys.* **69**, 27, 1981.

ELECTRON ACOUSTIC AND LOWER HYBRID DRIFT DISSIPATIVE INSTABILITIES IN MULTI-ION SPECIES PLASMAS

S. Guha and Mridul Bose

Department of Physics
Ravishankar University,
Raipur 492 010 (M.P.) India

Introduction

In mirror devices at fusion conditions, theta pinches as well as in space plasmas, $T_i > T_e$. At this condition, electron-acoustic mode appears. Davidson et al (1) and Davidson (2) explained that the anomalous transport and flute formation in a rapidly pulsed theta pinch experiments are due to the lower hybrid drift instabilities. We have studied the electron acoustic and the lower hybrid drift dissipative instabilities under the conditions $\omega_{ci} < \omega < \omega_{ce}$, $k_z v_{ti} \ll k_z v_{te} < \omega$ and $\omega < k_\perp v_{ti}$ in a multi-ion species plasma. In addition we have obtained magnetosonic-drift dissipative instability in multi as well as single ion species plasmas.

Theoretical Formulation

Consider a magnetic field applied in the z-direction. The basic equations used are

$$\frac{\partial n_e}{\partial t} + n_{oe} \nabla \cdot \vec{V}_e + \vec{V}_e \cdot \nabla n_{oe} = 0 \qquad (1)$$

$$\frac{\partial \vec{V}_e}{\partial t} = \frac{e}{m_e} \nabla \phi - \frac{e}{m_e} (\vec{V}_e \times \vec{B}_0) - v_{te}^2 \nabla \left(\frac{n_e}{n_{oe}} \right) \qquad (2)$$

$$\frac{\partial n_i}{\partial t} + n_{oj} \nabla \cdot \vec{V}_j + \vec{V}_j \cdot \nabla n_{oj} = 0 \qquad (3)$$

$$\frac{\partial \vec{V}_j}{\partial t} = -\frac{e}{m_j} \nabla \phi - v_{tj}^2 \nabla \left(\frac{n_j}{n_{oj}} \right) - \nu_j \vec{V}_j \qquad (4)$$

$$\nabla^2 \phi = -4\pi e \left(n_e - \sum_{j=1,2} n_j \right) \qquad (5)$$

In the frequency regime considered, the effective ionic collisional frequencies are larger than the ionic cyclotron frequencies and $\omega_{c1}, \omega_{c2} < \omega < \omega_{ce}$, so the electrons are considered as magnetized whereas the ions are unmagnetized. The electron satisfy the drift approximation and from the above eqns, we get

$$\frac{\partial^2 n_e}{\partial t^2} - \frac{c}{B_0}\frac{\partial}{\partial t}(\nabla\phi \times \hat{z})\cdot\nabla n_{0e} + \frac{c\,n_{0e}}{B_0\omega_{ce}}\frac{\partial^2}{\partial t^2}\nabla_\perp\phi + \frac{e n_{0e}}{m_e}\frac{\partial^2\phi}{\partial t^2} = 0 \qquad (6)$$

Solution of eqn. (6) gives the electron density as

$$n_e = -\frac{c}{\omega B_0}\left(\vec{K} \times \hat{z}\cdot\nabla n_{0e}\right)\phi + \frac{c\,n_{0e}}{B_0\omega_{ce}}K_\perp^2\phi - \frac{e n_{0e}}{m\omega^2}K_z^2\phi \qquad (7)$$

The number density of the ions as

$$n_j = \frac{n_{0j}\,e\,k^2}{m_j(\omega + i\nu_j)\omega}\left(1 - \frac{k^2 v_{tj}^2}{\omega(\omega + i\nu_j)}\right)^{-1} \qquad (8)$$

From Poison's eqn., eqn. (7) and (8) gives the dispersion relation as

$$\omega^2 K^2\lambda^2 + \frac{K_\perp^2\omega^2}{m_e\omega_{ce}}(T_1 + T_2) - \omega\omega^* - \frac{K_z^2(T_1+T_2)}{m_e} -$$

$$\frac{\omega^2 K^2(T_1+T_2)\left[\omega^2(n_{01}m_2 + n_{02}m_1) + i\omega(n_{01}m_2\nu_2 + n_{02}m_1\nu_1) - K^2(n_{01}T_2 + n_{02}T_1)\right]}{n_0\left[m_1m_2\omega^2(\omega+i\nu_1)(\omega+i\nu_2) - \omega K^2\{\omega(m_1T_2 + m_2T_1) + i(m_1\nu_1T_2 + m_2\nu_2T_1)\} + K^4T_1T_2\right]}$$

$$= 0, \qquad (9)$$

where $\omega^* = \dfrac{c(T_1+T_2)}{eB_0}\dfrac{K_\perp}{L}$ is ion-drift frequency

and $\lambda_D = (\lambda_{D1} + \lambda_{D2})$.

For the dissipative, inhomogeneous case, the dispersion relation for electron acoustic wave is

$$\omega^2 = \frac{K_z^2 T_1 T_2}{\left[K_z^2\dfrac{(m_1T_2 + m_2T_1)}{K^2} - \dfrac{K_z^2}{K^4}\nu_1\nu_2 m_1m_2 - \dfrac{m_e}{m_0}(n_{01}T_2 + n_{02}T_1) - \dfrac{i\omega^* m_e(m_1\nu_1T_2 + m_2\nu_2T_1)}{K^2(T_1+T_2)} + \dfrac{am_eT_1T_2}{(T_1+T_2)}\right]} \qquad (10)$$

and the growth rate when $\omega_r \gg \gamma$ turns out to be

$$\gamma = \frac{\omega^* m_e k_z \sqrt{T_1 T_2}\left(m_{01} v_1 T_2 + m_{02} v_2 T_1\right)}{2K^2(T_1+T_2)A\left[\frac{(m_1 T_2 + m_2 T_1)}{K^2} k_z^2 - \frac{k_z^2}{K^4} v_1 v_2 m_1 m_2 \frac{m_e}{n_0}\left(m_{01} T_2 + m_{02} T_1\right) + \frac{2 m_e T_1 T_2}{(T_1+T_2)}\right]^{3/2}} \quad . \quad (11)$$

The dispersion relation of the lower-hybrid drift dissipative wave is obtained as

$$\omega^2 = \left[v_1 v_2 + i\frac{\omega^*(v_1+v_2)}{a} + \frac{K^2(m_1 T_2 + m_2 T_1)}{m_1 m_2} + \frac{K^2(T_1+T_2)(m_{01} m_2 + m_{02} m_1)}{a m_0 m_1 m_2} + \frac{K_z^2(T_1+T_2)}{a m_e}\right] \quad (12)$$

and the growth rate as

$$\gamma = -\frac{\omega^*(v_1+v_2)}{2a\left[v_1 v_2 + \frac{K^2(m_1 T_2 + m_2 T_1)}{m_1 m_2} + \frac{K^2(T_1+T_2)}{m_2 n_0 m_1}(m_{01} m_2 + m_{02} m_1) + \frac{K_z^2(T_1+T_2)}{a m_e}\right]^{1/2}} \quad (13)$$

Magnetosonic drift dissipative instability can also be obtained from eqn. (12) under the limit $k_z \to 0$ and $\omega \ll \omega_{ci}$ as

$$\omega^2 = \left[v_1 v_2 + \frac{i\omega^*(v_1+v_2)}{\left(\frac{K_\perp^2 v_{ti}^2}{\omega_{pi}^2} + \frac{K_\perp^2 v_{ti}^2}{\omega_{ci}^2}\right)} + \frac{K_\perp^2(m_1 T_2 + m_2 T_1)}{m_1 m_2} + \frac{K_\perp^2(T_1+T_2)(m_{01} m_2 + m_{02} m_1)}{m_0 m_1 m_2\left(\frac{K_\perp^2 v_{ti}^2}{\omega_{pi}^2} + \frac{K_\perp^2 v_{ti}^2}{\omega_{ci}^2}\right)}\right] \quad (14)$$

and the growth rate as

$$\gamma = \frac{\omega^*(\nu_1+\nu_2)}{2a\left[\nu_1\nu_2 + \frac{K_\perp^2(m_1T_2+m_2T_1)}{m_1m_2} + \frac{K_\perp^2(T_1+T_2)}{a\omega_0 m_1 m_2}(\omega_{01}m_2+\omega_{02}m_1)\right]} \qquad (15)$$

Results: Some typical calculations $n_i \sim 10^{14}\,cm^{-3}$, $B_0 \simeq 10^4\,G$, $m_1/m_2 \sim 3600$, $m_2/m_e \sim 5400$, $T_i \sim 13\,KeV$, γ for electron acoustic drift dissipative instability $= 5 \times 10^4 \frac{k_z}{K_\perp L} s^{-1}$.

Growth rate of the lower-hybrid drift dissipative instability for E-region of ionosphere with $n \sim 2 \times 10^4 cm^{-3}$, $B_0 \sim 0.3$ G, $\nu_i \sim 10^3 s^{-1}$, and $\omega_{ce} \gg \nu_e$ we get $\gamma = (10^5/K_\perp L)\, s^{-1}$.

References

1. Davidson, R.C. Gladd, N.T., Wu, C.S. and Huba, J.D., Phys. Fluids 20, (1977) 301.
2. Davidson, R.C., Phys. Fluids 21, (1975), 1375.
3. Mohan, M. and Yu, M.Y., J.Plasma Physics 7, (1983), 205.

MODULATION INSTABILITY OF ELECTRON HELICON IN A MAGNETIZED COLLISIONAL PLASMA

M.Y. EL ASHRY * & N.A. PAPUASHVILI **

* Faculty of Science, Suez Canal University, Ismailia, Egypt .
** Institute of Physics, Academy of Science of the Georgian SSR , Tbilisi , USSR .

Recently, there has been considerable interest in the effects on plasma of an intense electromagnetic field which causes a relativistic oscillation of the electron mass. Nonlinear processes caused by relativistic effects were studied by Drake et al [1], whose results show that the relativistic electron motion can lead to the formation of shock waves . Tsintsadze and Tskhakaya [2] studied how the dependence of the electron mass on the amplitude of the pump field affects the propagation of electron-acoustic waves in a plasma with a negative dielectric constant. They showed that if the RF pressure force exceeds the gas pressure the solitary wave is a compressional wave .

Recently, Papuashvili et al [3] studied the interaction of a magnetized collisionless plasma with circularly polarized high-frequency wave, in whose field electrons can acquire relativistic velocities. Their results show that in the ultra-relativistic case ther are new types of waves one of which may be called an "electron helicon". Also they show that the external magnetic field strongly affects the interaction .

In the present paper we will study a circularly polarized RF wave interacting with a magnetized collisional plasma , in which the plasma electrons acquire relativistic velocities under the effect of such a wave .

To formulate the basic equation, let us consider the case in which intense electromagnetic radiation is propagated along the constant magnetic field $B(0,0,B_0)$ in a transparent plasma, and the wave length is much smaller than the characteristic distance over which the plasma density changes appreciably. The system of equations that describe the motion of particle $\alpha (= i, e)$ and the field is :

$$\frac{\partial \vec{P}}{\partial t} + \vec{v}_\alpha \frac{\partial P}{\partial \vec{r}} = e_\alpha \vec{E} + \frac{e_\alpha}{m_\alpha} \left(\vec{v}_\alpha \times \vec{B}_0 \right) - \delta P_\alpha$$

$$\frac{\partial n_\alpha}{\partial t} + \operatorname{div} n_\alpha \vec{v}_\alpha = 0 \quad ; \quad \vec{\nabla} \cdot \vec{E} = 4\pi \sum e_\alpha n_\alpha$$

$$\vec{\nabla} \times \vec{E} = -\frac{1}{c} \frac{\partial \vec{B}}{\partial t} \quad ; \quad \vec{\nabla} \times \vec{B} = \frac{1}{c} \frac{\partial \vec{E}}{\partial t} + \frac{4\pi}{c} \sum_\alpha e_\alpha n_\alpha v_\alpha$$

$$P_\alpha = m_{o\alpha} \vec{v}_\alpha / \left(1 - v_\alpha^2/c^2\right)^{1/2} \qquad (1)$$

where δ is the frequency of weak collision between electrons and ions .

It is well known [4] that an intense RF electromagnetic wave, under the effect of its field the plasma electrons acquire relativistic velocities, may be purely transverse, if it is circularly polarized. Therefore we shall be interested in studying the circularly polarized RF field propagating along a constant, uniform magnetic field $\vec{B}_o$.

Analysing system (1) by assuming $n(z,t) = n_o + \delta n(z,t)$, where n_o is the unperturbed density and δn is the perturbed density caused by the pendromotive force (also, of course, all the other hydrodynamic quantities should be expanded in the same way), and using the same method and approximation expanded in [3], one can come to the following equation which describes the plasma behavior in the field of RF wave :

$$\nabla^2 E_+ - \frac{1}{c^2}\frac{\partial^2}{\partial t^2} E_+ = \frac{\omega\, \omega_p^2 \left(1 + \delta n/n_o\right) E_+}{c^2 \left(w\sqrt{1+\nu^2} - \omega_c + i\delta\sqrt{1+\nu^2}\right)} \qquad (2)$$

where $E_+ = E_x + iE_y$, $w = (4\pi ne^2/m)^{1/2}$ is the electron langmuir frequency, δn is a slowly-varying density perturbation , $w_c = (eB_o/m\,c)$ is the electron cycltron frequency , $w = (k^2c^2/w_p^2)w_E$ is the electric helicon frequency, $w_E = eE_+/m_e c$ and

$$\nu^2 = \frac{p_e^2}{m_{oe}^2 c^2} = \frac{\omega_E^2 (1+\nu^2)}{\left(\omega\sqrt{1+\nu^2} - \omega_c\right)^2 + \delta^2(1+\nu^2)} \qquad (3)$$

Choosing a condition that

$$\left(\omega\sqrt{1+\nu^2} - \omega_c\right)^2 \gg \delta\,(1+\nu^2) \qquad (4)$$

it is easy from (3), in the ultra-relativistic case ($\nu \gg 1$) to obtain the following expression for the electric helicon :

$$\nu = \frac{\omega_c - \sqrt{\omega_E^2 - \delta^2}}{\omega} \simeq \frac{\omega_c}{\omega} \qquad (5)$$

providing that $w_c \gg (w_E^2 - \delta^2)^{1/2}$.

It is important to point out here that the quantity $(w\sqrt{1+\nu^2} - w_c)$ as it is shown in [3] should not be less than w_E . This condition differs from the non-relativistic case , in which w can reach the value w_c .

Thus , using the above mentioned notations and considering that all the hydrodynamic quantities and the field depend only on a single coordinate z , in addition to the time t , the following equation for the amplitude of the electric helicon is obtained from Eqn. (2) :

$$2i\omega\left(\frac{\partial}{\partial t}+v_g\frac{\partial}{\partial z}\right)E'+c^2\frac{\partial^2}{\partial z^2}E'+\frac{\omega_p^2\omega}{\omega_{E_0}}\left(\frac{\delta n}{n_0}-\frac{|E|-E_0}{E_0}\right)E'+$$
$$+i\delta\frac{\omega_c\omega_p^2}{\omega_{E_0}^2}\left(\frac{\delta n}{n_0}-2\frac{|E|-E_0}{E_0}\right)E'=0 \qquad (6)$$

where $v_g = kc^2/\omega$, $\omega_{E_0} = e|E|/m_{0e}c$ is the initial amplitude of the electromagnetic wave before the modulation and $(|E| - E_0)/E_0 \ll 1$.

Expressing E' as $E' = a\,e^{i\varphi}$, where a and φ are real functions of z and t , to obtain from (6) the following set of equations for a and φ :

$$-2\omega\left(\frac{\partial\varphi}{\partial t}+\frac{kc^2}{\omega}\frac{\partial\varphi}{\partial t}\right)a+c^2\frac{\partial^2 a}{\partial z^2}-c^2a\left(\frac{\partial\varphi}{\partial z}\right)^2+$$
$$\frac{\omega_p^2\omega}{\omega_{E_0}}\left(\frac{\delta n}{n_0}-\frac{|a|-a_0}{a_0}\right)a=0 \qquad (7)$$

and

$$2\omega\left(\frac{\partial a}{\partial t}+\frac{kc^2}{\omega}\frac{\partial a}{\partial z}\right)+2c^2\frac{\partial\varphi}{\partial z}\frac{\partial a}{\partial z}+c^2a\frac{\partial^2\varphi}{\partial z^2}+$$
$$+\delta\frac{\omega_c\omega_p^2}{\omega_{E_0}^2}\left(\frac{\delta n}{n_0}-2\frac{|a|-a_0}{a_0}\right)a=0 \qquad (8)$$

Linearizing (7) and (8) together with the continuity equation and the equation of ion motion , and seeking a solution of the form $\sim \exp(iqz - i\Omega t)$, to obtain the dispersion relation for the electric helicon in a magnetized collisional plasma :

$$(\Omega-v_g q)^2+i\delta\frac{\omega_c\omega_p}{\omega\,\omega_{E_0}^2}(\Omega-v_g q)-\frac{1}{4\omega^2}c^2q^2-$$
$$-\frac{c^2q^2}{4\omega^2}\frac{\omega_p^2\omega}{\omega_{E_0}}\Big\}(\Omega^2-v_s^2q^2)=\Big\{c^2q^2\frac{\omega_p^2\omega}{\omega_{E_0}}+2i\omega(\Omega-v_g q)\delta\frac{\omega_p^2\omega_c}{\omega_{E_0}^2}\Big\}\cdot$$
$$\cdot\frac{ec\,a_0}{m_i\omega}\left(q^2-i\delta\frac{kq}{\omega}\right)\frac{1}{4\omega^2} \qquad (9)$$

Substituting $\Omega = \Omega' + i\gamma$ where Ω' and γ are real values, and $\Omega' \gg \gamma$, into equation (9) to obtain the following equations governing Ω' and γ :

$$\left\{\left(\Omega'-v_g q'\right)^2-\frac{c^2q^2}{4\omega^2}\frac{\omega_p^2\omega}{\omega_{E_0}}\right\}(\Omega'^2-v_s^2q^2)=$$
$$=\frac{m_{0e}}{m_i}\left(c^2q^2\right)^2\left(k^2c^2/4\omega^2\right) \qquad (10)$$

and

$$\gamma^2 + \delta \frac{\omega_c \omega_p^2}{2\omega \omega_{E_0}^2} \gamma - \frac{1}{8} \delta \frac{k^2 c^2}{\omega^2} \left(\frac{m_e}{m_i}\right)\left(\frac{q_L c}{\omega}\right)\left(\frac{c}{v_s}\right) \omega_E = 0 \qquad (11)$$

From (11) we can get γ :

$$\gamma = -\delta \frac{\omega_c \omega_p^2}{2\omega \omega_{E_0}^2} \pm \frac{1}{2} \sqrt{\frac{\delta^2 \omega_c^2 \omega_p^4}{\omega^2 \omega_{E_0}^4} + \frac{1}{2} \delta \frac{k^2 c^2}{\omega^2} \left(\frac{m_{oe}}{m_i}\right)\left(\frac{q_L c}{\omega}\right)\left(\frac{c}{v_s}\right)\omega_E} \qquad (12)$$

Since,it is necessary that γ should be positive to get a modulation instability , then we shall consider only the positive sign (+) in equation (12) to describe and discuss the following two cases :

(i) The case in which

$$\delta \left(\omega_c \omega_p^4 / \omega_{E_0}^4\right) > \frac{1}{2} k^2 c^2 \left(\frac{m_{oe}}{m_i}\right)\left(\frac{q_L c}{\omega}\right)\left(\frac{c}{v_s}\right) \omega_E \qquad (13)$$

equation (12) simplifies to

$$\gamma_+ = \frac{1}{8} \left(k^2 c^2 / \omega^2\right) q_L c \left(m_{oe}/m_i\right)\left(\frac{c}{v_s}\right)\left(\omega_E^2 / \omega_c \omega_p^2\right) \qquad (14)$$

As is clear from (14),in this case the growth rate does not depend on the collision frequency,in spite of the fact that collision plays a significant role in the interaction. Also,it seems that the growth rate given by(14) is larger than that obtained in [5].

(ii) The case when

$$\left(\delta / q_L c\right) < \frac{1}{2} \left(\omega_E/\omega_p\right)^2 \left(\omega_E/\omega_c\right)^2 \left(c/V_{Te}\right)\left(m_{oe}/m_i\right) \qquad (15)$$

equation (12) becomes :

$$\gamma_+ = \frac{1}{2} \left(kc/\omega\right) \left[\delta \left(m_{oe}/m_i\right)\left(q_L c/\omega\right)\left(c/v_s\right)\omega_E\right]^{1/2} \qquad (16)$$

which shows the dependence of the growth rate on the collision frequency. It is important to note here that the condition (15) is an easy condition to fulfill experimetally.

REFERENCES

[1] S. Drake, Y.C. Lee, K.Nishikawa and N.L.Tsintsadze, Phys. Rev. Lett. 36,196 (1976).

[2] N.L. Tsintsadze and D.D. Tskhakaya,Sov.Phys.JETP 45, 252 (1977) .

[3] N.A. Papuashvili, E.G. Tsikharishvili and N.L.Tsintsadze, Sov. J. Plasma Phys. 6(3), 331 (1980) .

[4] A.I. Akhiezer and R.V. Polovin,Sov.Phys.JETP 3,969(1956/7).

[5] K.Nishikawa, N.L.Tsintsadze and M.Watanabe,Sov.J.Plasma Phys. 6, 713 (1980) .

MAGNETIC RECONNECTION AND INSTABILITES IN COAXIAL DISCHARGE

M.M. Masoud, H.M. Soliman, and T.A. El-Khalafawy

Plasma Physics and Accelerators Department,
Nuclear Research Centre, Cairo 13759, Egypt.

Introduction :

The interaction of plasma flow with magnetic field is the subject of extensive theoretical and experimental investigations carried out at present. This subject extended to deal with geophysical and astrophysical plasmas[1].

In the most of experimental electromagnetic driven plasma devices, the plasma flow possesses a considerable value of trapped magnetic field, which depends on the operational parameters of the plasma source[2]. The trapped magnetic field is due to the discharge current sheath, CS and reconnection diamagnetic effect which cause a disconnection of the magnetic field lines.

Different models suggest that the rearrangement of the sheath's magnetic topology is a source of energy release mechanism, leading to an effective plasma heating and particle acceleration to suprathermal energies [3]. Two types of energy release was proposed, flash energy release, and slow energy release. The flash energy release occurs during the current sheath formation, where the following mechanisms occur, development of tearing instability, heating of plasma sheath due to anomalous resistivity, and uniformed acceleration of plasma throughout the sheath. In slow energy release formation of trapped magnetic field occurs and in these magnetic island, relaxation oscillations in T_e and localization of energy release in magnetic island takes place.

In a T-tube, a fast energy wave packet pulse with velocity greater than 10^8 cm/s., accompanied by the discharge current disruption and sharp electric field was observed [4]. The destruction of the disrupted wave increase the plasma temperature and density.

This paper will present results of a coaxial ring electrodes discharge on the study of the formation of precursor pulse and magnetic reconnection.

Experimental arrangement :

The experiments were performed with a coaxial discharge system figure (1). The system consisted of a solid electrode of 1.8 cm diameter set back from a ring electrode of 3.6 cm diameter by 8 cm, at the end of expansion chamber 4 cm in diameter and 100 cm long. The electrodes were connected to a 10 K. Joule capacitor bank, with capacitance of 61.7 μF, through a

pressurised field distortion spark gap. The discharge current was 150 KA. with rise time of 4.5 μs. The test gas was hydrogen at 2 x 10^{-2} torr.

Measurements were carried out by miniature Rogovsky coils, magnetic probes, electric probes, diamagnetic loops, high speed camera, photomultipliers, and X-ray probe. Miniature Rogovsky coil was used to measure the current distribution inside the discharge system. X-ray probe was inserted in the expansion chamber to measure the energetic electrons.

Results and Discussion :

Electric probe results showed that, the test gas was preionized to a level = 2 x 10^{13} particles Cm^{-3}. The preionization was due to the plasma radiation and charged particles emitted from the discharge region. The discharge current sheath (J_r) was detected by the iminiature Rogovsky coil, while the shock front was detected by its luminousity, using 3 successive pinhole collimator and a photomultiplier. A separation of the piston (J_r front) from the shock front (light front) was observed, figure (2) in the pressure range between 2 x 10^{-2} torr and 1 x 10^{-1} torr. The J_r piston velocity was of order of 6 x 10^6 cm S^{-1} and the shock front velocity was 8 x 10^6 cm S^{-1} at 10 cm from ring electrode.

A precursor effect was observed as a step pulse propagating with velocity 4 x 10^7 cm S^{-1} ahead of the shock front. The velocity of the precursor remained almost constant but the shock slowed down. The structure of the precursor pulse was determined by the use of electric probe and it was found that the front of the pulse rose sharply (< 1 μs.) to a plateau. Also an igniting double electric probe working in the breakdown region showed several increases in the conductivity in the region of the precursor pulse, figure (2).

When a magnetic field with intensity varying from 6 - 10 KG was applied throughout the expansion chamber parallel to the direction of propagation, the shock front velocity was increased. On the other hand the precursor pulse appeared to be unaffected by this magnetic field. The magnetic field measurements showed a decrease of 10% of the magnetic field intensity in the precursor pulse region but the magnetic field lines were completely pushed out by the shock front. Such a precursor effects seem to have the same characteristics as the solitons. The pulse was splited sometimes into two or more pulses, have the same shape and structure of the original pulse.

The precursor pulse was distructed near the end of the expansion chamber and gave its energy to the working gas. The electric probe was used to measure the electron temperature and density, figure (3) showed a jump of temperature at the shock front to a 5 eV and at the precursor distruction region by 20 eV. The density measurements showed similar profile, with increase of density ≈ 4 times $\sim$ (7 x 10^{13} particles cm^{-1}) at the shock front and to peak value at the precursor region.

Magnetic field measurements showed a reversed field, was formed within the discharge region. The reversed field was accompanied by a sharp rise of electric field and energetic electrons, figure (4).

It has been thought that, the magnetic field lines were disconnected, when the plasma sheath has diamagnetic properties and its temperature increases, this was followed by magnetic field reconnection between its ends, and this will cause a sharp electric field due to the fast change of magnetic flux during the reconnection process. The plasma in that region will gain the energy of the magnetic flux, through acceleration of its ions, and some of the sharp deliver of energy, will be transfered to a solitary waves.

References :

(1) Dubois M.A., Gresillon D., and Bussac M.N., Proccedings of the international workshop on magnetic reconnection and turbulence, 1985. Les Editiors de Physique BP 112, 91944. Les Vils Cedex, France.

(2) Youssef A.M., Zaki A.A., Tsagas N.F., and Masoud M.M. Proceeding of sixth international conf. on "Gas discharges and their applications". Heriat-Watt Univ. Edinburgh, 1980. IEE Publication No. 189 part (2) pp. 134-138.

(3) Allyntsev A.T., Kasov V.I., Lebedev N.V., and Paperny V.V., Journal de Physique, Collogue (7) 1979. Supplement an No. 7, Tom 40, p. 723.

(4) Masoud M.M., Bourham M.A., Sharkwy W., and Saudy A.H., Z. Naturforsch, 1987. Vol. 42 a, p. 120.

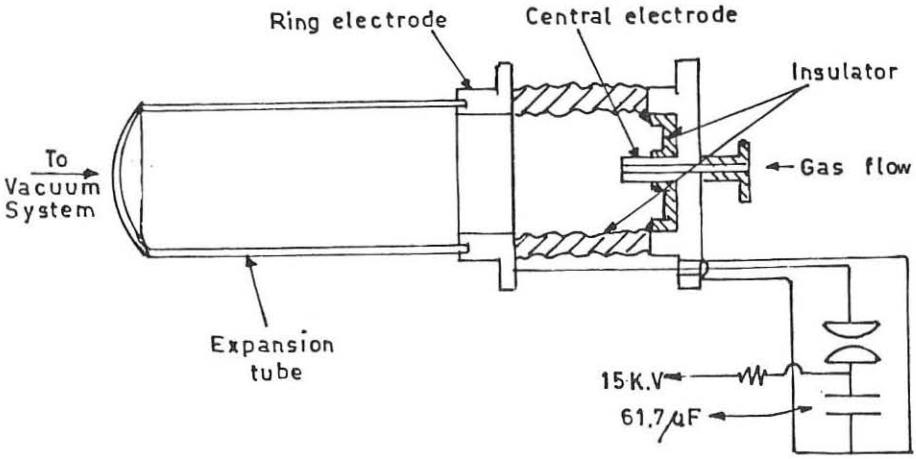

Fig.(1) Schematic diagram of the Coaxial discharge system.

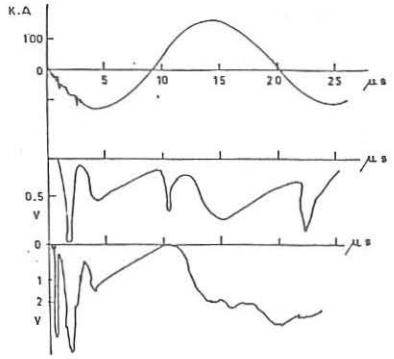

Fig. (2) Traces of discharge current, light pulse and electric probe current.

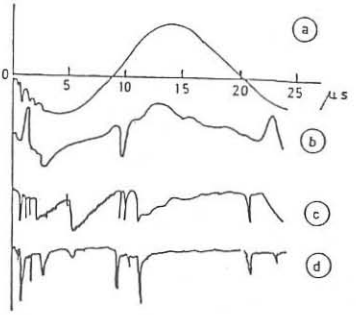

Fig. (4) Traces of the out-put signal of
a) Discharge current. b) Magnetic probe.
c) Igniting electric probe & d) X-ray probe.

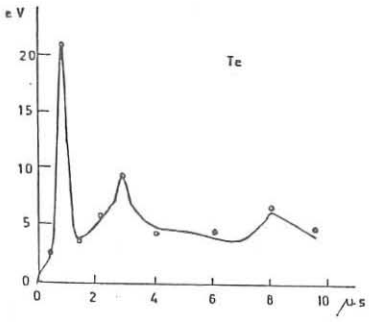

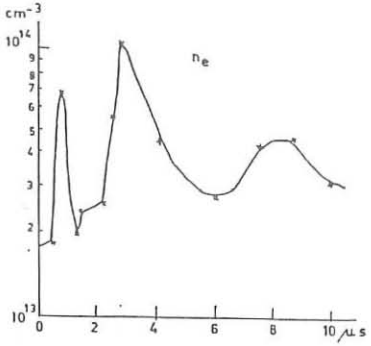

Fig. (3) Temperature and density variation with time, at 80 cm from the discharge.

EXPERIMENTS ON DOUBLE LAYERS

Čerček M. Jelić N.
J. Stefan Institute, E.Kardelj University of Ljubljana,
Jamova 39, 61000 Ljubljana, Yugoslavia

1. EXPERIMENTAL SET-UP

A strong double layer ($eV \gg kT_e$) generated in weakly magnetized plasma with additional discharge was investigated. Experiments were performed in the Single Plasma Machine at "Jožef Stefan" Institute. Experimental conditions were similar to those of Andersson [1] and Fujita et al [2]. The aparatus is shown in Figure 1. Plasma created by a hot tungsten filament cathode

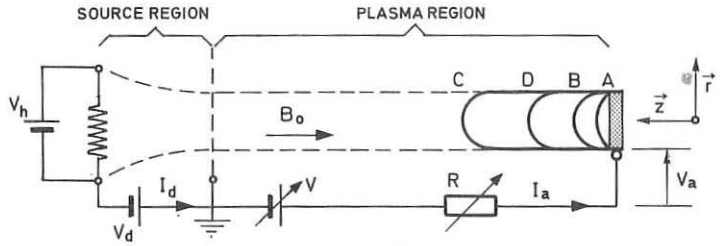

Figure 1: Schematic experimental device

source flowed along weakly converging magnetic field lines into stainless steel tube region (lenght $1.20\,m$, diameter $0.18\,m$) with homogenous magnetic field ($B_o = 70 \cdot 10^{-4}\,T$). Plasma in the experimental region was separated from the source region by a grid (G). Typically the source discharge current and voltage were $I_d = 1\,A$ and $V_d = 30\,V$ in order to obtain a highly stable discharge. The plasma in the experimental region had a space potential $V_s \simeq 0.5\,V$, a charged particle density $n = 2 \cdot 10^{15}\,m^{-3}$ and electron and ion temperatures $T_e = 2\,eV$ and $T_i = 0.1\,eV$ respectively. Plasma column diameter was approximately $5\,cm$. Working pressure of argon gas was typically $p = 4 \cdot 10^{-2}\,Pa$. For these parameters the electrons were magnetized whereas the ions were unmagnetized. To produce a double layer structure a tungsten anode plate (A) in the diameter of 1 or $2\,cm$ was biased up to $90\,V$. When the plate bias was increased to sufficiently high values above the ionization potential of the argon gas ($V_{ion} = 15.8\,eV$), a region with a new plasma in front of the anode was generated. The new plasma was occupying a well defined bright region and was characterised by a space potential close to the anode potential. The transition region between two plasmas where the potential diference is localised is known as a double layer.

2. EXPERIMENTAL RESULTS

The current-voltage characteristics for two anode plates ($d_1 = 2\,cm$, $d_2 = 1\,cm$)are shown in

Figure 2. It resembles a characteristic of a plane Langmuire probe showing first an exponential increase of the current followed by the saturation region when the plate potential is higher than plasma potential. When the potential increases further above the ionization potential for argon a thin bright sheath forms in front of the anode. With increasing plate potential it grows up to the thickness of approximately 1 cm (point B). Between the points B and D a region of negative resistance appears which is followed again by a steeper increase of current. In this region a new plasma is generated in front of the anode with a duble layer structure at the transition region to the (old) cathode plasma. The double layer moves further to the cathode side as the potential on the plate is increased. The potential difference between the anode and cathode plasma is not

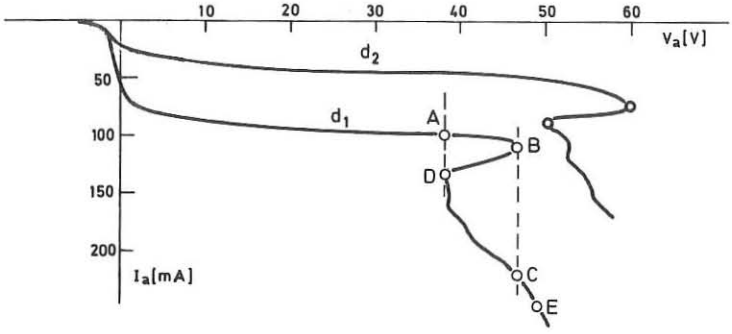

Figure 2: Anode circuit current-voltage characteristic

changed as the potential on the plate is increased. At the same time the double layer thicknees is slightly increasing. If the external resistance R is removed from the circuit, the current to the plate abruptly changes from B to C.When the potential is afterward decreasing, a hysteresys is observed ($C - D - A$). The electron and ion densities were measured axialy and radialy with cylindrical Langmuir probes (Figure 3). In the anode plasma three groups of electrons were

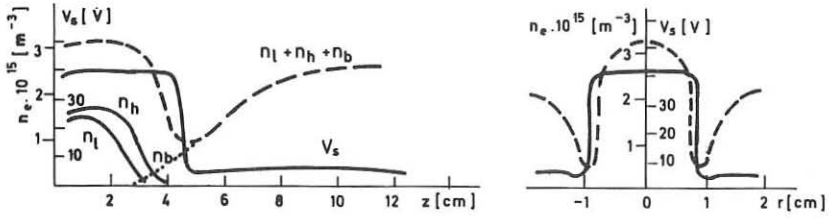

Figure 3: Plasma potential and electron densities profiles

observed(Figure 4). Two of them with approximately equal densities ($n_e{}^l = n_e{}^h = 1 \cdot 10^{15}\, m^{-3}$) having maxwellian velocity distributions were with highly diferent temperatures ($kT_e{}^l \simeq 2\, eV$, $kT_e{}^h \simeq 10\, eV$). The third group was identifyed as a maxwellian beam ($kT_e{}^b \simeq 2.5\, eV$) with drift velocity corresponding to the double layer potential. The density of the beam decreased to less than a three percent of the total electron density at the distance of a few milimeters from the

double layer. The thickness of the double layer in the axial direction is from 4 mm at the point D to 6 mm at the point C and in radial direction constantly about 2 mm. With the increasing lenght of the anode plasma the electron density is slightly increasing but the temperature is slightly decreasing (up to approximately $7eV$). Low frequency plasma potential oscilations ($60\,kHz$) as well as anode current oscilations are observed if the anode to plasma potential is positive. The amplitudes of the relative current oscilations were $I_a{}^{osc}/I_a = 0.3 \sim 0.5$. The

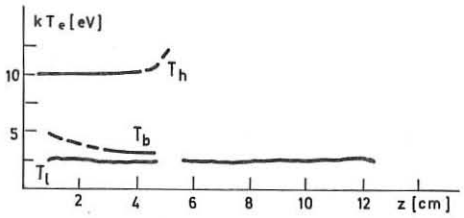

Figure 4: Electron temperature profiles

amplitude has periodical minima and maxima decaying exponentialy with increasing distance from the anode.

3. DISCUSSION

The observed hysteresis depends mainly on gas pressure and background plasma density. This phenomenon was described in [3] but the physical picture leading to such behaviour was not proposed. In this paper we shall use an extention of the simple model for the treshold for double layer formation first obtained by Torven and Andersson [4]. They started from the idea that for the formation of a double layer of such a type the ion loss rate must be balanced by the ionization rate. Furthermore the ratio of particle fluxes is expressed by the Langmuir condition $\Gamma_i/\Gamma_e = (m_e/m_i)^{\frac{1}{2}}$. They supposed that the ions are produced by the ionisation of atoms with beam electrons. The basic approximation was that the density and energy spectra of the beam are not changed because the mean free path for any kind of collissions in such plasmas is too long. We can express their considerations in the way as follows. The continuity equation for the ion flux is:

$$\nabla\mathbf{\Gamma}_i = n_a n_{eb} \int f_e(v_e)\sigma(v_e)\mathbf{v}_e d\mathbf{v}_e \tag{1}$$

where $\mathbf{\Gamma}_i$ is the ion flux, n_{eb}-electron beam density and n_a-neutral atom density. Electron beam distribution function is approximated by Dirac δ-function:

$$f_e(v_e) = \delta(v_e - ({v_{eo}}^2 + \frac{2eV_o}{m_e})^{\frac{1}{2}}) \tag{2}$$

where v_{eo} is the electron velocity in the low potential plasma and V_o is the double layer potential. Ionisation cross section is (neglecting v_{eo}) approximated by :

$$\sigma(v_e) = \alpha e(V - V_{ion}) = \alpha e\frac{m_e}{2}({v_e}^2 - {v_{ion}}^2) \tag{3}$$

where $\alpha \simeq 2.27 \cdot 10^{-21} m^2/eV$. Simple integration in velocity space gives:

$$\nabla \Gamma_i = \alpha e n_a \Gamma_e (V_o - V_{ion}) \tag{4}$$

If the problem is onedimensional with anode plasma lenght L_a the integration immediately gives:

$$\Gamma_i = \alpha e n_a \Gamma_e (V_o - V_{ion}) L_a \tag{5}$$

Using Langmuir condition the balance equation becomes:

$$\alpha e n_a (V_o - V_{ion}) L_a = (m_e/m_i)^{\frac{1}{2}} \tag{6}$$

For the experimental values $V_o = 45\,V$, $n_a = 9.5 \cdot 10^{18}\,m^{-3}$ we calculate the critical dimension $L_a = 6\,mm$ what is in excelent agreement with experimental value for the critical dimension of the sheath corresponding the knee B on the discharge curve. If the anode voltage is not allowed to fall with increasing current the B point is not stable and a jump into new anode plasma is observed. But our experimental results in the anode plasma with developed (region $D-E$)double layer show that the basic pressumption of constant beam density does not hold. Instead of the beam only two maxwellian populations were observed as in experiments of Lindberg [5]. Accordingly, we use again the balance equation (1), but choose electron distribution function to be maxwellian. After integrations, neglecting the low temperature electron population in collissional integral and using Langmuir condition, we get:

$$\alpha e n_a \sqrt{\frac{8}{\pi}} (2kT_e{}^h + V_{ion}) \exp\left(-\frac{eV_i}{kT_e{}^h}\right) L_{Th} = (m_e/m_i)^{\frac{1}{2}} \tag{7}$$

Using the experimental value $T_e{}^h = 7\,eV$ corresponding to anode voltage $V_a = 45\,V$ we calculated the critical distance for the double layer existence $L_{Th} = 3.5\,cm$ what is about $1\,cm$ less than the experimental value. With decreasing potential the temperature $T_e{}^h$ increases to $10eV$ giving shorter anode plasma in good agreement with experimental results. In our opinion the second critical point (D) corresponds to the critical dimension where the thermal ionisation is insufficient to maintain particle balance(for observed $T_e{}^h \simeq 10eV$ the plasma is about $1.5\,cm$ long). On the other hand, the beam is allready thermalised too much at this point and in the negative resistance region ($D - B$) so that the first model also can not be applied. A rigorous treatment in this region is planned. For more precisse quantitative analysis an energy balance equation should be included in the calculations. For this to performe thermalisation processes near the double layer as well as inside them must be studied. The nonhomogenity of the relevant parameters makes this problem extremly difficult.

REFERENCES

[1] Andersson D. *J.Phys.D*, **14**, 1403 (1981)

[2] H. Yagura S. and Matsuo K. *Phys.Fluids*, **27**, 2948 (1984)

[3] Amemyia H. and Nakamura Y. *Plasma Phys*, **28**, 1613 (1986)

[4] Torven S. and Andersson D. *J.Phys.D*, **12**, 717 (1979)

[5] Lindberg D. *Symposium on Plasma Double Layers*, Roskilde, Denmark, 164 (1982)

PONDEROMOTIVE VERSUS FLUID RESPONSE IN A FUSION PLASMA

M.M. Škorić and M. Kono*
The Boris Kidrič Institute of Nuclear Sciences, P. O. Box 522, 11001 Belgrade, Yugoslavia
* Research Institute for Applied Mechanics, Kyushy University, Kasuga, 516, Japan

Introduction

It has been currently understood [1)-6)] that the ponderomotive forces and the ponderomotive magnetization are complementary effects of the high frequency waves exerting the low frequency plasma motion. In this note these two are shown to be uniquely related to the ponderomotive potential which is simply expressed in terms of the linear susceptibility of a (possibly inhomogeneous) warm plasma. This work generalized a recent study, by these authors, devoted to a case of a cold magnetized plasma [5)]. Generally taken in a warm plasma, the temperature becomes perturbed under the action of high-frequency fields. However, when the temperature is given, such as in a fluid description, we show that similar formalism is applicable.

Derivation

Starting from a fluid equation

$$\partial_t \vec{v}_\alpha + (\vec{v}_\alpha \vec{\nabla})\vec{v}_\alpha = (e_\alpha/m_\alpha)[\vec{E} + \vec{v}_\alpha \times \vec{B}/c] - \vec{\nabla}\vec{P}_\alpha/m_\alpha n_\alpha \qquad (1)$$

we chose $\vec{P}_\alpha = n_\alpha[T_{\alpha\perp} 1 + (T_{\alpha\parallel} - T_{\alpha\perp})\vec{b}\vec{b}]$, $\vec{b} = \vec{B}_0/B_0$ and 1 is the unit dyadic, and taking a time average of Eq. (1) over the high frequency motion, we get an equation for the low frequency dynamics up to the second order with respect to the high frequency (hf) oscillations:

$$\partial_t \vec{v}_{\alpha 0} + (\vec{v}_{\alpha 0}\vec{\nabla})\vec{v}_{\alpha 0} = (e_\alpha/m_\alpha)[\vec{E}_0 + \vec{v}_{\alpha 0} \times \vec{B}_0/c] - \vec{\nabla}\vec{\vec{P}}_{\alpha 0}/m_\alpha N_\alpha - \langle(\tilde{v}_\alpha \nabla)\tilde{v}_\alpha - (e_\alpha/m_\alpha c)\tilde{v}_\alpha \times \tilde{B}\rangle$$

$$-(1/2N^2 m)\vec{P}_{\alpha 0}\vec{\nabla}(\langle \tilde{n}_\alpha^2 \rangle/N), \qquad (2)$$

where all the physical quantities have been splitted into high frequency ($\tilde{A}$) and low frequency (A_0) parts, and $\langle \cdots \rangle$ indicates the time average over the high frequency motion: $\langle \tilde{A} \rangle = 0$. For the nonlinear terms associated with

the high frequency motion in Eq.(2), we need only the linear response to the electric field.

Further, we introduce a vector potential $\tilde{A}$ and a displacement of the fluid through

$$\tilde{E} = -(1/c)\partial_t \tilde{A} \text{ and } \tilde{v}_\alpha = \partial_t \tilde{r}_\alpha \equiv \partial_t^2 \xi_\alpha, \tag{3}$$

where we have chosen the radiation gauge.

After integrating a linear h.f. equation of motion; we get

$$\tilde{v}_\alpha = (e_\alpha/m_\alpha c)[-\tilde{A}+\tilde{r}_\alpha \times \vec{B}_0]-(1/m_\alpha)\vec{\nabla}[(\vec{P}_{\alpha 0}/N_\alpha^2)\vec{\nabla}(N_\alpha \tilde{\xi}_\alpha)], \tag{4}$$

Taking the curl of Eq. (4) leads to

$$\vec{\nabla}\times\tilde{v}_\alpha + e_\alpha \tilde{B}/m_\alpha c = \vec{\nabla}\times(\tilde{r}_\alpha \times \vec{\Omega}); \quad \text{where } \vec{\Omega} = e_\alpha \vec{B}_0/m_\alpha c. \tag{5}$$

From Eqs. (2), (4) and (5) see Refs. 4&5 we obtain for the slow part of the equation of motion:

$$\partial_t \vec{v}_{\alpha 0} + (\vec{v}_{\alpha 0}\cdot\vec{\nabla})\vec{v}_{\alpha 0} = (e_\alpha/m_\alpha)\vec{E}_0 + [\vec{v}_{\alpha 0} + \langle n_\alpha \vec{v}_\alpha \rangle/N_\alpha]\times\vec{\Omega} - (1/2)\vec{\nabla}[\langle \tilde{v}_\alpha^2 \rangle + \vec{\Omega}\langle \tilde{v}_\alpha \times \tilde{r}\rangle$$
$$-(\vec{P}_{\alpha 0}/N_\alpha m_\alpha)\langle(\vec{\nabla}\tilde{r}_\alpha)^2\rangle] + (1/2N_\alpha)\vec{\Omega}\times\vec{\nabla}\times(N_\alpha \tilde{v}_\alpha \times \tilde{r}_\alpha). \tag{6}$$

In deriving Eq. (6) we have neglected the terms of order O(1/kL) where L is the scale length of theinhomogeneity: kL >> 1. From Eq. (6) the low frequency dynamics is self-consistently determined by the ponderomotive potential force

$$F_p = -(1/2)\vec{\nabla}[\langle \tilde{v}_\alpha^2 \rangle + \vec{\Omega}\langle \tilde{v}_\alpha \times \tilde{r}_\alpha \rangle - (\vec{P}_{\alpha 0}/N_\alpha m_\alpha)\langle(\vec{\nabla}\tilde{r}_\alpha)^2\rangle], \tag{7}$$

and the force involving the induced magnetization current

$$F_M = (1/2N_\alpha)\vec{\Omega}\times\vec{\nabla}\times\vec{M}_\alpha, \text{ where } \vec{M}_\alpha = \langle N_\alpha \tilde{v}_\alpha \times \tilde{r}_\alpha \rangle. \tag{8}$$

The above ponderomotive force and the magnetization are uniquely determined by the ponderomotive potential defined as

$$\phi^{(\alpha)} = (1/2)[\langle \tilde{v}_\alpha^2 \rangle + \vec{\Omega}\langle \tilde{v}_\alpha \times \tilde{r}_\alpha \rangle - (\vec{P}_{\alpha 0}/N_\alpha m_\alpha)\langle(\vec{\nabla}\tilde{r})^2\rangle], \tag{9}$$

through the following equations:

$$\vec{F}_p = -N_\alpha \vec{\nabla}\phi^{(\alpha)}, \quad \text{and} \quad \vec{M}_\alpha = N_\alpha \frac{\partial}{\partial \vec{\Omega}} \phi^{(\alpha)} \tag{10}$$

The magnetization gives a solenoidal (transverse) current which is equivalent to the stationary current as is clearly seen from the force-free condi-

tion in Eq. (6):

$$j_0^{(\alpha)} \equiv N_\alpha \vec{v}_{\alpha 0} + \langle \tilde{n}_\alpha \tilde{v}_\alpha \rangle = \vec{\nabla} \times \vec{M}_\alpha . \tag{11}$$

Next, we show a generalized K - χ theorem [6] on the basis of the fluid theory. Multiplying Eq. (8) by $\tilde{v}_\alpha$ and taking a time average, we obtain[5-6]

$$\langle \tilde{v}_\alpha^2 \rangle + \vec{\Omega} \langle \tilde{v}_\alpha \times \tilde{r}_\alpha \rangle - (T_\alpha/m_\alpha) \langle (\vec{\nabla} r_\alpha)^2 \rangle = -(e_\alpha/m_\alpha c) \langle \tilde{v}_\alpha \cdot \tilde{A} \rangle , \tag{12}$$

Which relates the ponderomotive potential (9) on the left side, to the linear response $\tilde{v}_\alpha$ on the right side of (12). Therefore Eq. (12) can be regarded as a generalized version of the K - χ theorem.

Turning to the eikonal representation

$$\tilde{A}_p(\vec{x},t) = \sum_j | \tilde{A}_p(\tilde{k}_j, \omega_j) 1^{i\theta_j} + c.c | , \tag{13}$$

Eq. (12) is readily reduced to the familiar expression in a homogeneous system[6]:

$$\Phi^{(\alpha)} = (1/8\pi N_\alpha m_\alpha) \chi_{pq}(\vec{k},\omega) \tilde{E}_p(\vec{k},\omega) \tilde{E}_q^*(\vec{k},\omega) , \tag{14}$$

where χ_{pq} is the linear warm plasma susceptibility.

Equation (14) is a relation between the ponderomotive potential and the linear susceptibility, which is a fluid counterpart of the so called K-χ theorem originally derived with the aid of the Lie transformation for the Vlasov plasma. This relation is powerul because it reduces the nonlinear calculation of the ponderomotive potential to the linear calculation of the susceptibility, which is usually a straightforward task.

Recently it was pointed out that the force associated with the magnetization current can be used to stabilize a flute instability[7]. Another important aspect of the foregoing magnetization is that it may be linked to experimental evidences of low-frequency nonpotential fluctuations in RF heated fusion plasmas.

Acknowledgements

This work was supported in part by the US-SFRY Joint Fund Project under US Department of Energy grant JFP-556/DOE.

References

1. L. Pitaevski, Sov. Phys. JETP 12, 1008 (1961)
2. R. Klima, Czech. J. Phys. B12, 1280 (1968)
3. Yu. S. Barash and V. I. Karpman, Sov. Phys. JETP 58, 1139 (1983)
4. M. Kono, M.M. Škorić and D. ter Haar, Phys. Fluids 30, 270 (1987)
5. M. M. Škorić, M. Kono, Phys. Fluids 31, 418 (1988)
6. J. R. Cary and A. N. Kaufman, Phys. Rev. Lett., 39 402 (1977)
7. P. L. Similon, A. N. Kaufman and D.D. Holm, Phys. Fluids 29, 1908 (1986)

A NUMERICAL STUDY OF A STABILITY OF UPPER-HYBRID SOLITONS

Hadžievski Lj., Škorić M. M.

The Boris Kidrič Institute of Nuclear Science
P.O.B.522,11001 Belgrade Yugoslavia

Introduction

A large amount of effort has been recently put into studies of plasma soliton stability problems using various analytical and numerical methods. As a rule, perturbed planar soliton appear to be unstable in two or three dimensional problems (e.g. NSE). Moreover, nonlinear stage of soliton instability often leads to a soliton collapse: a process of intensive field growth coupled to a rapid decrease of physical dimension. When the localized scale-length approachs the Debye scale, strong Landau damping plays a role of a dissipation.

In this paper we perform a two dimensional numerical investigation of a nonlinear stability of a plane upper-hybrid soliton with respect to transverse perturbations.

Basic equations

Equations describing the nonlinear interaction of high-frequency, upper-hybrid (UH) electron oscilations with low-frequency ion-sound motions are given in a dimensionless form |1-2| by

$$\nabla^2(i\psi_t + \nabla^2\psi) - \sigma\nabla_\perp^2\psi = \nabla(n\nabla\psi) \qquad (1)$$

$$n_{tt} - \nabla^2 n \pm \nabla^2|\nabla\psi|^2,$$

where ψ is the slowly varying envelope of the high frequency wave potential while n is the ion density perturbation.

Above equations written in dimensionless units |1|:

$$t \to \frac{3}{2}\left(\frac{M}{m}\right)\omega_{pe}^{-1}\, t \qquad \underline{r} \to \frac{3}{2}\sqrt{\frac{M}{m}}\, r_d\, \underline{r} \qquad (2)$$

$$n \to \frac{4}{3}(\frac{m}{M})n_0 \cdot n \qquad \psi \to (\frac{T_e}{e})\sqrt{12}\cdot\psi, \tag{3}$$

while σ has a form

$$\sigma = \frac{3}{4}\frac{\omega_{ce}^2}{\omega_{pe}^2}(\frac{M}{m}),$$

are valid in a weakly magnetized plasma ($\omega_{ce}^2 << \omega_{pe}^2$).

In the nonlinear regime of equations (1-2) the only known stationary localized solution is given in the form of a planar soliton |1-2| propagating along the magnetic field.

Assuming two-dimensional geometry with a magnetic field along the $\underline{x}$-axis and

$$\nabla \equiv \frac{\partial}{\partial x}\underline{x} + \frac{\partial}{\partial y}\underline{y}; \qquad \nabla_\perp \equiv \frac{\partial}{\partial y}\underline{y},$$

a planar soliton takes a form

$$E_s = \frac{\partial}{\partial x}\psi_s = \sqrt{2}(1-v^2)K \text{ sech } K(x-vt)\exp i[(K^2 - \frac{v^2}{4})t + \frac{Vx}{2}] \tag{4}$$

$$n_s = -|E_s|^2/(1-v^2), \tag{5}$$

here v is the soliton velocity and K is the soliton strength.
To investigate the stability on the background of the standing soliton (v=0) we introduce the transverse perturbation

$$\delta\psi = \phi\exp(iK^2t)\exp i(\Gamma t - k_y y), \quad \delta\psi << \psi_s \tag{6}$$

where ϕ is slowly varying on x and t, and k_y is the perturbation wavenumber, while Γ is the instability growth rate.

Numerical results

The equations (1-2) are solved numerically in two dimensions by the spectral Fourier method with respect to the space coordinates, assuming periodic boundary conditions with periodicity lengths L_x and L_y. Nonlinear terms are computed by transforming back to the x-y space. Time integration is performed by using an explicit method with an accuracy of a second order in a time step.

A spatial resolution of 32x32 points and a time step 0.001 has been used, with a regular check on the conservation of the plasmon number (N) and the Hamiltonian (H).

The initial conditions for the soliton potential are given by the equation (4) and the initially perturbed ion density by

$$n = n_s(1 + 2\varepsilon \cos k_y y) , \qquad (7)$$

where ε is the perturbation parameter.

Runs with $\sigma=0$ agree with the results of |3|, both, in its linear and developed (self similar like) stage of the instability. Moreover, the spectral dependance of Γ agrees with the analytical and numerical results of|4|.

In order to investigate an influence of a week magnetic field on: the linear growth rate (Γ) and a developed (self-similar like) stage of instabilities, we have chosen in all runs with $\sigma\neq0$, the following parameters:

$$K = 2,\ L_y = 6,\ L_y = 16\quad \varepsilon = 0.1$$

These calculations shows that an increase of a magnetic field strength ($\sigma\to0$-50) leads to an increase of the linear growth rate Γ, which is in an agreement with the analytical prediction of |5|. On fig.1. we plot the total wave energy $|E(x,y)|^2$ for a) $\sigma=0$, b) $\sigma=30$ in t=0.3 and t=0.8

In the developed stage of the instability numerical results show agreement with theoretical predictions of |2|. Namely, during the time evolution, the transverse dimension of the localized structure changesmore rapidly than the longitudinal dimension. Therefore its pancake shape becomes less asymmetic (fig. 2).

More detailed investigation is in progress.

References

|1|. E.H. Kuznetsov, A.M.Rubenchik, V.E. Zakharov, Phys. Reports 142(3), 105 (1986)

|2|. V.V. Krasnosel'skikh, V.I. Sotnikov, Fiz. Plazmy 3, 872 (1977)

|3|. N.R. Pereira, R.N. Sudan, Phys. Fluids 20(6), 936 (1977)

|4|. D. Anderson, A. Bondeson, M. Lisak, J. Plasma Physics 21(2) 259 (1979)

|5|. H.L. Rowland, Phys. Fluids 28(1), 190(1985)

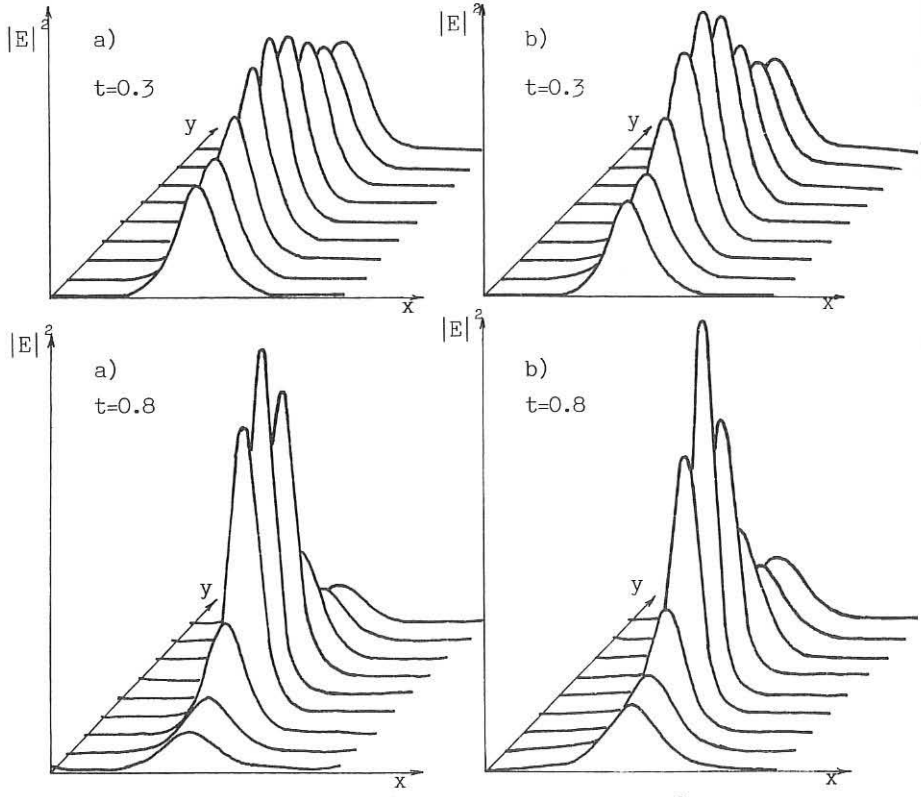

Fig.1.

Fig.2.

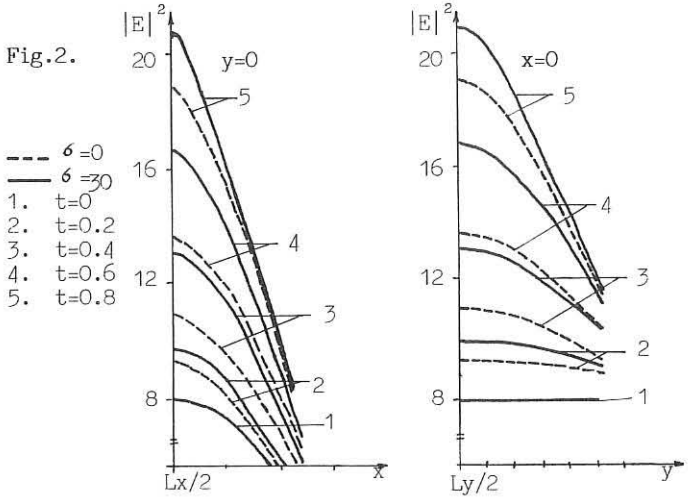

--- $\delta = 0$
—— $\delta = 30$

1. t=0
2. t=0.2
3. t=0.4
4. t=0.6
5. t=0.8

UPPER-HYBRID SOLITARY VORTICES

U. de Angelis
Department of Physics, University of Naples
80125 Naples, Italy

D. Jovanović
Institute of Physic, P.O.Box 57
11000 Belgrade, Yugoslavia

P. K. Shukla
Institute of Theoretical Physics, Ruhr-University Bochum
4630 Bochum, Federal Republic of Germany

Nonlinear theory of electrostatic uper-hybrid waves in magnetized plasmas has been inspired by the success of the theory of strong Langmuir turbulence. In a strictly one-dimensional case, interaction of an upper-hybrid wave, propagating perpendicularly to the ambient magnetic field with low frequency density perturbations in a weakly magnetized plasma, $|\Omega_e| \ll \omega_{pe}$ can be described by a nonlinear Schrodinger equation[1]. Consequently, one may expect that small density perturbations are parametrically unstable, saturating into NLS-type pancake solitons. It is well known that such solitons are unstable with respect to small perurbations perpendicular to the direction of their propagation. Low frequency density perturbations in magnetized plasmas are essentially two-dimensional in the nonlinear regime, due to the presence of the convective nonlinearity which is of the Poisson-bracket type, and the existence of pancake solitons in such systems is questionable. A dominating feature of the low frequency turbulence in magnetized plasmas is the existence of two-dimensional wortex structures, which may be associated with a large number of linear modes[2], such as convective cells, Alfven waves[3], drift waves[4], etc.

In this paper we study the quasi-three dimensional electrostatic turbulence of magnetized plasmas, which can be interpreted in terms of the interaction of upper-hybrid waves with plasma vortices, and we show that a new type of vortices becomes possible in the presence of the pump. We assume an electrostatic pump wave, propagating (almost) perpendicularly to the homogeneous magnetic field $\vec{e}_z B_o$. Plasma is weakly inhomogeneous, and the plasma density is given by $N(x) = N_o + x\frac{dN}{dx}$. Representing the high-frequency potential in the form:

$$\phi_H = \frac{1}{2}\,\phi_{HO}(\vec{r},t)\, e^{-i\omega_{pe}t} + c.c. \qquad (1)$$

where $\omega_{pe} = \left[\frac{N_o e^2}{m_e \varepsilon_o}\right]^{1/2}$, with the amplitude ϕ_{HO} being slowly varying compared to the rapid oscillations $e^{-i\omega_{pe}t}$, we can write the following equation for the evolution of the pump wave amplitude:

$$\nabla_\perp\left\{\left[\,2i\omega_{pe}\left(\frac{\partial}{\partial t}+\vec{v}_{eL}\nabla_\perp\right) - \Omega_e^2 - \frac{\omega_{pe}^2}{N_o}\left(x\frac{dN}{dx}+n_{eL}\right)+3v_{Te}^2\nabla_\perp^2\,\right]\nabla_\perp\phi_{HO}(\vec{r},t)\right\} = 0 \qquad (2)$$

Here $\vec{v}_{eL}$, and n_{eL} are low frequency components of the electron velocity, resp. density, and v_{Te} is the electron thermal velocity. In the derivation of (2) we used assumptions of a weakly magnetized plasma, $|\Omega_e| \ll \omega_{pe}$, and of purely electrostatic perturbations. On the low frequency scale we use the standard drift-wave scaling $\frac{\partial}{\partial t} \sim \vec{v}_{eL}\nabla \sim \vec{v}_{iL}\nabla \ll \Omega_i$ and assume cold, two-dimensional and linear ions. Then the ion continuity readily yields:

$$\left[\frac{\partial}{\partial t} + \frac{1}{B_o}(\vec{e}_z\times\nabla_\perp\phi_L)\nabla\right]\left[x\frac{dN}{dx} + n_{eL} + \frac{\varepsilon_o}{e}\left(1+\frac{\omega_{pi}^2}{\Omega_i^2}\right)\nabla_\perp^2\phi_L\right] = 0 \qquad (3)$$

while the parallel electron momentum equation in the zero electron mass limit yields a Boltzmann distribution:

$$\phi_L + \phi_P + \frac{T_e}{N_o e}\, n_{eL} = 0 \qquad (4)$$

The low-frequency electron velocity is then equal to zero:

$$\vec{v}_{eL} = \frac{1}{B_o}\vec{e}_z \times \nabla_\perp \left(\phi_L + \phi_P + \frac{T_e}{N_o e} n_{eL}\right) = 0 \qquad (5)$$

Here ϕ_L is the low-frequency potential, and ϕ_P is the ponderomotive potential:

$$\phi_P = \frac{e}{2m_e \omega_{pe}^2} \left| \nabla_\perp \phi_{HO}(\vec{r},t) \right|^2 \qquad (6)$$

Substitution of (4) into (5) gives the Hasegawa-Mima equation[4], driven by the ponderomotive force.

We seek a solution traveling along the y axis with the velocity v_g, $\frac{\partial}{\partial t} = -v_g \frac{\partial}{\partial y}$. We use the parametric approximation, assuming a long-wavelength pump (compared to the scale size of the LF perturbation) in the form $\nabla\phi_{HO} = -\vec{e}_y E_o + \nabla\delta\phi$, ($|\nabla\delta\phi| \ll E_o = \text{const.}$). Then we can write $\phi_P = \phi_{PO} + \delta\phi_P$, where:

$$\phi_{PO} = \frac{eE_o^2}{2m_e\omega_{pe}^2} \quad ; \quad \delta\phi_P = -\frac{\phi_{PO}}{E_o}\frac{\partial}{\partial y}(\delta\phi + \delta\phi^*) \qquad (7)$$

and eq. (2) is simlified to:

$$\left(9\frac{v_{Te}^2}{\omega_{pe}^2}\nabla_\perp^4 + 4\frac{v_g^2}{v_{Te}^2}\frac{\partial^2}{\partial y^2} \right) \frac{\delta\phi_P}{\phi_{PO}} = 6\frac{\partial^2}{\partial y^2}\frac{n_{eL}}{N_o} \qquad (8)$$

The LF equation (2) can be integrated once to give:

$$\left(\lambda_T^2\nabla_\perp^2 - 1\right)\left(\delta\phi_P + \frac{T_e}{N_o e} n_{eL}\right) + \delta\phi_P - B_o u x = F\left(\delta\phi_P + \frac{T_e}{N_o e} n_{eL} + B_o v_g x\right) \qquad (9)$$

where $u = \frac{dN}{dx}\frac{T_e}{eB_o N_o}$, $\lambda_T^2 = \frac{N_o T_e}{N_o e^2}\left(1 + \frac{\omega_{pi}^2}{\Omega_i^2}\right)$, and F is an arbitrary function. In the usual way, we adopt F to be a linear function, whose derivative $F'(=\text{const.})$ has different values inside, and outside of an arbitrary circle in the x-y plane with the radius r_o. Then, using (8), (9), we find the solution in the form of a dipole vortex:

$$n_{eL} = \cos\theta \left[\alpha_1 I_1(A_1 r) + \beta_1 K_1(A_1 r) + \alpha_2 I_1(A_2 r) + \beta_2 K_1(A_2 r) - \alpha r \right] + \phi_5 \qquad (10)$$

Here $r = (x^2+y^2)^{1/2}$, $\theta = \text{arctg}\,\frac{y}{x}$; I_1, K_1 are Bessel functions of the first order, and $\mathcal{O}_5$ is a small correction due to the presence of the fifth, and higher, cylindrical harmonics; α_i, β_i $(i=1,2)$ are constants of integration, and:

$$A_1^2 + A_2^2 = \frac{1}{\lambda_T^2}\left[1+F'-\varkappa\left(\frac{v_g^2}{v_{Te}^2}+\frac{3}{2}\frac{e\phi_{P0}}{T_e}\right)\right]$$

$$A_1^2 A_2^2 = \frac{\varkappa}{\lambda_T^4}\left[(1-F')\frac{v_g^2}{v_{Te}^2}-\frac{3}{2}\frac{e\phi_{P0}}{T_e}F'\right]$$

$$a = \frac{eN_0B_0}{T_e}\left(u+F'v_g\right)\left[F'+1+\frac{3}{2}\frac{e\phi_{P0}}{mv_g^2}\right]^{-1} \quad ; \quad \varkappa = \frac{1}{9}\left(1+\frac{\omega_{pi}^2}{\Omega_i^2}\right) \qquad (11)$$

All constants $(\alpha_1, \alpha_2, \beta_1, \beta_2, F')$ are discontinuous at $r=r_0$. Finiteness at $r\to\infty$ requires $\alpha_1^{(+)}=\alpha_2^{(+)}=\beta_1^{(-)}=\beta_2^{(-)}=0$, and $F'^{(+)}=-\frac{u}{v_g}$ (superscripts $(-)$, $(+)$ correspond to solutions for $r<r_0$, and $r>r_0$, resp.). Remaining five constants of integration, and the radius of the vortex core, r_0, can be calculated in terms of the group velocity v_g, which is a free parameter. We require continuity of n_{eL} and $\delta\phi_p$, and of their first and second derivatives, at $r=r_0$, which yields six equations from which we can find these six parameters.

Solution presented here contains a new nonlinear mode, which does not exist for the case of the non-driven Hasegawa-Mima equation. Furthermore, size of the vortex is not a free parameter, but it is determined by the characteristics of the pump. Upper-hybrid vortices are expected to be stable structures, representing the final stage in the development of the flute-type electrostatic turbulence. They can significantly contribute to the particle transport in RF heated fusion plasmas, since particles trapped in such vortices can be carried to large distances.

REFERENCES:

1. K. Dyste, E. Mjølhus, H. Pecseli, L. Stenflo: Plasma Phys. 20, 1087, (1978)
2. V. Petviashvili, O. Pokhotelov: Fiz Plazmy 12, 1127,(1978)
3. D. Jovanović: Phys. Fluids 30, 417, (1987)
4. A. Hasegawa, K. Mima: Phys. Fluids 21, 87, (1978)

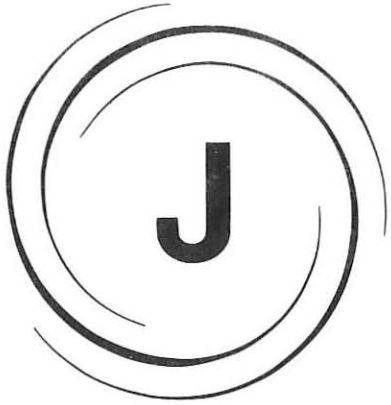

Inertial Confinement Physics

J

BINARY SHOCK WAVE FORMATION STRUCTURE IN HYDROGEN PLASMA

A.A.Filyukov

Keldysh Institute of Applied Mathematics
USSR Academy of Sciences

A stationary structure of plane shock wave (SW) in two--temperature hydrogen plasma was studied in [1-4]. An asymptotic stage of propagation of spherical SW in plasmas and gases was analized in connection with the theory of strong explosion [5-7]. The SW were investigated in the astrophysical hydrogen plasma [8], in the process of disassamble of laser pellets in rarefied atmosphere [9,10], and also in computation modelling of this effect [12].

The results of numerical experiments given in this paper are dealt with new effects of a nonstationary structure of spherically symmetrical SW propagating in hydrogen and its plasma. As was observed in computations the SW propagation has two distinct stages which may be characterized by different laws of propagation and qualitative structure properties. At the first stage of formation in the two-temperature hydrogen plasma a new phenomenon of emergency of secondary SW was discovered. This SW is localized at the electron heat conductivity wave front. According to the classical description[1] the electron flow front leaves far behind the hydrodynamical discontinuity which coincides with ion temperature jump. So at the formation stage the secondary SW propagates with the nonlinear front of electron heat conductivity against the undisturbed background ahead of the primary SW as its forerunner, forming in combination a binary nonstationary SW structure. Once the double structure has been formed its further evolution consists in the subsequent pursuit of the forerunner by the primary wave. It is completed by their join in a single asymptotic SW. The moment of joining means the start point of the second asymptotic stage of the propagation. The prolongation of the first formation stage has an order of the characteristic relaxation time for the electron-ion temperature disruption. In the asymptotic SW the disruption of temperatures is no longer observed.

The pursuit process as well as the joining of the primary and secondary SW run differently in the cases depending on the competition between the heat conductivity and electron--ion heat exchange. In the case of intensive heat conductivity the waves joining occurs so that the forerunner absorbs its primary SW, the last degrading step by step, and to the

joining moment its amplitude is considerably smaller in comparison with the forerunner. In the opposite case, when the energy flow to the forerunner zone is weaker than the rate of intercomponent exchange the primary SW is larger by amplitude than the forerunner at the last moment before joining.

In the diagrams cited below the pursuit process and the joining of primary (o) and secondary (•) SW are illustrated, where R_o denotes the joining radius.

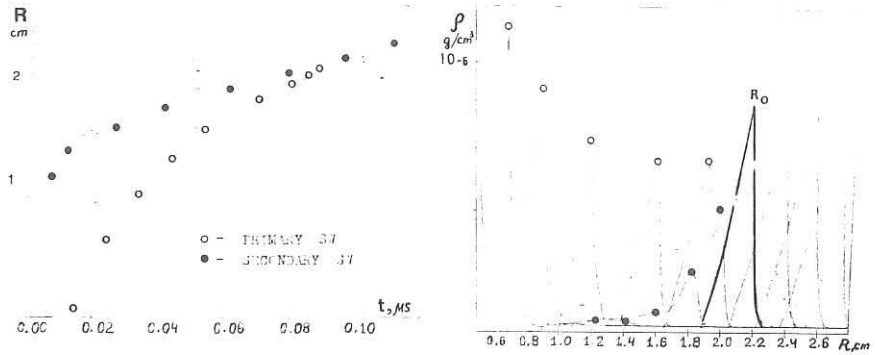

The origin and growth of the secondary SW are due to the energy pumping from the electron to ion component. This process is most intensive in hydrogen plasma in contrast to the heavier elements, for instance, nitrogen, that was taken for comparison in computational experiments. In nitrogen plasma the secondary SW does not emerge. The physical reasons of secondary SW localization are determined by rate of intercomponent energy exchange which reaches its maximum value exactly at the front where the electron temperature sharply falls to the background level. Due to local energy stream from electron to ion component, gradients of ion temperature and pressure here arise and grow. In the presence of viscosity they are the final reason of the secondary SW formation.

The primary (P), secondary (S) and asymptotic (A) SW possess the distinct propagation scaling laws-power functions form- that determine the radius with time dependence:

$$R_p = P\,t^i; \qquad R_s = S\cdot t^j; \qquad R_A = A\cdot t^a;$$

One may establish with sufficient accuracy the relation:

$$i + j = 2a$$

that allows to express the propagation law for the asymptotic SW with the help of laws for P and S waves

$$R_A = \sqrt{PS}\cdot t^{(i+j)/2};$$

In connection with this fact one may consider the stage of contemporary existence of two SW as a period of binary formation of asymptotic flow from two intermediate selfsimilar ones. The process as a whole is certainly not selfsimilar, though each flow considered separately on certain time and spatial intervals has typical features of intermediate selfsimilarity [7].

Specifically, the asymptotic SW propagating through the hydrogen plasma has the time index a=2/5, corresponding to the solution for the adiabatic point explosion [5]. In the case when the ionizing SW propagation through neutral hydrogen was considered with ionization in the quasi-equilibrium Saha approximation taken into account, the selfsimilarity index decreases to a=1/3. The profiles of main gasdynamic characteristics of the flow behind the ionizing SW (ISW) are maintained from the joining moment. They disagree with the Sedov-Taylor solution and essentially differ from the other limiting case described by Ryzhov-Taganov for the homothermal point explosion [6]. The computed R(t) diagrams for plasma shock wave (PSW) and ISW are cited below. Comparison of the relative density distributions in the steady selfsimilar flow for Sedov-Taylor (1), Ryzhov-Taganov (2) solutions, as well as for case of ISW (3) is given below.

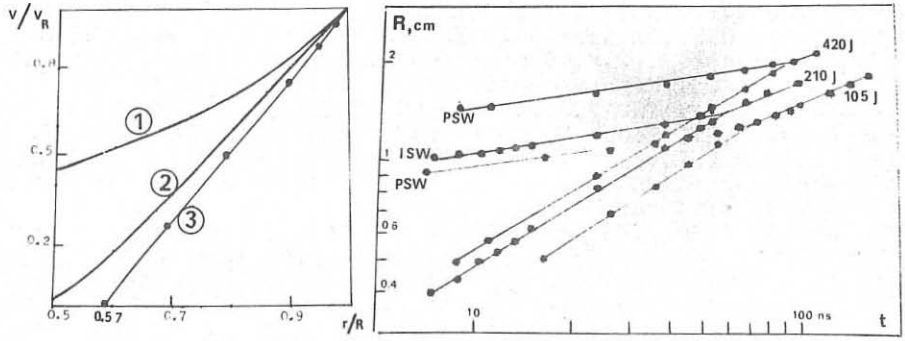

Disagreement in the velocity profile which changes its sign at r/R = 0.57 in case (3) of ISW is most significant. It means the existence of selfsimilar expanding region where the velocities are directed to the symmetry center. In the flow (2) there is an analogous central region extending to the relative radius r/R = 0.5 where the motion is absent, while in the solution (1) all velocities are positive. In connection with this it is interesting to notethat at joining moment the disassemble of the pellet matter terminates. The maintained profile of "frozen" in its matter temperature deminishes with the spread of central region.

As was shown by direct numerical experiments with various models of electron heat conductivity [11] the small value of conductivity coefficient or the introduction of definite limiting factor "f" for the electron heat conductivity have a great influence on the formation structure, and when the limiting factor has a value f = 0.1 the binary structure disappears. The experimental data [9] confirm the existence of double structure in hydrogen and its absence in air in accordance with the results of this paper. It allows us to consider the above value of the limiting factor as its minimum minimorum.

As was mentioned above, at the asymptotic stage the heat conductivity is not essential, and lets us to compare the ionizing explosion with the Barenblatt-Sivashinsky solution [7]. The value of a = 0.33 means in terms of this solution the similarity of ionizing explosions with equal product of explosion energy times the joining radius R_o.

References

1. Jukes Y., J.Fluid Mech. 1957,3,275
2. Tidman B.,Phys.Rev.1958,111,1439
3. Shafranov V.D.,JETP1957,32,1453
4. Imshennik V.S.,JETP1962,42,236
5. Sedov L.I.,PMM,1946,10,241
6. Ryzhov O.S.,Taganov G.I.,PMM,1956,20,545
7. Barenblatt G.I.,Sivashinsky G.I.,PMM,1970,34,685
8. Kaplan A.S. Mezhsvesdnaia sreda, M.:GIFML,1963
9. Zakharenkov Yu.A.,Zorev N.N.et al.Trudy FIAN,1983,133,147
10. Basov N.G., Masur M.Yu. et al. Pisma JETP,1987,46,8,320
11. Levanov E.I.,Sotsky E.N.,Filyukov A.A. Ob odnoi vosmojnosti eksperimentalnogo opredeleniya velichiny ogranicheniya potoka electronnoi teploprovodnosti. Zvenigorod,1985
12. Goldin V.Ya.,Chetverushkin B.N.,JETP,1975,68,1768

LASER SIMULATION OF IMPACT OF PARTICLES AND FOIL ACCELERATION

S. Borodziuk, J. Kostecki, J. Marczak

Kaliski Institute of Plasma Physics and Laser Microfusion
00-908 Warsaw, POLAND, P.O. Box 49

The paper presents experiments dealing with interaction of Nd:glass laser radiation with plane Al foils. Investigations contained laser simulation of the process of collisions between macroparticles and target and the measurement of velocity of accelerated foils.

Experimental system for laser simulation of particles impact against the target consists of the Nd:glass laser (λ = 1.06 μm, $E_L \leq 20$ J, $\tau_L \approx 3$ ns), vacuum chamber ($p = 5 \times 10^{-3}$ N/m^2) and of diagnostic apparatus: calorimeters for measurement of laser energy and angular distributions of scattered laser radiation, camera obscura for registration of hot plasma area, ion collectors for registration the expansion of ions emitted from the plasma, fast streak camera for measurement of plasma expansion velocity and foil acceleration (Borodziuk et al. 1984). Al targets were 4-6 mm in diameter and 12-3000 μm thick.

In the conditions of the carried experiment the diameter of craters appearing in targets changed in the range from 200 to 400 μm and their depth h_k in the range from 100 to 200 μm depending on the laser parameters .

The diameter of laser beam focus, equal to the diameter of particle simulated by laser, was about 100 μm. Both the diameter and the depth of craters increased with the laser pulse energy. At approximation by a power function it was achieved

$$\varnothing_k = 186 E_L^{0.25}$$

what is the result similar to the dependence obtained in the papers (Zwiegenbaum et al. 1977; Burton 1983)

$$\varnothing_k = 254 E_L^{0.25}.$$

Volume of the craters was from 2×10^{-6} to 2×10^{-5} cm^3. Mass of the matter thrown out of the crater was much greater than the mass of the target material ionized by laser radiation determined from measurements done by ion collectors.

Craters had a shape close to a hemisphere with characteristic bank around the edge; the bank was probably created in result of rapid solidification of liquid effluent target material. The height of this bank changed in the range 0-100 μm, in most

cases it was proportional to the laser energy.

The shape of craters made by the focused laser beam in our experiment (Kostecki et al. 1987) was similar to craters made by fast macroparticles (Schneider 1979). It confirms the correctness of simulations carried out so far. Fig. 1 shows the view of the target surface after laser shot and its intersection.

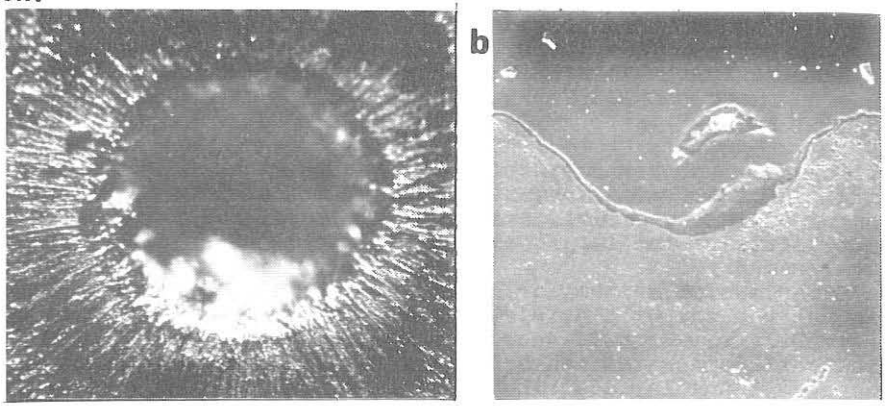

Figure 1. View of 1 mm Al target surface in vicinity (a) and intersection (b) of the crater (crater diameter 350 μm).

Backward surface of the target of the thickness of 1 mm was not disturbed even at maximum energies of the laser. However, for thinner targets we observed a bulge or a wrench of material and at last - there was a hole.

For 120 μm thick target it was stated that even the energy of the order 0.5-1.0 J causes tearing of the target backward surface on the diameter of the order 150-250 μm (crater is not perforated), while energy of 3-4 J causes creation of holes of the diameter about 200 μm (Fig. 2).

The aim of experimental laser simulation of collisions of superfast particles (e.g. cosmic dust) with solid targets (e.g. shield of a cosmic probe) was to find relation between the parameters of the used laser and the basic parameters of particles and to determine scaling laws for craters made in result of laser radiation interaction with the target.

The main idea of laser simulation of the analysed problem is the assumption that the effect of irradiation the target by a laser beam, pulse of which has energy E_L, time duration τ_L and focus diameter $\varnothing_L$, is similar as the one in the collision of target and particle of the diameter $\varnothing_p$, length L_p (cylindrical symmetry) and velocity v_p, under the condition that pressures, sizes and reaction time are equal, respectively

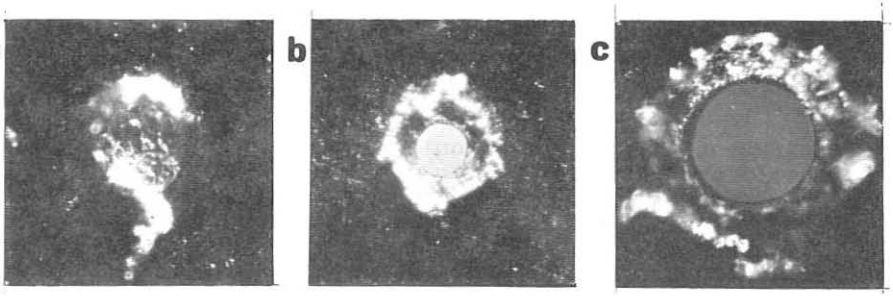

Figure 2. View of the back of the target (120 μm Al). a - 0.56J, b - 2.9 J, c - 4.4 J.

$$p_L = p_p \ , \ \tau_L = \tau_p \ , \ \varnothing_L = \varnothing_p \ .$$

Such attitude was used, among others, in the papers (Pirri 1977; Bibring et al. 1983; Borodziuk et al. 1984) and also it was a basis for the interpretation of results in this paper. Thus, the particle velocity can be calculated as follows

$$v_p = A^{1/2} - (a/2b)(1 + \sqrt{\varrho_p/\varrho_T})$$

where

$$A \cong (100/\varrho_p b)(1 + \sqrt{\varrho_p/\varrho_T})p^{2D} + [(a/2b)(1 + \sqrt{\varrho_p/\varrho_T})]^2.$$

Constants a and b are, respectively

for the variant "Al-Al": $a = 5.39 \times 10^5$ cm/s, $b = 1.34$
for the variant "1-Al": $a = 3.07 \times 10^6$ cm/s, $b = 1.30$.

The expression on the pressure p^{2D}, regarding laser beam geometry, was assumed in the form given by Harrach and Szoke (1982)

$$p^{2D}[\text{Mbar}] = 8I^{0.7}[10^{14}\ \text{W/cm}^2]/[1 + (L_{ac}/r_L)\sin\alpha]^{1.4}$$

where α is the half-angle determining the beam convergence, and $L_{ac} \sim c_s \tau_s$ (c_s is the sound velocity in the expanding plasma).

Having calculated the value v_p, then the length L_p of the simulated particle may be obtained from the following dependence

$$p_L \tau_L = \varrho_p L_p v_p .$$

Velocities of simulated particles, calculated in this way, are in the range $(1\text{-}2) \times 10^6$ cm/s ("Al-Al") or $(1.5\text{-}3) \times 10^5$ cm/s ("1-Al"). On the basis of these values, considering the craters measured in the experiment, it is possible to determine scaling laws for relative volume of craters as a function of velocity of simulated particles

$$K \equiv V_k / V_p$$

where V_k is the crater volume, and V_p is the particle-bullet volume. They are as follows

$$K_1 = 1.14v_1^{1.44} \quad \text{for "Al-Al"} \quad ; \quad K_2 = 1.02v_2^{1.21} \quad \text{for "1-Al".}$$

In case of "Al-Al" one should point out that there is a good compatibility with the results obtained by Bibring et al. (1983).

The laser radiation pulse used in the experiment enables to achieve the velocity of simulated collisions "particle-target" in the range 2×10^6 cm/s ("Al-Al") or 3×10^6 cm/s ("1-Al"). To obtain higher velocities one should use more intensive laser.

Analysing the problem of interaction between superfast macroparticles and metal targets, it is possible to use the laser to accelerate a fragment of thin foil obtaining a real, not simulated by laser, bullet (the velocity of the order 10^6 - 10^7 cm/s). The bullet obtained in such a way has the diameter equal to the diameter of the laser beam focus and the length equal to difference in thicknesses of the foil and the laser evaporated layer. Superfast shadowgraphy (with the use of a streak camera) was used in investigations of foil acceleration velocity. Maximum achieved and measured velocity was 2.2×10^6 cm/s for the 12 μm foil at the power density 3×10^{13} W/cm^2. When ablatively accelerated foil has a proper thickness of the order of several μm it is possible to obtain much higher velocities of collisions "particle-target". Such investigations are actually carried out and their main aim is, apart from the above mentioned possibility of achieving higher velocities of accelerated particles, to verify the method of laser simulation being the basis of this paper.

REFERENCES

BIBRING J. P. et al. (1983) J. Phys. Lett. **44**, 189.

BORODZIUK S., KOSTECKI J., NAGRABA S., PARYS P. (1984) IPPLM Report No 9/III/84.

BURTON W. M. (1983) Advances in Space Research, Proceedings of COSPAR Symposium on Impact Processes, Ottawa 1982, **2**, 12.

HARRACH R. J. and SZOKE A. (1982) Report UCRL-86798.

KOSTECKI J., BORODZIUK S., PARYS P., MARCZAK J., RYCYK A. (1987) IPPLM Report No 6/III/87.

PIRRI A. N. (1977) Phys. Fluids **20**, 221.

SCHNEIDER E. (1979) ESA Report SP-153, 103.

ZWEIGENBAUM S., GAZIT Y., KOMET Y. (1977) Plasma Physics **19**, 1035.

THE INVESTIGATION OF THE NONEQUILIBRIUM PROCESSES WITHIN THE LASER PRODUCED STREAMS.

V.A.Gribkov, V.Ya.Nikulin
P.N.Lebedev Phys.Inst., Moscow, USSR

G.I.Zmievskaya
M.V.Keldysh Inst.of Appl.Math., Moscow, USSR

Asbtract.

The nonequilibrium processes taking place in the colliding laser produced streams are investigated experimentally and numerically.

Under the experimental investigations of the laser produced plasma /1,2/ the anomalous ion polarisability of the carbon ions have been discovered. For the plasma experiment the installation analogous to the discribed one in /3/, have been used. The power flux density at the focusing point have been within the limits $(1\div5).10^{13}$ W/cm^2. The Nd-glass laser beam have been splitted into two beams with the energy of 30J each (pulse duration 12 ns). The focusing on every target have been performed on the side, looking for the other target. These targets are the $(CH_2)n$ particles, having the cubic shape of the 0.2 mm size. They are hung up with the 1 mm distance between them by means of very thin threads. In these experiments the method of the two wave-lengths interferometry have been used /3/ (λ_1=0.69 mkm, λ_2=0.35 mkm), due to which the interferograms of both free expanding and colliding laser flares have been displayed for the moment of time 10 ns later the begining of the heating pulse. The plasma refractive index is:

$$n-1=-4.49.10^{-14}\,\lambda^2\,Ne + 2\pi\sum_z\sum_i N_i^z\,\alpha_i^z \qquad (1)$$

where α_i^z - polarizability of the ion (atom) in i - state with the charge number Z. The results of the two wavelength interferogram prosession is shown in Fig.1. It is clear, that

the electron (2) and, especially, the ion (1) polarizabilities at the collapse region are increased sharply in comparison with those for free expanding plasma (3,4) from one particle. The polarizability of the excited ions /1,4/ is very close to the electron one. Special estimations show us /2,3/ the realization of "the freezing" of the ionization states and $T_e \ll T_i$ both for the free expanding and for the collapsing plasma streams. Anomalous high value of the ionic polarizability, recieved in the experiments of laser flare collapse, gives us an evidance, that the considerable quantity of the ions is in the excited states. The difference between the experimental ionic distribution function for the excited states and the equilibrium one can be resulted from the photorecombination and the inelastic collisions, including the charge-exchange processes. Indeed, under $T_e \sim 1$ eV, $Z \sim 10$ and $N_i \sim 10^{20}$ cm^{-3} the characteristic time of the photorecombination $\tau_{phr} \sim 10^{-9}$ s, i.e. smaller than τ_{ie}-time of the existance of the cold electrons. Time of the radiation decay of the ionic levels with a high quantum number n: $\tau_d \sim n^{4.5}/Z^4$ can be of the order of $10^{-9} \div 10^{-10}$ s. As for the inelastic ion-ion collisions, the corresponding crosssection can be smaller than 10^{-19} in case of the keV ions. Consequently, under $N_i \sim 10^{20}$ cm^{-3} the characteristic excitation time will be $\tau_{ex} \ll 10^{-9}$ s. Especially it is necessary to note the possibility of the creation of the inverse population in this kind of plasma due to methastable levels /2/ because of the very low electron temperature. So, this plasma can be used as an active media for the X-ray lasers. It is clear, that the abovementioned processes can take place also under the cylindrical cumulation (pinch-effect) and in the plasma of the cumulative streams.

For the investigation of the kinetics of the free streaming and colliding laser produced plasma streams we applied

the numerical methods of the solutions of the Bolzmann kinetic equations, which described a space - time evolution of the one-particle distribution function through the velocities and the nonequilibrium populated levels of the internal energy for the homogeneous expansion (compression) of the plasma /5/. It this way we have done the numerical procession of the stochastic differencial equation system /6/, where the collisions are reflected by the Markov jumps. The constancy of the expansion velocity allows us to use the equations, stochastic analog of which permits the space - homogeneous model. The grounds of such approach are contained in /7/.

So, during the time T in the media at first the process of the collisional relaxation is modeled in the unit volume with the step Δt_1, and then with the step Δt_2 the collisionless expansion with the velocity V_0 is examined; $\Delta t_{1,2} \in [0,T]$.

As an example of the model usage we analyse the ionization-recombination processes and super-elastic collisions, and also the processes of the excitation of the internal energy levels (due to e-i collisions). We have analysed two variants of the media - carbon plasma with T_e^o=1 keV and T_e^o=1 eV. At 1^{st} case the mixture has contained the multistriped ions at the ground state, and at the 2^{nd} case-two excited levels of the CVI ions have been taken into consideration. At Fig.2^a the deposit of the electron polarizability (1) is higher, than those from ions CV, CVI and Z=6(2). But from Fig.2^b it is shown, that in the plasma with the cold electrons and the excited ions the ion polarizability (2) appears to be of 1÷2 orders of magnitude higher than the electron one during all the time of the numerical experiment.

Authors are grateful to A.A.Pyarnpuu, V.I.Shematovich, O.N.Krokhin and M.Ya.Marov for the assistance and fruitful discussions.

References.

1. Gribkov V.A., Nikulin V.Ya., Sklizkov G.V., Lebedev Inst. Reports N 2, 45 (1971).
2. Afanasiev Yu.V., Gribkov V.A. et.al., Preprint FIAN N° 87, M. (1973).
3. Basov N.G., Gribkov V.A. et.al., JETP, 54, 1073 (1968).
4. Dalgarno A., Advances Phys., 11, N°44, 281 (1962).
5. Cheremisin F.G., DAN USSR, 163, N°2, 315 (1965).
6. Leontovich M.A., JETP, 5, 3÷4, 211 (1935).
7. Zmievskaya G.I., Pyarnpuu A.A., Shematovich V.I., Preprint IPM N 116, M.(1980); DAN USSR, 248, N 3, 561 (1979); DAN USSR, 258, N 4, 815 (1981); DAN USSR, 266, N 3, 573 (1982).

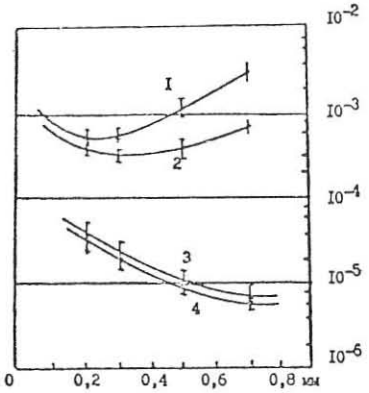

Fig.1

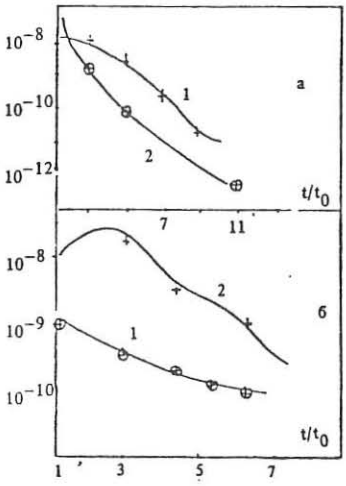

Fig.2

First Author Index

Full Author Index